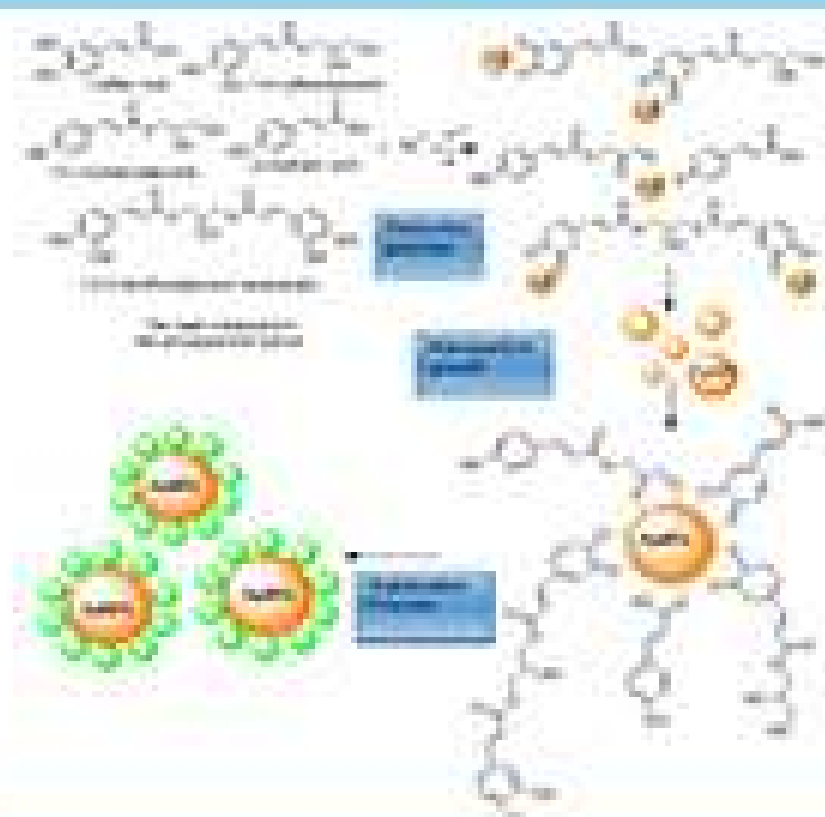


# Indonesian Journal of Chemistry

Vol. 21, No. 3, June 2021



Approved by the Indonesian  
Ministry of Education

## Enhancement of Cobalt Concentration Supported on Mesoporous Silica towards the Characteristics and Activities of Catalysts for the Conversion of Waste Coconut Oil into Gasoline and Diesel Oil

Wega Trisunaryanti\*, Triyono, Nugroho Raka Santoso, Savitri Larasati, Cahyarani Paramesti, and Dyah Ayu Fatmawati\*\*

Department of Chemistry, Faculty of Mathematics and Natural Sciences, Universitas Gadjah Mada, Sekip Utara, Yogyakarta 55281, Indonesia

\* **Corresponding author:**

email: [wegats@ugm.ac.id](mailto:wegats@ugm.ac.id);

[dyah.ayu.fatmawati@mail.ugm.ac.id](mailto:dyah.ayu.fatmawati@mail.ugm.ac.id)\*\*

Received: April 23, 2020

Accepted: July 11, 2020

DOI: 10.22146/ijc.55633

**Abstract:** The analysis of the effect of cobalt concentration supported on mesoporous silica (MS) has been evaluated. This study was aimed to observe the physical and chemical characteristics of the catalysts, and also to study the catalytic activity and its selectivity towards gasoline and diesel oil products in the hydrocracking process of waste coconut oil. The MS was produced using Lapindo mud, where the CTAB was used as the mesopore templating agent. The Co/MS catalyst was prepared by the wet impregnation method with various concentrations of Co. The characterization of the catalyst includes silica purity test by XRF, determination of Co content by AAS, the crystallinity by XRD, the catalyst porosity by SAA, physical pore structure by SEM and TEM, and total acidity by the gravimetric method using  $\text{NH}_3$  base vapor adsorption. The hydrocracking was carried out in a hydrocracking reactor using various concentrations of Co/MS catalysts with the ratio of catalyst/feed = 1/50. The products of the hydrocracking process were liquid, coke, and gas. The composition of the hydrocracking liquid products was analyzed by GC-MS. Based on the results of the catalytic activity test, it was concluded that the Co(1)/MS catalyst, which had the highest acidity, showed the best catalyst selectivity towards gasoline and diesel fractions.

**Keywords:** cobalt; CTAB; hydrocracking; Lapindo mud; mesoporous silica; waste coconut oil

### ■ INTRODUCTION

In the 21<sup>st</sup> century, many issues concerning energy sustainability, environmental problems, and rising fuel prices have been surfacing. Conventional fuels are known for polluting the air due to emissions of sulfur dioxides, carbon dioxides, particulate matter, and other gases [1]. Due to worldwide environmental concern and the increasing fuel demand, conventional energy sources are being steadily substituted by available renewable sources of liquid fuels such as biofuels, alcohol, and vegetable oil. The transformation of vegetable oil to biofuel offers environmental benefits since they are renewable, readily available, have low sulfur and aromatics, and are biodegradable. Similar to fossil fuels derived from petroleum, vegetable oil can be thermochemically converted to

biofuels such as unfinished gasoline, kerosene, and biodiesel [2].

However, the cost of feedstock and limited availability of edible vegetable oils are critical issues for biofuel production. The exploit of Waste Cooking Oil (WCO) as biofuel feedstock reduces the cost of biofuel production since the feedstock costs constitute approximately 70–95% of the overall cost of biofuel production [3]. There are several conversion methods of vegetable oils into biofuels, such as thermal cracking, catalytic cracking, and hydrocracking [4-6].

Thermal cracking, a conversion technique of vegetable oil to biofuel, is performed under conditions of high temperature and high pressure of hydrogen in the absence of a catalyst. These conditions cause the cost

of thermal cracking to be relatively high. Moreover, a large amount of gas and naphtha produced during the process is of relatively low quality due to over cracking [7]. Alternatively, the catalytic cracking process in the absence of high pressure of hydrogen increases a significant amount of desirable olefinic and aromatic compounds in the biofuels, and coke depositing on the catalyst. Hydrocracking is the combination of catalytic cracking and hydrogenation process. Properties of the hydrocracking products, i.e., gasoline or kerosene, showed improved oxidation stability and higher cetane numbers [8]. Hydrocracking reaction progress through a dual functional mechanism that requires two different types of catalytic sites. These sites are the acidic support that promotes cracking and isomerization and also the metallic sites that promote dehydrogenation, hydrogenation, and undesirable hydrogenolysis. In order to synthesize an optimal hydrocracking catalyst, a suitable balance between acid and metal site density has to be maintained [9].

Research on mesoporous material has been highly developed due to its superiority in various applications such as catalysts, adsorbents, and others. Mesoporous structure has large surface area sizes allowing for large-scale diffusion and adsorption of molecules in various applications [10]. The main components in the formation of mesoporous materials can be in the form of silica, alumina, and carbon. One of the basic components favored compared to others is silica because it is thermally stable, non-hazardous, and cheap [11]. Silica can be found in natural materials including the Lapindo mud in Sidoarjo, East Java, Indonesia. Lapindo mud can be used as the main potential source in the synthesis of mesoporous material due to high silica content (> 47%) [12].

One important factor in mesoporous material synthesis is the selection of templates. The main requirement for a template is to have an amphiphilic character and mesoporous-forming properties [13]. Commonly used types of mesoporous templates are cationic and neutral surfactants. A cationic surfactant such as CTAB (Cetyl Trimethyl Ammonium Bromide) is often used in MCM-41 synthesis [14-15].

MS contains pure silica material that only has a weak Lewis acid site content and has no Brønsted acid site,

making it difficult to be used directly as a catalyst and adsorbent. The Lewis acid site will increase if a transition metal is included in the MS structure. Improving the dispersion of the metal nanoparticles can increase the activity of the catalyst. The stability of the catalyst depends on the dispersion of the metal and the interaction between the metallic phase and the support [16-17]. The metals that are usually used in the catalyst are the transition metals such as Co, Ni, Cr, Fe, etc.

In a previous study, cobalt and molybdenum metal were used as the catalyst support on mesoporous silica-alumina (MSA) and showed that the cobalt supported catalyst had the highest liquid conversion of  $\alpha$ -cellulose oil pyrolysis compared to molybdenum in the hydrocracking process [18]. The nature and the dispersion of cobalt are the key factors in determining the activity and the selectivity of the supported catalyst.

The current research studies the synthesis of cobalt metal supported mesoporous silica catalyst using various concentrations of cobalt and also its application for the conversion of waste coconut oil. The correlation of the catalyst characteristics to its activity and selectivity is also reported.

## ■ EXPERIMENTAL SECTION

### Materials

Materials used in this research were Lapindo mud, hydrochloric acid (HCl, Fluka 37% p.a), sodium hydroxide (NaOH, Merck p.a), cetyltrimethylammonium bromide (CTAB), cobalt(II) nitrate hexahydrate ( $\text{Co}(\text{NO}_3)_2 \cdot 6\text{H}_2\text{O}$ ), silver nitrate ( $\text{AgNO}_3$ ), ammonia solution ( $\text{NH}_3$  sol 25%),  $\text{N}_2$  gas,  $\text{H}_2$  gas, demineralized water, Whatman filter paper No. 42 and 41, universal pH indicator strips (Merck), and waste coconut oil.

### Instrumentation

The purity of synthesized silica and the chemical content of the Lapindo mud were analyzed by X-ray Fluorescence (XRF, Analytical MiniPal 4). X-ray Diffractometer (XRD, Philips X-pert Powder Diffractometer) was used to observe the crystallinity of the catalysts. The amount of metal content of all samples was determined using Atomic Absorption Spectroscopy

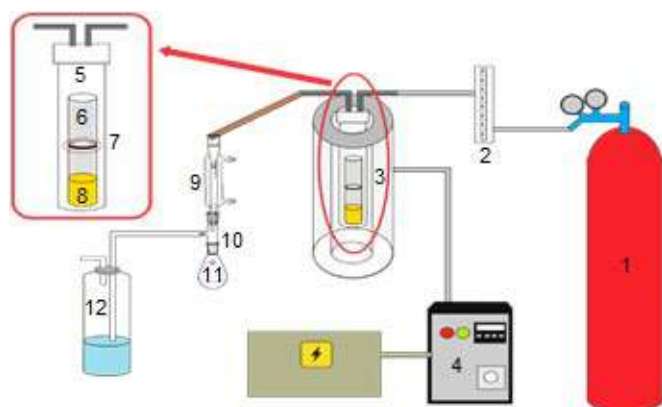


**Fig 1.** Schematic illustration of the hydrocracking reactor (1) gas tank, (2) flow meter, (3) reactor, (4) thermocouple, (5) feed vessel, (6) catalyst vessel, (7) iron gauze 200 mesh, (8) oil feed vessel, (9) Liebig condenser, (10) connector, (11) hearth flask, (12) gas trapper

(AAS, Perkin Elmer 3110). The surface parameters (surface area, pore-volume, and pore diameter) of the samples were analyzed using the Surface Area Analyzer (SAA, St 2 on NOVA touch 4LX). The surface morphology of the catalyst was analyzed using a Scanning Electron Microscope (SEM, JMS-6510LA). The pore images were taken using a Transmission Electron Microscope (TEM, JEM-1400). The liquid products obtained from hydrocracking of waste coconut oil were analyzed using Gas Chromatography-Mass Spectrophotometer (GC-MS, Shimadzu QP2010S).

## Procedure

### Silica extraction from Lapindo mud

Based on our XRF result, the Lapindo mud contained 45.49% of  $\text{SiO}_2$ , 17.24% of  $\text{Al}_2\text{O}_3$ , 8.19% of  $\text{Fe}_2\text{O}_3$ , and 29.08% of other compounds. The Lapindo mud was cleaned and washed with demineralized water and then dried. Afterwards, the Lapindo mud was sieved up to 100 mesh. Later, 100 g of Lapindo mud was refluxed with 400 mL of 6 M HCl (90 °C, 5 h). Afterwards, the sample was filtered and washed by demineralized water until it was free from Cl. The filtrate was dried at 100 °C for 24 h. The residue was then refluxed with 400 mL of 6 M NaOH (90 °C, 5 h). The refluxed mud was then filtered using Whatman 42, and the  $\text{Na}_2\text{SiO}_3$  solution was obtained. After that,  $\text{Na}_2\text{SiO}_3$  solution was added with 3 M HCl (until the

pH reaches 8) and was settled overnight until the white gel formed. The white gel that was formed was then filtered and dried at 100 °C overnight. The extracted silica was characterized by XRF and XRD.

### Synthesis of mesoporous silica (MS)

The ratio of silica/CTAB used in this research was ~2. Three point nine hundred and seventy five grams of CTAB was diluted in 65 mL demineralized water at 40 °C (under stirring). Meanwhile, 7.5 g of synthesized silica was diluted in 200 mL of 1.5 M NaOH, forming the  $\text{Na}_2\text{SiO}_3$  solution. The  $\text{Na}_2\text{SiO}_3$  solution was dropped carefully to the CTAB solution until it was homogenous. Afterwards, 3 M HCl was added to the solution until the pH became 10 and then the solution was settled for 4 h. After that, the solution was put in the autoclave (100 °C, 24 h). The white solids were then washed using demineralized water until the pH became neutral, then dried at 80 °C for 24 h. The formed solids were calcined at 550 °C for 5 h (10 °C  $\text{min}^{-1}$ ). The mesoporous silica was analyzed using XRD, AAS, and SAA.

### Preparation of Co/MS via wet-impregnation

Co/MS catalysts were prepared by impregnation method. An aqueous solution containing 0.00494 g of  $\text{Co}(\text{NO}_3)_2 \cdot 6\text{H}_2\text{O}$  was mixed with 0.5 g of MS in a beaker glass for a ratio of 1 wt.%. The solution was stirred until homogenous and kept overnight. The Co concentration was varied at 1, 3, and 5 wt.% towards the MS, which were subsequently mentioned as Co(1)/MS, Co(2)/MS, and Co(3)/MS. The solution was evaporated and dried by using an oven at 100 °C overnight. The dried mixture was then calcined with flowing  $\text{N}_2$  gas at flow rate of 20 mL  $\text{min}^{-1}$ , and temperature of 500 °C for 2 h. After that, the reduction process was conducted under  $\text{H}_2$  gas at flow rate of 20 mL  $\text{min}^{-1}$  for 3 h to remove oxygen from the Co/MS. The produced catalysts were analyzed using XRD, AAS, and SAA.

The acidity of the catalysts was tested by the gravimetric method using  $\text{NH}_3$  gas as the basic adsorbate. Point zero five grams of catalyst was placed in a porcelain crucible and put into a desiccator. The desiccator was vacuumed and flowed with  $\text{NH}_3$  vapor for 24 h. After that, the sample was taken out from the

desiccator and weighed as porcelain crucible with sample after adsorption. The acidity of the catalyst was determined using the following Eq. (1).

$$\text{Acidity}(\text{mmole/g}) = \frac{W_2 - W_1}{(W_1 - W_0) \times \text{MW NH}_3} \times 1000 \quad (1)$$

where,  $W_0$  = weight of empty porcelain crucible (g);  $W_1$  = weight of porcelain crucible + sample before adsorption (g);  $W_2$  = weight of porcelain crucible + sample after adsorption (g); and MW = molecular weight of  $\text{NH}_3$  ( $\text{g mol}^{-1}$ )

### Catalytic activity test

The weight ratio of catalyst/waste coconut oil that was used to test the catalytic activity was 1:50 (1 g of catalyst; 50 g of feed). The feed and catalyst were put in a container, and then the container was put into the conversion reactor. Afterwards, the sample was heated at  $450^\circ\text{C}$  with increasing temperature of  $10^\circ\text{C min}^{-1}$  and  $\text{H}_2$  gas with a flow rate of  $15 \text{ mL min}^{-1}$  inside the flask. The schematic illustration of the hydrocracking reactor is shown in Fig. 1. The result of the cracking process was then determined as its liquid conversion percentage (%) using Eq. (2).

$$\begin{aligned} \text{Liquid Product (\%)} &= \frac{M_c}{M_u} \times 100\% \\ \text{Coke Formation (\%)} &= \frac{M_k}{M_u} \times 100\% \\ \text{Residue Formation (\%)} &= \frac{M_r}{M_u} \times 100\% \\ \text{Gas Product (\%)} &= \frac{M_u - (M_c + M_k)}{M_u} \times 100\% \\ \text{Total Conversion (\%)} &= \frac{M_u - M_r}{M_u} \times 100\% \end{aligned} \quad (2)$$

where,  $M_c$  = liquid product mass (g);  $M_k$  = coke mass (g);  $M_r$  = residue mass (g); and  $M_u$  = mass of waste coconut oil (g)

The hydrocracking products were analyzed by GC-MS to determine the compound content in the liquid. The chromatogram result from the analysis of liquid product represented as the relative percentage for each compound contained in the liquid product. The selectivity percentage of the gasoline and diesel fraction on liquid oil waste product was determined using Eq. (3).

$$\begin{aligned} \text{Gasoline Fraction (\%)} &= \frac{R_a}{R_x} \times R_t(\%) \\ \text{Diesel Fraction (\%)} &= \frac{R_b}{R_x} \times R_t(\%) \\ \text{Organic Liquid Product} &= R_t(\%) - (\text{GF} + \text{DF}) \end{aligned} \quad (3)$$

where,  $R_a$  =  $\text{C}_5$ - $\text{C}_{12}$  GC area (%);  $R_b$  =  $\text{C}_{13}$ - $\text{C}_{17}$  GC area (%);  $R_x$  = Total relative (%);  $R_t$  = Liquid product conversion (%); GF = Gasoline Fraction; and DF = Diesel Fraction

## RESULTS AND DISCUSSION

### Silica Extraction

Based on the XRF analysis results, silica was proven to be the main component in the sample with an average content of 96.9%, which indicates that the silica extracted from the Lapindo mud has high purity. This result was also supported by the XRD data as shown in Fig. 2, which shows the amorphous silica phase in the range of  $15^\circ < 2\theta < 30^\circ$ . However the purity of the silica does not reach 100% due to the presence of impurities such as iron oxide (0.15%) and other compounds (2.99%). One hundred percent purity is very difficult to obtain from the extraction process; even more so, if the silica source comes from nature.

### Catalysts Characterization

The XRD pattern of MS, Co(1)/MS, Co(2)/MS, and Co(3)/MS are shown in Fig. 3. As expected, mesoporous silica did not show any sharp diffraction peaks consistent with the amorphous structure of the support. The broad peak at  $15^\circ < 2\theta < 30^\circ$  was observed for all catalysts, corresponding to the amorphous silica phase. The broad peak intensity of Co(1)/MS, Co(2)/MS, and Co(3)/MS decreased with increasing cobalt concentration [19]. This

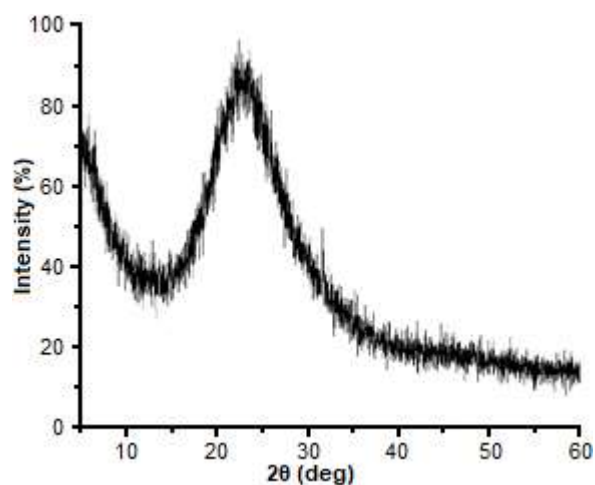
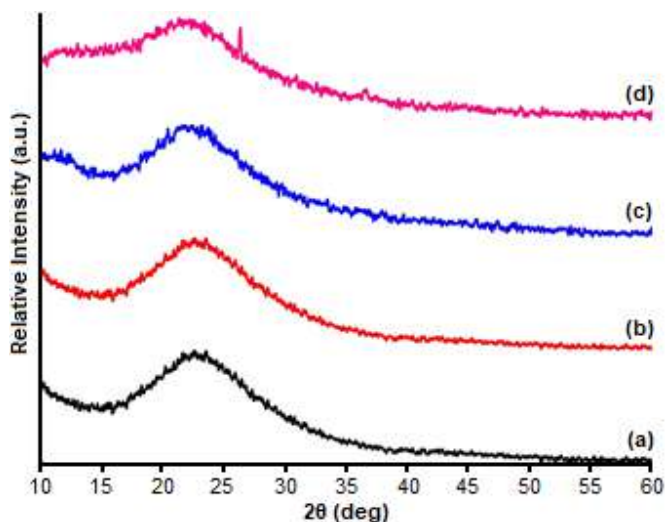


Fig 2. Wide-angle XRD of extracted silica



**Fig 3.** Wide-angle XRD pattern obtained from (a) MS, (b) Co(1)/MS, (c) Co(2)/MS, (d) Co(3)/MS

indicates that the impregnation of metal slightly reduced the amorphous area. This is because the surface of the mesoporous silica is attended by new species that should give rise to new crystalline peaks. However, there was not much metal in material, so this effect does not appear.

As seen in Fig. 3, Co(1)/MS, Co(2)/MS, and Co(3)/MS do not display significant peak of cobalt diffraction pattern, unlike high cobalt loaded catalysts. This can be attributed to the low content of cobalt metal species. Although the presence of cobalt metal in MS could not be proven in XRD analysis, the AAS analysis showed that there was cobalt metal content carried in MS.

The N<sub>2</sub> adsorption-desorption isotherm of MS and cobalt supported-catalysts are shown in Fig. 4. The isotherm of MS in Fig. 4(a) exhibits a type IV isotherm with H4 hysteresis according to the IUPAC classification. After loading of cobalt, the isotherm shades of the catalyst with different cobalt content were relatively similar to MS. This shows that the impregnation of cobalt did not give significant changes in the mesoporous structure of the catalyst. The hysteresis type of the cobalt supported catalysts were considered as the H4 type, which showed relatively uniform wormhole-like pores [20] as seen in the TEM image that will be displayed later.

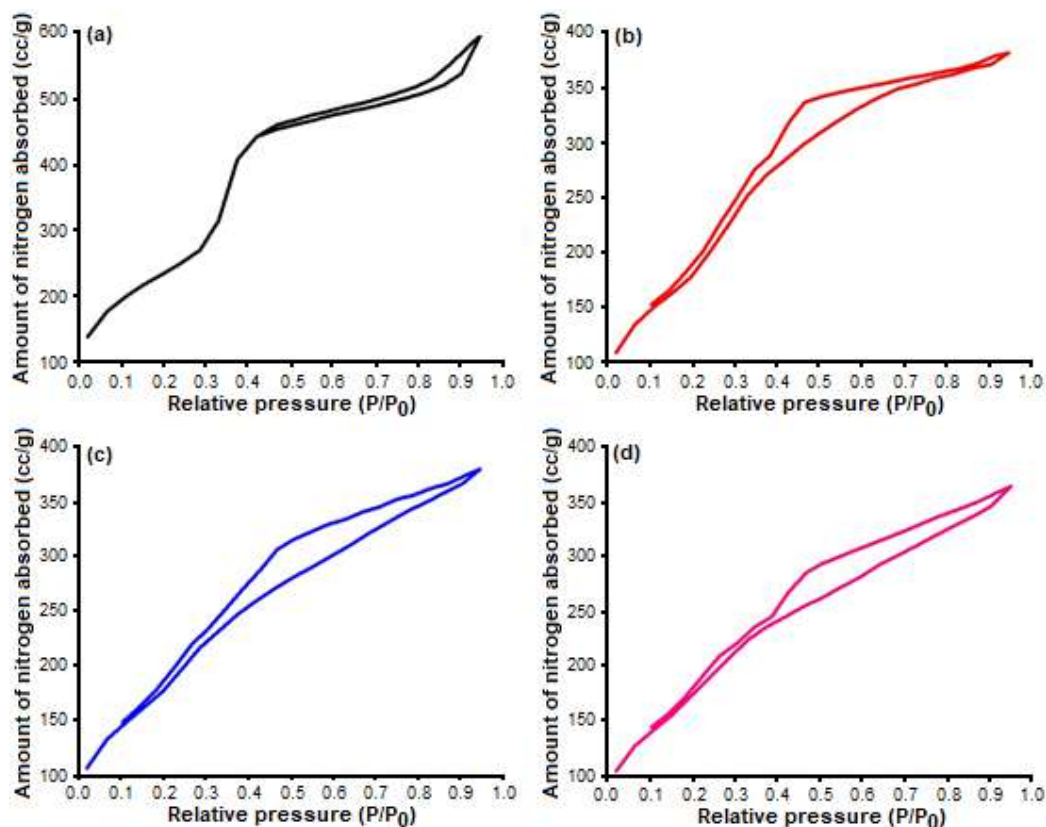


**Fig 4.** N<sub>2</sub> gas adsorption-desorption isotherm of (a) MS, (b) Co(1)/MS, (c) Co(2)/MS, and (d) Co(3)/MS

In this study, capillary condensation of Co(1)/MS, Co(2)/MS, and Co(3)/MS were shifted to lower relative pressure with a shoulder on the desorption branch. The presence of the shoulder on the desorption branch of the cobalt supported catalysts in Fig. 4(b), (c), and (d) at relative pressure ( $P/P_0$ ) of around 0.45, can be attributed to partial pore blockage due to the presence of the metal cobalt species in the aperture of the pores that cause a decrease in the specific surface area. This is known as the cavitation phenomenon.

Pore distribution of porous materials was calculated using the BJH method. In this research, the BJH method was used to calculate the pore distributions from the experimental isotherm using the Kelvin mode of pore filling. This method can be applied to the mesopore and all macropore size range. The size of the pore distribution peak indicates the pore size average. The narrow pore distribution peak means that the pore size is homogenous.

As seen in Fig. 5, MS has the narrowest peak among the other catalysts. This indicates that MS has the most homogenous pore size. Meanwhile, the peak distribution of the impregnated MS shows a less narrow peak, which means that the impregnated MS has less homogenous pore distribution compared to MS. The impregnation of cobalt metal into MS does affect the homogeneity of the pore distribution, which can be seen from the peak of Co(1)/MS, Co(2)/MS, and Co(3)/MS, in which the peak intensity continually decreased. All of the cobalt supported catalysts showed unimodal pore distribution, where it still increases at the smaller pore size. This suggests that there may be partial pore blockage or deposition of cobalt particles against the internal silica walls and/or at the pore apertures. This is also proven by the decrease of total pore volume, where the total pore volume of MS > Co(1)/MS > Co(2)/MS > Co(3)/MS as shown in Table 1. Although their pore size distributions

differ in homogeneity, the average pore size obtained by all catalysts was relatively similar to each other so their ability to absorb molecules contained in the substrate was also relatively similar.

The actual metal content of the impregnated MS that had been determined using AAS were slightly different from the loaded amount. This can happen possibly because some of the metal was left on the glassware that was used in the impregnation process, or it can also be caused by the uneven dispersion of the metal that caused unevenly distributed metal on the surface of the catalyst.

The addition of metal can give support to the acid sites in the catalyst system through the Lewis acid site. The cobalt metal contained in the catalyst sample can affect the acidity of the catalyst considering the empty 4p orbital that acts as the Lewis acid site. The acidity of the catalyst with higher metal content should also be higher. All data show a relationship between the loaded metal and the acidity of the catalyst, but there is an anomaly in this study. The Co(1)/MS had the highest acidity value

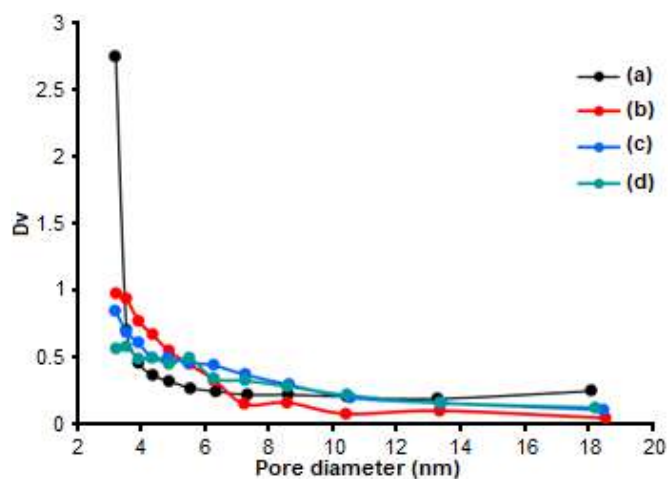


**Fig 5.** Pore size distribution (BJH desorption) of (a) MS, (b) Co(1)/MS, (c) Co(2)/MS, and (d) Co(3)/MS

**Table 1.** Summary of the textural properties of the catalysts

Catalyst samples	Total pore volume (cc/g)	Average pore diameter (nm)	BJH surface area ( $\text{m}^2 \text{g}^{-1}$ )	Cobalt content (%)	Acidity ( $\text{mmol g}^{-1}$ )
MS	0.93	3.28	291	0.00	13.24
Co(1)/MS	0.60	3.27	233	0.95	17.94
Co(2)/MS	0.59	3.28	224	1.39	13.91
Co(3)/MS	0.57	3.28	192	5.26	15.36

because the  $\text{NH}_3$  gases was completely absorbed on the surface of the catalyst where the metals were well dispersed, while for Co(2)/MS and Co(3)/MS, the  $\text{NH}_3$  gases were not completely adsorbed by the metal, possibly due to agglomeration or the pore blocking of the metal. As seen in Table 1, the order of acidity is Co(1)/MS > Co(3)/MS > Co(2)/MS > MS. It was predicted that the hydrocarbon product would follow the acidity content of the catalyst because acidic sites have a function to help the cracking process of large molecules into smaller molecules.

The morphology and the orderliness of MS and Co(1)/MS were analyzed using SEM. As seen in Fig. 6, the MS pores are shaped like slit-like pores. The SEM image of MS also shows that it consists of aggregates of uniform sphere-like particles but not too ordered. The pores formation on MS material was affected by the micelle shape from the CTAB templates that were used. The

synthesized MS material only showed the slit-like pores that were affected by the calcination process and did not fully degrade the CTAB template, leaving the remaining CTAB molecules in the MS. Furthermore, the SEM image of Co(1)/MS does not show any significant changes. However, it can be seen that the pores of the catalyst were slightly reduced, indicating that the cobalt metals were filling the pores of the catalyst.

Fig. 7 shows TEM images of Co(1)/MS before and after the hydrocracking process. The TEM result indicated that before hydrocracking, Co(1)/MS had a wormhole-like pore structure. This result was similar to the TEM images of Co/MS that were synthesized in previous work [18]. Meanwhile, the TEM image of Co(1)/MS after hydrocracking (coke) showed that there were no pores, indicating that the pores of the Co(1)/MS were blocked by the carbon that were trapped inside the pores.

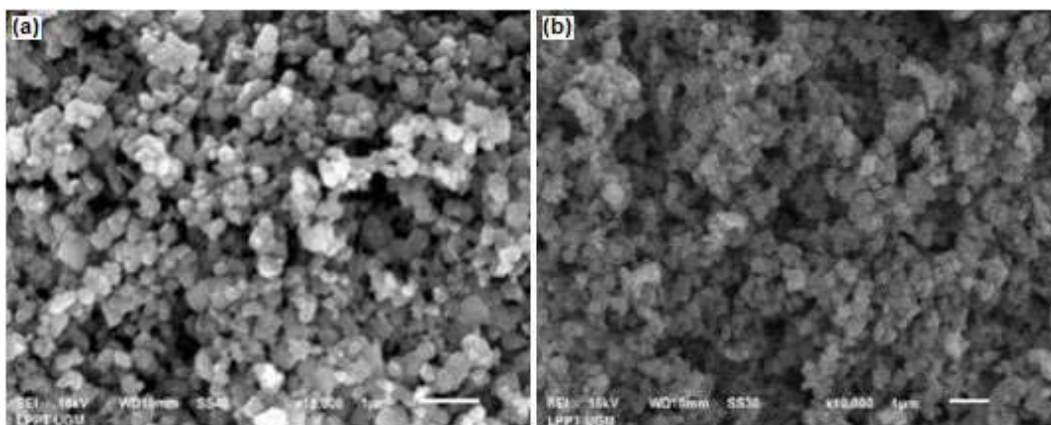


**Fig 6.** SEM images of (a) MS with 15,000× magnification and (b) Co(1)/MS with 10,000× magnifications

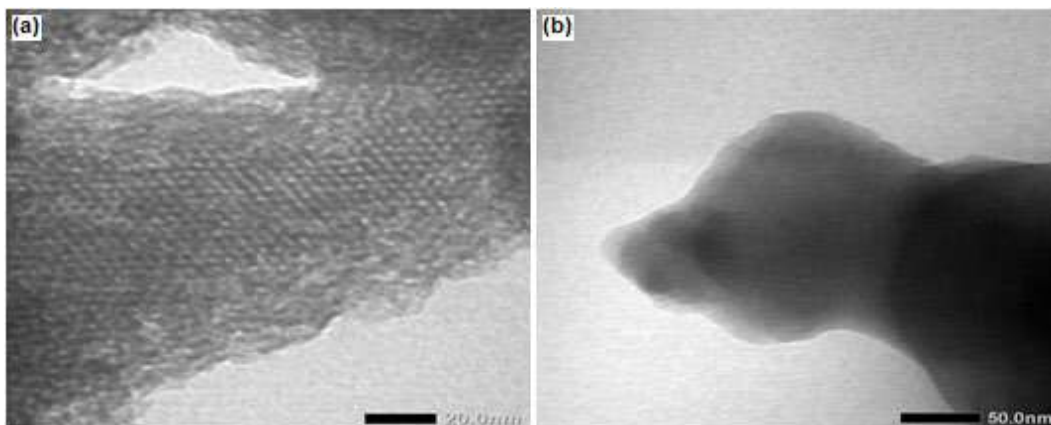


**Fig 7.** TEM images of Co(1)/MS (a) before and (b) after hydrocracking



### Catalytic activity and selectivity test

Waste coconut oil is a hydrocarbon compound with the carbon chain of  $\leq C_{18}$  that needs a catalyst with good catalytic activity in the cracking treatment. The cracking process in the current study was conducted using a fixed bed reactor with a temperature of 450 °C. As seen in Table 2, the hydrocracking process produced three phases of product, namely liquid, gas, and coke fraction, along with leftover residues.

The results show that the order of the amount of liquid product is Co(2)/MS > Co(3) > Co(1)/MS. This order follows the number of metal sites entrusted to MS. The more metals are loaded, the more d orbitals containing one electron are used as the electron place of hydrogen gas. This state facilitates the hydrogenation process.

It can be seen in Table 2 that higher amounts of metal impregnated to the MS relatively improves the conversion of the liquid product, except for the Co(3)/MS catalyst. The Co(2)/MS catalyst gave the highest conversion of the liquid product among the other catalysts because it had the optimal metal content in the catalyst. Meanwhile, the Co(3)/MS, which had the highest cobalt content, did not give the highest conversion of liquid product. This could happen possibly because the cobalt in the Co(3)/MS dispersed in the inner surface of the MS, and the feed was not able to reach every metal inside the pores of the MS due to blocking from other metals in the same pore. Another possibility is the occurrence of sintering of the metals embedded in MS

because of high hydrogen gas pressure. The liquid product from the hydrocracking process was analyzed by GC-MS to determine the compounds that were produced from the hydrocracking process of the waste coconut oil. The content of gasoline ( $C_5$ - $C_{12}$ ), diesel ( $C_{13}$ - $C_{17}$ ), and organic compound fractions contained in the liquid product of the hydrocracking process could be obtained from the peak area percentage of the GC-MS analysis result.

As seen in Table 3, it can be observed that the order of the total hydrocarbon products (gasoline and diesel fractions) is Co(1)/MS > Co(3)/MS > Co(2)/MS. This is based on the acidity value of the catalyst. The higher the acidity value, the easier the cracking process of the molecules [21]. The total of both gasoline and diesel fraction by Co(1)/MS, Co(3)/MS, and Co(2)/MS catalyst were 64.85, 57.18, 56.67 wt.% respectively. Therefore, it can be concluded that the Co(1)/MS catalyst with the highest acidity value had the highest selectivity towards the hydrocarbon fractions (gasoline and diesel).

### ■ CONCLUSION

In this study, the preparation of catalysts via the wet-impregnation method was successfully applied for Co/MS, and the results showed that the impregnation of metals did not significantly change the texture of the catalyst, which agreed with XRD, BET, SEM, and TEM results. The Co(1)/MS catalyst with the lowest Co content of 0.95% and highest acid sites of 17.94 mmol g<sup>-1</sup> showed

**Table 2.** Hydrocracking conversion products of waste coconut oil

Catalyst	Conversion (wt.%)			Residues	Total conversion (wt.%)
	Liquid fraction	Gas fraction	Coke		
Co(1)/MS	75.97	23.79	0.24	0.90	99.10
Co(2)/MS	79.17	20.77	0.06	0.59	99.41
Co(3)/MS	77.20	22.36	0.44	0.52	99.48

**Table 3.** The selectivity of the catalysts on the hydrocracking liquid products

Catalyst	Liquid product fraction selectivity (wt.%)		
	Gasoline fraction	Diesel fraction	Organic liquid product
Co(1)/MS	43.11	21.74	11.12
Co(2)/MS	39.93	16.74	22.49
Co(3)/MS	38.03	19.15	20.02

the best performance resulting in the lowest conversion of liquid product of 75.97%, but the highest total of hydrocarbon product with 43.11% gasoline and 21.74% diesel fractions.

## ■ ACKNOWLEDGMENTS

The author thanks Universitas Gadjah Mada for the financial support under the scheme of the RTA research grant 2019 (Contract Number: 3187/UN1/DITLIT/DIT-LIT/LT/2019).

## ■ REFERENCES

- [1] Raqeeb, M.A., and Bhargavi, R., 2015, Biodiesel production from waste cooking oil, *J. Chem. Pharm. Res.*, 7 (12), 670–681.
- [2] Yotsomnuk, P., and Skolpap, W., 2017, Biofuel production from waste virgin coconut oil by hydrocracking over HZSM-5 zeolite, *Int. J. Adv. Sci. Eng. Technol.*, 5 (2), 54–57.
- [3] Hafriz, R.S.R.M., Salmiaton, A., Yunus, R., and Taufik-Yap, Y.H., 2018, Green biofuel production via catalytic pyrolysis of waste cooking oil using Malaysian dolomite catalyst, *Bull. Chem. React. Eng. Catal.*, 13 (3), 489–501.
- [4] Obidike, L.I., 2016, Biofuel production from waste animal fat using pyrolysis (thermal cracking), *Thesis*, Faculty of Engineering and the Built Environment, University of the Witwatersrand.
- [5] Alvarez-Galvan, M.C., Campos-Martin, J.M., and Fierro, J.L.G., 2019, Transition metal phosphides for the catalytic hydrodeoxygenation of waste oils into green diesel, *Catalysts*, 9 (3), 293.
- [6] Salim, I., Trisunaryanti, W., and Arryanto, Y., 2016, Hydrocracking of coconut oil into gasoline fraction using Ni/modified natural zeolite catalyst, *Int. J. ChemTech Res.*, 9 (4), 492–500.
- [7] Verma, D., Rana, B.S., Kumar, R., Sibi, M.G., and Sinha, A.K., 2015, Diesel and aviation kerosene with desired aromatics from hydroprocessing of jatropha oil over hydrogenation catalysts supported on hierarchical mesoporous SAPO-11, *Appl. Catal., A*, 490, 108–116.
- [8] Liu, C., Liu, J., Zhou, G., Tian, W., and Rong, L., 2013, A cleaner process for hydrocracking of jatropha oil into green diesel, *J. Taiwan Inst. Chem. Eng.*, 44 (2), 221–227.
- [9] Ahmed, S., Ali, S.A., Hamid, H., and Honna, K., 2003, Preparation, characterization, and catalytic evaluation of first stage hydrocracking catalyst, *Stud. Surf. Sci. Catal.*, 145, 295–298.
- [10] Trisunaryanti, W., Falah, I.I., Prihandini, D.R., and Marsuki, M.F., 2019, Synthesis of Ni/mesoporous silica-alumina using Sidoarjo mud and bovine bone gelatin template for hydrocracking of waste lubricant, *Rasayan J. Chem.*, 12 (3), 1523–1529.
- [11] Trisunaryanti, W., Triyono, and Fatmawati, D.A., 2020, Synthesis of Co-NH<sub>2</sub>/mesoporous silica bifunctional catalyst using Sidoarjo mud and bovine bone gelatin template for conversion of used cooking oil into biofuel, *Rasayan J. Chem.*, 13 (1), 723–732.
- [12] Trisunaryanti, W., Triyono, Paramesti, C., Larasati, S., Santoso, N.R., and Fatmawati, D.A., 2020, Synthesis and characterization of Ni-NH<sub>2</sub>/mesoporous silica catalyst from Lapindo mud for hydrocracking of waste cooking oil into biofuel, *Rasayan J. Chem.*, 13 (3), 1386–1393.
- [13] Masykuroh, A., Trisunaryanti, W., Falah, I.I., and Sutarno, 2016, Preparation and characterization of Co and Co-Mo loaded on mesoporous silica for hydrocracking of waste lubricant, *Int. J. ChemTech Res.*, 9 (9), 598–606.
- [14] Triyono, Trisunaryanti, W., Putri, A.D., Lutfiana, A., and Dewi, K., 2018, Transesterification of waste cooking oil using NH<sub>2</sub>/MCM-41 base catalyst: effect of methanol/oil mole ratio and catalyst/oil weight ratio towards conversion of ester, *Asian J. Chem.*, 30 (5), 953–957.
- [15] Meléndez-Ortiz, H.I., Mercado-Silva, A., García-Cerda, L.A., Castruita, G., and Perera-Mercado, Y.A., 2013, Hydrothermal synthesis of mesoporous silica MCM-41 using commercial hydrothermal synthesis of mesoporous silica MCM-41 using commercial sodium silicate, *J. Mex. Chem. Soc.*, 57 (2), 73–79.
- [16] Parapat, R.Y., Saputra, O.H.I., Ang, A.P., Schwarze, M., and Schomäcker, R., 2014, Support effect in the

- preparation of supported metal catalysts via microemulsion, *RSC Adv.*, 4 (92), 50955–50963.
- [17] Prasiwi, A.D., Trisunaryanti, W., Tiyono, Falah, I.I., Santi, D., and Marsuki, M.F., 2019, Synthesis of mesoporous carbon from Merbau wood (*Intsia spp.*) by microwave method as Ni catalyst support for  $\alpha$ -cellulose hydrocracking, *Indones. J. Chem.*, 19 (3), 575–582.
- [18] Marsuki, M.F., Trisunaryanti, W., Falah, I.I., and Wijaya, K., 2018, Synthesis of Co, Mo, Co-Mo and Mo-Co catalysts, supported on mesoporous silica-alumina for hydrocracking of  $\alpha$ -cellulose pyrolysis oil, *Orient. J. Chem.*, 34 (2), 955–962.
- [19] Li, S., Li, X., Wu, H., Sun, X., Gu, F., Zhang, L., He, H., and Li, L., 2019, Mechanism of synergistic effect on electron transfer over Co–Ce/MCM-48 during ozonation of pharmaceuticals in water, *ACS Appl. Mater. Interfaces*, 11 (27), 23957–23971.
- [20] Behniafar, H., Yazdi, M., Farshad, S., and Malekshahinezhad, K., 2016, Poly(4,4'-oxydiphenylene-pyromellitimide) loaded by  $\text{NH}_2$ -functionalized silica: Optical and thermal behavior of new polyimide-based nanocomposites, *High Perform. Polym.*, 28 (10), 1228–1234.
- [21] Trisunaryanti, W., Triyono, Falah, I.I., Siagian, A.D., and Marsuki, M.F., 2018, Synthesis of Ce-mesoporous silica catalyst and its lifetime determination for the hydrocracking of waste lubricant, *Indones. J. Chem.*, 18 (3), 441–447.

## Influence of Calcination Temperature on Size, Morphology and Optical Properties of ZNO/C Composite Synthesized by a Colloidal Method

Siham Lhimr\*, Saidati Bouhlassa, and Bouchaib Ammary

Department of Chemistry, University of Mohammed V Agdal, Rabat, Morocco

\* **Corresponding author:**

tel: +212-676463299

email: siham.lhimr@gmail.com

Received: December 19, 2020

Accepted: March 31, 2021

DOI: 10.22146/ijc.56309

**Abstract:** ZnO is one of the most studied semiconductor materials because of its interesting chemicals, and from a technological point of view, mainly as a consequence of their outstanding properties, such as wurtzite type, non-toxic nature, large band gap, low cost, and environment-friendly. In this work, the ZnO/C composite was synthesized by a simple and fast low-temperature method; the solid product was calcination temperature at 100 to 400 °C. The influence of variation in calcination temperature was studied using X-ray diffraction (XRD), Fourier transforms infrared spectroscopy (FTIR), scanning electron microscopy (SEM), and UV-visible diffuse reflectance spectroscopy. The X-ray diffraction patterns indicated a high crystallinity and a nanocrystalline size of the ZnO/C composite hexagonal structure of wurtzite. The SEM image of the samples showed that the powder has a spherical structure of flakes aggregated in the common nucleus like a grid. The sphere consists of spindle and flower-like structures. The optical properties were determined by UV-vis diffuse reflectance spectroscopy, and it was found that the band gap energy of ZnO/C composite increase from 3.210 to 3.329 eV with an increase in calcination temperature from 100 to 400 °C. FTIR spectra and EDS analysis showed that the existence of carbon in the composite.

**Keywords:** ZnO/C composite; calcination temperature; colloidal method; morphology; optical properties

### ■ INTRODUCTION

Materials based on zinc oxide are the most interesting from a technological point of view, mainly because of their remarkable properties, such as the wide direct band gap of around 3.37 eV, a semiconductor material with a high exciton binding energy of 60 meV at room temperature [1], crystallizes in the typical hexagonal wurtzite structure with lattice parameters  $a = b = 0.325$  nm and  $c = 0.521$  nm [2]. All these properties make them widely applied in several fields, such as light-emitting diodes [3], solar cells [4], photocatalysis [5], and photovoltaic applications [6].

Carbon as a good candidate is used as a host material for composite because of its properties, such as high surface area and conductivity. The combination of ZnO with carbon will result in an intermediate energy level in the band gap of the material and reduce its absorption energy. Previous studies on ZnO/carbon composites have

improved the structural, morphological, vibrational properties and reduce the band gap of broadband semiconductors of ZnO [7]. Osman et al. [8] reported the synthesis of ZnO/C nanocomposite using glucose and observed enhanced visible-light photocatalytic activity. On the other hand, Jayalakshmi et al. [9] described the synthesis of ZnO/C Nanocomposite by the thermal decomposition using dextrose for the application of supercapacitors. There are different synthesis methods used to produce a ZnO/C composite, such as the sol-gel method [10], a hydrothermal method [11], micro-emulsion method [12], thermal decomposition [13], combustion method [14], and microwave-assisted method [15]. The Thermal treatment, for example, calcinations, would remove impurities, and the second chemical phase, used as a capping agent, would give a pure product. In addition, calcinations effectively modify the crystalline phase to obtain a homogeneous one.

Therefore, the combination of the two methods, chemical and thermal, makes it possible to produce nanoparticles of better size and better crystalline phase [16-17]. In this work, we report synthesized the ZnO/C composite using the colloidal method. It is a simple and inexpensive method and does not take much time to prepare the nanoparticles, and citric acid is used as a source of carbon. The aim of this research is The ZnO/C composite was then calcined at different temperatures 100, 300, and 400 °C to study the influence of heat treatment on the morphology and size of the ZnO/C composite. The structural properties, the particle size, the morphological and optical properties of the synthesized ZnO/C composite were characterized by Fourier Transform Infrared spectroscopy (FTIR), X-ray diffraction spectroscopy (XRD), scanning electron microscope (SEM), and UV-visible diffuse reflectance spectroscopy.

## ■ EXPERIMENTAL SECTION

### Materials

Materials used were Zinc nitrate hexahydrate ( $\text{Zn}(\text{NO}_3)_2 \cdot 6\text{H}_2\text{O}$ , Panreac, Espagne), citric acid monohydrate ( $\text{C}_6\text{H}_8\text{O}_7 \cdot \text{H}_2\text{O}$ , Panreac, Espagne), and sodium hydroxide (NaOH, Prolabo, Suisse).

### Instrumentation

The structure and particle size were characterized by X-ray diffraction (XRD) with CuK ( $\lambda = 0.1546 \text{ nm}$ ). The existence of carbon indicated by the infrared absorption spectra was recorded over a range of 4000 to 400  $\text{cm}^{-1}$  on an infrared spectrophotometer with Fourier transform. The morphology and the particle size of the product obtained were analyzed by scanning electron microscopy. The optical property was analyzed by UV-visible diffuse reflectance spectroscopy.

### Procedure

The used procedure was prepared by our previously reported method but modified by calcined at different temperatures for ZnO/C composite [18]. ZnO/C composite was prepared using the colloidal method. First, the Zinc nitrate hexahydrate ( $\text{Zn}(\text{NO}_3)_2 \cdot 6\text{H}_2\text{O}$ ; 0.954 g) and citric acid monohydrate ( $\text{C}_6\text{H}_8\text{O}_7 \cdot \text{H}_2\text{O}$ ; 2.101 g) were fully dissolved in distilled water (10 mL) and stirring at

room temperature for 30 min, Zinc Nitrate Hexahydrate to obtain 0.7 M and 1 M of citric acid.

Secondly, 1.4 M NaOH was directly and rapidly dropped into the first aqueous solutions with a molar ratio ( $r = n_{\text{OH}^-}/n_{\text{Zn}^{2+}} = 6:1$ ) at room temperature. Then the white colloidal was recovered by centrifugation and washed several times with distilled water. Then, the resulting products were placed in an oven at a temperature of 40 °C for 3 days. Finally, the powder obtained by the above process was thermal treatment at a different temperature such as 100, 300, and 400 °C in the air for 1 h.

### Different relations used for measurement of properties

The average size D can be calculated Debye-Scherrer formula [19]:

$$D = \frac{k\lambda}{B \cos \theta} \quad (1)$$

where D is average crystallite size,  $\lambda$  the wavelength of CuK $\alpha$ 1 taken as 0.1546 nm,  $\theta$  is the diffraction angle, and B the width of the peaks (FWHM) in radians.

The lattice parameters (a and c) have been determined by using the following formula [20]:

$$\frac{1}{d^2} = \frac{4}{3} \left( \frac{h^2 + hk + k^2}{a^2} \right) + \frac{l^2}{c^2} \quad (2)$$

Referring to Bragg law, it is possible to rewrite Eq. (2) as follows:

$$\frac{4 \sin^2 \theta}{\lambda^2} = \frac{4}{3} \left( \frac{h^2 + hk + k^2}{a^2} \right) + \frac{l^2}{c^2} \quad (3)$$

The lattice constant 'a' is derived for the plane (100) by the relation (4):

$$a = \frac{\lambda}{\sqrt{3} \sin \theta} \quad (4)$$

The lattice parameter C is calculated for the (002) plane using the following Eq. (5):

$$c = \frac{\lambda}{\sin \theta} \quad (5)$$

where d is lattice spacing, a and c are lattice constants; h, k, l are miller indices,  $\theta$  is the angle of the corresponding peak, and  $\lambda$  is the wavelength of X-ray used (1.5402 Å).

The volume of the unit cell for the hexagonal system has been calculated by using the relation given below (6):

$$V = 0.866 * a^2 * c \quad (6)$$

## RESULTS AND DISCUSSION

### FT-IR Analysis

FT-IR spectra were used to study the composition and structure of the ZnO and ZnO/C sample calcined at different temperatures are shown in Fig. 1. For all samples, the absorption bands in the 3380–3600  $\text{cm}^{-1}$  range can be assigned to the O–H stretching vibrations, and the band about at 1550–1600  $\text{cm}^{-1}$  range is attributed to O–H bending vibration of surface-adsorbed water molecules. The presence of the sharp peak at the 400–460  $\text{cm}^{-1}$  range can be attributed to the vibration of the zinc-oxygen bond. Besides, the absorption signals appeared around 702  $\text{cm}^{-1}$  and were assigned for the Zn–O stretching vibration of pure ZnO nanoparticles [21-22]. The presence of carbonyl groups at 1340  $\text{cm}^{-1}$  came from the citric acid material. Moreover, these absorption peaks are obviously stronger for ZnO/C

composite calcined at 100 °C than the other samples. When the calcination temperature was increased for ZnO/C composite samples to 300 °C, we observed that the peaks began to decrease because the carbon mass loss changed as indicated by EDS. Table 1 shows the type of vibration IR bands for ZnO/C composite at different calcination temperatures.

### X-Ray Analysis

Fig. 2 shows the XRD diffraction patterns of the ZnO pure and ZnO/C composite calcined at 100, 300, and 400 °C for 1 h. All the main diffraction peaks were indexed in the wurtzite structure of ZnO with (JCPDS card No.36-1451). No obvious peaks typical of the crystalline graphitic layers of a carbonaceous material were observed because the carbon species were in the amorphous phase.

As shown in Table 2, the calculated crystallite size,

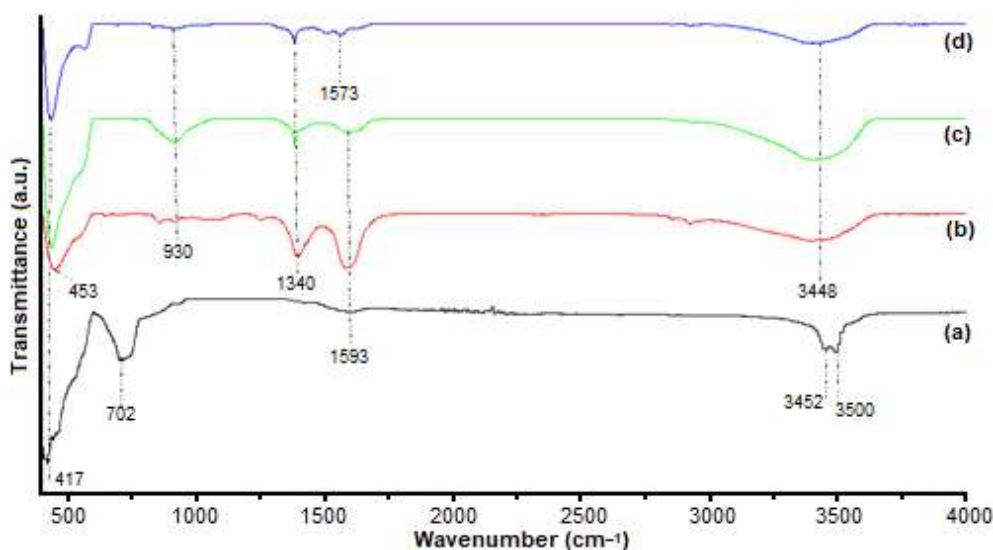


**Fig 1.** FTIR spectra of the synthesized ZnO and ZnO/C composite calcined at different temperatures: (a) pure ZnO (b) ZnO/C at 100 °C, (c) ZnO/C at 300 °C, and (d) ZnO/C at 400 °C

**Table 1.** The type of vibration IR bands for ZnO/C composite at different calcination temperatures

Type of vibration	Wavenumber ( $\text{cm}^{-1}$ )			
	ZnO	ZnO/C at 100 °C	ZnO/C at 300 °C	ZnO/C at 400 °C
assigned to O-H stretching vibrations [23-24]	3500			
	3452	3448	3448	3448
assigned to O-H bending vibrations [25]	1573	1573	1573	1593
assigned to C-O stretching vibrations [26]	-	1340	1340	1340
assigned to Zn-O bending vibration [21-22]	417			
	702	453	417	417

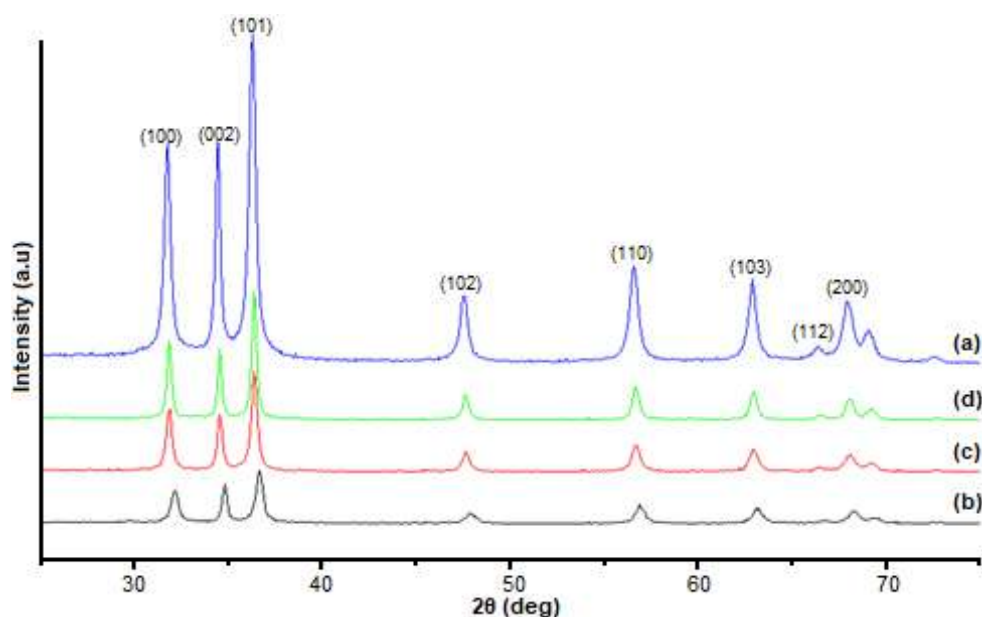


**Fig 2.** XRD spectra of the synthesized ZnO and ZnO/C composite calcined at different temperatures: (a) pure ZnO (b) ZnO/C at 100 °C, (c) ZnO/C at 300 °C, and (d) ZnO/C at 400 °C

**Table 2.** Crystallite sizes, lattice volume, and lattice parameters (a and c) for ZnO and ZnO/C composite calcined at different temperatures

	D (nm)	a (nm)	c (nm)	V (nm <sup>3</sup> )
ZnO pure	32.91	0.3249	0.4969	0.0454
ZnO/C at 100 °C	28.49	0.3210	0.4919	0.0439
ZnO/C at 300 °C	31.25	0.3241	0.4956	0.0451
ZnO/C at 400 °C	31.53	0.3241	0.4957	0.0451

lattice parameters, and unit cell volume of ZnO/C composite are indeed smaller than those of pure ZnO. It was observed that with the increase in calcination temperature from 100 to 400 °C with a gradual increase in crystallite size due to aggregation and also unevenly sized particles of surface atoms at higher temperatures which at higher temperatures above 100 °C reduces content carbon and improved the metal crystallinity [16].

### Scanning Electron Microscope (SEM)

Fig. 3 demonstrates the correspondent morphology and calcined size at different temperature ZnO/C composite samples, as investigated by SEM. Image of ZnO/C composite samples calcined at 100 °C shows the sphere is of flakes (nanosheet) aggregated in the common nucleus like a grid in Fig. 3(a). The particles are about 1 μm in diameter, whereas the ZnO/C composite samples calcined at 300 °C showed the sphere consists of the

spindle in the common nucleus (Fig. 3(b)). These microstructures have an average particle diameter of about 1–2 μm. The samples ZnO/C composite calcined at 400 °C showed well-defined the rods aggregated formed flowers-like with a diameter of 2–3 μm (Fig. 3(c)). These results indicate that the attained particle size increased with increasing calcination temperature. The ZnO nanosheet product gradually started to crumble and overlapped with the increment of calcination temperature from 300 °C. As we know, the high surface area to volume ratio of nano-size particles possesses higher surface energy. Therefore, they tend to agglomerate due to Van der Waals's force to stabilize the surface energy. Besides that, agglomeration often occurs at high temperatures due to the sintering effect in which the particles move closer to each other during the dehydration process [27-28]. From EDS spectra, the amount of C, O,

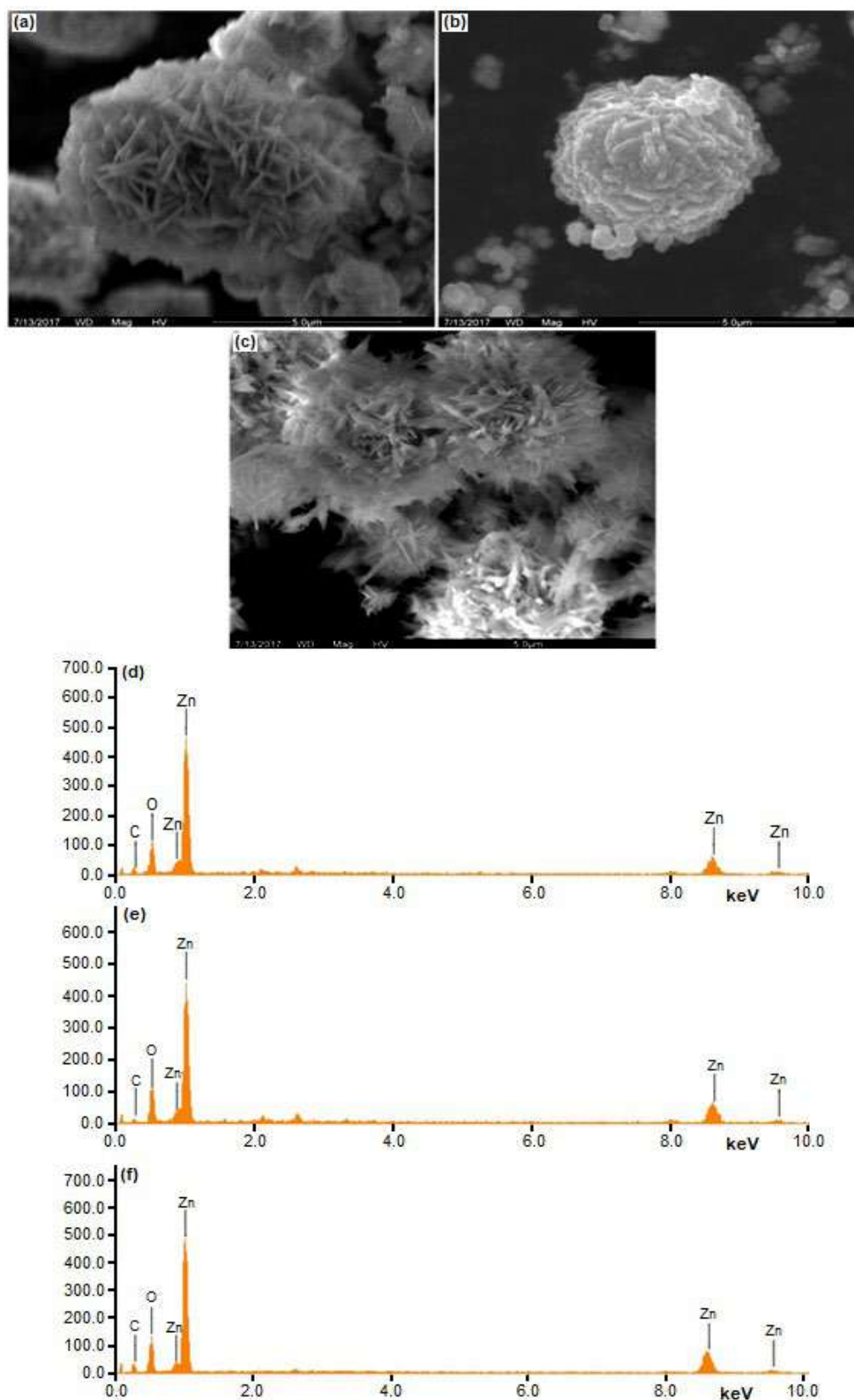


**Fig 3.** SEM images of the synthesized ZnO/C composite calcined: (a) ZnO/C at 100 °C (b) ZnO/C at 300 °C (c) ZnO/C at 400 °C and EDS microanalyses: (d) ZnO/C-100 °C (e) ZnO/C-300 °C (f) ZnO/C-400 °C



**Table 3.** The amount of C present in ZnO calcined at 100, 300, and 400 °C

Temperature of calcination (°C)	C content (%)	O content (%)	Zn content (%)
100	12.97	29.57	57.46
300	10.40	32.45	57.15
400	8.30	32.38	59.32

and Zn present in the sample was estimated as presented in Table 3, the content of carbon in the composite for the ZnO/C-100 °C, ZnO/C-300 °C, and ZnO/C-400 °C are about 12.97 wt.%, 8.30 wt.%, and 8.55 wt.%, respectively. These results reveal that the carbon content of the samples decreases with increasing the temperature of calcination.

### Optical Properties: UV-Vis

The Optical Properties of the ZnO and ZnO/C composite calcined at different temperatures 100, 300, and 400 °C were studied by the UV-visible absorption spectra shown in Fig. 4. Fig. 4 shows display the sharp fundamental absorption in the ultraviolet region with a band gap absorption edge of 350, 354, 362, and 369 nm for ZnO and ZnO/C-100 °C, ZnO/C-300 °C, ZnO/C-400 °C, respectively, which can be assigned to the intrinsic band-gap absorption of ZnO due to the electron transitions from the valance to the conduction band.

The band gap of semiconductors can be calculated by the Kubelka-Munk method [29]. The absorption

coefficient ( $\alpha$ ) versus photon energy ( $h\nu$ ) for the direct band gap semiconductor can be expressed as follows:

$$(\alpha h\nu)^2 = B(h\nu - E_g)^n = f(h\nu) \quad (7)$$

where  $\alpha$  is absorption coefficient,  $A$  the absorption of a sample, and  $t$  is the thickness of the sample,  $B$  is a constant,  $E_g$  the optical band gap,  $h$  is Plank's constant,  $\nu$  is the frequency of the incident photon. The value of  $n = 1/2, 3/2, 2,$  or  $3$  depending on the nature of the electronic transition responsible for absorption and  $n = 1/2$  for direct band gap semiconductor.

The value of the band gap is calculated by extrapolating the straight-line portion of the  $(\alpha h\nu)^2$  versus  $(h\nu)$  axis. The Plot  $(\alpha h\nu)^2$  as a function of the energy  $h\nu$  and extrapolating the linear part of the curve to the zero absorption are shown in Fig. 5.

We can see from Fig. 5 that the energy band gap for ZnO pure is calculated to be 3.385 eV, while the energy band gap of the ZnO/C composite calcined at 100 °C drops down to 3.290 eV, and it can be seen that the  $E_g$

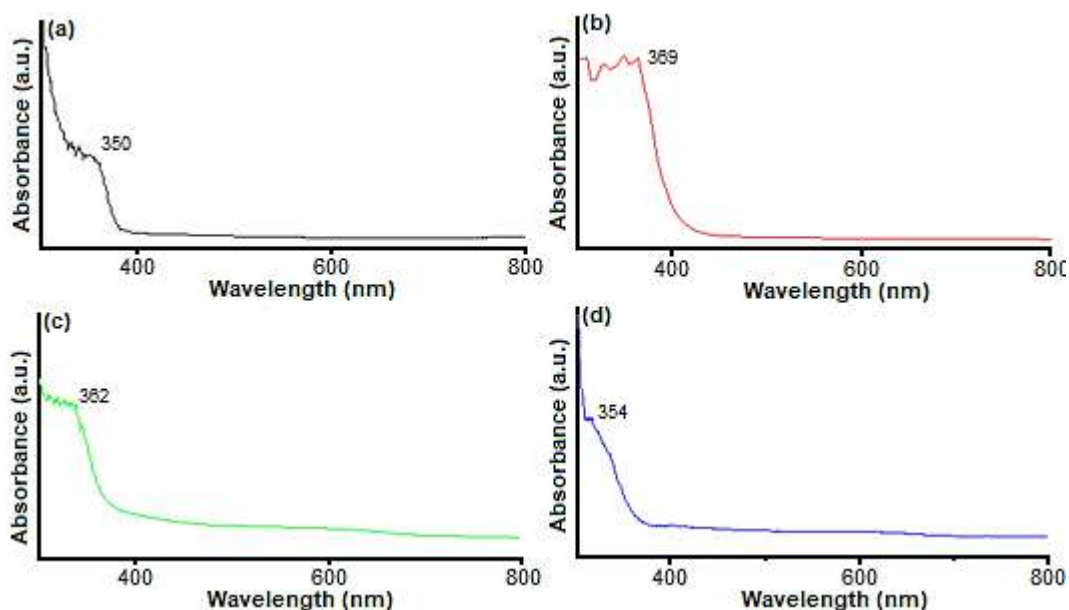


**Fig 4.** UV-visible absorption spectra of ZnO and ZnO/C composite calcined at different temperatures: (a) pure ZnO (b) ZnO/C at 100 °C, (c) ZnO/C at 300 °C, and (d) ZnO/C at 400 °C

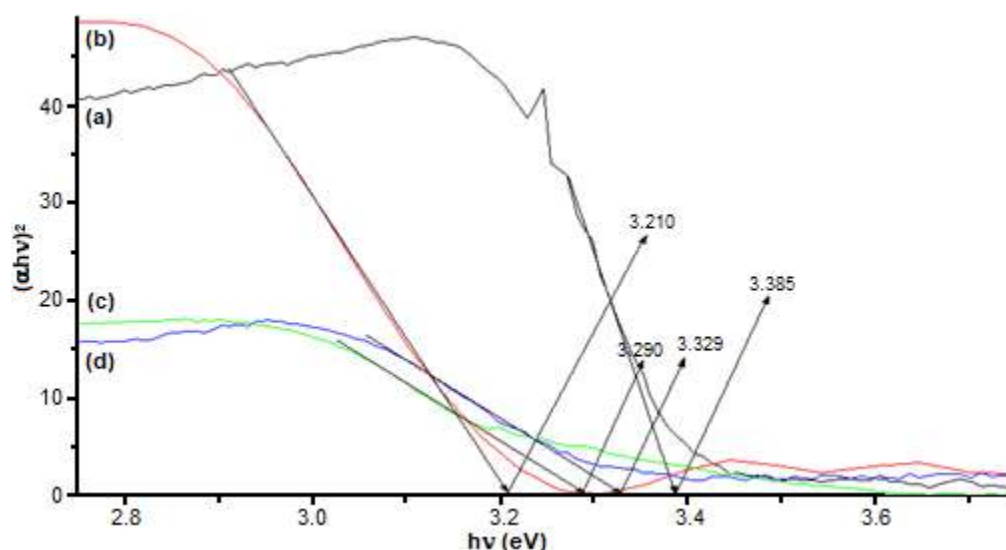


**Fig 5.** Plots of a function of  $h\nu$  for the ZnO and ZnO/C composite calcined at different temperatures: (a) pure ZnO (b) ZnO/C at 100 °C, (c) ZnO/C at 300 °C, and (d) ZnO/C at 400 °C

values of the composites increases as the calcination temperature increased. Accordingly, the existence of carbon-carrying ZnO can enhance the light absorption and widen the ultraviolet region range as described in ZnO/C composites. It is clear that the increase of  $E_g$  is correlated along with the grain size of the material, which increases with temperature calcination (Table 4).

### Comparison of Size and Morphology with Other Literature

The results of ZnO/C composite calcined at different temperatures are compared with those reported in the literature. Table 5 summarizes the morphology, size, optical band gap, and carbon source of the ZnO/C composite calcined at different temperatures and other publications.

### CONCLUSION

In this study, the effect of calcination temperature on the size, morphology, and optical properties of ZnO/C composite synthesis by the colloidal method was reported. The shapes and carbon amount-of-substance fractions of the samples were characterized by SEM, EDS, and FTIR. When the calcination temperature was

**Table 4.** Crystallite size, band gap energy of the ZnO and ZnO/C composite calcined at 100, 300, and 400 °C

Sample	Crystallite Size (nm)	$E_g$ (eV)
Pure ZnO	32.91	3.385
ZnO/C-100 °C	28.49	3.210
ZnO/C-300 °C	31.25	3.290
ZnO/C-400 °C	31.53	3.329

**Table 5.** The morphology, size, optical band gap, and carbon source of the ZnO/C composite and other publications

Method	Carbon source	Calcined temperature (°C)	Size (nm)	$E_g$ (eV)	Morphology	Reference
Colloidal method	Citric acid	100	28.49	3.210	- the sphere is of flakes	This work
		300	31.25	3.290	- the sphere is of spindle	
		400	31.53	3.329	- flowers like	
Sol gel method	sucrose (C <sub>12</sub> H <sub>22</sub> O <sub>11</sub> )	400	27.07	-	Spherical particles	[30]
Thermal decomposition	glucose(C <sub>6</sub> H <sub>12</sub> O <sub>6</sub> )	350	-	3.221	-	[8]
Combustion Synthesis	dextrose	650	-	-	spindle-like shapes	[9]
Assisted pyrolysis	Pluronic F127	500	21.8	2.98	-	[25]

increased, the carbon amount-of-substance fraction of the product also decreased. The XRD patterns of the synthesized ZnO and ZnO/C composite at different calcination temperatures revealed the presence of a single wurtzite ZnO phase. The particle size increased with increases in calcination temperature due to aggregation and unevenly sized particles; at higher temperatures above 100 °C, it reduced content carbon and improved the metal crystallinity. The band gap increases with increasing calcination temperature from 3.210 to 3.329 eV.

### ■ ACKNOWLEDGMENTS

The authors would like to thank the National Center for Scientific and Technical Research (CNRST) of Morocco for putting at our disposal the technical facilities of the UATRS.

### ■ AUTHOR CONTRIBUTIONS

SL conducted the experiment, SL and BA conducted the DFT calculations, SL, SB, and BA wrote and revised the manuscript. All authors agreed to the final version of this manuscript.

### ■ REFERENCES

- [1] Su, Y.K., Peng, S.M., Jie, L.W., Wu, C.Z., Cheng, W.B., and Liu, C.H., 2010, Ultraviolet ZnO nanorod photosensors, *Langmuir*, 26 (1), 603–606.
- [2] Liu, R., Vertegel, A.A., Bohannon, E.W., Sorenson, T.A., and Switzer, J.A., 2001, Epitaxial electrodeposition of zinc oxide nanopillars on single-crystal gold, *Chem. Mater.*, 13 (2), 508–512.
- [3] Fan, X., Zhou, Z., Wang, J., and Tian, K., 2011, Morphology and optical properties of tetrapod-like zinc oxide whiskers synthesized via equilibrium gas expanding method, *Trans. Nonferrous Met. Soc. China*, 21 (9), 2050–2060.
- [4] Baviskar, P., Ennaoui, A., and Sankapal, B., 2014, Influence of processing parameters on chemically grown ZnO films with low cost Eosin-Y dye towards efficient dye sensitized solar cell, *Sol. Energy*, 105, 445–454.
- [5] Tsuzuki, T., He, R., Dodd, A., and Saunders, M., 2019, Challenges in determining the location of dopants, to study the influence of metal doping on the photocatalytic activities of ZnO nanopowders, *Nanomaterials*, 9 (3), 481.
- [6] Gertman, R., Oshero, A., Golan, Y., and Visoly-Fisher, I., 2014, Chemical bath deposited PbS thin films on ZnO nanowires for photovoltaic applications, *Thin Solid Films*, 550, 149–155.
- [7] Lavand, A.B., and Malghe, Y.S., 2015, Visible light photocatalytic degradation of 4-chlorophenol using C/ZnO/CdS nanocomposite, *J. Saudi Chem. Soc.*, 19 (5), 471–478.
- [8] Osman, H., Su, Z., Ma, M., Liu, S., Liu, X., and Abduwayit D., 2016, Synthesis of ZnO/C nanocomposites with enhanced visible light photocatalytic activity, *Ceram. Int.*, 42 (8), 10237–10241.
- [9] Jayalakshmi, M., Palaniappa, M., and Balasubramanian, K., 2008, Single step solution combustion synthesis of ZnO/carbon composite and its electrochemical characterization for supercapacitor application, *Int. J. Electrochem. Sci.*, 3, 96–103.
- [10] Peña-García, R., Guerra, Y., Milani, R., Oliveira, D.M., de Souza, F.R., and Padrón-Hernández, E., 2019, Influence of Ni and Sr on the structural, morphological and optical properties of ZnO synthesized by sol gel, *Opt. Mater.*, 98, 109427.
- [11] Bazazi, S., Arsalani, N., Khataee, A., and Tabrizi, A.G., 2018, Comparison of ball milling-hydrothermal and hydrothermal methods for synthesis of ZnO nanostructures and evaluation of their photocatalytic performance, *J. Ind. Eng. Chem.*, 62, 265–272.
- [12] Rusli, R.A., and Hadi, N., 2017, Synthesis of carbon doped zinc oxide as visible-light driven photocatalyst, *eProceed. Chem.*, 2 (2), 279–282.
- [13] Jagtap, R.M., Kshirsagar, D.R., Khire, V.H., and Pardeshi, S.K., 2019, Facile fabrication of porous La doped ZnO granular nanocrystallites and their catalytic evaluation towards thermal decomposition of ammonium perchlorate, *J. Solid State Chem.*, 276, 194–204.
- [14] Ahmad, M., Ahmed, E., Zafar, F., Khalid, N.R., Niaz, N.A., Hafeez, A., Ikram, M., Khan, M.A., and

- Hong, Z., 2015, Enhanced photocatalytic activity of Ce-doped ZnO nanopowders synthesized by combustion method, *J. Rare Earths*, 33 (3), 255–262.
- [15] Liu, S., Yao, K., Wang, B., and Ma, M.G., 2017, Microwave assisted hydrothermal synthesis of cellulose/ZnO composites and its thermal transformation to ZnO/carbon composites, *Iran. Polym. J.*, 26 (9), 681–691.
- [16] Lee, P.J., Saion, E., Al-Hada, N.M., and Soltani, N., 2015, A simple up-scalable thermal treatment method for synthesis of ZnO nanoparticles, *Metal*, 5 (4), 2383–2392.
- [17] Parra, M.R., and Haque, F.Z., 2014, Aqueous chemical route synthesis and the effect of calcination temperature on the structural and optical properties of ZnO nanoparticles, *J. Mater. Res. Technol.*, 3 (4), 363–369.
- [18] Lhimr, S., Bouhlassa, S., and Ammary, B., 2019, Effect of molar ratio on structural and size of ZnO/C nanocomposite synthesized using a colloidal method at low temperature, *Indones. J. Chem.*, 19 (2), 422–423.
- [19] Ianoş, R., Lazău, I., Păcurariu, C., and Sfirloagă, P., 2011, Aqueous combustion synthesis and characterization of ZnO powders, *Mater. Chem. Phys.*, 129 (3), 881–886.
- [20] Sarfraz, M., Ahmed, N., Haq, K., Shahida, S., and Khan, M.A., 2019, Structural optical and magnetic properties of transition metal doped ZnO magnetic nanoparticles synthesized by sol-gel auto-combustion method, *Mater. Sci.-Pol.*, 37 (2), 280–288.
- [21] Awad, A., Abou-Kandil, A.I., Elsabbagh, I., Elfass, M., Gaafar, M., and Mwafy, E., 2014, Polymer nanocomposites part 1: Structural characterization of zinc oxide nanoparticles synthesized via novel calcination method, *J. Thermoplast. Compos. Mater.*, 28 (9), 1343–1358.
- [22] Kayani, Z.N., Iqbal, M., Riaz, S., Zia, R., and Naseem, S., 2015, Fabrication and properties of zinc oxide thin film prepared by sol-gel dip coating method, *Mater. Sci.-Pol.*, 33 (3), 515–520.
- [23] Puziy, A.M., Poddubnaya, O.I., Martínez-Alonso, A., Suárez-García, F., and Tascón, J.M.D., 2002, Synthetic carbons activated with phosphoric acid: I. Surface chemistry and ion binding properties, *Carbon*, 40 (9), 1493–1505.
- [24] Hasanpour, A., Niyafar, M., Asan, M., and Amighian, J., 2013, Synthesis and characterization of Fe and ZnO nanocomposites by the sol-gel method, *J. Magn. Magn. Mater.*, 334, 41–44.
- [25] Lanfredi, S., Silveira, G.S., Potensa, B.S., and Nobre, M.A.L., 2016, ZnO/Zn/amorphous carbon matrix nanostructured composite powder: A new photocatalyst for dye, *MRS Adv.*, 1 (19), 1327–1332.
- [26] Lanfredi, S., Nobre, M.A.L., Moraes, P.G.P., and Matos, J., 2014, Photodegradation of phenol red on a Ni-doped niobate/carbon composite, *Ceram. Int.*, 40 (7), 9525–9534.
- [27] Al-Hada, N.M., Saion, E., Shaari, A.H., Kamarudin, M.A., and Gene, S.A., 2014, The influence of calcination temperature on the formation of zinc oxide nanoparticles by thermal-treatment, *Appl. Mech. Mater.*, 446-447, 181–184.
- [28] Al-Hada, N.M., Saion, E., Shaari, A.H., Kamarudin, M.A., Flaifel, M.H., Ahmad, S., and Gene, S., 2014, A facile thermal-treatment route to synthesize ZnO nanosheets and effect of calcination temperature, *PLoS One*, 9 (8), e103134.
- [29] Ali, A.A., El Fadaly, E., and Ahmed, I.S., 2018, Near-infrared reflecting blue inorganic nano-pigment base on cobalt aluminate spinel via combustion synthesis method, *Dyes Pigm.*, 158, 451–462.
- [30] Sasirekha, C., Arumugam, S., and Muralidharan, G., 2018, Green synthesis of ZnO/Carbon (ZnO/C) as an electrode material for symmetric supercapacitor devices, *Appl. Surf. Sci.*, 499, 521–527.

## Phytochemical Analysis of Bioactive Extracts and Seed Oil of Three Euphorbia Species from Algerian Flora by LC-MS and GC-MS

Nadia Toudert<sup>1</sup>, Farida Zakkad<sup>2</sup>, Noureddine Dadda<sup>2</sup>, Abdelouaheb Djilani<sup>2</sup>, Amadou Dicko<sup>3</sup>, and Salah Eddine Djilani<sup>2\*</sup>

<sup>1</sup>Laboratory of Physical Chemistry of Materials, El Chadli Ben Djedid University, El Tarf, Algeria

<sup>2</sup>Laboratory of Synthesis and Organic Biocatalysis, Badji Mokhtar University, Annaba, Algeria

<sup>3</sup>Université de Lorraine, UR-AFPA (Unité de Recherche Animal et Fonctionnalité des Produits Animaux), France

\* **Corresponding author:**

tel: +213-552549827

email: djilanisalah2000@yahoo.fr

Received: August 11, 2020

Accepted: March 6, 2021

DOI: 10.22146/ijc.56679

**Abstract:** Euphorbia species possess pharmacological properties that have been widely used for medical purposes worldwide. In this paper, three plants belonging to the Euphorbia genus growing in North-East of Algeria were studied. The phenolic contents were identified using LC-MS, while the fatty acid composition of their fixed oils was determined with GC-MS. The quantification of the total condensed tannins and the leaves' entire anthocyanin content were performed using photometric methods. The main constituents of the polyphenolic compounds identified by LC-MS were ascorbic, chlorogenic, and ellagic acids. The oil yield of the seeds of *E. terracina*, *E. biumbellata*, and *E. dendroides* was 17.48%, 18.5%, and 20.05%, respectively. Quantitative analyses of these oils using GC-MS showed variations in the species' fatty acid constituents' concentrations and compositions. Besides, the phytochemical screening results showed that *E. terracina* possessed a high amount of tannin and anthocyanin content compared with other studied plants.

**Keywords:** Euphorbia; polyphenols; oil; LC-MS; GC-MS

### ■ INTRODUCTION

More attention has been given to plants as a human medicaments source, especially in some developing countries, as plant-derived medicines have made significant contributions to human health and wellbeing [1-3]. Among the natural products found in plants, polyphenols constitute one of the largest classes of the plant's secondary metabolite, which has an important role in preventing and restricting free radicals.

The plant *Euphorbia* belongs to the family Euphorbiaceae that is widespread worldwide and widely present in the tropical region. It is a large family of flowering plants, including 300 genera and over 5000 species [4-5].

The *Euphorbia* species are considered critical medicinal plants used mainly in folk medicine all over the world. In Africa, *Euphorbia* species were used to treat various diseases such as skin disease, migraines,

gonorrhoea, fungal and inflammatory disorders, and sexual transmission [6-7]. In Nepal, the latex of *E. milii* is used to cure sprains [8], while in China, it is used to cure hepatitis [9]. In Pakistan *E. helioscopia* leaves are used to relieve constipation [10]. In India, *E. neriifolia* is known for its medicinal value, such as antibacterial, antifungal, antiviral, and antioxidant [11]. In Nigeria, essential oils from the leaves of *E. milii* are used for insecticidal action [12].

Few previous works are reported on the use of *E. biumbellata*, *E. terracina*, and *E. dendroides* in folk medicine. According to ethnobotanical investigations, it was observed that *E. terracina* leaves have been used as a remedy for paralysis and fever [13]. And *E. dendroides* was used as a fish poison and as a cathartic, while *E. biumbellata* latex has been used to cure warts [4].

Phytochemical studies of *Euphorbia dendroides* exhibited the presence of polyphenols, flavonoids, and

jatropane esters [4], while in previous research studies, *Euphorbia terracina* was found to contain a variety of bioactive chemical compounds such as saponins, tannins [13], triterpenes, flavenoids and coumarins [14].

This research aims to identify the chemical constituents contained in the seeds and leaves of the three Algerian plants: *E. biumbellata*, *E. dendroides*, and *E. terracina*, with LC-MS. An additional goal is to determine the fatty acid composition of oil obtained from their seeds using GC-MS analysis.

## ■ EXPERIMENTAL SECTION

### Materials

*E. biumbellata*, *E. dendroides*, and *E. terracina* were collected from El Kala National Park in the northeast of Algeria in March 2019. The identification was carried out by the botanists of the Biology Department, Badji Mokhtar University. **ph005\_48**, **ph005\_49**, **ph006\_04**, voucher specimens of *E. biumbellata*, *E. dendroides*, and *E. terracina*, respectively, were deposited in the Herbarium of Gérard De Belair.

The plants were cleaned and air-dried in the shade at room temperature for three weeks. The dry seeds and sheets were ground at the mill until they obtain fine homogeneous powders and stored in dark glass flasks to protect them from humidity and light till their use in further analysis.

### Instrumentation

The main apparatus used in the research were rotary evaporator (Buchi R-124), analytical balance, Shimadzu Spectrophotometer UV-1800, gas chromatography-mass spectrometer (GC-MS) (Shimadzu QP-2010S), liquid chromatography-mass spectrometry (Shimadzu LCMS-2020S).

### Procedure

#### Extract preparation

The weighed amount of each part (sheets and seeds) of the samples was extracted in a known volume of the solvent MeOH-H<sub>2</sub>O (70/30: v/v) for 24 h with intermittent shaking. Each extracted material is filtered through Whatman filter paper No.1 and centrifuged at 4000 rpm for 15 min. The supernatant is then stored at

-4 °C for further use in the phytochemical analysis, total anthocyanin contents, determination of antioxidant activity, and LC-MS analysis.

#### Analysis of chemical composition

**Total condensed tannin contents (TCT).** The tannin contents were estimated with the vanillin-HCl method [15] with slight modification, using catechin as a reference compound. In brief, 1 g of dry residue was added to 15 mL of MeOH-HCl (1%) in a test tube. The tube was placed in a water bath at 35 °C for 30 min, centrifuged at 1532 × g, and finally filtered. Aliquots (0.5 mL) of extract were mixed with 3 mL of vanillin-HCl reagent (4% in methanol) in test tubes. After 20 min of incubation at room temperature, the absorbance was read at 500 nm, using a UV-visible spectrophotometer. The estimation of condensed tannins was carried out in triplicate, and the results were expressed as mg catechin equivalent/g of dry matter.

**Total anthocyanin compounds (TAC).** The samples' total anthocyanins compounds were determined using a Vis- spectrophotometer according to the pH-differential method [16]. Two buffer systems, potassium chloride buffer, pH 1.0 (0.025 M), and sodium acetate buffer, pH 4.5 (0.4 M), were used. Absorbance was measured at 520 and 700 nm. TAC Results were expressed as cyanidin-3-glucoside equivalents and calculated using the formula:

$$TA \text{ (mg / g)} = \frac{\Delta A \times MW \times DF \times 1000}{\epsilon \times l}$$

where  $\Delta A$ : difference of absorbance; DF = dilution factor; MW (molecular weight) = 449.2 g/mol;  $l$  = cuvette pathlength in cm;  $\epsilon$  = 26,900 L/mol.cm.

#### Evaluation of total antioxidant capacity by phosphomolybdate (PPM) method.

The total antioxidant capacity assay of plant extract was carried out by the phosphomolybdenum method [17-18]. A 0.1 mL of sample solution was mixed with 1 mL of reagent solution (0.6 M sulfuric acid, 28 mM sodium phosphate, and 4 mM ammonium molybdate). Against a blank containing 0.1 mL of methanol mixed with 1 mL of reagent solution. The test tube contained the reaction mixture was covered with aluminum foil and incubated at 95 °C for 90 min. After the samples were cooled to room temperature, the absorbance was measured at 695 nm.

Ascorbic acid was used as a standard. The antioxidant capacity was estimated using the following formula:

$$\text{Tot. antioxidant cap. (\%)} = \frac{\text{Abs. of control} - \text{Abs. of sample}}{\text{Abs. of control}} \times 100$$

Total antioxidant activity was expressed as mg vitamin C equivalent/1g dry weight, and the values are presented as the means of triplicate analysis.

### Fixed oil analysis

**Oil extraction.** Seeds powder of different plants *E. biumbellata*, *E. dendroides*, and *E. terracina* was extracted by Soxhlet method with hexane solvent for 8 h. After solvent evaporation under reduced pressure, the oil was recovered and stored in glass vials at 4 °C for further analysis.

**Chemical characteristics of oil.** Oil characteristics, namely saponification number (SP), iodine value (IV), and acidity, were determined according to AOCS standard methods [19].

### GC-MS analysis

The fatty acid composition is determined as the methyl esters of fatty acids by gas-liquid chromatography. Methyl esters of the fatty acids (FAME) of the three seed oils were prepared according to a convenient method [20], using BF<sub>3</sub>-methanol at 60 °C.

The FAME was recovered using *n*-hexane, and an aliquot (2 µL) was injected automatically in splitless mode into the GC-MS apparatus. The carrier gas was helium, the temperatures of the injector and detector were held at 300 °C. Electron impact ionization was achieved with ionization energy IE of 70 eV. The identification of the components was based on the comparison of their mass spectra with those of the NIST 11 mass spectral library.

### LC-MS analysis

The concentration of standards solution was 1 mg in 1 mL of methanol-water (1:1) solution. Measurements

were carried out at 280 nm wavelength. Standards and extracts were filtered through a Millipore membrane (0.45 µm). LC-MS method was used for the determination of bioactive ingredient content in our plant's hydro-methanolic extracts.

An aliquot of extract (20 µL) was injected onto a Gemin C-18 column (4.6 mm i.d. × 150 mm). The solvents used were formic acid-acidified water at 0.5% (A) and acetonitrile (B). The elution gradient was 35 min with a flow rate of 0.6 mL/min (Table 1). Spectra were recorded in negative ionization mode in full scan between 0 and 1000 Da.

## RESULTS AND DISCUSSION

### Chemical Composition

Previous phytochemical screening of the phytochemical constituents of various extracts from the three plants [21] showed that they are very rich in polyphenols, lipids, tannins, flavonoids, fats and oils, anthocyanins, sterols, and terpenes. In contrast, alkaloids and starch were not detected, and *E. dendroides* extract gave a negative result for cardenolides.

### TAC, TTC, and phosphomolybdate assay

The results of TAC, TTC, and PPM tests of leave extracts are shown in Table 2. The quantitative estimation of chemical constituents revealed that *E. terracina* leaves contained the highest tannins and anthocyanin levels with 15.54 mg catechin/g and 1.070 cy-3-gly/g, respectively,

**Table 1.** Gradient elution

Instants (min)	A% : B%
0–22.50	90:10 to 50:50
22.50–23	50:50 to 10:90
23–29	10:90
29–29.50	10:90 to 90:10
29.50–35	90:10

**Table 2.** Values of total anthocyanins content (TAC), total tannins content (TTC), and total antioxidant capacity (phosphomolybdate assay) of different leaves extracts

TEST	<i>E. biumbellata</i>	<i>E. dendroides</i>	<i>E. terracina</i>
TTC (CE mg/g Dm)	6.41 ± 0.13	7.31 ± 0.33	15.54 ± 0.56
TAC (AC mg/g Dm)	0.23 ± 0.42	0.35 ± 0.32	1.070 ± 0.98
PPM (VCE mg/g Dm)	9.05 ± 0.02	8.17 ± 0.03	8.75 ± 0.07

**Dm:** dry matter

exceeding the contents of *E. dendroides* and *E. bumbellata*. It was reported that these phytochemical compounds (tannins and anthocyanin) are known to provide support for the bioactive properties of plants [22-23].

The results obtained from the phosphomolybdic acid assay of the three *Euphorbia* leaves extracts show that all the tested extracts possessed a scavenging activity (Table 2). *E. biumbellata* sheets extract exhibited a higher activity than the other two extracts, while *E. dendroides* extract was the least active.

### Fixed Oil Analysis

The yields of oils extracted from *E. terracina*, *E. biumbellata*, and *E. dendroides* were 17.48%, 18.5%, and 20.05%, respectively.

### Chemical characteristics of the oils

Results of the chemical characteristics of the three samples are displayed in Table 3. The data indicate considerable variations in acid values, saponification values, and iodine values between the three seed oils.

The acid index is a parameter that demonstrates the quality of the oil. However, the acid value of the oil must not be too high; an acid value of 0.00 to 3.00 mg KOH/g oil is recommended for oil to find application in cooking [24]. All the vegetable oils under study with a high acid

value of 5.83 to 10.99 mg KOH/g, this denotes a high content of free fatty acids, which causes the oil to turn sour and a less storage quality [25].

Iodine value is a measure of the degree of unsaturation. It is used to quantify the number of double bonds present in the oil. Among the different oils analyzed, *E. dendroides* seed oil displayed the highest iodine value, which reflected a high concentration of unsaturated fatty acids in the oil. On the other hand, *E. biumbellata* seeds oil showed a low degree of unsaturated fatty acid, which indicated that the oil could be used as a nondrying oil, which helps manufacture soap [26].

The saponification value is inversely compared to the molecular weight of the oil. It helps assess the chain lengths of fatty acids in the oil. All of the analyzed oils showed a high SP number, but *E. biumbellata* recorded the highest value.

### GC-MS Reports

The GC-MS analysis of seed oils from the three *Euphorbia* species allowed us to identify numerous compounds belonging to different chemical families. The active compounds with their molecular mass, retention time, and concentration are presented in Table 4.

**Table 3.** Chemical properties of the seeds oil

Chemical characteristics	<i>E. biumbellata</i>	<i>E. dendroides</i>	<i>E. terracina</i>
Acid value: <b>AV</b> (mg KOH/g)	5.83	10.09	10.99
Iodine value: <b>IV</b> (gI <sub>2</sub> /100 g)	47.58	90.41	63.45
Saponification: <b>SP</b> (mg KOH/g)	266.47	210.30	162.32

**Table 4.** Principal compounds in oils from seeds

Compounds	Molar mass (g/mol)	Retention time (min)	<i>Euphorbia</i>	<i>Euphorbia</i>	<i>Euphorbia</i>
			<i>biumbellata</i>	<i>dendroides</i>	<i>terracina</i>
Concentration (%)					
Hexadecanoic acid, methyl ester	270	19.35	2.08 ± 0.2	10.05 ± 0.7	8.5 ± 1.2
8,11-Octadeca-dienoic acid, methyl ester	294	21.22	14.6 ± 2.7	-	-
11,14,17-Eicosatrienoic acid, methyl ester	320	21.64	11.3 ± 1.7	-	13.55 ± 0.3
Linoleic acid, methyl ester	294	21.19	-	37 ± 1.2	31.05 ± 1.2
Linolenic acid, methyl ester	292	21.27	-	2.3 ± 0.9	-
Stearic acid, methyl ester	298	21.47	-	14.35 ± 0.5	-
Ascorbic acid, dipalmitate	652	19.92	-	-	3.95 ± 0.2



The GC-MS chromatogram of the compounds detected is shown in Fig. 1. Results showed that hexadecanoic acid and linoleic acid are present in the various oils. The predominant unsaturated fatty acid is linoleic acid (37% in *E. dendroides*, 31.05% in *E. terracina*, and 14.06% in *E. buimbelatta*). Besides, only *E. terracina* oil contains a rare and important compound of 1-(+)-ascorbic acid 2,6-dihexadecanoate (Fig. 1). Ascorbic acid, dipalmitate has been reported to have many biological properties such as antioxidant, anti-inflammatory, and anti-nociceptive properties [27-28].

### LC-MS Analysis

Different peaks at different retention times were obtained through LC-MS analysis in all three samples, and ten phenolic compounds were identified, and the

chromatographic profile of standards and their retention times are represented by Fig. 2 and Table 5.

The standards retention time values are grouped in Table 5. The results of the chromatographic analysis of the

**Table 5.** Standards retention time

Standard	Retention time (min)
Ascorbic acid	3.00
Gallic acid	4.70
Chlorogenic acid	8.70
Syringic acid	10.55
Rutin	12.53
Ellagic acid	13.35
Ferulic acid	13.85
Colchecin	17.30
Quercitin	19.90
Cinnamic acid	20.70

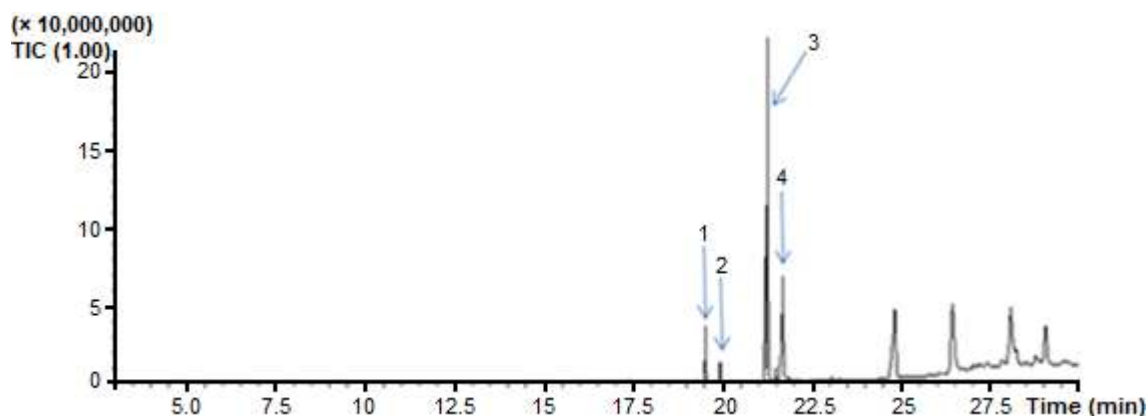


**Fig 1.** Chromatographic profiles of seeds oil of *Euphorbia terracina*

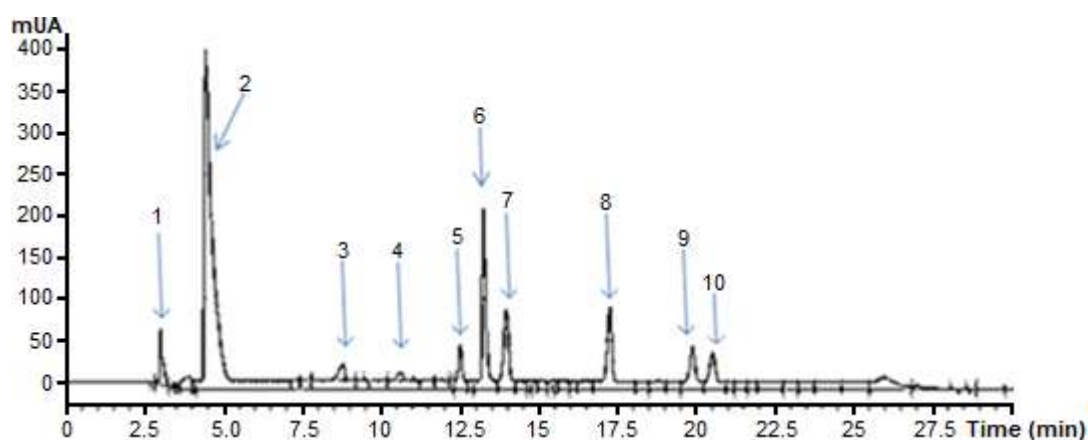


**Fig 2.** Chromatographic profiles of standards at 280 nm at 1 mg/mL: 1: ascorbic acid; 2: gallic acid; 3: chlorogenic acid; 4: syringic acid; 5: rutin; 6: ellagic acid; 7: ferulic acid; 8: colchicin; 9: quercitin; 10: cinnamic acid

**Table 6.** Important compounds identified by LC-MS

Standards	<i>Euphorbia biumbelatta</i>		<i>Euphorbia dendroides</i>		<i>Euphorbia terracina</i>	
	Leaves	Seeds	Leaves	Seeds	Leaves	Seeds
Ascorbic acid	+	+	+	+	+	+
Gallic acid	+	+	-	+	-	+
Chlorogénicacid	+	+	+	+	+	+
Syringic acid	-	+	+	+	+	-
Rutin	+	+	-	-	+	+
Ellagic acid	+	+	+	+	+	+
Ferulic acid	+	+	+	+	+	-
Colchicin	+	+	-	-	+	-
Quercitin	+	+	-	-	-	-
Cinnamic acid	-	-	-	-	-	-

different leaves and seeds extracts are compiled in Table 6. The compound's chemical structures are elucidated from the standard reference graphs, using the molecular weight data.

From the standard reference graphs, the compounds are elucidated using the molecular weight. The results showed the presence of ascorbic acids, chlorogenic acids, and ellagic acids in the different extracts. The species that contains the more standards are *Euphorbia biumbelatta*.

Most of the phytoconstituents identified are very important in medicine. They exhibit various pharmacological activities such as antioxidant, antidiabetic, anti-inflammatory, and anticancer [29-30].

## ■ CONCLUSION

The present work has demonstrated the potential of *Euphorbia* species growing in Algeria as an important source of secondary metabolites.

Hydro-alcoholic extracts from sheets of the three plants were subjected to quantitative estimation of chemical constituents and antioxidant activity essay. Results showed that total tannin and anthocyanin contents were higher in *Euphorbia terracina* extract, compared to the two other generates. Whereas, the total antioxidant activity was higher in *Euphorbia buimbelatta* extract, and was found to be equal in *Euphorbia dendroides* and *Euphorbia terracina* extract. In addition, chemical compositions of hydro-methanolic extracts of leaves were analyzed by the LC-MS technique, which

leads to the identification of ten compounds with considerable concentrations.

On the other hand, fixed oils of seeds were obtained with the Soxhlet method and analyzed by GC-MS apparatus. Linoleic acid was detected as the main FAME among the identified FAMES in the various oils. From LC-MS and GC-MS results, an appreciable abundance of secondary metabolites in the studied plants was noticed. These results demonstrated the importance of *Euphorbia* genre as a promising source of new bioactive compounds.

## ■ ACKNOWLEDGMENTS

The authors would like to thank Pr. Amado DIKOU for his assistant in carrying out the GC-MS and LC-MS analysis. We are also grateful to the anonymous reviewers for their constructive comments on this Manuscript.

## ■ REFERENCES

- [1] Bagewadi, Z.K., Siddanagouda, R.S., and Baligar, P.G., 2014, Phytoconstituents investigation by LC-MS and evaluation of antimicrobial and antipyretic properties of *Cynodon dactylon*, *Int. J. Pharm. Sci. Res.*, 5(7), 2874–2889.
- [2] Savithramma, N., Rao, M.L., and Ankanna, S., 2012, Preliminary Phytochemical Screening of Some Important Medicinal Plants, *Int. J. Ayurveda Res.*, 2 (1), 139–145.

- [3] Azmathullah, N.M., Sheriff, M.A., and Mohideen, A.K.S., 2011, Phytochemical screening of *Calotropis procera* flower extracts and their bio-control potential on *Culex sp.* mosquito larvae and pupae, *Int. J. Pharm. Biol. Arch.*, 2 (6), 1718–1721.
- [4] Ghout, A., Zellagui, A., Gherraf, N., Demirtas, I., Sahin, Y.A., Boukhenaf, M., Lahouel, M., Nieto, G., and Akkal, S., 2018, Antiproliferative and antioxidant activities of two extracts of the plant species *Euphorbia dendroides* L., *Medicines*, 5 (2), 36.
- [5] Saleem, U., Hussain, K., Ahmad, M., Bukhari, N.I., Malik, A., and Ahmad, B., 2014, Report: Physicochemical and phytochemical analysis of *Euphorbia helioscopia* (L.), *Pak. J. Pharm. Sci.*, 27 (3), 577–585.
- [6] Titilope, K.K., Rashidat, E.A., Christiana, O.C., Kehinde, E.R., Omobolaji, J.N., and Olajide, A.J., 2012, In-vitro antimicrobial activities of *Euphorbia hirta* against some clinical Isolates, *Agric. Biol. J. North Am.*, 3 (4), 169–174.
- [7] Özbilgin, S., and Saltan Citoğlu, G., 2012, Uses of some *Euphorbia* species in traditional medicine in Turkey and their biological activities, *Turk. J. Pharm. Sci.*, 9 (2), 241–256.
- [8] Qaisar, M., Gilani, S.N., Farooq, S., Rauf, A., Naz, R., Shaista, and Pervees, S., 2012, Preliminary comparative phytochemical screening of *Euphorbia* species, *Am.-Eurasian J. Agric. Environ. Sci.*, 12 (8), 1056–1060.
- [9] Sun, Y.X., and Liu, J.C., 2011, Chemical constituents and biological activities of *Euphorbia fischeriana* Steud, *Chem. Biodivers.*, 8 (7), 1205–1214.
- [10] Badshah, L., and Hussain, F., 2011, People preferences and use of local medicinal flora in District Tank Pakistan, *J. Med. Plants Res.*, 5 (1), 22–29.
- [11] Sharma, V., Janmeda, P., and Singh, L., 2011, A review on *Euphorbia neriifolia* (Sehund), *Spatula DD*, 1 (2), 107–111.
- [12] Okonkwo, C.O., and Ohaeri, O.C., 2018, Essential oils from the leaves of *Euphorbia Mili* exert insecticidal activity through disruption in ionic composition, *IOSR J. Pharm. Biol. Sci.*, 13 (4), 46–53.
- [13] Jannet, S.B., Hymery, N., Bourgou, S., Jdey, A., Lachaal, M., Magné, C., and Ksouri, R., 2017, Antioxidant and selective anticancer activities of two *Euphorbia* species in human acute myeloid leukemia, *Biomed. Pharmacother.*, 90, 375–385.
- [14] El-Amier, Y.A., Al-Hadithy, O.N., Abdulhadi, H.L., and Fayed, E.M., 2016, Evaluation of antioxidant and antimicrobial activities of *Euphorbia terracina* L. from deltaic mediterranean coast, Egypt, *J. Nat. Prod. Resour.*, 2 (2), 83–85.
- [15] Wafa, G., Amadou, D., Larbi, K.M., and Héla, E.F.O., 2014, Larvicidal activity, phytochemical composition, and antioxidant properties of different parts of five populations of *Ricinus communis* L., *Ind. Crops Prod.*, 56, 43–51.
- [16] Sutharut, J., and Sudarat, J., 2012, Total anthocyanin content and antioxidant activity of germinated colored rice, *Int. Food Res. J.*, 19 (1), 215–221.
- [17] Ahmed, D., Khan, M.M., and Saeed, R., 2015, Comparative analysis of phenolics, flavonoids, and antioxidant and antibacterial potential of methanolic, hexanic and aqueous extracts from *Adiantum caudatum* leaves, *Antioxidants*, 4 (2), 394–409.
- [18] Jan, S., Khan, M.R., Rashid, U., and Bokhari, J., 2013, Assessment of antioxidant potential, total phenolics and flavonoids of different solvent fractions of *Monothea buxifolia* fruit, *Osong Public Health Res. Perspect.*, 4 (5), 246–254.
- [19] Cunniff, P., 1995, *Official Methods of Analysis*, 16<sup>th</sup> Ed., Association of Official Analytical Chemists, Washington DC, US.
- [20] Raharjo, T.J., Nurliana, L., and Mastjeh, S., 2011, Phospholipids from pumpkin (*Cucurbita moschata* (Duch.) Poir) seed kernel oil and their fatty acid composition, *Indones. J. Chem.*, 11 (1), 48–52.
- [21] Zeghad, F., Djilani, S.E., Djilani, A., and Dikou, A., 2016, Antimicrobial and antioxidant activities of three *Euphorbia* species, *Turk. J. Pharm. Sci.*, 13 (1), 47–56.
- [22] Elhassan, G.O.M., Adhikari, A., Abdalla, O.M., Shukrulla, A., Khalid, A., Choudhary, M.I., Mesaik,

- M.A., and Yagi, S., 2015, Chemical constituents of *Euphorbia polyacantha* Boiss. and their immunomodulatory properties, *Rec. Nat. Prod.*, 9 (1), 146–152.
- [23] Vijayabaskar, P., and Shiyamala, V., 2012, Antioxidant properties of seaweed polyphenol from *Turbinaria ornate* (Turner) J. Agardh, 1848, *Asian Pac. J. Trop. Biomed.*, 2 (1), S90–S98.
- [24] Agboola, J.B., Abubakre, O.K., Mudiare, E., Adeyemi, M.B., and Hassan, S.B., 2015, Physicochemical characteristics and fatty acids composition of some selected Nigerian vegetable oils for quenching medium, *Br. J. Appl. Sci. Technol.*, 8 (3), 246–253.
- [25] Youssef, M.K.E., Eshak, N.S., and Hana, R.S., 2013, Physicochemical characteristics, nutrient content and fatty acid composition of *Nigella sativa* oil and sesame oil, *Food Public Health*, 3 (6), 309–314.
- [26] Bello, M.O., Akindele, T.L., Adeoye, D.O., and Oladimejir, A.O., 2011, Physicochemical properties and fatty acids profile of seed oil of *Telfairia occidentalis* Hook F., *Int. J. Basic Appl. Sci.*, 11 (06), 9–14.
- [27] Kumar, P.P., Kumaravel, S., and Lalitha, C., 2010, Screening of antioxidant activity, total phenolics and GC-MS study of *Vitex negundo*, *Afr. J. Biochem. Res.*, 4 (7), 191–195.
- [28] Okwu, D.E., and Ighodaro, B.U., 2010, GC-MS evaluation of bioactive compounds and antibacterial activity of the oil fraction from the leaves of *Alstonia boonei* De Wild, *Der Pharma Chem.*, 2 (1), 261–272.
- [29] Vankar, P.S., and Srivastava, J., 2010, Evaluation of anthocyanin content in red and blue flowers, *Int. J. Food Eng.*, 6 (4), 7.
- [30] Mohamed, A.H.H., Hegazy, M.E.F., Moustafa, M.F.M., El-Sayed, M.A., Abdel-Farid, I.B., Esmail, A.M., Abdelrazik, M.H., Mohamed, N.S., Nenaah, G., Mohamed, T.A., Shahat, A.A., Karchesy, J., Matsuda, H., and Pare, P.W., 2012, *Euphorbia helioscopia*: Chemical constituents and biological activities, *Int. J. Phytopharmacol.*, 3 (1), 78–90.

## Equilibrium Modeling of Astaxanthin Extraction from *Haematococcus pluvialis*

Putri Restu Dewati<sup>1,2</sup>, Rochmadi<sup>2</sup>, Abdul Rohman<sup>3</sup>, Avido Yuliestyan<sup>1</sup>, and Arief Budiman<sup>2,4\*</sup>

<sup>1</sup>Chemical Engineering Department, Universitas Pembangunan Nasional Veteran Yogyakarta, Jl. SWK No. 104, Yogyakarta 55283, Indonesia

<sup>2</sup>Department of Chemical Engineering, Universitas Gadjah Mada, Jl. Grafika 2, Yogyakarta 55284, Indonesia

<sup>3</sup>Department of Pharmaceutical Chemistry, Faculty of Pharmacy, Universitas Gadjah Mada, Yogyakarta, 55281, Indonesia

<sup>4</sup>Center of Excellence for Microalgae Biorefinery, Universitas Gadjah Mada, Sekip K1A, Yogyakarta 55284, Indonesia

\* **Corresponding author:**

tel: +62-8164262111  
email: abudiman@ugm.ac.id

Received: June 17, 2020  
Accepted: December 3, 2020

DOI: 10.22146/ijc.56965

**Abstract:** Astaxanthin is a natural antioxidant, and the highest content of this compound is found in *Haematococcus pluvialis* microalgae. Microwave-assisted extraction (MAE) is one of the environmentally friendly extraction methods and has many advantages. This study aims to investigate the extraction of astaxanthin through the MAE method using various solvents. Several equilibrium models were proposed to describe this solid-liquid equilibrium. The solid-liquid extraction equilibrium parameters were determined by minimizing the sum of squares of errors (SSE), in which equilibrium constants were needed for scaling up purposes. Previously, the microalgae were pretreated with HCl to soften their cell walls thus improving the extraction recovery. In this study, dichloromethane, acetone, methanol, and ethanol were used as the solvents for the extraction process. The astaxanthin concentration was determined by high-performance liquid chromatography (HPLC) and spectrophotometry. Astaxanthin was found to attain equilibrium at 57.42% recovery in a single-step extraction. Thus, several steps were required in sequence to obtain optimum recovery. The experimental data were fitted to three equilibrium models, namely, Henry, Freundlich, and Langmuir models. The experimental data were well fitted to all the models for the extraction in dichloromethane, methanol, ethanol and acetone, as evident from a similar SSE value for each model.

**Keywords:** equilibrium constant; mass transfer coefficient; astaxanthin; extraction; *Haematococcus pluvialis*

### ■ INTRODUCTION

Astaxanthin, with a molecular formula of  $C_{40}H_{52}O_4$  and molecular weight of 596.84 g/mol, is an antioxidant from the carotenoid group. Its antioxidant capacity is 100–500 times higher than those of vitamin E [1-2] and vitamin C [3], and also 40–600 times higher than that of  $\alpha$ -tocopherol [4]. Astaxanthin has an essential role in maintaining liver function and preventing inflammation, oxidation due to UV rays, and cell damage due to the aging process. Astaxanthin is also known for its ability to prevent heart cancer disease by enhancing the immune system, thereby increasing life expectancy, and has several other important functions in the physiological system.

Astaxanthin is widely used in the pharmaceutical, cosmetic, and food industries [1,3,5-8].

Astaxanthin can be obtained from *Haematococcus pluvialis* (*H. pluvialis*) microalgae in up to 0.5–5% of dry weight content [9-11]. There are several methods, categorized as conventional and non-conventional methods, for extracting astaxanthin from *H. pluvialis*. Maceration or solvent extraction is a conventional method, while microwave-assisted extraction (MAE), ultrasound-assisted extraction (UAE), supercritical fluid extraction (SFE), etc., are non-conventional methods. Based on the astaxanthin recovery in these methods, SFE and MAE have been reported to provide a high yield of astaxanthin [6].

Besides the aspect of astaxanthin recovery, the MAE method is an interesting technique. It has several advantages, such as the requirement of simple equipment and small solvent volumes, high extraction efficiency, short extraction time, and minimum solvent waste [6,12-13]. The short extraction time is extremely beneficial for minimizing the degradation of astaxanthin [14]. Although astaxanthin extraction using the MAE method has been studied previously [13-16], the studies were limited to determining the optimum extraction conditions.

An equilibrium model is required to represent the extraction equilibrium and it is extremely beneficial for the design and scaling up of laboratory processes to the pilot and industrial scales [17-18]. To the best of our knowledge, the equilibrium for astaxanthin extraction from *H. pluvialis* microalgae using MAE has not been studied before. This study aims to determine the equilibrium constant and mass transfer coefficient through minimization of the sum of squares of errors (SSE) between the experimental data and simulated data of the equilibrium model. Three equilibrium models, namely, Henry, Freundlich, and Langmuir models, were used for describing the solid-liquid extraction process. Evaluation of the extraction equilibrium constants was based on the unsteady-state process.

Fig. 1 depicts the theoretical scheme of the astaxanthin mass transfer process. In this figure,  $N_A$  is the mass transfer rate,  $C_{Ap}$  is the astaxanthin concentration on solid microalgae surface,  $C_{As}$  is astaxanthin concentration

at equilibrium, and  $C_A$  is the astaxanthin concentration in the solvent. Astaxanthin was assumed to transfer from the microalgae through the boundary layer lying between the solid microalgae surface and solvent.

Astaxanthin was transferred continuously until the equilibrium condition has been reached. Upon the attainment of equilibrium, astaxanthin from microalgae did not dissolve any further in the solvent [19].

In a solid-liquid extraction process, the mass transfer of a solute from the solid to liquid phase occurs in two stages. The first stage involves the internal diffusion from the interior of the solid microalgae to its surface, and the second stage involves mass transfer from the surface to the solvent [20].

Due to the small size of microalgae, as for the case of astaxanthin extraction, the internal diffusion was considered to occur very fast. The astaxanthin concentration in the microalgae ( $C_{Ap}$ ) could then be assumed to be homogeneous, i.e., no concentration gradient existed within the solid. Therefore, the overall mass transfer between the two phases would be entirely controlled by the mass transfer process.

The rate of astaxanthin mass transfer and its coefficient ( $k_c$ ) can be derived from its mass balance equation, as given by Eq. (1).

$$-M \frac{dC_{Ap}}{dt} = A_s \cdot k_c \cdot (C_{As} - C_A) \quad (1)$$

Another important parameter in solid-liquid extraction is the equilibrium constant [19]. In this case, the distribution of a solute between the solid and liquid phases can be determined from the adsorption isotherm, which can be explained using several equilibrium models such as the Henry, Freundlich, and Langmuir models, as given by Eq. (2), (3), and (4).

Henry equilibrium model:

The Henry model is represented by a simple linear equation, as given by Eq. (2).

$$C_{As} = H \cdot C_{Ap} \quad (2)$$

$H$ , the Henry constant, represents the equilibrium constant; a high  $H$  value indicates stronger interaction between the solute and solid, while a low  $H$  value indicates a weaker solute-solid interaction [18]. This model is suitable for low concentrations of liquid [21].

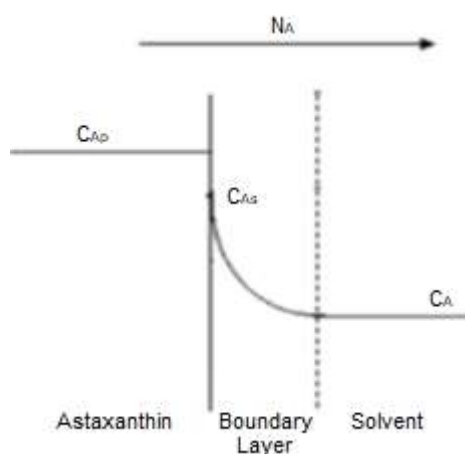


Fig 1. Scheme of astaxanthin mass transfer process

Freundlich equilibrium model:

The Freundlich model is given by Eq. (3).

$$C_{Ap} = K_F \cdot C_{As}^{(1/n)} \quad (3)$$

This model is suitable for heterogeneous, monolayered porous solid surfaces [21]. In Equation (3),  $K_F$  is the equilibrium constant.  $1/n$  is always positive and generally not an integer. It can be determined by plotting  $\log C_{Ap}$  vs.  $\log C_{As}$  [19].

Langmuir equilibrium model

Eq. (4) represents the Langmuir model. This model is suitable for homogeneous, monolayered flat solid surfaces.

$$C_{Ap} = \frac{K_L \cdot q_m \cdot C_{As}}{1 + K_L \cdot C_{As}} \quad (4)$$

Here,  $k_L$  is the equilibrium constant, and  $q_m$  is the monolayer capacity approached at large concentrations. These can be determined by plotting  $1/C_{Ap}$  vs.  $1/C_{As}$  [19].

The experimental data were fit to the above equilibrium models using MATLAB. The equilibrium constant and mass transfer coefficient were determined from the fitting parameters. The accuracy of the fit was optimized by minimizing the SSE, which is defined by Eq. (5).

$$SSE = \sum (C_{\text{experiment}} - C_{\text{calculation}})^2 \quad (5)$$

## ■ EXPERIMENTAL SECTION

### Materials

In this study, astaxanthin was extracted from *H. pluvialis* microalgae obtained from Xi'an Saiyang Bio-Technology Co., Ltd, China. EMSURE grade of acetone, methanol, ethanol, and dichloromethane were purchased from Merck and used as the solvents. An astaxanthin standard with a purity of 98%, CAS 472-61-7, was purchased from Sigma Aldrich, Singapore, as the reference standard for HPLC.

### Instrumentation

HPLC and spectrophotometry techniques were used to determine the astaxanthin concentration. UV-visible spectroscopy was performed on a UV Mini 1240 Shimadzu UV/Vis spectrophotometer. The wavelength at 476, 475, 477, and 480 nm were detected when ethanol, methanol, acetone, and dichloromethane, respectively,

were used as the extraction solvents. For comparison, HPLC Shimadzu LC-2010CHT with photodiode array detector SPD-M10A<sub>VP</sub> was performed on a C18 column, with 0.05% trifluoroacetic acid/methanol (3:97 (v/v)) as the mobile phase. The retention time was 5.5 min.

### Procedure

#### Pretreatment process

The pretreatment process was conducted to soften the thick cell wall of the microalgae, as hard cell walls can hinder the extraction of astaxanthin. Based on a previous study [22], the microalgae used in this study were pretreated by mixing them with 4 M HCl at 70 °C for 2 min. Afterward, the mixture was cooled to ambient temperature and washed with distilled water until the pH of the mixture was 7. Then, the wet microalgae were dried in a refrigerator at ~4 °C for 24 h. The sample was used for the next stage of the extraction process.

#### Astaxanthin extraction

The extraction was performed using the MAE method. Microwaves (Electrolux type MM823AB4-POOC) with 800-W power and frequency of up to 2450 MHz were used. The microwave treatment leads to the resonance of the water molecules in the microalgae cells, producing heat due to molecular friction. This results in the disruption of cell walls due to increased internal pressure. As the cell wall disrupts, the rate of mass transfer of astaxanthin from the solid microalgae to the solvent increases remarkably [16]. During the extraction, the astaxanthin concentration in the solution continues to increase till equilibrium is attained [17]. The microalgae to solvent ratio was maintained at 10:1 (w/v), following the previously reported procedures [5,22]. The extraction temperature was 5 °C at the boiling point of each solvent.

#### Hydrolysis

In the microalgae extract, astaxanthin is present in the form of free astaxanthin (5%), monoester astaxanthin (70%), and diester astaxanthin (25%) [15,23]. The complexity of the ester form renders the analysis difficult. Thus, the ester bond is cleaved by hydrolysis to form free astaxanthin, thereby rendering the analysis easier. The effectiveness of hydrolysis is

evident in the Fourier transform infrared (FTIR) spectra Thermo Nicolet IS 10, wherein the change in the absorbance ratio of the alternating C–O–R to C–O–H bonds on the hydrolyzed sample can be clearly identified. Additionally, the spectrophotometric analysis confirmed the enhancement of free astaxanthin recovery after this process [26].

Hydrolysis was conducted by mixing the microalgae extract with 0.02 M alcoholic NaOH, according to previously reported studies [24–25]. Alcoholic NaOH was prepared by mixing NaOH with methanol. It was reported that a 1:2 (v/v) ratio of the sample to alcoholic NaOH was effective for hydrolysis [26].

## ■ RESULTS AND DISCUSSION

### Effect of Pretreatment on Astaxanthin Recovery

Fig. 2 shows a comparison of the astaxanthin concentration recovered from the extraction process with and without the initial pretreatment, using acetone and ethanol as the solvents (Fig. 2(a) and 2(b), respectively).

In both figures, a sharp increase in the astaxanthin recovery is observed for the pretreated samples in the first two minutes, before reaching equilibrium, as shown by the steady concentration. In contrast, the release of astaxanthin during extraction seems difficult without pretreatment, and a longer time is required to attain the

equilibrium. In Fig. 2(a), the extraction is shown to increase by 74% upon pretreatment compared to the case without pretreatment. Similar behavior is observed for the case of ethanol (Fig. 2(b)), where 79% of the astaxanthin could be extracted after the pretreatment. Thus, pretreatment not only shortens the extraction time but also improves the maximum astaxanthin recovery. This suggests that pretreatment can successfully soften the cell walls of the microalgae, thereby facilitating the extraction process; this phenomenon is similar to that reported previously [22,27].

With an aim to observe the morphology, the microalgae were visualized under the focused beam of electrons of a scanning electron microscope (SEM). The images are shown in Fig. 3. At 1000 times magnification, the differences between the pretreated and non-pretreated samples were fairly obvious—much darker spots were observed for the cell walls of the microalgae that were pretreated. The openings were deeper in this sample, probably because of the damage on its surface as a consequence of the cell wall disruption.

### Determination of Astaxanthin Concentration by Spectrophotometry

Fig. 4 depicts the spectrophotometrically determined astaxanthin concentration [28–30] upon extraction using different solvents.

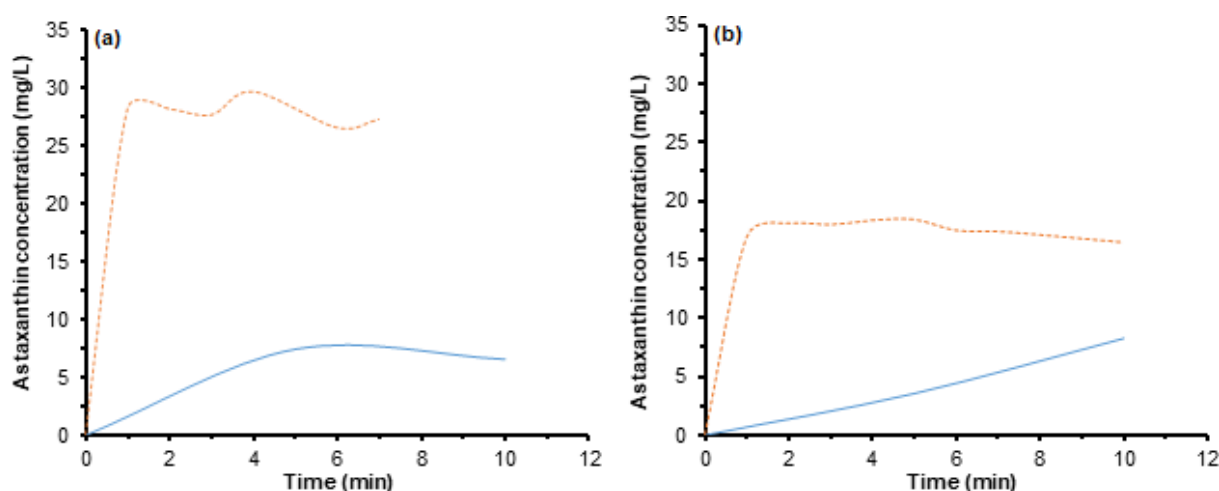


**Fig 2.** Comparison of the outcome of pretreated and non-pretreated samples on astaxanthin extract using (a) acetone and (b) ethanol as the extraction solvent. Blue line shows the astaxanthin concentration without a pretreatment process while orange dotted line shows the astaxanthin concentration with a pretreatment process



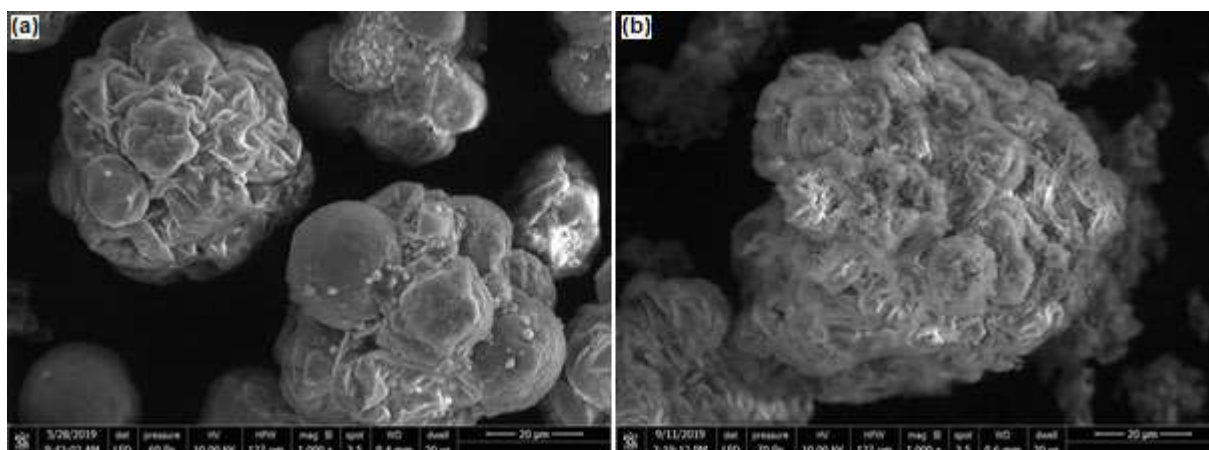


Fig 3. SEM images of microalgae (a) without and (b) with pretreatment

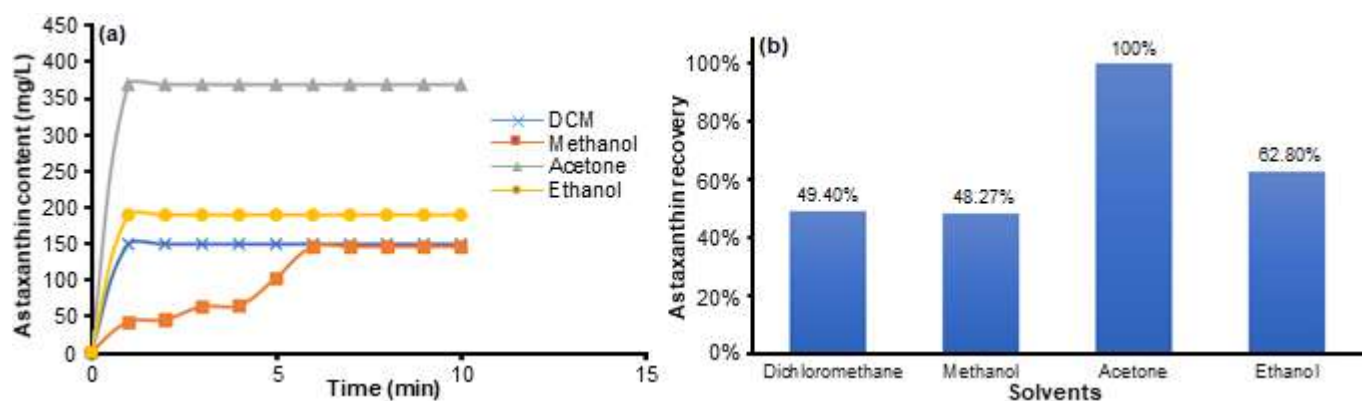
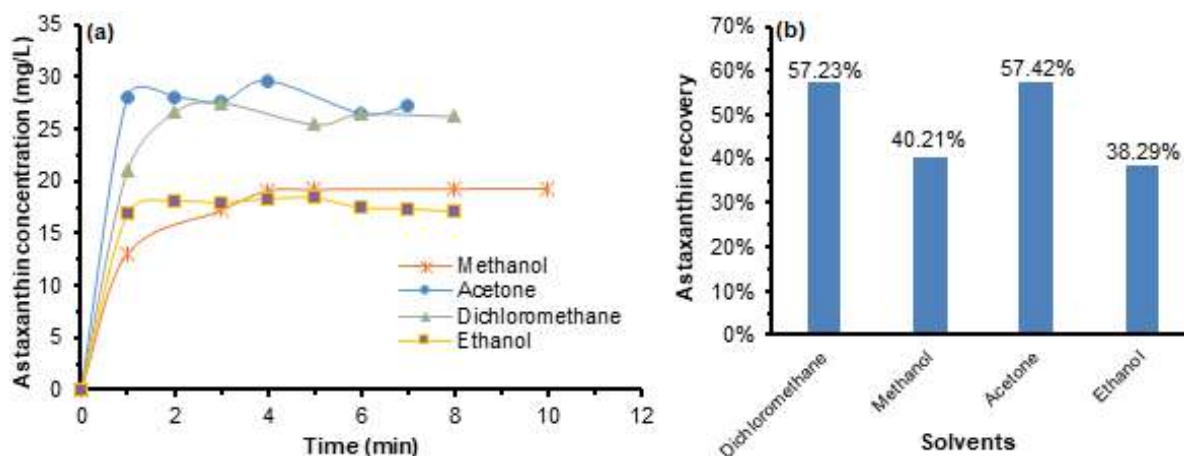


Fig 4. Astaxanthin concentration analyzed by spectrophotometry: (a) evolution of concentration with extraction time and (b) recovery percentage in various solvents

Fig. 4(a) suggests that all the solvents tested can be used to extract astaxanthin from microalgae, and an equilibrium is attained in the process. The extraction in acetone, dichloromethane, and ethanol reaches equilibrium within a minute. For methanol, a slightly slower mass transfer rate seems to be responsible for the longer time required to reach the equilibrium condition (Fig. 4(b)) shows that the extraction of astaxanthin from dry powder microalgae proceeds with 100% recovery in acetone, followed by 62.80, 49.40, and 48.27% recovery in ethanol, dichloromethane, and methanol, respectively. Thus, spectrophotometric analysis suggests that the compatibility between astaxanthin and the solvent plays a significant role in determining the extraction kinetics and total recovery, with acetone being the best choice among the tested solvents for extracting astaxanthin from microalgae.

#### Determination of Astaxanthin Concentration by HPLC

The recovery of astaxanthin extraction, as determined using HPLC [13-14,22,31-33], is shown in Fig. 5. Fig. 5 suggests that both the rate and recovery percentage are affected by the solvent. Rate analysis suggests that the extraction takes the maximum time to attain the equilibrium in methanol, and astaxanthin can no longer diffuse into the solvent in this state [19]. A fraction of astaxanthin (13 mg/L) dissolves into the methanol in less than a minute. The equilibrium was reached directly in the first minute in acetone, in the second minute in dichloromethane, and ethanol (Fig. 5(a)). However, when methanol was used for the extraction, equilibrium was attained in 5 min. Acetone gives the highest astaxanthin recovery percentage, as



**Fig 5.** Astaxanthin concentration analyzed by HPLC: (a) evolution of concentration with extraction time and (b) percentage recovery in various solvents

evident from Fig. 5(b). Compared to other organic solvents such as methanol, ethanol, and acetonitrile [14], the highest astaxanthin recovery was obtained in acetone ( $44 \pm 1\%$ ). Acetone was the most appropriate solvent because its structure is very similar to that of astaxanthin, which contains many carbonyl groups. Since astaxanthin extraction reached equilibrium with 100% recovery, the extraction process must be conducted in a stepwise manner.

### Equilibrium of Astaxanthin Extraction

Three equilibrium models were investigated in this study—the Henry, Freundlich, and Langmuir models. Fig. 6(a) depicts the plot of astaxanthin concentration vs. extraction time and its fit using the Henry equilibrium model. The Henry constant ( $H$ ) is obtained by plotting  $C_{Ap}$  and  $C_{As}$ . Meanwhile,  $k_c$  is derived from the mass balance. Their values are summarized in Table 1. For the Freundlich model, the Freundlich constants ( $n$  and  $k_L$ ) are obtained by plotting  $\log C_{Ap}$  vs.  $\log C_{As}$  and solving the mass balance equation, respectively. Table 1 and Fig. 6(b) show the corresponding values and the fitting curves for the various solvents used.

Fig. 6(c) shows the fit of the experimental data to the Langmuir model. Parameters  $k_L$  and  $q_m$  derived from the plot of  $1/C_{Ap}$  vs.  $1/C_{As}$  are listed in Table 1. Besides,  $k_c$  is determined by solving the mass balance equation and is given in the same table. From Table 1  $H$  is the Henry constant,  $k_F$  and  $1/n$  are the Freundlich constants, and  $k_L$  and  $q_m$  are the Langmuir constants. The  $k_c$  value gives an

estimate of the extraction rate, wherein higher  $k_c$  values correspond to a faster mass transfer rate and hence, a shorter extraction time.

### Comparison of the Henry, Freundlich, and Langmuir Models

Comparison of the Henry, Freundlich, and Langmuir models based on the SSE in each solvent is presented in Table 2. The smallest SSE value corresponding to each solvent represents the best fit. For acetone, methanol, ethanol, and dichloromethane, the experimental data were well fitted to all models, as the SSE values are almost equal regardless of the model used. For acetone,  $H$  and  $k_c$  values from the Henry model were  $13.505 \text{ g microalgae/dm}^3$  and  $20.405 \text{ dm/min}$ , respectively. In the Freundlich model,  $1/n$ ,  $k_F$ , and  $k_c$  were  $0.093$ ,  $1.516 \text{ dm}^3/\text{g microalgae}$ , and  $3.200 \text{ dm/min}$ , respectively. In the Langmuir model,  $k_L$ ,  $q_m$ , and  $k_c$  were  $0.021 \text{ dm}^3/\text{mg astaxanthin}$ ,  $5.549 \text{ mg astaxanthin/g microalgae}$ , and  $15.847 \text{ dm/min}$ , respectively.

For methanol,  $H$  and  $k_c$  values from the Henry model were  $6.675 \text{ g microalgae/dm}^3$  and  $5.600 \text{ dm/min}$ , respectively. In the Freundlich model,  $1/n$ ,  $k_F$ , and  $k_c$  were  $1.052$ ,  $0.129 \text{ dm}^3/\text{g microalgae}$ , and  $5.735 \text{ dm/min}$ , respectively. In the Langmuir model,  $k_L$ ,  $q_m$ , and  $k_c$  were  $0.005 \text{ dm}^3/\text{mg astaxanthin}$ ,  $33.454 \text{ mg astaxanthin/g microalgae}$ , and  $5.305 \text{ dm/min}$ , respectively. For ethanol,  $H$  and  $k_c$  values from the Henry model were  $5.922 \text{ g microalgae/dm}^3$  and  $14.563 \text{ dm/min}$ , respectively. In the

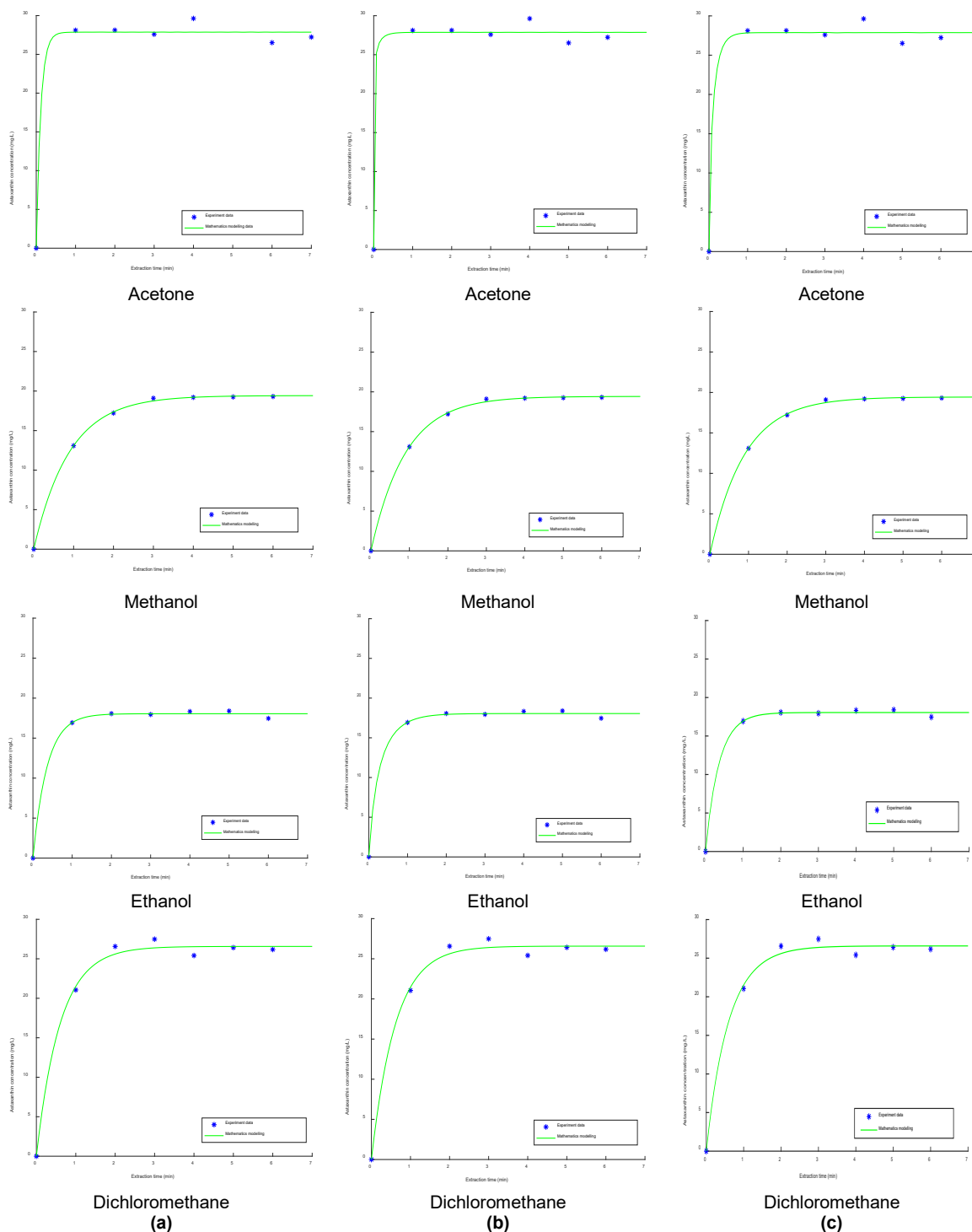


**Fig 6.** Equilibrium models for the extraction in different solvents. (a) Henry model, (b) Freundlich model, (c) Langmuir model

Freundlich model,  $1/n$ ,  $k_F$ , and  $k_c$  were 0.245, 1.498 dm<sup>3</sup>/g microalgae, and 5.544 dm/min, respectively. In the Langmuir model,  $k_L$ ,  $q_m$ , and  $k_c$  were 0.005 dm<sup>3</sup>/mg

astaxanthin, 38.396 mg astaxanthin/g microalgae, and 0.549 dm/min, respectively.

For dichloromethane,  $H$  and  $k_c$  values from the

**Table 1.** Model constants for the tested solvents

Solvents	Henry Model	Freundlich Model	Langmuir Model
	$H = g$ microalgae/dm <sup>3</sup> $k_c = dm/min$	$k_F = dm^3/g$ microalgae $k_c = dm/min$	$k_L = dm^3/mg$ astaxanthin $q_m = mg$ astaxanthin/g microalgae $k_c = dm/min$
Acetone	$H = 13.485$ $k_c = 73.895$	$1/n = 0.093$ $k_F = 1.516$ $k_c = 3.200$	$k_L = 0.021$ $q_m = 5.549$ $k_c = 15.847$
Methanol	$H = 6.675$ $k_c = 5.600$	$1/n = 1.052$ $k_F = 0.129$ $k_c = 5.735$	$k_L = 0.005$ $q_m = 33.454$ $k_c = 5.305$
Ethanol	$H = 5.922$ $k_c = 14.563$	$1/n = 0.245$ $k_F = 1.498$ $k_c = 5.544$	$k_L = 0.005$ $q_m = 38.396$ $k_c = 14.009$
Dichloromethane	$H = 12.097$ $k_c = 6.254$	$1/n = 1.336$ $k_F = 0.027$ $k_c = 7.412$	$k_L = 0.002$ $q_m = 44.004$ $k_c = 5.969$

**Table 2.** SSE of the fit of the Henry, Freundlich, and Langmuir models to the experimental data

SSE	Henry Model	Freundlich Model	Langmuir Model
Acetone	5.515	5.505	5.511
Methanol	0.157	0.156	0.162
Ethanol	0.549	0.557	0.549
Dichloromethane	3.773	3.684	3.834

Henry model were 12.097 g microalgae/dm<sup>3</sup> and 6.254 dm/min, respectively. In the Freundlich model,  $1/n$ ,  $k_F$ , and  $k_c$  were 1.336, 0.027dm<sup>3</sup>/g microalgae, and 7.412 dm/min, respectively. In the Langmuir model,  $k_L$ ,  $q_m$ , and  $k_c$  were 0.002 dm<sup>3</sup>/mg astaxanthin, 44.004 mg astaxanthin/g microalgae, and 5.969 dm/min, respectively.

## ■ CONCLUSION

Astaxanthin can be extracted from microalgae using the microwave-assisted extraction method. Acetone, methanol, ethanol, and dichloromethane were examined for extraction. Among these solvents, acetone was found as the best solvent for obtaining the highest recovery. The experimental data were fit to three equilibrium models, namely, Henry, Freundlich, and Langmuir models, using MATLAB. The experimental data were well fitted to all the three models for the extraction in acetone, methanol, ethanol, and dichloromethane, as evident from the almost same SSE value for each model.

## ■ ACKNOWLEDGMENTS

The authors acknowledge the financial support in research and publication from the Ministry of Research and Technology/National Agency for Research and Innovation of the Republic of Indonesia.

## ■ REFERENCES

- [1] Lee, S.A., Lee, N., Oh, H.M., Kim, D.G., and Ahm, C.Y., 2020, Fast-track production of astaxanthin by reduced cultivation time with the “red cell inoculation system” (RCIS) and various chemical cues in *Haematococcus lacustris*, *J. Appl. Phycol.*, 32 (1), 41–50.
- [2] Krichnavaruk, S., Shotipruk, A., Goto, M., and Pavasant, P., 2008, Supercritical carbon dioxide extraction of astaxanthin from *Haematococcus pluvialis* with vegetable oils as co-solvent, *Bioresour. Technol.*, 99 (13), 5556–5560.
- [3] Wang, L., Yang, B., Yan, B., and Yao, X., 2012,

- Supercritical fluid extraction of astaxanthin from *Haematococcus pluvialis* and its antioxidant potential in sunflower oil, *Innovative Food Sci. Emerg. Technol.*, 13, 120–127.
- [4] Ambati, R.R., Phang, S.M., Ravi, S., and Aswathanarayana, R.G., 2014, Astaxanthin: Sources, extraction, stability, biological activities and its commercial applications—A review, *Mar. Drugs*, 12 (1), 128–152.
- [5] Dong, S., Huang, Y., Zhang, R., Wang, S., and Liu, Y., 2014, Four different methods comparison for extraction of astaxanthin from green alga *Haematococcus pluvialis*, *Sci. World J.*, 2014, 694305.
- [6] Zhao, T., Yan, X., Sun, L., Yang, T., Hu, X., He, Z., Liu, F., and Liu, X., 2019, Research progress on extraction, biological activities and delivery systems of natural astaxanthin, *Trends Food Sci. Technol.*, 91, 354–361.
- [7] Khoo, K.S., Chew, K.W., Ooi, C.W., Ong, H.C., Ling, T.C., and Show, P.L., 2019, Extraction of natural astaxanthin from *Haematococcus pluvialis* using liquid biphasic flotation system, *Bioresour. Technol.*, 290, 121794.
- [8] Fan, Y., Niu, Z., Xu, C., Yang, L., Chen, F., and Zhang, H., 2019, Biocompatible protic ionic liquids-based microwave-assisted liquid-solid extraction of astaxanthin from *Haematococcus pluvialis*, *Ind. Crops Prod.*, 141, 111809.
- [9] Haque, F., Dutta, A., Thimmanagari, M., and Chiang, Y.W., 2016, Intensified green production of astaxanthin from *Haematococcus pluvialis*, *Food Bioprod. Process.*, 99, 1–11.
- [10] Shang, M., Ding, W., Zhao, Y., Xu, J.W., Zhao, P., Li, T., Ma, H., and Yu, X., 2016, Enhanced astaxanthin production from *Haematococcus pluvialis* using butylated hydroxyanisole, *J. Biotechnol.*, 236, 199–207.
- [11] Sun, H., Guan, B., Kong, Q., Geng, Z., and Wang, N., 2016, Repeated cultivation: Non-cell disruption extraction of astaxanthin for *Haematococcus pluvialis*, *Sci. Rep.*, 6 (1), 20578.
- [12] Morais, S., 2013, “Ultrasonic- and microwave-assisted extraction and modification of algal components”, in *Functional Ingredients from Algae for Foods and Nutraceuticals*, Woodhead Publishing, Cambridge, United Kingdom, 585–605.
- [13] Chuyeng, H.V., Nguyen, M.H., Roach, P.D., Golding, J.B., and Parks, S.E., 2018, Microwave-assisted extraction and ultrasound-assisted extraction for recovering carotenoids from Gac peel and their effects on antioxidant capacity of the extracts, *Food Sci. Nutr.*, 6 (1), 189–196.
- [14] Ruen-ngam, D., Shotipruk, A., and Pavasant, P., 2011, Comparison of extraction methods for recovery of astaxanthin from *Haematococcus pluvialis*, *Sep. Sci. Technol.*, 46 (1), 64–70.
- [15] Zhao, X., Zhang, X., Fu, L., Zhu, H., and Zhang, B., 2016, Effect of extraction and drying methods on antioxidant activity of astaxanthin from *Haematococcus pluvialis*, *Food Bioprod. Process.*, 99, 197–203.
- [16] Zhao, L., Chen, G., Zhao, G., and Hu, X., 2009, Optimization of microwave-assisted extraction of astaxanthin from *Haematococcus pluvialis* by response surface methodology and antioxidant activities of the extracts, *Sep. Sci. Technol.*, 44 (1), 243–262.
- [17] Shakir, I.K., 2017, Mass transfer coefficient of the extraction process of essential oil from *Myrtus communis* L. plants using different solvents, *The 8<sup>th</sup> Jordan International Chemical Engineering Conference (JICChEC 2017)*, Jordan, November 7–9, 2017.
- [18] Honarvar, B., Sajadian, S.A., Khorram, M., and Samimi, A., 2013, Mathematical modeling of supercritical fluid extraction of oil from canola and sesame seeds, *Braz. J. Chem. Eng.*, 30 (1), 159–166.
- [19] Perry, R.H., and Green, D.W., 1999, “Adsorption and ion exchange” in *Perry’s Chemical Engineers’ Handbook*, 7<sup>th</sup> Ed., Mc. Graw Hill, USA, 1497–1562.
- [20] Megawati, Fardhyanti, D.S., Sediawan, B.W., and Hisyam, A., 2019, Kinetics of mace (*Myristicaceae arillus*) essential oil extraction using microwave assisted hydrodistillation: Effect of microwave power, *Ind. Crops Prod.*, 131, 315–322.
- [21] Seader, J.D., Henley, E.J., and Roper, D.K., 2011, “Adsorption, ion exchange, chromatography, and

- electrophoresis” in *Separation Process Principle: Chemical and Biochemical Operation*, 3<sup>rd</sup> Ed., John Wiley & Sons, Inc., USA, 568–632.
- [22] Sarada, R., Vidhyavathi, R., Usha, D., and Ravishankar, G.A., 2006, An efficient method for extraction of astaxanthin from green alga *Haematococcus pluvialis*, *J. Agric. Food Chem.*, 54 (20), 7585–7588.
- [23] Galarza, J.I., Arredondo-Vega, B.O., Villón, J., and Henríquez, V., 2019, Deesterification of astaxanthin and intermediate esters from *Haematococcus pluvialis* subjected to stress, *Biotechnol. Rep.*, 23, e00351.
- [24] Di Caprio, F., Altimari, P., Toro, L., and Pagnanelli, F., 2015, Effect of lipids and carbohydrates extraction on astaxanthin stability in *Scenedesmus sp.*, *Chem. Eng. Trans.*, 43, 205–210.
- [25] Saini, R.K., and Keum, Y.S., 2018, Carotenoid extraction methods: A review of recent development, *Food Chem.*, 240, 90–103.
- [26] Dewati, P.R., Rochmadi, Rochman, A., and Budiman, A., 2020, A preliminary study of extraction and purification processes of astaxanthin from *Haematococcus pluvialis* as a natural antioxidant, *IOP Conf. Ser.: Mater. Sci. Eng.*, 778, 012032.
- [27] Kim, D.Y., Vijayan, D., Praveenkumar, R., Han, J.I., Lee, K., Park, J.Y., Chang, W.S., Lee, J.S., and Oh, Y.K., 2016, Cell-wall disruption and lipid/astaxanthin extraction from microalgae: *Chlorella* and *Haematococcus*, *Bioresour. Technol.*, 199, 300–310.
- [28] Li, Y., Miao, F., Geng, Y., Lu, D., Zhang, C., and Zeng, M., 2012, Accurate quantification of astaxanthin from *Haematococcus* crude extract spectrophotometrically, *Chin. J. Oceanol. Limnol.*, 30 (4), 627–637.
- [29] Takeungwongtrakul, S., and Benjakul, S., 2016, Astaxanthin degradation and lipid oxidation of Pacific white shrimp oil: Kinetic study and stability as affected by storage condition, *Int. Aquat. Res.*, 8 (1), 15–27.
- [30] Su, F., Xu, H., Yang, N., Liu, W., and Liu, J., 2018, Hydrolytic efficiency and isomerization during de-esterification of natural astaxanthin esters by saponification and enzymolysis, *Electron. J. Biotechnol.*, 34, 37–42.
- [31] Reyes, F.A., Mendiola, J.A., Ibanez, E., and del Valle, J.M., 2014, Astaxanthin extraction from *Haematococcus pluvialis* using CO<sub>2</sub>-expanded ethanol, *J. Supercrit. Fluids*, 92, 75–83.
- [32] Tzanova, M., Argirova, M., and Atanasov, V., 2016, HPLC quantification of astaxanthin and canthaxanthin in Salmonidae eggs, *Biomed. Chromatogr.*, 31 (4), e3852.
- [33] Hu, J., Lu, W., Lv, M., Wang, Y., Ding, R., and Wang, L., 2019, Extraction and purification of astaxanthin from shrimp shells and the effects of different treatments on its content, *Rev. Bras. Farmacogn.*, 29 (1), 24–29.

## Synthesis of Cu<sup>2+</sup> Doped ZnO by the Combination of Sol-Gel-Sonochemical Methods with Duck Egg Albumen as Additive for Photocatalytic Degradation of Methyl Orange

Sherly Kasuma Warda Ningsih<sup>1\*</sup>, Hary Sanjaya<sup>2</sup>, Bahrizal<sup>1</sup>, Edi Nasra<sup>3</sup>, and Syuhada Yurnas<sup>1</sup>

<sup>1</sup>Inorganic Chemistry Laboratory, Faculty of Mathematics and Natural Sciences, Universitas Negeri Padang, Kampus Air Tawar, Jl. Prof. Dr. Hamka, West Sumatera 25131, Indonesia

<sup>2</sup>Physical Chemistry Laboratory, Faculty of Mathematics and Natural Sciences, Universitas Negeri Padang, Kampus Air Tawar, Jl. Prof. Dr. Hamka, West Sumatera 25131, Indonesia

<sup>3</sup>Analytical Chemistry Laboratory, Faculty of Mathematics and Natural Sciences, Universitas Negeri Padang, Kampus Air Tawar, Jl. Prof. Dr. Hamka, West Sumatera 25131, Indonesia

\* **Corresponding author:**

email: sherly14@fmipa.unp.ac.id

Received: June 20, 2020

Accepted: February 11, 2021

DOI: 10.22146/ijc.57077

**Abstract:** Cu<sup>2+</sup> doped ZnO by green synthesis was successfully prepared by using a combination of the Sol-Gel-Sonochemical method. Duck egg albumen was used as an additive, a substitute for chemical additives, such as monoethanolamine (MEA) and diethanolamine (DEA). Zn(CH<sub>3</sub>COO)<sub>2</sub>·2H<sub>2</sub>O was used as a precursor, Cu(CH<sub>3</sub>COO)<sub>2</sub>·H<sub>2</sub>O was used as a dopant source with concentrations of 5 wt.%, and isopropanol was used as the solvent. The addition of albumen variations was 10, 20, 30, 40, and 50 mL. The prepared catalyst was applied for the degradation of the methyl orange dyes by using photosynthesis with variations of the degradation time of methyl orange for 30, 60, 90, 120, 150, 180, and 240 min. FTIR spectra showed stretching at 400–550 cm<sup>-1</sup> indicating the presence of Zn–O and Zn–O–Cu metal oxides. The optimum bandgap energy value was 2.82 eV with the addition of 30 mL of albumen. XRD analysis showed the optimum particle size of 16.62–53.21 nm after adding 30 mL of additives. The SEM image showed a spherical shape with an average diameter of 2.7 μm. The optimum percentage of degradation obtained was 94.88%, with the irradiation time under UV light for 210 min.

**Keywords:** Cu<sup>2+</sup> doped ZnO; duck egg albumen; sol-gel-sonochemistry; spherical; methyl orange

### ■ INTRODUCTION

ZnO is a nanostructured semiconductor material with high conductivity and low thermal expansion. ZnO nanostructured has environmental stability and low cost [1] as compared with other binary metal oxide nanoparticles [2-3]. Electrical and optical properties are what make this semiconductor widely applied to gas sensors, catalysts, to solar cell conversion. ZnO is a semiconductor group II-VI [4] because, in the periodic table, zinc and oxygen are group II and group VI respectively. ZnO has a band gap of 3.37 eV [5] with the ability to bind free electrons of 60 MeV at room temperature [6]. Pure ZnO has the disadvantage that the

surface area of the small volume and the energy of the band gap is less suitable when applied to visible light, so to optimize the properties of the semiconductor, it is necessary to do the doping.

Doping is the process of inserting other atoms in a semiconductor to give a band gap value that is smaller than the original material. In this research, Cu is used as a dopant. Cu is chosen because it has an ionic radius that is smaller than Zn, has conductivity properties similar to Zn, has abundant resources, and is a relatively cheap metal. Cu is preferred for the doping of ZnO as compared with other transition metals due to the easily overlapping process of its d electrons with the ZnO valence bond [7]. Cu doping can improve the electrical,

magnetic, and optical properties of ZnO [8]. In addition, the results of Cu ion insertion on Zn have been successful with certain concentrations of dopants to produce hexagonal wurtzite.

Cu doped ZnO synthesis has been reported with various methods such as solvothermal [9], hydrothermal method [10], coprecipitation method [11-13], sonochemical method [14] and sol-gel method [15]. The solvothermal method is a method with the principle of crystal growth based on the solubility of the material in the solvent under high-pressure conditions so that when a work accident occurs, it will cause more fatal consequences. The hydrothermal method is a process that involves heating reactants in an autoclave using water with the weakness of corrosive hydrothermal slurry, which can cause danger when an accident occurs. The coprecipitation method is a method of synthesis of nanoparticles by the addition of a precipitating agent. Still, this method has the disadvantage that the resulting particle size is not homogeneous. In contrast, sonochemical methods have good homogeneity, and sol-gel is a method that produces better sizes and can take place at low temperatures and does not require expensive costs in the synthesis process. Based on the mentioned methods, the sol-gel and sonochemical methods were chosen because of their superiority, such as they can control the size and growth of crystalline.

The sonochemical method can control the growth of ZnO crystals, which is successful in controlling the shape and size of the particles produced [16]. This method also has the advantage of being able to break the aggregates from large crystals into nano-sized crystals. The sonolysis method has a working principle that is utilizing ultrasonic waves with a high frequency, which are irradiated into the solution.

Additives are substances that can produce materials with high homogeneity and are stabilizing. The addition of this additive can produce products that have a large per volume surface area [17]. One of the additives commonly used in the synthesis of a nanomaterial is monoethanolamine (MEA). The MEA molecule contains 3 hydrogen atoms, 1 nitrogen atom, and 2 CH<sub>2</sub> molecules. MEA is an additive that is relatively expensive. The

downside makes researchers interested in looking for alternatives that are environmentally friendly and are expected to be a substitute for MEA as an additive to synthesize a nanoparticle.

The albumen of the duck egg and the chicken egg can be used as an additive replacing MEA in nanoparticle synthesis. The albumen of the duck egg has an alkaline pH that ranges from 9–11. The albumen of the chicken egg has a lower pH (7.6) than the duck egg white. ZnO nanoparticles can be synthesized by using egg whites (albumen) [18-20] through the sol-gel method. The main advantage obtained in the synthesis of nanoparticles using egg white additives is egg white (albumen) acting as a gelling agent and emulsifier to give a long-term stability of the nanoparticles by preventing agglomeration (accumulation of crystal particles). Egg white can control the crystal size of ZnO particles [21]. Albumen in egg white plays a role in increasing the rate of reaction and producing nano-sized ZnO crystals.

Methyl orange dye is a dye that has a very high toxic level, contamination in water, causes turbidity to water, and is very dangerous for the environment [22]. Methyl orange can cause irritation to the skin, eyes, digestive disorders, and respiratory disorders. Organic compounds are stable, which makes them difficult to degrade, so the need for a compound or catalyst that can degrade these dyes to reduce the threat to the environment. Methyl orange has been widely used in foodstuffs, textiles [23], and paper [24]. ZnO is very stable and has the catalytic activity that can degrade methyl orange [25]. Therefore, it is expected that ZnO metal oxides [26] doped with Cu can degrade methyl orange dyes.

Photosynthesis is a process that combines photolysis and sonolysis [27-28]. Irradiation of the catalyst with UV light will cause an excited state of electrons from the valence band to the conduction band in the semiconductor. Electrons are excited after absorbs sufficient energy that will cause holes (electron holes) that can interact with water solvents to form OH radicals that are reactive to decompose organic compounds.

In this paper, we report the synthesis of Cu doped ZnO by using duck egg albumen as an additive and the



application of Cu doped ZnO nanoparticles that have the lowest band gap for degradation of methyl orange by photosynthesis.

## ■ EXPERIMENTAL SECTION

### Materials

The materials used include  $\text{Zn}(\text{CH}_3\text{COO})_2 \cdot 2\text{H}_2\text{O}$  (Merck),  $\text{Cu}(\text{CH}_3\text{COO})_2 \cdot \text{H}_2\text{O}$  (Merck), isopropanol (p.a), and duck egg albumen, methyl orange, deionized water.

### Instrumentation

The equipments used were glassware, magnetic stirrer (brand ATE VELP Scentipica magnetic stirrer) stirrer bar, digital ultrasonic cleaner machine (45 Hz) used for sonication, porcelain cups, analytical balance, (precisa XT 220 A brand), oven (Oven) France Etuves XU 225) and furnaces (NEYCRAFT), X-Ray Diffraction (XRD) X-Pert<sup>3</sup> Pro material PAnalytical, Fourier Transform Infra-Red (FTIR) Perkin Elmer Frontier Optica, UV-Vis Diffuse Reflectance Spectrophotometer (UVDRS) Analytik Jena, Scanning Electron Microscopy (SEM) Hitachi (Hitachi FlexSEM 100), and UV-Vis Spectrophotometer Agilent 8453.

### Procedure

#### Preparation of catalyst

$\text{Zn}(\text{CH}_3\text{COO})_2 \cdot 2\text{H}_2\text{O}$  was dissolved in isopropanol and stirred with a magnetic stirrer for 40 min.  $\text{Cu}(\text{CH}_3\text{COO})_2 \cdot \text{H}_2\text{O}$  in the amount of 5 wt.% was added to the solution. The solution was continuously stirred for 40 min. The albumen of the duck egg was added to the solution with the various volumes of 10, 20, 30, 40, and 50 mL and stirred for 60 min. The solution was placed in a container for sonication for 30 min at 45 W. The solution was left one night to get a stable sol, placed into the vaporizer cup, and dried in the oven at 110 °C for 1 h. The formed gel was calcined in the furnace at 600 °C for 3 h.

#### Characterization

The peaks obtained in the XRD data were compared with the database contained in the ICDD (International Center for Diffraction Data). After this comparison, the type of phase corresponding to the  $\text{Cu}^{2+}$  doped ZnO sample was obtained. The estimated average size of

crystallite  $\text{Cu}^{2+}$  doped ZnO particles can be calculated by using the Scherrer formula.

$$D = \frac{k\lambda}{\beta \cos \theta} \quad (1)$$

where: D = diameter of crystallite; K = Scherrer's constant (0.89);  $\lambda$  = wavelength of the X-ray diffraction used ( $\lambda = 1.5406 \text{ \AA}$ );  $\beta$  = overall width of half the maximum diffraction peak (FWHM);  $\theta$  = angle comes to the field of Bragg.

#### Photocatalytic activity test

The methyl orange solution was prepared by dissolving 0.5 g of methyl orange in deionized water to the boundary mark in a 1 L flask (10 ppm). Methyl orange mother liquor in the amount of 20 mL was taken and put into a 1000 mL volumetric flask. The solution was homogenized so that a solution of methyl orange was obtained with a concentration of 10 ppm. Degradation of methyl orange was carried out by taken 80 mL of 10 ppm methyl orange solution. The  $\text{Cu}^{2+}$  doped ZnO catalyst was added in an amount of 0.1 g to the methyl orange solution. The photosynthesis irradiation times were 30, 60, 90, 120, 150, 150, 180, and 240 min. After the degradation process, the solution was centrifuged for 10 min.

## ■ RESULTS AND DISCUSSION

$\text{Cu}^{2+}$  doped ZnO can be synthesized through several steps consisting of sample preparation by dissolving precursors, dopants, and additives. The results of this stage are soles that can be stabilized by additives. The additive used was albumen. The second step was drying the sol to get a stiffer gel structure, followed by the calcination step to obtain the metal oxide, which will be characterized using FTIR (Fourier Transform-Infra Red) to determine the metal oxide bond formed from  $\text{Cu}^{2+}$  doped ZnO nanoparticles, UV-DRS (UV-Diffuse reflectance) to determine the band gap values obtained from  $\text{Cu}^{2+}$  doped ZnO nanoparticles, XRD (X-Ray Diffraction Spectroscopy) to determine the crystal structure and  $\text{Cu}^{2+}$  doped ZnO particle size, and SEM (Scanning Electron Microscopy) to determine the surface morphology of ZnO doped  $\text{Cu}^{2+}$  doped nanoparticles.

The FTIR spectra can provide information about the bonds and functional groups of  $\text{Cu}^{2+}$  doped ZnO. The absorbance band can be seen in (Fig. 1) at a wavenumber of  $1000\text{--}400\text{ cm}^{-1}$ . The absorbance band of  $400\text{--}550\text{ cm}^{-1}$  indicates the stretching of Zn–O, the absorbance band around the area of  $500\text{--}600\text{ cm}^{-1}$  indicates the presence of the Zn–O–Cu bond. Zn–O and Zn–O–Cu stretching was in the range of  $600\text{--}800\text{ cm}^{-1}$  [14], Zn–O bonds were obtained at  $480\text{--}490\text{ cm}^{-1}$ , and the Cu–O–metal showed at  $430\text{--}620\text{ cm}^{-1}$  [13]. Absorption for pure ZnO is obtained in the range of wavenumbers of  $443$  and  $497\text{ cm}^{-1}$  which is a stretching vibration of ZnO [29].

The band gap values of  $\text{Cu}^{2+}$  doped ZnO nanoparticles were calculated using the Kubelka-Munk equation. Testing with UV-DRS is performed in the wavelength range of  $200\text{--}800\text{ nm}$ . The band gap value of the sample has smaller than the ZnO pristine (Table 1). The results obtained were in accordance with the results reported by [25], which states that the band gap energy produced from ZnO material will be decreased with the addition of  $\text{Cu}^{2+}$  as the dopant. The band gap value curve is shown in Fig. 2.

The value of the band gap can be seen in (Fig. 2), which shows a decrease in the value of the band gap after carrying out the use of Cu metal by adding variations in the volume of albumen. Band gap values of  $\text{Cu}^{2+}$  doped ZnO are in the range  $2.82\text{--}2.90\text{ eV}$  (Table 1).

The band gap value of  $\text{Cu}^{2+}$  doped ZnO can go down to  $2.82\text{ eV}$ . This research obtains the smallest band gap value in the addition of  $30\text{ mL}$  of albumen. The band gap value of  $\text{Cu}^{2+}$  doped ZnO resulted by another researcher ranged from  $2.85\text{--}2.96\text{ eV}$  [30]. The band gap value for ZnO without doping is  $3.1\text{ eV}$  [31]. Cu doped ZnO with the addition of  $30\text{ mL}$  albumen has a band gap of  $2.82\text{ eV}$  so that it can be applied to photocatalysis. This decrease in band gap occurs due to interactions between the electron band and electron delocalization of the transition ion and the occurrence of metal ion substitution.

Fig. 3(a) showed X-ray diffractograms from undoped ZnO nanoparticles without the addition of albumen and  $\text{Cu}^{2+}$  doped ZnO nanoparticles with variations in the addition of albumen additives of  $10, 20, 30, 40,$  and  $50\text{ mL}$ . ZnO without doping obtained

hexagonal wurtzite structure, while for doping treatment also obtained hexagonal wurtzite ion structure of Cu which is substituted to the Zn lattice, but there is no peak showing a change in the structure of ZnO without doping [25].

Fig. 3(b) showed the position of  $2\theta$  addition of  $10\text{ mL}$  albumen at  $31.71^\circ; 34.36^\circ; 36.18^\circ; 56.52^\circ; 62.79^\circ$  and  $75.16^\circ$  with crystal size respectively obtained using the Scherrer equation are  $45.60, 45.92, 46.15, 57.18, 59.01,$  and  $13.24\text{ nm}$ . This value proves that ZnO, which

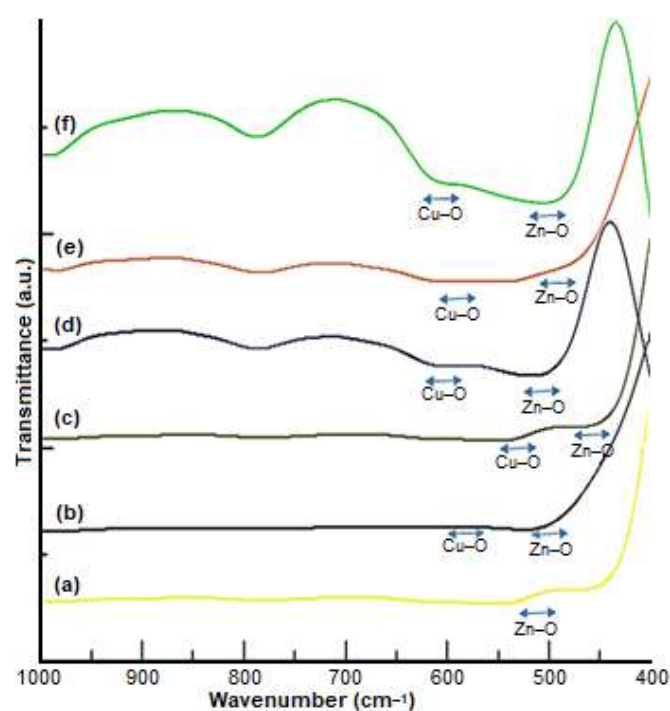


**Fig 1.** FTIR spectra of nanoparticles (a) pure ZnO, (b)  $\text{Cu}^{2+}/\text{ZnO}$  ( $10\text{ mL}$  albumen), (c)  $\text{Cu}^{2+}/\text{ZnO}$  ( $20\text{ mL}$  albumen), (d)  $\text{Cu}^{2+}/\text{ZnO}$  ( $30\text{ mL}$  albumen), (e)  $\text{Cu}^{2+}/\text{ZnO}$  ( $40\text{ mL}$  albumen), and (f)  $\text{Cu}^{2+}/\text{ZnO}$  ( $50\text{ mL}$  albumen)

**Table 1.** Band gap values of pure ZnO and  $\text{Cu}^{2+}$  doped ZnO

Samples	Band gap (eV)
Pure ZnO	3.10
$\text{Cu}^{2+}$ doped ZnO ( $10\text{ mL}$ albumen)	2.90
$\text{Cu}^{2+}$ doped ZnO ( $20\text{ mL}$ albumen)	2.88
$\text{Cu}^{2+}$ doped ZnO ( $30\text{ mL}$ albumen)	2.82
$\text{Cu}^{2+}$ doped ZnO ( $40\text{ mL}$ albumen)	2.90
$\text{Cu}^{2+}$ doped ZnO ( $50\text{ mL}$ albumen)	2.89

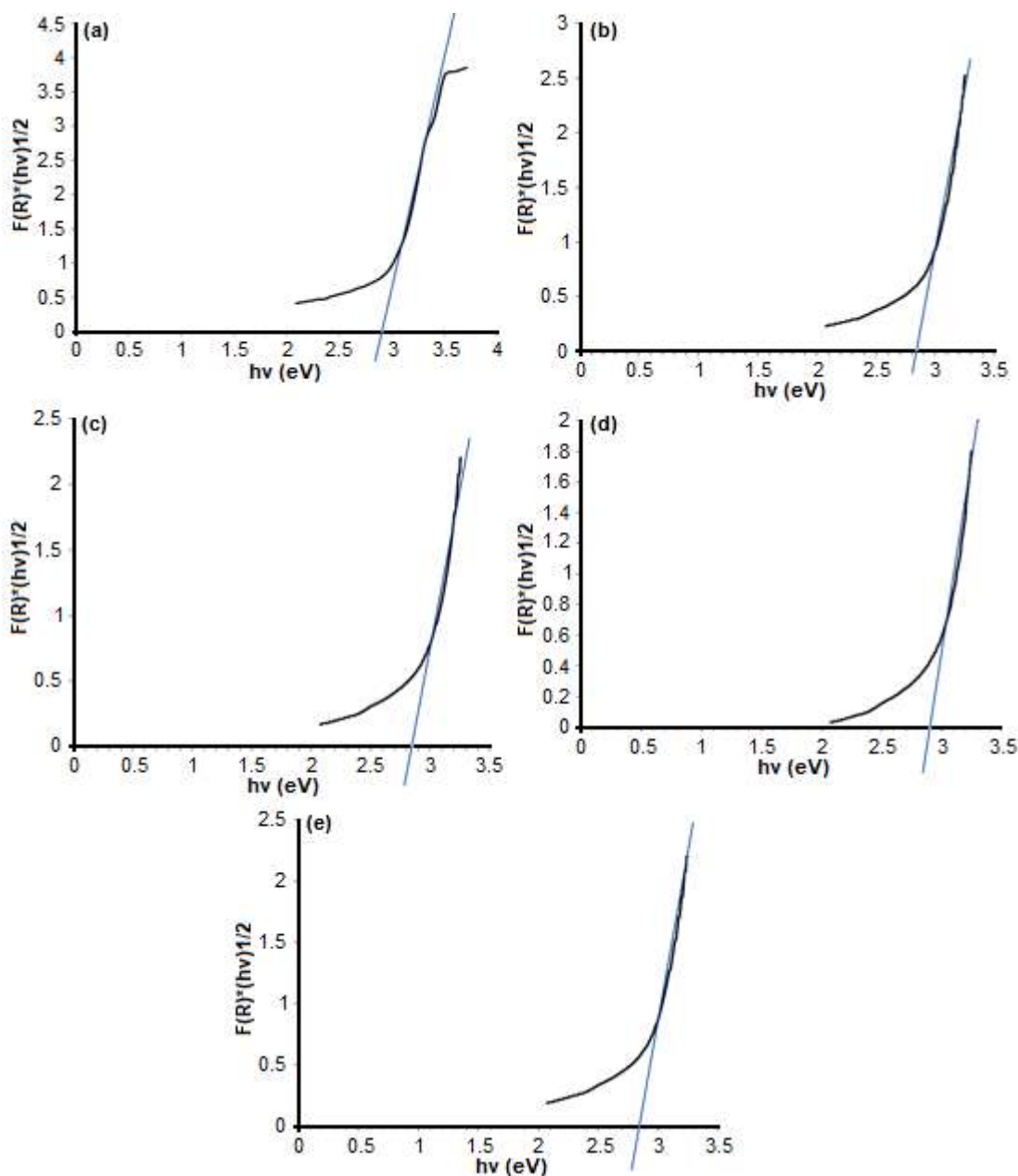


**Fig 2.** Band gap energy curves of  $\text{Cu}^{2+}$  doped ZnO (a) 10 mL, (b) 20 mL, (c) 30 mL, (d) 40 mL, and (e) 50 mL

is doped with Cu with the addition of albumen additives, is a nanoparticle material.

The resulting peaks address the hexagonal wurtzite crystal structure according to ICSD-ICDD (Inorganic Structure Database-International Center for Diffraction Data) data No. 01-076-0704 for  $\text{Cu}^{2+}$  doped ZnO nanoparticles with the addition of 10 mL of albumen. Egg white (albumen) is a gelling agent as well as an emulsifier that has a role in the long-term stability of nanoparticles,

which can prevent agglomeration (accumulation of crystal particles) so that with the presence of albumen, the particle size can be well controlled. Particle sizes for ZnO without doping and without the addition of albumen additives were around 38–74 nm [31].

Fig. 3(c) showed the position of  $2\theta$  addition of 20 mL of albumen at  $31.72^\circ$ ;  $34.38^\circ$ ;  $36.20^\circ$ ;  $56.53^\circ$ ;  $62.80^\circ$  and  $83.39^\circ$  with the crystal size obtained using the Scherrer equation is 53.21, 53.58, 46.15, 71.48, 73.76, and 14.05 nm,

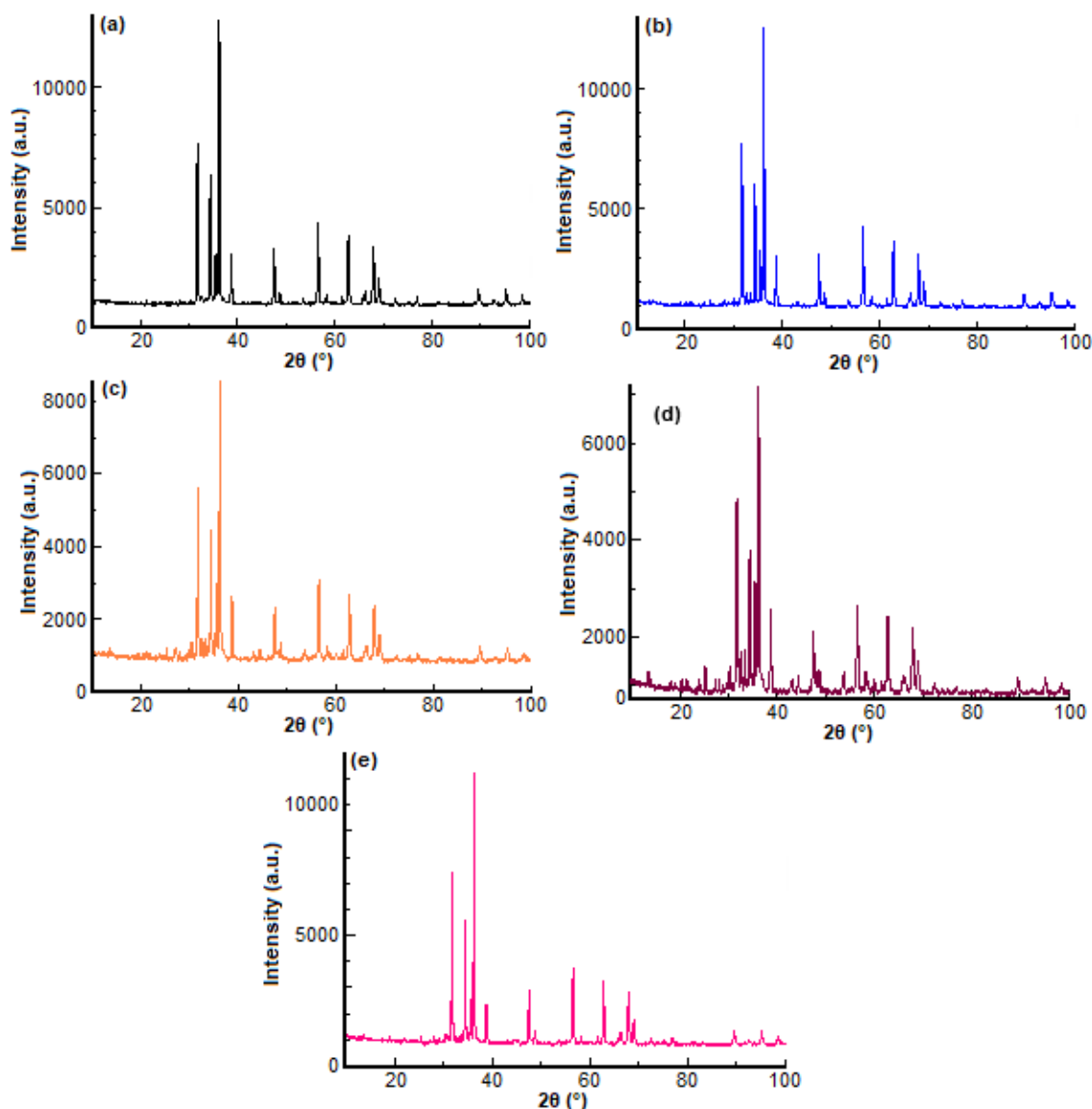


**Fig 3.** Diffractogram of nanoparticles (a)  $\text{Cu}^{2+}/\text{ZnO}$  (10 mL of albumen), (b)  $\text{Cu}^{2+}/\text{ZnO}$  (20 mL of albumen), (c)  $\text{Cu}^{2+}/\text{ZnO}$  (30 mL of albumen), (d)  $\text{Cu}^{2+}/\text{ZnO}$  (40 mL of albumen), and (e)  $\text{Cu}^{2+}/\text{ZnO}$  (50 mL of albumen)

respectively. Fig. 3(d) showed the position of  $2\theta$  addition of 30 mL of albumen at  $31.68^\circ$ ;  $34.34^\circ$ ;  $35.45^\circ$ ;  $36.17^\circ$ ;  $56.48^\circ$  and  $81.47^\circ$  with the corresponding crystal sizes obtained using the Scherrer equation is 53.21, 45.92, 40.30, 46.15, 47.64, and 16.62 nm, respectively. Fig. 3(e) showed the position of  $2\theta$  addition of 40 mL of albumen at  $10.40^\circ$ ;  $31.69^\circ$ ;  $34.36^\circ$ ;  $35.45^\circ$ ;  $36.17^\circ$ ; and  $56.50^\circ$  with the respective crystal sizes being obtained using the Scherrer equation is 12.85, 53.21, 45.92, 46.06, 40.36, and 58.11 nm. Fig. 3(f) showed the position of  $2\theta$  addition of 50 mL of albumen at  $31.704^\circ$ ,  $34.36^\circ$ ,  $36.18^\circ$ ;  $21.86^\circ$ ;  $56.51^\circ$

and  $62.8^\circ$  with the crystal size successively obtained using Scherrer's equation is 53.21, 45.92, 46.15, 19.55, 71.47, and 59.01 nm. This value proves that ZnO, which is doped with Cu with the addition of albumen additives, is a nanoparticle material. Albumen prevents the buildup of crystal particles so that with the presence of albumen, the particle size can be controlled properly.

Egg white has the ability to associate with metal ions in solution, and egg white is used as a binder to form a nanoparticle [32]. In general, high and sharp peak intensities are obtained at  $2\theta$ , which is the peak

characteristic of Cu<sup>2+</sup> doped ZnO nanoparticle samples. This shows that the sample shows a high degree of crystallinity, the width of the peak indicates the sample is nano-sized (Table 2).

The surface analysis of Cu<sup>2+</sup> doped ZnO samples with the addition of 30 mL of albumen can be seen in Fig. 4. SEM is an analytical technique used to see the topography and surface of a material. SEM images resulting from Cu<sup>2+</sup> doped ZnO nanoparticle samples with the addition of albumen obtained a spheric shape with a diameter of 2.72–2.89 μm for ZnO doped Cu samples. The results of the characterization using SEM (Figure 4) showed that the presence of dopant on the morphology of ZnO nanoparticles is characterized by Cu in the form of needle-shaped crystals. The morphology of ZnO nanoparticles was influenced by the dopants [33].

Degradation of methyl orange (Fig. 5) was measured by UV-Vis at a wavelength of 400–800 nm. The maximum wavelength for methyl orange was 511 nm. Degradation is done by varying the time during irradiation under UV light that is 30, 60, 90, 120, 150, 180, 210, and 240 min.

The curves of each absorbance are shown in Fig. 6.

Fig. 6 shows the absorbance value of methyl orange after being degraded with a Cu doped ZnO catalyst. The results of initial absorbance measurements of methyl orange with a concentration of 10 ppm are used as a comparison of absorbance after degradation. The percent degradation can be calculated by using the following formula:

$$D = \frac{A_0 - A_t}{A_0} \times 100\% \quad (2)$$

where: A<sub>0</sub> is the initial absorbance, A<sub>t</sub> is the absorbance of methyl orange after degradation at time t [34].

**Table 2.** Particle sizes of pure ZnO and Cu<sup>2+</sup> doped ZnO

Samples	Particle sizes (nm)
Pure ZnO	40-61
Cu <sup>2+</sup> doped ZnO (10 mL of albumen)	13.24-59.01
Cu <sup>2+</sup> doped ZnO (20 mL of albumen)	14.05-73.71
Cu <sup>2+</sup> doped ZnO (30 mL of albumen)	16.62-53.21
Cu <sup>2+</sup> doped ZnO (40 mL of albumen)	12.85-58.11
Cu <sup>2+</sup> doped ZnO (50 mL of albumen)	19.55-71.47

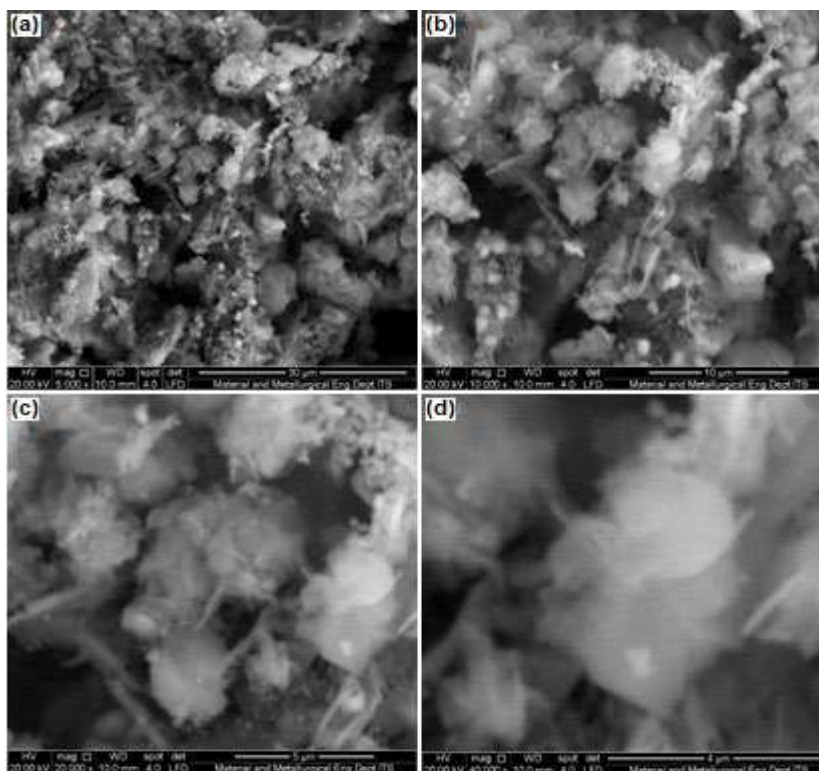


**Fig 4.** SEM Images of Cu<sup>2+</sup> doped ZnO nanoparticles with magnification of (a) 5000×, (b) 10000×, (c) 20000×, (d) 40000×

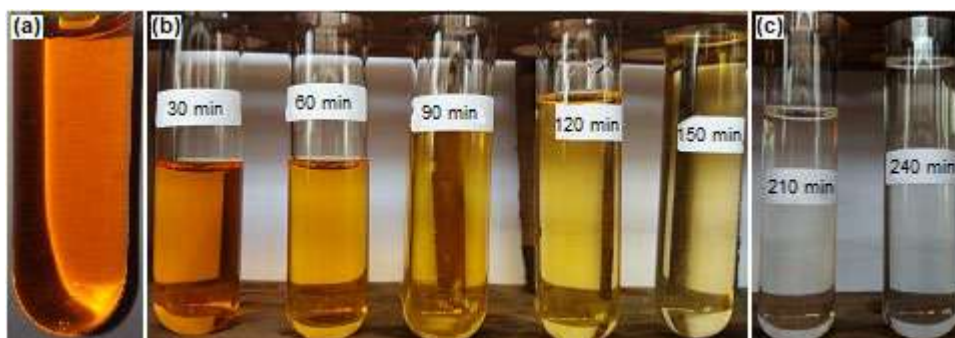
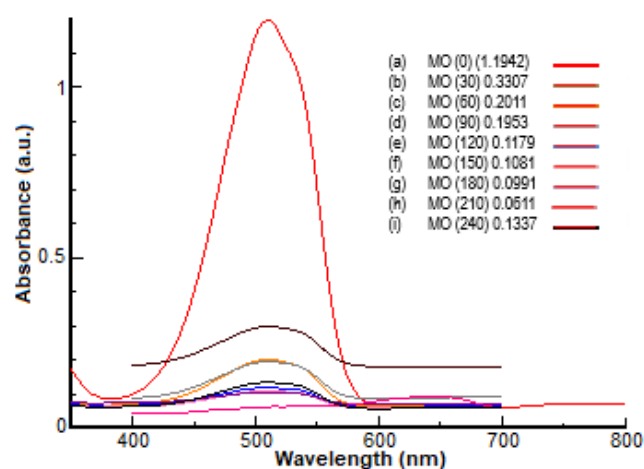


**Fig 5.** Methyl orange (a) before degradation, (b) after degradation process (30, 60, 90, 120, 150 min), (c) after degradation process (210 and 240 min)

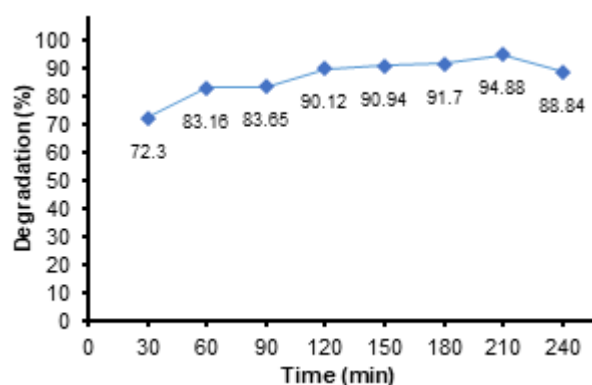
Based on measurements by using UV-DRS, absorbance decreases until 210 min with a percent degradation of 94.88% so that the degradation percent increases and the absorbance increases at 240 min so that the degradation percent decreases. Increased absorbance caused by excess  $\bullet\text{OH}$  is generated so that it reacts with  $\text{H}_2\text{O}_2$ , which causes the formation of  $\bullet\text{OOH}$ , which is unstable. This decrease in absorbance occurs due to contact between the solution of methyl orange and Cu doped ZnO catalyst with the help of UV light and sonication, which will accelerate degradation.

Fig. 7 shows the percent degradation of the methyl orange dyes by using the photolysis method. The data shows the optimum degradation process is found after 210 min with a degradation percentage of 94.88%, due to the more photons that hit the catalyst. This process increases the amount of  $\bullet\text{OH}$  radicals attacking the dyes to give a stable bond in the dye, such as the azo group. Degradation of methyl orange can also be influenced by the particle size and band gap values of the material. The smallest particle size has the greatest kinetic energy, so the reaction is faster. The band gap energy increases between the valence band and the conduction band by decreasing the particle size. This is due to the confinement of the holes and electrons. The electron can easily be excited and easily produce  $\bullet\text{OH}$  if the band gap value is small and the catalytic activity will increase under visible light.

Percent degradation of the methyl orange has decreased after 240 min. This is due to the excess of the  $\text{H}_2\text{O}_2$  that has been produced during the sonication process,

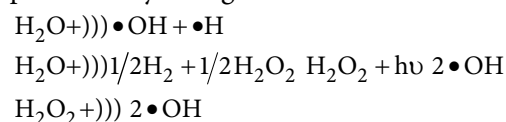


**Fig 6.** Absorbance curves of (a) methyl orange before degradation (0 min), (b) after 30 min degradation, (c) after 60 min degradation, (d) after 90 min degradation, (e) after 120 min degradation, (f) after 150 min degradation, (g) after 180 min degradation, (h) after 210 min degradation and (i) after 240 min degradation



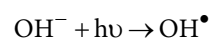
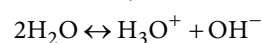
**Fig 7.** Photolysis curve for degradation of methyl orange

and the  $\text{H}_2\text{O}_2$  reacts with  $\cdot\text{OH}$  to produce hydroperoxy radicals ( $\cdot\text{OOH}$ ).  $\text{H}_2\text{O}_2$  [35] is the factor that decreases the percent degradation of the methyl orange. A general equation for the reaction that occurs during photolysis degradation can be written as follows:

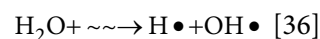


where  $\text{UV}$  shows the sonication process [35].

Photolysis takes place through UV radiation, which causes the bonding of a compound by  $\text{OH}\cdot$ . The principle of photolysis is the chemical reactions by using light and solid catalysts.



Degradation of the methyl orange is done by using ultrasonication in a water medium. It can produce  $\text{OH}\cdot$ , and  $\text{H}\cdot$  during the sonication and cavitation effects. The cavitation effect will produce bubbles that will be broken down by ultrasonic waves. The Reaction can be written as follows:



$\sim\sim$  = ultrasonic wave

## CONCLUSION

Albumen can influence the synthesis of  $\text{Cu}^{2+}$  doped ZnO in terms of particle size makes them smaller than pure ZnO. Characterization of  $\text{Cu}^{2+}$  doped ZnO using FTIR shows the presence of metal oxide bonds at wavenumbers of 400–800  $\text{cm}^{-1}$ . The smallest bandgap value measured by UV-DRS was obtained from the addition of 30 mL of albumen with particle size measured using XRD ranging at 16.62–53.21 nm. The morphology produced after being measured using SEM has a spherical shape.  $\text{Cu}^{2+}$  doped ZnO catalyst can degrade methyl orange dyes with the most optimum percent degradation that is 94.88%, with an irradiation time of 210 min.

## ACKNOWLEDGMENTS

The authors would like to thank the Ministry of Research and Higher Education, Indonesia, for providing financial support through research decentralization,

Penelitian Strategis Nasional Institusi (PSNI) No. 830/UN35.2/PG/2018.

## REFERENCES

- [1] Beitollahi, H., Tajik, S., Nejad, F.G., and Safaei, M., 2020, Recent advances in ZnO nanostructure-based electrochemical sensors and biosensors, *J. Mater. Chem. B*, 8 (27), 5826–5844.
- [2] Saravanan, R., Karthikeyan, S., Gupta, V.K., Sekaran, G., Narayanan, V., and Stephen, A., 2013, Enhanced photocatalytic activity of ZnO/CuO nanocomposite for the degradation of textile dye on visible light illumination, *Mater. Sci. Eng., C*, 33 (1), 91–98.
- [3] Karimi-Shamsabadi, M., Behpour, M., Babaheidari, A.K., and Saberi, Z., 2017, Efficiently enhancing photocatalytic activity of NiO-ZnO doped onto nanozeoliteX by synergistic effects of p-n heterojunction, supporting and zeolite nanoparticles in photo-degradation of Eriochrome Black T and methyl orange, *J. Photochem. Photobiol., A*, 346, 133–143.
- [4] Ningsih, S.K.W., Nizar, U.K., Bahrizal, Nasra, E., and Suci, R.F., 2019, Effect of egg white as additive for synthesis and characterization of Al doped ZnO nanoparticles by using sol-gel method, *J. Phys.: Conf. Ser.*, 1185, 012029.
- [5] Trandafilović, L.V., Jovanović, D.J., Zhang, X., Ptasińska, S., and Dramićanin, M.D., 2017, Enhanced photocatalytic degradation of methylene blue and methyl orange by ZnO:Eu nanoparticles, *Appl. Catal., B*, 203, 740–752.
- [6] Omri, K., Najeh, I., Dhahri, R., El Ghoul, J., and El Mir, L., 2014, Effects of temperature on the optical and electrical properties of ZnO nanoparticles synthesized by sol-gel method, *Microelectron. Eng.*, 128, 53–58.
- [7] Khan, S.A., Noreen, F., Kanwal, S., Iqbal, A., and Hussain, G., 2018, Green synthesis of ZnO and Cu-doped ZnO nanoparticles from leaf extracts of *Abutilon indicum*, *Clerodendrum infortunatum*, *Clerodendrum inerme* and investigation of their

- biological and photocatalytic activities, *Mater. Sci. Eng., C*, 82, 46–59.
- [8] Ghahramanifard, F., Rouhollahi, A., and Fazlollahzadeh, O., 2018, Electrodeposition of Cu-doped p-type ZnO nanorods; Effect of Cu doping on structural, optical and photoelectrocatalytic property of ZnO nanostructure, *Superlattices Microstruct.*, 114, 1–14.
- [9] Wu, C., Shen, L., Yu, H., Zhang, Y., and Huang, Q., 2012, Solvothermal synthesis of Cu-doped ZnO nanowires with visible light-driven photocatalytic activity, *Mater. Lett.*, 74, 236–238.
- [10] Lee, J.S., Lee, Y.M., and Boo, J.H., 2015, Doping control of Cu in pH-tuned hydrothermal growth of ZnO nanowires, *Appl. Surf. Sci.*, 354, 66–70.
- [11] Prasad, N., and Karthikeyan, B., 2017, Cu-doping and annealing effect on the optical properties and enhanced photocatalytic activity of ZnO nanoparticles, *Vacuum*, 146, 501–508.
- [12] Kanade, K.G., Kale, B.B., Baeg, J.O., Lee, S.M., Lee, C.W., Moon, S.J., and Chang, H., 2007, Self-assembled aligned Cu doped ZnO nanoparticles for photocatalytic hydrogen production under visible light irradiation, *Mater. Chem. Phys.*, 102 (5), 98–104.
- [13] Singhal, S., Kaur, J., Namgyal, T., and Sharma, R., 2012, Cu-doped ZnO nanoparticles: Synthesis, structural and electrical properties, *Physica B*, 407 (8), 1223–1226.
- [14] Othman, A.A., Ali, M.A., Ibrahim, E.M.M., and Osman, M.A., 2016, Influence of Cu doping on structural, morphological, photoluminescence, and electrical properties of ZnO nanostructures synthesized by ice-bath assisted sonochemical method, *J. Alloys Compd.*, 683, 399–411.
- [15] Omri, K., Bettaibi, A., Khirouni, K., and El Mir, L., 2018, The optoelectronic properties and role of Cu concentration on the structural and electrical properties of Cu doped ZnO nanoparticles, *Physica B*, 537, 167–175.
- [16] Yadav, R.S., Mishra, P., and Pandey, A.C., 2008, Growth mechanism and optical property of ZnO nanoparticles synthesized by sonochemical method, *Ultrason. Sonochem.*, 15 (5), 863–868.
- [17] Ningsih, S.K.W., 2016, *Sintesis Anorganik*, UNP Press, Padang, Indonesia.
- [18] Camaratta, R., Orozco-Messana, J., and Bergmann, C.P., 2015, Synthesis of ZnO through biomimetization of eggshell membranes using different precursors and its characterization, *Ceram. Int.*, 41 (10), 14826–14833.
- [19] Bhunia, A.K., Kamilya, T., and Saha, S., 2016, Synthesis, characterization of ZnO nanorods and its interaction with albumin protein, *Mater. Today: Proc.*, 3 (2), 592–597.
- [20] Dhara, S., and Bhargava, P., 2001, Egg white as an environmentally friendly low-cost binder for gelcasting of ceramics, *J. Am. Ceram. Soc.*, 84 (12), 3048–3050.
- [21] Thangaraj, P., Rajan, J., Durai, S., Kumar, S., Ratnaphani, A., and Neri, G., 2011, The role of albumen (egg white) in controlled particle size and electrical conductivity behavior of zinc oxide nanoparticles, *Vacuum*, 86 (2), 140–143.
- [22] Torres-Hernández, J.R., Ramírez-Morales, E., Rojas-Blanco, L., Pantoja-Enriquez, J., Oskam, G., Paraguay-Delgado, F., Escobar-Morales, B., Acosta-Alejandro, M., Díaz-Flores, L.L., and Pérez-Hernández, G., 2015, Structural, optical and photocatalytic properties of ZnO nanoparticles modified with Cu, *Mater. Sci. Semicond. Process.*, 37, 87–92.
- [23] Subha, P.P., and Jayaraj, M.K., 2015, Solar photocatalytic degradation of methyl orange dye using TiO<sub>2</sub> nanoparticles synthesised by sol-gel method in neutral medium, *J. Exp. Nanosci.*, 10 (14), 1106–1115.
- [24] Chen, T., Zheng, Y., Lin, J.M., and Chen, G., 2008, Study on the photocatalytic degradation of methyl orange in water using Ag/ZnO as catalyst by liquid chromatography electrospray ionization ion-trap mass spectrometry, *J. Am. Soc. Mass Spectrom.*, 19 (7), 997–1003.
- [25] Prasad, N., Saipavitra, V.M.M., Swaminathan, H., Thangaraj, P., Viswanathan, M.R., and Balasubramanian, K., 2016, Microstress, strain, band gap tuning and photocatalytic properties of



- thermally annealed and Cu-doped ZnO nanoparticles, *Appl. Phys. A Mater. Sci. Process.*, 122 (6), 590.
- [26] Kumar, R., Kumar, G., and Umar, A., 2013, ZnO nano-mushrooms for photocatalytic degradation of methyl orange, *Mater. Lett.*, 97, 100–103.
- [27] He, Y., Grieser, F., and Ashokkumar, M., 2011, The mechanism of sonophotocatalytic degradation of methyl orange and its products in aqueous solutions, *Ultrason. Sonochem.*, 18 (5), 974–980.
- [28] Kumar, R., Kumar, G., Akhtar, M.S., and Umar, A., 2015, Sonophotocatalytic degradation of methyl orange using ZnO nano-aggregates, *J. Alloys Compd.*, 629, 167–172.
- [29] Ali, I., Suhail, M., Alothman, Z.A., and Alwarthan, A., 2018, Recent advances in syntheses, properties and applications of TiO<sub>2</sub> nanostructures, *RSC Adv.*, 8, 30125–30147.
- [30] Amutha, C., Thanikaikarasan, S., Ramadas, V., and Natarajan, B., 2015, Structural, morphological and optical properties of Albumen mediated ZnO nanoparticles, *Optik*, 126 (24), 5748–5752.
- [31] Ningsih, S.K.W., Nizar, U.K., and Novitria, U., 2017, Sintesis dan karakterisasi nanopartikel ZnO doped Cu<sup>2+</sup> melalui metoda sol-gel, *Eksakta*, 18 (2), 39–51.
- [32] Ahmed, M.A., Okasha, N., and El-Dek, S.I., 2011, Novelty, preparation, characterization and enhancement of magnetic properties of Mn nanoferrites using safety binder (egg white), *Solid State Sci.*, 13 (10), 1840–1843.
- [33] Labhane, P.K., Huse, V.R., Patle, L.B., Chaudhari, A.L., and Sonawane, G.H., 2015, Synthesis of Cu doped ZnO nanoparticles: Crystallographic, optical, FTIR, morphological and photocatalytic study, *J. Mater. Sci. Chem. Eng.*, 3 (7), 39–51.
- [34] Sriram, S., Lalithambika, K.C., and Thayumanavan, A., 2017, Experimental and theoretical investigations of photocatalytic activity of Cu doped ZnO nanoparticles, *Optik*, 139, 299–308.
- [35] Joseph, C.G., Taufiq-Yap, Y.H., and Krishnan, V., 2017, Ultrasonic assisted photolytic degradation of reactive black 5 (RB5) simulated wastewater, *ASEAN J. Chem. Eng.*, 17 (2), 37–50.
- [36] Sanjaya, H., Rida, P., and Ningsih, S.K.W., 2017, Degradasi methylene blue menggunakan katalis ZnO-PEG dengan metode fotosonolisis, *Eksakta*, 18 (2), 21–29.

### Supplementary Data

This supplementary data is a part of paper entitled "Synthesis, Antiproliferative and Antimalarial Activities of Dinuclear Silver(I) Complexes with Triphenylphosphine and Thiosemicarbazones Ligands".

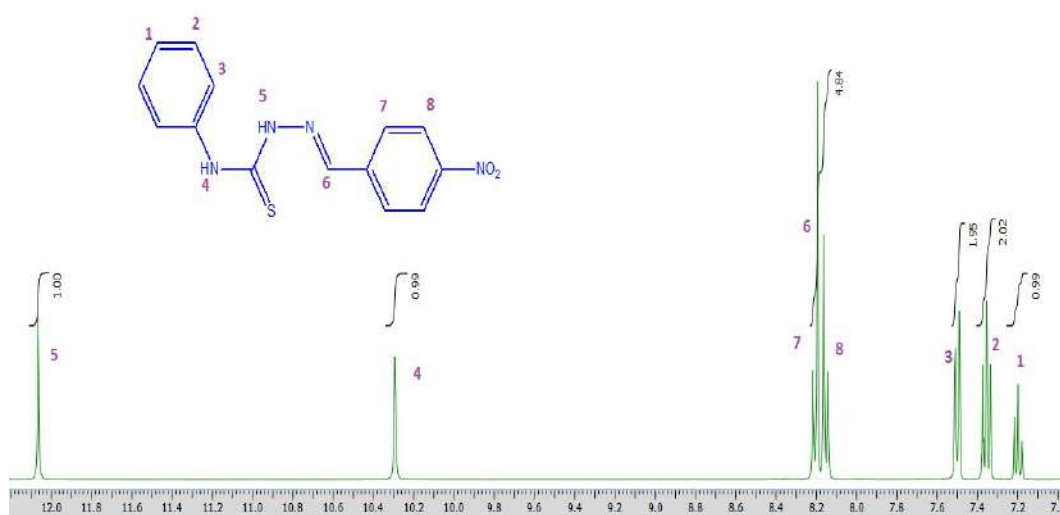


Fig 1.  $^1\text{H-NMR}$  of ligand 1 (L1)

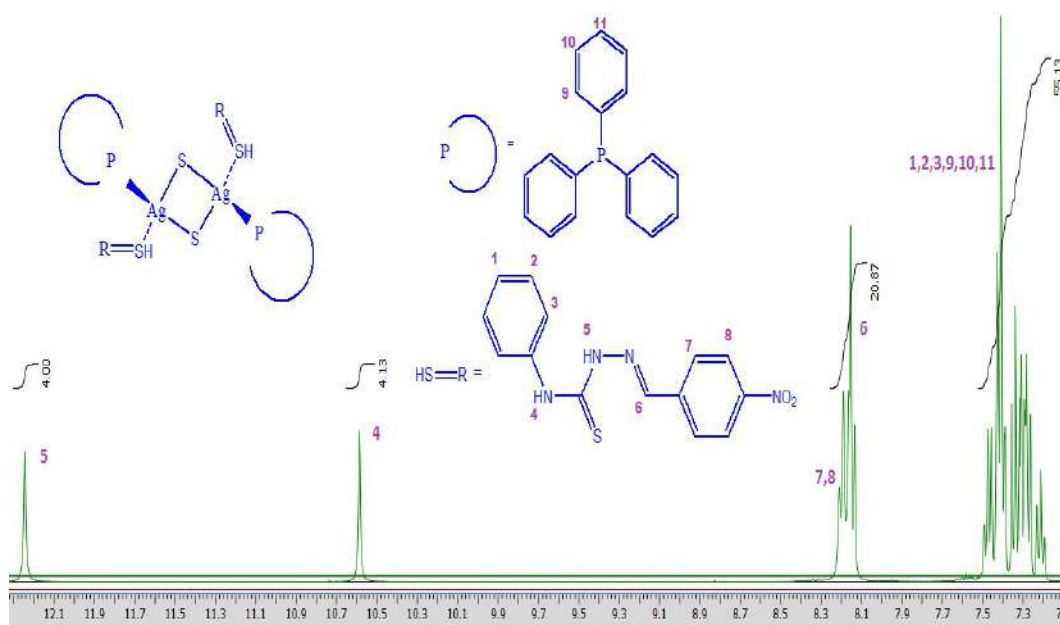
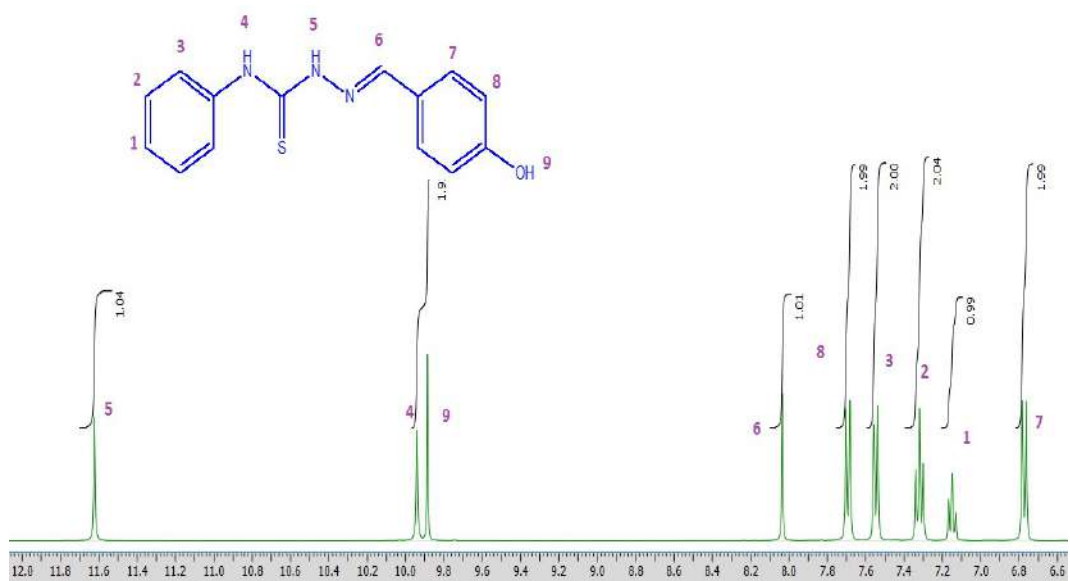
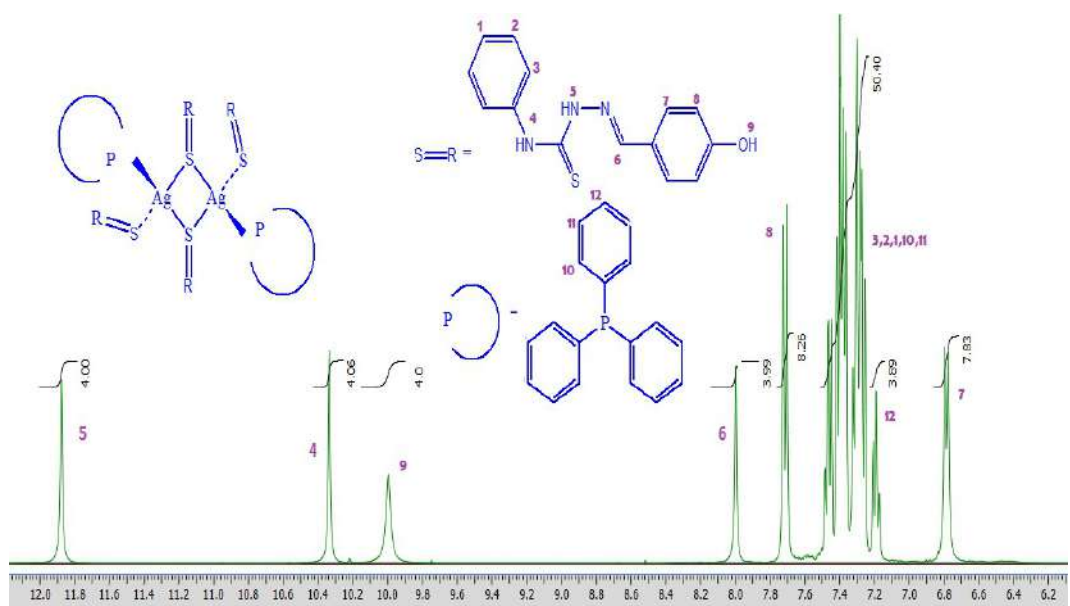


Fig 2.  $^1\text{H-NMR}$  of complex 1 (P1)

Fig 3. <sup>1</sup>H-NMR of ligand 2 (L2)Fig 4. <sup>1</sup>H-NMR of complex 2 (P2)

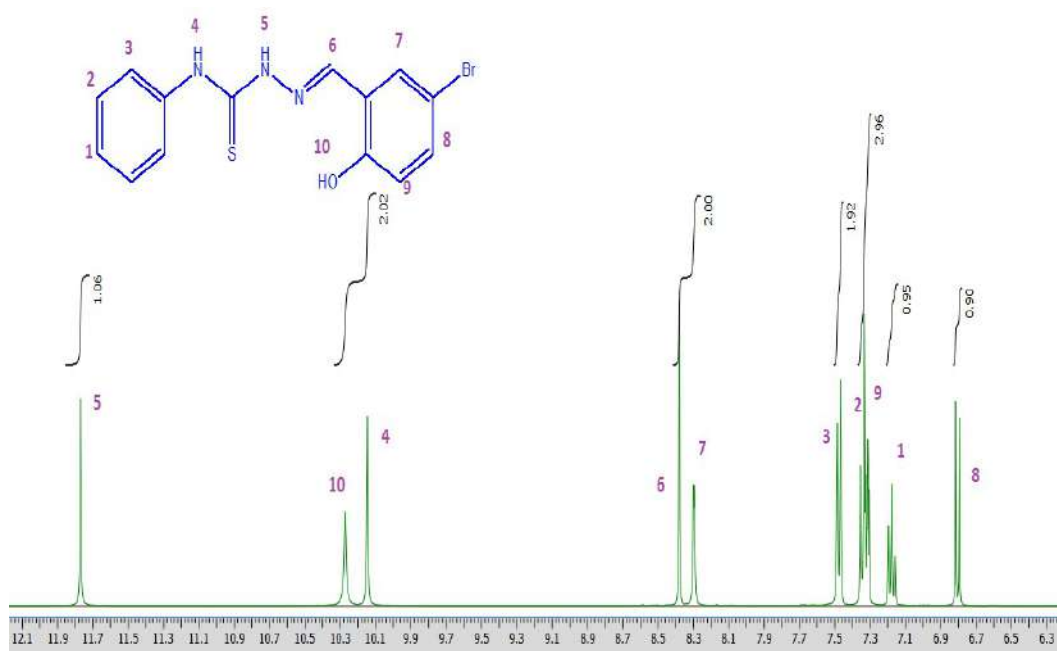


Fig 5. <sup>1</sup>H-NMR of ligand 3 (L3)

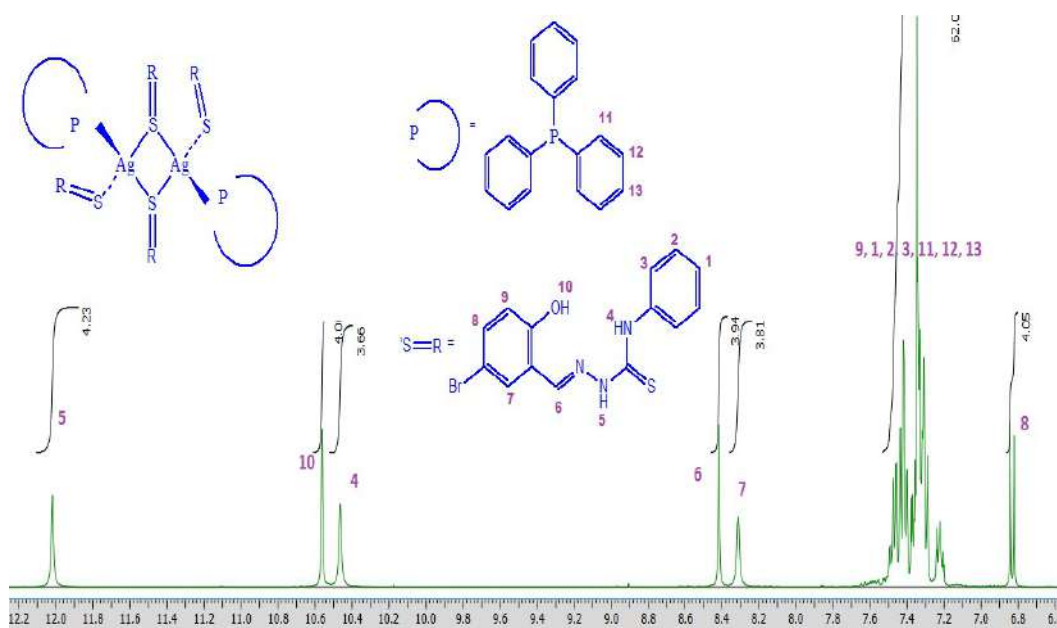
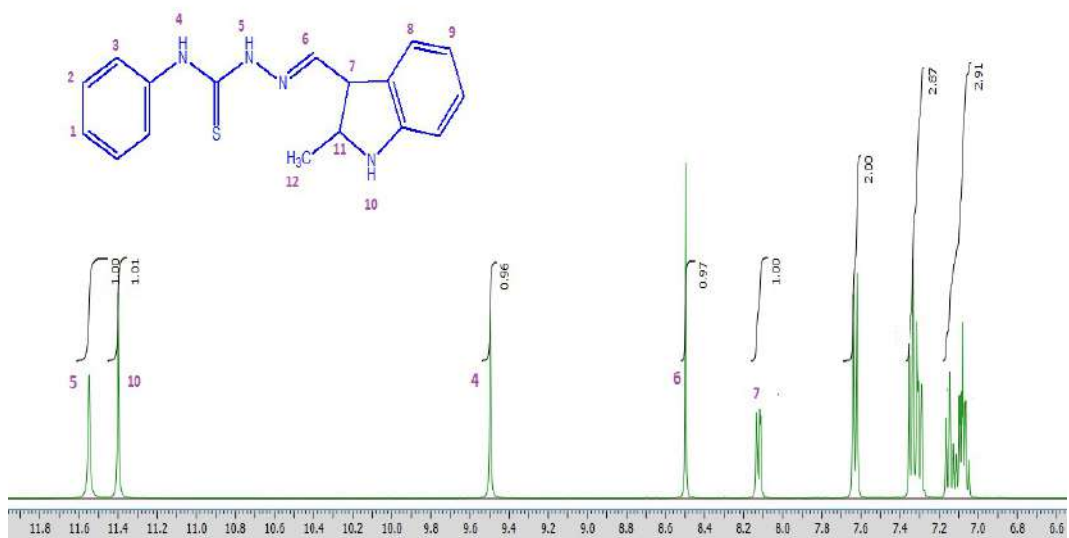
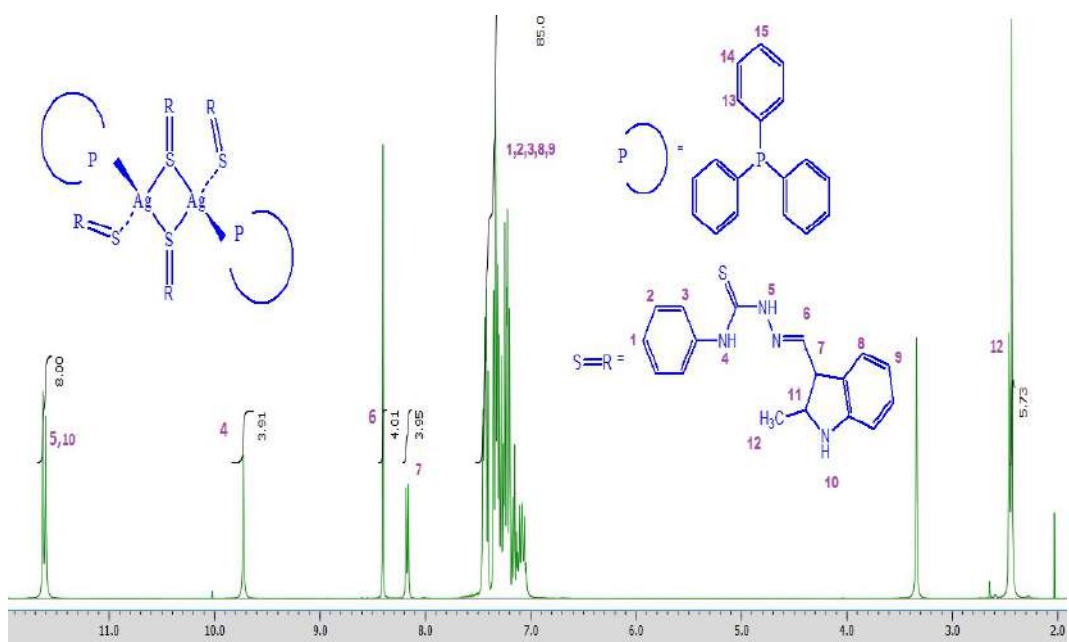


Fig 6. <sup>1</sup>H-NMR of complex 3 (P3)

Fig 7.  $^1\text{H-NMR}$  of ligand 4 (L4)Fig 8.  $^1\text{H-NMR}$  of complex 4 (P4)

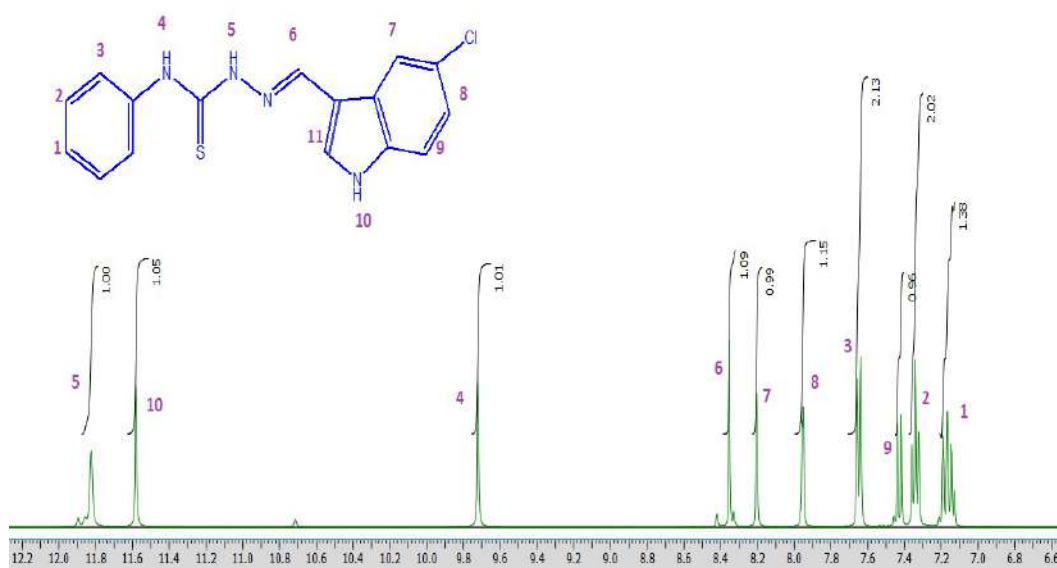


Fig 9. <sup>1</sup>H-NMR of ligand 5(L5)

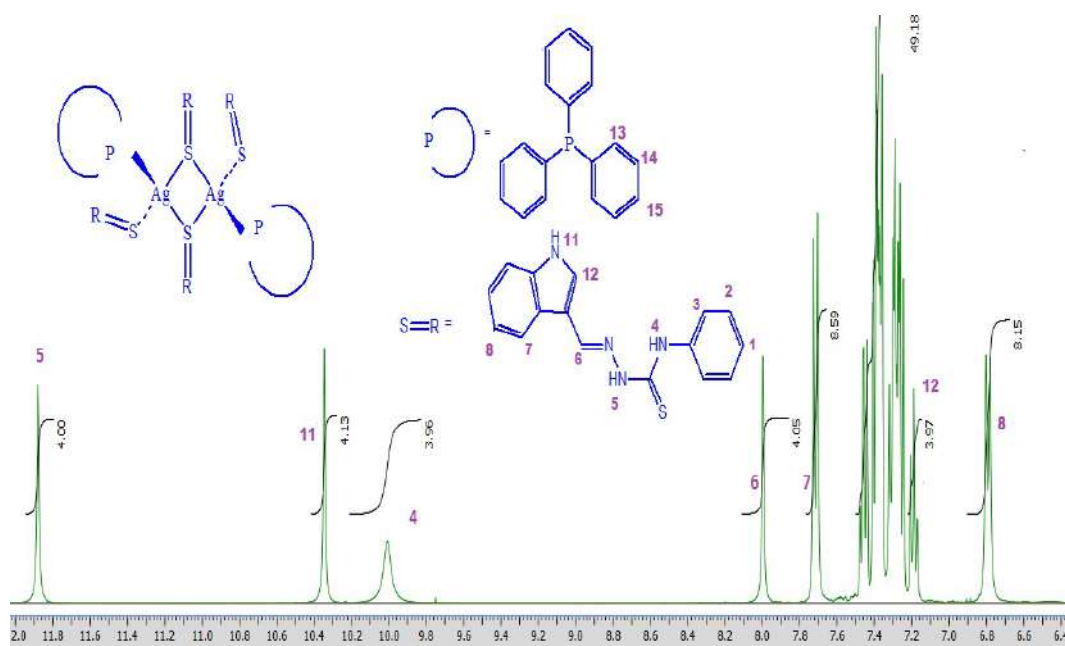
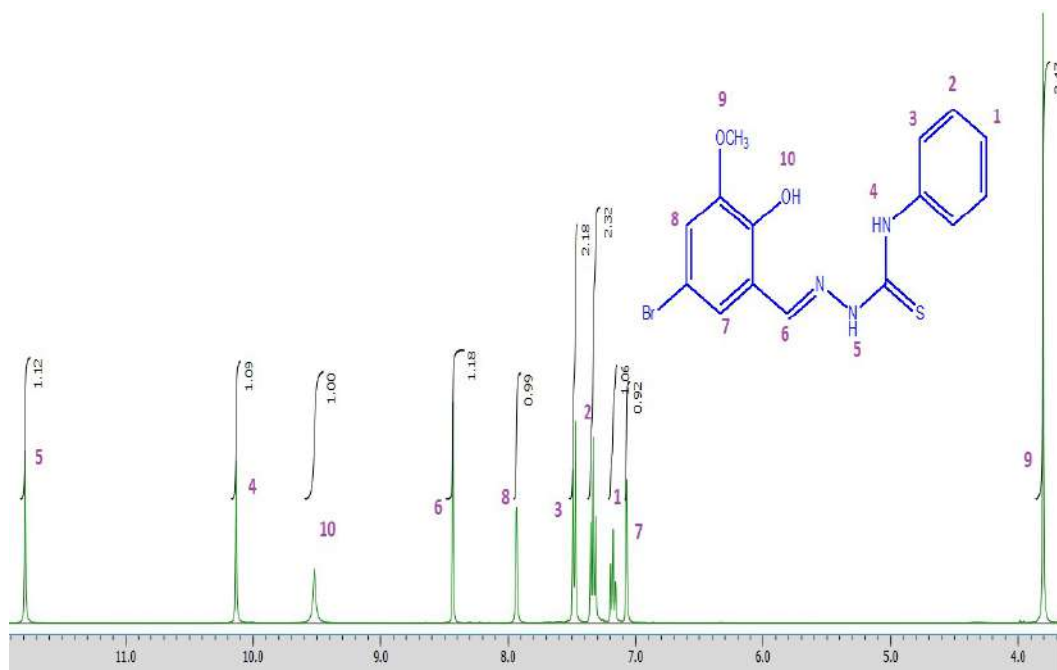
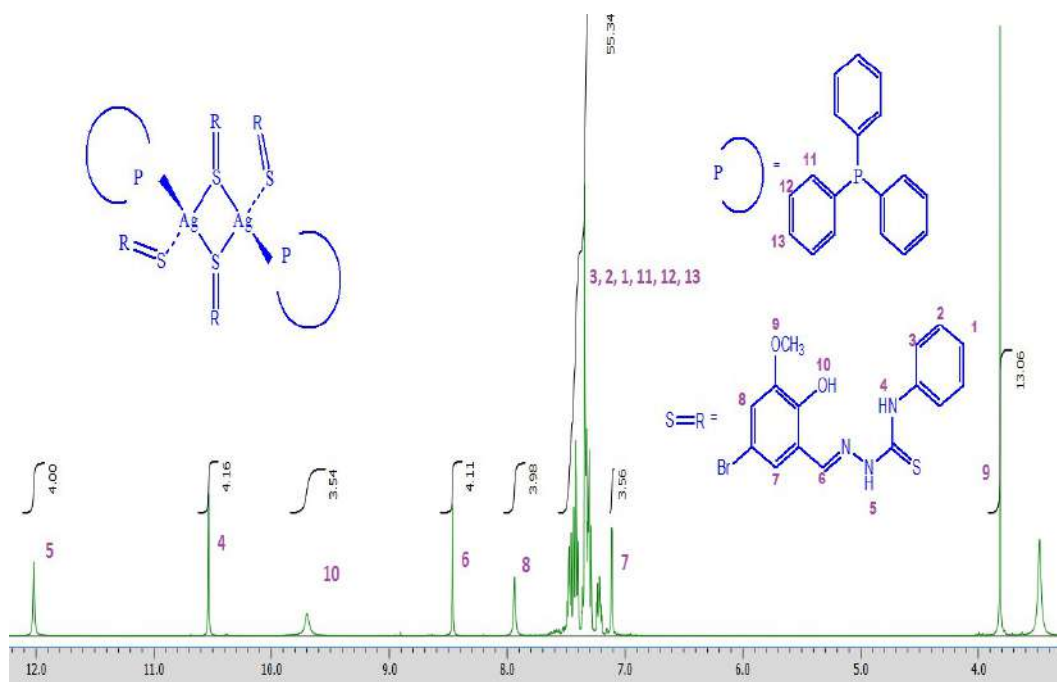


Fig 10. <sup>1</sup>H-NMR of complex 5 (P5)

Fig 11. <sup>1</sup>H-NMR of ligand 6 (L6)Fig 12. <sup>1</sup>H-NMR of complex 6 (P6)

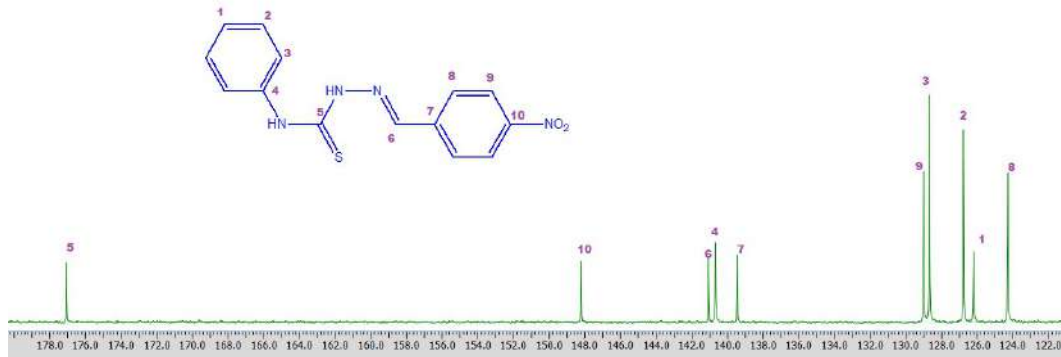


Fig 13.  $^{13}\text{C}$ -NMR of ligand 1 (L1)

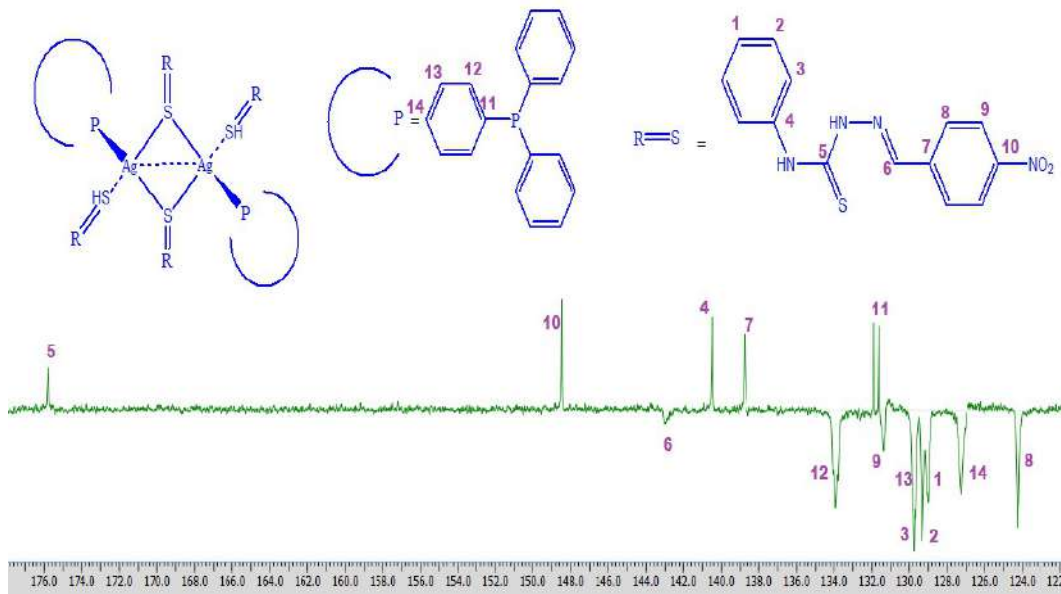
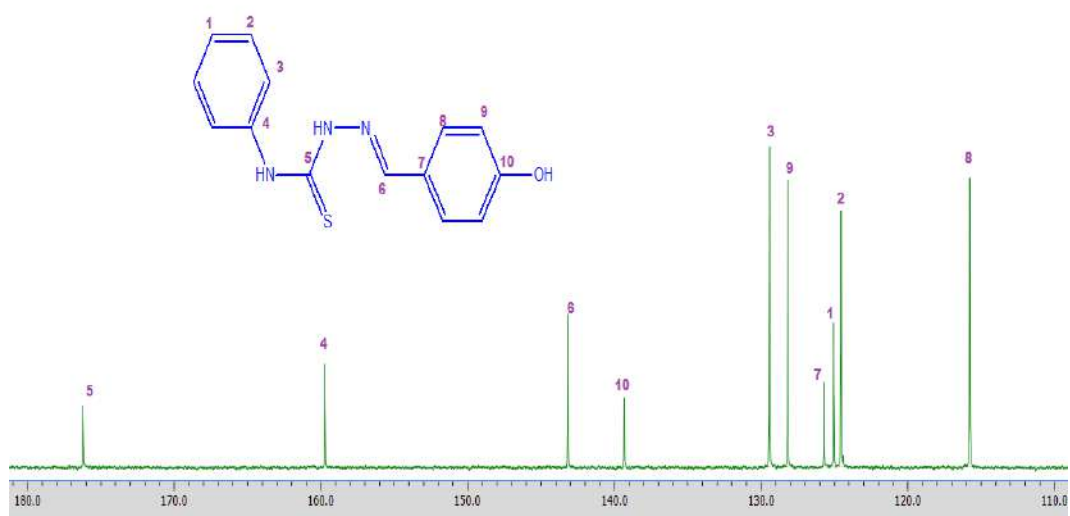
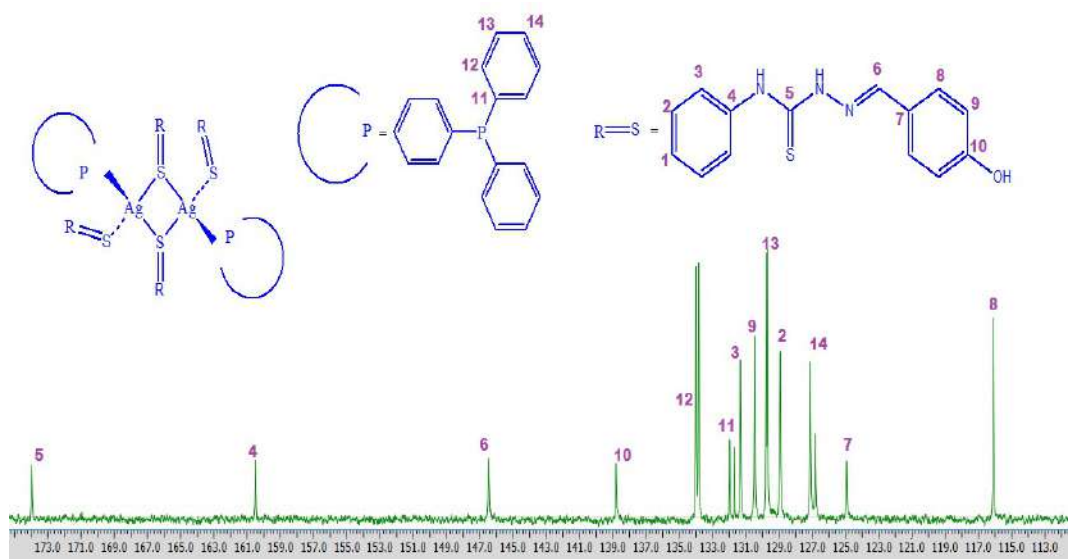


Fig 14.  $^{13}\text{C}$ -NMR of complex 1 (P1)



Fig 15.  $^{13}\text{C}$ -NMR of ligand 2 (L2)Fig 16.  $^{13}\text{C}$ -NMR of complex 2 (P2)

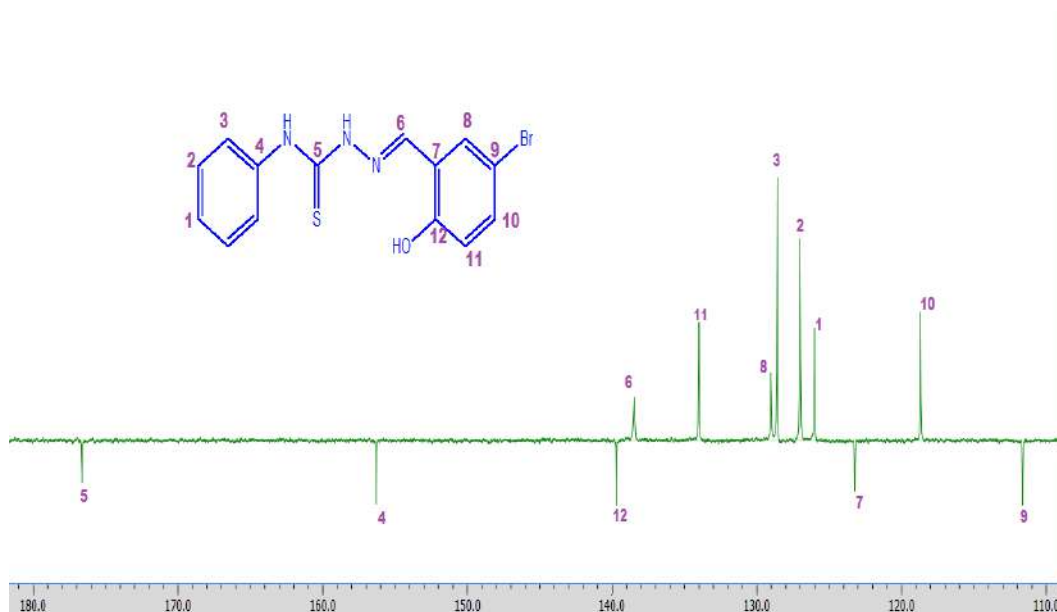


Fig 17.  $^{13}\text{C}$ -NMR of ligand 3 (L3)

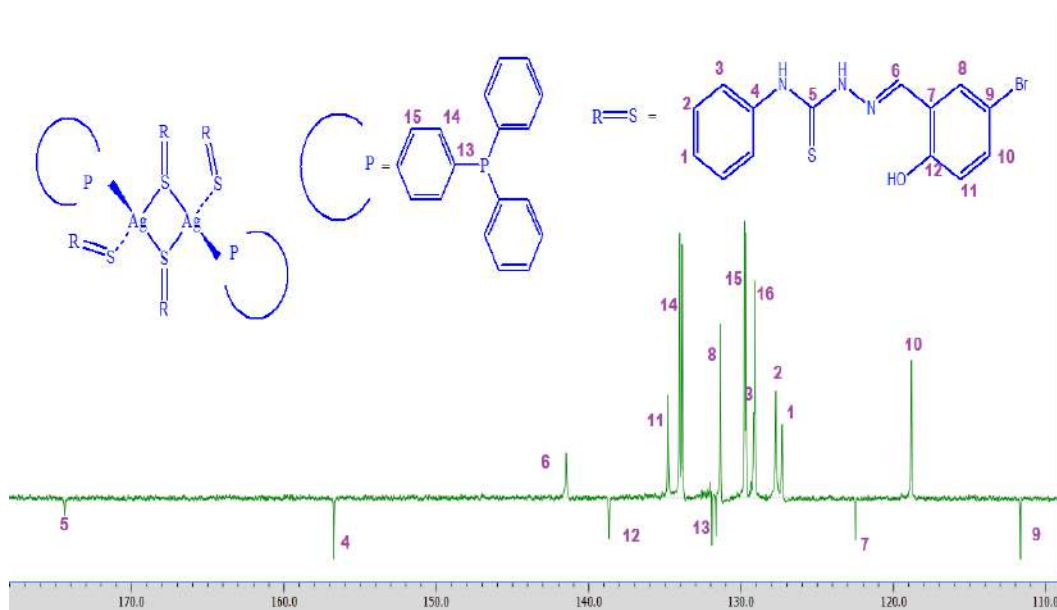
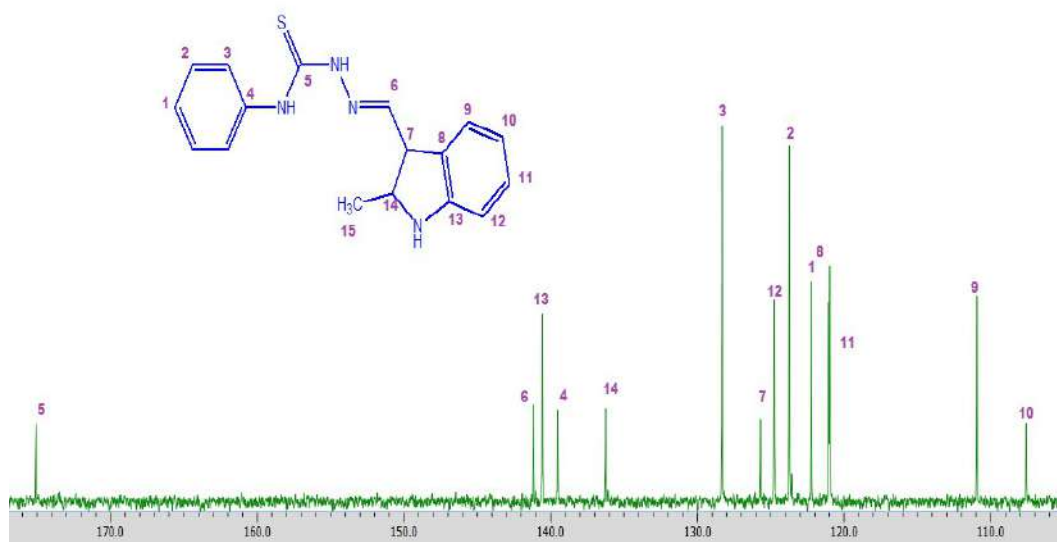
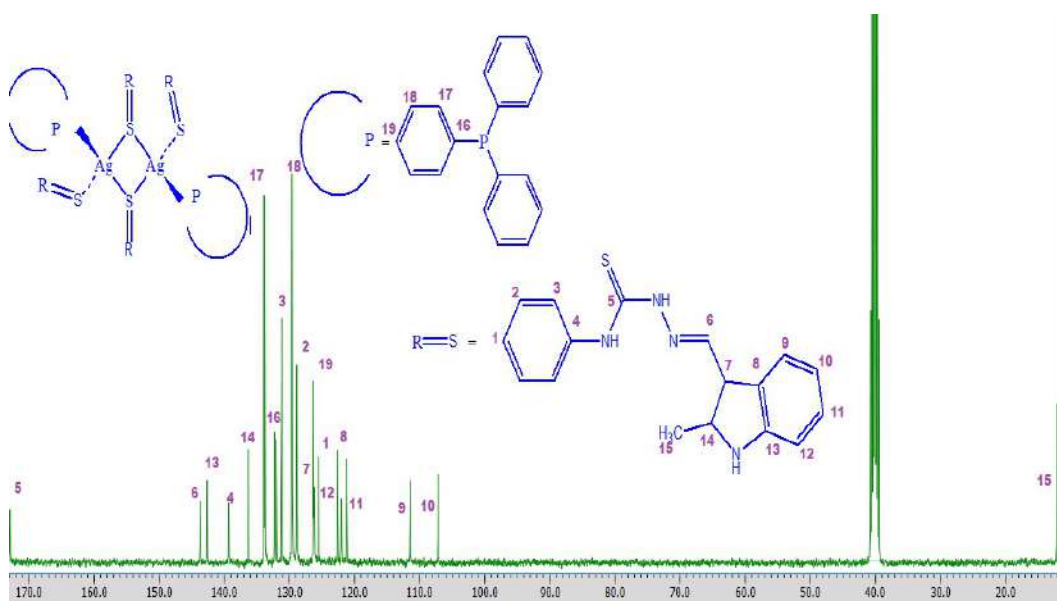


Fig 18.  $^{13}\text{C}$ -NMR of complex 3 (P3)

Fig 19. <sup>13</sup>C-NMR of ligand 4 (L4)Fig 20. <sup>13</sup>C-NMR of complex 4 (P4)

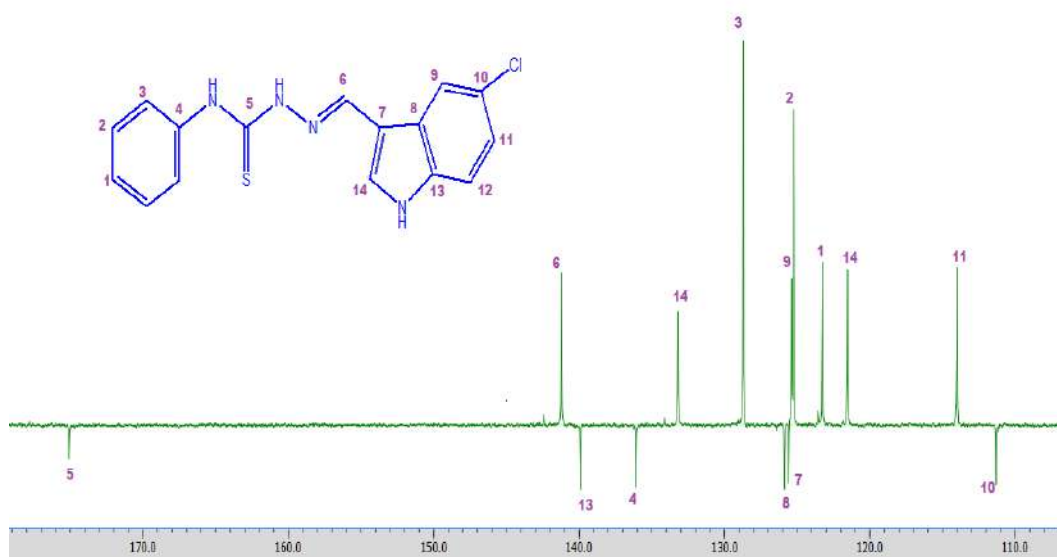


Fig 21. <sup>13</sup>C-NMR of ligand 5 (L5)

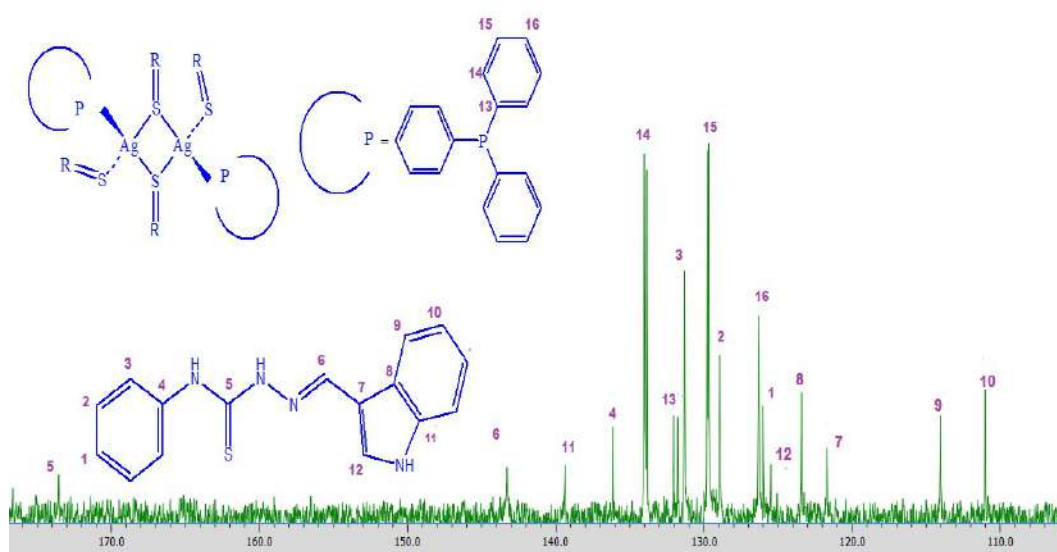
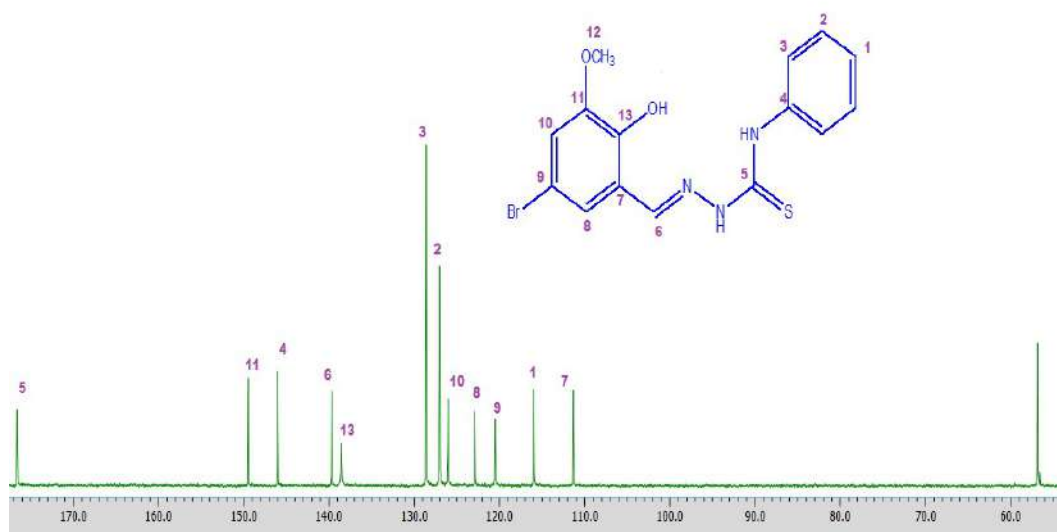
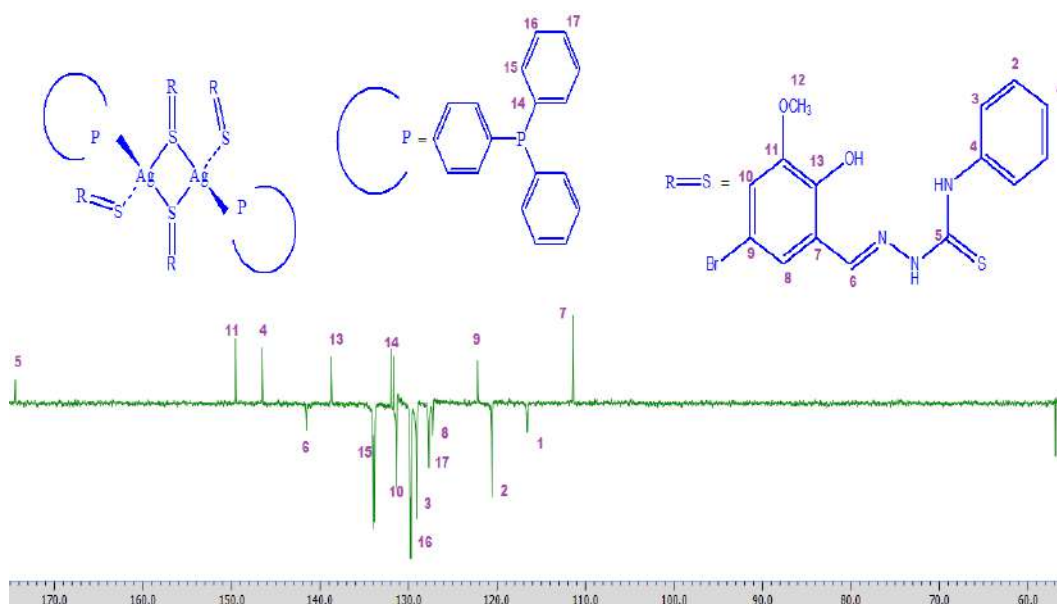


Fig 22. <sup>13</sup>C-NMR of complex 5 (P5)

Fig 23.  $^{13}\text{C}$ -NMR of ligand 6 (L6)Figure 24.  $^{13}\text{C}$ -NMR of complex 6 (P6)

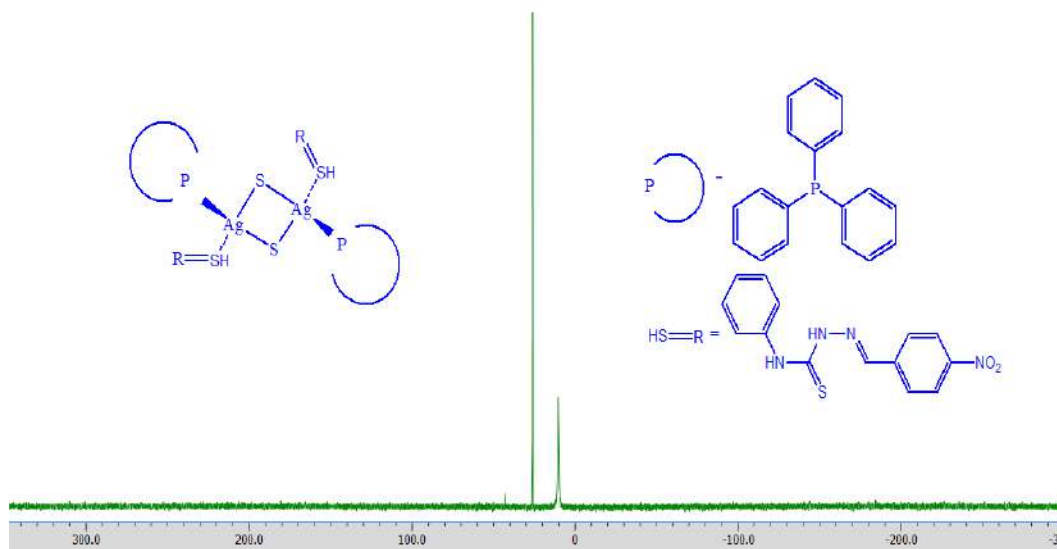


Fig 25.  $^{31}\text{P}$ -NMR of complex 1 (P1)

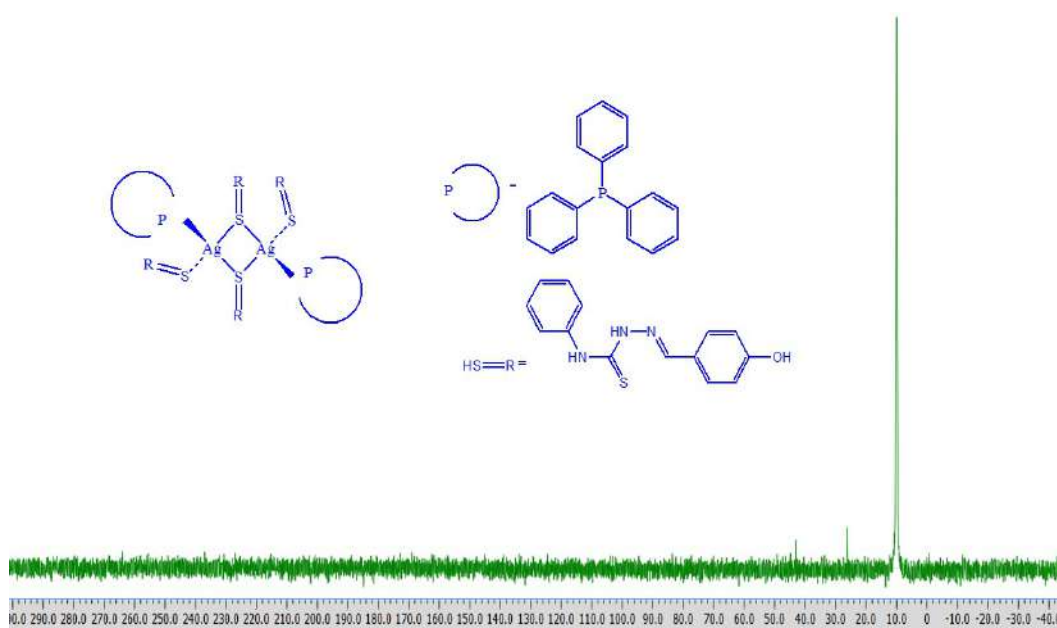
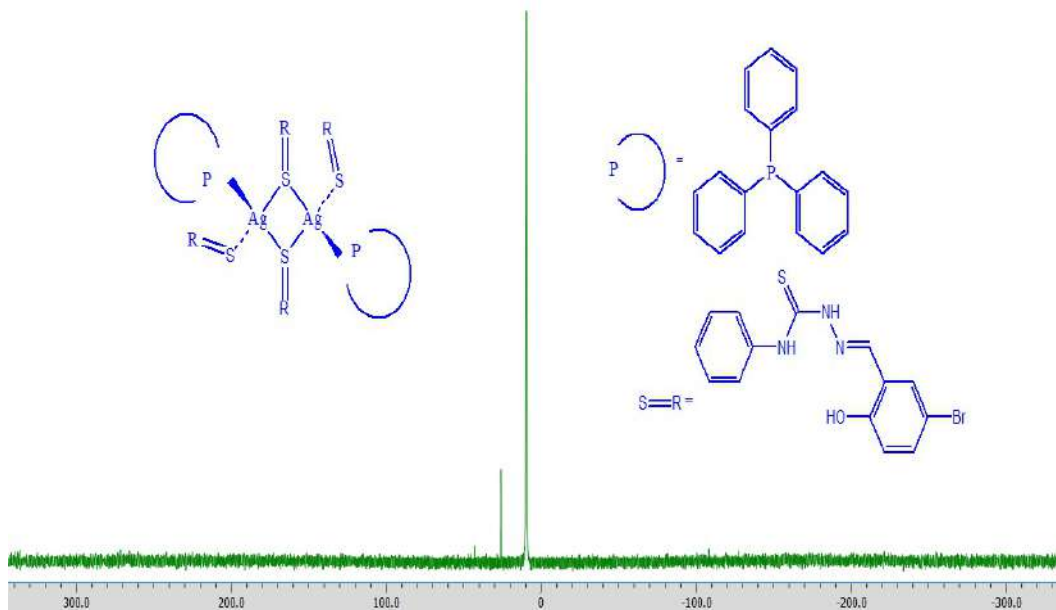
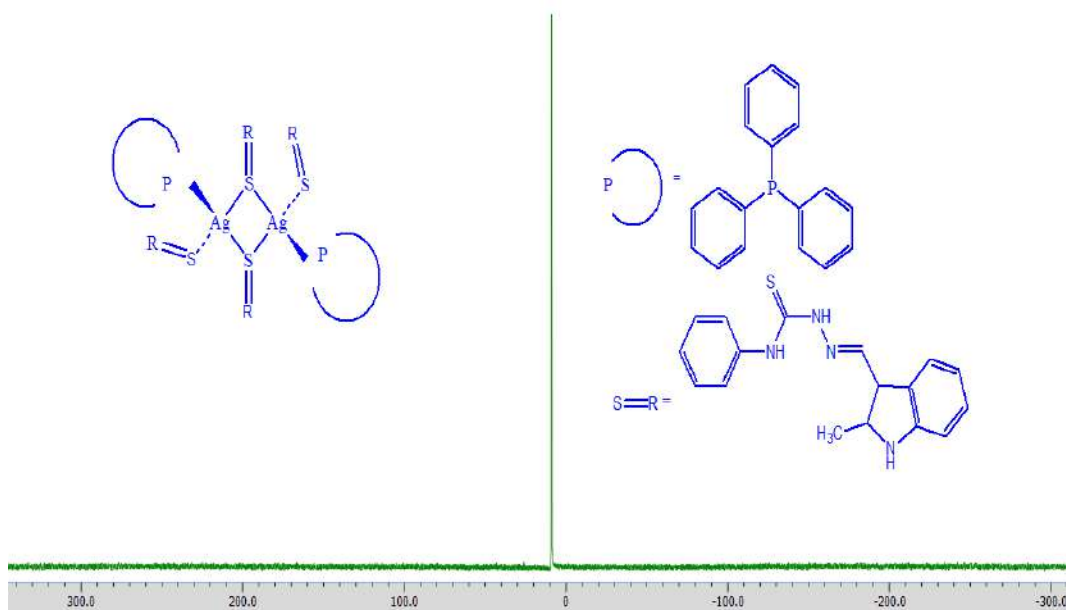


Fig 26.  $^{31}\text{P}$ -NMR of complex 2 (P2)

Fig 27.  $^{31}\text{P}$ -NMR of complex 3 (P3)Fig 28.  $^{31}\text{P}$ -NMR of complex 4 (P4)

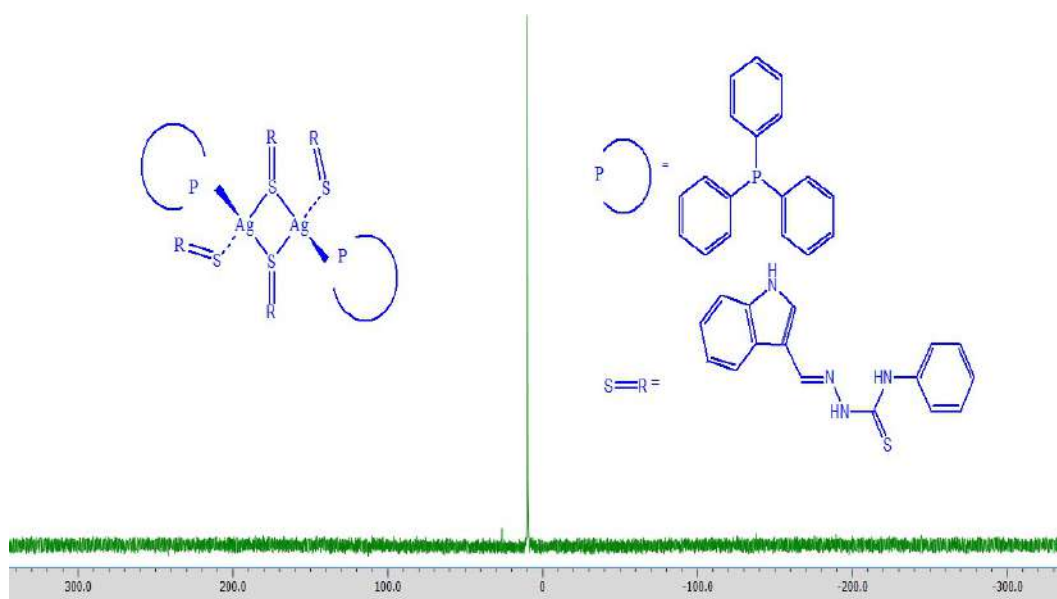


Fig 29.  $^{31}\text{P}$ -NMR of complex 5 (P5)

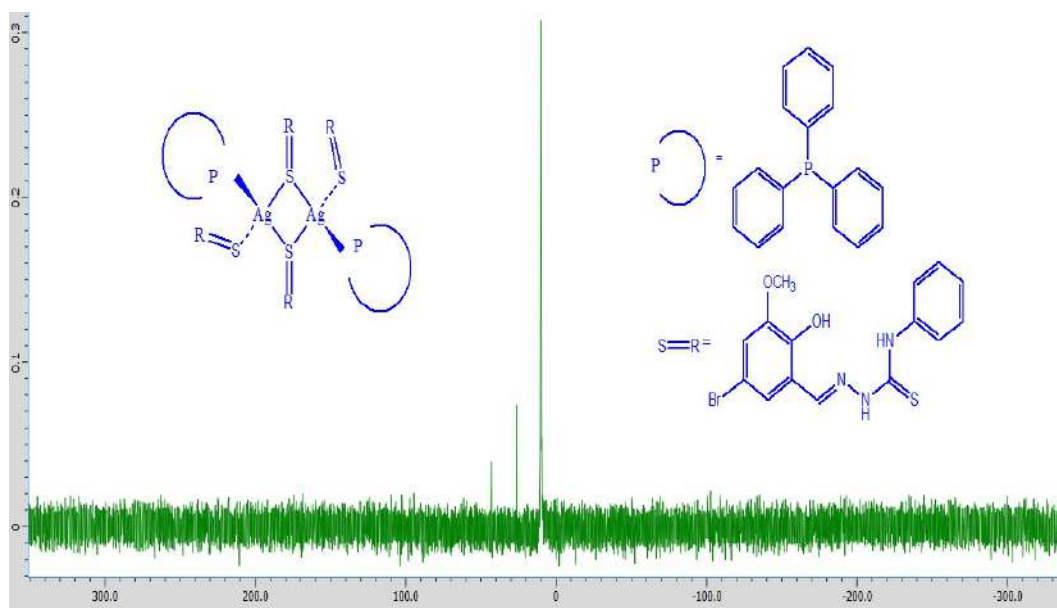
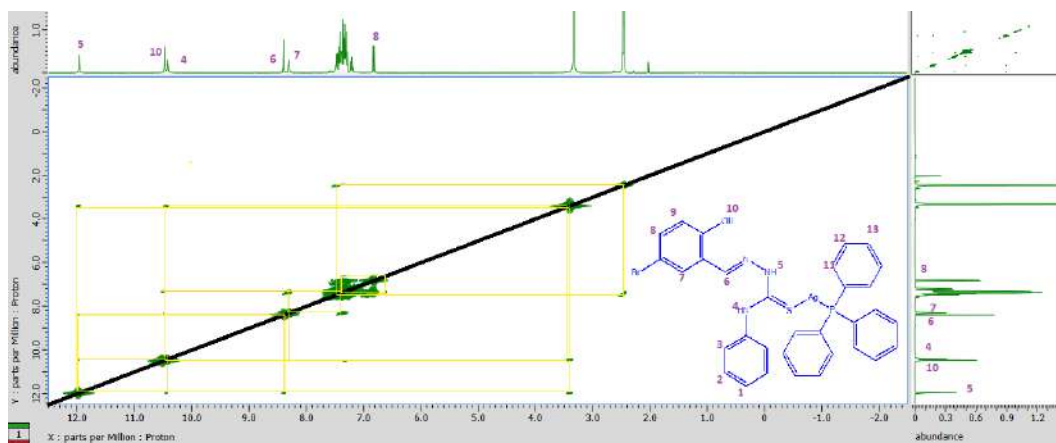
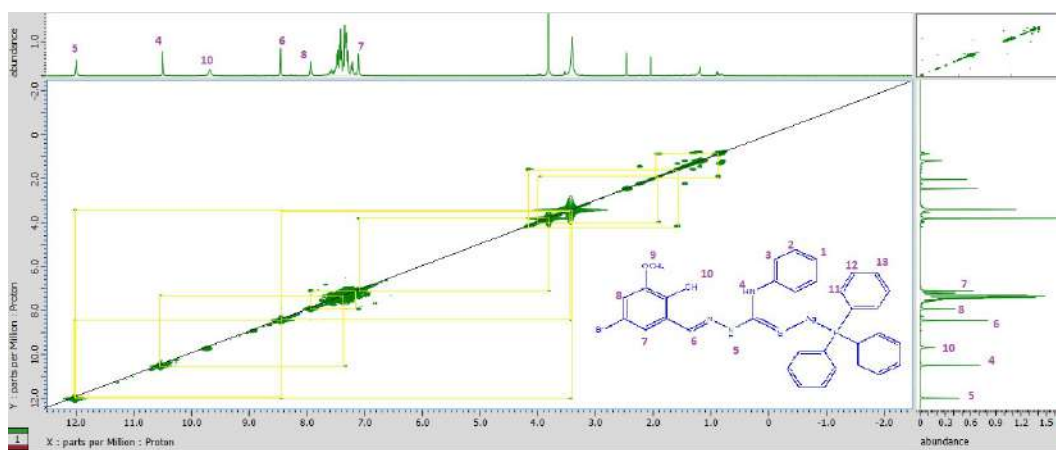


Fig 30.  $^{31}\text{P}$ -NMR of complex 6 (P6)



Fig 31. <sup>1</sup>H-COSY of complex P3Fig 32. <sup>1</sup>H-COSY of complex P6

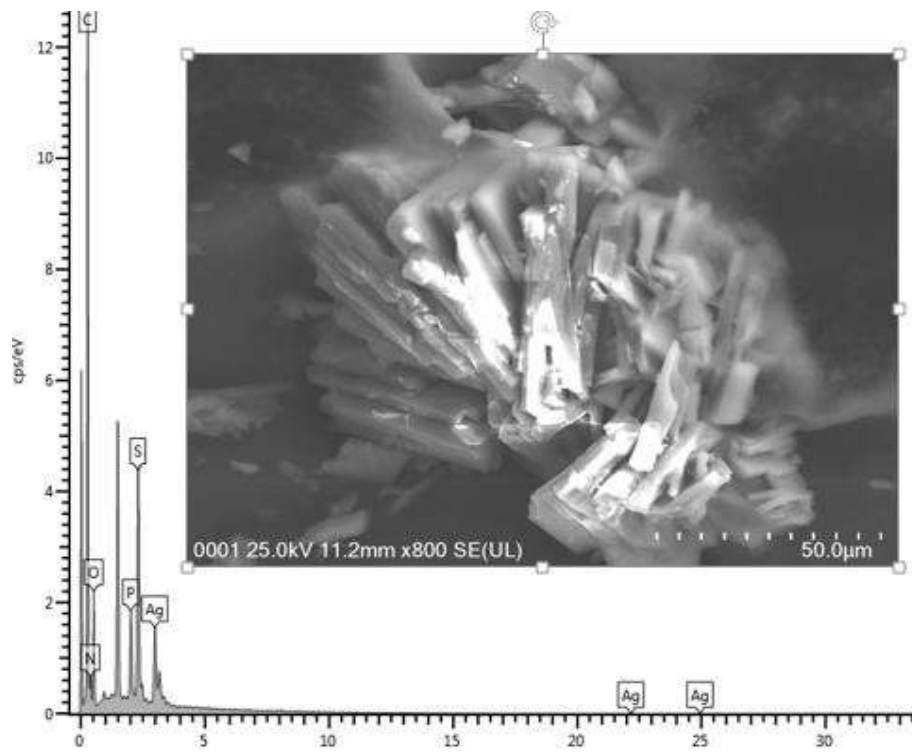


Fig 33. EDX data on complex P1

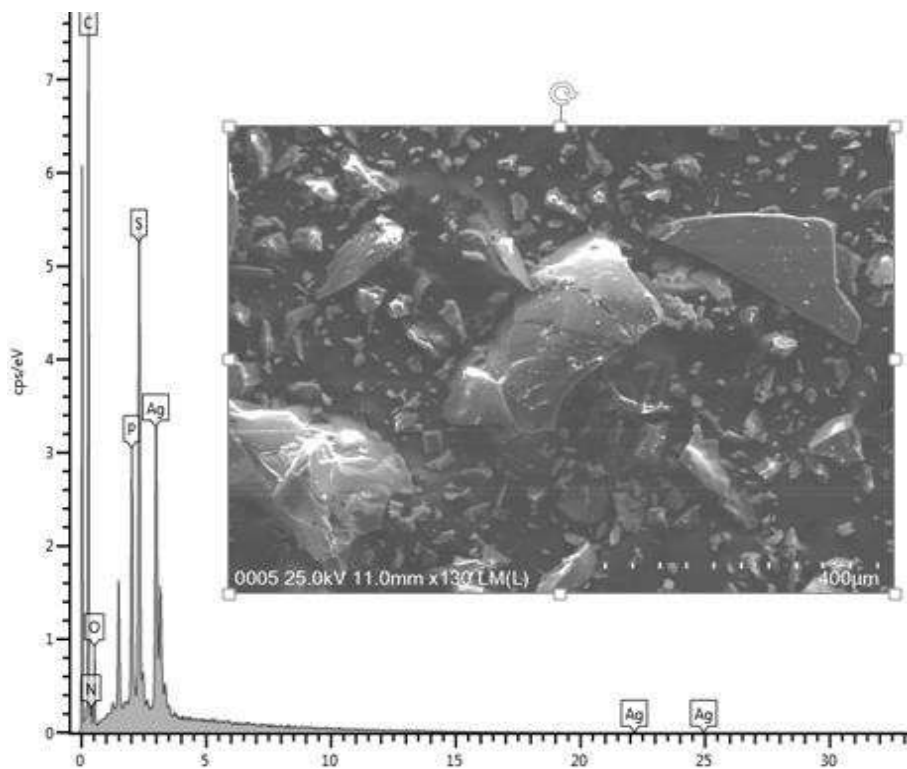


Fig 34. EDX data on complex P2

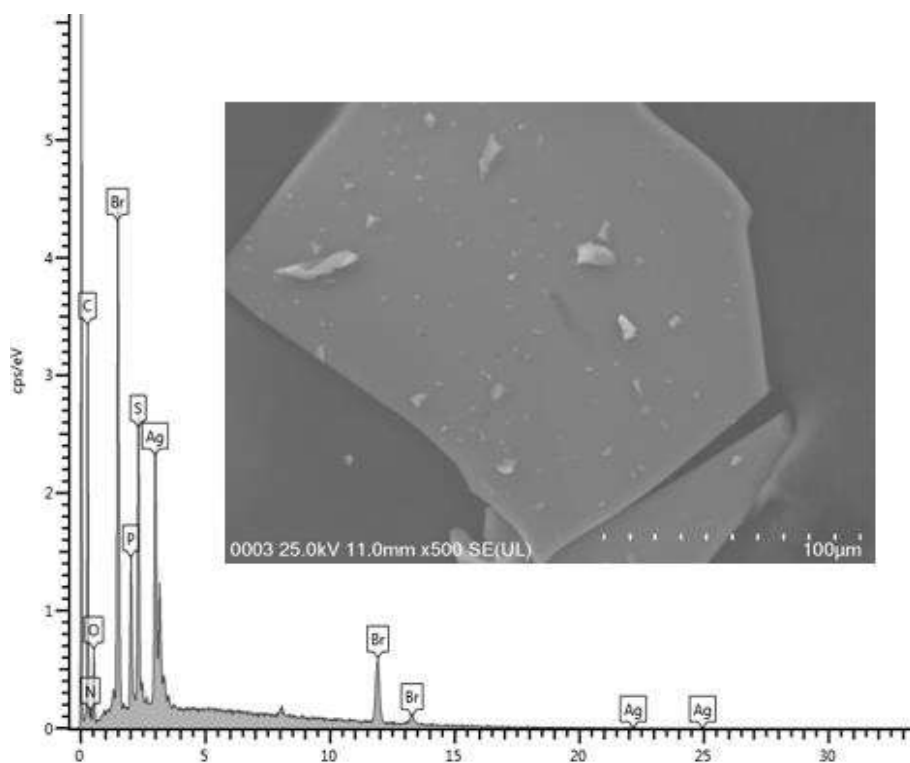


Fig 35. EDX data on complex P3

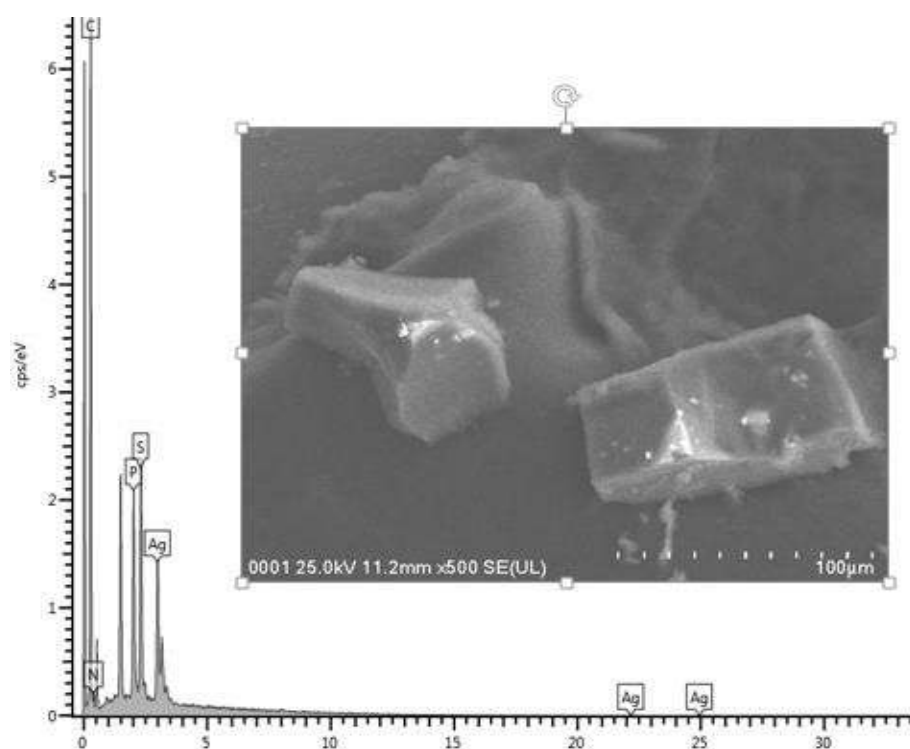


Fig 36. EDX data on complex P4

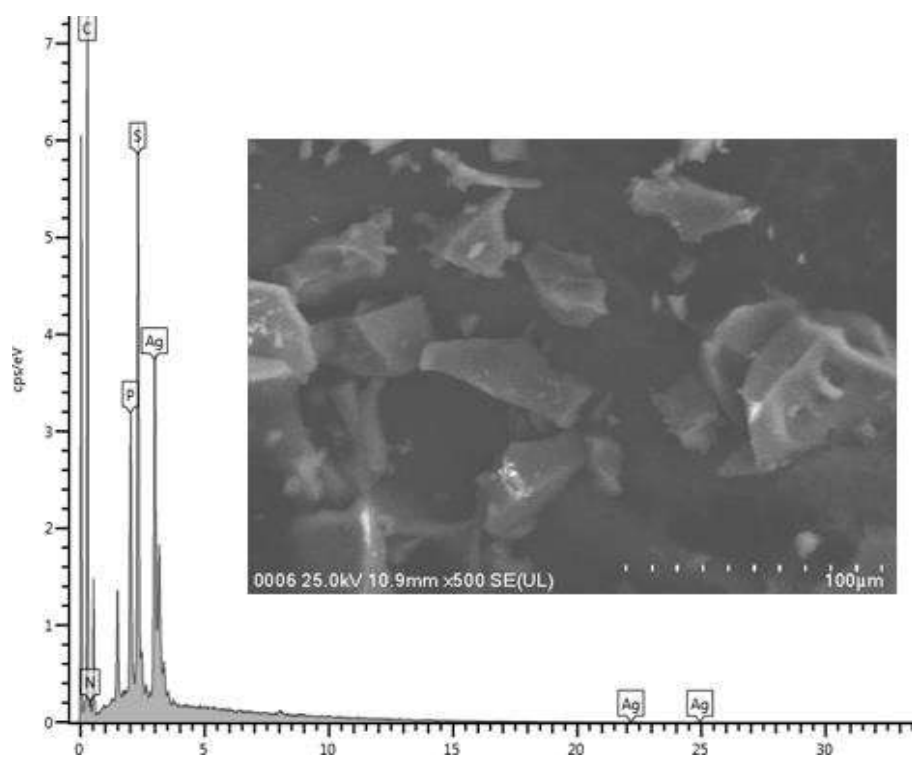


Fig 37. EDX data on complex P5

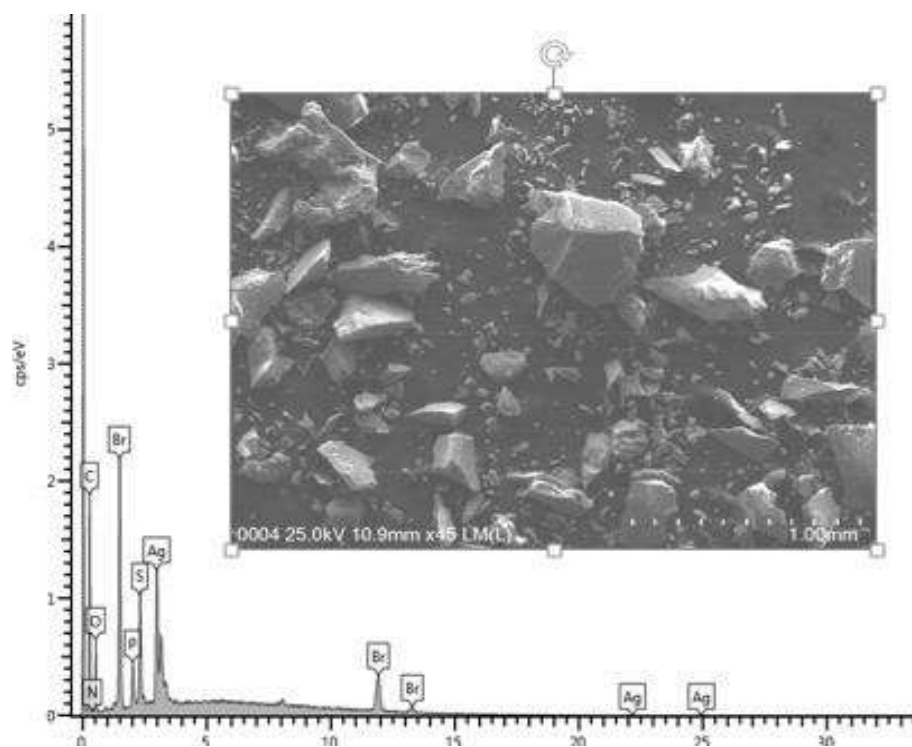


Fig 38. EDX data on complex P6

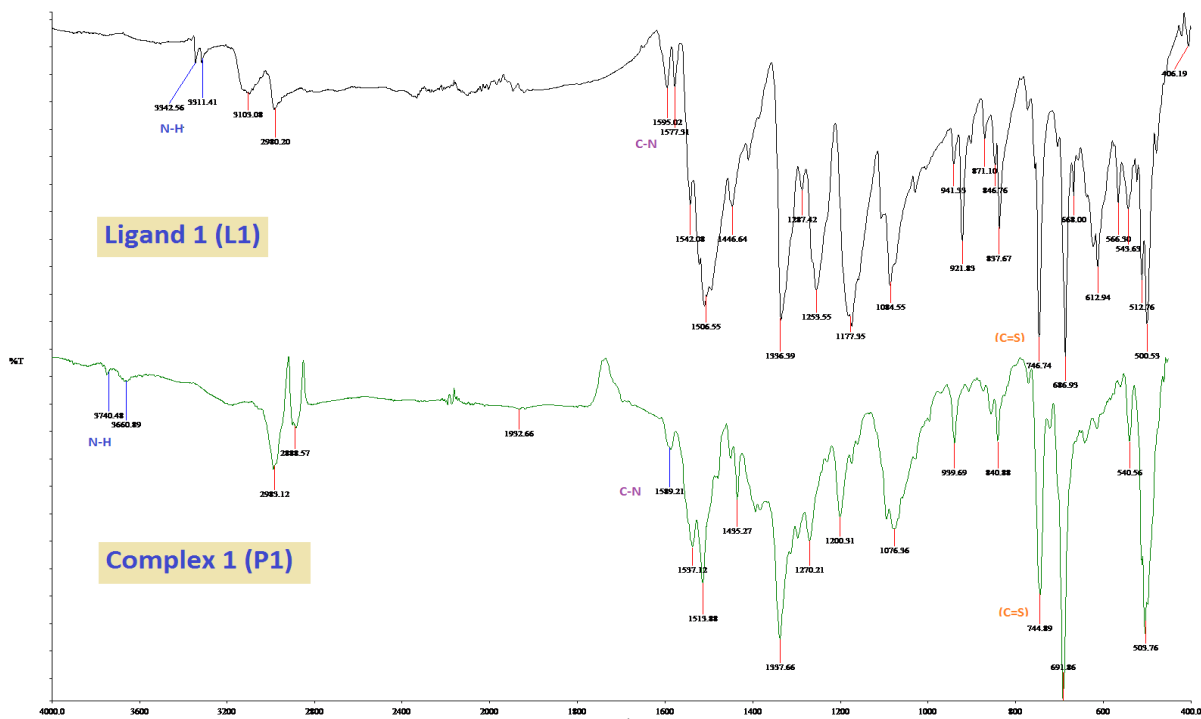


Fig 39. IR data for L1 and P1

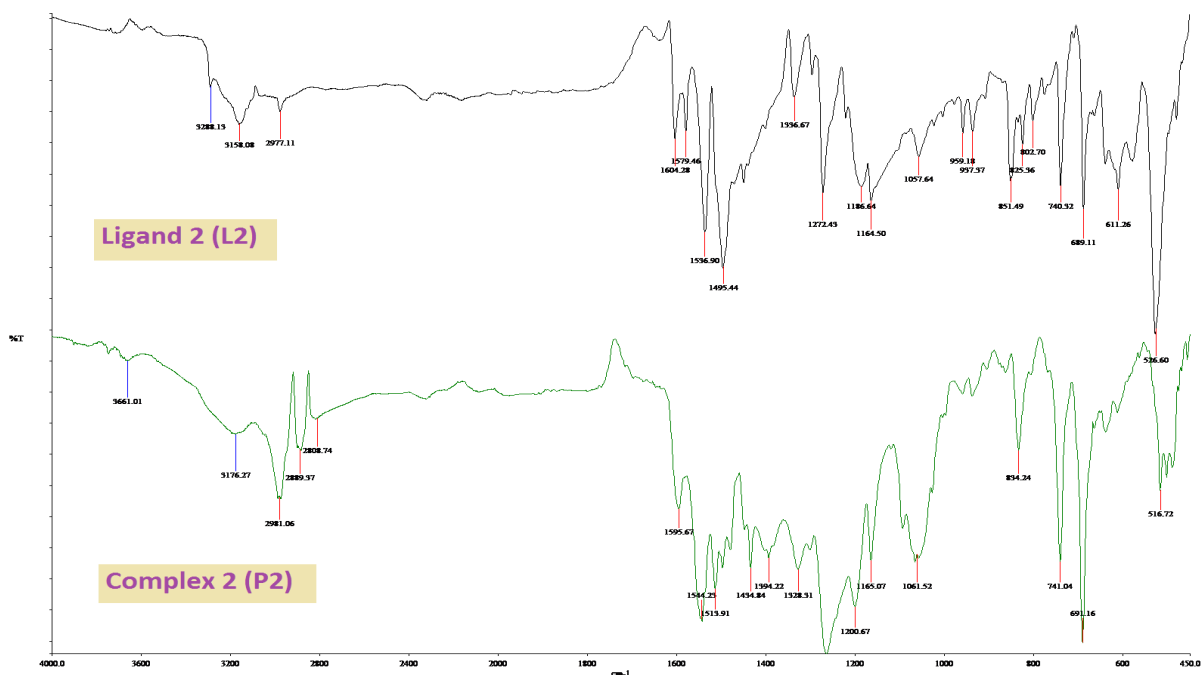


Fig 40. IR data for L2 and P2

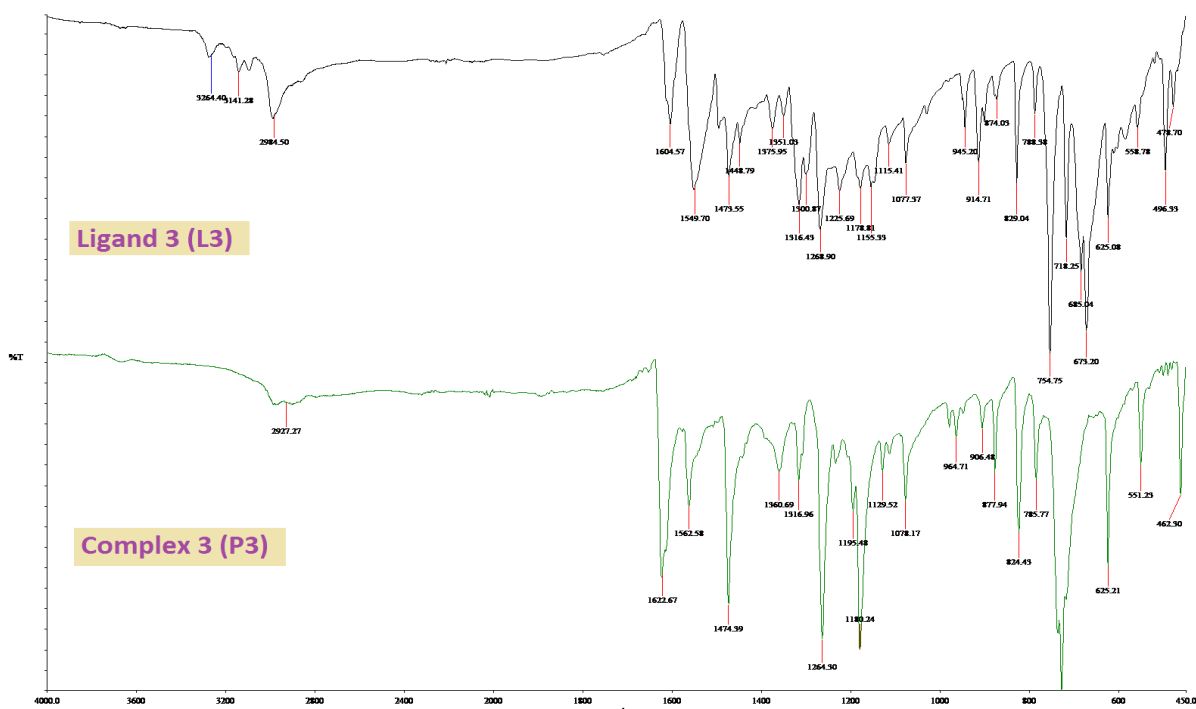


Fig 41. IR data for L3 and P3

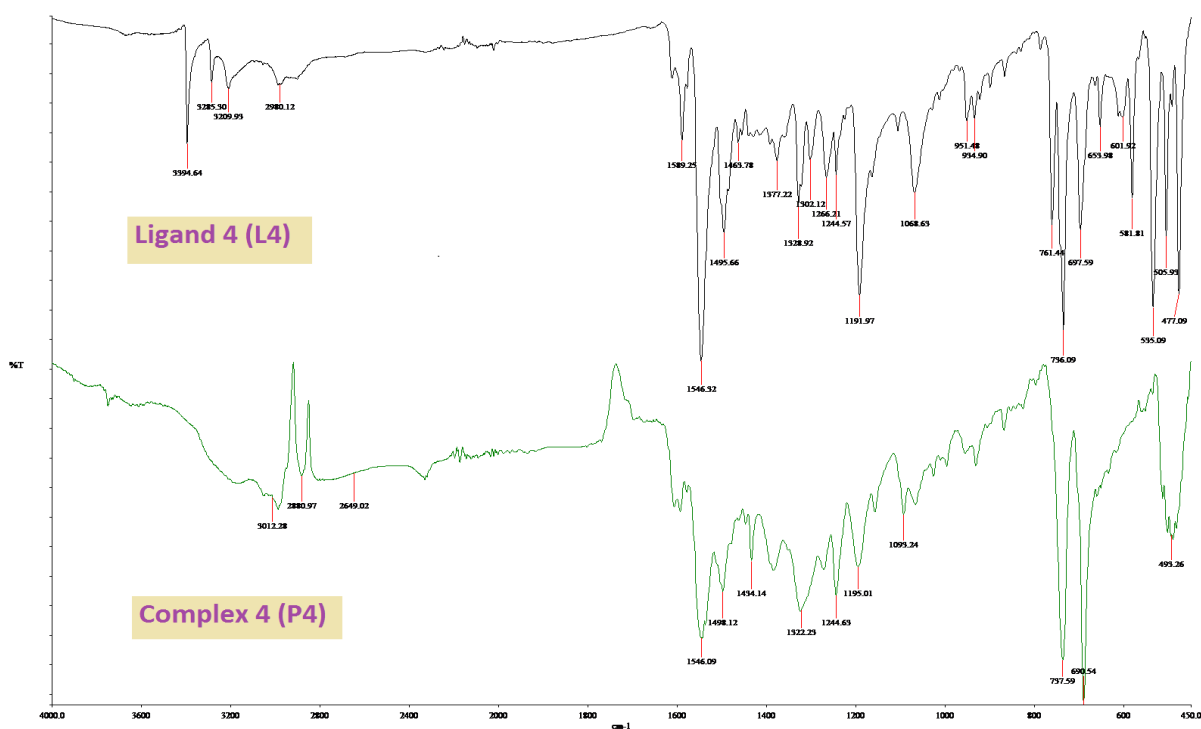


Fig 42. IR data for L4 and P4

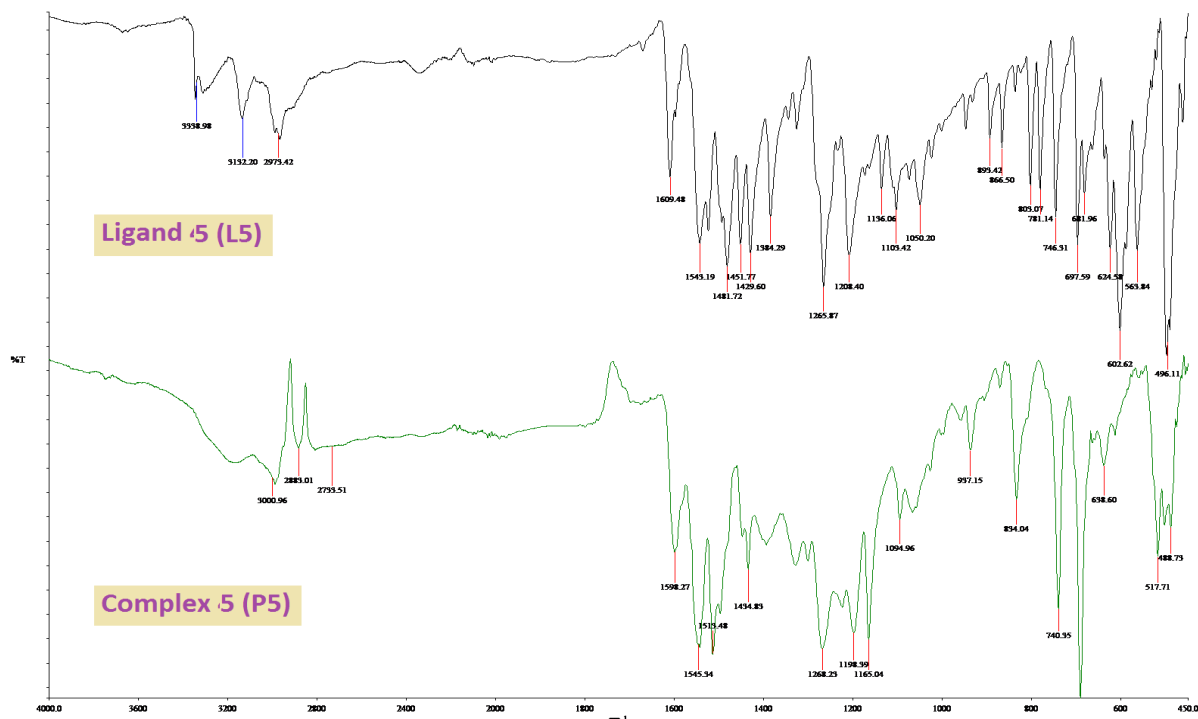


Fig 43. IR data for L5 and P5

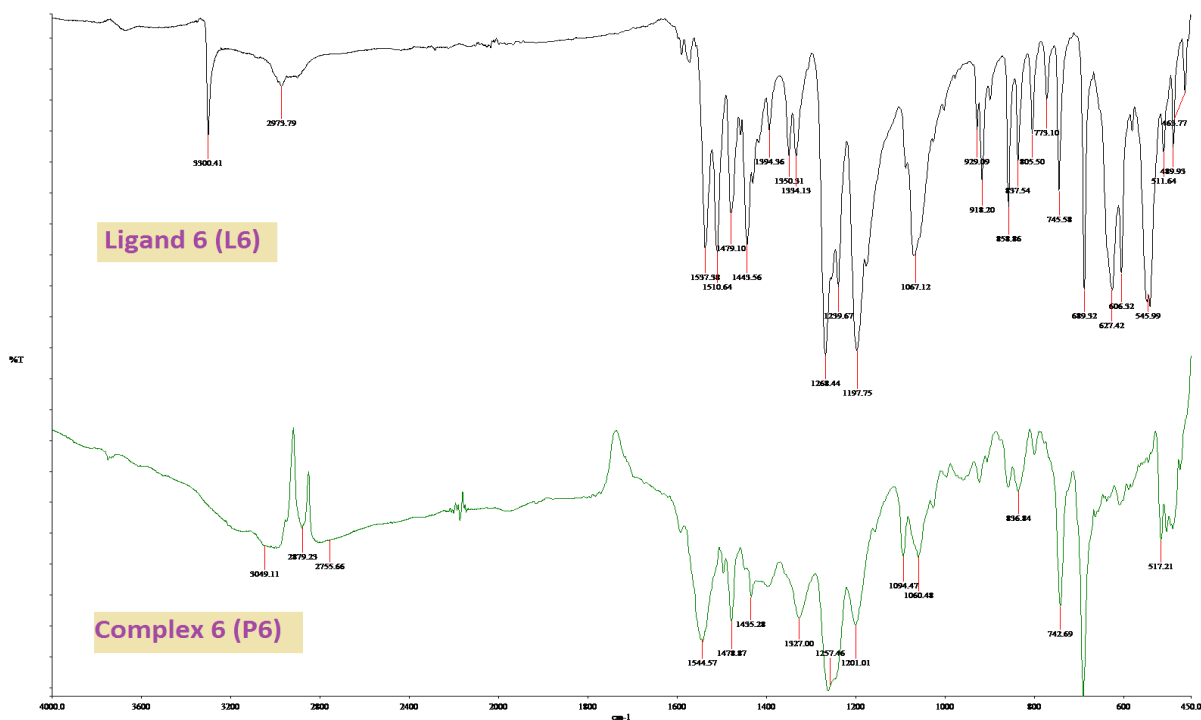
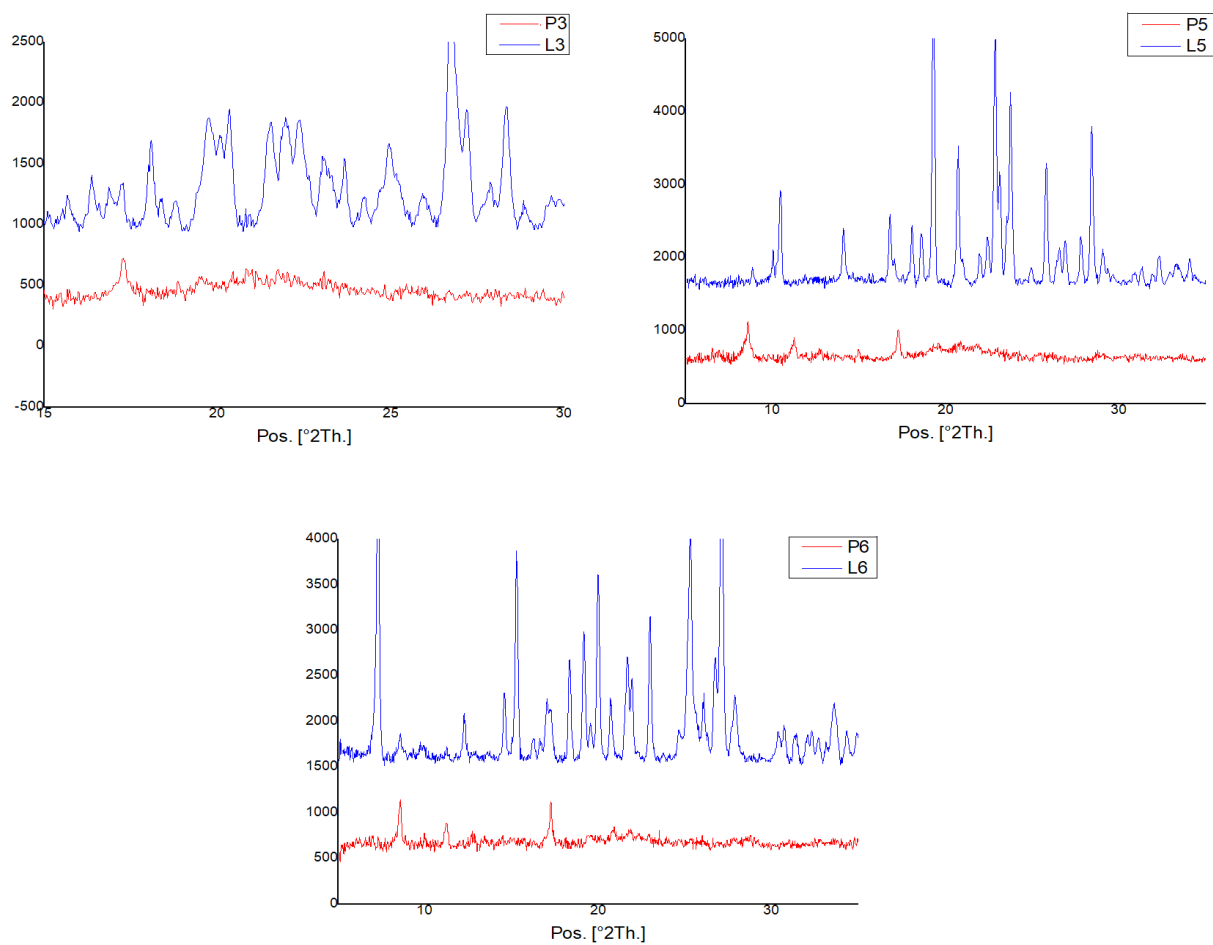


Fig 44. IR data for L6 and P6



**Fig 45.** PXRD diffratograms for ligands and complexes 3, 5 and 6



## Synthesis, Antiproliferative and Antimalarial Activities of Dinuclear Silver(I) Complexes with Triphenylphosphine and Thiosemicarbazones Ligands

Nur Adila Fatin Mohd Khir<sup>1</sup>, Mohd Ridzuan Mohd Abd Razak<sup>2</sup>, Fariza Juliana Nordin<sup>3</sup>, Nur Rahimah Fitrah Mohd Sofyan<sup>1</sup>, Nor Fadilah Rajab<sup>3</sup>, and Rozie Sarip<sup>1\*</sup>

<sup>1</sup>Department of Chemistry, Faculty of Science, University of Malaya (UM), Lembah Pantai, 50603 Kuala Lumpur, Malaysia

<sup>2</sup>Bioassay Unit, Herbal Medicine Research Centre (HMRC), Institute for Medical Research (IMR), Jl. Pahang, 50588 Kuala Lumpur, Malaysia

<sup>3</sup>Faculty of Health Sciences, Universiti Kebangsaan Malaysia (UKM), Kuala Lumpur Campus, Jl. Raja Muda Abdul Aziz, 50300 Kuala Lumpur, Malaysia

### \* Corresponding author:

tel: +603-79677022 ext. 2534

email: rozie@um.edu.my

Received: June 30, 2020

Accepted: September 20, 2020

DOI: 10.22146/ijc.57343

**Abstract:** A series of six sulfur-bridged dinuclear silver(I) thiosemicarbazone complexes were synthesized through the reaction of silver(I) nitrate with 4-phenyl-3-thiosemicarbazone derivatives together with triphenylphosphine (PPh<sub>3</sub>) (in a 1:1:2 molar ratio). Following structural characterizations using various techniques such as elemental analysis, Fourier-transform infrared (FTIR) spectroscopy, as well as <sup>1</sup>H, <sup>13</sup>C, <sup>31</sup>P{<sup>1</sup>H}s, COSY, and <sup>1</sup>H-<sup>13</sup>C nuclear magnetic resonance (NMR) spectroscopy, it was found that the thiosemicarbazone ligand exists in the form of a thione rather than thiol tautomer. Subsequently, MDA-MB-231 and MCF-7 breast cancer cell lines, as well as the HT-29 colon cancer cell lines, were used to investigate the in vitro antiproliferative activities of these complexes. In all cases, the IC<sub>50</sub> values were in the potent micromolar range. Besides, the aforementioned complexes also had good antiplasmodial activity against chloroquine-resistant *P. falciparum*, as per the results of histidine-rich protein 2 (HRP2) assays and cytotoxicity evaluations of MDBK cells.

**Keywords:** thiosemicarbazone; silver complexes; antiplasmodial; antiproliferative; phosphine

## ■ INTRODUCTION

The synthesis of metal complexes containing mixed ligand systems that have electron-donating potential has attracted much attention owing to their catalytic abilities [1], unique structures [2], and most importantly, applications in the medical field [3-4]. In particular, metal complexes with phosphine and thiosemicarbazone ligands have been explored due to the ability of thiosemicarbazone to coordinate a wide range of metallic ions that can be attributed to the extended delocalization of the electron density of the NH-CS-NH-N system [5]. The employment of transition metals in drug discovery has become a favorite approach, especially when it is attached to compounds of common therapeutic value like thiosemicarbazones in an effort to fight drug resistance

[6]. In addition, metal coordination also helps to increase the lipophilicity of a compound, hence increasing the speed of the compound's entry into the cell [7].

Research interest in these compounds is also fueled by their broad spectrum of biological activities, including antibacterial [8], antiviral [9], antitubercular [10], and antitumor [11], anticancer and antimalarial activities [5]. Evidently, silver complexes and their therapeutic abilities are interesting topics among researchers [12]. A previous study combining the ligands of thio and phosphine has shown a promising activity towards antibacterial activity [13]. Another study used a similar group of ligands (thio and phosphine), but gold also showed higher cytotoxicity, better antitumor activity,

and selectivity than the cisplatin [14]. However, to the ability of our knowledge, there is a lacking recent report on the screening for the anticancer potential and the antiplasmodial properties of the silver(I) complexes with thiosemicarbazone and triphenylphosphine ligands.

Hence, as a part of continuing interest in this area of research, we synthesized a series of thiosemicarbazone-derivative ligands, which were then attached to a silver center along with triphenylphosphine ligands. The silver complexes were later characterized using few elemental and spectral analyses to confirm their structure. Basic elemental analysis like CHNS and PXRD was used to confirm the composition and types of elements present in the complexes. Afterward, more detailed spectroscopy techniques like FTIR, 1D NMR, and 2D NMR were used to justify the structure of the complexes.

## ■ EXPERIMENTAL SECTION

### Materials

Chemicals of 4-nitrobenzaldehyde, 4-hydroxybenzaldehyde, 5-bromosalicylaldehyde, 5-bromoindole-3-carboxaldehyde (98%, Sigma Aldrich), 2-methylindole-3-carboxaldehyde, (5-bromo-2-hydroxy-3-methoxybenzaldehyde (97%, Sigma Aldrich), triphenylphosphine, 4-phenyl thiosemicarbazide (99%, Sigma Aldrich) were used in this study. All reagents and solvents used were of reagent grade without prior purification unless otherwise stated. The progress of these reactions was observed via thin-layer chromatography performed on 2.00 × 6.00 cm aluminium sheets pre-coated with silica gel 60 (HF-254, Merck) of thickness 0.25 mm.

### Instrumentation

The Fourier-transform infrared (FTIR) spectra were recorded by a Perkin Elmer Spectrum One FT-IR spectrophotometer (ATR) at 450–4000  $\text{cm}^{-1}$ . The  $^1\text{H}$ ,  $^{13}\text{C}$ ,  $^{31}\text{P}\{^1\text{H}\}$ , COSY, and  $^1\text{H}$ - $^{13}\text{C}$  nuclear magnetic resonance (NMR) spectra were analyzed using a JEOL FT-NMR ECX 400 (ECX 400) spectrometer, whereby deuterated dimethyl sulfoxide (DMSO) and chloroform were the solvents. Meanwhile, Perkin Elmer CHNS/O Analyzer 2400 Series II was used to perform the elemental analyses, while Energy Dispersive X-Ray spectroscopy (EDX) was

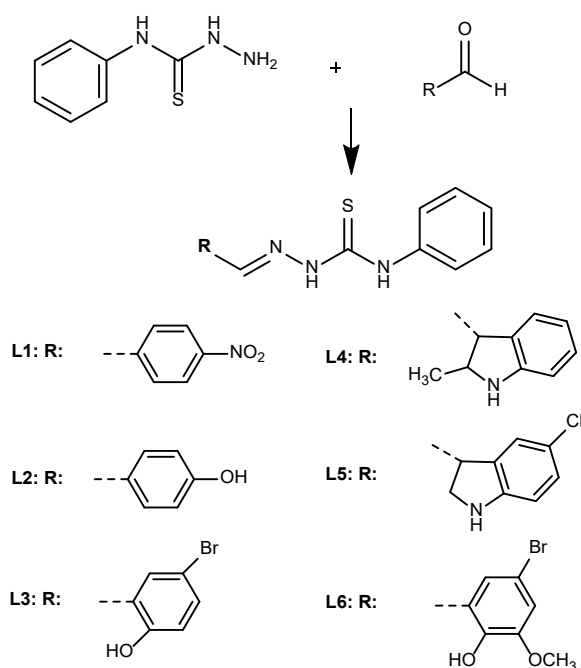
used to detect the presence of silver metal. X-ray diffractometer (PANalytical, Netherlands) was used to examine Powder X-ray diffraction (PXRD) with a scanning scope of  $2\theta$  from 0 to  $50^\circ$  and scanning rate of  $4.25^\circ/\text{min}$  at room temperature ( $25^\circ\text{C}$ ), with Cu K $\alpha$  characteristic radiation ( $\lambda = 0.154\text{ nm}$ ) at the current of 40 mA and voltage of 40 kV.

### Procedure

#### Synthesis of thiosemicarbazone ligands (L1-L6)

All thiosemicarbazone ligands (L1-L6) were prepared by the procedure described in Ref. [15], with slight modifications (Scheme 1). First, 4-phenyl-3-thiosemicarbazide (1 g, 6 mmol) was dissolved in ethanol (33 mL). Next, the corresponding aldehyde (which was pre-dissolved in ethanol) was added to the mixture along with a few small drops of glacial acetic acid. The solution was then refluxed for 3–4 h and later dried in a vacuum for analysis. The ligands were white or yellow powders soluble in ethanol, methanol, acetone, DMSO, dichloromethane, or chloroform.

**L1: 4-nitrobenzaldehyde-N-phenyl-thiosemicarbazone.** Yield: 70%, M.p.  $260^\circ\text{C}$ . Anal. Calc. for  $\text{C}_{14}\text{H}_{12}\text{N}_4\text{O}_2\text{S}$ : C, 56.00; H, 4.02; N, 18.63. Found: C, 55.20; H, 3.73; N, 18.59. IR data ( $\text{cm}^{-1}$ ): (N-H) 3103.08, 2980.20,



Scheme 1. Synthesis of thiosemicarbazone ligands

(C=N) 1595.02, (C=S) 846.76, <sup>1</sup>H-NMR data (δ, ppm; DMSO): 12.06 (s, 1H) (N-H), 10.29 (s, 1H) (N-H), 8.20 (C-H, 1H) (CH=N), 7.2–8.2 (m) (CH, CH<sub>2</sub>, CH<sub>3</sub>); <sup>13</sup>C-NMR data (δ, ppm; DMSO): 177.10 (C=S), 140.70 (C-Ph).

**L2: 4-hydroxybenzaldehyde-N-phenyl-thiosemicarbazone.** Yield: 60%, M.p. 240 °C. Anal. Calc. for C<sub>14</sub>H<sub>13</sub>N<sub>3</sub>OS: C, 61.97; H, 4.83; N, 15.49. Found: C, 61.24; H, 4.92; N, 14.98. IR data (cm<sup>-1</sup>): (N-H) 3158.08, 2977.11 (C=N) 1604.28 (C=S) 851.49, <sup>1</sup>H-NMR data (δ, ppm; DMSO): 11.62 (s, 1H) (N-H), 9.94 (s, 1H) (N-H), 9.88 (s, 1H) (C-OH), 8.04 (s, 1H) (CH=N), 6.8–8.1 (m) (CH, CH<sub>2</sub>, CH<sub>3</sub>); <sup>13</sup>C-NMR data (δ, ppm; DMSO): 175.90 (C=S), 144.00 (C-Ph).

**L3: 5-bromo-2-hydroxybenzaldehyde-N-phenyl-thiosemicarbazone.** Yield: 65%, M.p. 250 °C. Anal. Calc. for C<sub>14</sub>H<sub>12</sub>BrN<sub>3</sub>OS: C, 48.01; H, 3.45; N, 12.00. Found: C, 48.24; H, 3.44; N, 12.12. IR data (cm<sup>-1</sup>): (N-H) 3141.28, 2984.50 (C=N) 1604.57 (C=S) 829.04, <sup>1</sup>H-NMR data (δ, ppm; DMSO): 11.78 (s, 1H) (N-H), 10.14 (s, 1H) (N-H), 10.28 (s, 1H) (C-OH), 8.38 (s, 1H) (CH=N), 6.7–7.5 (m) (CH, CH<sub>2</sub>, CH<sub>3</sub>); <sup>13</sup>C-NMR data (δ, ppm; DMSO): 176.60 (C=S), 139.50 (C-Ph).

**L4: 2-methylindole-3-carboxaldehyde-N-phenyl-thiosemicarbazone.** Yield: 80%, M.p. 230 °C. Anal. Calc. for C<sub>17</sub>H<sub>16</sub>N<sub>4</sub>S: C, 65.78; H, 5.84; N, 18.05. Found: C, 66.01; H, 5.19; N, 17.32. IR data (cm<sup>-1</sup>): (N-H) 3394.64, 3285.30, 3209.93, (C=N) 1589.25 (C=S) 839.31, <sup>1</sup>H-NMR data (δ, ppm; DMSO): 11.55 (s, 1H) (N-H<sub>indole</sub>); 11.40 (s, 1H) (N-H), 9.50 (s, 1H) (N-H), 8.50 (s, 1H) (CH=N), 6.7–7.0 (m) (CH, CH<sub>2</sub>, CH<sub>3</sub>); <sup>13</sup>C-NMR data (δ, ppm; DMSO): 174.50 (C=S), 141.70 (C-Ph).

**L5: 5-chloroindole-3-carboxaldehyde-N-phenyl-thiosemicarbazone.** Yield: 45%, M.p. 210 °C. Anal. Calc. for C<sub>16</sub>H<sub>15</sub>ClN<sub>4</sub>S: C, 58.09; H, 4.57; N, 16.93. Found: C, 57.65; H, 3.95; N, 16.20. IR data (cm<sup>-1</sup>): (N-H) 3338.98, 3132.20, 2973.42 (C=N) 1609.25 (C=S) 866.50, <sup>1</sup>H-NMR data (δ, ppm; DMSO): 11.83 (s, 1H) (N-H), 11.58 (s, 1H) (N-H<sub>indole</sub>), 9.72 (s, 1H) (N-H), 8.35 (s, 1H) (CH=N), 7.0–8.2 (m) (CH, CH<sub>2</sub>, CH<sub>3</sub>) <sup>13</sup>C-NMR data (δ, ppm; DMSO): 175.10 (C=S), 141.20 (C-Ph).

**L6: 5-bromo-2-hydroxy-3-methoxybenzaldehyde-N-phenyl-thiosemicarbazone.** Yield: 70%, M.p. 190 °C. Anal. Calc. for C<sub>15</sub>H<sub>14</sub>BrN<sub>3</sub>O<sub>2</sub>S: C, 47.38; H, 3.71; N, 11.05.

Found: C, 47.89; H, 3.75; N, 11.08. IR data (cm<sup>-1</sup>): (N-H) 3300.41, 2973.79 (C=N) 1604.00, (C=S) 858.86. <sup>1</sup>H-NMR data (δ, ppm; DMSO): 11.80 (s, 1H) (N-H), 10.10 (s, 1H) (N-H), 9.49 (s, 1H) (OH), 8.43 (s, 1H) (CH=N), 3.81 (s, 1H) (OCH<sub>3</sub>), 7.0–7.6 (m) (CH, CH<sub>2</sub>, CH<sub>3</sub>); <sup>13</sup>C-NMR data (δ, ppm; DMSO): 176.60 (C=S), 140.00 (C-Ph).

### Synthesis of complexes (P1-P6)

AgNO<sub>3</sub> (0.17 g, 1 mmol) was first dissolved in a 20 mL mixture of acetonitrile and methanol (2:3), following which the respective thiosemicarbazone ligands (L1-L6) (2 mmol) were added. The mixture was refluxed at 55 °C for 3–4 h. The mixture was further added with triphenylphosphine (0.262 g, 1 mmol) in 5 mL of acetonitrile/methanol (2:3) and further refluxed for 2–3 more hours. The latter step could result in the solubilization of the precipitates obtained in the first step, if any. Thin-layer chromatography is used to monitor the reaction's progress. The resulting solution was filtered and later thoroughly dried via evaporation. Further purification was performed before the analysis. The silver complexes were brown and black powders and soluble in either DMSO or a mixture of methanol and acetonitrile.

**P1: [Ag<sub>2</sub>(PPh<sub>3</sub>)<sub>2</sub>(L1)<sub>4</sub>](NO<sub>3</sub>)<sub>2</sub>·H<sub>2</sub>O.** Yield: 50%, M.p. 157–160 °C. Anal. Calc. for C<sub>92</sub>H<sub>78</sub>Ag<sub>2</sub>N<sub>16</sub>O<sub>8</sub>P<sub>2</sub>S<sub>4</sub> C, 56.91; H, 4.05; N, 11.54; S, 6.61. Found: C, 56.30; H, 3.57; N, 11.65; S, 6.61. IR data (cm<sup>-1</sup>): (N-H) 2983.12, 2888.57, (C=N) 1589.21 (C=S) 840.88. <sup>1</sup>H-NMR data (δ, ppm; DMSO): 12.33 (s, 4H) (N-H), 10.72 (s, 4H) (N-H), 8.18 (C-H, 4H) (CH=N), 7.1–8.3 (m) (CH, CH<sub>2</sub>, CH<sub>3</sub>). <sup>13</sup>C-NMR data (δ, ppm; DMSO): 175.80 (C=S), 143.00 (C-Ph).

**P2: [Ag<sub>2</sub>(PPh<sub>3</sub>)<sub>2</sub>(L2)<sub>4</sub>](NO<sub>3</sub>)<sub>2</sub>·H<sub>2</sub>O.** Yield: 45%, M.p. 135–138 °C. Anal. Calc. for C<sub>92</sub>H<sub>82</sub>Ag<sub>2</sub>N<sub>12</sub>O<sub>4</sub>P<sub>2</sub>S<sub>4</sub> C, 60.53; H, 4.53; N, 9.21; S, 7.03. Found: C, 58.90; H, 3.82; N, 9.26; S, 6.48. IR data (cm<sup>-1</sup>): (N-H) 2981.06, 2889.37 (C=N) 1595.67, (C=S) 834.24. <sup>1</sup>H-NMR data (δ, ppm; DMSO): 11.88 (s, 4H) (N-H), 10.22 (s, 4H) (N-H), 7.99 (s, 4H) (CH=N), 9.98 (s, 4H) (O-H), 6.6–7.5 (m) (CH, CH<sub>2</sub>, CH<sub>3</sub>); <sup>13</sup>C-NMR data (δ, ppm; DMSO): 173.90 (C=S), 146.60 (C-Ph).

**P3: [Ag<sub>2</sub>(PPh<sub>3</sub>)<sub>2</sub>(L3)<sub>4</sub>](NO<sub>3</sub>)<sub>2</sub>·H<sub>2</sub>O.** Yield: 40%. M.p. 140–143 °C. Anal. Calc. for: C<sub>92</sub>H<sub>78</sub>Ag<sub>2</sub>Br<sub>4</sub>N<sub>12</sub>O<sub>4</sub>P<sub>2</sub>S<sub>4</sub> C, 51.60; H, 3.67; N, 7.85; S, 5.99. Found: C, 49.65; H, 3.17; N, 7.81; S, 5.31. IR data (cm<sup>-1</sup>): (N–H) 3141.28, 2984.50 (C=N) 1604.57, (C=S) 824.43. <sup>1</sup>H-NMR data (δ, ppm; DMSO): 12.02 (s, 4H) (N–H), 10.46 (s, 4H) (N–H), 8.42 (s, 4H) (CH=N), 10.58 (s, 4H) (O–H) 6.8–7.5 (m) (CH, CH<sub>2</sub>, CH<sub>3</sub>); <sup>13</sup>C-NMR data (δ, ppm; DMSO): 174.00 (C=S), 141.50 (C-Ph).

**P4: [Ag<sub>2</sub>(PPh<sub>3</sub>)<sub>2</sub>(L4)<sub>4</sub>](NO<sub>3</sub>)<sub>2</sub>·H<sub>2</sub>O.** Yield: 45%. M.p. 127–130 °C. Anal. Calc. for C<sub>104</sub>H<sub>94</sub>Ag<sub>2</sub>N<sub>16</sub>P<sub>2</sub>S<sub>4</sub> C, 63.28; H, 4.80; N, 11.35; S, 6.50. Found: C, 59.62; H, 4.34; N, 10.98; S, 5.89. IR data (cm<sup>-1</sup>): (N–H) 3012.28, 2880.97, 2649.02 (C=N) 1600.00 (C=S) 830.01. <sup>1</sup>H-NMR data (δ, ppm; DMSO): 11.63 (s, 1H) (N–H<sub>indole</sub>), 11.60 (s, 4H) (N–H), 9.73 (s, 4H) (N–H), 8.41 (s, 4H) (CH=N), 7–7.5 (m) (CH, CH<sub>2</sub>, CH<sub>3</sub>). <sup>13</sup>C-NMR data (δ, ppm; DMSO): 172.90 (C=S), 144.00 (C-Ph).

**P5: [Ag<sub>2</sub>(PPh<sub>3</sub>)<sub>2</sub>(L5)<sub>4</sub>](NO<sub>3</sub>)<sub>2</sub>·H<sub>2</sub>O.** Yield: 40%. M.p. 131–134 °C. Anal. Calc for C<sub>100</sub>H<sub>86</sub>Ag<sub>2</sub>N<sub>16</sub>P<sub>2</sub>S<sub>4</sub> C, 62.63; H, 4.52; N, 11.69; S, 6.69 Found: C, 59.89; H, 3.89; N, 10.91; S, 6.53. IR data (cm<sup>-1</sup>): (N–H) 3000.96, 2883.01, 2733.51, (C=N) 1598.27, (C=S) 834.04. <sup>1</sup>H-NMR data (δ, ppm; DMSO): 11.88 (s, 1H) (N–H<sub>indole</sub>), 10.35 (s, 4H) (N–H), 10.01 (s, 4H) (N–H), 8.00 (s, 4H) (CH=N), 6.8–7.8 (m) (CH, CH<sub>2</sub>, CH<sub>3</sub>). <sup>13</sup>C-NMR data (δ, ppm; DMSO): 173.70 (C=S), 133.80 (C-Ph).

**P6: [Ag<sub>2</sub>(PPh<sub>3</sub>)<sub>2</sub>(L6)<sub>4</sub>](NO<sub>3</sub>)<sub>2</sub>·H<sub>2</sub>O.** Yield: 40%. M.p. 137–140 °C. Anal. Calc for C<sub>96</sub>H<sub>86</sub>Ag<sub>2</sub>Br<sub>4</sub>N<sub>12</sub>O<sub>8</sub>P<sub>2</sub>S<sub>4</sub> C, 50.99; H, 3.83; N, 7.43; S, 5.67. Found: C, 48.09; H, 3.38; N, 7.72; S, 6.02. IR data (cm<sup>-1</sup>): (N–H) 3049.11, 2879.23, (C=N) 1599.12 (C=S) 742.69. <sup>1</sup>H-NMR data (δ, ppm; DMSO): 12.00 (s, 4H) (N–H), 10.53 (s, 4H) (N–H), 8.46 (s, 4H) (CH=N), 9.52 (s, 4H) (O–H), 7.0–7.4 (m) (CH, CH<sub>2</sub>, CH<sub>3</sub>). <sup>13</sup>C-NMR data (δ, ppm; DMSO): 174.40 (C=S), 836.84 (C-Ph)

### Biological procedures

**Antiplasmodial assays.** The antiplasmodial activities of all compounds were evaluated *in vitro* through HRP2 assays [16-17] as described in Ref. [18] with some alterations. First, the compounds were solubilized in 100% DMSO and serially diluted into mixtures whose concentrations range from 25 μM to 0.39 μM in wells A1

to A7 of a 96-well plate. Some 15 μL of each serially-diluted stock extract was moved accordingly into plates with 225 μL of sterile H<sub>2</sub>O. Aliquots from the plates would be used in the HRP2 assays. Next, ring-infected red blood cells (RBCs) of 5% parasitemia were tuned so that the parasitemia and hematocrit were 0.05% and 1.5%, respectively. Ten μL of each serially-diluted extract was moved to a test plate containing parasitized RBCs and later incubated in a candle jar at 37 °C for 72 h. The final test concentrations ranged from 0.156 μM to 0.002 μM, while DMSO was 0.3%. Artemisinin (Art) (Sigma, USA), chloroquine (CQ) (Sigma, USA), mefloquine (Mef) (Sigma, USA), and quinine (Q) (Sigma, USA) – whose final test concentrations were 1772.6–27.7 nM for CQ, 3495–54.6 nM for Q, 601.3–9.4 nM for Mef, and 51.2–0.8 nM for Art – were the standard controls used to validate the test. Meanwhile, the negative controls comprised infected RBCs without extracts or with sterile H<sub>2</sub>O only. Following incubation for 72 h, the test plates were then kept overnight at -80 °C. It was then thawed at room temperature to lyse the infected RBCs. Subsequently, the activities of the compounds against the parasite were measured via HRP2 assays [17,19].

**Cytotoxicity assays (in vitro).** The MDBK cells were preserved in complete Dulbecco's Modified Eagle Medium (DMEM) comprising 25 mM 4-(2-hydroxyethyl)-1-piperazineethanesulfonic acid (HEPES), 100 U of Pen-strep (100 U penicillin and 100 U streptomycin), 0.4% sodium bicarbonate (NaHCO<sub>3</sub>) accompanied with 10% fetal bovine serum (FBS). 3-(4,5-dimethylthiazol-2-yl)-2,5-diphenyltetrazolium bromide (MTT) assays were used to test the cytotoxicities of the extracts [20]. Briefly, MDBK cells (1 × 10<sup>3</sup> cells/well) which have been cultured overnight were exposed to serially diluted (2-fold-diluted) compounds whose final concentrations ranged from 0.25 μM to 0.004 μM. The final concentrations of DMSO in all tests were less than 1%. All tests were performed in duplicates. Cell suspension lacking the test material was the positive control for cell growth, while the negative control cell contains suspension with 0.05% Triton X 100. The test culture was kept for 72 h at 37 °C in a 5% CO<sub>2</sub> incubator. To each well, some 50 μL of MTT solution (2.5 mL

DMEM and 5 mg MTT in 1 mL PBS) were added. It was then kept for 4 h at 37 °C in the said incubator. Next, the medium was removed and replaced with 200  $\mu$ L of DMSO to solubilize the MTT formazan product. It was then mixed for 15 min before its absorbance was measured using a microplate reader (FLUOstar Omega, Germany) at 540 nm. The  $IC_{50}$  and growth inhibition percentage were predicted with reference to a dose-response curve.

**Antiproliferative assays.** Sulforhodamine B (SRB) assays were performed to determine the  $IC_{50}$  of the test compounds as described in previous studies [21]. Briefly, the cells were treated with 5.053–161.686  $\mu$ M, 4.843–154.960  $\mu$ M, 4.189–134.055  $\mu$ M, 4.680–149.752  $\mu$ M, or 3.936–125.944  $\mu$ M sets of concentrations for all the synthesized complexes. Forty-eight hours later, using 50  $\mu$ L of 50% (w/v) trichloroacetic acid (TCA), the cells were secured to the plates and kept further incubated at 4 °C for an hour. The plates were then washed five times using tap water, air-dried, stained with 100  $\mu$ L of 0.4% (w/v) SRB staining solution, and further incubated for another 10 min at room temperature. Consequently, the plates were washed three times with 1% (v/v) acetic acid to remove the unbound stains. Following air-drying, 200  $\mu$ L of 10 mM Trizma base was added into the wells, shaken for 10 min. The reading of the absorbance is taken using a microplate reader at 490 nm, and the  $IC_{50}$  calculated using the formula;  $IC_{50} = (OD \text{ sample}/OD \text{ control}) \times 100$ . All experiments were performed in triplicates.

## RESULTS AND DISCUSSION

The six silver(I) complexes which were synthesized in a molar ratio of 1:1:2 (Ag:PPh<sub>3</sub>:thiosemicarbazone) were either brown and black, were structurally characterized by nuclear magnetic resonance (NMR), Fourier-transform infrared (FTIR) spectroscopy, energy-dispersive X-ray (EDX), powder X-ray diffraction (PXRD), and elemental analysis. The spectroscopic data interpreted that all the ligands and their corresponding complexes existed in the form of thione tautomers. The formation of silver complexes occurred when silver received a lone pair of electrons from donor sulfur and phosphorus atoms. These complexes were believed to bind tightly to the metal center through M-S bridging

bonds as they were synthesized in a molar ratio of 1:1:2 [22]. In agreement with the results of previous studies [22–23], the silver complexes were dinuclear, with each silver atom tetrahedrally coordinated to one S atom with a thiosemicarbazone terminal, and two S atoms with a bridging thiosemicarbazone group, and one P atom of triphenylphosphine (PPh<sub>3</sub>) as shown in Fig. 1.

### Fourier-Transform Infrared Spectroscopy (FTIR)

To investigate the points of attachment of the ligands to the metal center in the complexes, the FTIR spectra of the free ligands were compared to its synthesized complexes. The infrared spectra of the corresponding complexes confirmed the coordination of the ligand as  $\nu(C=N)$  vibrational modes were detected in all of the ligands and complexes. The shifting of the  $\nu(C=S)$  bands to lower energies in the complexes meant that the thiosemicarbazone ligands were coordinated to the silver (I) metal via donor sulfur atoms. Meanwhile, the absence of  $\nu(S-H)$  bands at the 2800–2550  $cm^{-1}$  regions of both ligands and complexes revealed that the

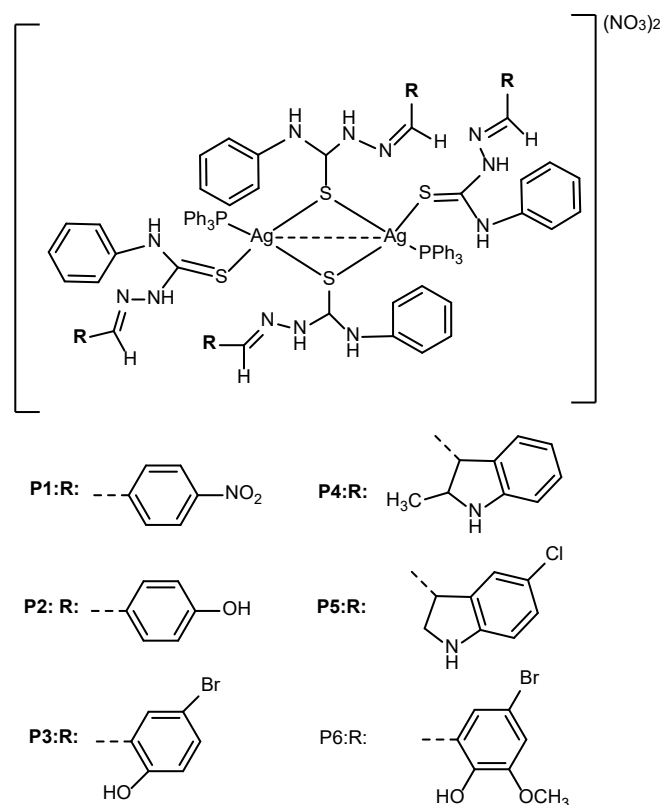


Fig 1. Structures of the silver complexes P1–P6

complexes only had thione tautomers which were retained from their free ligands. Intra- and intermolecular hydrogen bonds of the hydroxyl and amino groups, which gave rise to band-broadening in the 3500–3000  $\text{cm}^{-1}$  regions, were also present. A characteristic  $\nu(\text{P}-\text{C}_{\text{Ar}})$  peak at around 1090  $\text{cm}^{-1}$  denoted the presence of triphenylphosphine that was coordinated to the silver center. A sharp band around 1300  $\text{cm}^{-1}$  was detected in all complexes, suggesting non-coordinated  $\text{NO}_3^-$  ions. However, the FTIR spectrum of **P5** did not reveal a  $-\text{C}-\text{Cl}$  peak, unlike that of its ligand (**L5**). This occurrence further proposed the detachment of  $-\text{Cl}$  to form  $\text{HCl}$  in the reaction mixture.

### Nuclear Magnetic Resonance (NMR) Spectroscopy

In the  $^1\text{H}$ -NMR spectra of the complexes, signals from the aromatic protons were confirmed by the presence of multiplet peaks observed at 6.00–8.00 ppm. Concurrently, following coordination with silver metal, the N–H signals from the metal complexes were shifted downfield by around 0.20–0.50 ppm from their original positions in the free ligands ( $\delta = 9.5$ –12.0 ppm). As for

compounds **P2**, **P3**, and **P6**, the hydroxyl proton peaks at  $\delta = 9.98$ , 10.58, and 9.70 ppm were also shifted slightly downfield. On the same note, **P6** also gave rise to a methoxy-proton peak in the form of a triplet at  $\delta = 3.80$  ppm. The coordination of the triphenylphosphine ligand was evidenced by the presence of additional aromatic protons at  $\delta = 7.10$ –7.50 ppm in the complexes; these were not otherwise present in their respective ligands. Fig. 2 shows the assignments of protons in the  $^1\text{H}$ -NMR spectrum of compounds **4**.

In the  $^{13}\text{C}$ -NMR spectra, the bonding between the thiosemicarbazone and phosphine ligands to the metal centers was also proven by the presence of  $\text{C}=\text{S}$  signals in which the chemical shift value was around 2.0 ppm. This was in view of the decrease of the  $\text{C}=\text{S}$  bond when attached to metal [24], as well as a shift in the  $\text{N}\rightarrow\text{C}$  electron density, which gave rise to a partial bond characteristic in the  $\text{C}-\text{N}$  bond [25]. With reference to compounds **P2**, **P3**, and **P6**, the C-hydroxyl resonance at the thiosemicarbazone ligand was observed at  $\delta = 139.00$  ppm. In further detail, the spectrum for the

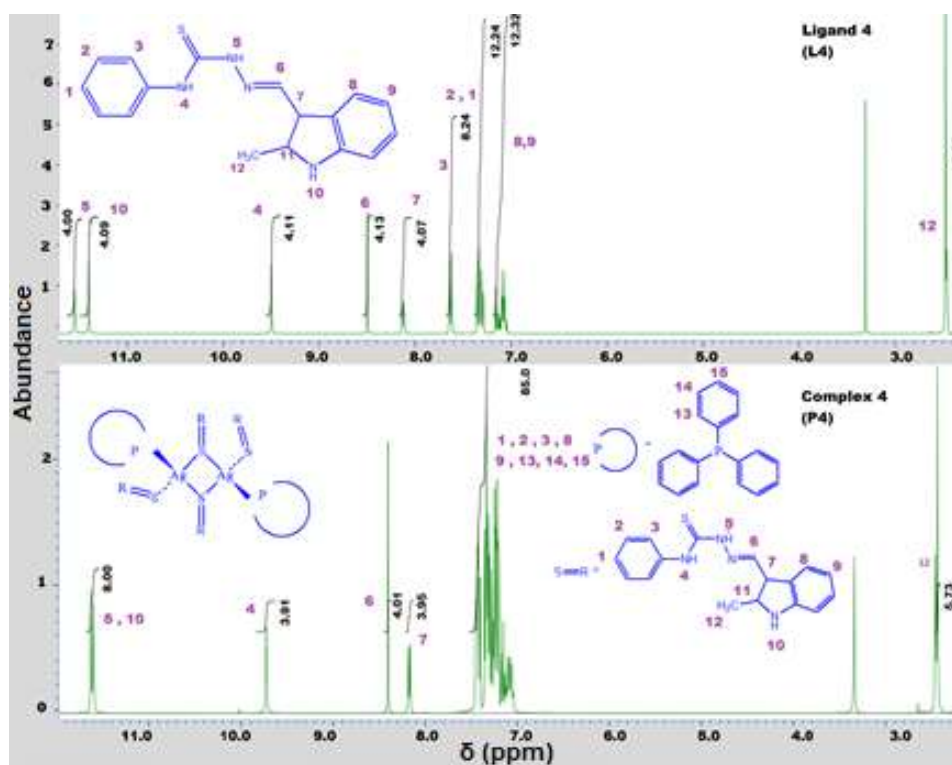


Fig 2.  $^1\text{H}$ -NMR spectra of compounds **L4** and **P4**

compound **P6** had a C-methoxy resonance at  $\delta = 57.0$  ppm, while the C-methyl resonance in compound **P4** was observed at  $\delta = 12.0$  ppm. In all complexes, the resonances of the aromatic carbons in triphenylphosphine and thiosemicarbazone revealed significant upfield shifts at  $\delta = 131.0$ – $132.0$  ppm. Since the aromatic C on triphenylphosphine appeared as doublets and singlet, these further confirmed the attachment of the triphenylphosphine ligand to the silver center [25]. Fig. 3 shows the assignments of carbon peaks for the ligand and complex **4**.

The  $^1\text{H}$ - $^1\text{H}$  COSY NMR has further authenticated the correlation between the equivalent proton pairs with the adjacent protons wherein the cross peak resulting from the correlation appears in the same region. Fig. 4 shows the COSY spectrum for complexes **P3**. From the figure, the proton H5 is correlated to the proton H4 and H6. Meanwhile, H10 is correlated to the aromatic proton area near 7 ppm. A similar phenomenon can also be found by H7 which correlates with the aromatic proton area near 7 ppm while the H8 correlates to the aromatic

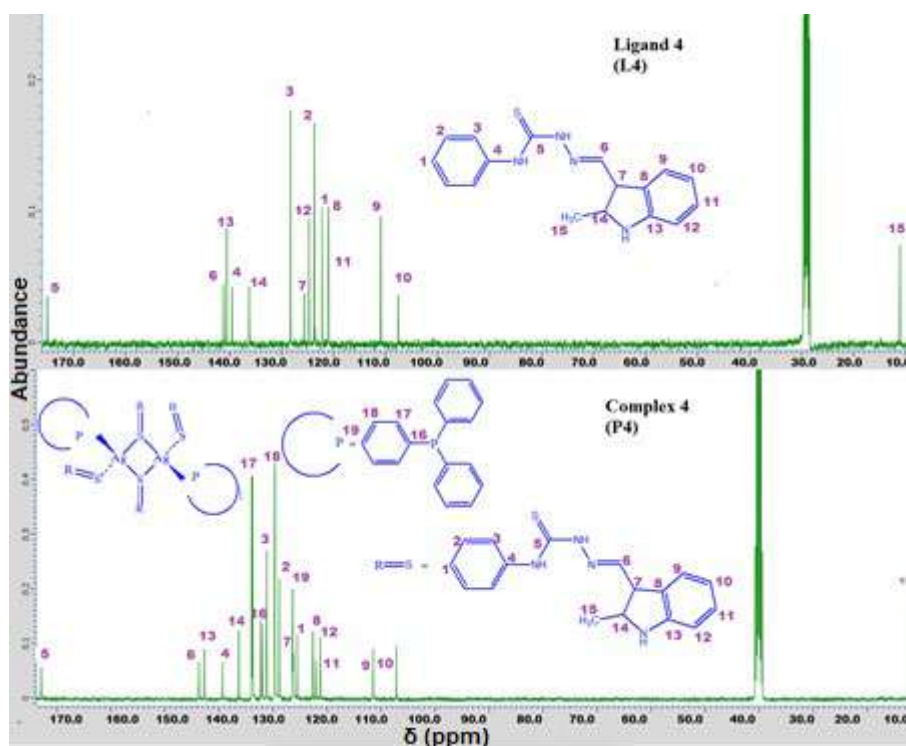


Fig 3.  $^{13}\text{C}$ -NMR spectra of L4 and P4

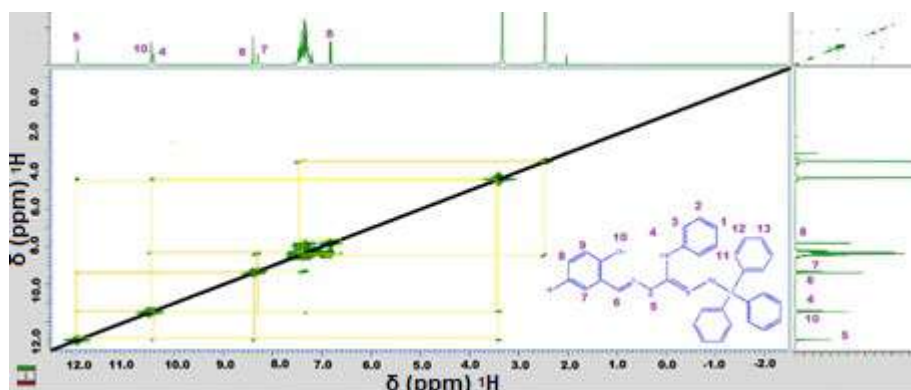


Fig 4. COSY NMR spectrum of complexes **P3**

proton peak indisputably H9. The COSY spectra also reveal that the H10 adjacent to the O atom in the hydroxyl group and H5 connected to the N atom is correlated with the H<sub>2</sub>O peak from the deuterated DMSO.

The <sup>1</sup>H-<sup>13</sup>C HSQC spectra of compounds demonstrate the interaction between the protons and the carbon atoms which are attached. As a representative, the discussion will be based on the spectrum for ligand and complex **P6** (Fig. 5). It can be deduced from Fig. 2 that the H6 is correlated with C6. A similar phenomenon can also be found on the H8, which relates to C10 as justified in the structure numbering shown in the figure. The aromatic carbons in the compound were established via the connectivities between the carbon and its neighboring proton by HSQC correlation spectra. H1, H2, H3, H11, H12, H13, and H7 in the aromatic ring are correlated with C1, C2, C3, C14, C15, C16, and C8, respectively.

In the <sup>31</sup>P{<sup>1</sup>H}-NMR spectra of complexes **P1** to **P6**, a sharp singlet was observed at  $\delta = 10.0$  ppm. This result suggested that the resonance of phosphorus in

triphenylphosphine has shifted downfield as compared to that of its free ligand [13] ( $\delta = -5.5$  ppm). In other words, complexation occurred between the silver center and the triphenylphosphine ligand. Fig. 6 shows the <sup>31</sup>P-NMR spectra of triphenylphosphine and silver complex **P4**.

#### Powder X-Ray Diffraction (PXRD) Analysis

To produce sufficient crystals for single-crystal X-ray analyses, the crystals of all synthesized complexes were grown several times using various methods, including those of previous studies that have managed to generate single crystals [22-26]. Some of these methods included slow evaporation at room temperature and low temperature (refrigerator) for several days, as well as recrystallization of the products scraped from organic solvents (DMF, DMSO, acetonitrile, methanol). However, crystals were not successfully grown that can be further used for X-ray diffraction studies. According to Altaf et al., silver compounds whose ligands contained

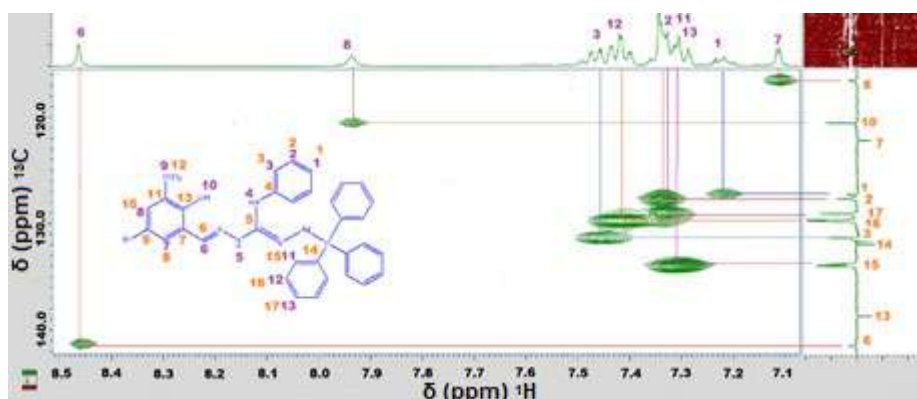


Fig 5. HSQC spectrum for complexes **P6**

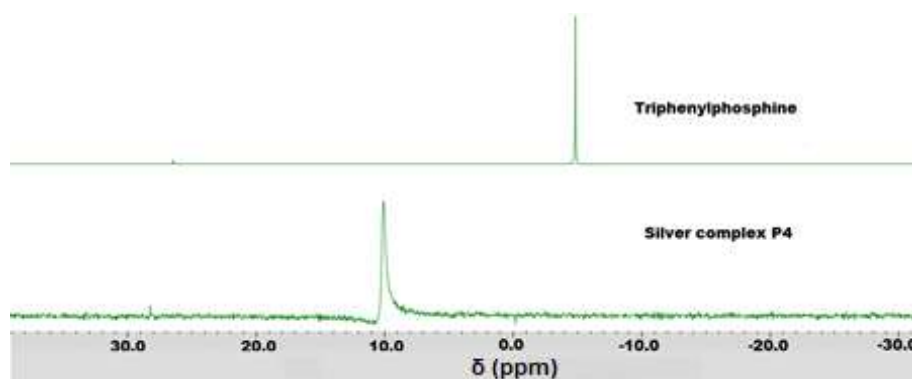


Fig 6. <sup>31</sup>P{<sup>1</sup>H}-NMR spectra of free ligand (triphenylphosphine) and silver complex



nitrogen and sulfur were hard to crystallize owing to their tendency to form intramolecular interactions and polymeric states [22]. Thus, we probed the complexes via PXRD analysis to determine their phases, unit cell dimensions, as well as sample purities. Fig. 7 shows the PXRD pattern for compound **5** (L5 and P5). All other diffractograms can be found in Supplementary Information associated with this report. The PXRD diffractograms were taken within  $2\theta$  ranges of 5–40°. The observed broad peaks were attributed to the non-crystalline samples.

### Energy Dispersive X-ray (EDX) Spectroscopy

EDX spectroscopy was also conducted to verify the existence of silver metal in all complexes (see Supplementary Information). Based on the results of the analyses, silver metal was present in all six series of

complexes. Other elements such as carbon, nitrogen, oxygen, sulfur, phosphorus, and bromine, which were expected to be present in the ligands, were also present in the complexes.

### Antiplasmodial Study

All complexes demonstrate suitable antiplasmodial activities in the *in vitro* *P. falciparum* HRP2 assays against chloroquine-resistant *P. falciparum* parasites (in the asexual cycle) in red blood cells (Table 1). All silver complexes (except **P1**) were tested for this study. The cytotoxic activity of the compounds on MDBK cells was evaluated in terms of the proportion of cytotoxicity to biological activity (SI). The biological efficacy was not attributable to *in vitro* cytotoxicity when the index was  $\geq 10$  [27]. However, the compounds better inhibited the growths of normal cell lines, MDBK cells,

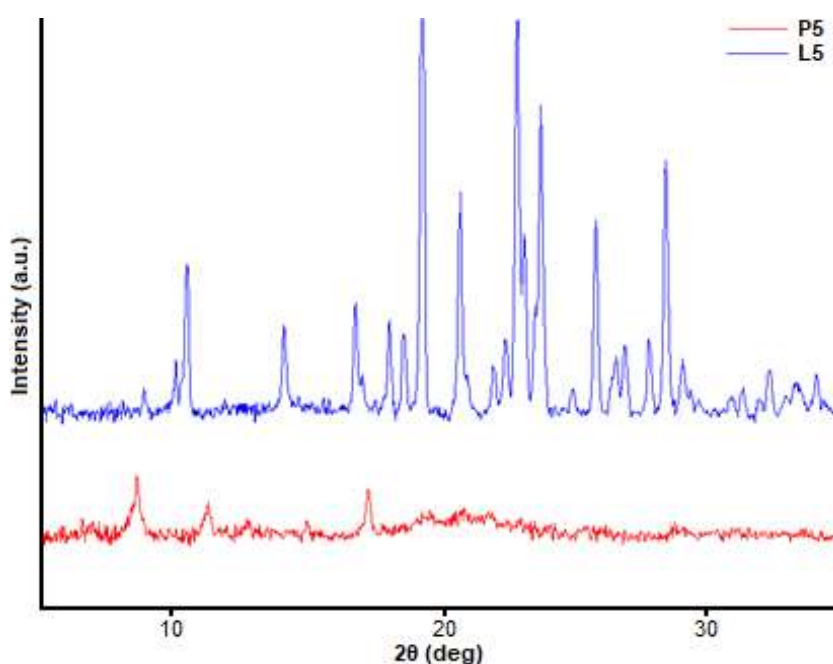


Fig 7. PXRD diffractograms of ligand and complex **P5**

Table 1. Antiplasmodial and cytotoxicity activity of silver complexes **1-6** (EC<sub>50</sub> in  $\mu\text{M}$ )

Complexes	<i>P. falciparum</i> HRP2	Normal MDBK	Selectivity Index (SI)
<b>P1</b>	-	-	-
<b>P2</b>	1.739 $\pm$ 0.243	1.215 $\pm$ 0.180	0.699
<b>P3</b>	4.000 $\pm$ 0.142	0.821 $\pm$ 0.068	0.205
<b>P4</b>	2.120 $\pm$ 1.184	0.945 $\pm$ 0.102	0.446
<b>P5</b>	3.776 $\pm$ 0.280	0.984 $\pm$ 0.046	0.261
<b>P6</b>	4.266 $\pm$ 0.311	1.675 $\pm$ 0.183	0.393

than *P. falciparum* (Table 1). Specifically, the SI of each compound was less than 10, thereby suggesting that the antiplasmodial activities of the compounds could be due to *in vitro* cytotoxicity.

Concerning the selectivity indices of silver complexes, **P2** had the highest SI (0.699) while **P3** the lowest (0.205). This could be explained by the existence of a hydroxyl group at the *-para* position in **P2** rather than the *-ortho* position in **P3**. Additionally, the latter complex also contained a bromide group at the *-meta* position. Meanwhile, the presence of a methoxy group at the *-meta* position in **P6** caused a higher SI value of 0.393 than that of **P3**. Based on the results of previous studies, the insertion of methyl [28] and hydroxyl [29-30] groups into the compounds enhanced the antiplasmodial activity. Nonetheless, it remained uncertain for the role of each functional group in improving the selectivity of the silver complexes.

### Antiproliferative Activities

Transition metals like silver have long been known to be antimicrobial agents. However, there is still much to be discovered concerning its ability to act as an anticancer agent [31-32], even though there are reports that silver has anticancer activity *in vitro* [33]. The advantage of silver is that its toxicity is lower than those of other metals like platinum (e.g., cisplatin) [34]. On another note, thiosemicarbazones have a wide range of antiproliferative activities on different tumor cell lines, apart from displaying the common features of all compounds with carcinogenic potencies [35-36]. Meanwhile, silver phosphine has been shown to exert *in vitro* antiproliferative effects [37-38]. Based on the IC<sub>50</sub> values, complexes **P2**, **P3**, **P4**, **P5**, and **P6** exerted modest antiproliferative effects on the human breast cancer MCF-7 and colon cancer HT-29 cell lines (Table 2). However, **P1** had the weakest antiproliferative potential in all cancer cell lines tested. However, as for the MDA-MB-231 carcinoma cancer cell line, good antiproliferative effects were also observed for **P2**, **P4**, and **P5**. This might be due to the hydroxyl group's presence [39] in **P2** and the indolic group of **P4** and **P5**. Therefore, more in-depth studies are warranted concerning the roles of these silver compounds as metallotherapeutic drugs for cancers.

**Table 2.** Antiproliferative activities of silver complexes **1-6** (IC<sub>50</sub> in  $\mu$ M)

Complexes	MDA-MB-231	HT-29	MCF-7
<b>P1</b>	15.11 $\pm$ 4.24	-	19.62 $\pm$ 4.87
<b>P2</b>	6.81 $\pm$ 1.69	7.23 $\pm$ 0.10	4.48 $\pm$ 0.86
<b>P3</b>	-	6.86 $\pm$ 0.17	3.51 $\pm$ 1.13
<b>P4</b>	5.48 $\pm$ 1.16	5.79 $\pm$ 1.92	7.13 $\pm$ 0.71
<b>P5</b>	5.27 $\pm$ 1.44	6.03 $\pm$ 0.76	4.34 $\pm$ 1.69
<b>P6</b>	-	7.14 $\pm$ 0.76	4.39 $\pm$ 0.74

### CONCLUSION

Six silver complexes containing mixed ligands (4-phenyl-3-thiosemicarbazone derivatives and triphenylphosphine) have been successfully synthesized. The silver complexes were found to be dinuclear with tetrahedral geometry supported by the spectroscopic data discussed in the earlier section. Antiproliferative activities were investigated using MCF-7 breast and MDA-MB-231 carcinoma cancer cell lines and the HT-29 colon cancer cell line. Compounds **P2-P6** were worthy of in-depth studies as metallotherapeutic agents as their result exerted modest antiplasmodial activity against most cancer cells tested. On another note, all the compounds mentioned above had good activity against chloroquine-resistant *P. falciparum* parasites, but they were not as selective as conventional drugs. Consequently, modifications of the structural frame of 4-phenyl-3-thiosemicarbazone could improve the SI value of the resulting compound.

### ACKNOWLEDGMENTS

This work was supported by the Geran Penyelidikan Universiti Malaya (UMRG) - AFR Frontier Science (Grant no. RG357-15AFR) and University of Malaya IPPP Grant (Grant no. PG002-2015A).

### AUTHOR CONTRIBUTIONS

The project was conceived by Rozie Sarip and Nor Fadilah Rajab. Chemical synthesis and characterizations were performed mainly by Nur Adila Fatin Mohd Khir with the help of Nur Rahimah Fitrah Mohd Sofyan. *In vitro* studies of the antiplasmodial and antiproliferative activity were done by Mohd Ridzuan Mohd Abd Razak and Fariza Juliana Nordin, respectively. The manuscript

was written by Nur Adila Fatin Mohd Khir, Mohd Ridzuan Mohd Abd Razak, Fariza Juliana Nordin, and Rozie Sarip.

## ■ REFERENCES

- [1] Chen, J.J., Gan, Z.L., Huang, Q., and Yi, X.Y., 2017, Well-defined dinuclear silver phosphine complexes based on nitrogen donor ligand and their high efficient catalysis for A<sup>3</sup>-coupling reaction, *Inorg. Chim. Acta*, 466, 93–99.
- [2] Papanikolaou, P.A., Papadopoulos, A.G., Andreadou, E.G., Hatzidimitriou, A., Cox, P.J., Pantazaki, A.A., and Aslanidis, P., 2015, The structural and electronic impact on the photophysical and biological properties of a series of Cu<sup>I</sup> and Ag<sup>I</sup> complexes with triphenylphosphine and pyrimidine-type thiones, *New J. Chem.*, 39 (6), 4830–4844.
- [3] Engelbrecht, Z., Meijboom, R., and Cronjé, M.J., 2018, The ability of silver(I) thiocyanate 4-methoxyphenyl phosphine to induce apoptotic cell death in esophageal cancer cells is correlated to mitochondrial perturbations, *BioMetals*, 31 (2), 189–202.
- [4] Human, Z., Munyaneza, A., Omondi, B., Sanabria, N.M., Meijboom, R., and Cronjé, M.J., 2014, The induction of cell death by phosphine silver(I) thiocyanate complexes in SNO-esophageal cancer cells, *BioMetals*, 28 (1), 219–228.
- [5] Chaves, J.D.S., Neumann, F., Francisco, T.M., Corrêa, C.C., Lopes, M.T.P., Silva, H., Fontes, A.P.S., and de Almeida, M.V., 2014, Synthesis and cytotoxic activity of gold(I) complexes containing phosphines and 3-benzyl-1,3-thiazolidine-2-thione or 5-phenyl-1,3,4-oxadiazole-2-thione as ligands, *Inorg. Chim. Acta*, 414, 85–90.
- [6] Adams, M., Barnard, L., de Kock, C., Smith, P.J., Wiesner, L., Chibale, K., and Smith, G.S., 2016, Cyclopalladated organosilane-tethered thiosemicarbazones: Novel strategies for improving antiplasmodial activity, *Dalton Trans.*, 45 (13), 5514–5520.
- [7] Haas, K.L., and Franz, K.J., 2009, Application of metal coordination chemistry to explore and manipulate cell biology, *Chem. Rev.*, 109 (10), 4921–4960.
- [8] Viñuelas-Zahínos, E., Luna-Giles, F., Torres-García, P., and Fernández-Calderón, M.C., 2011, Co(III), Ni(II), Zn(II) and Cd(II) complexes with 2-acetyl-2-thiazoline thiosemicarbazone: Synthesis, characterization, X-ray structures and antibacterial activity, *Eur. J. Med. Chem.*, 46 (1), 150–159.
- [9] Mustafa, A.Z.A., Altaf, M., Monim-ul-Mehboob, M., Fettouhi, M., Wazeer, M.I.M., Isab, A.A., Dhuna, V., Bhatia, G., and Dhuna, K., 2014, Tetrakis(1-3-diazinane-2-thione)platinum(II) chloride monohydrate complex: Synthesis, spectroscopic characterization, crystal structure and *in vitro* cytotoxic activity against A549, MCF7, HCT15 and HeLa human cancer lines, *Inorg. Chem. Commun.*, 44, 159–163.
- [10] Netalkar, P.P., Netalkar, S.P., and Revankar, V.K., 2014, Nickel(II) complexes of thiosemicarbazones: synthesis, characterization, X-ray crystallographic studies and *in vitro* antitubercular and antimicrobial studies, *Transition Met. Chem.*, 39 (5), 519–526.
- [11] Shahsavani, E., Khalaji, A.D., Feizi, N., Kučeráková, M., and Dušek, M., 2015, Synthesis, characterization, crystal structure and antibacterial activity of new sulfur-bridged dinuclear silver(I) thiosemicarbazone complex [Ag<sub>2</sub>(PPh<sub>3</sub>)<sub>2</sub>(μ-S-Brcatsc)<sub>2</sub>(η<sup>1</sup>-S-Brcatsc)<sub>2</sub>](NO<sub>3</sub>)<sub>2</sub>, *Inorg. Chim. Acta*, 429, 61–66.
- [12] Hemmert, C., Fabié, A., Fabre, A., Benoit-Vical, F., and Gornitzka, H., 2013, Synthesis, structures, and antimalarial activities of some silver(I), gold(I) and gold(III) complexes involving N-heterocyclic carbene ligands, *Eur. J. Med. Chem.*, 60, 64–75.
- [13] Isab, A.A., Nawaz, S., Saleem, M., Altaf, M., Monim-ul-Mehboob, M., Ahmad, S., and Evans, H.S., 2010, Synthesis, characterization and antimicrobial studies of mixed ligand silver(I) complexes of thioureas and triphenylphosphine; crystal structure of {[Ag(PPh<sub>3</sub>)(thiourea)(NO<sub>3</sub>)]<sub>2</sub>·[Ag(PPh<sub>3</sub>)(thiourea)]<sub>2</sub>(NO<sub>3</sub>)<sub>2</sub>}, *Polyhedron*, 29 (4), 1251–1256.

- [14] Chaves, J.D.S., Tunes, L.G., de J. Franco, C.H., Francisco, T.M., Corrêa, C.C., Murta, S.M.F., Monte-Neto, R.L., Silva, H., Fontes, A.P., and de Almeida, M.V., 2017, Novel gold(I) complexes with 5-phenyl-1,3,4-oxadiazole-2-thione and phosphine as potential anticancer and antileishmanial agents, *Eur. J. Med. Chem.*, 127, 727–739.
- [15] Benmohammed, A., Khoumeri, O., Djafri, A., Terme, T., and Vanelle, P., 2014, Synthesis of novel highly functionalized 4-thiazolidinone derivatives from 4-phenyl-3-thiosemicarbazones, *Molecules*, 19 (3), 3068–3083.
- [16] Noedl, H., Bronnert, J., Yingyuen, K., Attlmayr, B., Kollaritsch, H., and Fukuda, M., 2005, Simple histidine-rich protein 2 double-site sandwich enzyme-linked immunosorbent assay for use in malaria drug sensitivity testing, *Antimicrob. Agents Chemother.*, 49 (8), 3575–3577.
- [17] Noedl, H., Wernsdorfer, W.H., Miller, R.S., and Wongsrichanalai, C., 2002, Histidine-rich protein II: A novel approach to malaria drug sensitivity testing, *Antimicrob. Agents Chemother.*, 46 (6), 1658–1664.
- [18] Mohd Abd Razak, M.R., Afzan, A., Ali, R., Amir Jalaluddin, N.F., Wasiman, M.I., Shiekh Zahari, S.H., Abdullah, N.R., and Ismail, Z., 2014, Effect of selected local medicinal plants on the asexual blood stage of chloroquine resistant *Plasmodium falciparum*, *BMC Complementary Altern. Med.*, 14 (1), 492.
- [19] Noedl, H., Wernsdorfer, W.H., Kollaritsch, H., Looareesuwan, S., Miller, R.S., and Wongsrichanalai, C., 2003, Malaria drug-susceptibility testing. HRP2-based assays: current data, future perspectives, *Wien. Klin. Wochenschr.*, 115 (Suppl. 3), 23–27.
- [20] Mosmann, T., 1983, Rapid colorimetric assay for cellular growth and survival: Application to proliferation and cytotoxicity assays, *J. Immunol. Methods*, 65 (1-2), 55–63.
- [21] Vichai, V., and Kirtikara, K., 2006, Sulforhodamine B colorimetric assay for cytotoxicity screening, *Nat. Protocols*, 1 (3), 1112–1116.
- [22] Altaf, M., Stoeckli-Evans, H., Cuin, A., Sato, D.N., Pavan, F.R., Leite, C.Q.F., Ahmad, S., Bouakka, M., Mimouni, M., Khardli, F.Z., and Hadda, T.B., 2013, Synthesis, crystal structures, antimicrobial, antifungal and antituberculosis activities of mixed ligand silver(I) complexes, *Polyhedron*, 62, 138–147.
- [23] Sultana, R., Lobana, T.S., Sharma, R., Castineiras, A., Akitsu, T., Yahagi, K., and Aritake, Y., 2010, Heterocyclic thioamide derivatives of coinage metals (Cu, Ag): Synthesis, structures and spectroscopy, *Inorg. Chim. Acta*, 363 (13), 3432–3441.
- [24] Sharma, R., Lobana, T.S., Kaur, M., Thathai, N., Hundal, G., Jasinski, J.P., and Butcher, R.J., 2016, Variable coordinating activity of sulfur in silver(I) complexes with thiophene based N-1-substituted thiosemicarbazones: First case of thiophenyl-thione sulfur bridging in a dinuclear complex, *J. Chem. Sci.*, 128 (7), 1103–1112.
- [25] Nawaz, S., Isab, A.A., Merz, K., Vasylyeva, V., Metzler-Nolte, N., Saleem, M., and Ahmad, S., 2011, Synthesis, characterization and antimicrobial studies of mixed ligand silver(I) complexes of triphenylphosphine and heterocyclic thiones: Crystal structure of bis[ $\{(\mu^2\text{-diazinane-2-thione})(\text{diazinane-2-thione})(\text{triphenylphosphine})\text{silver(I) nitrate}\}$ ], *Polyhedron*, 30 (9), 1502–1506.
- [26] Venkatachalam, T.K., Pierens, G.K., Bernhardt, P.V., Stimson, D.H.R., Bhalla, R., Lambert, L., and Reutens, D.C., 2016, Heteronuclear NMR spectroscopic investigations of gallium complexes of substituted thiosemicarbazones including X-ray crystal structure, a new halogen exchange strategy, and  $^{18}\text{F}$  radiolabelling, *Aust. J. Chem.*, 69 (9), 1033–1048.
- [27] Waiganjo, B., Moriasi, G., Onyancha, J., Elias, N., and Muregi, F., 2020, Antiplasmodial and cytotoxic activities of extracts of selected medicinal plants used to treat malaria in Embu county, Kenya, *J. Parasitol. Res.*, 2020, 8871375.
- [28] Souza, M.C., Padua, T.A., Torres, N.D., Costa, M.F.S., Facchinetti, V., Gomes, C.R.B., Souza, M.V.N., and Henriques, M.G., 2015, Study of the antimalarial properties of hydroxyethylamine derivatives using green fluorescent protein transformed *Plasmodium berghei*, *Mem. Inst. Oswaldo Cruz*, 110 (4), 560–565.

- [29] Loginova, N.V., Koval'chuk, T.V., Gres, A.T., Osipovich, N.P., Polozov, G.I., Halauko, Y.S., Faletrov, Y.V., Harbatsevich, H.I., Hlushko, A.V., Azarko, I.I., and Bokshits, Y.V., 2015, Redox-active metal complexes of sterically hindered phenolic ligands: Antibacterial activity and reduction of cytochrome c. Part IV. Silver(I) complexes with hydrazone and thiosemicarbazone derivatives of 4,6-di-*tert*-butyl-2,3-dihydroxybenzaldehyde, *Polyhedron*, 88, 125–137.
- [30] Wani, W.A., Jameel, E., Baig, U., Mumtazuddin, S., and Hun, L.T., 2015, Ferroquine and its derivatives: New generation of antimalarial agents, *Eur. J. Med. Chem.*, 101, 534–551.
- [31] Medici, S., Peana, M., Nurchi, V.M., Lachowicz, J.I., Crisponi, G., and Zoroddu, M.A., 2015, Noble metals in medicine: Latest advances, *Coord. Chem. Rev.*, 284, 329–350.
- [32] Banti, C.N., and Hadjikakou, S.K., 2013, Anti-proliferative and anti-tumor activity of silver(I) compounds, *Metallomics*, 5 (6), 569–596.
- [33] Majeed, S., Abdullah, M.S., Nanda, A., and Ansari, M.T., 2016, In vitro study of the antibacterial and anticancer activities of silver nanoparticles synthesized from *Penicillium brevicompactum* (MTCC-1999), *J. Taibah Univ. Sci.*, 10 (4), 614–620.
- [34] Ndagi, U., Mhlongo, N., and Soliman, M.E., 2017, Metal complexes in cancer therapy - an update from drug design perspective, *Drug Des., Dev. Ther.*, 11, 599–616.
- [35] Arora, S., Agarwal, S., and Singhal, S., 2014, Anticancer activities of thiosemicarbazides/thio semicarbazones: A review, *Int. J. Pharm. Pharm. Sci.*, 6 (9), 34–41.
- [36] Serda, M., Kalinowski, D.S., Rasko, N., Potůčková, E., Mrozek-Wilczkiewicz, A., Musiol, R., Małecki, J.G., Sajewicz, M., Ratuszna, A., Muchowicz, A., Gołęb, J., Šimůnek, T., Richardson, D.R., and Polanski, J., 2014, Exploring the anti-cancer activity of novel thiosemicarbazones generated through the combination of retro-fragments: Dissection of critical structure-activity relationships, *Plos One*, 9 (10), e110291.
- [37] Human-Engelbrecht, Z., Meijboom, R., and Cronjé, M.J., 2017, Apoptosis-inducing ability of silver(I) cyanide-phosphines useful for anti-cancer studies, *Cytotechnology*, 69 (4), 591–600.
- [38] Kyros, L., Kourkoumelis, N., Kubicki, M., Male, L., Hursthouse, M.B., Verginadis, I.I., Gouma, E., Karkabounas, S., Charalabopoulos, K., and Hadjikakou, S.K., 2010, Structural properties, cytotoxicity, and anti-inflammatory activity of silver(I) complexes with tris(*p*-tolyl)phosphine and 5-chloro-2-mercaptobenzothiazole, *Bioinorg. Chem. Appl.*, 2010, 386860.
- [39] Abdul Halim, S.N.A., Nordin, F.J., Mohd Abd Razak, M.R., Mohd Sofyan, N.R.F., Abdul Halim, S.N., Rajab, N.F., and Sarip, R., 2019, Synthesis, characterization, and evaluation of silver(I) complexes with mixed-ligands of thiosemicarbazones and diphenyl(*p*-tolyl)phosphine as biological agents, *J. Coord. Chem.*, 72 (5-7), 879–893.

## Deposition of Hydroxyapatite on Silica Made from Rice Husk Ash to Produce the Powder Component of Calcium Phosphate Cement

Tri Windarti<sup>1,2\*</sup>, Widjijono<sup>3</sup>, and Nuryono<sup>2\*\*</sup>

<sup>1</sup>Department of Chemistry, Faculty of Science and Mathematics, Universitas Diponegoro, Jl. Prof. Soedharto SH, Tembalang, Semarang 50275, Indonesia

<sup>2</sup>Department of Chemistry, Faculty of Mathematics and Natural Sciences, Universitas Gadjah Mada, Sekip Utara, Yogyakarta 55281, Indonesia

<sup>3</sup>Department of Dental Biomaterials, Faculty of Dentistry, Universitas Gadjah Mada, Jl. Denta 1, Sekip Utara, Yogyakarta 55281, Indonesia

\* **Corresponding author:**

email: tri.windarti@lecturer.undip.ac.id\*;  
nuryono\_mipa@ugm.ac.id\*\*

Received: July 16, 2020

Accepted: September 10, 2020

DOI: 10.22146/ijc.57900

**Abstract:** Hydroxyapatite (HA) has been deposited on silica (SiO<sub>2</sub>) particles to produce HA-SiO<sub>2</sub> composite that will be used as the powder component of calcium phosphate cement. HA was expected to be on the composite surface to maintain its bioactivity. SiO<sub>2</sub> was made by the sol-gel method, in which silicate solution was extracted from rice husk ash with NaOH solution. Deposition of HA on SiO<sub>2</sub> was carried out by wet chemical deposition method at various Ca/Si molar ratio (in a range of 5–25) followed by calcination at 600 °C for 2 h. Results showed that HA was successfully deposited on SiO<sub>2</sub> particles. The cell parameters of the HA crystals were slightly distorted by the presence of SiO<sub>2</sub> and HA in the composite had a bigger cell volume than pure HA. The crystallite size of HA in the composites increased with the increase of the Ca/Si ratio but the values were smaller than pure HA. SiO<sub>2</sub> acted as a morphology directing agent. At low Ca/Si ratio, the HA-SiO<sub>2</sub> particles were in a form of short rod-like particles with sizes of < 50 nm, while at high Ca/Si ratio, a mixture of short and long rod-like particles with the size of < 100 nm was obtained. The zeta potential of composites was almost similar to pure HA. These properties indicated that HA-SiO<sub>2</sub> composites support the bioactivity of injectable calcium phosphate cement.

**Keywords:** hydroxyapatite; silica; rice husk ash; calcium phosphate cement

### ■ INTRODUCTION

Calcium phosphate cement (CPC) has been widely developed due to its ability to induce bone formation and vascularization. Injectable CPC consists of powder and liquid components. Calcium phosphate and its mixture are common materials used as the powder component and an aqueous solution of calcium or phosphate ion is used as the liquid component. The mixture of the two components produces a paste that can be injected into a damaged bone. Inside the body, the paste may harden to result in a temporary bone substitute [1-3]. Additives are often added to improve the property of CPC. One of the most studied additives with a strong influence on the

property of CPC is siliceous solids like silica (SiO<sub>2</sub>) and calcium silicate (CaSiO<sub>3</sub>) [4-9]. For instance, the addition of 5% fibrous CaSiO<sub>3</sub> into CPC increased the compressive strength of the resulting cement by 250% (from 14.5 MPa to 50.4 MPa) [10]. The setting reaction of CPC with silica precursor produced a porous composite with pore diameters in the range of 1–10 nm [11]. Moreover, CPC-silica composite was found to have an ability to improve cell adhesion and proliferation as well as stimulating osteogenic differentiation [12-14].

To adjust the contribution of silica additives to the improvement of CPC's properties, modification of the powder component, typically calcium phosphate in the form of hydroxyapatite [HA, (Ca<sub>10</sub>(PO<sub>4</sub>)<sub>6</sub>(OH)<sub>2</sub>], has

been intensively studied. Synthetic HA is known as a good bone substitute due to its properties such as being osteoconductive, biocompatible, and bioactive [15-18]. Normally, modification of HA with SiO<sub>2</sub> that is performed under alkaline conditions, produce composites in which silica covers the HA particles [19]. Moreover, under high Ca/P reactant ratios, which are usually used to produce HA, CaO is formed as a secondary product. The presence of CaO decreases the composite surface area. This is undesirable for the powder component of CPC because the presence of silica on the composite surface and the reduced surface area of the composite reduce the bioactivity of HA. On the other hand, a study about HA-SiO<sub>2</sub> morphology showed that the composite was built in such a way that silica interacted with the *a*-plane of HA and then HA crystals grew along the *c*-axis and produced needle-like particles [20]. However, the formation of such shaped particles should be avoided for injectable CPC, because it reduces the injectability of the paste material.

Silica is silicon dioxide (SiO<sub>2</sub>), which forms a three-dimensional framework through siloxane (Si-O-Si) bonds to build an amorphous and porous structure. Silica material has important properties such as soluble in water, chemically inert, thermally stable, and compatible for biomedical applications [21-23]. One of the sources of silica in nature is rice husk ash, in which rice is a very abundant and renewable commodity. Simple extraction of rice husk ash with NaOH produces silica with the same chemical and physical properties as commercial silica [24]. Silica from rice husk ash has a high purity and is a nano-sized material, and has also been applied for several industries such as pharmaceuticals and cosmetics [22].

In this study, the modification of HA with silica was conducted by depositing HA on SiO<sub>2</sub> to produce nano-sized HA-SiO<sub>2</sub> composites. Owing to such structure, it is expected that HA in the composite directly interacts with living bone tissue when the composite is used as CPC. In addition, composite particles are expected to have a shape that is suitable to improve the cement's injectability. This study was based on a previous work regarding *in situ* synthesis of mesoporous silica MCM-41/HA composite [23]. The research found that the arrangement of HA and

SiO<sub>2</sub> in the composite depended on the aging time. At shorter aging times, SiO<sub>2</sub> was found on the composite surface while at longer aging times, the composite was covered by HA. It can be concluded that, thermodynamically, during the synthesis process, SiO<sub>2</sub> and HA particles tried to get the lowest free energy. At first, silica was well dispersed in the reactant solution and the HA crystal was built on the silica surface by silanol-Ca interaction. The HA particles tended to interact with each other, which resulted in HA being inside of the composite and SiO<sub>2</sub> on the surface. With the increase of aging time, SiO<sub>2</sub> was then covered with HA that was built next from the reactant solution. That is why the position of SiO<sub>2</sub> and HA in the composite surface is seen to have changed during aging time. In the current work, these phenomena are predicted to occur when synthesis of the HA-SiO<sub>2</sub> composite is conducted at various Ca/Si reactant ratio. The silica was synthesized from rice husk ash by the sol-gel method and the formation of HA-SiO<sub>2</sub> composite was done by the wet chemical deposition method. The chemical structure, surface properties, and zeta potential of the HA-SiO<sub>2</sub> composite were studied according to the properties needed for the powder component of CPC.

## ■ EXPERIMENTAL SECTION

### Materials

Rice husk as the silica source was collected from a rice mill in Karanganyar, Central Java, Indonesia. Chemicals including NaOH (Merck), HCl (Merck), and deionized water were used in the silica preparation. For the synthesis of the HA-SiO<sub>2</sub> composite, Ca(NO<sub>3</sub>)<sub>2</sub>·4H<sub>2</sub>O (Merck) and KH<sub>2</sub>PO<sub>4</sub> (Merck) were used as Ca and P precursors, respectively. Double distilled water (Ikapharmindo Putramas) and NH<sub>4</sub>OH 32% (Merck) were used as solvent and for pH adjustment, respectively. All chemicals were in analytical grade and used without further purification.

### Instrumentation

The functional groups of the samples were analyzed with Fourier Transform Infrared (FTIR) spectrophotometer (Shimadzu) through a KBr pellet

method at a wavenumber range of 400–4000  $\text{cm}^{-1}$  (Scan step wavenumber of 7.715264  $\text{cm}^{-1}$ ). The crystal structure was characterized by X-Ray Diffraction (XRD) (Rigaku type Miniflex600) that was equipped with monochromatic Cu K $\alpha$  radiation, operated at 40kW ( $\lambda = 1.54 \text{ \AA}$ ) and scanned for  $2^\circ \leq 2\theta \leq 90^\circ$  at a scan step degree of 0.02°. XRD data was fitted by using the Origin software. Cell parameters were calculated with mathematic equations based on hexagonal structure and Bragg's law. Crystallite size was calculated by Scherrer equation. Surface morphology, element distribution, shape and size of particles on surfaces were observed using Scanning Electron Microscope-Energy Dispersive Spectroscopy (SEM-EDS) (Hitachi type SU3500) and Hitachi MC1000 sputter ion for sample coating with gold in a thickness of 1 nm. The shape and size of the particles were observed with Tunneling Electron Microscope (TEM) (JEOL type JEM-1400) by using ethanol as the dispersant. Zetaziser Nano form Malvern was used to record zeta potential value. The measurement was conducted at room temperature at pH 7 for samples that were dispersed in water and 1% (v/v) Tween 80.

## Procedure

### Preparation of silica

Rice husk was burned in fire to produce charcoal. The charcoal was then calcined at 700 °C for 4 h to obtain rice husk ash (RHA). The RHA sample was crushed and sieved with a 200 mesh sieve to obtain RHA powder. Afterwards, about 10 g of RHA powder was mixed with 60 mL of 2 M NaOH solution. The mixture was heated at 65 °C and stirred for 1 h to obtain a suspension. The suspension was then filtered, and the residue was mixed again for the second time with 30 mL of 2M NaOH solution. The obtained filtrate was added with HCl 25% dropwise to reach pH 7.0 or until a white gel was formed. The obtained gel was washed with deionized water by sonication for 1 h to get a white residue and then the white residue was heated at 400 °C for 4 h. The product was later crushed and sieved with a 200 mesh sieve and the obtained powders were considered as silica.

### Deposition of hydroxyapatite on silica

A certain weight of  $\text{Ca}(\text{NO}_3)_2 \cdot 4\text{H}_2\text{O}$  and silica were

**Table 1.** The composition of precursors for the preparation of HA-SiO<sub>2</sub> composites at various Ca/Si<sub>(R)</sub> molar ratios<sup>\*)</sup>

Sample code	Ca(NO <sub>3</sub> ) <sub>2</sub> ·4H <sub>2</sub> O (g)	KH <sub>2</sub> PO <sub>4</sub> (g)	Ca/Si <sub>(R)</sub>
A0	19.719	6.804	-
A1	4.912	1.699	5
A2	9.824	3.397	10
A3	14.736	5.095	15
A4	19.647	6.793	20
A5	24.560	8.491	25

<sup>\*)</sup> Ca/P ratio and SiO<sub>2</sub> content were kept constant at 1.67 and 0.25 g

mixed with double distilled water to produce 50 mL of solution I. Fifty mL of solution II was prepared by dissolving a certain weight of KH<sub>2</sub>PO<sub>4</sub> in double-distilled water. Solution II was then slowly added to solution I with gentle stirring. Afterwards, about 15 mL of NH<sub>4</sub>OH 32% was added into the mixture to reach pH > 9. The stirring process was continued for 1 h and then the mixture was kept at room temperature for 24 h. The formed precipitate was washed with 2 L of double distilled water and dried in an electric oven at 50 °C for 48 h to obtain a white powder. The product was called as-precipitate powder. The as-precipitate powder was calcined in an electric furnace at 600 °C for 2 h at air atmosphere to obtain the HA-SiO<sub>2</sub> composite (calcined powder). The composition of the precursors and the sample codes are presented in Table 1.

## RESULTS AND DISCUSSION

The transformation of the chemical and crystal structure of the products at various Ca/Si reactant molar ratio (Ca/Si<sub>(R)</sub>) were studied for the as-precipitate and calcined powder. Meanwhile, the surface properties and zeta potential were studied for the calcined powder.

### FTIR Analysis

Fig. 1 shows the FTIR spectra of SiO<sub>2</sub> and the HA-SiO<sub>2</sub> composite. For the SiO<sub>2</sub> spectrum, characteristic peaks of SiO<sub>2</sub> appeared at 1100, 805 and 466  $\text{cm}^{-1}$  that are attributed to the antisymmetric stretching vibration of Si–O–Si, symmetric vibration of Si–O–Si and bending vibration of Si–O–Si, respectively. A broad peak around 3500  $\text{cm}^{-1}$  is attributed to the vibration of the silanol group. For the as-precipitate powder, the antisymmetric



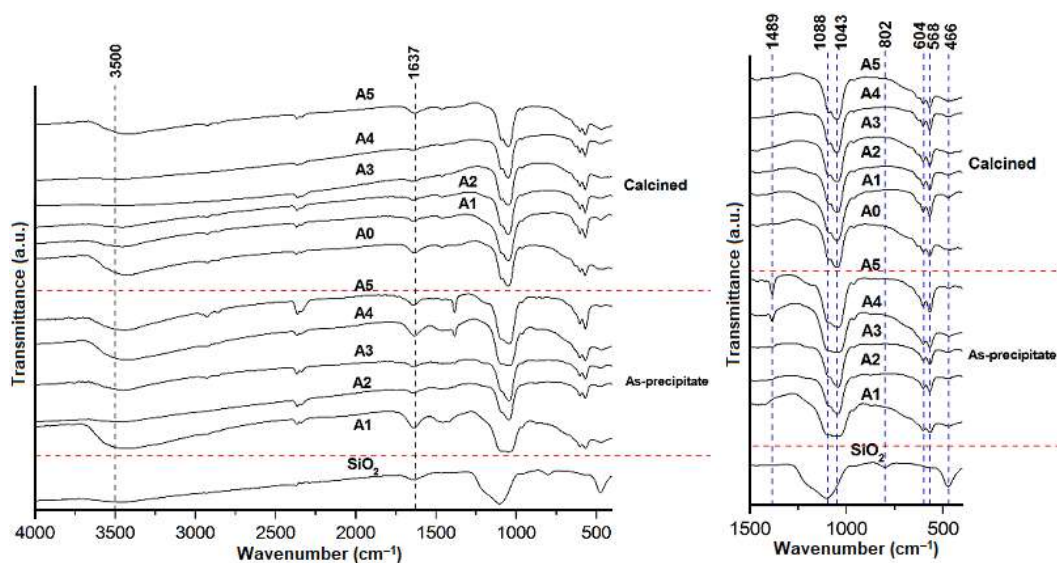


Fig 1. FTIR spectra of SiO<sub>2</sub> and HA-SiO<sub>2</sub> composites

stretching vibration of Si–O–Si overlapped with the peak of the asymmetric stretching vibration of PO<sub>4</sub><sup>3-</sup> at 1088 cm<sup>-1</sup>. The peak of the bending vibration of Si–O–Si at around 466 cm<sup>-1</sup> decreased significantly and the peak of the symmetric vibration of Si–O–Si at 805 cm<sup>-1</sup> disappeared. This phenomenon has been explained by a literature, which stated that introducing Ca<sup>2+</sup> ions into a SiO<sub>2</sub> network may damage some Si–O–Si bonds to form Si–O–Ca–O–Si groups [25].

During the deposition process, the silanol groups in SiO<sub>2</sub> released H<sup>+</sup> due to the alkaline condition produced by the Si–O<sup>-</sup> site. The Si–O<sup>-</sup> site then interacted with Ca<sup>2+</sup> to form Si–O–Ca<sup>+</sup> which interacted further with PO<sub>4</sub><sup>3-</sup> and another Ca<sup>2+</sup> until HA crystal seeds were formed. The crystal seed grew continuously on the SiO<sub>2</sub> surface in 3 dimensions. The tetrahedral symmetry of the PO<sub>4</sub><sup>3-</sup> group such as the asymmetric stretching ( $\nu_3$ ) appeared as sharp peaks at 1088 and 1043 cm<sup>-1</sup> and the asymmetric deformation ( $\nu_4$ ) appeared at 568 and 604 cm<sup>-1</sup> [26-27]. A wide peak around 3500 cm<sup>-1</sup> indicated the presence of stretching O–H groups with hydrogen bonds of HA or absorbed H<sub>2</sub>O. The presence of absorbed H<sub>2</sub>O is proven by a peak at 1637 cm<sup>-1</sup>. CO<sub>3</sub><sup>2-</sup> groups that substitute PO<sub>4</sub><sup>3-</sup> site appeared at 1489 cm<sup>-1</sup> [28-29]. The spectra of calcined powder A0–A5 looks similar to the as-precipitate spectra but with sharper peaks. Calcination of the as-precipitate powder at 600 °C for 2 h caused molecules arrangement

and the release of small molecules such as CO<sub>2</sub> and H<sub>2</sub>O, causing the CO<sub>3</sub><sup>2-</sup> peak to disappear, and the H<sub>2</sub>O peak became shorter.

### XRD Analysis

Crystal analysis based on XRD patterns is shown in Fig. 2. The characteristic peak of SiO<sub>2</sub> appeared as a broad peak at  $2\theta = 22^\circ$ . This peak disappeared when SiO<sub>2</sub> was composited with HA, due to the strong interaction of silica – HA [30]. For all as-precipitate powder, HA with low crystallinity was formed in the composites. The intensity of the peaks and sharpness increased with the increase of the Ca/Si molar ratio of the reactants (Ca/Si<sub>(R)</sub>). The peaks of the calcined powder were sharper than the as-precipitate powder. These peak patterns confirmed that the composites contained HA in hexagonal crystal lattice according to JCPDS card no 090432. The crystal cell parameters of the standard were  $a = b = 0.9418 \text{ nm}$   $c = 0.6884 \text{ nm}$ ,  $\alpha = \beta = 90^\circ$   $\gamma = 120^\circ$  and cell volume = 1.586 nm<sup>3</sup>. Broad peaks of HA that appeared at  $2\theta$  of around 25, 31, 32, 33, 34, 40, 47 and 49° are attributed to the crystal plane of (002), (211), (112), (300), (202), (212), (222), and (213), respectively. The low crystallinity of HA is desirable for biomaterial because it produces high bioactivity [31]. The effect of the Ca/Si<sub>(R)</sub> molar ratio to the HA crystal formation can be seen from the increase of peak intensity and the sharpening of the

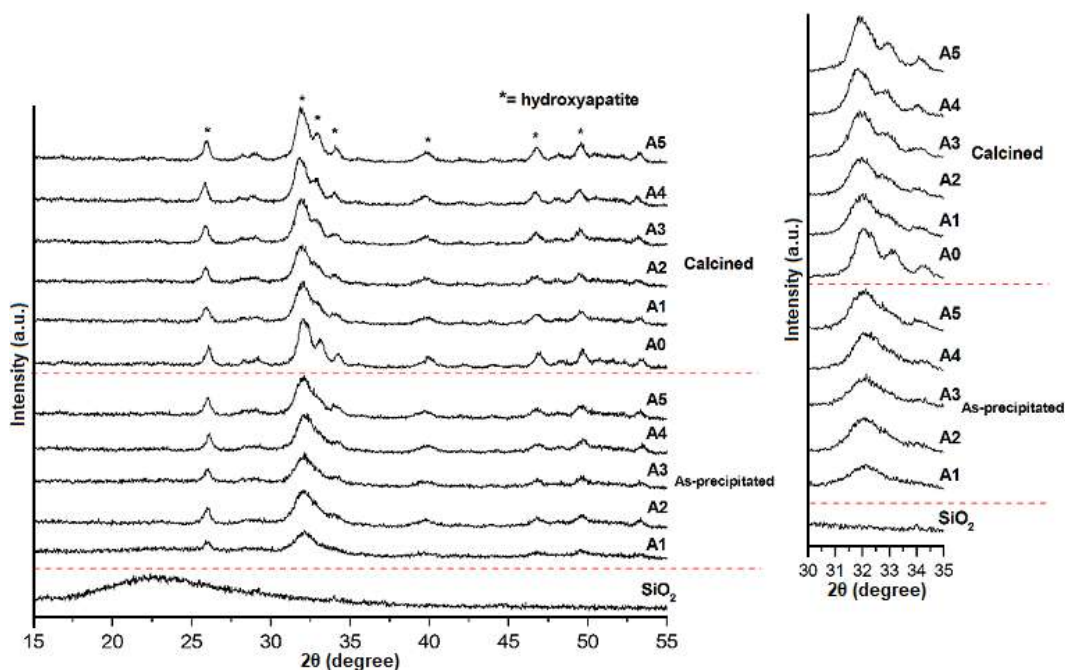


Fig 2. XRD patterns of SiO<sub>2</sub> and HA-SiO<sub>2</sub> composites

peak shape as the Ca/Si<sub>(R)</sub> ratio increases (Fig 2. inset). At high Ca/Si<sub>(R)</sub> molar ratio, the effect of silica on the formation of HA was not significant.

From the diffraction data that were fitted with Origin, the 2θ position and FWHM of every single peaks was able to be determined. The d-spacing that was calculated using Bragg's law and the information of miller indices from JCPDS data was used to determine the a and c parameters of HA crystal in A0–A5 samples. Also, the Scherrer equation was used to calculate the crystallite size. The cell parameters and crystallite size of HA in A0–A5 samples are shown in Table 2. The a value for all samples was almost the same. Meanwhile, the c value, as well as the cell volume of HA in the composites, were larger than pure HA but those values were fluctuated to Ca/Si<sub>(R)</sub>. The

formation of HA crystal was slightly distorted by the presence of SiO<sub>2</sub>. The crystallite size of HA in A1–A5 samples was in the range of 7.557 ± 0.164–9.581 ± 0.144 nm which was lower than pure HA (12.788 ± 0.450 nm). The crystallite size increased with the increase of Ca/Si<sub>(R)</sub>. The HA-SiO<sub>2</sub> composite is predicted to have a higher bioactivity than pure HA due to its higher volume and lower crystallite size. All parameters of the HA cell products were lower than the HA standard in JCPDS card no 090432. It is well known that HA cell parameters are dependent on the synthesis method used [31].

### SEM, EDS and TEM Analysis

SEM images of sample A1–A5 showed different morphologies for each Ca/Si<sub>(R)</sub> molar ratio (Fig. 3). For

Table 2. Cell parameters and crystallite size of HA in A0–A5 samples

Sample	a (nm)	c (nm)	V (nm <sup>3</sup> )	Crystallite size (nm)
A0	0.935 ± 6. 10 <sup>-4</sup>	0.683 ± 3. 10 <sup>-4</sup>	1.549 ± 1.2. 10 <sup>-3</sup>	12.788 ± 0.450
A1	0.933 ± 5. 10 <sup>-4</sup>	0.687 ± 3. 10 <sup>-4</sup>	1.554 ± 1.0. 10 <sup>-3</sup>	7.557 ± 0.164
A2	0.935 ± 5. 10 <sup>-4</sup>	0.688 ± 3. 10 <sup>-4</sup>	1.561 ± 0.9. 10 <sup>-3</sup>	7.783 ± 0.230
A3	0.935 ± 4. 10 <sup>-4</sup>	0.688 ± 2. 10 <sup>-4</sup>	1.562 ± 0.8. 10 <sup>-3</sup>	8.413 ± 0.126
A4	0.937 ± 4. 10 <sup>-4</sup>	0.689 ± 2. 10 <sup>-4</sup>	1.572 ± 0.8. 10 <sup>-3</sup>	8.971 ± 0.152
A5	0.935 ± 4. 10 <sup>-4</sup>	0.686 ± 2. 10 <sup>-4</sup>	1.559 ± 0.8. 10 <sup>-3</sup>	9.581 ± 0.144

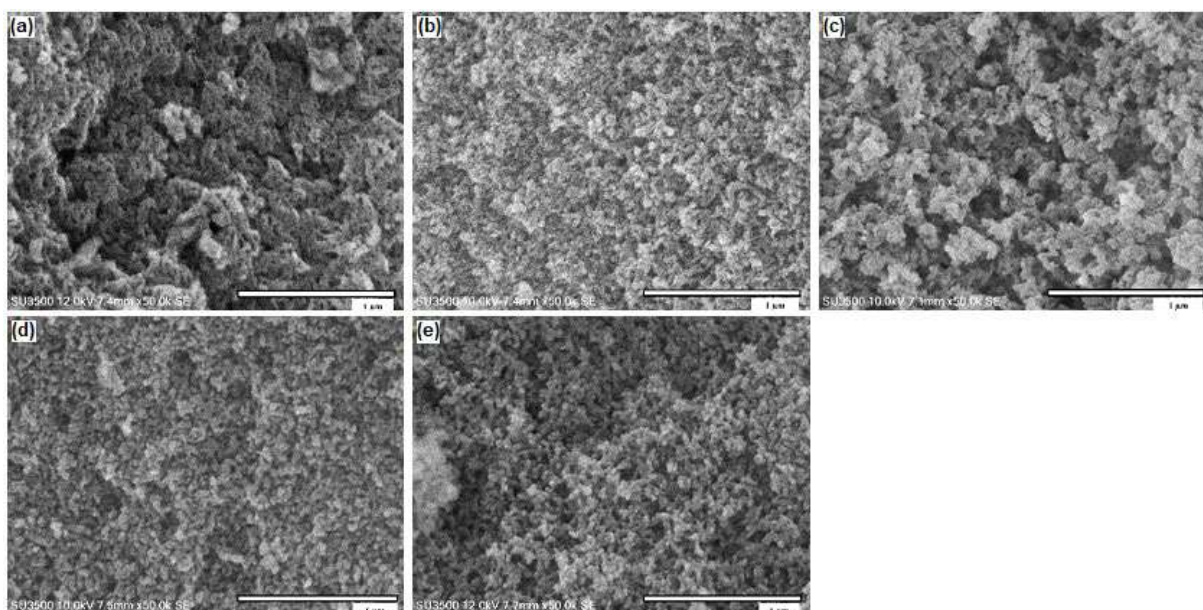


**Fig 3.** Surface topography of A1 (a), A2 (b), A3 (c), A4 (d), and A5 (e) sample

Ca/Si<sub>(R)</sub> = 5 (A1), the image showed a rough surface that compose of regular shape particles with size < 100 nm. For Ca/Si<sub>(R)</sub> = 10 (A2), the surface morphology was flat with more tightly arranged particles. A different image was shown for Ca/Si<sub>(R)</sub> = 15 (A3), where the particles were larger than A1 and A2, and agglomerated without a pattern. For Ca/Si<sub>(R)</sub> = 20 (A4) and 25 (A5), the images were nearly the same as A2, in which the particles have a regular shape with size < 100 nm.

TEM images of samples A0, A1, and A5 showed that particles of pure HA were different in shape and size compared to HA-SiO<sub>2</sub> composite particles (Fig. 4). Pure HA particles were in the form of long rod-like shapes with particle size < 100 nm. Particles of the HA-SiO<sub>2</sub> composite in sample A1 were regular-shaped in the form of rod-like

particles but in smaller sizes (< 50 nm). A different phenomenon occurred to sample A5, in which its shape and size were a combination of A0 and A1 samples. Short rod-like particles with particle sizes of < 50 nm were mixed with long rod-like particles with particle sizes of < 100 nm. These images as well as the crystallite size data confirmed that SiO<sub>2</sub> acted as a morphology directing agent. Through silanol - Ca interactions, the Ca<sub>9</sub>(PO<sub>4</sub>)<sub>6</sub> clusters were formed on the SiO<sub>2</sub> surface, and then these intermediate states grew in 3 dimensions to build HA crystallite on the silica surface [30]. The other HA-SiO<sub>2</sub> clusters inhibited further growth of HA so that HA-SiO<sub>2</sub> composite with lower Ca/Si ratio had smaller particles, hence suitable to be used as the powder component of CPC. The particles can produce a paste

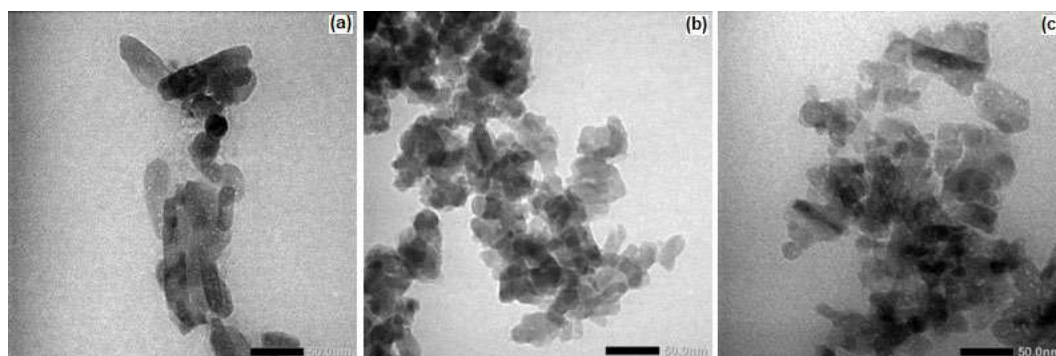


**Fig 4.** TEM images of A0 (a), A1 (b) and A5 (c) sample

with high viscosity due to the low particle-particle and particle-syringe wall friction.

Table 3 shows the elemental composition of the surface of the HA-SiO<sub>2</sub> composites. By increasing the Ca/Si<sub>(R)</sub> molar ratio, the Si content decreased from 2.72 to 0.54%, while the P content tended to be stable at 11.81–13.68%. The O content increased from 61.92 to 68.98%, while the Ca content fluctuated around 18.67–23.32%. The Ca/Si<sub>(p)</sub> ratio of the composites tended to increase linearly with Ca/Si<sub>(R)</sub>, except for sample A3. Meanwhile, Ca/P<sub>(p)</sub> or Ca/P ratio of the composites tended to decrease by the increase of Ca/Si<sub>(R)</sub>, except for sample A4. This can happen due to the tendency of HA and SiO<sub>2</sub> particles to agglomerate [23]. For all Ca/Si<sub>(R)</sub> ratios except for Ca/Si<sub>(R)</sub> = 15 (A3), the Ca/Si<sub>(p)</sub> was higher than Ca/Si<sub>(R)</sub> (Table 1). This data confirmed that SiO<sub>2</sub> tended to be in the inside of the HA-SiO<sub>2</sub> composite while HA covered the composite surface.

The formation of HA-SiO<sub>2</sub> composites with HA deposited on the SiO<sub>2</sub> surface was confirmed with EDS element mapping (Fig. 5). Mapping was done for Ca, P, Si, and O on the sample surface area of 750 μm<sup>2</sup>. For

Ca/Si<sub>(R)</sub> of 5 (A1), the mapping of Ca and P showed that both elements were evenly distributed on the sample surface with the same color intensity. Both images showed dark holes in the same position. Si element mapping confirmed that the dark holes were Si aggregates and there were at least five Si aggregates. The absence of black holes in the element mapping of O indicated that the composite surface was filled with oxygen. The image for element O showed that the composite surface was rough. For Ca/Si<sub>(R)</sub> of 25 (A5), the element mapping of Ca and P was not as intense as for the A1 sample. The images showed two dark holes in the same position. Image mapping of Si confirmed that only 1 of the holes was Si aggregate and from image mapping of O, the second hole indicated that the composite surface was rough. Besides appearing as an agglomerate, Si was also distributed evenly on the composite surface. At high Ca/Si ratios, Si had a low tendency to form aggregates. The surface phenomenon of sample A5 was related to the element composition in Table 3. The value of Ca/P<sub>(p)</sub> and Ca/Si<sub>(p)</sub> indicated that HA covered the composite surface. For CPC application, the presence of

**Table 3.** Elements composition, Ca/P<sub>(p)</sub> and Ca/Si<sub>(p)</sub> ratio on HA-SiO<sub>2</sub> composite surface

Sample	Element (%)				Ca/P <sub>(p)</sub> Ratio	Ca/Si <sub>(p)</sub> Ratio
	Ca	P	Si	O		
A1	22.48	12.88	2.72	61.92	1.75	8.26
A2	22.59	13.68	1.33	62.40	1.65	16.98
A3	20.50	12.65	1.47	65.37	1.62	13.95
A4	23.32	12.22	0.76	63.70	1.91	30.68
A5	18.67	11.81	0.54	68.98	1.58	34.57

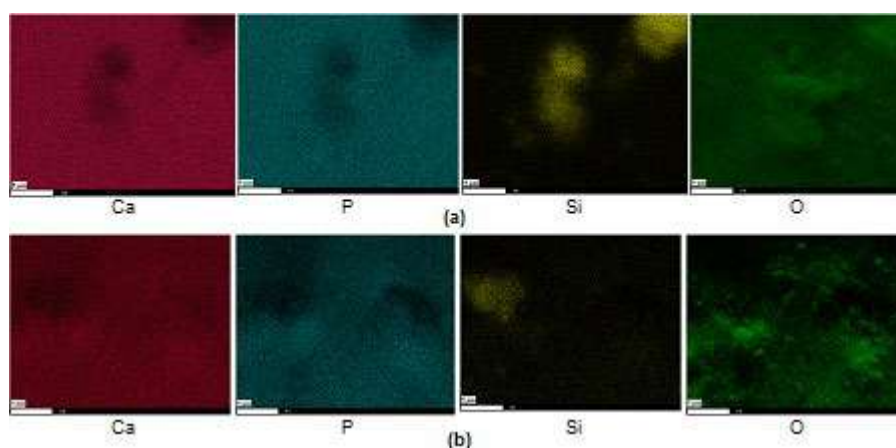


**Fig 5.** Surface element mapping of A1 (a) and A5 (b) sample

**Table 4.** The zeta potential of SiO<sub>2</sub> and A0–A5 samples

Sample	Zeta Potential (mV)
SiO <sub>2</sub>	-43.895 ± 0.061
A0	-1.623 ± 0.025
A1	-1.759 ± 0.028
A2	-0.259 ± 0.027
A3	-1.481 ± 0.027
A4	-1.411 ± 0.057
A5	-2.935 ± 0.030

HA on the composite surface is highly expected due to the HA ability to interact with living bone tissues [1-3]. In addition, the rough surface of the composite will support the attachment of CPC on the bone tissue surface [31].

### Measurement of Zeta Potential

Table 4 shows the zeta potential of SiO<sub>2</sub> and A0–A5 samples in water. The zeta potential value of SiO<sub>2</sub> was -43.895 ± 0.061 mV, which indicated that the SiO<sub>2</sub> dispersion in water was stable. In contrast, a previous study found that silica nanoparticles made from *Bambusa vulgaris* leaves had a zeta potential value of -0.29 mV [32]. Sample A1 that contained pure HA had a zeta potential of -1.623 ± 0.025 mV, which indicated that HA dispersion in water was unstable and had a great tendency to form aggregates quickly. The same condition occurred to samples A1–A5. The zeta potential of HA-SiO<sub>2</sub> composites was about -0.259 ± 0.027 to -2.935 ± 0.030 mV. The stability of SiO<sub>2</sub> dispersion changed due to the deposition of HA. HA that was deposited on the SiO<sub>2</sub> surface decreased the repulsion energy of the particles in water. The negative zeta potential value of the HA-SiO<sub>2</sub> composite will be beneficial to CPC because it will drive Ca<sup>2+</sup> ions in the body liquid to attach to the CPC surface. Furthermore, a negative zeta potential value is required in bone cell adhesion [26]. Therefore, the composite is predicted to have good bioactivity [33].

### CONCLUSION

The obtained HA-SiO<sub>2</sub> composite had excellent properties such as being covered by HA, resulting in greater lattice volume and smaller crystallite size compared to pure HA. The shape of the HA-SiO<sub>2</sub> particles was similar to pure HA but smaller in size. The

composites surface was rough with zeta potential values almost the same as pure HA. These properties make HA-SiO<sub>2</sub> composite a promising material to be used as a powder component of injectable calcium phosphate cement.

### ACKNOWLEDGMENTS

The authors gratefully acknowledge Universitas Gadjah Mada, Yogyakarta, Indonesia for the financial support through the research grant “*Rekognisi Tugas Akhir (RTA)*” with the contract number: 3204/UN1/DITLIT/DIT-LIT/LT/2019.

### AUTHOR CONTRIBUTIONS

Tri Windarti carried out the experiment, Tri Windarti and Nuryono analyzed data and wrote the manuscript, Nuryono and Widjijono supervised the experiment. All authors approved the manuscript.

### REFERENCES

- [1] Larsson, S., Stadelmann, V.A., Arnoldi, J., Behrens, M., Hess, B., Procter, P., Murphy, M., and Pioletti, D.P., 2012, Injectable calcium phosphate cement for augmentation around cancellous bone screws. In vivo biomechanical studies, *J. Biomech.*, 45 (7), 1156–1160.
- [2] Apelt, D., Theiss, F., El-Warrak, A.O., Zlinszky, K., Bettschart-Wolfisberger, R., Bohner, M., Matter, S., Auer, J.A., and von Rechenberg, B., 2004, In vivo behavior of three different injectable hydraulic calcium phosphate cements, *Biomaterials*, 25 (7-8), 1439–1451.
- [3] Heinemann, S., Rössler, S., Lemm, M., Ruhnaw, M., and Nies, B., 2013, Properties of injectable ready-to-use calcium phosphate cement based on water-immiscible liquid, *Acta Biomater.*, 9 (4), 6199–6207.
- [4] Motisuke, M., Mestres, G., Renó, C.O., Carrodegua, R.G., Zavaglia, C.A.C., and Ginebra, M.P., 2017, Influence of Si substitution on the reactivity of  $\alpha$ -tricalcium phosphate, *Mater. Sci. Eng., C*, 75, 816–821.
- [5] Zhou, S., Ma, J., Shen, Y., Haapasalo, M., Ruse, N.D., Yang, Q., and Troczynski, T., 2013, In vitro

- studies of calcium phosphate silicate bone cements, *J. Mater. Sci. Mater. Med.*, 24 (2), 355–364.
- [6] Sowjanya, J.A., Singh, J., Mohita, T., Sarvanan, S., Moorthi, A., Srinivasan, N., and Selvamurugan, N., 2013, Biocomposite scaffolds containing chitosan/alginate/nano-silica for bone tissue engineering, *Colloids Surf., B*, 109, 294–300.
- [7] Sopcak, T., Medvecký, L., Giretova, M., Stulajterova, R., Durisin, J., Girman, V., and Faberova, M., 2016, Effect of phase composition of calcium silicate phosphate component on properties of brushite based composite cements, *Mater. Charact.*, 117, 17–29.
- [8] Heinemann, S., Heinemann, C., Wenisch, S., Alt, V., Worch, H., and Hanke, T., 2013, Calcium phosphate phases integrated in silica/collagen nanocomposite xerogels enhance the bioactivity and ultimately manipulate the osteoblast/osteoclast ratio in a human co-culture model, *Acta Biomater.*, 9 (1), 4878–4888.
- [9] Szurkowska, K., and Kolmas, J., 2017, Hydroxyapatites enriched in silicon–Bioceramic materials for biomedical and pharmaceutical applications, *Prog. Nat. Sci.*, 27 (4), 401–409.
- [10] Motisuke, M., Santos, V.R., Bazanini, N.C., and Bertran, C.A., 2014, Apatite bone cement reinforced with calcium silicate fibers, *J. Mater. Sci. Mater. Med.*, 25 (10), 2357–2363.
- [11] Geffers, M., Barralet, J.E., Groll, J., and Gbureck, U., 2015, Dual-setting brushite-silica gel cements, *Acta Biomater.*, 11, 467–476.
- [12] Ahn, G., Lee, J.Y., Seol, D.W., Pyo, S.G., and Lee, D., 2013, The effect of calcium phosphate cement-silica composite materials on proliferation and differentiation of pre-osteoblast cells, *Mater. Lett.*, 109, 302–305.
- [13] Kao, C.T., Huang, T.H., Chen, Y.J., Hung, C.J., Lin, C.C., and Shie, M.Y., 2014, Using calcium silicate to regulate the physicochemical and biological properties when using  $\beta$ -tricalcium phosphate as bone cement, *Mater. Sci. Eng., C*, 43, 126–134.
- [14] Tomoaia, G., Mocanu, A., Vida-Simiti, I., Jumate, N., Bobos, L.D., Soritau, O., and Tomoaia-Cotisel, M., 2014, Silicon effect on the composition and structure of nanocalcium phosphates: In vitro biocompatibility to human osteoblasts, *Mater. Sci. Eng., C*, 37, 37–47.
- [15] Song, Z., Liu, Y., Shi, J., Ma, T., Zhang, Z., Ma, H., and Cao, S., 2018, Hydroxyapatite/mesoporous silica coated gold nanorods with improved degradability as a multi-responsive drug delivery platform, *Mater. Sci. Eng., C*, 83, 90–98.
- [16] Grandfield, K., and Zhitomirsky, I., 2008, Electrophoretic deposition of composite hydroxyapatite-silica-chitosan coatings, *Mater. Charact.*, 59 (1), 61–67.
- [17] Jia, Z.Q., Guo, Z.X., Chen, F., Li, J.J., Zhao, L., and Zhang, L., 2018, Microstructure, phase compositions and in vitro evaluation of freeze casting hydroxyapatite-silica scaffolds, *Ceram. Int.*, 44 (4), 3636–3643.
- [18] Villacampa, A.I., and García-Ruiz, J.M., 2000, Synthesis of a new hydroxyapatite-silica composite material, *J. Cryst. Growth*, 211 (1-4), 111–115.
- [19] Karimi, R., Abbas, A., Nourbakhsh, N., Nourbakhsh, M., and Mackenzie, K.J.D., 2017, Phase formation, microstructure and setting time of MCM-48 mesoporous silica nanocomposites with hydroxyapatite for dental applications: Effect of the Ca/P ratio, *Ceram. Int.*, 43 (15), 12857–12862.
- [20] Yamada, S., Nishikawa, M., and Tagaya, M., 2018, Mesoporous silica formation on hydroxyapatite nanoparticles, *Mater. Lett.*, 211, 220–224.
- [21] Shen, Y., 2017, Rice husk silica derived nanomaterials for sustainable applications, *Renewable Sustainable Energy Rev.*, 80, 453–466.
- [22] Pode, R., 2016, Potential applications of rice husk ash waste from rice husk biomass power plant, *Renewable Sustainable Energy Rev.*, 53, 1468–1485.
- [23] Yousefpour, M., and Taherian, Z., 2013, The effects of ageing time on the microstructure and properties of mesoporous silica-hydroxyapatite nanocomposite, *Superlattices Microstruct.*, 54, 78–86.
- [24] Nayak, J., and Bera, J., 2009, A simple method for production of humidity indicating silica gel from rice husk ash, *J. Met. Mater. Miner.*, 19 (2), 15–19.
- [25] Pajchel, L., and Kolodziejski, W., 2018, Synthesis and characterization of MCM-48/hydroxyapatite

- composites for drug delivery: Ibuprofen incorporation, location and release studies, *Mater. Sci. Eng., C*, 91, 734–742.
- [26] Fahami, A., Beall, G.W., and Betancourt, T., 2016, Synthesis, bioactivity and zeta potential investigations of chlorine and fluorine substituted hydroxyapatite, *Mater. Sci. Eng., C*, 59, 78–85.
- [27] Malakauskaite-Petruleviciene, M., Stankeviciute, Z., Niaura, G., and Garskaite, E., 2016, Characterization of sol-gel processing of calcium phosphate thin films on silicon substrate by FTIR spectroscopy, *Vib. Spectrosc.*, 85, 16–21.
- [28] Nurlidar, F., and Kobayashi, M., 2019, Succinylated bacterial cellulose induce carbonated hydroxyapatite deposition in a solution mimicking body fluid, *Indones. J. Chem.*, 19 (4), 858–864.
- [29] Hamzah, S., Yatim, N.I., Alias, M., Ali, A., Rasit, N., and Abuhabib, A., 2019, Extraction of hydroxyapatite from fish scales and its integration with rice husk for ammonia removal in aquaculture wastewater, *Indones. J. Chem.*, 19 (4), 1019–1030.
- [30] Shiba, K., Motozuka, S., Yamaguchi, T., Ogawa, N., Otsuka, Y., Ohnuma, K., Kataoka, T., and Tagaya, M., 2015, Effect of cationic surfactant micelles on hydroxyapatite nanocrystal formation: An investigation into the inorganic–organic interfacial interactions, *Cryst. Growth Des.*, 16 (3), 1463–1471.
- [31] Dorozhkin, S.V., 2017, "Calcium orthophosphate-based bioceramics and its clinical applications" in *Clinical Applications of Biomaterials*, Eds. Kaur, G., Springer International, Switzerland, 123–226.
- [32] Durairaj, K., Senthilkumar, P., Velmurugan, P., Dhamodaran, K., Kadirvelu, K., and Kumaran, S., 2019, Sol-gel mediated synthesis of silica nanoparticle from *Bambusa vulgaris* leaves and its environmental applications: Kinetics and isotherms studies, *J. Sol-Gel Sci. Technol.*, 90 (3), 653–664.
- [33] Latifi, S.M., Fathi, M., Sharifnabi, A., and Varshosaz, J., 2017, *In vitro* characterisation of a sol-gel derived *in situ* silica-coated silicate and carbonate co-doped hydroxyapatite nanopowder for bone grafting, *Mater. Sci. Eng., C*, 75, 272–278.

## Polarity Effect on the Electronic Structure of Molybdenum Dichalcogenides MoXY (X, Y = S, Se): A Computational Study Based on Density-Functional Theory

Salsabila Amanda Putri<sup>1\*</sup>, Edi Suharyadi<sup>2</sup>, and Moh. Adhib Ulil Absor<sup>2\*\*</sup>

<sup>1</sup>Graduate School of Physics, Department of Physics, Faculty of Mathematics and Natural Sciences, Universitas Gadjah Mada, Sekip Utara BLS 21, Yogyakarta 55281, Indonesia

<sup>2</sup>Department of Physics, Faculty of Mathematics and Natural Sciences, Universitas Gadjah Mada, Sekip Utara BLS 21, Yogyakarta 55281, Indonesia

\* **Corresponding author:**

email: salsabila.amanda@mail.ugm.ac.id\*;  
adib@ugm.ac.id\*\*

Received: July 19, 2020

Accepted: December 10, 2020

DOI: 10.22146/ijc.57949

**Abstract:** Computational research based on the Density Functional Theory (DFT) has been performed to explore the electronic structure of monolayer material Transition Metal Dichalcogenides (TMDCs) Molybdenum Dichalcogenides MoXY (X, Y = S; Se) in the first Brillouin zone by breaking its mirror symmetry due to the polarity effect. Our study discovered that Rashba spin-splitting could be identified around the  $\Gamma$  point by proposing the polarity effect on the system. Moreover, the anisotropic characteristic of Rashba spin-splitting in this system can be explicitly analyzed by using  $\bar{k} \cdot \bar{p}$  perturbation theory and the third-order symmetry group analysis. By performing the spin textures analysis, this research also recognizes the in-plane direction of spin textures. The tunable characteristic of the Rashba parameter of this monolayer polar MoSSe system under the strain effects control exhibits its potential to be the candidate of semiconductor material for the Spin Field Effect Transistor (SFET) device.

**Keywords:** TMDCs; spin-splitting; polarity; DFT; Rashba; strain

### ■ INTRODUCTION

The significant evolvement in the research scope of low-dimensional material for spin-field effect transistor (SFET) device was first generated by the astonishing isolation of graphene in 2004, which emerged various predominances [1]. As the pioneering of the wonder material, the researchers' inquisitiveness in other varieties of low-dimensional materials is also expanding. One of the prospective materials discoveries is transition metal dichalcogenides (TMDCs). In contrast to graphene, which has a zero bandgap [2-3], TMDCs are narrow-gap semiconductor materials with numerous excellence comparable to graphene, which is flexible [4], easy to fabricate [5], have a tunable electronic structure [6], as well as considerably thin and transparent [7]. One of the remarkable attractions of TMDCs is the presence of spin-orbit interactions (SOI), which leads to an emerging strong relativistic effect in the solid-state physics manifests as a large spin-splitting [8-9]. This

phenomenon can be controlled by applying some physical effects such as crystal defect [10], charge doping [11], atomic doping [12], electric field [13-14], polar structure [14-15] or strain effect [14,16-17]. The advantage of the phenomenon in TMDCs material conducts to an excellent concept for spintronics application such as valley hall effect [18], quantum dots, and qubits [19].

In consequence of the SOI emergence, the spin-splitting called Zeeman spin-splitting is intrinsically found in TMDCs [20-21]. The existence of time-reversal symmetry in TMDCs basically prompts the degeneration of around  $\Gamma$  and M points, but a Zeeman spin-splitting manifests at K point due to the broken time-reversal symmetry [9,22]. As in a computational study conducted by [3], the Zeeman spin-splitting was confirmed to appear at the K point in the first Brillouin zone of TMDCs electronic structure. However, the existence of out-of-plane mirror symmetry results in the



only Zeeman spin-splitting to be noticed. Nevertheless, the application of TMDCs for the SFET device requires another type of spin-splitting, namely Rashba spin-splitting, which can be identified in the electronic structure around  $\Gamma$  points [23]. The Rashba spin-splitting becomes essential for the SFET device since it generates a vital process called a spin precession [24], allowing to control the spin transport of the carriers in the SFET device by using gate voltage. The Rashba effect occurs in the systems lacking inversion symmetry. The absence of the inversion symmetry leads to the out-of-plane potential gradient, together with the SOI, induces the significant spin splitting of the bands called the Rashba spin-splitting [25]. For a two-dimensional electron gas system, the Rashba effect leads to the band dispersion of  $E(k) = \frac{\hbar^2}{2m^*} (|k| \pm k_R)^2 + E_R$ , where  $E_R$  and  $k_R$  are the Rashba energy and momentum offset, respectively. Both  $E_R$  and  $k_R$  characterized the Rashba parameter,  $\alpha_R = 2E_R/k_R$ , which are important to stabilize spin precession and achieve a phase offset for different spin channels in the SFET device.

In an equilibrium state, the TMDCs system has a mirror-symmetry in the out-of-plane direction, which only yields a spin-splitting called Zeeman spin-splitting to be noticed. The computational study by Affandi and Absor revealed that the TMDCs  $WX_2$  material (X: S, Se, Te), which is subjected to an external electric field, is proven to induce the Rashba spin-splitting due to mirror-symmetry breaking in the out-of-plane direction [26]. This mirror-symmetry breaking can be distinguished through the unequal bond length of  $W-Te_{(1)}$  and  $W-Te_{(2)}$ . The result of the Hamiltonian Rashba in the study also ascertained that the existence of the second and third-order of the Rashba parameters contributed to an anisotropic spin-splitting [26]. This broken symmetry also leads to the reduced point group of the TMDCs system [27].

Another approach as the implementation to induce Rashba spin-splitting is by proposing a polar structure that is rearranged from an initial structure  $MX_2$  to become an  $MXY$  polar structure [14-15]. This polar structure has already taken the attention since it has a great output on both optical and electrical properties [28]. The study of

the electronic structure a TMDCs polar structure of  $WSe_2$  reveals a shorter band gap rather than the non-polar structure  $WS_2$ , although both still obtain the identical substantial bandgap [29].

The synthesis of TMDCs material has been successfully accomplished in several experimental methods such as annealing [30] and chemical vapor deposition [31-32]. In the case of polar  $MoSSe$  material, one of the well-qualified methods is via the sulfurization [33] or selenization [34] methods. The result of the bandgap experimentation using photoluminescence (PL) spectroscopy confirms a consistent value with the computational calculations by using the density-functional theory (DFT) method with 1.68 eV [33]. The computational research in the heterostructure TMDCs is also confirmed successfully produced a large Rashba spin-splitting, meaning that TMDCs can be proposed as the candidate of heterostructure material in the spintronics application [35-36]. Meanwhile, in the heterostructures application, the strain effect becomes important, especially in the fabrication system, related to the misfit dislocations while forming a material having a different lattice parameter with the substrate [37-38].

By conducting the DFT-based computational study, we carried out the electronic structure of TMDCs material focused on the Molybdenum Dichalcogenides  $MoXY$  (X, Y = S, Se) material by breaking the mirror-symmetry through the polarity effect. The study will focus on the Rashba effects and its tunability characteristic under the strain effect. In addition, the anisotropic characteristic of Rashba spin-splitting in this system is explicitly analyzed by using  $\vec{k} \cdot \vec{p}$  perturbation theory and the third-order symmetry group analysis. By performing the spin textures analysis, this research also recognizes the in-plane direction of the spin textures calculation.

## ■ COMPUTATIONAL DETAILS

Our DFT calculations are performed using the generalized gradient approximation [39], implemented in the OpenMX code [40]. We adopted norm-conserving pseudopotentials [41] with an energy cutoff of 200 Rydberg for charge density. The  $8 \times 8 \times 1$  k-point

mesh was used for discretization of the real space Hamiltonian. The wave functions were expanded by a linear combination of multiple pseudoatomic orbitals generated using a confinement scheme [42-43], where two s-, two p-, and one d-character numerical pseudoatomic orbitals were used. The SOC interaction was included self consistently in all calculations by using j-dependent pseudopotentials [44]. The spin textures in the k-space were calculated using the spin density matrix of the spinor wave functions obtained from the DFT calculations that we applied recently to various 2D materials [10,12,16,26,29,45-48].

The primary materials used in the computational calculations are the representatives of the  $\text{MoX}_2$  structure monolayer, which consists of  $\text{MoS}_2$  and  $\text{MoSe}_2$ , as well as the representative of  $\text{MoXY}$  structure monolayer, which is  $\text{MoSSe}$ . The geometry represents both the polar  $\text{MoX}_2$  and non-polar  $\text{MoXY}$  monolayers are shown in Fig. 1(a) and 1(b), respectively, where the first Brillouin zone is characterized by several high symmetry points (K,  $\Gamma$ , M) is given in Fig. 1(c). We assumed that the monolayers are

highly clean systems without any impurities such as vacancy defect, interstitial, or atomic doping so that according to the Bloch theorem, the monolayers can be represented only by the primitive unit cell consisting of the three atoms. In fact, the highly crystalline quality of the systems for both the non-polar  $\text{MoX}_2$  and polar  $\text{MoXY}$  monolayer has been experimentally reported [30-34]. Here, we used the vacuum layer of 24 Å to avoid contiguous inter-layer interaction.

Table 1 summarizes that the  $\text{MoSSe}$  polar structure material establishes a lattice parameter of 3.25 Å, which is higher than the lattice parameter belonging to the non-polar  $\text{MoS}_2$  (3.20 Å) but relatively smaller over  $\text{MoSe}_2$  (3.40 Å). Besides, we also found that corresponds to the previous experimental [33-34] and computational [49] results, the lattice parameters are entirely consistent.

In this study, the crystal structure of TMDCs is established with a trigonal prismatic or known as the type 2H polymorph, which manifests as the most stable structure of TMDCs under the room-temperature. This structure consists of one transition metal atom M which

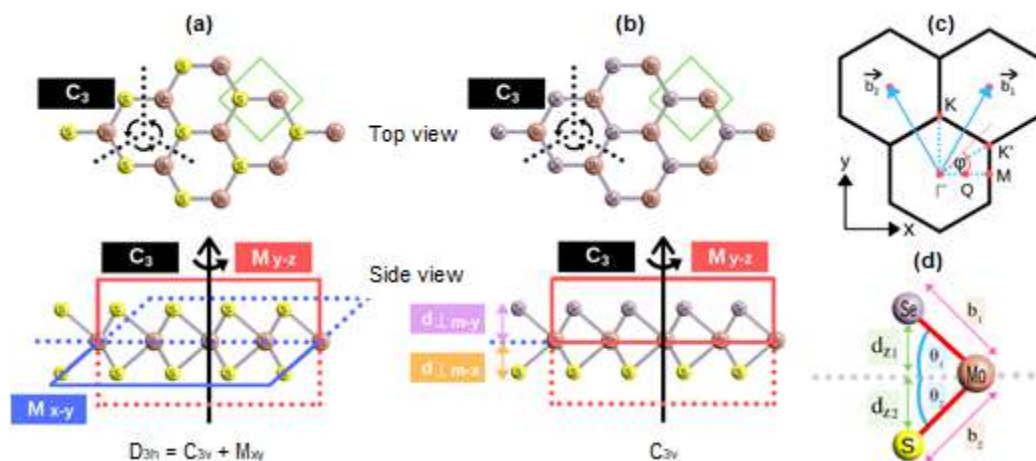


**Fig 1.** The structure of TMDCs systems (a) Non-polar  $\text{MX}_2$  and (b) Polar  $\text{MX}_Y$  in  $M = \text{Mo}$  and  $X, Y = \text{S}, \text{Se}$ , (c) The highest symmetry points in the first Brillouin zone as the observation points with  $\theta$  angle (d) Atomic distances in the z-axis direction, bond length, and angles between atoms in the  $\text{MoSSe}$  polar monolayer system

**Table 1.** Lattice parameter optimization result of monolayer system  $\text{MoS}_2$ ,  $\text{MoSe}_2$ , and  $\text{MoSSe}$

Monolayer Systems	Lattice parameter a (Å)		
	Optimization Result	Experimental Result	Optimization Result
$\text{MoS}_2$	3.20	$\text{MoS}_2$	3.20
$\text{MoSe}_2$	3.40	$\text{MoSe}_2$	3.40
$\text{MoSSe}$	3.25	$\text{MoSSe}$	3.25

bonds two chalcogen atoms in the +z and -z directions; hence one monolayer system will form one X-M-X combination along the z-direction. Although the bulk phase of  $\text{MX}_2$  appears centrosymmetric with the  $D_{6h}$  point group, however, in the monolayer phase, the broken inversion symmetry will occur and drive the point group transformation into  $D_{3h}$ . Precisely, the  $D_{3h}$  point group is composed of the  $C_{3v}$  point group including  $M_{xy}$  out-of-plane mirror symmetry, which is identified by the identical distance between the M-Y ( $d_{z1}$ ) and M-X ( $d_{z2}$ ) in the out-of-plane direction. However, in the case where the  $d_{z1} \neq d_{z2}$  due to the polar structure, the system will yield a broken mirror symmetry; therefore, the remaining point group is  $C_{3v}$  only (see Fig. 1(a) and 1(b)). This point group will be the basis of the perturbation theory analysis.

The structural optimization with the force criterion of  $10^{-5}$  Hartree/Bohr clearly shows obvious distinctions between polar and non-polar monolayer systems. According to the polar effect, the MXY system produces a different number between  $d_{z1}$  and  $d_{z2}$  (See Table 2), or in other words, the mirror symmetry breaking occurs and proven leads to the symmetry group transformation from  $D_{3h}$  to  $C_{3v}$ .

## RESULTS AND DISCUSSION

We next calculated the electronic structure with several visible results in Fig. 2. First off, Fig. 2(a)–2(c) show the direct bandgap properties of the non-polar systems in K point, while the polar system obtains the indirect one with conduction band minimum (CBM) and

**Table 2.** The distance of the atom in the direction of the z-axis, the length of the bond, and the angle between the atoms in the MoSSe polar monolayer system of the equilibrium state

Monolayer System	$d_{z1}$ (Å)	$d_{z2}$ (Å)	$b_1$ (Å)	$b_2$ (Å)	$\theta_1$ (°)	$\theta_2$ (°)
MoS <sub>2</sub>	1.59	1.59	2.44	2.44	40.66	40.66
MoSe <sub>2</sub>	1.67	1.67	2.58	2.58	41.30	41.30
MoSSe	1.73	1.56	2.53	2.42	43.15	40.18

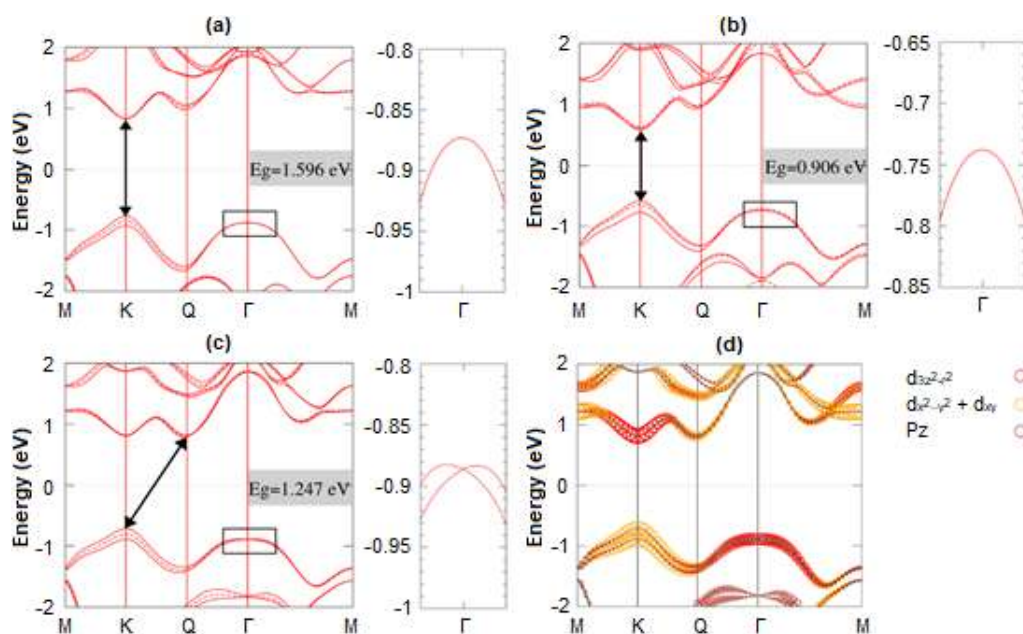


**Fig 2.** The electronic structure of equilibrium systems (a) MoS<sub>2</sub>, (b) MoSe<sub>2</sub>, (c) MoSSe with (dotted lines) and without SOI calculation (undotted lines) provided with each magnification in around  $\Gamma$  point. The spin-splitting around K referred to as Zeeman splitting, and around the  $\Gamma$  point, referred to as the Rashba splitting, are clearly shown. (d) The projected orbital band of MoSSe with the colored contributed orbital and the spectral weights are represented by the circle radius

valence band maximum (VBM) at the Q and K points, respectively. Since the high crystalline quality of the systems for both the non-polar  $\text{MoX}_2$  and polar  $\text{MoXY}$  monolayer has been experimentally achieved [30-34], in our calculations, we, therefore, considered only for the primitive unit cell. Our calculations revealed that there are no folding states found in the band structures in the first-Brillouin zone, which is consistent-well with the experiment of angle-resolved photoemission spectroscopy [50]. In our band structures calculations, the band gap value of  $\text{MoSSe}$  is 1.247 eV, which is slightly smaller than  $\text{MoS}_2$  (1.596 eV) but larger than  $\text{MoSe}_2$  (0.906 eV). It is discovered from the projected orbital band calculation of  $\text{MoSSe}$  (Fig. 2(d)) that both CBM and VBM are dominated by the coupling between the in-plane atomic orbital contribution of  $d_{x^2-y^2} + d_{xy}$ , which are enhanced and being responsible for the dropped band gap value.

It is also clearly noticeable that by including the SOI (undotted red lines), the calculation of the electronic structure without any strains applied for monolayer systems  $\text{MoS}_2$ ,  $\text{MoSe}_2$ , and  $\text{MoSSe}$ , particularly in VBM, all systems are producing Zeeman splitting around K point due to the time-reversal symmetry breaking [Fig. 2(a)-2(c)]. On the contrary, there is an additional splitting assured appearing around  $\Gamma$  point only on the polar system  $\text{MoSSe}$ , namely Rashba spin-splitting, which

is considered as a contribution of both out-of-plane atomic orbital  $d_{3z^2-r^2}$  and  $p_z$  (see Fig. 2(d)).

Next, we consider the compressive and expansive strain effects with the range from -4% to +8%. These small strains can be experimentally expected, in particular, if we introduce the substrates during the growth process of the monolayer [31-34]. Let us take the representative of the compressive strain with -4% strain as well as the expansive strain with +4% strain applied to the polar system  $\text{MoSSe}$ . Consequently, from the Fig. 3(a)-3(c), the CBM and VBM transition is clearly remarked from Q and K points in the equilibrium system into K and  $\Gamma$  points affected by the expansive strain, while no shifting occurs between CBM and VBM in consequence of the compressive strain. As a result, the indirect band gap remains, but the optical transition changes dramatically from the K (CBM)- $\Gamma$  (VBM) to the K (VBM)- $\Gamma$  (CBM) under the compressive strain (see Fig. 3(c)).

The polarity effect maintained by the  $\text{MoSSe}$  system is confirmed, causing spin-splitting at  $\Gamma$  points as shown by the green rectangular at  $\Gamma$  point in Fig. 3(a)-3(c). Basically, the Rashba effect occurs in a system due to the presence of the out-of-plane potential gradient induced by the absence of the inversion symmetry of the crystal [24]. However, in the case of the non-polar  $\text{MoX}_2$  monolayer, the existence of the  $M_{xy}$  out-of-plane mirror

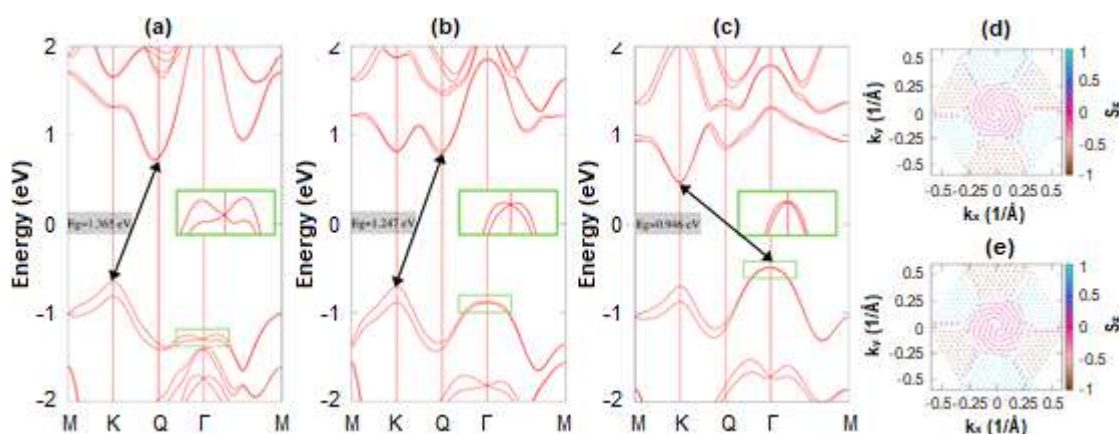


**Fig 3.** The electronic structure of the polar monolayer  $\text{MoSSe}$  system in (a) compressive strain (-4%), (b) no strain, (c) expansive strain (+4%) with green rectangle around  $\Gamma$  point denotes the Rashba spin-splitting and the additional magnification figure. (d) The representative of spin textures of the spin splitting around  $\Gamma$  point in  $k_x$  and  $k_y$  plane, with counterclockwise spin polarization, and (e) clockwise spin polarization, as the function of the out-of-plane spin polarization ( $S_z$ ) in the energy range of -1.25 to -1.4 eV of monolayer  $\text{MoSSe}$  system with compressive strain (-4%)

symmetry removes the out-of-plane potential gradient (Fig. 1(a)), and thus there is no Rashba splitting found in this system (Fig. 2(a)-(b)). In contrast, for the polar MoSSe system, the mirror symmetry  $M_{xy}$  is broken, characterized by the out-of-plane distance difference  $\Delta z = |d_{z1} - d_{z2}|$  between S and Se atoms (Fig. 1(b)). This leads to the fact that the out-of-plane potential gradient is induced, which is responsible for inducing the Rashba spin splitting around the  $\Gamma$  point (see Fig. 2(c) and Fig. 3(a)-3(c)). Importantly, by controlling the magnitude of the  $\Delta z$ , it is possible to modulate the Rashba splitting, opening an avenue to control the Rashba splitting, for example, by applying the strain, as shown in Fig. 3(a) and Fig. 3(c).

To further analyze the Rashba spin-splitting manifests in the MoSSe polar monolayer system, which is based on the  $C_{3v}$  point group, an analysis based on the  $\bar{k}\bar{p}$  perturbation theory and symmetry group is practiced. Hamiltonian Rashba can be obtained by calculating the irreducible representation of the system with a specific symmetry group. As formulated by Vajna et al. [51], Hamiltonian Rashba up to the third-order for the  $C_{3v}$  point group is as follows:

$$\hat{H}_R = \alpha_1(\bar{k}_x\sigma_y - \bar{k}_y\sigma_x) + \alpha_3^1[(\bar{k}_x^3 + \bar{k}_x\bar{k}_y^2)\sigma_y - (\bar{k}_x^2\bar{k}_y + \bar{k}_y^3)\sigma_x] + \alpha_3^2(\bar{k}_x^3 - 3\bar{k}_x\bar{k}_y^2)\sigma_z \quad (1)$$

By adjusting the coordinates of  $k_x$  and  $k_y$  in the first Brillouin zone, as shown in Fig. 1(c), Eq. (1) can be rewritten as:

$$\hat{H}_R = (\alpha_1\bar{k} + \alpha_3^1\bar{k}^3)(\cos\varphi\sigma_y - \sin\varphi\sigma_x) + \alpha_3^2\bar{k}^3\cos 3\varphi\sigma_z \quad (2)$$

To produce the final equation of the Rashba spin-splitting, an angle adjustment is made according to the measurement point ( $k$ -path) chosen in the first Brillouin zone. By using  $\varphi = \arctan \frac{\bar{k}_y}{\bar{k}_x}$ , and the direction of  $\Gamma - K$

point ( $\varphi = 0^\circ, 60^\circ, \dots$ ) and  $\Gamma - M$  point ( $\varphi = 30^\circ, 90^\circ, \dots$ ) can be written as follows:

$$(\Delta\varepsilon_R)_{(\Gamma-K)}^2 = (\alpha_1\bar{k} + \alpha_3^1\bar{k}^3)^2 + (\alpha_3^2\bar{k}^3)^2 \quad (3)$$

$$(\Delta\varepsilon_R)_{(\Gamma-M)}^2 = (\alpha_1\bar{k} + \alpha_3^1\bar{k}^3)^2 \quad (4)$$

Eq. (3) and (4) will be used to find the Rashba parameter of each strained and unstrained system.

The Rashba spin-splitting energy fitting results are represented by the MoSSe polar monolayer system of equilibrium (0% strain effect) and by applying compressive (-4%) and expansive strain effects (+4%). The fitting result reveals that the Rashba spin-splitting energy data is nearly fit at  $k$  of small value, with  $k = 0.6$  (1/Å) for  $\Gamma - K$  direction and  $k = 0.2$  (1/Å) for  $\Gamma - M$  direction. This means that the  $\bar{k}\bar{p}$  perturbation theory effectively explains the Rashba spin-splitting phenomenon around  $\Gamma$  points for the small  $k$  values. Nevertheless, our fitting calculation found that the  $\alpha_1$  value of the MoSSe polar monolayer system in the  $\Gamma - M$  direction overall has a higher value than in the  $\Gamma - K$  direction, which exhibits the fact of anisotropic Rashba Parameter characteristic of MoSSe material. For example, in the equilibrium, we find that the  $\alpha_1$  value of the MoSSe for  $\Gamma - K$  direction is 0.669 eVÅ, which is smaller than that for  $\Gamma - M$  direction (1.224 eVÅ). The  $\alpha_1$  is comparable with that observed on the doped-PtSe<sub>2</sub> monolayer [12] and polar tungsten dichalcogenide monolayer [26,29]. In addition to  $\alpha_1$ , the system's anisotropic characteristic is also the result of the first and third-order Rashba parameters contribution, namely  $\alpha_3^1$  and  $\alpha_3^2$  (see Table 3).

To further confirm the evidence of the Rashba splitting in the polar MoSSe monolayer, we calculate the spin polarization around the  $\Gamma$  point. We perform the spin textures calculation by plotting the expectation value

**Table 3.** The first, first-third, and second-third order of Rashba Parameter fitting result in monolayer polar MoSSe system by applying the strain effect

Strain Effect (%)	$\Gamma - K$ (eVÅ)			$\Gamma - M$ (eVÅ)	
	$\alpha_1$	$\alpha_3^1$	$\alpha_3^2$	$\alpha_1$	$\alpha_3^1$
-4	0.669	-9.054	0.016	1.224	-56.719
0	0.151	0.425	0.002	0.335	-6.806
4	0.191	0.265	0.000	0.218	-4.714

of spin in the  $x$ ,  $y$ , and  $z$  directions. The Rashba effect is confirmed appearing in all the polar system MoSSe with the in-plane polarization, both strained and unstrained systems with similar results of the spin textures visualization, having two components of spins consist of the counter-clockwise and the clockwise one (Fig. 3(d)–3(e)). It can be clearly seen that by observing  $k_x$  and  $k_y$  planes from 0 to 0.25, overall, all the spin textures of the MoSSe polar monolayer system seem to have a circular pattern. This implies that the Rashba effect characteristic of the system at a small value of  $k_x$  and  $k_y$  tend to be isotropic. Nevertheless, at  $k_x$  and  $k_y$ , which are more than 0.25, the spin polarization turns gradually into a hexagonal warping, meaning that the system assures shifts into the anisotropic one. This typical hexagonal pattern of the spin textures is similar to that observed on the doped-PtSe<sub>2</sub> monolayer [12]. We also figure out that the out-of-plane spin polarization on the higher  $k$  value appears as the contribution of the third-order Rashba parameter. Thus, the spin textures of the system are integrated by both in-plane and out-of-plane spin polarization, especially in the higher number of  $k$ .

Now, we discuss the effect of strain on the electronic properties and the Rashba spin splitting in the polar MoSSe monolayer. It is noticeable here that the

application of strain significantly affects the out-of-plane distance difference  $\Delta z$  between S and Se atoms, in which we found that the magnitude of the  $\Delta z$  is an inversely proportional percentage of the strain effect (Fig. 4(a)). As a result, the band gap modulation is achieved (Fig. 4(a)), which is due to the shifting energy between the  $\Gamma$  and K point in both the CBM and VBM [see Fig. 3(a)–3(c)]. At the same time, the change of the  $\Delta z$  by the strain is expected to affect the polarity of the MoSSe monolayer and thus sensitively changes the magnitude of the Rashba spin-splitting energy. As it is depicted in Fig. 4(c), we can find that overall, the third-order Rashba parameter is growing up by adding the strain percentage to the polar system MoSSe. In addition, the result of the Rashba parameter in the strained system manifests a relatively similar trend of the first-order Rashba parameter  $\alpha_1$  in both  $\Gamma$  - K and  $\Gamma$  - M directions, which tends to increase strongly by increasing the compressive strain (Fig. 4(c)). However, we observed an opposite trend of the third-order Rashba parameters  $\alpha_3^1$ , in particular for the bands along the  $\Gamma$  - M direction, where the enhancement of the third-order Rashba parameters  $\alpha_3^1$  is achieved under the increase of the expansive strain (Fig. 4(d)). These facts indicate that the strain effect is beneficial for the electronic structure

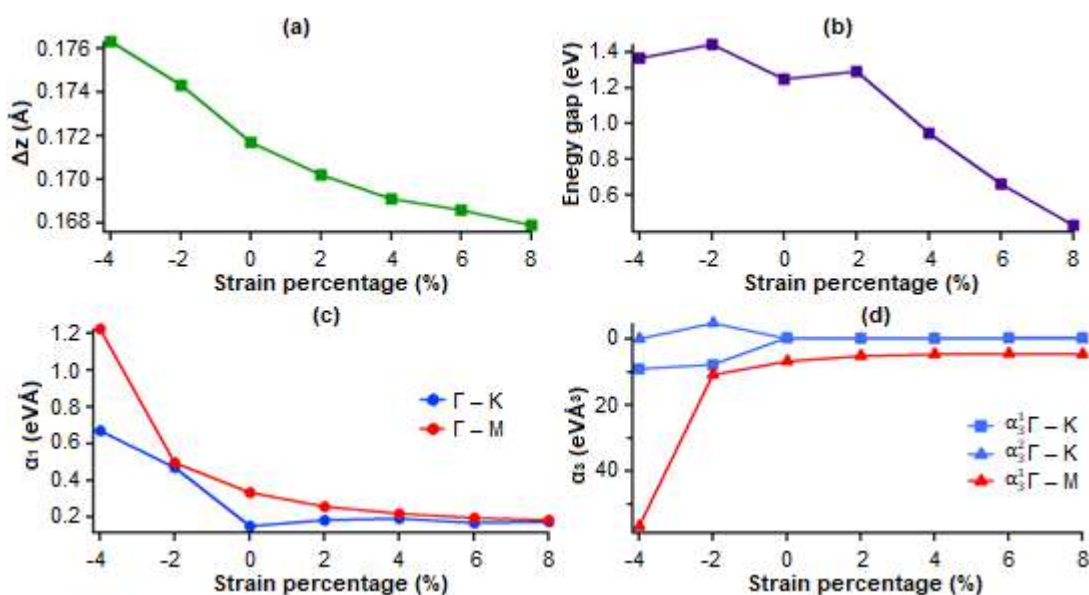


**Fig 4.** The strain percentage of the polar monolayer MoSSe systems as the function of (a) the out-of-plane distance ( $\Delta z$ ), (b) the energy gap, (c) the first-order Rashba parameter in  $\Gamma$  - K and  $\Gamma$  - M direction, (d) the third-order Rashba parameter in  $\Gamma$  - K and  $\Gamma$  - M direction, all from -4% to 8% strain effect

and Rashba splitting controls, suggesting the suitability of the MoSSe polar monolayer system for the spintronics device material application.

We noted here that the existence of the Rashba splitting found in the polar MoSSe monolayer system could be accessed experimentally in the spirit of the experimental observation of the spin splitting in the MoS<sub>2</sub> monolayer [50]. Since the Rashba splitting is observed near the  $\Gamma$  point in the VBM, observation of the Rashba splitting requires hole doping. Recently, the electron/hole doping techniques in various 2D materials are under rapid development realizing by the ion liquid gating technique [52-53]. Thus the application of the electron doping in polar MoSSe monolayer is plausible. Here, the hole doping can move the VBM around the  $\Gamma$  point close to the Fermi level; thus, the bands can be resolved by using ARPES [50]. Furthermore, the higher-order term of the Rashba effect can be further confirmed through the hexagonal warping of the Fermi surface obtained from the ARPES measurement. Therefore, we expect that our predictions will stimulate further theoretical and experimental efforts in the exploration of the Rashba effect in polar MoSSe monolayers, thus broadening the range of the 2D materials for future spintronic applications.

## ■ CONCLUSION

To conclude, the proposed polarity effect of the TMDCs monolayer material from the MoX<sub>2</sub> structure to polar MoXY conveyed into the electronic properties evolution, which raises Rashba spin-splitting around  $\Gamma$  point. The Rashba parameter and spin textures analysis can be adequately explained using  $\vec{k}\cdot\vec{p}$  perturbation theory and the third-order symmetry group analysis. This shows that the anisotropic characteristic of the Rashba parameter in MoSSe polar monolayer system is contributed by the third-order Rashba parameter, namely  $\alpha_3^1$  and  $\alpha_3^2$ . Moreover, by providing both compressive and expansive strains to the system, it is recognized that MoSSe polar monolayer system is proven in effectively controlling the Rashba parameter and suitable to be a candidate for spintronic material for SFET device.

## ■ ACKNOWLEDGMENTS

This work was supported by the PDUPT (2774/UN1/DITLIT/DIT-LIT/PT/2020) research grant and PD (1950/UN1/DITLIT/DIT-LIT/PT/2020) research grant supported by RISTEK-BRINT, Republic of Indonesia. The computations in this research were performed using the computer facilities at Universitas Gadjah Mada.

## ■ AUTHOR CONTRIBUTIONS

Moh. Adhib Ulil Absor led the project and provided the conceptualization. Salsabila Amanda Putri conducted the DFT calculations and wrote the initial draft preparation. Moh. Adhib Ulil Absor, Edi Suharyadi, and Salsabila Amanda Putri wrote and revised the manuscript. All authors agreed to the final version of this manuscript.

## ■ REFERENCES

- [1] Novoselov, K.S., Geim, A.K., Morozov, S.V., Jiang, D., Zhang, Y., Dubonos, S.V., Grigorieva, I.V., and Firsov, A.A., 2004, Electric field effect in atomically thin carbon films, *Science*, 306 (5696), 666–669.
- [2] Partoens, B., and Peeters, F.M., 2006, From graphene to graphite: Electronic structure around the K point, *Phys. Rev. B*, 74 (7), 075404.
- [3] Chen, C., Avila, J., Arezki, H., Yao, F., Nguyen, V.L., Lee, Y.H., Boutchich, M., and Asensio, M.C., 2017, Structural and electronic inhomogeneity of graphene revealed by Nano-ARPES, *J. Phys. Conf. Ser.*, 864, 012029.
- [4] Bertolazzi, S., Brivio, J., and Kis, A., 2011, Stretching and breaking of ultrathin MoS<sub>2</sub>, *ACS Nano*, 5 (12), 9703–9709.
- [5] Wang, Q.H., Kalantar-Zadeh, K., Kis, A., Coleman, J.N., and Strano, M.S., 2012, Electronics and optoelectronics of two-dimensional transition metal dichalcogenides, *Nat. Nanotechnol.*, 7 (11), 699–712.
- [6] Mak, K.F., Lee, C., Hone, J., Shan, J., and Heinz, T.F., 2010, Atomically thin MoS<sub>2</sub>: A new direct gap semiconductor, *Phys. Rev. Lett.*, 105 (13), 136805.

- [7] Radisavljevic, B., Radenovic, A., Brivio, J., Giacometti, V., and Kis, A., 2011, Single-layer MoS<sub>2</sub> transistors, *Nat. Nanotechnol.*, 6 (3), 147–150.
- [8] Kośmider, K., González, J.W., and Fernández-Rossier, J., 2013, Large spin splitting in the conduction band of transition metal dichalcogenide monolayers, *Phys. Rev. B*, 88 (24), 245436.
- [9] Zhu, Z.Y., Cheng, Y.C., and Schwingenschlögl, U., 2011, Giant spin-orbit-induced spin splitting in two-dimensional transition-metal dichalcogenide semiconductors, *Phys. Rev. B*, 84 (15), 153402.
- [10] Absor, M.A.U., Santoso, I., Harsojo, Abraha, K., Ishii, F., and Saito, M., 2017, Defect-induced large spin-orbit splitting in monolayer PtSe<sub>2</sub>, *Phys. Rev. B*, 96 (11), 115128.
- [11] Chen, J., Wu, K., Ma, H., Hu, W., and Yang, J., 2020, Tunable Rashba spin splitting in Janus transition metal dichalcogenide monolayers *via* charge doping, *RSC Adv.*, 10 (11), 6388–6394.
- [12] Absor, M.A.U., Santoso, I., Harsojo, Abraha, K., Kotaka, H., Ishii, F., and Saito, M., 2018, Strong Rashba effect in the localized impurity states of halogen-doped monolayer PtSe<sub>2</sub>, *Phys. Rev. B*, 97 (20), 205138.
- [13] Yuan, H., Bahramy, M.S., Morimoto, K., Wu, S., Nomura, K., Yang, B.J., Shimotani, H., Suzuki, R., Toh, M., Kloc, C., Xu, X., Arita, R., Nagaosa, N., and Iwasa, Y., 2013, Zeeman-type spin splitting controlled by an electric field, *Nat. Phys.*, 9 (9), 563–569.
- [14] Yao, Q.F., Cai, J., Tong, W.Y., Gong, S.J., Wang, J.Q., Wan, X., Duan, C.G., and Chu, J.H., 2017, Manipulation of the large Rashba spin splitting in polar two-dimensional transition-metal dichalcogenides, *Phys. Rev. B*, 95 (16), 165401.
- [15] Hu, T., Jia, F., Zhao, G., Wu, J., Stroppa, A., and Ren, W., 2018, Intrinsic and anisotropic Rashba spin splitting in Janus transition-metal dichalcogenide monolayers, *Phys. Rev. B*, 97 (23), 235404.
- [16] Absor, M.A.U., Kotaka, H., Ishii, F., and Saito, M., 2016, Strain-controlled spin splitting in the conduction band of monolayer WS<sub>2</sub>, *Phys. Rev. B*, 94 (11), 115131.
- [17] Hanakata, P.Z., Rodin, A.S., Park, H.S., Campbell, D.K., and Castro Neto, A.H., 2018, Strain-induced gauge and Rashba fields in ferroelectric Rashba lead chalcogenide Pb X monolayers (X = S, Se, Te), *Phys. Rev. B*, 97 (23), 235312.
- [18] Zhou, B.T., Taguchi, K., Kawaguchi, Y., Tanaka, Y., and Law, K.T., 2019, Spin-orbit coupling induced valley Hall effects in transition-metal dichalcogenides, *Commun. Phys.*, 2 (1), 26.
- [19] Kormányos, A., Zólyomi, V., Drummond, N.D., and Burkard, G., 2014, Spin-orbit coupling, quantum dots, and qubits in monolayer transition metal dichalcogenides, *Phys. Rev. X*, 4 (1), 011034.
- [20] Rybkovskiy, D.V., Gerber, I.C., and Durnev, M.V., 2017, Atomically inspired *k-p* approach and valley Zeeman effect in transition metal dichalcogenide monolayers, *Phys. Rev. B*, 95 (15), 155406.
- [21] Wang, T., Miao, S., Li, Z., Meng, Y., Lu, Z., Lian, Z., Blei, M., Taniguchi, T., Watanabe, K., Tongay, S., Smirnov, D., and Shi, S.F., 2019, Giant valley-Zeeman splitting from spin-singlet and spin-triplet interlayer excitons in WSe<sub>2</sub>/MoSe<sub>2</sub> heterostructure, *Nano Lett.*, 20 (1), 694–700.
- [22] Zollner, K., Faria Junior, P.E., and Fabian, J., 2019, Proximity exchange effects in MoSe<sub>2</sub> and WSe<sub>2</sub> heterostructures with CrI<sub>3</sub>: Twist angle, layer, and gate dependence, *Phys. Rev. B*, 100 (8), 085128.
- [23] Bychkov, Y.A., and Rashba, E.I., 1984, Properties of a 2D electron gas with lifted spectral degeneracy, *J. Exp. Theor. Phys. Lett.*, 39, 78.
- [24] Nitta, J., Akazaki, T., Takayanagi, H., and Enoki, T., 1997, Gate control of spin-orbit interaction in an inverted In<sub>0.53</sub>Ga<sub>0.47</sub>As/In<sub>0.52</sub>Al<sub>0.48</sub>As heterostructure, *Phys. Rev. Lett.*, 78 (7), 1335–1338.
- [25] Rashba, E.I., and Sheka, V.I., 1959, Symmetry of energy bands in crystals of wurtzite type II. Symmetry of bands with spin-orbit interaction included, *Fiz. Tverd. Tela*, 2, 162–176.
- [26] Affandi, Y., and Absor, M.A.U., 2019, Electric field-induced anisotropic Rashba splitting in two dimensional tungsten dichalcogenides WX<sub>2</sub> (X: S, Se, Te): A first-principles study, *Physica E*, 114, 113611.



- [27] Li, X., Chen, H., and Niu, Q., 2020, Out-of-plane carrier spin in transition-metal dichalcogenides under electric current, *Proc. Natl. Acad. Sci. U. S. A.*, 117 (29), 16749–16755.
- [28] Wang, J., Shu, H., Zhao, T., Liang, P., Wang, N., Cao, D., and Chen, X., 2018, Intriguing electronic and optical properties of two-dimensional Janus transition metal dichalcogenides, *Phys. Chem. Chem. Phys.*, 20 (27), 18571–18578.
- [29] Absor, M.A.U., Santoso, I., Harsojo, Abraha, K., Kotaka, H., Ishii, F., and Saito, M., 2017, Polarity tuning of spin-orbit-induced spin splitting in two-dimensional transition metal dichalcogenides, *J. Appl. Phys.*, 122 (15), 153905.
- [30] Bai, H., Ma, J., Wang, F., Yuan, Y., Li, W., Mi, W., Han, Y., Li, Y., Tang, D., Zhao, W., Li, B., and Zhang, K., 2017, A controllable synthesis of uniform MoS<sub>2</sub> monolayers on annealed molybdenum foils, *Mater. Lett.*, 204, 35–38.
- [31] Li, Y., Wang, F., Tang, D., Wei, J., Li, Y., Xing, Y., and Zhang, K., 2018, Controlled synthesis of highly crystalline CVD-derived monolayer MoSe<sub>2</sub> and shape evolution mechanism, *Mater. Lett.*, 216, 261–264.
- [32] Chen, K., Wan, X., and Xu, J., 2017, Epitaxial stitching and stacking growth of atomically thin transition-metal dichalcogenides (TMDCs) heterojunctions, *Adv. Funct. Mater.*, 27 (19), 1603884.
- [33] Zhang, J., Jia, S., Kholmanov, I., Dong, L., Er, D., Chen, W., Guo, H., Jin, Z., Shenoy, V.B., Shi, L., and Lou, J., 2017, Janus monolayer transition-metal dichalcogenides, *ACS Nano*, 11 (8), 8192–8198.
- [34] Lu, A.Y., Zhu, H., Xiao, J., Chuu, C.P., Han, Y., Chiu, M.H., Cheng, C.C., Yang, C.W., Wei, K.H., Yang, Y., Wang, Y., Sokaras, D., Nordlund, D., Yang, P., Muller, D.A., Chou, M.Y., Zang, X., and Li, L.J., 2017, Janus monolayers of transition metal dichalcogenides, *Nat. Nanotechnol.*, 12 (8), 744–749.
- [35] Xiang, L., Ke, Y., and Zhang, Q., 2019, Tunable giant Rashba-type spin splitting in PtSe<sub>2</sub>/MoSe<sub>2</sub> heterostructure, *Appl. Phys. Lett.*, 115 (20), 203501.
- [36] Din, H.U., Idrees, M., Albar, A., Shafiq, M., Ahmad, I., Nguyen, C.V., and Amin, B., 2019, Rashba spin splitting and photocatalytic properties of GeC–MSSe ( $M = \text{Mo}, \text{W}$ ) van der Waals heterostructures, *Phys. Rev. B*, 100 (16), 165425.
- [37] Chen, Y., and Washburn, J., 1996, Structural transition in large-lattice-mismatch heteroepitaxy, *Phys. Rev. Lett.*, 77 (19), 4046–4049.
- [38] Gabrys, P.A., Seo, S.E., Wang, M.X., Oh, E., Macfarlane, R.J., and Mirkin, C.A., 2018, Lattice mismatch in crystalline nanoparticle thin films, *Nano Lett.*, 18 (1), 579–585.
- [39] Perdew, J.P., Burke, K., and Ernzerhof, M., 1996, Generalized gradient approximation made simple, *Phys. Rev. Lett.*, 77 (18), 3865–3868.
- [40] Ozaki, T., Kino, H., Yu, J., Han, M.J., Kobayashi, N., Ohfuti, M., Ishii, F., Ohwaki, T., Weng, H., and Terakura, K., 2009, *OpenMX (Open source package for Material eXplorer) Version 3.8.*, <http://www.openmx-square.org/>
- [41] Troullier, N., and Martins, J.L., 1991, Efficient pseudopotentials for plane-wave calculations, *Phys. Rev. B*, 43 (3), 1993–2006.
- [42] Ozaki, T., 2003, Variationally optimized atomic orbitals for large-scale electronic structures, *Phys. Rev. B*, 67 (15), 155108.
- [43] Ozaki, T., and Kino, H., 2004, Numerical atomic basis orbitals from H to Kr, *Phys. Rev. B*, 69 (19), 195113.
- [44] Theurich, G., and Hill, N.A., 2001, Self-consistent treatment of spin-orbit coupling in solids using relativistic fully separable *ab initio* pseudopotentials, *Phys. Rev. B*, 64 (7), 073106.
- [45] Anshory, M., and Absor, M.A.U., 2020, Strain-controlled spin-splitting in the persistent spin helix state of two-dimensional SnSe monolayer, *Physica E*, 124, 114372.
- [46] Absor, M.A.U., and Ishii, F., 2019, Intrinsic persistent spin helix state in two-dimensional group-IV monochalcogenide MX monolayers ( $M = \text{Sn}$  or  $\text{Ge}$  and  $X = \text{S}, \text{Se},$  or  $\text{Te}$ ), *Phys. Rev. B*, 100 (11), 115104.
- [47] Absor, M.A.U., and Ishii, F., 2019, Doping-induced persistent spin helix with a large spin splitting in monolayer SnSe, *Phys. Rev. B*, 99 (7), 075136.

- [48] Absor, M.A.U., Santoso, I., Yamaguchi, N., and Ishii, F., 2020, Spin splitting with persistent spin textures induced by the line defect in the 1T phase of monolayer transition metal dichalcogenides, *Phys. Rev. B*, 101 (15), 155410.
- [49] Defo, R.K., Fang, S., Shirodkar, S.N., Tritsarlis, G.A., Dimoulas, A., and Kaxiras, E., 2016, Strain dependence of band gaps and exciton energies in pure and mixed transition-metal dichalcogenides, *Phys. Rev. B*, 94 (15), 155310.
- [50] Jin, W., Yeh, P.C., Zaki, N., Zhang, D., Liou, J.T., Sadowski, J.T., Barinov, A., Yablonskikh, M., Dadap, J.I., Sutter, P., Herman, I.P., and Osgood, Jr., R.M., 2015, Substrate interactions with suspended and supported monolayer MoS<sub>2</sub>: Angle-resolved photoemission spectroscopy, *Phys. Rev. B*, 91 (12), 121409.
- [51] Vajna, S., Simon, E., Szilva, A., Palotas, K., Ujfalussy, B., and Szunyogh, L., 2012, Higher-order contributions to the Rashba-Bychkov effect with application to the Bi/Ag(111) surface alloy, *Phys. Rev. B*, 85 (7), 075404.
- [52] Zhang, Y.J., Oka, T., Suzuki, R., Ye, J.T., and Iwasa, Y., 2014, Electrically switchable chiral light-emitting transistor, *Science*, 344 (6185), 725–728.
- [53] Mak, K.F., McGill, K.L., Park, J., and McEuen, P.L., 2014, The valley Hall effect in MoS<sub>2</sub> transistors, *Science*, 344 (6191), 1489–1492.

## Groundwater Recharge Area Based on Hydrochemical and Environmental Isotopes Analysis in the South Bandung Volcanic Area

Rizka Maria<sup>1,2\*</sup>, Satrio<sup>1,3</sup>, Teuku Yan Waliyana Muda Iskandarsyah<sup>1</sup>, Bombom Rachmat Suganda<sup>1</sup>, Robert Mohammad Delinom<sup>2</sup>, Dyah Marganingrum<sup>2</sup>, Wahyu Purwoko<sup>2</sup>, Dady Sukmayadi<sup>2</sup>, and Hendarmawan Hendarmawan<sup>1</sup>

<sup>1</sup>Faculty of Geological Engineering, Padjadjaran University, Jl. Raya Bandung Sumedang Km 21, Jatinangor, Sumedang 45363, Indonesia

<sup>2</sup>Research Center for Geotechnology LIPI, Jl. Sangkuriang, Bandung 40135, Indonesia

<sup>3</sup>Center for Isotopes and Radiation Application – BATAN, Jl. Lebak Bulus Raya No. 49, Jakarta 12440, Indonesia

\* **Corresponding author:**

tel: +62-81321409165

email: rizka\_maria@yahoo.com

Received: August 14, 2020

Accepted: November 20, 2020

DOI: 10.22146/ijc.58633

**Abstract:** The determination of recharge areas needs to support the groundwater conservation in the southern volcanic Bandung area. This study aims to determine the recharge area based on environmental isotopes and hydrochemical. A sampling of 26 groundwater was carried out at springs, dug wells, and drilling wells. The variation in groundwater chemistry principally is controlled by a combination of ion exchange, silicate weathering, calcite, and dolomite dissolution of minerals. The hydrochemical facies were CaCl, CaMgCl, CaMgHCO<sub>3</sub>, CaHCO<sub>3</sub>, and NaKHCO<sub>3</sub>. The CaHCO<sub>3</sub> facies describe moderate groundwater flows. The NaKHCO<sub>3</sub> facies shows the mixing of shallow and deep groundwater. The recharge area in the central, proximal, and medial facies zone consists of 3 groups. Group I is considered water originating from local rainwater infiltration; Group II is considered the infiltration elevation, which ranges from 980–1230 m asl; Group III estimated to be derived from the recharge elevation between 750–970 m asl, Group IV are more likely to show symptoms of evaporation or interaction with surface water. The discharge area is characterized by less active groundwater circulation, with dominant HCO<sub>3</sub><sup>-</sup> and TDS values in the distal facies zone. Hydrochemical variation helped the identification of recharge areas in the volcanic facies.

**Keywords:** volcanic facies; recharge; groundwater; environmental isotopes

### ■ INTRODUCTION

A volcanic area is a place for groundwater recharge and water resources for the surrounding community [1]. The need for groundwater is increasing along with the development and population growth [2]. Excessive groundwater extraction will cause environmental changes such as reduced groundwater reserves, drought in the dry season, and groundwater pollutants. Groundwater recharge is influenced by environmental changes and anthropogenic conditions [3-4]. The South Bandung volcanic area is part of the upstream Citarum watershed located in Bandung Regency. The potential of abundant water resources in this area is the main buffer for the

fulfillment of raw water for Bandung Municipality and Bandung Regency [5]. Expansion of built land for settlements in the South Bandung area is feared to affect the groundwater conservation area [6]. There has been a deficit of groundwater in South Bandung in 2015, amounting to 170,215,063 m<sup>3</sup>/year [5]. The large potential of water sources must be preserved.

One of the methods used to validate hydrogeological conditions is an environmental isotope and hydrochemical analysis [1-2,4,7-9]. Isotope composition in hydrological systems in nature are influenced by physical variables, namely air temperature, air pressure, humidity, geographical

location, and altitude [10]. The reaction between groundwater and minerals in aquifers affects groundwater quality, such as cation and anion exchange reactions [8]. Groundwater genesis can be seen from the composition of groundwater, and the processes occur when passing through aquifer media [9]. Research on hydrochemical and stable isotopes in hydrogeological systems at Bandung-Soreang and Batujajar Groundwater Basin has been widely carried out by several researchers [6,11-17]. Previous isotope research for groundwater recharge in the Bandung Basin has been carried out based on groundwater type. Even though in one kind of groundwater, it does not necessarily indicate groundwater system the same. The differences with the previous studies, in this study, the groundwater recharge was determined based on the isotope value and hydrochemical volcanic facies analysis. The study aimed

to identify recharge areas with stable isotope and hydrochemical analysis of volcanic facies. Environmental isotopes used are the stable isotope deuterium ( $\delta^2\text{H}$  or D) and oxygen-18 ( $\delta^{18}\text{O}$ ). The stable isotopes Deuterium and oxygen-18 are also used to determine the origin of groundwater.

## ■ EXPERIMENTAL SECTION

### Location and Sampling

The research was conducted in the South Bandung volcanic area, geographically located at  $107^{\circ}30'\text{E}$ – $107^{\circ}45'\text{E}$  and  $7^{\circ}00'\text{S}$ – $7^{\circ}10'\text{S}$  (Fig. 1). The southern part of the Bandung Basin is surrounded by Malabar Wayang Windu Patuha volcanoes [18]. The geological condition from the study area consists of: The Beser Formation (Tmb) is the oldest rock in the late Miocene, consist of tuffaceous breccias, lava, andesite and basalt. Quaternary

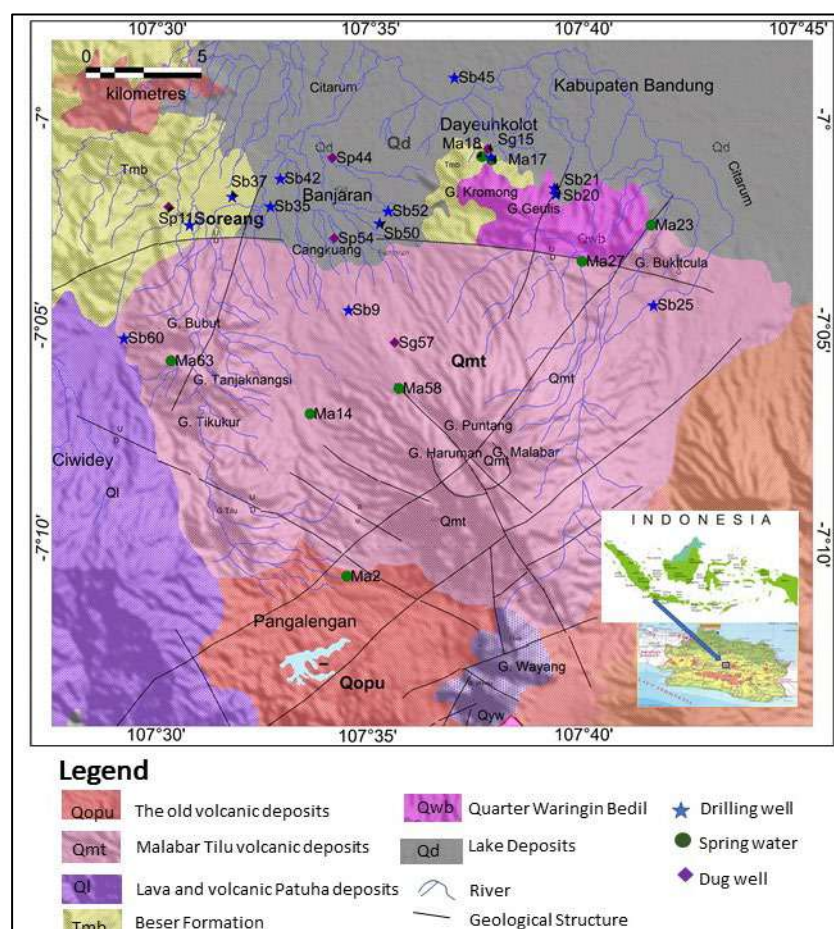


Fig 1. Research location on geological map [27-28]

volcanic rocks overlay Tertiary volcanic rocks. Old unraveled volcanic deposits (Qopu) of Pleistocene age, consisting of fine-coarse crystalline tuff, dacite, tuff breccia containing old pumice and andesite lava deposits. The youngest rock unit is lake deposits (Qd) of the Holocene age. The distribution of springs is located in the old volcanic deposits (Qopu) and the Malabar volcanic deposits (Qmt) [19-20].

Volcanic facies have characteristics based on the geological condition, sedimentary structures, and biological conditions [18]. The study area's volcanic facies consist of the central, proximal, medial, and distal facies. The central facies are located in the Pangalengan area, the proximal facies on the upper slopes of Mount Malabar, the medial facies on the lower slopes, and the distal facies plain area of the lake deposits.

### Instrumentation

Retrieval of 26 groundwater samples consist of 5 dug wells, 13 drillings wells, and 8 springs were taken during the rainy season. Field parameters such as pH, electrical conductivity, and temperature were measured at each site using Horiba measuring instruments. Water samples from dug wells are taken from the top, middle, and bottom of the well to maintain homogeneity using a vertical water sampler made of 600 mL volume glass fiber. The water samples are put into a 500 mL polyethylene bottle and preserved. The process of taking stable isotope  $\delta^2\text{H}$  and  $\delta^{18}\text{O}$  samples is by taking water samples in 100 mL polyethylene bottles tightly closed to prevent evaporation. Stable isotope analysis was performed on the hydrogeochemistry laboratory of Institute Technology Bandung. The values of  $\delta^2\text{H}$  and  $\delta^{18}\text{O}$  were measured relative to the Vienna Standard Mean Ocean Water (VSMOW) using the Picaro L-2130-i Analyzer. The allowable error in the analysis is  $\pm 0.2\%$  for  $\delta^{18}\text{O}$  or  $\pm 1.0\%$  for  $\delta^2\text{H}$ . The local meteoric water line (LMWL) equation is determined by considering a weighted total factor, namely the monthly rainfall at each rainwater sampling location [21].

### Procedure

#### Major ion analysis

Laboratory analysis was carried out for the Total

Dissolve Solid (TDS) and major ions:  $\text{Ca}^{2+}$ ,  $\text{Mg}^{2+}$ ,  $\text{Na}^+$ ,  $\text{K}^+$ ,  $\text{SO}_4^{2-}$ ,  $\text{Cl}^-$ ,  $\text{HCO}_3^-$ . The analysis was carried out in the groundwater laboratory of the Research Center for Geotechnology LIPI. The  $\text{Na}^+$ ,  $\text{K}^+$  were analyzed by atomic absorption spectrophotometry methods. The  $\text{HCO}_3^-$  was carried out by acidimetric methods. The  $\text{SO}_4^{2-}$  was investigated by turbidimetry methods. The  $\text{Cl}^-$  was carried out using argentometry methods. Gravimetry methods determined TDS analysis. The concentrations of  $\text{Ca}^{2+}$  and  $\text{Mg}^{2+}$  were analyzed by complexometric titration with EDTA. A hydrochemical analysis is validated with ion balance. The quality of laboratory analysis results can be seen from the charge balance error (CBE), with the formula [22]:

$$\text{BE} = \frac{\sum Zm_c - \sum Zm_a}{\sum Zm_c + \sum Zm_a} \times 100 \quad (1)$$

Z notation is ion valence,  $m_c$  is the molality of cation, and  $m_a$  is the anion's molality.

CBE values can be accepted if  $< 5\%$  [22]. Laboratory analysis results are presented using graphical methods, bivariate analysis, and correlation statistics. The combination of graphical and statistical analysis will produce an accurate classification that supports the accuracy of research results [23]. This result can be used as a groundwater facies indicator.

#### Correlation analysis

The correlation coefficient uses the Spearman method to determine the relationship between several hydrochemical parameters [24]. The correlation values ( $r$ )  $> 0.7$  indicating strong correlation, between  $0.5-0.7$  indicating moderate correlation, and  $< 0.3$  indicating weak correlation [24]. The closeness of the relationship between variables was analyzed using the Spearman method processed with Minitab.19 software.

#### Hydrogeochemical analysis

A hydrogeochemical analysis is one of the techniques used to study groundwater quality [24]. Piper diagram analysis was carried out to show groundwater's evolution and the relationship between various dissolved ions from geochemical data analysis [25]. One of the groundwater facies type determinants is the dissolving of plagioclase, ferromagnesian minerals,

carbonates, and cation exchange process [26]. Groundwater with a predominance of bicarbonate ( $\text{HCO}_3^-$ ) concentrations comes from shallow and young groundwater. The main source of  $\text{HCO}_3^-$  is  $\text{CO}_2$  dissolved in rainwater and infiltrated into the soil [9].

### Isotope analysis

Determination of the recharge area elevation from isotope can be performed using natural isotope methods, namely  $\delta^2\text{H}$  and  $\delta^{18}\text{O}$  isotope in water molecules [2,21]. Water-rock interactions, evaporation, mixing, water origin, and accompanying processes are known by comparing the isotopic composition of water with reference [3,16]. The altitude effect and the amount of rainfall can be used to find the relationship between the isotope composition of rainwater and the altitude of a recharge area [27]. Determination of groundwater origin was carried out using the ratio of heavy isotopes to light isotopes, which were determined in terms of the difference in the rate of  $\delta^2\text{H}$  and  $\delta^{18}\text{O}$  isotopes. The isotope ratio  $\delta^2\text{H}$  and  $^{18}\text{O}$  will experience fractionation when there is a physical change in water molecules due to differences in isotopic mass in the hydrological cycle [27]. Rainwater falls at different elevations will have different isotope ratios where the higher the height of a place will be depleted the isotope composition [28].

The analysis of the  $\delta^{18}\text{O}$  and  $\delta^2\text{H}$  isotope composition of the water samples was performed using the Picaro L-2130-i Instrument. The abundance of  $\delta^2\text{H}$  and  $\delta^{18}\text{O}$  molecules in water is not measured in absolute ratio but in terms of their relative abundance to a standard. The relative abundance of the  $\text{HD}^{16}\text{O}$  molecule is called the relative abundance of deuterium ( $\delta^2\text{H}$ ), and the close lot of  $\text{H}_2^{18}\text{O}$  is called the  $\delta\text{O}^{18}$ . The relative mass of  $\delta^{18}\text{O}$  and  $\delta^2\text{H}$  in water molecules is measured relative to an international standard SMOW (Standard Mean Ocean Water). The relative lot of  $^2\text{H}$  is written as  $\delta^2\text{H}$ , with the formula:

$$\delta = \frac{R_{\text{Sample}} - R_{\text{SMOW}}}{R_{\text{SMOW}}} \times 1000 \text{ ‰} \quad (2)$$

where,  $R_{\text{sample}}$  = the isotope ratio ( $\delta^2\text{H}$  or  $\delta^{18}\text{O}$ ) of the sample, in ‰;  $R_{\text{SMOW}}$  = the isotope ratio ( $\delta^2\text{H}$  or  $\delta^{18}\text{O}$ ) of the SMOW

## RESULTS AND DISCUSSION

### Groundwater Hydrochemical Processes

The summary of the physical and chemical properties is given in Table 1 and 2. The physico-chemical properties from the field data collection and the chemical properties are taken from laboratory analysis.

**Table 1.** The summary of the physico-chemical properties in the research area

Type of sample	X	Y	Type of groundwater	Elevation (m)	pH	Temp (°C)	Conductivity ( $\mu\text{S}/\text{cm}$ )
Ma2	784217	9205750	Spring	1427	5.4	22.6	220
Sb9	784363	9217295	Drilling well	809	7.4	28.4	100
Sp11	776614	9221798	Dug well	816	6.9	25.3	370
Ma14	782672	9212796	Spring	915	7.1	25.5	160
Sg15	790418	9224231	Dug well	700	7.2	26.0	700
Sb16	790554	9223882	Drilling well	701	6.7	27.7	230
Ma17	790591	9223757	Spring	718	7.2	26.9	160
Ap18	790159	9223906	Lake	720	7.5	25.4	160
Sb20	793352	9222272	Drilling well	707	7.3	27.6	300
Sb21	793292	9222526	Drilling well	720	7.3	28.8	330
Ma23	797460	9220890	Spring	716	6.9	28.5	230
Sb25	797545	9217430	Drilling well	810	6.4	26.4	70
Ma27	794474	9219337	Spring	855	6.7	26.7	130
Sb35	781008	9221806	Drilling well	700	7,9	25.4	460
Sb37	779361	9222239	Drilling well	749	7,7	27.2	350
Sb42	781448	9223008	Drilling well	703	7.4	29.3	460

**Table 1.** The summary of the physico-chemical properties in the research area (*Continued*)

Type of sample	X	Y	Type of groundwater	Elevation (m)	pH	Temp (°C)	Conductivity (µS/cm)
Sb42	781448	9223008	Drilling well	703	7.4	29.3	460
Sp44	783701	9223886	Dug well	692	7.4	29.8	390
Sb45	788997	9227341	Drilling well	689	7.7	28.9	440
Sb 49	777512	9221024	Drilling well	734	7.7	31.2	550
Sb50	785689	9920350	Drilling well	706	7.7	28.7	230
Sb52	786103	9221573	Drilling well	696	7.6	28.9	400
Sp54	783759	9220403	Dug well	705	7.3	28.2	330
Sg57	786348	9215868	Dug well	965	6.1	24.8	50
Ma58	786522	9213881	Spring	1179	6.5	24.2	60
Sb60	774648	9216127	Drilling well	1059	7.5	26.3	170
Ma63	776683	9215129	Spring	1222	7.4	28.2	70

**Table 2.** The summary of the major ion's chemical analysis in the research area

Type of sample	TDS (mg/L)	Na <sup>+</sup> (mg/L)	K <sup>+</sup> (mg/L)	Mg <sup>2+</sup> (mg/L)	Ca <sup>2+</sup> (mg/L)	Cl <sup>-</sup> (mg/L)	SO <sub>4</sub> <sup>2-</sup> (mg/L)	HCO <sub>3</sub> <sup>-</sup> (mg/L)	CBE (%)
Ma2	96	15.0	3.3	10.7	13.4	56.2	10.3	18.5	4.1
Sb9	126	10.1	5.0	3.9	7.7	6.9	6.4	63.2	-3.4
Sp11	326	16.6	2.5	16.3	37.8	66.8	8.7	98.5	2.0
Ma14	114	14.2	4.7	4.9	14.6	9.6	6.7	81.7	-1.3
Sg15	518	36.4	30.9	16.2	66.5	78.5	48.0	216.7	-3.5
Sb16	244	15.0	1.5	4.4	28.4	20.7	9.8	97.5	1.7
Ma17	196	10.1	1.1	7.1	18.8	5.5	5.3	94.9	-4.1
Ap18	160	11.7	1.4	6.1	17.3	12.4	11.0	73.8	-3.4
Sb20	238	13.0	1.3	12.4	36.4	5.5	5.0	168.7	-1.5
Sb21	206	14.6	1.7	17.4	35.3	13.8	5.1	176.6	-3.7
Ma23	152	14.2	0.6	9.2	24.8	16.5	14.9	89.9	4.0
Sb25	28	7.7	0.6	1.2	5.8	9.4	8.2	22.3	-3.9
Ma27	48	3.7	0.6	3.9	15.0	12.4	6.2	47.4	-3.9
Sb35	376	42.4	3.3	7.4	20.9	22.0	5.7	139.4	-3.5
Sb37	246	26.8	10.9	7.3	31.2	11.0	11.8	200.8	-3.3
Sb42	186	27.6	8.6	18.1	29.8	13.8	4.8	258.3	-3.6
Sp44	200	7.3	7.1	11.2	42.3	6.9	4.6	220.3	-5.0
Sb45	280	25.4	6.2	16.6	36.1	16.5	4.7	228.3	-4.2
Sb49	320	44.3	3.2	13.4	31.9	55.3	7.5	141.2	-3.7
Sb50	172	25.4	3.4	6.1	15.1	20.7	4.9	103.3	-3.7
Sb52	308	32.9	2.8	7.9	20.6	53.8	4.6	107.0	-2.8
Sp54	252	20.8	2.5	21.1	25.5	12.4	8.3	191.8	4.0
Sg57	130	2.6	0.5	2.7	6.4	12.4	6.1	10.5	1.3
Ma58	20	2.0	0.5	2.4	4.9	6.9	6.1	16.4	-4.5
Sb60	266	9.1	1.4	12.4	16.6	6.9	5.0	115.4	2.0
Ma63	106	3.3	0.7	3.8	8.2	6.9	8.2	36.2	-4.5

The correlation coefficient uses the Spearman method to determine the relationship between several hydrochemical parameters. The relationship between variables was analyzed using the Spearman method processed because the data observations are random samples with a uniform distribution (Table 3). Correlation analysis was performed on the hydrochemical data of conductivity, TDS, pH,  $\text{Ca}^{2+}$ ,  $\text{Mg}^{2+}$ ,  $\text{Na}^+$ ,  $\text{K}^+$ ,  $\text{SO}_4^{2-}$ ,  $\text{Cl}^-$ ,  $\text{HCO}_3^-$ ,  $\text{CO}_3^-$ .

The results of chemical and physical analysis of 26 samples with correlation analysis showed the dominance of  $\text{Ca}^{2+} > \text{Na}^+ > \text{Mg}^{2+}$  cations and  $\text{HCO}_3^- > \text{Cl}^- > \text{SO}_4^{2-}$  anions. The moderate to very strong correlation shows the dissolving reaction of rock minerals in groundwater. In the study area, almost all types showed the predominance of  $\text{Ca}^{2+}$  and  $\text{HCO}_3^-$ , followed by  $\text{Mg}^{2+}$  and C, this condition is influenced by hydrochemical and geological formation [29]. The related ions are influenced by environmental and rock factors [30].

There are three groups of conductivity and TDS values:

- (i) Group A, the upper zone is characterized by active groundwater flushing with low TDS value  $< 200$  mg/L and conductivity  $< 300$   $\mu\text{S}/\text{cm}$ , found in old volcanic deposits (Qopu) and Mt. Malabar volcanic Deposits (Qmt).
- (ii) Group B, the intermediate zone is characterized by less active groundwater circulation, with moderate TDS value 200–300 mg/L and conductivity with

values 170–460  $\mu\text{mhos}/\text{cm}$ , is present in the Fm Beser (Tmb) and lake deposits (Qd).

- (iii) Group C, the lower zone is characterized by passive groundwater with a high TDS value  $> 300$  mg/L and conductivity value of  $< 370$   $\mu\text{mhos}/\text{cm}$ , is found in lake deposits (Qd) (Fig. 2). Sources of material availability from TDS and conductivity come from the geological conditions and the influence of human activities such as industry, households, and agriculture [31]. Variation in TDS values indicates groundwater recharge areas [6]. A high TDS value indicates the travel time for groundwater [32]. The TDS value caused by anthropogenic effects is validated by Nitrate concentrations (Fig. 3). High nitrate values are situated in livestock, and plantation areas were located in the Pangalengan. The average nitrate concentration in Pangalengan is 23.03 mg/L. The nitrate concentration is getting lower downstream.

Groundwater hydrogeochemistry is controlled by several processes such as evaporation, precipitation, ion exchange, oxidation-reduction, weathering, and dissolving [32]. The  $\text{Ca}^{2+}/\text{Mg}^{2+}$  molar ratio indicates the dissolution of calcite, dolomite, and silicate. The ratio of  $\text{Ca}^{2+}/\text{Mg}^{2+} = 1$  indicates dolomite dissolution,  $\text{Ca}^{2+}/\text{Mg}^{2+} > 1$  ratio indicates calcite dissolution and ration  $\text{Ca}^{2+}/\text{Mg}^{2+} > 2$  ratio indicates silicate dissolution [33]. The dolomite dissolution occurs in Beser formation and volcanic deposits with  $\text{Ca}^{2+}/\text{Mg}^{2+}$  values 0.73–0.81 meq/L.

**Table 3.** Matrix of Spearman's correlation

Parameter	pH	Temp (°C)	Cond ( $\mu\text{S}/\text{cm}$ )	TDS (mg/L)	$\text{Na}^+$ (mg/L)	$\text{K}^+$ (mg/L)	$\text{Mg}^{2+}$ (mg/L)	$\text{Ca}^{2+}$ (mg/L)	$\text{Cl}^-$ (mg/L)	$\text{SO}_4^{2-}$ (mg/L)	$\text{HCO}_3^-$ (mg/L)	$\text{CO}_3^-$ (mg/L)
pH	1.00											
Temp	0.53	1.00										
Cond	0.56	0.46	1.00									
TDS	0.56	0.25	0.83	1.00								
$\text{Na}^+$	0.54	0.31	0.86	0.73	1.00							
$\text{K}^+$	0.53	0.33	0.68	0.46	0.67	1.00						
$\text{Mg}^{2+}$	0.36	0.39	0.80	0.68	0.62	0.49	1.00					
$\text{Ca}^{2+}$	0.37	0.43	0.85	0.77	0.57	0.50	0.79	1.00				
$\text{Cl}^-$	0.08	0.02	0.59	0.47	0.73	0.35	0.38	0.35	1.00			
$\text{SO}_4^{2-}$	-0.36	-0.43	-0.14	-0.09	0.06	-0.08	-0.14	-0.05	0.26	1.00		
$\text{HCO}_3^-$	0.64	0.59	0.87	0.74	0.64	0.67	0.81	0.85	0.20	-0.30	1.00	
$\text{CO}_3^-$	0.30	0.09	0.44	0.44	0.43	0.13	0.36	0.46	0.32	-0.02	0.32	1.00



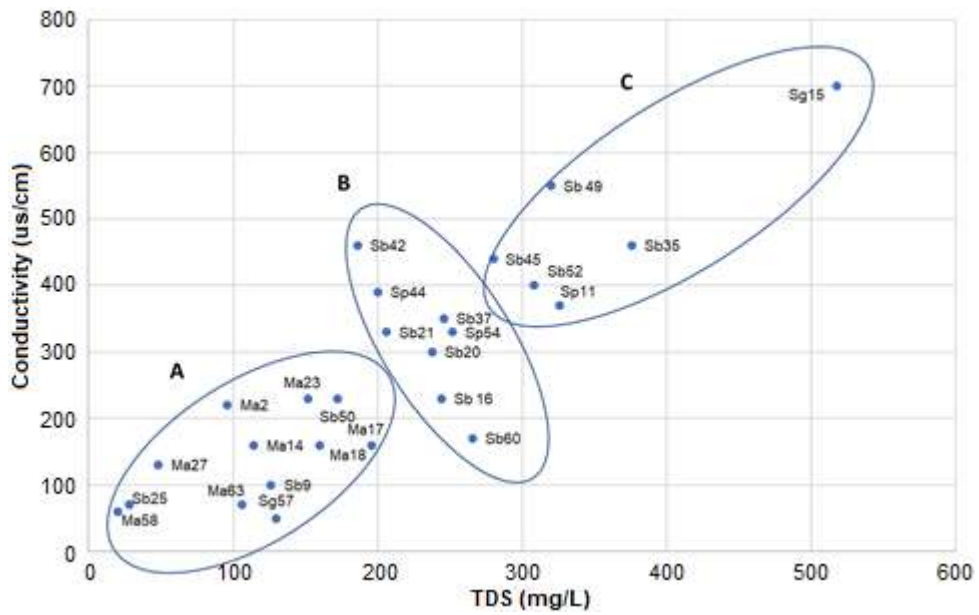


Fig 2. Groundwater conductivity correlation to TDS

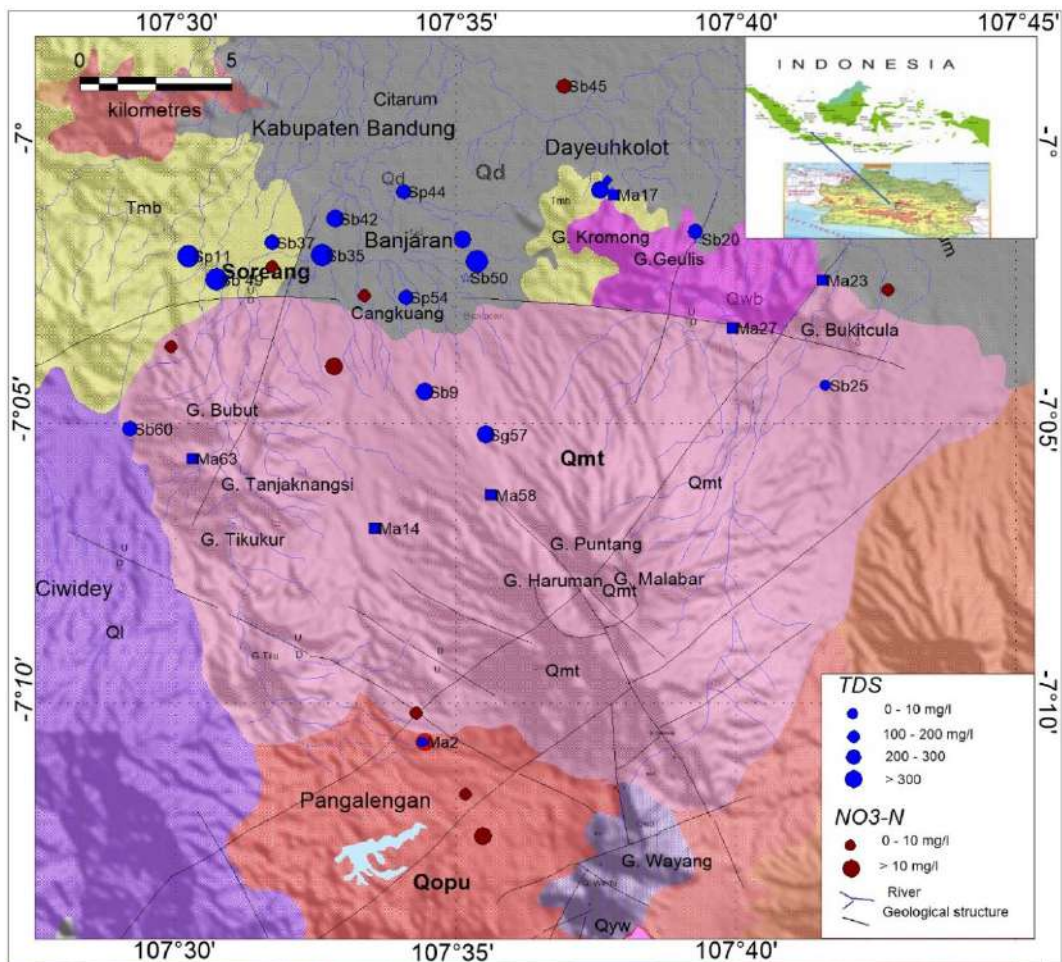


Fig 3. TDS and NO<sub>3</sub>-N concentration in the research area

Calcite dissolution dominates the entire area with even distribution of volcanic deposits and lake sediments with  $\text{Ca}^{2+}/\text{Mg}^{2+}$  values 1.00–1.81 meq/L. Silicate weathering occurs in Beser formation and lake sediments with  $\text{Ca}^{2+}/\text{Mg}^{2+}$  values 2.28–3.93 meq/L. The dominance of groundwater in the study area is influenced by calcite minerals dissolution (Fig. 4). The relatively high value of the  $\text{Ca}^{2+}/\text{Mg}^{2+}$  ratio indicates that the interaction process between rock and water is quite long.

Groundwater hydrochemical processes control the mechanism of groundwater originating from the dominance of rainwater, rock weathering, crystallization, or evaporation. The TDS process in groundwater evolution has a low value, and the composition of the

dominant bicarbonate ion shows the water source comes from shallow aquifers [33]. The Gibbs diagram distinguishes the effects of rock weathering interactions, evaporation, and the impact of rainwater on groundwater chemical processes [34]. Based on the analysis, rock weathering has influenced the groundwater chemical process (Fig. 5, 6).

The ratio of TDS to  $\text{Cl}^-/(\text{Cl}^- + \text{HCO}_3^-)$  anions show that the groundwater is affected by rock weathering (Fig. 5). Group A consists of Ma2 and Sg57, which are springs and dug wells in the volcanic deposits area in the proximal facies. Group A has a high Cl value due to the influence of hydrothermal alteration. Group B consists of Sg15, Sb52, Sb49, and Sp11, located in lake deposits and

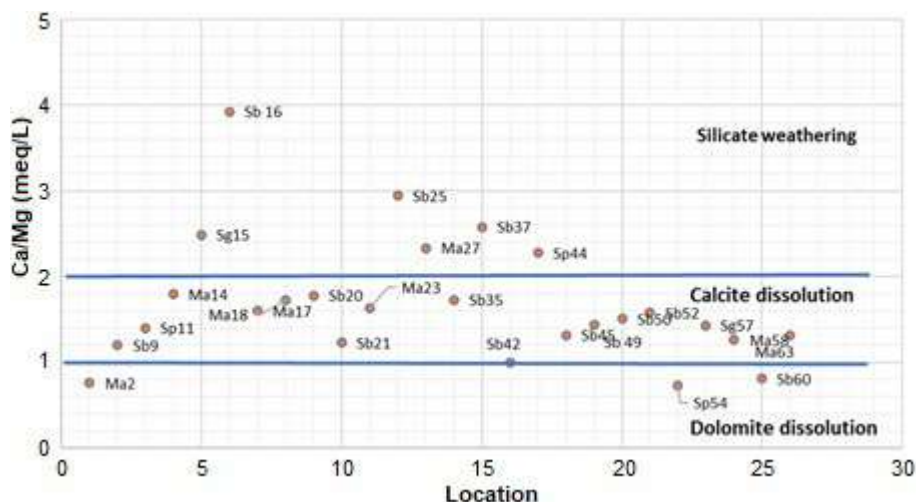


Fig 4. Bivariate  $\text{Ca}^{2+}/\text{Mg}^{2+}$  in the study area

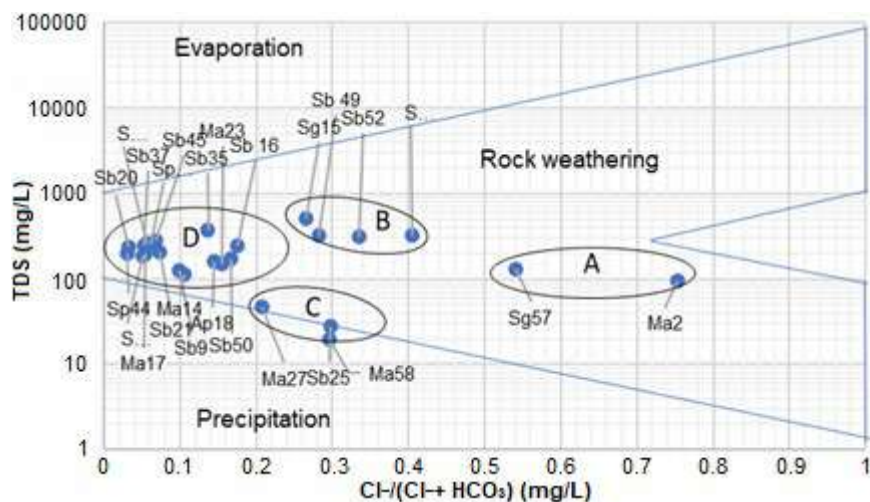


Fig 5. Gibbs diagram of the ratio of TDS with anion  $\text{Cl}^-/(\text{Cl}^- + \text{HCO}_3^-)$

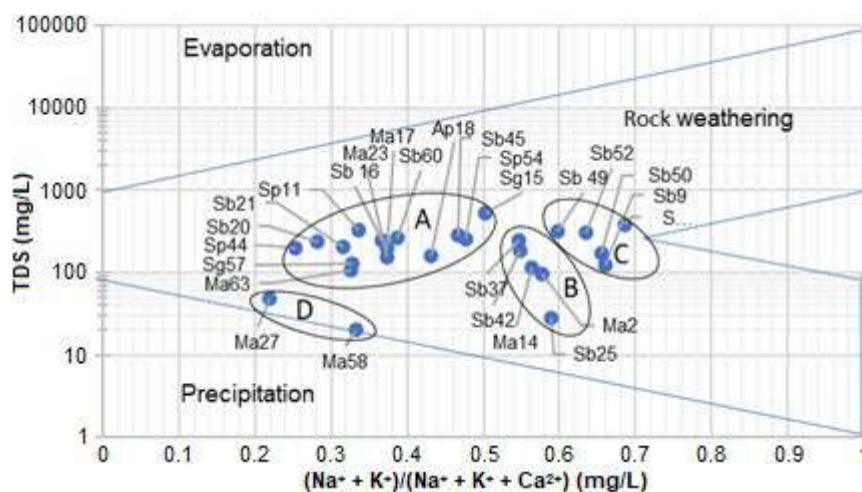


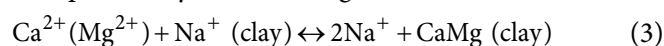
Fig 6. Gibbs diagram of the ratio of TDS with cations  $(\text{Na}^+ + \text{K}^+)/(\text{Na}^+ + \text{K}^+ + \text{Ca}^{2+})$

Beser formation deposits in the distal facies. Higher TDS values in group B indicate this area is much influenced by anthropogenic activity. Group C consists of Sb25, ma27, ma58, which are water sources located in the Malabar volcanic deposits and Beser formation deposits in the medial facies. Group C has low TDS and  $\text{Cl}^-$  values because it comes from springs in the hills with little anthropogenic influence. Group D is groundwater in the medial and distal facies. The TDS value in group D is high due to anthropogenic effects.

The ratio of TDS to the cation  $(\text{Na}^+ + \text{K}^+)/(\text{Na}^+ + \text{K}^+ + \text{Ca}^{2+})$  shows that the groundwater is affected by rock weathering (Fig. 6). Group A consists of Ma2, ma14, Sb25, Sb37, and Sb42, springs, and drilling wells in volcanic deposits in the proximal and medial facies. Higher TDS in group A indicate anthropogenic influenced activity. Group B consists of Sb9, Sb35, Sb49, Sb50, and Sb52, deep groundwater drilling wells located in lake deposits, and Beser formation deposits in the distal facies. Groundwater in Type C is located in the medial and distal facies. Group D consists of ma27 and ma58, water resources located in the Malabar volcanic deposits, and Beser formation deposits in the medial facies. Differences in each group of these facies show rock properties greatly influence groundwater chemistry. The high ratio of  $\text{HCO}_3^-$  shows rock weathering as a major ion [32]. Hydrochemical conditions are a reflection of the length of the short residence time in the aquifer. The longer groundwater

interacts and circulates in the aquifer, the total dissolved solids' total concentration will increase until it reaches an equilibrium condition.

The cation exchange process indicates the interaction between rock and groundwater occurs for a long time. The plot of  $(\text{Ca}^{2+} + \text{Mg}^{2+}) - (\text{HCO}_3^- - \text{SO}_4^{2-})$  versus  $\text{Na}^+ - \text{Cl}^-$  was prepared to evaluate the ion-exchange process [33]. The dominant process of ion exchange will form a line with a slope of -1. The reverse ion exchange will form a line with a slope of > 1. It can be explained by the following reaction [35].



The ion exchange process is located in Sb52, Ma63, Ma58, Ma27, Sg57, Sg15, Ma2, Sp11. The reverse ion exchange is dominated in the area (Fig. 7).

### Hydrochemical Facies

The shallow groundwater tends to be influenced by local rainwater infiltration. It has a low bicarbonate concentration. However, the deep groundwater has a higher bicarbonate concentration than shallow groundwater; the process of deep groundwater from the recharge area dissolves more carbonate rocks [34]. To determine the hydrochemical facies and groundwater characteristics, the hydrochemical data is plotted on the Piper diagram [8]. Based on the piper diagram analysis, the dominant types of hydrochemical facies are CaCl, CaMgCl, CaMgHCO<sub>3</sub>, CaHCO<sub>3</sub>, and NaKHCO<sub>3</sub> (Fig. 8).

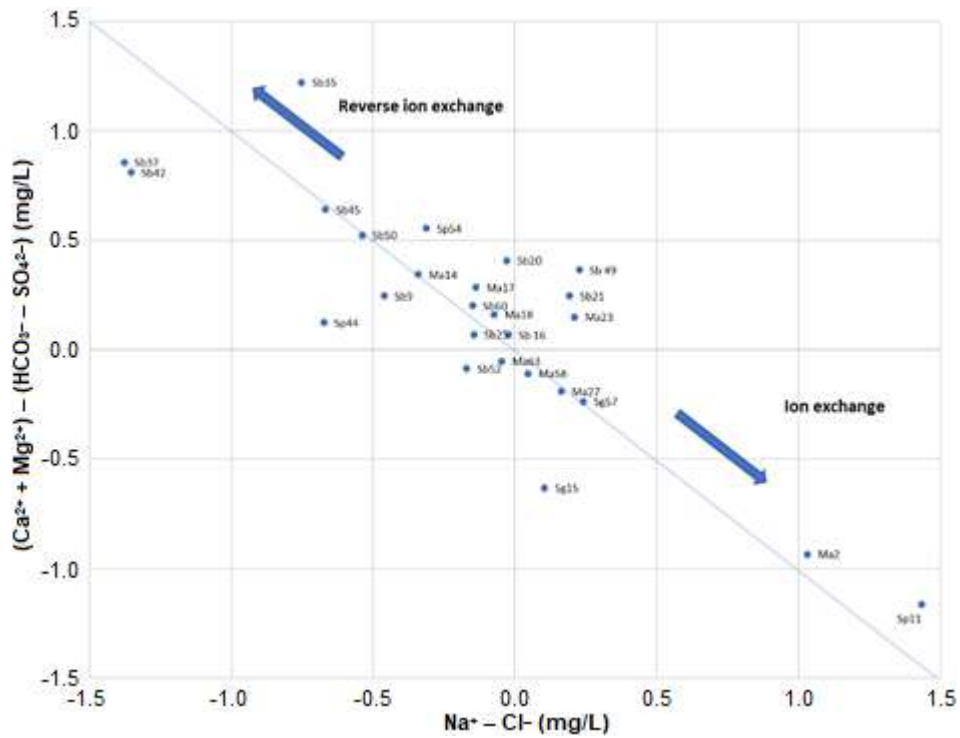


Fig 7. Bivariate  $(Ca^{2+} + Mg^{2+}) - (HCO_3^- - SO_4^{2-})$  versus  $Na^+ - Cl^-$  in the study area

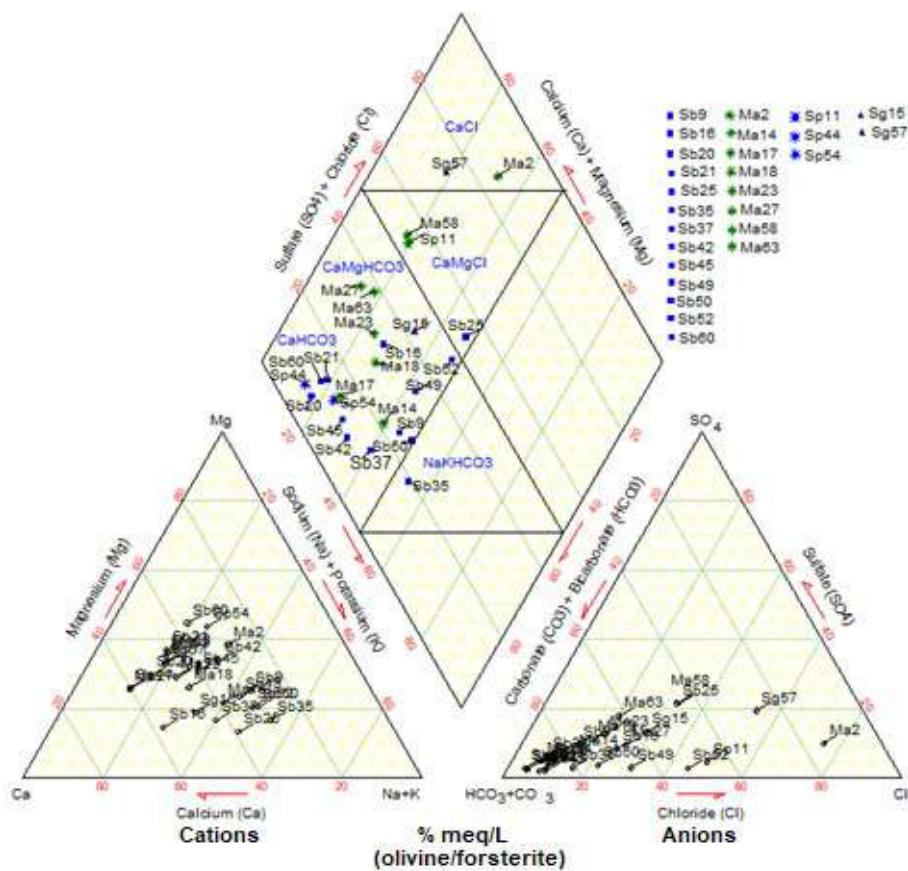
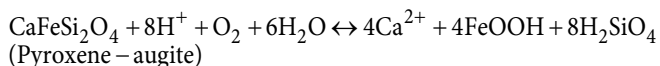
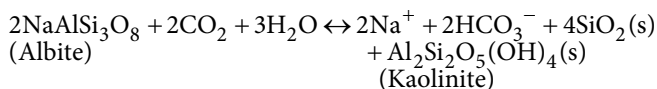
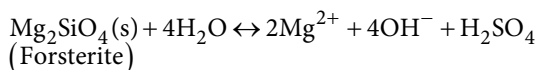


Fig 8. Piper diagram of the groundwater samples

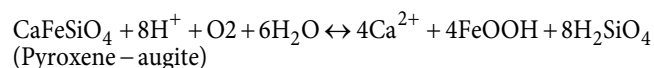
The groundwater CaCl facies are located at Sg57 and Ma2 in the central volcano facies. These facies lies in the hydrothermal alteration zone. Cl<sup>-</sup> ions' density comes from the weathering of the feldspathoid sodalite mineral (Na<sub>2</sub>Cl<sub>2</sub>·Al<sub>2</sub>SiO<sub>4</sub>) as a constituent of porous volcanic rock [35]. Several factors that cause Cl<sup>-</sup> enrichment in the study area are contamination of geothermal fluids and anthropogenic effects.

The CaMgCl facies in the Ma58 and Sp11 locations in the Malabar Tilu volcanic deposit. The calcium-magnesium dominance is generated from the weathering of silica minerals rich in Ca<sup>2+</sup> from basaltic andesitic volcanic rocks. Aquifers are formed by coarse tuff alternating basalt lava. The constituent minerals are feldspar (albite-labradorite, olivine, pyroxene, and chlorite [35]). The weathering process of aquifer constituent minerals is described as follows:



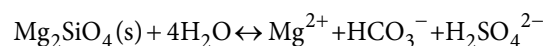
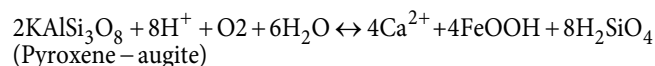
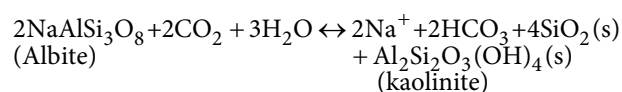
The CaMgHCO<sub>3</sub> is dominates the hydrochemical type in the Malabar Tilu volcanic deposits. This is located in Ma14, Ma17, Ma18, Ma23, Ma27, Ma63, Sg15, Sp54, Sb18, Sb9, Sb16, Sb37, Sb42, Sb45, Sb49, Sb50, Sb52, Sb54. This type is formed due to the interaction between rocks and groundwater for a long time due to mixing, this can be seen from the amount of enrichment of Ca<sup>2+</sup> and Mg<sup>2+</sup> ions balanced.

The CaHCO<sub>3</sub> facies are at locations Sp44, Sb20, Sb21, Sb60 scattered in the proximal and medial facies. This group shows that groundwater circulation is not too far away. The dominant Ca<sup>2+</sup> content is due to the interaction with volcanic rocks. The presence of HCO<sub>3</sub><sup>-</sup> indicates that the groundwater has been mixed with shallow groundwater as a local recharge. The presence of Ca<sup>2+</sup> cations is affected by the weathering of rocks, while bicarbonate anions (HCO<sub>3</sub><sup>-</sup>) is influenced by the time of storing water in rocks and the atmospheric condition [8]. The chemical reaction indicates weathering process of the minerals CaHCO<sub>3</sub> facies [35]:



The NaKHCO<sub>3</sub> facies are located at Sb35, scattered on distal facies. Volcanic deposit rocks have mineral compositions of Na-feldspar (NaAlSi<sub>3</sub>O<sub>8</sub>), K-feldspar (KAl<sub>2</sub>Si<sub>2</sub>O<sub>8</sub>), pyroxene (KAlSi<sub>3</sub>O<sub>8</sub>), and olivine (Mg<sub>2</sub>SiO<sub>4</sub>) [35]. The result of the weathering of these rock minerals is the source of the presence of Na<sup>+</sup> cations and HCO<sub>3</sub><sup>-</sup> anions.

The reaction indicates the formation of NaKHCO<sub>3</sub> facies [35]:



The cation exchange process in groundwater evolution is characterized by decreasing Ca<sup>2+</sup> and Mg<sup>2+</sup> values and enriching Na<sup>+</sup> values [8]. Na<sup>+</sup> ions' enrichment is due to the cation exchange process between Ca<sup>2+</sup> ions and Mg<sup>2+</sup> ions, and it becomes Na<sup>+</sup> ions. In the research area, this process occurs in the distal area because there are many clay inserts. The adsorption rate of Na<sup>+</sup> cations on clay minerals tends to be weaker than that of Ca<sup>2+</sup> ions. The adsorption tendencies among the main cations are [32]: (strong adsorption) Ca<sup>2+</sup> < Mg<sup>2+</sup> < K<sup>+</sup> < Na<sup>+</sup> (weakly adsorbed).

### **Stable isotopes to determine groundwater recharge**

The stable isotopes δ<sup>18</sup>O and δ<sup>2</sup>H have varying ratios related to elevation functions and rainfall values. The various isotopic compositions can be grouped using local meteoric lines (LMWL), determining groundwater processes, i.e., groundwater and rock interactions, evaporation, and mixing processes [21]. Analysis of the recharge area with stable isotope requires three types of isotope graphs, the local meteoric water line (LMWL) graph, the depletion gradient graph δ<sup>18</sup>O for elevation, and the depletion gradient graph δ<sup>2</sup>H for height [27].

The Local Meteoric water line (LMWL) determination uses research from the Geological Agency [17], which observed rainfall isotopes from January 2008 to July 2009. The stations selected in the study area were

PT. Safilindo, Cikalong hydropower, and Malabar plantation (Table 4). The equation of the local meteoric line (LMWL) from the measurement results [17] with the equation:

$$\begin{aligned} \delta^2\text{H} &= 8.3\delta^{18}\text{O} + 14.3 \\ R^2 &= 0.9873 \end{aligned} \quad (4)$$

Data on the results of physical measurements of  $\delta^{18}\text{O}$  and  $\delta^2\text{H}$  isotopes in groundwater in the southern Bandung groundwater basin are shown in Table 5.

Groundwater isotope values were plotted on the Bandung Meteoric Water to determine the relationship between groundwater and meteoric water (Fig. 9) and also

**Table 4.** Rainwater isotope  $\delta^{18}\text{O}$  and  $\delta^2\text{H}$  analysis for the period of January 2008–July 2009

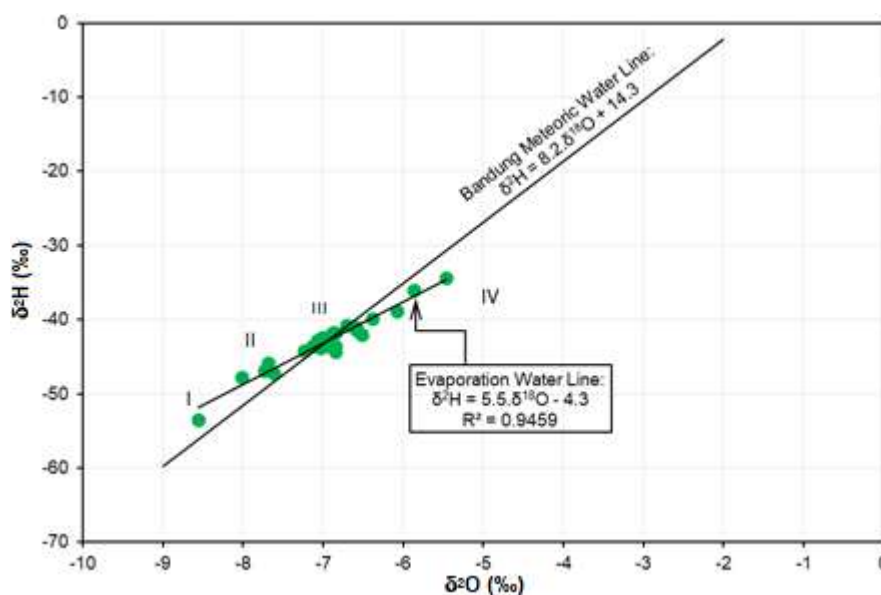
Month	PT Safilindo (829 m asl)		Cikalong (1255 m asl)		Malabar (1560 m asl)	
	$\delta^{18}\text{O}$ (‰)	$\delta^2\text{H}$ (‰)	$\delta^{18}\text{O}$ (‰)	$\delta^2\text{H}$ (‰)	$\delta^{18}\text{O}$ (‰)	$\delta^2\text{H}$ (‰)
16-May-08	-5.40	-31.1	-5.04	-26.1	–	–
13-Jun-08	-3.48	-10.4	-3.43	-13.0	–	–
14-Jul-08	-2.71	-10.7	–	–	-6.53	-37.2
13-Agt-08	-3.99	-20.0	-4.23	-17.0	–	–
14-Sep-08	-3.88	-17.3	-4.16	-17.0	-5.41	-27.6
13-Oct-08	–	–	–	–	-5.18	-24.7
12-Nov-08	-6.58	-45.0	-6.38	-36.3	-6.72	-43
13-Dec-08	-8.65	-55.4	-10.9	-73.1	-10.95	-73.5
13-Jan-09	-11.49	-77.4	-9.68	-68.1	-11.35	-80.6
13-Feb-09	-8.54	-57.2	-10.13	-70.6	-10.65	-73.2
13-Mar-09	-9.83	-66.6	-8.61	-58.4	-9.66	-65.9
13-Apr-09	-6.88	-47.3	-6.22	-40.8	-7.37	-49.2
14 May 09	-5.96	-38.5	-6.30	-38.5	-9.03	-57.9
15-Jun-09	-7.98	-48.9	-7.73	-45.8	-7.30	-45.05
13-Jul-09	-1.81	-1.6	-3.22	-12.0	-4.66	-24.2
Average	-6.22	-37.7	-6.62	-39.7	-7.90	-50.17

**Table 5.** Physical measurements of  $\delta^{18}\text{O}$  and  $\delta^2\text{H}$  isotopes in the southern Bandung

No	Type of sample	X	Y	Elevation (m)	$\delta^{18}\text{O}$ (‰)	$\delta^2\text{H}$ (‰)
1	Ma2	784217	9205750	1427	-8.56	-53.5
2	Ma14	782672	9212796	915	-6.51	-42.0
3	Ma17	790591	9223757	718	-7.01	-42.4
4	Ma23	797460	9220890	716	-6.58	-41.1
5	Ma27	794474	9219337	855	-7.61	-47.2
6	Ma58	786522	9213881	1179	-6.39	-39.8
7	Ma63	776683	9215129	1222	-7.12	-43.5
8	Ma18	790159	9223906	720	-5.86	-36.1
9	Sb9	784363	9217295	809	-8.02	-47.7
10	Sb 16	790554	9223882	701	-6.88	-41.7
11	Sb20	793352	9222272	707	-7.08	-43.5
12	Sb21	793292	9222526	720	-7.13	-43.5
13	Sb25	797545	9217430	810	-6.98	-43.6
14	Sb35	781008	9221806	700	-7.07	-42.8
15	Sb37	779361	9222239	749	-6.70	-40.8
16	Sb42	781448	9223008	703	-6.84	-41.8
17	Sb45	788997	9227341	689	-7.23	-44.2
18	Sb 49	777512	9221024	734	-6.91	-42.2

**Table 5.** Physical measurements of  $\delta^{18}\text{O}$  and  $\delta^2\text{H}$  isotopes in the southern Bandung (*Continued*)

No	Type of sample	X	Y	Elevation (m)	$\delta^{18}\text{O}$ (‰)	$\delta^2\text{H}$ (‰)
19	Sb50	785689	9920350	706	-7.73	-46.9
20	Sb52	786103	9221573	696	-7.68	-45.9
21	Sb60	774648	9216127	1059	-7.03	-43.8
22	Sp44	783701	9223886	692	-5.46	-34.4
23	Sp11	776614	9221798	816	-6.85	-44.3
24	Sg15	790418	9224231	700	-6.85	-43.5
25	Sg57	786348	9215868	965	-6.58	-41.4
26	Sp54	783759	9220403	705	-6.08	-38.8

**Fig 9.** Relationship between  $\delta^2\text{H}$  and  $\delta^{18}\text{O}$  of groundwater in the study area

to estimate the elevation of the recharge area.

Furthermore, Fig. 10 shows the relationship between elevation and mean  $\delta^2\text{H}$  and  $\delta^{18}\text{O}$  isotopes of monthly rainwater.

Based on Fig. 10, the groundwater in the study area can be classified into four groups as follows:

- (i) Group I: groundwater Ma2, which is at an elevation of 1427 m asl, from the  $^{18}\text{O}$  and  $^2\text{H}$  isotope values do not indicate water originating from a higher elevation and is considered water originating from local rainwater infiltration.
- (ii) Group II: groundwater Ma27, Sb9, Sb50, and Sb52, which are at an elevation of 696–855 m asl, are considered to come from the same infiltration elevation, which ranges from 980–1230 m asl.
- (iii) Group III: groundwater Ma17, Ma23, Sb16, Sb20, Sb21, Sb25, Sb35, Sb37, Sb42, Sb45, Sb49, Sp11, Sg15, which are at an elevation between 700–816 m asl is estimated to be derived from the recharge elevation between 750–970 m asl. Meanwhile, groundwater Ma63 and Sb60, which are in this group, from the  $^{18}\text{O}$  and  $^2\text{H}$  isotope values, more indicate local rainwater origin.
- (iv) Group IV: groundwater Ma14, Ma58, Ma18, Sp44, Sg57, Sp54 are more likely to show symptoms of evaporation or interaction with surface water.

The hydrogeological system's identification in this study was based on hydrochemical and stable isotope analysis of  $\delta^{18}\text{O}$  and  $\delta^2\text{H}$ . The CaCl facies is located in the hydrothermal alteration zone.  $\text{Cl}^-$  ions' density comes

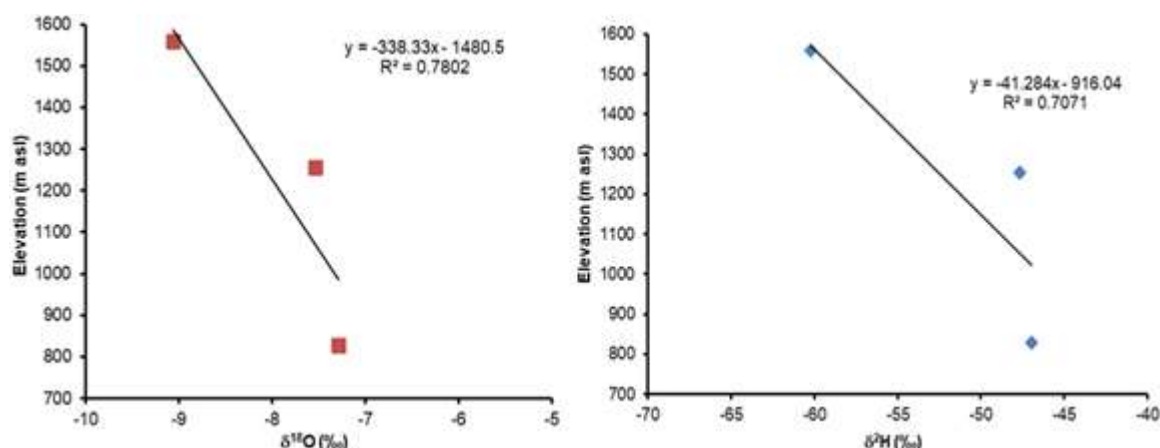


Fig 10. Graph of elevation vs.  $\delta^{18}\text{O}$  and  $\delta^2\text{H}$  in the study area

from contamination of geothermal fluids and the weathering of the feldspathoid sodalite mineral as a constituent of porous volcanic rock. The CaMgCl facies is a mixed water type. The calcium-magnesium dominance is generated from the weathering of silica minerals rich in  $\text{Ca}^{2+}$  from basaltic andesitic volcanic rocks. The CaMgHCO<sub>3</sub> type is formed due to the interaction between rocks and groundwater for a long time due to mixing, this can be seen from the amount of enrichment of  $\text{Ca}^{2+}$  and  $\text{Mg}^{2+}$  ions tare balanced. The CaHCO<sub>3</sub> facies shows groundwater circulation is not too far away. The dominant  $\text{Ca}^{2+}$  is due to the interaction with volcanic rocks. The presence of  $\text{HCO}_3^-$  indicates groundwater has been mixed with shallow groundwater as a local recharge.

The presence of  $\text{Ca}^{2+}$  cations comes from the weathering of rocks, while the presence of bicarbonate anions ( $\text{HCO}_3^-$ ) is influenced by the time of storing water in rocks and the influence of the atmosphere. The CaHCO<sub>3</sub> facies describe the groundwater flow with a short distance from shallow to moderate groundwater flows. The NaKHCO<sub>3</sub> facies are on distal facies. The cation exchange process in groundwater evolution is characterized by decreasing  $\text{Ca}^{2+}$  and  $\text{Mg}^{2+}$  and enriching  $\text{Na}^+$  ions. The adsorption rate of  $\text{Na}^+$  cations on clay minerals tends to be weaker than  $\text{Ca}^{2+}$  ions. Groundwater facies NaKHCO<sub>3</sub> shows groundwater flow intensity over a long-distance mixing shallow and deep groundwater (Fig. 11).

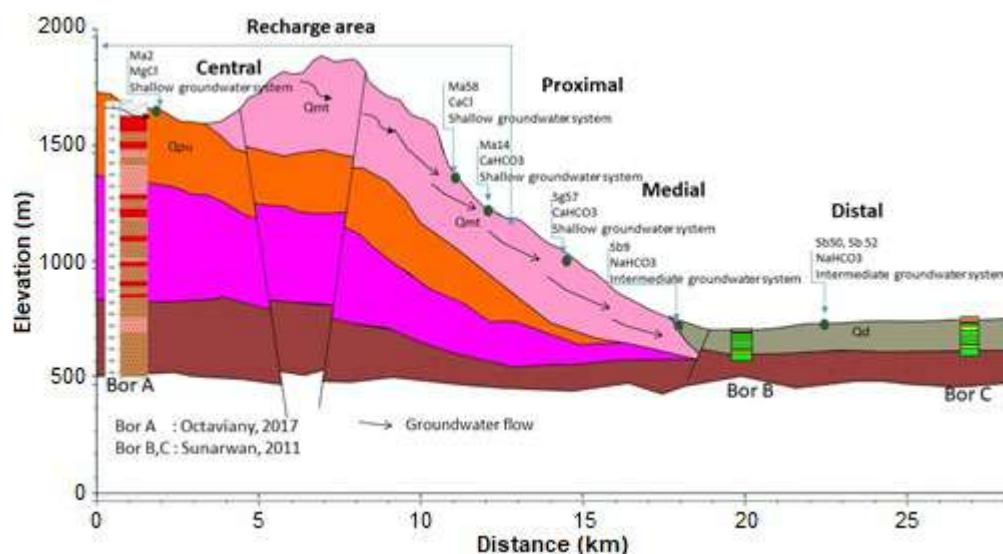


Fig 11. The hydrogeological system's identification in the study area



Groundwater flow systems are classified into the middle flow or intermediate systems [1]. The concentration of TDS is also an indication of a recharge area. TDS has a low value in the central facies area and increases upward to the distal region. The catchment area located in the upper zone is characterized by active groundwater flushing with a low TDS value, seen in central and proximal facies. The discharge area is characterized by less active groundwater circulation, with dominant  $\text{HCO}_3^-$  and high TDS values are seen in the medial zone. The lower zone is characterized by passive groundwater with high sodium concentrations and TDS in distal facies.

Stable isotope analysis reveals irregular patterns, and localized catchments represent a complex hydrogeological system. Isotope analysis shows the groundwater recharge location follows the groundwater circulation flow. Groundwater in the study area can be classified into four groups as follows: Group I, which is at an elevation of 1427 m asl, from the  $^{18}\text{O}$  and  $^2\text{H}$  isotope values do not indicate water originating from a higher elevation and is considered water originating from local rainwater infiltration; Group II: which are at an elevation of 696–855 m asl, is considered to come from the same infiltration elevation, which ranges from 980–1230 m asl; Group III which are at an elevation between 700–816 m asl is estimated to be derived from the recharge elevation between 750–970 m asl, Group IV are more likely to show symptoms of evaporation or interaction with surface water.

## ■ CONCLUSION

The results of hydrogeological, hydrochemical, and stable isotope analysis have determined groundwater recharge. The variation in groundwater chemistry of this area is principally controlled by a combination of ion exchange, silicate weathering, calcite, and dolomite dissolution of minerals. The hydrochemical facies were  $\text{CaCl}$ ,  $\text{CaMgCl}$ ,  $\text{CaMgHCO}_3$ ,  $\text{CaHCO}_3$ , and  $\text{NaKHCO}_3$ . Changes in  $\text{Ca}^{2+}$  to  $\text{Mg}^{2+}$  cations mean it has been a hydrochemical evolution. The  $\text{CaHCO}_3$  facies describe moderate groundwater flows. The  $\text{NaKHCO}_3$  Groundwater facies shows the mixing of shallow and deep

groundwater into intermediate flow systems. The recharge area in the central, proximal, and medial facies zone consists of 4 groups. Group I, which is at an elevation of 1427 m asl, from the  $^{18}\text{O}$  and  $^2\text{H}$  isotope values do not indicate water originating from a higher elevation and is considered water originating from local rainwater infiltration; Group II: which are at an elevation of 696–855 m asl, are considered to come from the same infiltration elevation, which ranges from 980–1230 m asl; Group III which are at an elevation between 700–816 m asl is estimated to be derived from the recharge elevation between 750–970 m asl, Group IV are more likely to show symptoms of evaporation or interaction with surface water. The discharge area in the distal facies zone is characterized by less active groundwater circulation, with dominant  $\text{HCO}_3^-$  and TDS values. Hydrochemical variation helped the identification of recharge areas in the volcanic facies.

## ■ ACKNOWLEDGMENTS

The author would like to thanks the Saintek Scholarship Program of the Ministry of Research and Technology, which has funded the education program. Thanks are also given to the Head of the Research Center for Geotechnology, Indonesian Institute of Science, Dr. Eko Yulianto, who has given permission for providing laboratory facilities to carry out the water sample analysis. Thanks are also given to Mr. Sudaryanto, MT, who has provided guidance.

## ■ AUTHOR CONTRIBUTIONS

Rizka Maria conducted the experiment, calculations, wrote, and revised the manuscript. Satrio conducted, wrote, and revised the manuscript. TYWM Iskandarsyah conducted, wrote, and revised the manuscript. B.R. Suganda conducted, wrote, and revised the manuscript. M.R. Delinom revised the manuscript. Hendarmawan conducted, wrote, and revised the manuscript. D. Marganingrum provided guidance before wrote manuscript. Dady Sukmayadi and W. Purwoko have helped a lot in laboratory analysis. All authors agreed to the final version of this manuscript.

## ■ REFERENCES

- [1] Hendarmawan, and Satrio, 2011, Recharge area on the slopes of volcano based on geological setting, content of deuterium and oxygen isotopes of groundwater chemistry: Case study on the slopes of Salak mountain, West Java, *J. Trop. Soils*, 16 (3), 245–256.
- [2] Satrio, Hendarmawan, Hadian, M.S.D., and Pujiindiyati, E.R., 2016, Karakteristik air tanah dangkal kota Semarang pada musim penghujan berdasarkan pendekatan isotop stabil ( $^{18}\text{O}$ ,  $^2\text{H}$ ) dan kimia air, *J. Ilm. Apl. Isot. Radiasi*, 11 (1), 73–86.
- [3] Toulrier, A., Baud, B., de Montety, V., Lachassagne, P., Leonardi, V., Pistre, V., Dautria, J.M., Hendrayana, H., Fajar, M.H.M., Muhammad, A.S., Beon, O., and Jourde, H., 2019, Multidisciplinary study with quantitative analysis of isotopic data for the assessment of recharge and functioning of volcanic aquifers: Case of Bromo-Tengger volcano, Indonesia, *J. Hydrol.: Reg. Stud.*, 26, 100634.
- [4] Abidi, J.H., Farhat, B., Ben Mammou, A., and Oueslati, N., 2017, Characterization of recharge mechanisms and sources of groundwater salinization in Ras Jbel coastal aquifer (Northeast Tunisia) using hydrogeochemical tools, environmental isotopes, GIS, and statistics, *J. Chem.*, 2017, 8610894.
- [5] Resubun, M.L., Wahjunie, E.D., and Tarigan, S.D., 2018, Analisis potensi ketersediaan dan kebutuhan air di Daerah Aliran Sungai Cisangkuy, *JITL*, 20 (2), 57–62.
- [6] Hendrasto, F., and Sunarwan, B., 2013 Pemanfaatan isotop lingkungan di daerah cekungan airtanah Bandung, *Jurnal Teknik*, 14 (2), 1–11.
- [7] Pujiindiyati, E.R., Satrio, and Prasetyo, R., 2019, Major ions for tracing leachate migration within shallow ground water in the vicinity of municipal landfill in Bantar Gebang –Bekasi, *Indones. J. Chem.*, 19 (1), 19–29.
- [8] Krishnaraj, S., Murugesan, V., Vijayaraghavan, K., Sabarathinam, C., Paluchamy, A., and Ramachandran, M., 2011, Use of hydrochemistry and stable isotopes as tools for groundwater evolution and contamination investigations, *Geosciences*, 1 (1), 16–25.
- [9] Wu, H., Chen, J., Qian, H., and Zhang, X., 2015, Chemical characteristics and quality assessment of groundwater of exploited aquifers in Beijiao water source of Yinchuan, China: A case study for drinking, irrigation, and industrial purposes, *J. Chem.*, 2015, 726340.
- [10] Hendarmawan, 2002, Unconfined aquifer system of volcanics in the northern part of Bandung basin, West Java, Indonesia, *J. Geosci., Osaka City Univ.*, 45, 1–12.
- [11] Delinom, R.M., and Suriadarma, A., 2010, Groundwater flow system of Bandung basin based on hydraulic head, subsurface temperature, and stable isotopes, *JRGP*, 20 (1), 55–68.
- [12] Iskandar, I., Notosiswoyo, S., Purnandi, C., and Pasaribu, T., 2013, Type and origin of springs and hotspots at surrounding ridges of Bandung basin, related with its potential natural contamination, *Procedia Earth Planet. Sci.*, 6, 262–268.
- [13] Sunarwan, B., 2011, Penentuan satuan hidrostratigrafi (HSU) di daerah vulkanik (Studi kasus: Daerah cekungan Bandung), *Jurnal Teknik*, 12 (2), 44–56.
- [14] Oktaviany, V., Hutabarat, J., and Haryanto, A.D., 2017, Estimasi temperatur bawah permukaan berdasarkan kehadiran mineral alterasi pada sumur 'X' lapangan panas bumi Wayang Windu, Pangalengan, Kabupaten Bandung, Provinsi Jawa Barat, *Bul. Sumber Daya Geol.*, 12 (2), 123–133.
- [15] Taufiq, A., Effendi, A.J., Iskandar, I., Hosono, T., and Hutasoit, L.M., 2019, Controlling factors and driving mechanisms of nitrate contamination in groundwater system of Bandung basin, Indonesia, deduced by combined use of stable isotope ratios, CFC age dating, and socioeconomic parameters, *Water Res.*, 148, 292–305.
- [16] Suhendar, R., Hadian, M.S.D., Muljana, Setiawan, T., and Hendarmawan, 2020, Geochemical evolution and groundwater flow system in Batujajar groundwater basin area, West Java, Indonesia, *Indones. J. Geosci.*, 7 (1) 87–104.
- [17] Matahelumual, B.C., and Wahyudin, 2010, Penelitian hidrogeologi daerah imbuhan air tanah dengan

- metode isotop dan hidrokimia di cekungan air tanah Bandung- Soreang, Provinsi Jawa Barat (Tahap III), *Field Report*, Pusat Vulkanologi dan Mitigasi Bencana Geologi, Badan Geologi, Bandung, Indonesia.
- [18] Bronto, S., Koswara, A., and Lumbanbatu, K., 2006, Stratigrafi gunung api daerah Bandung Selatan, Jawa Barat, *Indones. J. Geosci.*, 1 (2), 89–101.
- [19] Silitonga, P.H., 1973, *Geologic Map of the Bandung Quadrangle, Java*, scale 1:100.000, Geological Agency of the Ministry of Energy and Mineral Resources, Bandung, Indonesia.
- [20] Alzwar, M., Akbar, N., and Bachri S., 1992, *Peta geologi lembar Garut dan Pemeungpeuk, Jawa*, Pusat Penelitian dan Pengembangan Geologi, Bandung.
- [21] Clark, I., 2015, *Groundwater Geochemistry and Isotopes*, 1<sup>st</sup> Ed., CRC Press, Boca Raton, Florida, US.
- [22] Freeze, R.A., and Cherry, J.A., 1979, *Groundwater*, Prentice Hall, Inc., Englewood Cliffs, New Jersey.
- [23] Ahamed, A.J., Loganathan, K., Ananthakrishnan, S., Ahmed, J.K.C., and Ashraf, M.A., 2016, Evaluation of graphical and multivariate statistical methods for classification and evaluation of groundwater in Alathur block, Perambalur District, India, *Appl. Ecol. Environ. Res.*, 15 (3), 105–116.
- [24] Gaikwad, S., Gaikwad, S., Meshram, D., Wagh, V., Kandekar, A., and Kadam, A., 2020, Geochemical mobility of ions in groundwater from the tropical western coast of Maharashtra, India: Implication to groundwater quality, *Environ. Dev. Sustain.*, 22 (3), 2591–2624.
- [25] Pujiindiyati, E.R., Sidauruk, P., Prayogi, T.E., and Abdillah, F., 2020, Hydrochemical evolution in Ciliwung River - Java, Indonesia: Study of sea water mixture and mineral dissolution, *Indones. J. Chem.*, 20 (6), 1360–1373.
- [26] Mohamed, A.K., Liu, D., Song, K., Mohamed, M.A.A., Aldaw, E., and Elubid, B.A., 2019, Hydrochemical analysis and fuzzy logic method for evaluation of groundwater quality in the North Chengdu plain, China, *Int. J. Environ. Res. Public Health*, 16 (3), 302.
- [27] Mook, W.G., 2001, *Environmental Isotopes in the Hydrological Cycle: Principles and Applications, Volume I: Introduction: Theory, Methods, Review*, International Atomic Energy Agency and United Nations Educational, Scientific and Cultural Organization.
- [28] Coplen, T.B., Herczeg, A.L., and Barnes, C., 2000, “Isotope engineering—using stable isotopes of the water molecule to solve practical problems” in *Environmental Tracers in Subsurface Hydrology*, Springer, Boston, MA, 79–110.
- [29] Kumar, P.J.S., and James, E.J., 2016, Identification of hydrogeochemical processes in the Coimbatore district, Tamil Nadu, India, *Hydrol. Sci. J.*, 61 (4), 719–731.
- [30] Setiawan, T., Alam, B.Y.C.S.S.S., Haryono, E., and Hendarmawan, 2020, Hydrochemical and environmental isotopes analysis for characterizing a complex karst hydrogeological system of Watuputih area, Rembang, Central Java, Indonesia, *Hydrogeol. J.*, 28 (4), 1635–1659.
- [31] Rusydi, A.F., Naili, W., and Lestiana, H., 2015, Domestic and agricultural waste pollution of shallow groundwater in Bandung Regency, *JRGP*, 25 (2), 87–97.
- [32] Kehew, A.E., 2001, *Applied Chemical Hydrogeology*, Prentice Hall, New Jersey.
- [33] Paul, R., Brindha, K., Gowrisankar, G., Tan, M.L., and Singh, M.K., 2019, Identification of hydrogeochemical processes controlling groundwater quality in Tripura, Northeast India using evaluation indices, GIS, and multivariate statistical methods, *Environ. Earth Sci.*, 78 (15), 470.
- [34] Singh, A.K., Raj, B., Tiwari, A.K., and Mahato, M.K., 2013, Evaluation of hydrogeochemical processes and groundwater quality in the Jhansi district of Bundelkhand region, India, *Environ. Earth Sci.*, 70 (3), 1225–1247.
- [35] Hem, J.D., 1985, Study and interpretation of the chemical characteristics of natural water, *Water Supply Paper 2254*, U.S. Geological Survey.

## Morphology of NdFeB-Type Permanent Magnet Coercivity Enhancement by Heat Treatment Process

Eva Afrilinda<sup>1\*</sup>, Dagus Resmana Djuanda<sup>1</sup>, Shinta Viridhian<sup>1</sup>, Martin Doloksaribu<sup>1</sup>, Moch Iqbal Zaelana Muttahar<sup>1</sup>, and Sri Bimo Pratomo<sup>2</sup>

<sup>1</sup>Metal Industries Development Center (MIDC), Ministry of Industry of The Republic of Indonesia, Jl. Sangkuriang No. 12, Bandung 40135, West Java, Indonesia

<sup>2</sup>Department of Metallurgical Engineering, Faculty of Manufacturing Technology, Universitas Jenderal Achmad Yani, Jl. Terusan Jenderal Gatot Subroto, PO Box 807, Bandung 40285, West Java, Indonesia

\* **Corresponding author:**

tel: +62-22-2503171  
email: eva.afirilinda@gmail.com

Received: August 28, 2020  
Accepted: November 9, 2020

DOI: 10.22146/ijc.59096

**Abstract:** To understand the morphology of the coercivity enhancement by heat treatment, a commercial sintered NdFeB-type permanent magnet is annealed, and the coercivity is measured by Permagraph. It is shown that the coercivity is increased compared to the initial. Observation by X-Ray Diffraction (XRD) analysis and Scanning Electron Microscope-Energy Dispersive X-ray Spectroscopy (SEM-EDS) is then conducted. The XRD result shows the amount of NdFeB content in the NdFeB-type permanent magnet is increased after heat treatment. The more significant amount of NdFeB content causes higher coercivity. The maximum coercivity, 19 kOe, is achieved at 850 °C of heat treatment temperature, where the NdFeB content is at the highest amount. Microstructural characterizations using SEM-EDS show that at 850 °C of heat treatment temperature, the iron (Fe) content in the grain boundaries is the lowest. It causes higher coercivity. This is due to the magnetically decoupled between NdFeB grains. The decoupling magnet of the NdFeB grains is affected by the Fe content in the grain boundaries. High-temperature heat treatment at 900 and 1050 °C led to the decomposition of NdFeB content in the grains and increased the Fe content in the grain boundaries, which resulted in a substantial reduction of magnetic coercivity.

**Keywords:** NdFeB; heat treatment; coercivity; magnetically decoupled; decomposed

### ■ INTRODUCTION

One of the sintered magnets which can produce high energy  $(BH)_{\max}$  is Nd-Fe-B sintered magnets. These magnets were made by Sepehri-Amin et al. [1]. Nd-Fe-B sintered magnets are utilized for different applications, e.g., voice coil motors for hard disk drives and engines for hybrid electric vehicles (HEVs) or electric vehicles (EVs). Ecological issues caused by carbon emission affected the developing business sector of an electric vehicle, so that HEVs and EVs have drawn a great deal of consideration to be produced. Even though Nd-Fe-B sintered magnets have high  $(BH)_{\max}$ , it has low intrinsic coercivity. This is contributed by the  $Nd_2Fe_{14}B$  compound, the prime phase of this magnet, which arrives at around 12% of the

anisotropy field of its prime phase [2]. The methods used to keep up high magnetic properties at the high-temperature environments in HEVs, are additional Dy or Tb into the Nd-Fe-B sintered magnets. It will create  $Dy_2Fe_{14}B$  and  $Tb_2Fe_{14}B$  compounds with a higher anisotropy field than  $Nd_2Fe_{14}B$  [3].

Additional of Dy gives the Nd-Fe-B sintered magnets with several transformations such as better thermal stability but reduces the remanence and  $(BH)_{\max}$  value [4]. Besides, these added substance components are quite rare to be found, and their material costs rise significantly. If the perfect coercivity of  $Nd_2Fe_{14}B$  is acquired, the thermal ability would be improved without the addition of any substantial rare earth components. To attain high coercivity, two strategies have been proposed.

One is to get uniform distribution of the Nd-rich stage, which helps to diminish the nucleation site of reversed magnetic domains. If there are found some imperfections on the outer of the  $\text{Nd}_2\text{Fe}_{14}\text{B}$  grains, the reversed magnetic domains will show up at the low reverse magnetic field. Once a reversed magnetic domain appears in the grain, the domain wall moves, and magnetic reversal occurs without any problem. When a switched attractive space shows up in the grain, the area divider moves, and attractive inversion happens without any problem. In this case, it is required to diminish defects at the outer of  $\text{Nd}_2\text{Fe}_{14}\text{B}$  grains to increase the coercivity value. The phase that plays a vital part in diminishing nucleation sites of the reversed magnetic domain amid the annealing process is the Nd-rich phase. This phase contributes to enhance the coercivity [5-6]. The other is to control grain sizes underneath the single domain size of  $0.3\ \mu\text{m}$  in sintered magnets. These approaches appear that the control of microstructures of Nd-Fe-B magnets is very vital to get high coercivity [5].

Recently, sintered magnets with a grain measure around  $1\ \mu\text{m}$  with 20 kOe of coercivity, without the expansion of any heavy rare-earth elements were manufactured successfully on Nd-Fe-B type magnets by Sasaki et al. [7]. The methods to reduce the grain dimension are not the only reason to increase coercivity value. Subsequently, it is observed that Dy-free magnets with high coercivity were accomplished by reducing grain size, as well as reducing the nucleation sites of the reversed magnetic domain. Sepehri-Amin et al. [1] have researched the microstructure of the grain boundary for these magnets and the continuous grain boundary in sintered magnets through filtering electron microscopy (SEM), transmission electron microscopy (TEM), and atom probe tomography techniques. Moreover, they specified that the homogenous scattering of the Nd-rich phases at a triple junction was required to make a continuous grain boundary. Hence, the Nd-rich stage at the triple junction works as an asset to create grain boundary layers during the heat treatment process, particularly the annealing process [3].

It is notable that heat treatment of sintered Nd-Fe-B magnet emphatically builds the coercivity and improves the squareness of the demagnetizing  $J/H$  loops [8]. The temperature and time of this heat treatment, called annealing, the composition of the magnet should be considered then followed by fast quenching to optimize both the intrinsic coercivity and the hysteresis loop squareness. Numerous researchers have portrayed the impact of the annealing treatment and demonstrated a few patterns to associate the coercivity increment with an appearing mechanism in the grain boundary of the  $\text{RE}_2\text{Fe}_{14}\text{B}$  magnetic phase [9]. Nowadays, a few mechanisms are proposed. Some consider the impact of the RE-rich (RE: Rare Earth, for the most part, Nd-boundary phase as magnetic protection of the  $\text{RE}_2\text{Fe}_{14}\text{B}$  magnetic phase, and others ignore the participation of the boundary phase) [10].

There are necessarily two conceivable outcomes when it comes to creating coercivity at high temperatures. The outcomes are upgrading the intrinsic temperature reliance of the materials or creating sufficient coercivity value at room temperature to remain when the magnet is faced with high-temperature environments [11]. NdFeB magnets create their coercivity following a nucleation- type coercivity mechanism. It is crucial to locally increase the HA within the external shell of the grains, to the proximity of much less than a micron, as any new another rare earth in the  $\text{RE}_2\text{Fe}_{14}\text{B}$  grains [12]. It will substantially decrease the value of the magnetization.

The purpose of this study was to use several experimental techniques to define the relationship between the optimized annealing conditions and metallurgical transformations, also the microstructure change due to annealing in the NdFeB grains and grain boundary phase. The test samples were prepared by several annealing conditions at various temperatures. The magnetic properties were then measured and analyzed by Permagraph, X-Ray Diffraction (XRD), and Scanning Electron Microscope (SEM)-Energy-Dispersive X-ray Spectroscopy (EDS) observations.

## ■ EXPERIMENTAL SECTION

### Materials

The material used in this experiment was a commercial NdFeB-type permanent magnet sample that has an initial coercivity of 13.7 kOe, which compositions are listed in Table 1.

### Instrumentation

Instruments used included SANTE-High Temperature Vacuum Tube Furnace, Lab made grinding and polishing machine, Permagraph Magnet Physik, JEOL SEM machine type JSM636OLA, and Maxima XRD machine.

### Procedure

The un-magnetized samples were cut to the dimension of  $12 \times 12 \times 5$  mm and then put into the argon-filled vacuum heat treatment furnace. Afterward, they were annealed using several annealing conditions and various temperatures. The annealing temperature is set at 800, 850, 900, 950, 1000, and 1050 °C and held for 2 h. Subsequently, the post-annealing temperature is set at 500 °C, also held for 2 h. The heat treatment cycle of this research is shown in Fig. 1.

The value of magnetic coercivity is obtained by permagraph observation, which measures the reverse magnetic field that is applied to the sample, which changes the magnetized sample into fully demagnetized. Meanwhile, the chemical composition and metallurgical transformations appearing in the grains and grain boundary of the  $RE_2Fe_{14}B$  magnetic phase are observed by X-Ray Diffraction (XRD) and Scanning Electron

Microscope (SEM)/Energy-Dispersive X-ray Spectroscopy (EDS).

## ■ RESULTS AND DISCUSSION

### Permagraph Result Analysis

NdFeB-phase is the main element of the magnetic force in the NdFeB-type permanent magnet. The amount of NdFeB is related to high coercivity. The more of NdFeB contained, the higher coercivity is achieved. The presence of NdFeB-phase can be produced by casting NdFeB alloy. However, not all the elements are combined to developed NdFeB-phase by casting only; many of them are spread out become  $\alpha$ -Fe, Nd Rich, FeB, and so on. The Heat treatment for NdFeB-type permanent magnet is one of the processes that can be conducted to recombine the spread out elements into developing new NdFeB-phases.

The permagraph result shows that magnetic coercivity is increased after the heat treatment process. It is noticed that the highest coercivity (19 kOe) is achieved at 850 °C of annealing temperature [13]. Afterward, the coercivity is gradually decreased when the temperature is increased, but still higher than the initial coercivity, shown in Fig. 2.

**Table 1.** Composition of commercial NdFeB-type permanent magnet for the experiment

No.	Element	wt (%)
1	Nd (Neodymium)	28.07
2	Fe (Iron)	70.2
3	B (Boron)	1.1
4	Nb (Niobium)	0.3
5	Ga (Gallium)	0.33

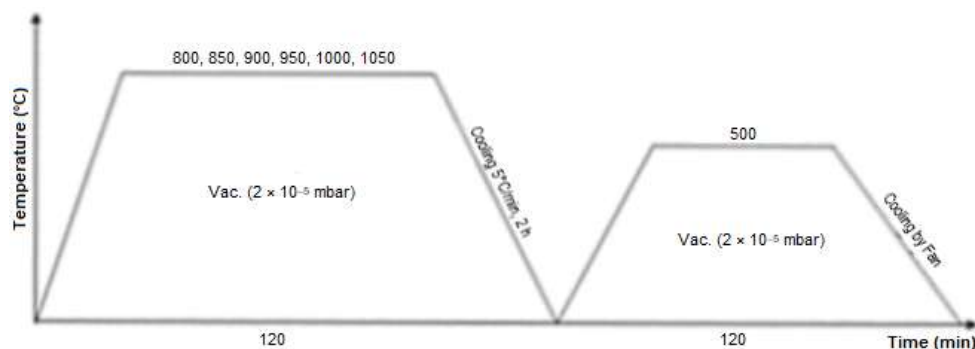


**Fig 1.** Variable of time and temperature for heat treatment process

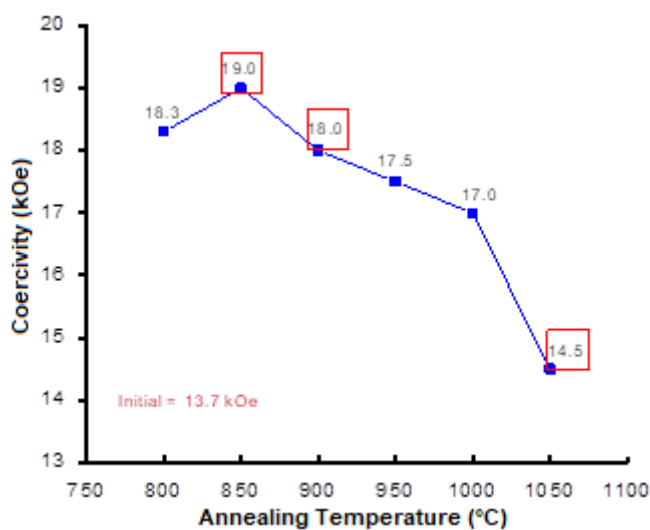


**Fig 2.** The change of coercivity at increased annealing temperature

The selected temperatures for the characterization of this research in the microstructure phase by XRD and microstructure composition by SEM from samples after heat treatment are at 850, 900, and 1050 °C are conducted and analyzed. The temperatures 850 and 1050 °C are selected because they show the highest and lowest coercivity, respectively. The 900 °C annealing temperature presents a condition where the coercivity is starting to decrease. The annealing condition at 800, 950, and 1000 °C are not being analyzed any further since 800 °C is already represented by initial coercivity, which is before optimum temperature. The 850 °C annealing condition is very important, because at this temperature, the coercivity is at the maximum value. Because the decrease of coercivity is already started at 900 °C, after optimum condition at 850 °C, the 950 °C annealing condition will not be significant anymore. The 1050 °C annealing condition, where the coercivity is the lowest, has a significant difference in the data compare to 1000 °C. By having data at optimum condition (850 °C), before optimum condition

(initial), and after optimum condition (900 and 1050 °C), the discussion is compact and comprehensive.

Annealing temperature and annealing time are the crucial parameters for controlling grain development. The crystallizations are depending on the composition [14]. With quick annealing tempering of 60 s at 500 °C, it is conceivable to get the grain sizes of 50 nm and a coercive field  $H_c$  up to 20 kOe [15].

### XRD Result Analysis

The XRD results in Fig. 3 show a phase-change in the samples after the heat treatment process. At 850 °C, which is the optimum temperature for coercivity enhancement, contain the highest amount of NdFeB-phase [16]. A compelling way to extend coercivity is to decrease the grain size underneath the single domain particle size. This can be frequently found in NdFeB layers, where the size is indeed more significant than the lateral grain size [17]. The switchover of coupling between neighboring grains leads to the interaction for each domain. For the most part, the domain walls will take after the grain boundaries, illustrating their pinning impact. In this manner, the coercivity enhancement follows the decline of grain size and the magnetically decouple of the closest grains.

From the XRD analysis result, it is described that there are phase-changed in the samples after heat treatment. The amount of NdFeB-phase is increased after heat treatment at 850 °C. However, when the heat treatment temperature is set at a higher temperature (900, 1050 °C), the coercivity is decreased due to the decomposition of the NdFeB-phase. Table 2 shows the change of coercivity value because of the NdFeB-phase composition amount.

In Nd-Fe-B sintered magnets, there are several secondary phases, such as  $\alpha$ -Fe, NdFe (Nd-rich), FeB, and

**Table 2.** The relation between phase composition and coercivity

Samples	Phase composition (%)					Coercivity samples (kOe)
	Fe	Nd	NdFe	FeB	FeB	
Initial	2.1	0.3	5.2	92.3	0.1	13.7
850 °C	25.2	3.1	14.5	13.2	44	19
900 °C	5.5	0.6	9.8	76.7	7.4	17.5
1050 °C	21.5	0	73.1	3.7	1.6	14.5

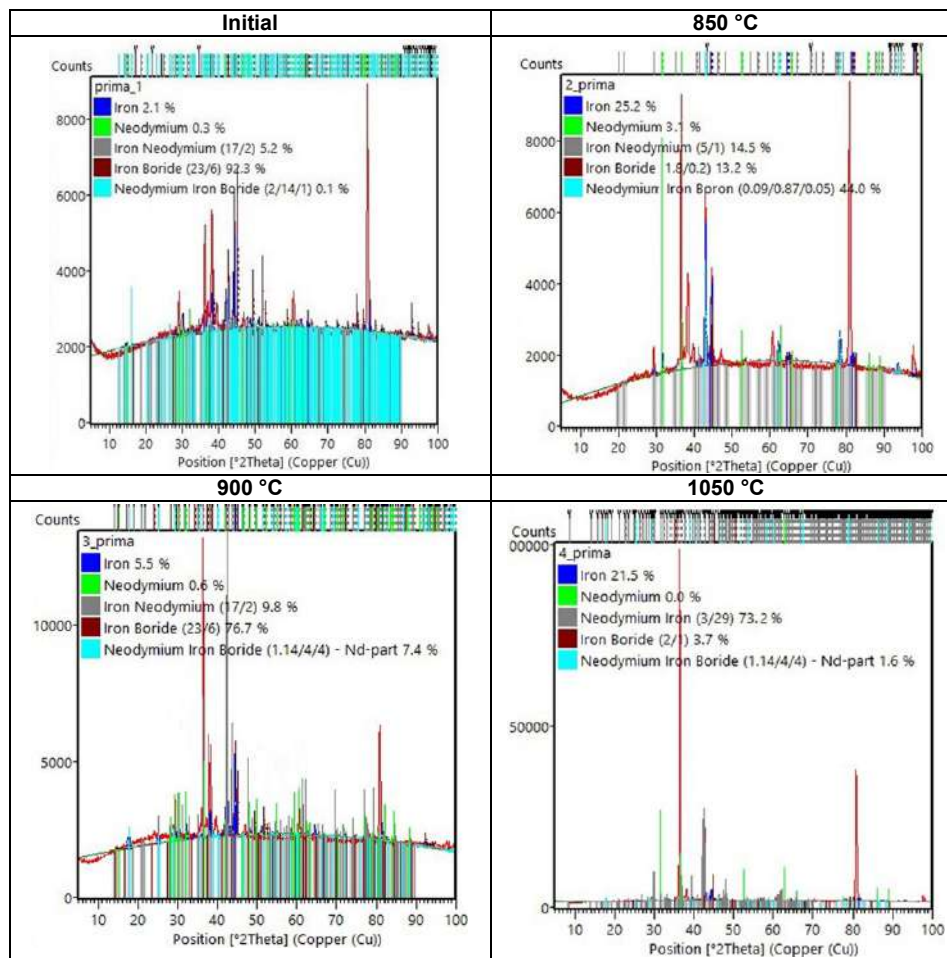


Fig 3. Phase-change at samples after heat treatment process by XRD

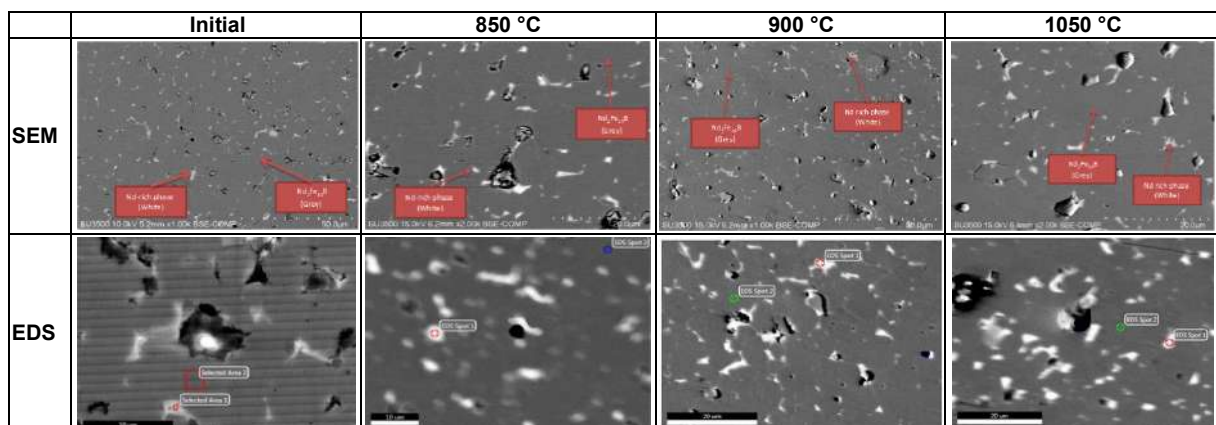


Fig 4. Microstructure of samples after heat treatment by SEM

oxides [18]. At the 850 °C annealing temperature, those secondary phase compositions are transformed into new NdFeB-phase. These cause an increase of coercivity due to the increased annealing temperature.

### SEM-EDS Result Analysis

The SEM observation results of samples after heat treatment are shown in Fig. 4. The images point to a grey and white area. The grey area represents the NdFeB grain,



and the white area represents grain boundaries [19-20].

The EDS results show that the composition in the grey area and white area. Fig. 5 shows the composition content of the grey area and white area, where the rare-earth and Fe composition are shown in Table 3.

The white area is representing the grain boundaries. The lowest Fe content (12.22%) in the grain boundaries is observed at 850 °C, as shown in Table 3. When the Fe content is low, the grain will be considered as magnetically separated (magnetic decoupling) that gives

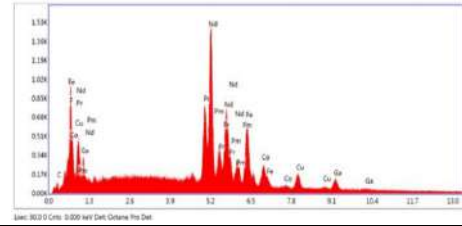
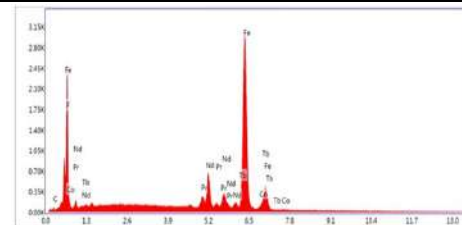
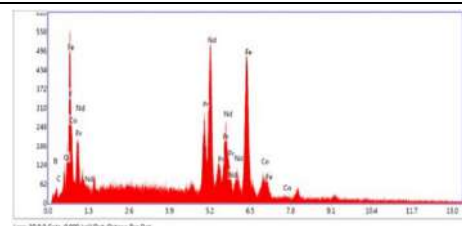
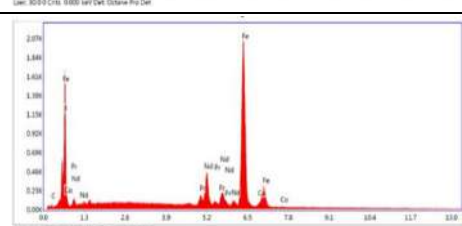
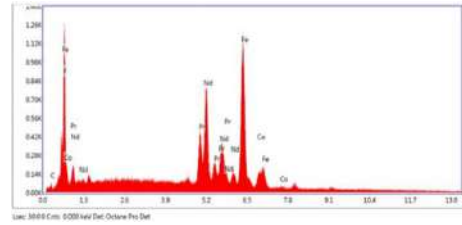
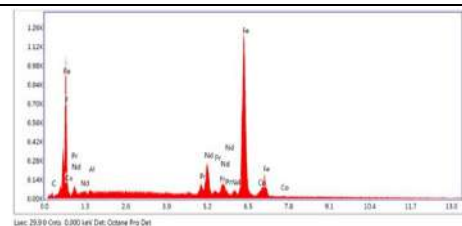
	Area	SEM-EDS																																																																																										
Initial	White	 <table border="1"> <thead> <tr> <th>Element</th> <th>Weight %</th> <th>Atomic %</th> <th>Net Int.</th> <th>Error %</th> <th>Kratio</th> <th>Z</th> <th>R</th> <th>A</th> <th>F</th> </tr> </thead> <tbody> <tr><td>CK</td><td>3.44</td><td>29.26</td><td>20.61</td><td>13.49</td><td>0.0166</td><td>1.4600</td><td>0.7692</td><td>0.3330</td><td>1.0000</td></tr> <tr><td>FK</td><td>1.13</td><td>4.22</td><td>33.05</td><td>15.19</td><td>0.0081</td><td>1.2900</td><td>0.7926</td><td>0.5504</td><td>1.0000</td></tr> <tr><td>PL</td><td>17.92</td><td>9.01</td><td>168.93</td><td>10.55</td><td>0.1850</td><td>0.9055</td><td>1.0849</td><td>1.0349</td><td>1.1002</td></tr> <tr><td>NdL</td><td>40.57</td><td>19.92</td><td>343.25</td><td>6.79</td><td>0.3964</td><td>0.8979</td><td>1.0874</td><td>1.0344</td><td>1.0522</td></tr> <tr><td>FeK</td><td>33.02</td><td>41.97</td><td>451.20</td><td>4.48</td><td>0.3416</td><td>1.1936</td><td>0.9360</td><td>0.9022</td><td>1.0299</td></tr> <tr><td>CoK</td><td>3.95</td><td>4.72</td><td>44.89</td><td>13.77</td><td>0.0394</td><td>1.0903</td><td>0.9422</td><td>0.8844</td><td>1.0371</td></tr> </tbody> </table>	Element	Weight %	Atomic %	Net Int.	Error %	Kratio	Z	R	A	F	CK	3.44	29.26	20.61	13.49	0.0166	1.4600	0.7692	0.3330	1.0000	FK	1.13	4.22	33.05	15.19	0.0081	1.2900	0.7926	0.5504	1.0000	PL	17.92	9.01	168.93	10.55	0.1850	0.9055	1.0849	1.0349	1.1002	NdL	40.57	19.92	343.25	6.79	0.3964	0.8979	1.0874	1.0344	1.0522	FeK	33.02	41.97	451.20	4.48	0.3416	1.1936	0.9360	0.9022	1.0299	CoK	3.95	4.72	44.89	13.77	0.0394	1.0903	0.9422	0.8844	1.0371																				
	Element	Weight %	Atomic %	Net Int.	Error %	Kratio	Z	R	A	F																																																																																		
CK	3.44	29.26	20.61	13.49	0.0166	1.4600	0.7692	0.3330	1.0000																																																																																			
FK	1.13	4.22	33.05	15.19	0.0081	1.2900	0.7926	0.5504	1.0000																																																																																			
PL	17.92	9.01	168.93	10.55	0.1850	0.9055	1.0849	1.0349	1.1002																																																																																			
NdL	40.57	19.92	343.25	6.79	0.3964	0.8979	1.0874	1.0344	1.0522																																																																																			
FeK	33.02	41.97	451.20	4.48	0.3416	1.1936	0.9360	0.9022	1.0299																																																																																			
CoK	3.95	4.72	44.89	13.77	0.0394	1.0903	0.9422	0.8844	1.0371																																																																																			
Grey	 <table border="1"> <thead> <tr> <th>Element</th> <th>Weight %</th> <th>Atomic %</th> <th>Net Int.</th> <th>Error %</th> <th>Kratio</th> <th>Z</th> <th>R</th> <th>A</th> <th>F</th> </tr> </thead> <tbody> <tr><td>CK</td><td>1.83</td><td>9.09</td><td>24.26</td><td>15.90</td><td>0.0204</td><td>1.1763</td><td>0.7998</td><td>0.2991</td><td>1.0000</td></tr> <tr><td>FK</td><td>3.88</td><td>8.98</td><td>294.24</td><td>7.90</td><td>0.0202</td><td>1.2350</td><td>0.9344</td><td>0.9729</td><td>1.0000</td></tr> <tr><td>PL</td><td>9.39</td><td>2.52</td><td>177.92</td><td>10.72</td><td>0.0228</td><td>0.8979</td><td>1.1293</td><td>1.0994</td><td>1.1610</td></tr> <tr><td>NdL</td><td>18.28</td><td>7.08</td><td>484.31</td><td>6.56</td><td>0.1032</td><td>0.8494</td><td>1.1311</td><td>1.0384</td><td>1.0965</td></tr> <tr><td>TdL</td><td>5.78</td><td>2.17</td><td>117.74</td><td>14.78</td><td>0.0497</td><td>0.8187</td><td>1.1353</td><td>1.0099</td><td>1.0458</td></tr> <tr><td>FeK</td><td>53.50</td><td>67.95</td><td>2709.10</td><td>2.44</td><td>0.8583</td><td>1.0923</td><td>0.9711</td><td>0.9846</td><td>1.0394</td></tr> <tr><td>CoK</td><td>1.73</td><td>1.76</td><td>91.61</td><td>17.82</td><td>0.0174</td><td>1.0309</td><td>0.9771</td><td>0.9410</td><td>1.0345</td></tr> </tbody> </table>	Element	Weight %	Atomic %	Net Int.	Error %	Kratio	Z	R	A	F	CK	1.83	9.09	24.26	15.90	0.0204	1.1763	0.7998	0.2991	1.0000	FK	3.88	8.98	294.24	7.90	0.0202	1.2350	0.9344	0.9729	1.0000	PL	9.39	2.52	177.92	10.72	0.0228	0.8979	1.1293	1.0994	1.1610	NdL	18.28	7.08	484.31	6.56	0.1032	0.8494	1.1311	1.0384	1.0965	TdL	5.78	2.17	117.74	14.78	0.0497	0.8187	1.1353	1.0099	1.0458	FeK	53.50	67.95	2709.10	2.44	0.8583	1.0923	0.9711	0.9846	1.0394	CoK	1.73	1.76	91.61	17.82	0.0174	1.0309	0.9771	0.9410	1.0345											
Element	Weight %	Atomic %	Net Int.	Error %	Kratio	Z	R	A	F																																																																																			
CK	1.83	9.09	24.26	15.90	0.0204	1.1763	0.7998	0.2991	1.0000																																																																																			
FK	3.88	8.98	294.24	7.90	0.0202	1.2350	0.9344	0.9729	1.0000																																																																																			
PL	9.39	2.52	177.92	10.72	0.0228	0.8979	1.1293	1.0994	1.1610																																																																																			
NdL	18.28	7.08	484.31	6.56	0.1032	0.8494	1.1311	1.0384	1.0965																																																																																			
TdL	5.78	2.17	117.74	14.78	0.0497	0.8187	1.1353	1.0099	1.0458																																																																																			
FeK	53.50	67.95	2709.10	2.44	0.8583	1.0923	0.9711	0.9846	1.0394																																																																																			
CoK	1.73	1.76	91.61	17.82	0.0174	1.0309	0.9771	0.9410	1.0345																																																																																			
850 °C	White	 <table border="1"> <thead> <tr> <th>Element</th> <th>Weight %</th> <th>Atomic %</th> <th>Net Int.</th> <th>Error %</th> <th>Kratio</th> <th>Z</th> <th>R</th> <th>A</th> <th>F</th> </tr> </thead> <tbody> <tr><td>CK</td><td>2.16</td><td>16.49</td><td>37.23</td><td>12.39</td><td>0.0199</td><td>1.9040</td><td>0.7367</td><td>0.3391</td><td>1.0000</td></tr> <tr><td>FK</td><td>1.09</td><td>4.95</td><td>87.50</td><td>11.12</td><td>0.0077</td><td>1.3440</td><td>0.7674</td><td>0.3227</td><td>1.0000</td></tr> <tr><td>PL</td><td>22.80</td><td>13.82</td><td>609.42</td><td>6.90</td><td>0.2367</td><td>0.9410</td><td>1.0566</td><td>1.0209</td><td>1.0902</td></tr> <tr><td>NdL</td><td>47.22</td><td>38.22</td><td>1147.92</td><td>3.95</td><td>0.4702</td><td>0.8323</td><td>1.0594</td><td>1.0200</td><td>1.0454</td></tr> <tr><td>FeK</td><td>12.22</td><td>18.66</td><td>478.79</td><td>6.41</td><td>0.1266</td><td>1.1970</td><td>0.9118</td><td>0.8776</td><td>1.0338</td></tr> <tr><td>CoK</td><td>4.24</td><td>6.20</td><td>139.37</td><td>11.17</td><td>0.0432</td><td>1.1388</td><td>0.9187</td><td>0.8895</td><td>1.0400</td></tr> <tr><td>CaK</td><td>4.46</td><td>6.03</td><td>110.69</td><td>11.65</td><td>0.0470</td><td>1.1264</td><td>0.9097</td><td>0.9095</td><td>1.0639</td></tr> <tr><td>SiK</td><td>4.48</td><td>6.91</td><td>78.05</td><td>15.16</td><td>0.0467</td><td>1.0942</td><td>0.9517</td><td>0.9166</td><td>1.0993</td></tr> </tbody> </table>	Element	Weight %	Atomic %	Net Int.	Error %	Kratio	Z	R	A	F	CK	2.16	16.49	37.23	12.39	0.0199	1.9040	0.7367	0.3391	1.0000	FK	1.09	4.95	87.50	11.12	0.0077	1.3440	0.7674	0.3227	1.0000	PL	22.80	13.82	609.42	6.90	0.2367	0.9410	1.0566	1.0209	1.0902	NdL	47.22	38.22	1147.92	3.95	0.4702	0.8323	1.0594	1.0200	1.0454	FeK	12.22	18.66	478.79	6.41	0.1266	1.1970	0.9118	0.8776	1.0338	CoK	4.24	6.20	139.37	11.17	0.0432	1.1388	0.9187	0.8895	1.0400	CaK	4.46	6.03	110.69	11.65	0.0470	1.1264	0.9097	0.9095	1.0639	SiK	4.48	6.91	78.05	15.16	0.0467	1.0942	0.9517	0.9166	1.0993
	Element	Weight %	Atomic %	Net Int.	Error %	Kratio	Z	R	A	F																																																																																		
CK	2.16	16.49	37.23	12.39	0.0199	1.9040	0.7367	0.3391	1.0000																																																																																			
FK	1.09	4.95	87.50	11.12	0.0077	1.3440	0.7674	0.3227	1.0000																																																																																			
PL	22.80	13.82	609.42	6.90	0.2367	0.9410	1.0566	1.0209	1.0902																																																																																			
NdL	47.22	38.22	1147.92	3.95	0.4702	0.8323	1.0594	1.0200	1.0454																																																																																			
FeK	12.22	18.66	478.79	6.41	0.1266	1.1970	0.9118	0.8776	1.0338																																																																																			
CoK	4.24	6.20	139.37	11.17	0.0432	1.1388	0.9187	0.8895	1.0400																																																																																			
CaK	4.46	6.03	110.69	11.65	0.0470	1.1264	0.9097	0.9095	1.0639																																																																																			
SiK	4.48	6.91	78.05	15.16	0.0467	1.0942	0.9517	0.9166	1.0993																																																																																			
Grey	 <table border="1"> <thead> <tr> <th>Element</th> <th>Weight %</th> <th>Atomic %</th> <th>Net Int.</th> <th>Error %</th> <th>Kratio</th> <th>Z</th> <th>R</th> <th>A</th> <th>F</th> </tr> </thead> <tbody> <tr><td>CK</td><td>2.40</td><td>11.28</td><td>20.59</td><td>15.85</td><td>0.0083</td><td>1.3699</td><td>0.8292</td><td>0.2547</td><td>1.0000</td></tr> <tr><td>FK</td><td>2.64</td><td>7.83</td><td>167.23</td><td>7.71</td><td>0.0193</td><td>1.2191</td><td>0.9441</td><td>0.6888</td><td>1.0000</td></tr> <tr><td>PL</td><td>6.29</td><td>2.12</td><td>101.16</td><td>17.66</td><td>0.0563</td><td>0.8453</td><td>1.1391</td><td>1.0637</td><td>1.1644</td></tr> <tr><td>NdL</td><td>18.91</td><td>7.40</td><td>319.74</td><td>8.10</td><td>0.1845</td><td>0.8368</td><td>1.1408</td><td>1.0632</td><td>1.0964</td></tr> <tr><td>FeK</td><td>68.66</td><td>69.36</td><td>1855.22</td><td>2.49</td><td>0.7013</td><td>1.0265</td><td>0.8792</td><td>0.9692</td><td>1.0274</td></tr> <tr><td>CoK</td><td>2.10</td><td>2.01</td><td>47.62</td><td>16.77</td><td>0.0208</td><td>1.0160</td><td>0.9848</td><td>0.9453</td><td>1.0343</td></tr> </tbody> </table>	Element	Weight %	Atomic %	Net Int.	Error %	Kratio	Z	R	A	F	CK	2.40	11.28	20.59	15.85	0.0083	1.3699	0.8292	0.2547	1.0000	FK	2.64	7.83	167.23	7.71	0.0193	1.2191	0.9441	0.6888	1.0000	PL	6.29	2.12	101.16	17.66	0.0563	0.8453	1.1391	1.0637	1.1644	NdL	18.91	7.40	319.74	8.10	0.1845	0.8368	1.1408	1.0632	1.0964	FeK	68.66	69.36	1855.22	2.49	0.7013	1.0265	0.8792	0.9692	1.0274	CoK	2.10	2.01	47.62	16.77	0.0208	1.0160	0.9848	0.9453	1.0343																					
Element	Weight %	Atomic %	Net Int.	Error %	Kratio	Z	R	A	F																																																																																			
CK	2.40	11.28	20.59	15.85	0.0083	1.3699	0.8292	0.2547	1.0000																																																																																			
FK	2.64	7.83	167.23	7.71	0.0193	1.2191	0.9441	0.6888	1.0000																																																																																			
PL	6.29	2.12	101.16	17.66	0.0563	0.8453	1.1391	1.0637	1.1644																																																																																			
NdL	18.91	7.40	319.74	8.10	0.1845	0.8368	1.1408	1.0632	1.0964																																																																																			
FeK	68.66	69.36	1855.22	2.49	0.7013	1.0265	0.8792	0.9692	1.0274																																																																																			
CoK	2.10	2.01	47.62	16.77	0.0208	1.0160	0.9848	0.9453	1.0343																																																																																			
900 °C	White	 <table border="1"> <thead> <tr> <th>Element</th> <th>Weight %</th> <th>Atomic %</th> <th>Net Int.</th> <th>Error %</th> <th>Kratio</th> <th>Z</th> <th>R</th> <th>A</th> <th>F</th> </tr> </thead> <tbody> <tr><td>CK</td><td>2.09</td><td>12.46</td><td>22.48</td><td>14.29</td><td>0.0096</td><td>1.4441</td><td>0.7645</td><td>0.3197</td><td>1.0000</td></tr> <tr><td>FK</td><td>2.13</td><td>8.00</td><td>119.80</td><td>9.02</td><td>0.0156</td><td>1.2830</td><td>0.7972</td><td>0.5642</td><td>1.0000</td></tr> <tr><td>PL</td><td>18.16</td><td>9.21</td><td>322.04</td><td>7.95</td><td>0.1868</td><td>0.9024</td><td>1.0900</td><td>1.0378</td><td>1.0987</td></tr> <tr><td>NdL</td><td>36.69</td><td>18.18</td><td>595.00</td><td>6.96</td><td>0.3686</td><td>0.8938</td><td>1.0924</td><td>1.0370</td><td>1.0546</td></tr> <tr><td>FeK</td><td>37.38</td><td>47.95</td><td>985.72</td><td>3.61</td><td>0.3873</td><td>1.1083</td><td>0.9391</td><td>0.9076</td><td>1.0296</td></tr> <tr><td>CoK</td><td>3.53</td><td>4.29</td><td>76.23</td><td>11.21</td><td>0.0394</td><td>1.0966</td><td>0.9462</td><td>0.8996</td><td>1.0269</td></tr> </tbody> </table>	Element	Weight %	Atomic %	Net Int.	Error %	Kratio	Z	R	A	F	CK	2.09	12.46	22.48	14.29	0.0096	1.4441	0.7645	0.3197	1.0000	FK	2.13	8.00	119.80	9.02	0.0156	1.2830	0.7972	0.5642	1.0000	PL	18.16	9.21	322.04	7.95	0.1868	0.9024	1.0900	1.0378	1.0987	NdL	36.69	18.18	595.00	6.96	0.3686	0.8938	1.0924	1.0370	1.0546	FeK	37.38	47.95	985.72	3.61	0.3873	1.1083	0.9391	0.9076	1.0296	CoK	3.53	4.29	76.23	11.21	0.0394	1.0966	0.9462	0.8996	1.0269																				
	Element	Weight %	Atomic %	Net Int.	Error %	Kratio	Z	R	A	F																																																																																		
CK	2.09	12.46	22.48	14.29	0.0096	1.4441	0.7645	0.3197	1.0000																																																																																			
FK	2.13	8.00	119.80	9.02	0.0156	1.2830	0.7972	0.5642	1.0000																																																																																			
PL	18.16	9.21	322.04	7.95	0.1868	0.9024	1.0900	1.0378	1.0987																																																																																			
NdL	36.69	18.18	595.00	6.96	0.3686	0.8938	1.0924	1.0370	1.0546																																																																																			
FeK	37.38	47.95	985.72	3.61	0.3873	1.1083	0.9391	0.9076	1.0296																																																																																			
CoK	3.53	4.29	76.23	11.21	0.0394	1.0966	0.9462	0.8996	1.0269																																																																																			
Grey	 <table border="1"> <thead> <tr> <th>Element</th> <th>Weight %</th> <th>Atomic %</th> <th>Net Int.</th> <th>Error %</th> <th>Kratio</th> <th>Z</th> <th>R</th> <th>A</th> <th>F</th> </tr> </thead> <tbody> <tr><td>CK</td><td>2.93</td><td>13.36</td><td>14.84</td><td>16.68</td><td>0.0101</td><td>1.3666</td><td>0.9112</td><td>0.2654</td><td>1.0000</td></tr> <tr><td>FK</td><td>2.66</td><td>7.70</td><td>93.63</td><td>8.93</td><td>0.0192</td><td>1.2192</td><td>0.9461</td><td>0.9939</td><td>1.0000</td></tr> <tr><td>ALK</td><td>0.44</td><td>0.89</td><td>9.75</td><td>49.16</td><td>0.0016</td><td>1.1726</td><td>0.9362</td><td>0.3036</td><td>1.0039</td></tr> <tr><td>PL</td><td>6.46</td><td>2.13</td><td>82.00</td><td>20.36</td><td>0.0688</td><td>0.8424</td><td>1.1412</td><td>1.0842</td><td>1.1823</td></tr> <tr><td>NdL</td><td>18.34</td><td>6.99</td><td>184.50</td><td>9.95</td><td>0.1784</td><td>0.8339</td><td>1.1426</td><td>1.0637</td><td>1.0989</td></tr> <tr><td>FeK</td><td>67.77</td><td>66.67</td><td>1009.50</td><td>2.86</td><td>0.6905</td><td>1.0320</td><td>0.9800</td><td>0.9600</td><td>1.0276</td></tr> <tr><td>CoK</td><td>2.41</td><td>2.24</td><td>32.49</td><td>19.01</td><td>0.0238</td><td>1.0114</td><td>0.9964</td><td>0.9462</td><td>1.0344</td></tr> </tbody> </table>	Element	Weight %	Atomic %	Net Int.	Error %	Kratio	Z	R	A	F	CK	2.93	13.36	14.84	16.68	0.0101	1.3666	0.9112	0.2654	1.0000	FK	2.66	7.70	93.63	8.93	0.0192	1.2192	0.9461	0.9939	1.0000	ALK	0.44	0.89	9.75	49.16	0.0016	1.1726	0.9362	0.3036	1.0039	PL	6.46	2.13	82.00	20.36	0.0688	0.8424	1.1412	1.0842	1.1823	NdL	18.34	6.99	184.50	9.95	0.1784	0.8339	1.1426	1.0637	1.0989	FeK	67.77	66.67	1009.50	2.86	0.6905	1.0320	0.9800	0.9600	1.0276	CoK	2.41	2.24	32.49	19.01	0.0238	1.0114	0.9964	0.9462	1.0344											
Element	Weight %	Atomic %	Net Int.	Error %	Kratio	Z	R	A	F																																																																																			
CK	2.93	13.36	14.84	16.68	0.0101	1.3666	0.9112	0.2654	1.0000																																																																																			
FK	2.66	7.70	93.63	8.93	0.0192	1.2192	0.9461	0.9939	1.0000																																																																																			
ALK	0.44	0.89	9.75	49.16	0.0016	1.1726	0.9362	0.3036	1.0039																																																																																			
PL	6.46	2.13	82.00	20.36	0.0688	0.8424	1.1412	1.0842	1.1823																																																																																			
NdL	18.34	6.99	184.50	9.95	0.1784	0.8339	1.1426	1.0637	1.0989																																																																																			
FeK	67.77	66.67	1009.50	2.86	0.6905	1.0320	0.9800	0.9600	1.0276																																																																																			
CoK	2.41	2.24	32.49	19.01	0.0238	1.0114	0.9964	0.9462	1.0344																																																																																			

Fig 5. Composition of white and grey area in the sample after heat treatment by EDS

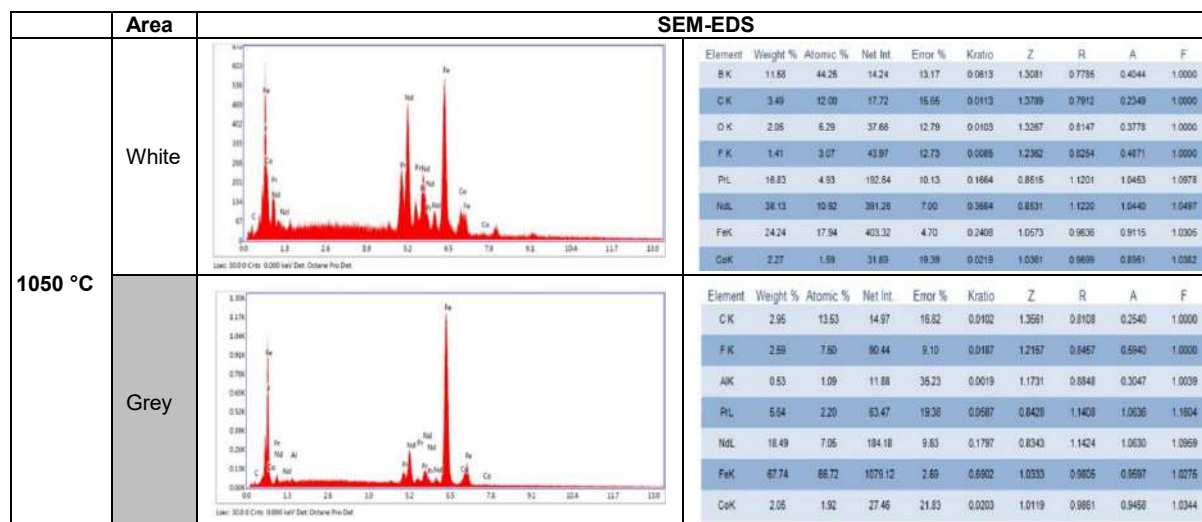


Fig 5. Composition of white and grey area in the sample after heat treatment by EDS (Continued)

Table 3. Composition of Rare-Earth (RE) and Fe in white and grey area of the sample after heat treatment by EDS

Area Color	Composition (%)							
	Initial		850 °C		900 °C		1050 °C	
	RE	Fe	RE	Fe	RE	Fe	RE	Fe
White	58.39	33.02	71.38	12.22	55.15	37.39	56.96	24.24
Grey	29.98	63.6	24.2	68.66	23.8	67.77	24.13	67.74
Coercivity (kOe)	13.7		19		17.5		14.5	

high coercivity. On the other hand, when the Fe content in the white area is high (37.39% at 900 °C), the coercivity is lower. These can be explained as Fe has high magnetic conductivity (ferromagnetic) [21]. If the grain boundaries have high Fe content, then the neighboring grains will be considered as one big grain that causes low coercivity.

Paramagnetic component addition, such as RE (Rare-Earth), in this case, neodymium in NdFeB, creates a neodymium-rich intergranular paramagnetic stage that decouples the ferromagnetic NdFeB grains. The decoupling avoids the nucleation initiated by the closest grains and heighten the coercivity. The highest RE content (71.38%) in the grain boundaries is observed at 850 °C, as shown in Table 3. When the RE content is high, then the grain will be considered as magnetically separated (magnetic decoupling) that gives high coercivity. However, the grain size will shrink, and the energy production can be achieved effectively with neodymium concentrations higher than the stoichiometric composition [22].

A previous study in manipulating grain boundaries [23] shows that the continuous grain boundaries are developed after annealing, which causes the increase of magnetic coercivity for the NdFeB-type permanent magnet. Our study result compliments their data by defining the continuous grain boundaries crystal phase where the RE or Fe content in the grain boundaries gives a significant effect to coercivity value, as shown in Table 3. Further study is needed to determine the homogeneity of the metal distribution in the sample by Electron Probe Micro Analyzer (EPMA), despite localize measurement from EDS.

## CONCLUSION

From the experiments, it shows clearly that the coercivity enhancement of NdFeB type permanent magnet by heat treatment process is due to the increasing amount of NdFeB-phase in the grain and the magnetically separation between the neighboring grains.

This result gives the necessary information for any effort in increasing the magnetic properties of NdFeB-type permanent magnet.

## ■ ACKNOWLEDGMENTS

This research was financially supported by the Korean Institute of Materials Science (KIMS).

## ■ AUTHOR CONTRIBUTIONS

All authors conducted the experiment, calculations, wrote, and revised the manuscript then agreed to the final version of this manuscript.

## ■ REFERENCES

- [1] Sepehri-Amin, H., Une, Y., Ohkubo, T., Hono, K., and Sagawa, M., 2011, Microstructure of fine-grained Nd-Fe-B sintered magnets with high coercivity, *Scr. Mater.*, 65 (5), 396–399.
- [2] Poenaru, I., Lixandru, A., Güth, K., Malfliet, A., Yoon, S., Škulj, I., and Gutfleisch, O., 2020, HDDR treatment of Ce-substituted Nd<sub>2</sub>Fe<sub>14</sub>B-based permanent magnet alloys - phase structure evolution, intergranular processes and magnetic property development, *J. Alloys Compd.*, 814, 152215.
- [3] Goto, R., Matsuura, M., Sugimoto, S., Tezuka, N., Une, Y., and Sagawa, M., 2012, Microstructure evaluation for Dy-free Nd-Fe-B sintered magnets with high coercivity, *J. Appl. Phys.*, 111 (7), 07A739.
- [4] Li, X., Liu, S., Cao, X., Zhou, B., Chen, L., Yan, A., and Yan, G., 2016, Coercivity and thermal stability improvement in sintered Nd-Fe-B permanent magnets by intergranular addition of Dy-Mn alloy, *J. Magn. Magn. Mater.*, 407, 247–251.
- [5] Soderžnik, M., Rožman, K.Ž., Kobe, S., and McGuinness, P., 2012, The grain-boundary diffusion process in Nd-Fe-B sintered magnets based on the electrophoretic deposition of DyF<sub>3</sub>, *Intermetallics*, 23, 158–162.
- [6] Vial, F., Joly, F., Nevalainen, E., Sagawa, M., Hiraga, K., and Park, K.T., 2002, Improvement of coercivity of sintered NdFeB permanent magnets by heat treatment, *J. Magn. Magn. Mater.*, 242-245 (Part 2), 1329–1334.
- [7] Sasaki, T.T., Ohkubo, T., Hono, K., Une, Y., and Sagawa, M., 2013, Correlative multi-scale characterization of a fine grained Nd-Fe-B sintered magnet, *Ultramicroscopy*, 132, 222–226.
- [8] Kim, S., Ko, D.S., Lee, H.S., Kim, D., Roh, J.W., and Lee, W., 2019, Enhancing the coercivity of Nd-Fe-B sintered magnets by consecutive heat treatment-induced formation of Tb-diffused microstructures, *J. Alloys Compd.*, 780, 574–580.
- [9] Yin, W., Chen, R., Tang, X., Ju, J., and Yan, A., 2019, Effect of pressless heat treatment on the magnetic performance and microstructure of hot-deformed Nd-Fe-B magnet, *J. Magn. Magn. Mater.*, 482, 9–13.
- [10] Loewe, K., Benke, D., Kübel, C., Lienig, T., Skokov, K.P., and Gutfleisch, O., 2017, Grain boundary diffusion of different rare earth elements in Nd-Fe-B sintered magnets by experiment and FEM simulation, *Acta Mater.*, 124, 421–429.
- [11] Li, Y., Zhu, M., Li, A., Feng, H., Huang, S., Li, W., Du, A., and Qi, Y., 2014, Relationship between controllable preparation and microstructure of NdFeB sintered magnets, *J. Rare Earths*, 32 (7), 628–632.
- [12] Liu, Y., Pan, Q., Li, H., Huang, Z., Ye, J., and Li, M., 2019, Revealing the evolution of microstructure, mechanical property and corrosion behavior of 7A46 aluminum alloy with different ageing treatment, *J. Alloys Compd.*, 792, 32–45.
- [13] Pratomo, S.B., Djuanda, D.R., Fauzi, M.N., Afrilinda, E., and Nurqiat, P.R., 2019, Peningkatan koersivitas magnet permanen tipe Nd<sub>2</sub>Fe<sub>14</sub>B dengan metoda perlakuan panas, *Jurnal Teknologi Bahan dan Barang Teknik*, 9 (1), 1–6.
- [14] Zhou, Q., Li, W., Hong, Y., Zhao, L., Zhong, X., Yu, H., Huang, L., and Liu, Z., 2018, Microstructure improvement related coercivity enhancement for sintered NdFeB magnets after optimized additional heat treatment, *J. Rare Earths*, 36 (4), 379–384.
- [15] Krasny, Y.P., Kovalenko, N.P., and Krey, U., 1997, Thermodynamics of amorphous magnets with ferromagnetic and antiferromagnetic coupling, *Physica B*, 240 (1-2), 173–182.

- [16] Wang, Y., You, C., Wang, J., Tian, N., Lu, Z., and Ge, L., 2012, Coercivity enhancement of Nd<sub>2</sub>Fe<sub>14</sub>B/ $\alpha$ -Fe nanocomposite magnets through neodymium diffusion under annealing, *J. Rare Earths*, 30 (8), 757–760.
- [17] Gouteff, P.C., Folks, L., and Street, R., 1998, MFM study of NdFeB and NdFeB/Fe/NdFeB thin films, *J. Magn. Magn. Mater.*, 177-181 (Part 2), 1241–1242.
- [18] Li, J., Yang, D., and Zhu, X., 2017, Effects of aging time and annealing temperature on structural and optical properties of sol-gel ZnO thin films, *AIP Adv.*, 7 (6), 065213.
- [19] Zhou, L., Li, J., Cheng, X., Liu, T., Yu, X., and Li, B., 2017, Dy gradient and coercivity in grain boundary diffusion processed Nd-Fe-B magnet, *J. Rare Earths*, 35 (6), 559–566.
- [20] Hu, S.Q., Peng, K., and Chen, H., 2017, Influence of annealing temperature on the Dy diffusion process in NdFeB magnets, *J. Magn. Magn. Mater.*, 426, 340–346.
- [21] Coey, J.M.D., 2011, Hard magnetic materials: A perspective, *IEEE Trans. Magn.*, 47 (12), 4671–4681.
- [22] Piramanayagam, S.N., Matsumoto, M., Morisako, A., and Takei, S., 1998, Studies on NdFeB thin films over a wide composition range, *J. Alloys Compd.*, 281 (1), 27–31.
- [23] Li, W.F., Ohkubo, T., and Hono, K., 2009, Effect of post-sinter annealing on the coercivity and microstructure of Nd-Fe-B permanent magnets, *Acta Mater.*, 57 (5), 1337–1346.

## Hierarchical Structure of Magnetic Nanoparticles -Fe<sub>3</sub>O<sub>4</sub>- Ferrofluids Revealed by Small Angle X-Ray Scattering

Gea Fitria<sup>1</sup>, Arum Patriati<sup>2</sup>, Mujamilah<sup>2</sup>, Maria Christina Prihatiningsih<sup>1</sup>, Edy Giri Rachman Putra<sup>1,2\*</sup>, and Sิริwat Soontaranon<sup>3</sup>

<sup>1</sup>Department of Nuclear Chemical Engineering, Polytechnic Institute of Nuclear Technology, Indonesia, Jl. Babarsari, Yogyakarta 55281, Indonesia

<sup>2</sup>Center for Science and Technology of Advanced Materials, National Nuclear Energy Agency of Indonesia, Kawasan Puspiptek Serpong, Banten 15314, Indonesia

<sup>3</sup>Synchrotron Light Research Institute of Thailand, 111 University Avenue, Nakhon Ratchasima 30000, Thailand

\* Corresponding author:

email: giri@batan.go.id

Received: August 28, 2020

Accepted: November 20, 2020

DOI: 10.22146/ijc.59114

**Abstract:** Small-angle X-ray scattering (SAXS) experiments were set up to investigate the form and structure of Fe<sub>3</sub>O<sub>4</sub> magnetic nanoparticles (MNPs) using BL1.3:SAXS at the Synchrotron Light Research Institute (SLRI) of Thailand in the range of scattering vector  $q$ ,  $0.7 < q \text{ (nm}^{-1}\text{)} < 4$ . The scattering data from samples, background, and empty cells were collected and then subtracted using small-angle X-ray scattering image tool (SAXSIT) software. The analysis of the corrected scattering patterns for four different pH, i.e., 2, 3, 4, and 5, has been revealed by applying log-normal spherical and mass fractal models calculation. The results showed that the SAXS measurement could investigate the hierarchical structures of MNPs Fe<sub>3</sub>O<sub>4</sub> containing primary and secondary particles. The two-dimensional fractal ( $D_f$ ) aggregates as secondary particles (in volume) have various sizes ranging from 21 to 103 nm in diameter, confirming the correlation to their pH. Those structures consist of primary particles with a mean length of 2 nm in radius and the particle size distribution ( $\sigma$ ) of 0.5.

**Keywords:** magnetic nanoparticles Fe<sub>3</sub>O<sub>4</sub>; ferrofluids; small-angle scattering; X-ray synchrotron; nanostructures; hierarchical structure

### ■ INTRODUCTION

Ferrofluids are highly stable colloidal systems containing magnetic nanoparticles (MNPs) Fe<sub>3</sub>O<sub>4</sub>, which can be physically controlled using external magnetic fields. The study of ferrofluids has progressed in recent years due to many possible applications in the biomedical field. As described in a review paper by Wu et al., magnetic nanoparticles have been used for medical applications such as drug delivery agents, biosensing, and bioseparation [1]. However, due to the magnetic properties of MNPs Fe<sub>3</sub>O<sub>4</sub>, they tend to form clusters or aggregate in volume. The presence of aggregates and their internal structure will strongly influence the properties of MNPs. For example, the number of primary particles forming aggregate can affect the strength of magnetic

interaction. The larger aggregate with more primary particles and interaction with each of them will result in strong magnetic properties [2]. Usually, the surface of magnetic nanoparticles is altered to prevent interparticle surface interactions [3].

As a fundamental understanding, the importance of the aggregation and the properties of the hierarchical structure of MNPs Fe<sub>3</sub>O<sub>4</sub> becomes a crucial matter that must be explored further due to its effects on magnetic properties and applications. Rodriquez et al. [4] and Sulungbudi et al. [5] have measured magnetic nanoparticles' structure using dynamic light scattering (DLS) and transmission electron microscopy (TEM). By comparing the size that was measured using DLS and TEM, they pointed out that the particles formed

aggregates. However, in the case of aggregate structures, both of the measurements simply give the information about the overall size of aggregates and could not provide the information about the size of each primary particles that formed aggregate to reveal its hierarchical structure. Therefore, it is necessary to employ the other techniques that could show the hierarchical structure of MNPs  $\text{Fe}_3\text{O}_4$  to obtain a deep understanding of the aggregation mechanism.

Small-angle scattering (SAS), including X-ray (SAXS) and neutron (SANS), is a powerful technique to investigate size disorders of material structures, ranging from 1 to 100 nm. Detailed information of the nanostructures such as aggregate phenomena, fractal structure, and dimensions of MNPs  $\text{Fe}_3\text{O}_4$  as well as its hierarchical structures can be obtained through this technique [6-7].

Previously, the study of fractal aggregates of MNPs using the small-angle scattering technique has been undertaken by many researchers. Taufiq et al. [8] and Putra et al. [9] reported the measurement of MNPs  $\text{Fe}_3\text{O}_4$  using small-angle neutron scattering (SANS). They pointed out by using two model combinations that the hierarchical structure could be measured. In this case, SAS measurement's vital process is how to cultivate and acquire the valuable information from scattering data that is usually carried out through fitting analysis. However, the two previous works still briefly explain the detailed analysis, including each step for the analysis process and the meaning for each obtained parameter.

In this work, a series of MNPs  $\text{Fe}_3\text{O}_4$  was prepared via co-precipitation method as a pH function and then characterized using SAXS instrument. The established data analysis was applied to cultivate the scattering data to understand better and explain aggregation phenomena, fractal structure, and hierarchy structure.

## ■ EXPERIMENTAL SECTION

### Sample Preparation

Magnetic nanoparticles (MPNs)  $\text{Fe}_3\text{O}_4$  were synthesized by co-precipitation method at Center for Science and Technology of Advanced Materials, BATAN-Indonesia. A detailed explanation about the synthesis

process has been published in previous work [5]. The SAXS measurement was carried out at room temperature using a liquid cell with an aperture of  $4 \times 10$  mm and thickness of 1.5 mm for each sample. The samples' concentration was 1 mg/mL with different pH conditions, i.e. 2, 3, 4, and 5.

### Small Angle X-ray Scattering (SAXS) Measurement

The SAXS experiments were performed at BL 1.3: SAXS at SLRI, Thailand. A 2-dimensional charge-coupled device (CCD, Rayonix SX165, LX170HS) detector with a diameter of 165 mm was put 1.5 m and 4.5 m away from the sample. The 1.5 m and 4.5 m setups provided  $q$  range of  $0.07 < q \text{ (nm}^{-1}\text{)} < 0.4$  with  $q = (4\pi/\lambda) \sin \theta$ , where  $\theta$  is the scattering angle, and  $\lambda$  is the wavelength of the incident beam.

Scattering intensities of each sample were subtracted from the empty cell and the solvent backgrounds (pure  $\text{H}_2\text{O}$ ) using data reduction software, SAXSIT [10]. The corrected scattering intensity data were normalized and then fitted with a combination of two models calculation, log-normal spherical and mass fractal models using data analysis software, SASfit [11].

### Data Analysis

#### Data import

**Analyze standard.** Analyze Standard using SAXSIT software is carried out for calibration of SAXS measurement called  $q$ -range calibration using silver behenate crystal as a standard. The crystal has several peaks that give the same  $d$ -spacing structure of 5.838 nm. There are two parameters needed to determine i.e., sample detector distance (SDD) or  $L$  and the distance between the direct beam and scattering ring or  $D$  to calibrate the  $q$ -range [10].

**Data reduction.** The 2-dimensional scattering intensities were normalized using the background subtraction process to reduce the cell's scattering effect and the solvent backgrounds during experiments. Afterward, the scattering profile is calculated to radially averaged from the 2-dimensional pattern to  $q$  into the 1-dimensional pattern, consisting of two parameters, intensity  $I(q)$  and scattering vector  $q$ . While the intensity is obtained from the measurement, the scattering vector

is resulted from the calculation using parameters D and L, the distance between the direct beam to scattering ring, and sample detector distance (SDD), respectively, through q-calibration, Eq. (1),

$$2\theta = \tan^{-1}\left(\frac{D}{L}\right) \quad (1)$$

Then, the scattering vector (q) is found from Eq. (2) [12],

$$q = \frac{4\pi}{\lambda} \sin\theta \quad (2)$$

### Model fitting

The main aim of the SASfit program is to adjust the fitting model calculation to the scattering pattern of the sample. The fitting process is carried out to obtain the high suitability between the intensity of the  $I_{\text{mod}}(q)$  or theoretical and the intensity of the  $I_{\text{exp}}(q)$  or experiment.

The scattering intensity  $I(q)$  from all samples as a function of scattering vector was calculated using Eq. (3),

$$I(q) \approx S(q) \cdot P(q) \quad (3)$$

where  $S(q)$  is the structure factor that, in this case, explains the aggregate structures, and  $P(q)$  is the form factor that explains the size and shape of primary particles. The simplest form model, the sphere, was used to investigate particle morphology. In contrast, a log-normal distribution model was applied due to the MNP's tendency to form aggregate and had broad distribution. Hence, a log-normal spherical model as a form factor calculation, which is a good approximation to start the calculation, was applied to fit the experimental data. The scattering function for the sphere particle with radius  $r$  is calculated with the Eq. (4),

$$P(q) = \phi V_p^2 \Delta\rho^2 F(qr_0)^2 f(r) \quad (4)$$

where  $P(q)$  is form factor,  $\phi$  is volume fraction,  $\Delta\rho$  is scattering length density difference. With the particle volume  $(V_p) = (4/3) \pi r_0^3$ , the spherical form factor is given by,

$$F(qr_0) = \frac{3[\sin(qr_0) - qr_0 \cos(qr_0)]}{(qr_0)^3} \quad (5)$$

The term of  $f(r)$  in Eq. (4) could be explained with the Eq. (6),

$$f(r) = \frac{N}{C_{\text{LN}}} \frac{1}{r^p} \exp\left(\frac{1}{2\sigma^2} (\ln r - \ln r_{\text{med}})^2\right) \quad (6)$$

Where

$$C_{\text{LN}} = \sqrt{2\pi} r_{\text{med}}^{1-p} \exp\left((1-p)^2 \frac{\sigma^2}{2}\right) \quad (7)$$

In the global fitting, besides the log-normal spherical model, the fractal model as structure factor was also applied to explain the interaction between the MNPs or, in this case, called fractal aggregate. Therefore, the scattering intensity can be expressed as [13],

$$I(q) = \int N(r_0) F^2(qr_0) dr_0 S(q, \xi, D_f, r_0) \quad (8)$$

where  $N$ ,  $F(q, r_0)$  and  $S(q, \xi, D_f, r_0)$  are the number density of the particles, the scattering amplitude, and the structure factor. The characteristics of the structure factor of the samples are given in the following equation,

$$S(q) = 1 + \frac{D_f \Gamma(D_f - 1)}{(qr_0)^{D_f} \left[1 + 1/(q^2 \xi)^2\right]^{(D_f - 1)/2} \times \sin\left[(D_f - 1) \tan^{-1}(q\xi)\right]} \quad (9)$$

where  $\Gamma$  is the gamma function,  $D_f$  is the fractal dimensions, and  $\xi$  is correlation length or the size of fractal an aggregate.

The best fit corresponds to the minimum residuum and chi-square values. These values show the difference between theoretical calculation and experimental fits, which are the fit parameters' estimates. The best-fitting results can be seen from the residuum not oscillating, and the data spread evenly. This indicates that there is high suitability between the model calculation and experimental data.

## RESULTS AND DISCUSSION

The corrected scattering intensity data were obtained by subtraction of each raw data sample using the SAXSIT program. The process was carried out to subtract the scattering intensities to get scattering from particles only, see Fig. 1(a).

Furthermore, Fig. 1(b) shows the final result of the data reduction process where a 1-dimensional plot is radially averaged intensity as a function of scattering vector  $q$  from the 2-dimensional pattern. Thus, this pattern will be used for further analysis using SASfit.

According to Fig. 2, the scattering pattern at the first region at large- $q$  values shows the characteristic of the interference between the scattering object and the

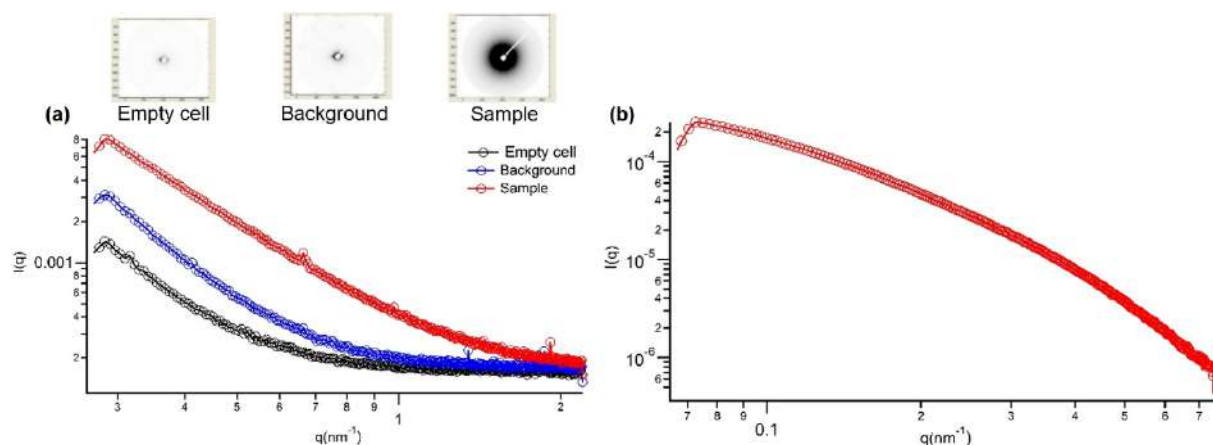


**Fig 1.** (a) Small-angle scattering pattern of the three measurements (2-dimensional and 1-dimensional patterns), namely empty cell, background, and sample (b) The corrected 1-dimensional scattering pattern

solvent. This region is called the Porod zone, which means that the primary particles' scattering intensity decreases following a power law of  $I(q) \sim q^{-4}$ . In this region, the scattering pattern is started at the high to intermediate  $q$  region as  $S(q) \approx 1$ . Then the size of the primary particles and polydispersity of the primary particles can be determined. The existence of particles with broad size distribution can be confirmed by the absence of an oscillatory behavior on the scattering curve.

The second region in Fig. 2 defined for intermediate to the low- $q$  range with the data as  $I(q) \approx S(q)$ . The nonlinearity at the low- $q$  range can be caused by the interference effects with the neighboring particles. The slope in the low  $q$  range appeared, indicating the particles'

aggregation effect, and the Guiner behavior does not occur. This effect makes larger particles that are measured by the SAXS technique. This showed that many spherical particles as primary particles formed aggregates or fractal objects as secondary particles. In this region, the scattering intensity falls, following a power law of  $I(q) \sim q^{-D_f}$  and the size of aggregate can be determined [12]. The correlation of particles formed aggregate within the system occurred due to the large surface and the magnetic forces and the ionic force.

Both of the two regions are fitted separately with a combination of two models calculation to obtain the best fitting results and parameters fitting in the two regions. These two models are determined based on the direct

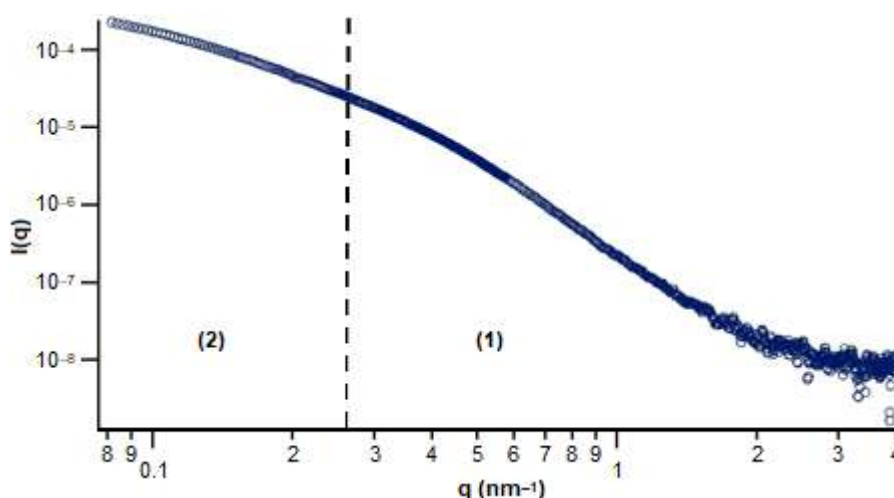


**Fig 2.** Different phenomenon is measured based on scattering pattern (1) First region at high- $q$  values (2) Second region at low- $q$  values



analysis of scattering patterns and literature such as previous papers to acquire the initial assumptions about the MNPs. Moreover, other techniques such as dynamic light scattering (DLS) were also applied to make initial assumptions and ensure the fitting results.

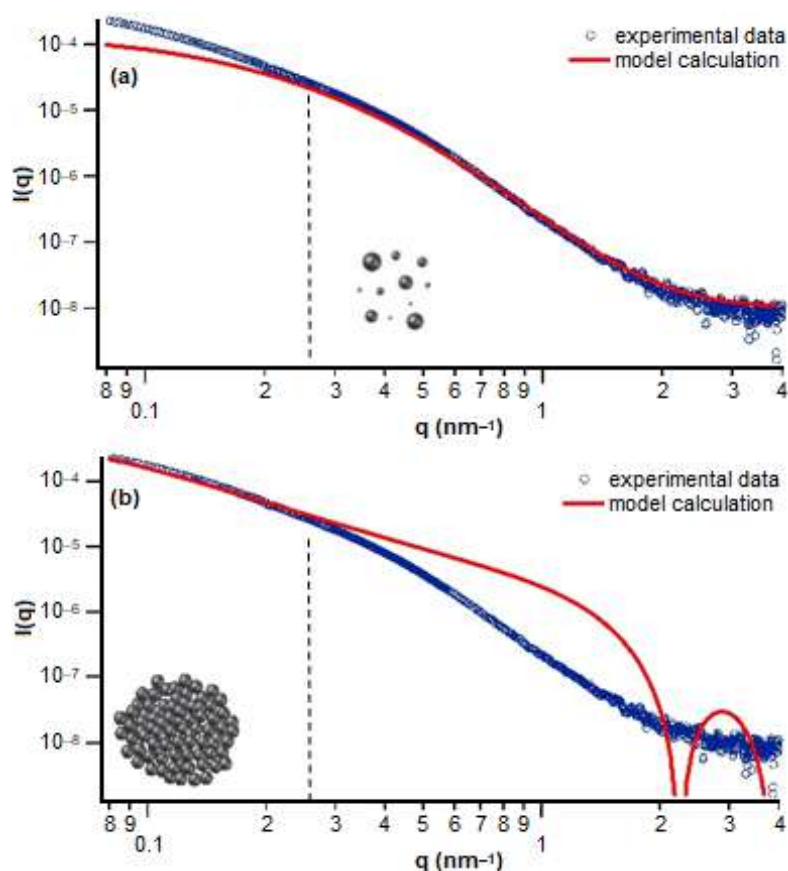
The first assumption that can be applied through model fitting is correlated particles to get the suitable structural information. Fig. 3(a) shows the fitting process by following the log-normal sphere model calculation for the first region. According to the fitting process result, a mean primary radius is 2 nm with the polydispersity 0.5. Fig. 3(b) shows the fitting process's result through the mass fractal model calculation for the second region, and the primary particles were assumed in a spherical shape and monodisperse. The size of fractal objects or aggregates is about 21 nm to 103 nm as the variation of pH.

Fig. 4 shows the scattering pattern in all samples' log-log plot; the black dash line shows that the scattering

is close to  $q^{-2}$  behavior as a slope -2 in agreement at low  $q$  region or  $q < 0.03 \text{ nm}^{-1}$ . This means that the fractal objects had a two-dimensional structure in the range of  $1.9 \leq D_f \leq 2.1$ .

The combination of two theoretical models resulted in the best-fitted data and also proved that Porod law (high to intermediate  $q$  range) and power-law scattering (intermediate to low  $q$  range) are appearing for all the pH variation. With increasing the pH, the existence of primary particles and aggregates are always detected. From the fitting results through the mass fractal model, the size of aggregates is 21 nm, 24 nm, 33 nm, and 103 nm in diameter for the pH of 2, 3, 4, and 5, respectively.

The results from DLS measurement that confirmed SAXS measurement are hydrodynamic diameter ( $d_H$ ) as the overall diameter of MNPs  $\text{Fe}_3\text{O}_4$  aggregates, see Table 1.



**Fig 3.** Fitting process of SAXS profiles of ferrofluid sample fitted with two model calculations (a) log-normal sphere model at high to intermediate  $q$  region and (b) mass fractal model at intermediate to low  $q$  region

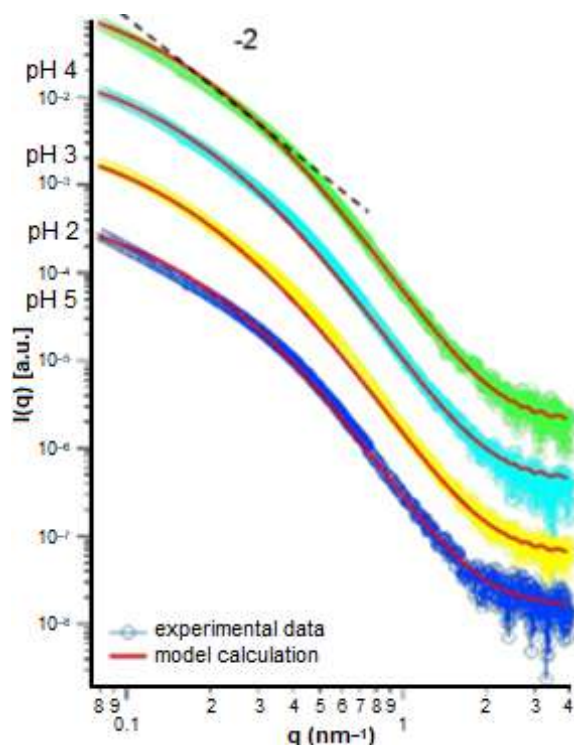


**Fig 4.** One dimensional SAXS profile of MNPs  $\text{Fe}_3\text{O}_4$  as a function of pH fitted by combining two model calculations in a different region, log-normal sphere and mass fractal

**Table 1.** The particle diameter of magnetic nanoparticles with pH variation, Hydrodynamic diameters ( $d_H$ , nm), size of fractal aggregate ( $\xi$ , nm)

pH samples	Size (nm)		Pdl
	$d_H$	$\xi$	
2	21	21	0.2
3	25	24	0.2
4	35	33	0.3
5	165	103	0.6

The DLS result confirms the appearance of aggregates measured using the SAXS technique, then the presumption of hierarchical structures of MNPs  $\text{Fe}_3\text{O}_4$  can be verified. Even though the primary particles of aggregates could not be investigated through DLS measurement, the value of  $d_H$  can be employed to be compared with the value of  $\xi$  from SAXS measurement.

Based on Derjaguin, Landau, Verwey, Overbeek (DLVO) theory, stability or instability of charged colloidal systems is influenced by competition between London-

van der Waals forces of attraction and electrostatic forces of repulsion [14]. Due to the oxidation state of a metal oxide, iron oxide can form an amphoteric oxide with a pH-dependent surface [15]. This characteristic makes iron oxide's surface become positive in the acidic condition or at low pH and negative in the basic condition or at high pH. Theoretically, in an aqueous solution, iron oxide's surface properties will be altered to form surface hydroxyl groups (Fe-OH sites). Under this condition, the proton transfer could occur with surface protonation ( $\text{Fe-OH} + \text{H}^+ \leftrightarrow \text{Fe-OH}_2^+$ ) and deprotonation ( $\text{Fe-OH} \leftrightarrow \text{Fe-O}^- + \text{H}^+$ ) [16]. Therefore, at the low pH condition, the surface of iron oxide particles was positive charged due to protonation reaction ( $\text{Fe-OH}_2^+$ ). The surface charge will generate electrostatic forces of repulsion and decrease the aggregation of particles.

As the result of SAXS measurement, we found that the hierarchical structure of fractal aggregate reflected the aggregation phenomenon as the function of pH solution. The increasing of pH solution will increase the fractal size, which means that the amphoteric surface of MNPs  $\text{Fe}_3\text{O}_4$  can control the aggregation of particles.

Table 1 shows the pH-dependent of iron oxide influence the aggregation particles. At pH 2, the measurement using DLS technique resulted in  $d_H$  ca. 21 nm, while the SAXS measurement resulted  $\xi$  ca. 21 nm. These sizes increase with the increase of pH until pH 5 with  $d_H$  ca. 165 nm and  $\xi$  ca. 103 nm. This condition proved that the surface charge particles become stronger at low pH, and the electrostatic repulsion forces become higher. These phenomena will decrease the aggregation of particles and formed smaller size of aggregates. The surface charge and electrostatic stability reach a minimum point at isoelectric point or point of zero charges (PZC) with  $\text{pH} = \text{PZC} = 7.4$ . If the pH is closer to the PZC, so the tendency of magnetic nanoparticles forming the aggregate is higher [16].

The existence of a larger aggregate size at a higher pH value can be explained as the charge neutralization phenomenon [17-18]. As explained before, the MNPs  $\text{Fe}_3\text{O}_4$  are highly positively charged in low pH, and with the increasing of pH the positive charge will decrease until the point of zero charges. The positive charge on

particles' surface will enhance the electrostatic forces of repulsion among particles and decrease the aggregation. While the increase of the pH solution will reduce the positive charge, and as a result, the aggregate will become larger due to the decreasing of electrostatic forces of repulsion among the particles.

Concerning aggregation, there is a correlation between polydispersity and aggregation particles. Aggregation alters the magnetic nanoparticle's size distribution. The increasing aggregation effect on magnetic nanoparticles will increase particles' size distribution, which can be seen as log-normal distribution on scattering data analysis.

The standard deviation of particle size distribution gives important information about the width of the distribution. Log-normal distribution has an asymmetrical curve, skewed with low mean values, variances large and positive values, see Fig. 5. Generally, distribution appears with a symmetrical curve called normal distribution, which can easily be characterized and described by additive calculation of mean and standard deviation. On the other hand, the log-normal distribution has a different kind of calculation called multiplicative, which is the log-transformed variable mean and standard deviation model.

Galton has described particle distribution range with multiplying and dividing ( $\times$  or times/divide) [19]. Concerning this experimental result using log-normal distribution, the range of particle size is  $6.68^x/3.16$  or 2.11–21.10 nm.

The mechanism of aggregate formation influences the dimension of fractal objects. The aggregates fractal dimension determined in this work indicated that a reaction-limited cluster aggregation (RLCA) mechanism occurred in the magnetic nanoparticles system [20]. In this mechanism, particles' collisions formed a more compact aggregate due to the slow diffusion of particles into the center of aggregate. A sheet-like aggregate would have a fractal dimension closer to two.

The illustration model of aggregate fractal or primary particles formed a building block is shown in Fig. 6. The two fractal dimensions indicate correlations between points on each particle forming a single cluster.

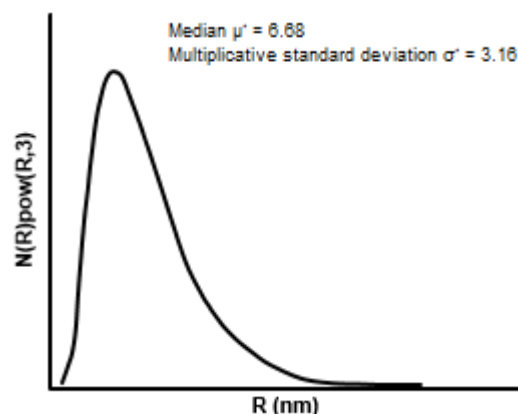


**Fig 5.** Log-normal distribution fitted to the experimental data ferrofluids

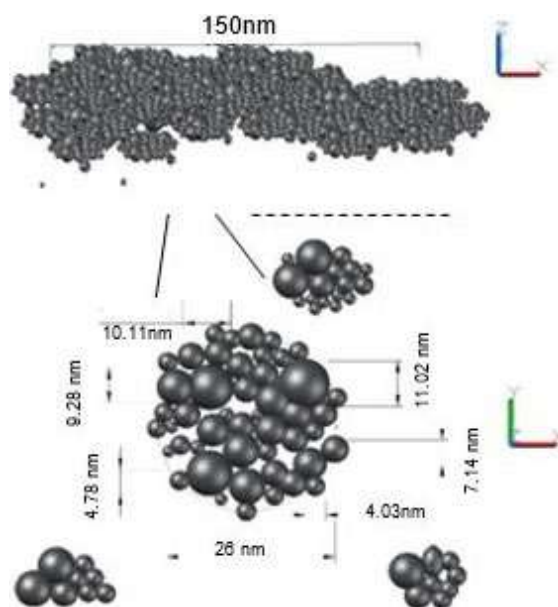


**Fig 6.** The illustration model presenting fractal objects of magnetic nanoparticle

The single cluster then interacted with each other to form a 2-dimensional fractal aggregate with a sheet-like structure.

Moreover, as the overall result of this experiment, it can be confirmed that the hierarchical structures of materials can be investigated using the SAXS technique. In contrast, DLS measurement is not able to provide information related to those structures. The primary particle with the size of 2 nm in a radius resulting from SAXS measurement is important information to be investigated. The other techniques measure the overall aggregate size.

## ■ CONCLUSION

The structure of a series of magnetic nanoparticles Fe<sub>3</sub>O<sub>4</sub> or ferrofluid as pH variation has been successfully characterized using Small Angle X-ray Scattering (SAXS). The fitting analysis of the scattering pattern of ferrofluids was conducted by applying global fitting with the combination of a log-normal sphere and mass fractal models. It confirmed that the hierarchical structures containing primary particles and fractal aggregate of MNP Fe<sub>3</sub>O<sub>4</sub> can be investigated using SAXS measurement. The aggregates have a similar particle size of 2 nm in radius with the particle size distribution of 0.5 for all the pH variations, then the size of fractal aggregate from ca. 21 nm to 103 nm in diameter for the pH of 2, 3, 4 and 5, respectively. The log-normal sphere and the mass fractal model calculations have high suitability fitted to SAXS data of ferrofluids

## ■ ACKNOWLEDGMENTS

This work was supported partially by the Synchrotron Light Research Institute of Thailand (SLRI–Thailand) and the Centre for Science and Technology of Advanced Materials–BATAN. The authors were also appreciative of the Polytechnic Institute of Nuclear Technology for providing a research grant Reg. No. 69/STTN/VI/2018 to support this work.

## ■ REFERENCES

- [1] Wu, Y., Yang, X., Yi, X., Liu, Y., Chen, Y., Liu, G., and Li, R., 2015, Magnetic nanoparticles for biomedicine applications, *J. Nanotechnol. Nanomed. Nanobiotechnol.*, 2, 003.
- [2] Engelman, U., Buhl, E.M., Baumann, M., Schmitz-Rode, T., and Slabu, I., 2017, Agglomeration of magnetic nanoparticles and its effects on magnetic hyperthermia, *Curr. Dir. Biomed. Eng.*, 3 (2), 457–460.
- [3] Chu, X., Yu, J., and Hou, Y.L., 2015, Surface modification of magnetic nanoparticles in biomedicine, *Chin. Phys. B*, 24 (1), 014704.
- [4] Rodriguez, A.F.R., Rocha, C.O., Piazza, R.D., dos Santos, C.C., Morales, M.A., Faria, F.S.E.D.V., Iqbal, M.Z., Barbosa, L., Chaves, Y.O., Mariuba, L.A., Jafelicci, M., and Marques, R.F.C., 2018, Synthesis, characterization, and applications of maghemite beads functionalized with rabbit antibodies, *Nanotechnology*, 29 (36), 365701.
- [5] Sulungbudi, G.T., Yuliani, Lubis, W.Z., Sugiarti, S., and Mujamilah, 2017, Controlled growth of iron oxide magnetic nanoparticles via co-precipitation method and NaNO<sub>3</sub> addition, *JUSAMI*, 18 (3), 136–143.
- [6] Anitas, E.M., 2015, Fractal fragmentation and small angle scattering, *J. Phys. Conf. Ser.*, 633, 012119.
- [7] Anitas, E.M., 2017, “Small-angle scattering from mass and surface fractals” in *Complexity in Biological and Physical Systems – Bifurcations, Solitons and Fractals*, Eds. Lopez-Ruiz, R., IntechOpen, London, United Kingdom.
- [8] Taufiq, A., Sunaryono, Hidayat, N., Hidayat, A., Putra, E.G.R., Okazawa, A., Watanabe, I., Kojima, N., Pratapa, S., and Darminto, 2017, Studies on nanostructure and magnetic behaviors of Mn-doped black iron oxide magnetic fluids synthesized from iron sand, *Nano*, 12 (9), 1750110.
- [9] Putra, E.G.R., Seong, B.S., Shin, E., Ikram, A., Ani, S.A., and Darminto, 2010, Fractal structures on Fe<sub>3</sub>O<sub>4</sub> ferrofluid: A small-angle neutron scattering study, *J. Phys. Conf. Ser.*, 247, 012028.
- [10] Rugmai, S., and Soontaranon, S., 2013, *Manual for SAXS/WAXS data processing using SAXSIT*, <https://www.slri.or.th/en/bl13w-saxs.html>.
- [11] Kohlbrecher, J., and Bressler, I., 2011, *Software package SASfit for fitting small-angle scattering curve*, Laboratory for Neutron Scattering, Paul Scherrer Institut, Switzerland.
- [12] Londoño, O.M., Tancredi, P., Rivas, P., Muraca, D., Socolovsky, L.M., and Knobel, M., 2018, “Small angle X-ray scattering to analyze the morphological properties of nanoparticulated systems, in *Handbook of Materials Characterization*, Eds. Sharma, S., Springer, Cham, Switzerland.
- [13] Teixeira, J., 1988, Small-angle scattering by fractal systems, *J. Appl. Crystallogr.*, 21 (6), 781–785.
- [14] Choi, Y.W., Lee, H., Song, Y., and Sohn, D., 2015, Colloidal stability of iron oxide nanoparticles with

- multivalent polymer surfactants, *J. Colloid Interface Sci.*, 443, 8–12.
- [15] Meng, X., Ryu, J., Kim, B., and Ko, S., 2016, Application of iron oxide as a pH-dependent indicator for improving the nutritional quality, *Clin. Nutr. Res.*, 5 (3), 172–179.
- [16] Pfeiffer, C., Rehbock, C., Hühn, D., Carrillo-Carrion, C., de Aberasturi, D.J., Merk, V., Barcikowski, S., and Parak, W.J., 2014, Interaction of colloidal nanoparticles with their local environment: The (ionic) nanoenvironment around nanoparticles is different from bulk and determines the physico-chemical properties of nanoparticles, *J. R. Soc. Interface*, 11 (96), 20130931.
- [17] Cruz, D., Pimentel, M., Russo, A., and Cabral, W., 2020, Charge neutralization mechanism efficiency in water with high color turbidity ratio using aluminium sulfate and flocculation Index, *Water*, 12 (2), 572.
- [18] Vereda, F., Martin-Molina, A., Hidalgo-Alvarez, R., and Quesada-Pérez, M., 2015, Specific ion effects on the electrokinetic properties of iron oxide nanoparticles: Experiments and simulations, *Phys. Chem. Chem. Phys.*, 17 (26), 17069–17078.
- [19] Limpert, E., Stahel, W.A., and Abbt, M., 2001, Log-normal distributions across the sciences: Keys and clues: On the charms of statistics, and how mechanical models resembling gambling machines offer a link to a handy way to characterize log-normal distributions, which can provide deeper insight into variability and probability—normal or log-normal: That is the question, *BioScience*, 51 (5), 341–352.
- [20] Jungblut, S., Joswig, J.O., and Eychmüller, A., 2019, Diffusion- and reaction-limited cluster aggregation revisited, *Phys. Chem. Chem. Phys.*, 21 (10), 5723–5729.

## Modeling and Thermodynamic Values of Complex Equilibrium of Cobalt(II) with Diethylenetriaminepentaacetic Acid in Aqueous Solution

Ghusoon Faidhi Hameed<sup>1</sup>, Fawzi Yahya Wadday<sup>2\*</sup>, and Nahla Shakir Salman<sup>1</sup>

<sup>1</sup>Department of Chemistry, Faculty of Education, Al-Qadisiyah University, Al-Qadisiyah, Iraq

<sup>2</sup>Department of Chemistry, Faculty of Science, Kufa University, Al-Najaf, Iraq

\* **Corresponding author:**

tel: +964-7811443061

email: Fawzi.almuwashi@uokufa.edu.iq

Received: August 31, 2020

Accepted: October 26, 2020

DOI: 10.22146/ijc.59169

**Abstract:** The paper reports the study of the complex formation of cobalt (II) with diethylenetriaminepentaacetic acid (DTPA, H<sub>5</sub>L) based on spectrophotometric (SF) and potentiometric data (pH). Complexes of different compositions were found, and equilibrium constants, as well as the stability constants of these complexes, were determined. Accumulation of complexes in proportion is calculated based on the acidity of the medium. The experimental data have been carried out by using mathematical models to assess the solution's possible existence with a wide spectrum of complex particles and to point out those which are quite sufficient to copy the experimental data. In addition, thermodynamic parameters ( $\Delta G^\circ$ ,  $\Delta H^\circ$ , and  $\Delta S^\circ$ ) for the studying complexes were calculated according to the values of stability constant ( $K_{ST}$ ) at 25 °C obtained from the temperature dependence of stability constant by using van't Hoff equation.

**Keywords:** cobalt; stability constants; spectrophotometer; potentiometer

### ■ INTRODUCTION

It is known that DTPA, being an octadentate pentabasic ligand, forms stable water-soluble complexes with many metal cations including cobalt(II). These complexes are widely used in various fields of science, technology, agriculture, and medicine [1-2]. It is known that all animal and plant organisms need trace elements. The latter should be introduced into living organisms in a biologically active form, easily transported and absorbed. The use of inorganic metal salts for these purposes is ineffective. The most promising substances in this regard are biologically active complexes, especially, DTPA. The introduction of metal complexes into the soil contributes not only to an increase in micronutrient fertilizers but also to their mobility. Some metal complexes with DTPA contribute to the growth and productivity of crops and increase the yield and quality of potato tubers. Iron complexonate with DTPA is a useful tool in the fight against plant chlorosis. Some of the biochemical-complexes are used in animal husbandry and the food industry [3-5]. In medicine, metal complexes can play the role of antidotes, regulators of mineral metabolism, as

anticancer and antiviral, antimicrobial, and diagnostic drugs [6-8]. It should be noted that the cumulative properties of complexions and their complexes are very weakly expressed. Accumulation coefficients indicate a low potential risk of developing chronic poisoning with these drugs.

Cobalt, on the other hand, is a biologically active metal. Excessive "technogenic" intake of this metal in the body has a toxic effect on metabolism and has a carcinogenic effect on the cell [9]. The widespread use of cobalt and DTPA salts necessitates a detailed study of equilibrium in the Co(II)-DTPA system. In the previous studies, cobalt and DTPA complexes have been widely used in agriculture and medicine, the researchers used spectrophotometer measurements and did not use voltage measurements data and programs while the thermodynamic values of the complexes were not calculated [3], thus it is necessary to be studied in more detail. In our current study, the equilibrium constants were measured based on spectrophotometer (SF) and voltage data (pH), and the stability constants of these complexes are determined by using mathematical

modeling and also calculated the thermodynamic parameters ( $\Delta G^\circ$ ,  $\Delta H^\circ$  and  $\Delta S^\circ$ ) for complexes.

The thermodynamic parameters represented by standard free energy change where values of stability constants can be expressed in terms of free energy or standard Gibbs ( $\Delta G^\circ$ ) [10-12], as in Eq. (1):

$$\Delta G^\circ = RT \ln K_{eq} \quad (1)$$

Standard enthalpy change  $\Delta H^\circ$  of equilibrium constant can be determined from Eq. (2) as follows [12-14]:

$$\ln K_{eq} = -\Delta H^\circ / RT + \text{constant} \quad (2)$$

The standard entropy change  $\Delta S^\circ$  for each compound was calculated by using the following Eq. (3) [12-16]:

$$\Delta G^\circ = \Delta H^\circ - T\Delta S^\circ \quad (3)$$

## ■ EXPERIMENTAL SECTION

### Materials

The chemical reagents used in this research were diethylenetriaminepentaacetic (DTPA,  $C_{14}H_{23}N_3O_{10}$ ), potassium hydroxide (KOH), sodium hydroxide (NaOH), sodium nitrate ( $NaNO_3$ ), hydrochloric acid (HCl fuming 37%), cobaltous sulfate heptahydrate ( $CoSO_4 \cdot 7H_2O$ ) were purchased from Sigma-Aldrich, Merck (Germany and British). All reagents were used without further purification.

### Instrumentation

Instruments used in this research were Spectrophotometer SF-2000 No. 03 11 1120 00 (Russia), pH Meter PW 9421 Philips (England), Electric Balance + 0.0001g L420 B Sartorius (Germany), and Distillate Water Lab Tech (Korea).

### Procedure

The complex solution was prepared by dissolving 3.929 g from a reagent grade DTPA in 250 mL distilled water. The solution that concentration 0.04 M of DTPA was clarified by pH-metric titration with a standard solution of 0.1 M KOH. A 0.04 M cobalt(II) solution was prepared by dissolved 2.808 g of  $CoSO_4 \cdot 7H_2O$  salt in 250 mL of distilled water. Then  $Co^{2+}$  ions were standardized by redox metric titration with a DTPA solution. The necessary acidity of the medium was supported by 0.1 M for both HCl and NaOH solutions. A constant ionic strength ( $I = 0.1$  M) was created with  $NaNO_3$  solution.

The optical density of the solutions was measured on an SF-2000 spectrophotometer using quartz cuvettes with an absorbing layer length of 1 cm. The concentration of hydrogen ions was measured on an I-160 M ion meter (ES-10601/7 working electrode and ESr-10101 reference electrode). The main absolute error of pH measurement was  $\pm 0.01$ . The redox potential value was measured using a platinum electrode EPL-02. All measurements were carried out at a temperature of  $20 \pm 2$  °C. The calculation of equilibrium parameters in the Co(II)-DTPA system was carried out using the computer programs HypSpec (spectrophotometer) and Hyperquad 2008 (potentiometer) [17-18].

## ■ RESULTS AND DISCUSSION

To study the complexation process in the Co(II)-DTPA system, the absorption spectra of solutions were collected for various values of the acidity of the medium (Fig. 1). A comparison of the obtained spectra with the spectra of Co(II) solution shows that Co(II) complexes with DTPA were already formed in a strongly acidic medium ( $pH = 0.5-6.88$ ). In DTPA's presence, the absorption band of hydrated Co(II) ions at 350 nm disappears while the optical density increases in the region of 450-550 nm with a maximum at 506 nm.

To calculate the composition and stability of the resulting Co(II) complexes with DTPA, the HypSpec program was used. This program allows us to analyze the experimental dependence of the optical density on pH simultaneously for different wavelengths of 300-750 nm in accordance with the selected complexation model. For complexes of the molar composition Co(II):DTPA = 1:1,  $Co(H_iL)^{i-3}$  ( $i = 0-5$ ) and  $Co(OH)_jL^{(3+j)-}$  ( $j = 0-1$ ), and also hydroxo complexes  $Co(OH)_k$  ( $k = 1-3$ ), we performed calculations for various compositional models, including complexness. In the calculations, we used fixed values of the DTPA dissociation constants, previously determined by us by pH metric titration as below. The total hydrolysis constants of Co (II) were taken from the literature as ( $K_i = [Co(OH)_i^{3-i}][H^+]^i/[Co^{2+}]$ ):  $pK_{1w} = 9.7$ ;  $pK_{2w} = 9.1$ ;  $pK_{3w} = 12.7$  ( $I = 0.1$ ,  $t = 25$  °C) [19-20]. The HypSpec program allows modeling in automatic mode by comparing the experimental and

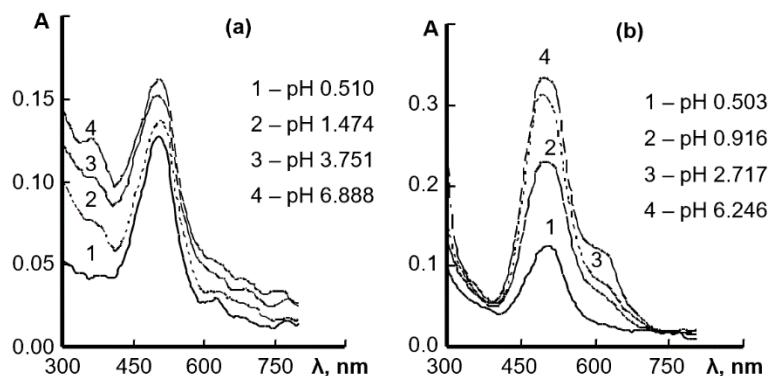


**Fig 1.** Absorption spectra of (a) Co (II) solution, and (b) Co(II)-DTPA complex.  $C_{\text{Co(II)}} = 1.6 \times 10^{-2}$  mol/L,  $C_{\text{DTPA}} = 2.4 \times 10^{-2}$  mol/L

calculated spectra represented by the sum of the spectra of all absorbing particles.

For Co(II)-DTPA system in the studied range of medium acidity ( $0 < \text{pH} < 7$ ), the minimum standard deviation corresponds to a model that includes the following particles:  $\text{Co}^{2+}$ ,  $\text{CoH}_2\text{L}^-$ ,  $\text{CoHL}^{2-}$ ,  $\text{CoL}^{3-}$ . The calculated values of the total stability constants are presented in Table 1. Fig. 2 shows a comparison of the experimental and calculated optical density values (at 506 nm) for the established complexation model, which shows their good agreement. At  $\text{pH} > 11$ , hydrolysis proceeds in the system, and turbidity appears in the solution.

Spectrophotometer method established complex compounds of cobalt with DTPA at different ionic strengths values;  $[\text{CoH}_4\text{L}]^+$  ( $\lg\beta = 30.18$ ,  $I = 0.1$ ,  $25^\circ\text{C}$ )

$[\text{CoL}^{3-}]$  ( $\lg\beta = 19.72$ ,  $[\text{CoHL}^{2-}]$  ( $\lg\beta = 22.47$ , ( $I = 0$ ,  $20^\circ\text{C}$ ) [22].

The diagram of the molar distribution of complexes in the Co(II)-DTPA system (Fig. 2(b)) allows us to compare the observed spectral changes with the regions of existence of individual complexes characterized by the spectra shown in Fig. 3.

**Table 1.** Composition and stability constants of complexes in the Co(II)-DTPA system

Complex	$\lg\beta$	Terms, Method
$\text{CoH}_2\text{L}^-$	26.55 ( $\pm 0.01$ ) SF	I = 0.1 (NaNO <sub>3</sub> ), 21 °C SF, pH
	25.38 ( $\pm 0.04$ ) pH	
$\text{CoHL}^{2-}$	22.87 ( $\pm 0.05$ ) SF	
	22.67 ( $\pm 0.02$ ) pH	
$\text{CoL}^{3-}$	18.39 ( $\pm 0.10$ ) SF	
	17.79 ( $\pm 0.03$ ) pH	

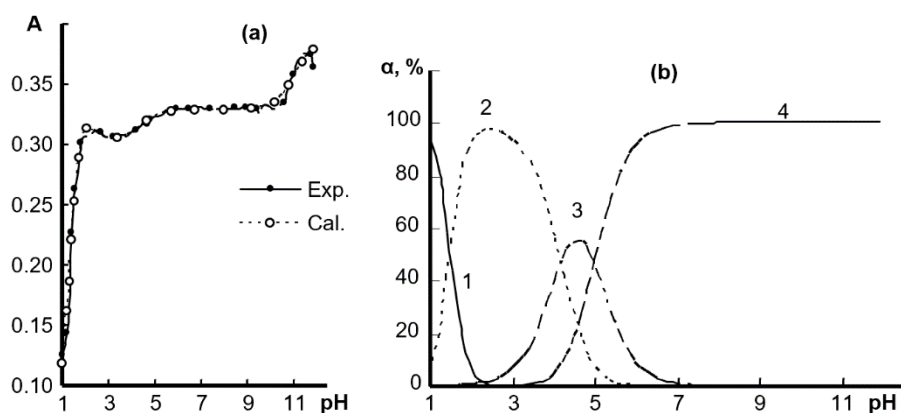


**Fig 2.** (a) Experimental and calculated dependences of optical density ( $\lambda = 506$  nm) and diagram of the molar distribution of complexness. (b) Versus pH for the system Co(II)-DTPA, where Co(II) (1),  $\text{CoH}_2\text{L}^-$  (2),  $\text{CoHL}^{2-}$  (3),  $\text{CoL}^{3-}$  (4),  $C_{\text{Co(II)}} = 1.6 \times 10^{-2}$  mol/L,  $C_{\text{DTPA}} = 2.4 \times 10^{-2}$  mol/L



Three buffer regions are observed on the pH metric DTPA titration curve ( $0 < a < 3$ ;  $3 < a < 4$ ;  $a > 4$ ;  $a$  = degree of titration) and one distinct jump at  $a = 3$  (Fig. 4). In the presence of Co(II) cations, a decrease in the pH of solutions associated with complexation is observed. To calculate the equilibrium in the Co(II)–DTPA system, the Hyperquad 2008 program was used, designed to process various potentiometer data, including pH-metric ones. Initially, the DTPA dissociation constants were calculated from the DTPA titration curve ( $pK_1 = 2.2$ ;  $pK_2 = 2.9$ ;  $pK_3 = 4.4$ ;  $pK_4 = 8.7$ ;  $pK_5 = 10.04$ ), which were then used as fixed values when calculating the composition and stability of the resulting Co(II) complexes as depicted in Table 1.

In the alkali medium, the oxidation of cobalt in the main layers occurs much more slowly, the final product of which is  $CoO(OH)$  or  $Co_2O_3 \cdot H_2O$  Fig. 4 [23]. In the absence of oxidation, that is, without access to air, the blue form ( $\alpha$ -form) turns into pink ( $\beta$ -form). The unstable  $\alpha$ -form is distinguished, which is associated with its organization of two-dimensional particles, which can be considered as the initial structure of a hexagonal layered lattice corresponding to a stable monomorphic  $\beta$ -form. Particles of the  $\alpha$ -form are characterized by smaller sizes and a lower degree of perfection of the crystal lattice compared to particles of the  $\beta$ -form.

The experimental and calculated titration curves exhibited a good agreement with the entire pH range and the complexes' corresponding distribution diagram as shown in Fig 5. Compared with spectrophotometer technique, the pH-metric method does not identify the presence of the  $CoH_3L$  complex in the system since its existence region lies at lower pH values than those studied. A potentiometer study shows that, at  $pH > 7$ , the  $CoL^{3-}$  complex is formed in solution in the middle region as shown in Fig. 5. The stability constants of complexes established by both methods are reasonably close as given in Table 1.

Thus, the work results show that, at Co (II) concentrations in the range of  $2 \times 10^{-4}$ – $2 \times 10^{-3}$  mol/L with the excess of DTPA, only soluble complexes are formed in the solution. The formation of insoluble polynuclear complexes under these conditions is not observed. DTPA

is characterized by the formation of protonated complexes with Co(II) already in a strongly acidic medium. In the pH range close to neutral in solution, there is an average  $CoL^-$  complexions, whose stability ( $\log\beta = 17$ – $18$ ) is only slightly inferior to the stability of the Co(II)–EDTA $^{2-}$  complex ( $\log\beta = 16.31$ ) [24]. The results obtained are consistent with some published data (see Table 1). The high stability and wide pH range of the existence of Co(II) complexes with DTPA are a positive factor when using DTPA for various practical purposes [3,17]. The strong binding of Co(II) cations

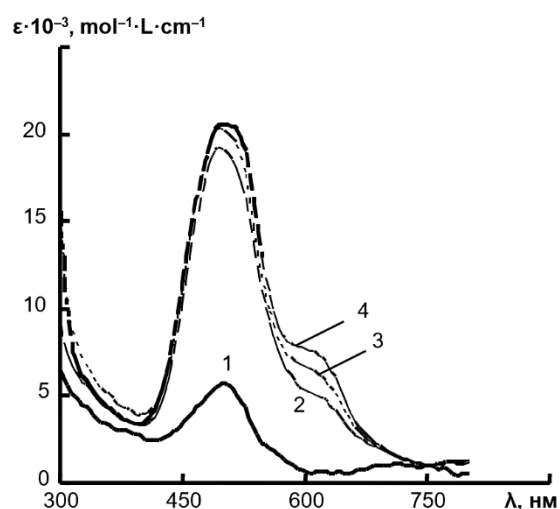


**Fig 3.** The calculated absorption spectra of the complexes Co(II) with DTPA for Co(II) (1),  $CoH_2L^-$  (2),  $CoHL^{2-}$  (3) and  $CoL^{3-}$  (4),  $C_{Co(II)} = C_{DTPA} = 1.62 \times 10^{-3}$  mol/L

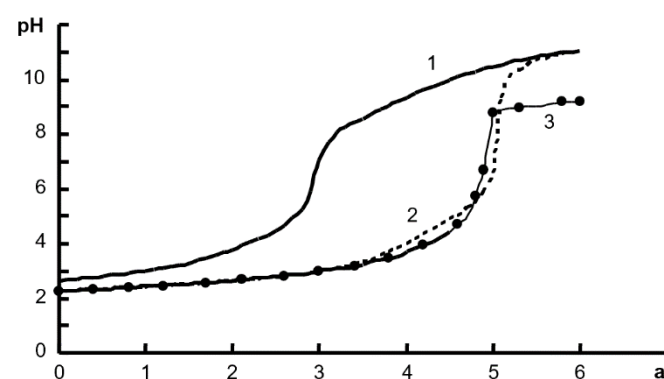


**Fig 4.** Curves of pH-metric titration of DTPA and its complex with Co(II) for DTPA (1),  $C_{DTPA} = 2 \times 10^{-3}$  mol/L and mixtures Co(II)–DTPA with the ratio 1:2 (2) and 1:1 (3)

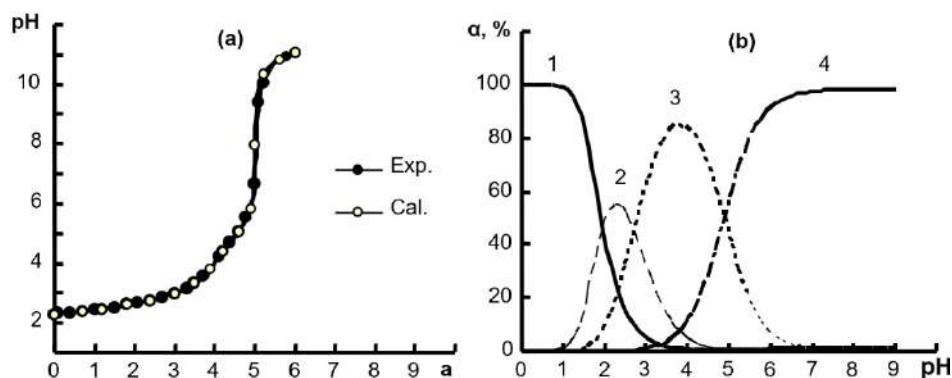


**Fig 5.** (a) Experimental and calculated pH-metric titrated curves, (b) The molar distribution diagram of complexes in the Co(II) – DTPA system as a function of pH For Co (II) (1),  $\text{CoH}_2\text{L}^-$  (2),  $\text{CoHL}^{2-}$  (3) and  $\text{CoL}^{3-}$  (4),  $C_{\text{Co(II)}} = C_{\text{DTPA}} = 2 \times 10^{-3} \text{ mol/L}$

under the action of DTPA allows the use of DTPA as a stabilizer of peroxides in household detergents and bleaches. Despite the lack of data on various forms of DTPA in the environment, it can be assumed that a significant proportion of DTPA in natural waters will be in the form of complexes with Co(II) and other metals. This photolysis leads to the degradation of DTPA in nature.

From the dependence of  $K_{\text{eq}}$  on temperature (T), the thermodynamic function ( $\Delta G^\circ$ ,  $\Delta H^\circ$ ,  $\Delta S^\circ$ ) were calculated. The values were summarized in Table 2 at 25 °C. The  $\Delta G^\circ$  values were obtained from the reaction of complexes indicating a spontaneous reaction. The positive values of  $\Delta H^\circ$  (endothermic reaction) were obtained for complexes by using van't Hoff equation. Meanwhile, the  $\Delta S^\circ$  values indicate that complexes are brought into being [25-27].

The positive value of  $\Delta H^\circ$  is the indicative of

endothermic processes, and the formation of these complexes is favored under high temperature. Meanwhile, the negative values of  $\Delta G^\circ$  indicate the spontaneous process in each case. On the other hand, the positive values of  $\Delta S^\circ$  indicate some randomness degree during the formation presses.

## CONCLUSION

Co(II) complexes have been identified by absorption spectroscopy, pH-meter, and computer-assisted mathematical modeling in the Co(II)-DTPA system. Complexation begins in strongly acidic media and occurs in the range of  $\Delta\text{pH}$  0.5–6.2 for a 1:1 system. On the other hand, in an alkaline medium in solutions of Co(II) salts, hydrolysis processes are enhanced. In this case, a blue precipitate first forms with increasing pH, while the blue precipitate gradually turns to be purple and finally in pink color.

**Table 2.** The values of a standard thermodynamic functions ( $\Delta G^\circ$ ,  $\Delta H^\circ$ ,  $\Delta S^\circ$ ) of equilibrium constants for  $\text{CoH}_2\text{L}^-$ ,  $\text{CoHL}^{2-}$  and  $\text{CoL}^{3-}$  complexes in 25 °C

Complex	$\lg K_{\text{eq}}$	$\Delta G^\circ \text{ kJ mol}^{-1}$	$\Delta H^\circ \text{ kJ mol}^{-1}$	$\Delta S^\circ \text{ J mol}^{-1} \text{ K}^{-1}$
$\text{CoH}_2\text{L}^-$	7.37 ( $\pm 0.02$ ) SF	-4.948	16.606	39.120
	6.208 ( $\pm 0.03$ ) pH	-4.523	15.180	35.761
$\text{CoHL}^{2-}$	12.29 ( $\pm 0.04$ ) SF	-6.215	20.858	49.137
	12.09 ( $\pm 0.02$ ) pH	-6.175	20.721	48.812
$\text{CoL}^{3-}$	18.39 ( $\pm 0.10$ ) SF	-7.214	24.208	57.026
	17.79 ( $\pm 0.03$ ) pH	-7.132	23.932	56.375

## ■ ACKNOWLEDGMENTS

The authors would like to thank the Department of Chemistry, College of Education for Pure Science, University of Al-Qadisiyah, and College of Science, Kufa University in Iraq for funding this work.

## ■ REFERENCES

- [1] Dyatlova, N.M., Temkina, V.Y., and Popov, K.I., 1988, *Kompleksy i kompleksonaty metallov (Complexones and Compexonates of Metals)*, Khimiya, Moscow.
- [2] Martak, F., Cahyani, N.W.D., Nugraheni, Z.V., and Utomo, W.P., 2016, Properties and toxicity of cobalt(II) complex with 2,4,5-triphenyl-1H-imidazole ligand, *Indones. J. Chem.*, 16 (3), 260–267.
- [3] Rawat, K.S., Kumar, R., and Singh, S.K., 2019, Topographical distribution of cobalt in different agro-climatic zones of Jharkhand state, India, *Geol. Ecol. Landsc.*, 3 (1), 14–21.
- [4] Hall, L.H., Spijkerman, J.J., and Lambert, J.L., 1968, Preparation and coordination studies of the complex acid, dihydrogen diethylene-triaminepentaacetato ferrate(III) dihydrate, and several of its metal(I) salts, *J. Am. Chem. Soc.*, 90 (8), 2044–2048.
- [5] Sugiyarto, K.H., Kusumawardani, C., and Wulandari, K.E., 2018, Synthesis and structural analysis of powder complex of tris(bipyridine) cobalt(II) trifluoromethanesulfonate octahydrate, *Indones. J. Chem.*, 18 (4), 696–701.
- [6] El-Sherif, A.A., Shoukry, M.M., Abd Elkarim, A.T., and Barakat, M.H., 2014, Protonation equilibria of biologically active ligands in mixed aqueous organic solvents, *Bioinorg. Chem. Appl.*, 2014, 626719.
- [7] Sucipto, T.H., Churrotin, S., Setyawati, H., Mulyatno, K.C., Amarullah, I.H., Ueda, S., Kotaki, T., Sumarsih, S., Wardhani, P., Bendryman, S.S., Aryati, A., Soegijanto, S., and Kameoka, M., 2017, Inhibitory activity of cobalt(II)–morin complex against the replication of dengue virus type 2, *IJTID*, 6 (6), 141–144.
- [8] Rakhmanin, Y.A., 2016, Actualization of methodological problems of regimentation of chemical pollutions on the environment, *Gig. Sanit.*, 95 (8), 701–707.
- [9] Cui, P., Yin, Q., Gong, J., Wang, Y., Hao, H., Xie, C., Bao, Y., Zhang, M., Hou, B., and Wang, J., 2013, Thermodynamic analysis and correlation of solubility of candesartan cilexetil in aqueous solvent mixtures, *Fluid Phase Equilib.*, 337, 354–362.
- [10] Wang, Z., Long, Z.W., Long, C.Y., and Zhang, W., 2015, On the thermodynamic properties of the spinless Duffin-Kemmer-petiau oscillator in noncommutative plane, *Adv. High Energy Phys.*, 2015, 901675.
- [11] Kumar, A., Rout, S., Ghosh, M., Singhal, R.K., and Ravi, P.M., 2013, Thermodynamic parameters of U (VI) sorption onto soils in aquatic systems, *SpringerPlus*, 2 (1), 530.
- [12] Batool, F., Akbar, J., Iqbal, S., Noreen, S., and Bukhari, S.N.A., 2018, Study of isothermal, kinetic, and thermodynamic parameters for adsorption of cadmium: An overview of linear and nonlinear approach and error analysis, *Bioinorg. Chem. Appl.*, 2018, 343724.
- [13] Hussein, A.A., Kareem, L.K.A., and Mohammed, S.S., 2020, Preparation, diagnosis, thermodynamic and biological studies of new complexes derived from heterocyclic ligand, *Syst. Rev. Pharm.*, 11 (5), 445–450.
- [14] Nwabanne, J.T., 2012, Kinetics and thermodynamics study of oil extraction from fluted pumpkin seed, *IJMSE*, 3 (2), 11–15.
- [15] Anwer, M., Muqtader, M., Iqbal, M., Ali, R., Almutairy, B.K., Alshetaili, A., Alshahrani, S.M., Aldawsari, M.F., Alalaiwe, A., and Shakeel, F., 2019, Estimating the solubility, solution thermodynamics, and molecular interaction of aliskiren hemifumarate in alkylimidazolium based ionic liquids, *Molecules*, 24 (15), 2807.
- [16] Blokhina, S.V., Sharapova, A.V., Ol'khovich, M.V., Volkova, T.V., Proshin, A.N., and Perlovich G.L., 2017, Thermodynamic aspects of solubility and solvation of bioactive bicyclic derivatives in organic solvents, *J. Chem. Eng. Data*, 62 (12), 4288–4295.

- [17] Jastrzab, R., Kaczmarek, M.T., Tylkowski, B., and Odani, A., 2018, Computer analysis of potentiometric data of complexes formation in the solution, *Phys. Sci. Rev.*, 3 (3), 140.
- [18] Singh, J., Srivastav, A.N., Singh, N., and Singh, A., 2019, "Stability constants of metal complexes in solution" in *Stability and Applications of Coordination Compounds*, IntechOpen Limited, London, UK, 90183.
- [19] Plyasunova, N.V., Zhang, Y., and Muhammed, M., 1998, Critical evaluation of thermodynamics of complex formation of metal ions in aqueous solutions. V. Hydrolysis and hydroxo-complexes of  $\text{Co}^{2+}$  at 298.15 K, *Hydrometallurgy*, 48 (2), 153–169.
- [20] Mehdi, S.H., and Budesinsky, B.W., 1974, Protonated metal complexes of diethylenetriaminepentaacetic acid (DTPA), *J. Coord. Chem.*, 3 (4), 287–292.
- [21] Jelecevic, A. Horn, D., Eigner, H., Sager, M., Liebhard, P., Moder, K., and Vollprecht, D., 2019, Kinetics of lead release from soils at historic mining and smelting sites, determined by a modified electro-ultrafiltration, *Plant Soil Environ.*, 65, 298–306.
- [22] Remy, G., 1966, *A Course of Inorganic Chemistry*, Vol. 2, Mir, Moscow.
- [23] Kornev, V.I., and Alabdulla, G.F., 2017, Simulation of equilibria of formation of mono-and polynuclear heteroligand cobalt(II) and nickel(II) complexonates in aqueous solutions, *Russ. J. Inorg. Chem.*, 62 (8), 1127–1133.
- [24] Krajewska, B., and Brindell, M., 2016, Thermodynamic study of competitive inhibitors' binding to urease, *J. Therm. Anal. Calorim.*, 123 (3), 2427–2439.
- [25] Tamiji, Z., Yazdanipour, A., and Niazi, A., 2018, Spectrophotometric and thermodynamic study on the dimerization equilibrium of neutral red in the water and micelle environments by chemometrics methods, *Int. J. Exp. Spectrosc. Tech.*, 3, 15.
- [26] Baikusheva-Dimitrova, G., Genieva, S., and Yankova, R., 2017, Synthesis, thermal behavior and thermodynamic data of hafnium selenite tetraaqua complex dihydrate, *Int. J. Sci. Eng. Appl. Sci.*, 2 (3), 137–144.

## Analysis and Characterization of Solid and Liquid Organic Fertilizer from Hydrothermal Carbonization (HTC) of Chicken Feather and Blood Waste

Agus Kuncaka\*, Rizky Ibnufaatih Arvianto\*\*, Almas Shafira Ramadhanty Bunga Latifa, Munawir Ramadhan Rambe, Adhitasari Suratman, and Sugeng Triono

Department of Chemistry, Faculty of Mathematics and Natural Sciences, Universitas Gadjah Mada, Sekip Utara, Yogyakarta 55281, Indonesia

\* **Corresponding author:**

tel: +62-274-545188

email: akuncaka@ugm.ac.id;

rizkyibnu6@gmail.com\*\*

Received: September 2, 2020

Accepted: March 15, 2021

DOI: 10.22146/ijc.59353

**Abstract:** Conversion of feather and blood from chicken slaughterhouse waste for producing solid and liquid organic fertilizer excluding composting process with a variation of the mass ratio of feather and blood of a chicken has been conducted. The nitrogen, sulfur, and iron content in the solid and liquid product of the hydrothermal carbonization process were analyzed to identify and characterize the possibility of hydrolysate as a source of nitrogen, sulfur, and iron in soil fertilizer. Feather and blood of chicken waste were introduced to a hydrothermal carbonization reactor with the addition of limestone at a temperature range of 160–170 °C for the preparation of solid and liquid organic fertilizer. According to the FTIR interpretation, the solid product had functional groups such as NH, OH, CH  $sp^3$ , SH, C=O, C=C, C–O–C, and C–H aromatic. The nitrogen, sulfur, and iron content of the optimal ratio in the solid phase were 4.67%, 1.63%, and 3694.56 ppm, while their contents in the liquid fertilizer were 3.76%, 1.80%, and 221.56 ppm, respectively. The vibration of 478  $cm^{-1}$  is attributed to Fe–O paramagnetic ( $Fe_2O_3$ ) confirmed by TEM images showed the diameter size less than 20 nm indicating the presence of superparamagnetic material.

**Keywords:** hydrolysate; hydrothermal carbonization; feather; blood

### ■ INTRODUCTION

The composting process requires a very long time to produce organic fertilizer; otherwise, it is only several hours if the hydrothermal carbonization (HTC) process is used. Production of organic fertilizer from poultry feather wastes, excluding the composting process of chicken feathers generated in large quantities by the poultry industry, are hazardous for the natural environment because of their poor digestibility and their potential as a source of microbiological pathogens [1]. Mazzoto et al. [2] explained that chicken meat consumption increases the waste problem like feathers and blood. This waste produced by chicken slaughterhouse waste causes terrible odor due to releasing  $NH_3$  and  $H_2S$  gas. The soil undergoes hardening when this waste disposes directly into the soil (especially for feathers waste) due to disulfide bonds (S–S). Meanwhile, the chicken slaughter waste, such as poultry litter and manure, and feathers can be

functioned as a soil amendment [2] due to the high nitrogen, sulfur and iron chelate organic complex contents [2,4–6].

Kuncaka [7] proposed a synthetic humus preparation technique called New Road of Synthetic Humification, which explained how to make synthetic humus by Partial Hydrothermal Carbonization (PHTC). This technique produces a high aromatization degree called hydrochar and some materials like carbohydrate, protein, and lipid or hydrolysate material like amino acid and fatty acid. These molecules interact with each other using hydrogen bonding [8]. This humus like structure has suitable to the modern humus definition [8]. This humus like structure is called a Slow Release Organic Paramagnetic (SROP) Fertilizer.

Adiabati et al. [8] explained feather waste contains protein about 80–90%, while blood contains protein about 4.5–5.2 g/L [9]. Both proteins in feather and blood

are useful as a source of nitrogen [3-5]. Feather is the main sulfur source in disulfide bonds (S-S), contained in a feather as much as 17% [2]. Blood contains hemoglobin as much as 8.65 g/L [10-11]. Each hemoglobin contains iron in the heme protein [5]. Based on this, a combination of feather and blood can be converted into hydrolysate. Suwardi and Wijaya [12] studied one of the problems in Indonesian soil is leveling off. This condition occurs when the soil organic matter (SOM) is very low. SOM is classified into three categories according to soil organic carbon (SOC) content, i.e., low (less than 2%), normal (2–3%), and high (up to 3%) [13]. Indonesia's soil agriculture, around 73%, has a low SOC [14].

Chicken feathers and blood waste contain many microbes, pathogens, and parasites in raw biomass; then this study aims to develop hydrothermal carbonization (HTC) using feather and blood chicken waste as a precursor for producing solid and liquid organic fertilizer instead of the composting process. The nitrogen, sulfur, and iron content in the solid and liquid organic fertilizer were analyzed to identify and characterize the possibility of hydrolysate as nitrogen, sulfur, and iron source in solid and liquid organic fertilizer. In this research, feathers and blood of chicken waste as precursors were obtained from the Ar-Royan Chicken Slaughterhouse, Yogyakarta province, Indonesia.

## ■ EXPERIMENTAL SECTION

### Materials

The materials used in this research were feather and blood of chicken waste (obtained from the Ar-Royan Chicken Slaughterhouse, Bantul, Yogyakarta, Indonesia), limestone (CaO), universal pH indicator, filter paper, distilled water, H<sub>2</sub>SO<sub>4</sub> 96%, Fe(NO<sub>3</sub>)<sub>3</sub>, H<sub>3</sub>BO<sub>3</sub>, NaOH, Na<sub>2</sub>S<sub>2</sub>O<sub>3</sub>, K<sub>2</sub>SO<sub>4</sub>, HgO, HCl 37%, HNO<sub>3</sub> 68%, BaCl<sub>2</sub>, and Mr-BCG indicator (a mixture of methyl red and cresol green bromine) from Sigma Aldrich in pro analysis grade.

### Instrumentation

The solid organic fertilizer was characterized by Fourier Transform Infra-Red spectrophotometry (FTIR, Prestige-21) with KBr pellet and Transmission Electron Microscopy (TEM, JEOL-JEM1400). The liquid organic

fertilizer was characterized by High Performance Liquid Chromatography (HPLC, Dionex Ultimate-3000). The content of nitrogen (N), sulfur (S), and iron (Fe) in both solid organic and liquid organic fertilizer were determined using the Kjeldahl method, gravimetric method, and atomic absorption spectrophotometer, respectively.

### Procedure

#### Hydrolysate preparation

Feather and blood of chicken waste were mixed with a mass ratio of feather and blood, i.e., 500 g of feather and 500 g of blood (1:1), 750 g of feather and 250 g of blood (3:1), and 250 g feather and 750 g of blood (1:3). Limestone (CaO) was added to the mixture of feather and blood until a pH of 12–13 showed by universal pH indicator. Then, the mixture was introduced to HTC Reactor without a stirring system, as shown in Fig. 1. The HTC process using this reactor was done at temperatures around 160–170 °C and pressure of 9–10 atm for 3 h. HTC products were separated using the Buchner filter. The solid phase was dried using an oven at 100 °C for 24 h. The dry matter was weighed with an analytical balance. The liquid phase obtained was placed in a bottle for further analysis.

#### Nitrogen determination by Kjeldahl method

Nitrogen determination was carried out for a solid organic fertilizer and liquid organic fertilizer. The Kjeldahl method consists of 3 stages, i.e., destruction, distillation, and titration. For the first stage, destruction, 0.2 g of sample was put into 30 mL Kjeldahl flask. As much as 0.7 g of N catalyst (a mixture of K<sub>2</sub>SO<sub>4</sub> and HgO with a ratio of 20:1), 4 mL of concentrated H<sub>2</sub>SO<sub>4</sub> solution,

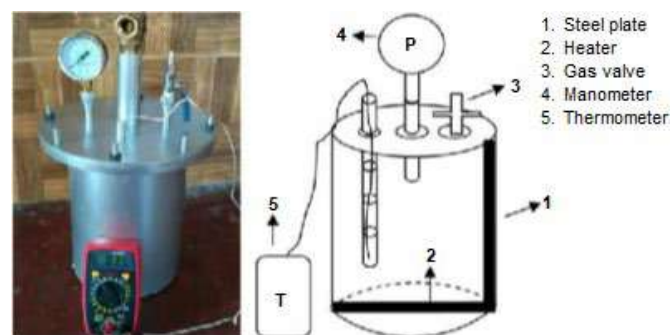


Fig 1. Scheme of HTC Reactor without stirring system

and boiling chips were added to the Kjeldahl flask. The flask was then boiled in a fume hood for 1 h until the sample turns green clearly. After this, the flask was cooled until it reaches room temperature. Ten milliliters of distilled water was added to the cold Kjeldahl flask. The second step is distillation; the product of destruction was moved from the Kjeldahl flask to the distillation flask. Erlenmeyer 125 mL was placed under the condenser. The Erlenmeyer was then filled with 4% H<sub>3</sub>BO<sub>3</sub> solution and 4 drops of the Mr-BCG indicator. The tip of the condenser must be submerged in Erlenmeyer. A solution of 20 mL of NaOH-thiosulfate (a mixture of NaOH 40% and Na<sub>2</sub>S<sub>2</sub>O<sub>3</sub>) was put into a distillation flask which had been filled with a sample that had been destroyed. The distillation process was carried out until 60 mL of distillate was obtained in Erlenmeyer (the color changed from red to blue). The third stage is titration; a standard of 0.02 M HCl solution was used for the titration process until the color of the sample was changed from blue to red. Nitrogen percentage (%N) was calculated by using this equation:

$$\%N = \frac{v \times M \times Ar_N}{w} \times 100\%$$

where *v* is the volume of HCl solution used for titration (mL), *M* is the concentration of HCl used (0.02 M), *Ar<sub>N</sub>* is the relative mass of nitrogen (14.007 g/mol), and *w* is the mass of sample (mg).

#### **Sulfur determination by gravimetric method**

Sulfur determination was carried out for a solid organic fertilizer and liquid organic fertilizer. A total of 2 g of sample (solid phase) was inserted into the porcelain dish. Then, the sample was heated in a muffle furnace to give ash. Ash was crushed by porcelain mortar and then was added with 25 mL of HNO<sub>3</sub> (1:3). The solution was filtered using filter paper. Five milliliters of the filtrate was taken and then put into 5 mL centrifuge tube. The tube was centrifuged to form a sediment, and the sediment was separated using filter paper. The sediment obtained was then dried in an oven until it reached a constant mass. The sulfur percentage (%S) was calculated using this equation:

$$\%S = \frac{m \times \frac{Ar_S}{Mr_{BaSO_4}}}{w} \times 100\%$$

where *m* is the mass of sediment (g), *Ar<sub>S</sub>* is the relative

atomic mass of S, *Mr<sub>BaSO<sub>4</sub></sub>* is the relative mass of BaSO<sub>4</sub>, and *w* is the mass of sample (g).

#### **Iron (Fe) determination**

The Fe containing in each solid organic fertilizer and liquid organic fertilizer (3:1, 1:1, 1:3) was determined using Atomic Absorption Spectrophotometer (AAS). A standard curve of Fe(NO<sub>3</sub>)<sub>3</sub> was used for the quantitative analysis of Fe.

## **RESULTS AND DISCUSSION**

### **FTIR Characterization of Solid Aggregate of Hydrolysate**

The solid organic fertilizer was characterized by an FTIR spectrophotometer to show the functional group changes during the HTC process. FTIR spectra were showed in Fig. 2. The broad band at 3400 cm<sup>-1</sup> was attributed to O–H stretching vibration in carboxyl and hydroxyl groups from an amino acid in polyaromatic structure. This band can be correlated to the hydrophilic surface of polyaromatic compounds in a solid aggregate of hydrolysate [15]. The band at 2924 and 2855 cm<sup>-1</sup> were attributed to the vibration of the CH sp<sup>3</sup> group. This band was associated with an aliphatic group from an amino acid in the polyaromatic structure of a solid organic fertilizer.

The band at 2515 cm<sup>-1</sup> was associated with the thiol group (–SH), which is appeared due to the hydrolysis process of a disulfide bond (S–S) from keratin. The formation of a thiol group (–SH) indicated the loss of undegradable character in chicken feathers [16]. Thiol group (–SH) was associated with cysteine adsorbed in polyaromatic structure in solid organic fertilizer. The band at 1651 cm<sup>-1</sup> was associated with the C=O bond from the polyaromatic surface as the product of polycondensation of hydroxymethylfurfural (HMF) [15]. This band proved that the surface of polyaromatic was hydrophilic.

A new band that appeared at 1623 cm<sup>-1</sup> was attributed to the stretching vibration of the C=C aromatic bond from a polyaromatic structure. The aromatic structure was present in a solid aggregate of hydrolysate strengthened by a new band at 872 cm<sup>-1</sup> attributed to the vibration of CH aromatic. Both of these

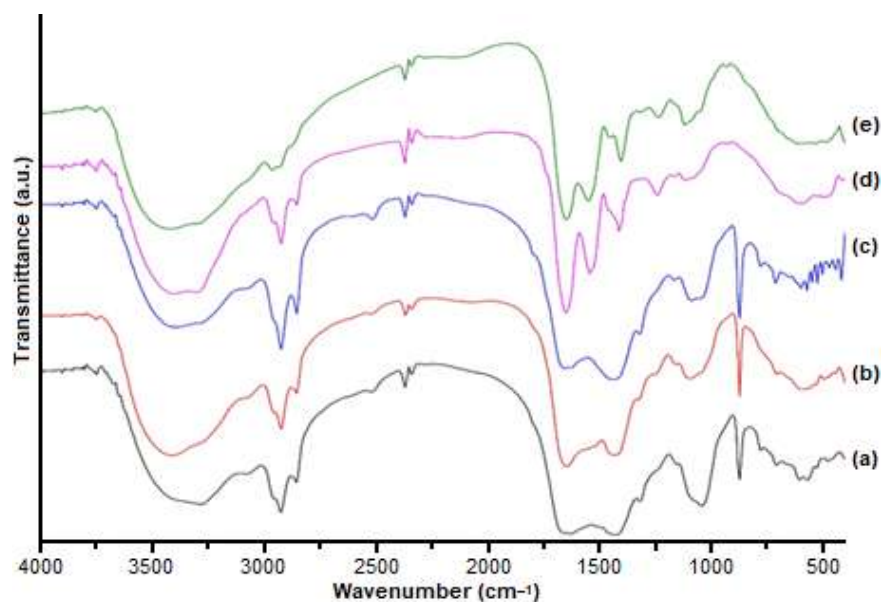


**Fig 2.** FTIR spectra of solid aggregates of hydrolysates of (a) 1:3, (b) 1:1, (c) 3:1, (d) chicken feather raw material, and (e) chicken blood raw material

new bands indicated the aromatization process during HTC. The aromatization was also present in the previous study [15-18]. Polyaromatic structure in solid aggregate of hydrolysate plays a role in bonding some nutrients such as nitrogen and sulfur in the soil. In this study, amino acid and the polyaromatic structure were bonded via hydrogen bonds through an amine, carboxyl, and hydroxyl groups from the amino acid. In addition, the band at  $1080\text{ cm}^{-1}$  was attributed to the vibration of the C–O–C bond from the product of HMF polycondensation in the polyaromatic surface. The band at  $478\text{ cm}^{-1}$  was attributed to Fe–O vibration from paramagnetic material ( $\text{Fe}_2\text{O}_3$ ) in a solid organic fertilizer, and the band located at  $500\text{--}700\text{ cm}^{-1}$  in raw chicken feather and raw blood were attributed to N–H vibration.

This solid organic fertilizer should also be able to play a role as soil amendments. The requirement of soil amendment material was the high aromatization degree [17]. The two bands that showed the aromatization degree were at  $1623$  and  $872\text{ cm}^{-1}$ . After making a comparison of the five samples, it was found that the characteristic peaks are similar to each other and comparable with other studies except the absorption ratio of band intensity at  $872\text{ cm}^{-1}$  and the absorption band of  $1080\text{ cm}^{-1}$  was relatively different in 1:3 compared with the ratio of 1:1 and

3:1. Therefore during HTC of ratio 1:1, the deposit of solid organic fertilizer starts to settle well. The difference in aromatization degree in each ratio is caused by the ability of the system to raise sub-critical water conditions that are affected by water content [18]. More water content could cause low sub-critical water conditions. A solid organic fertilizer with a ratio of 1:3 has higher water content (from blood used) in the system than the 1:1 and 3:1 ratio. Therefore, the 1:3 ratio has low subcritical water conditions that cause a low hydrolysis reaction.

### TEM Characterization of Solid Aggregate of Hydrolysate

TEM images are shown in Fig. 3. Two agglomeration products have been identified in the TEM images to give a primary and secondary agglomeration. A secondary agglomerate consists of some combined primary agglomerates, while a primary agglomerate consists of some incorporated primary nanoparticles. The agglomeration could occur because the hydroxyl (–OH) and carbonyl (C=O) groups in the surface of polyaromatics undergo dehydration reactions [19]. The diameter of the agglomerate has a size less than 20 nm, and if this result was combined with the result from FTIR vibration of Fe–O at  $478\text{ cm}^{-1}$ , it may be assumed



that the primary nanoparticles have the superparamagnetic property [19].

### Nitrogen and Sulfur Analysis

Each ratio of a solid organic fertilizer and liquid organic was analyzed by Kjeldahl and gravimetric methods to determine the percentage of nitrogen and sulfur. Fig. 4 and 5 represent the percentage of nitrogen

and sulfur of each solid organic fertilizer and liquid organic fertilizer, respectively. Nitrogen and sulfur percentage increased in the solid phase from 3:1 to 1:3 ratio, while decreased in the liquid phase from 3:1 to 1:3 ratio. Nitrogen and sulfur in the liquid phase indicated the hydrolysis of protein in chickens' feathers and blood into soluble amino acids [16].

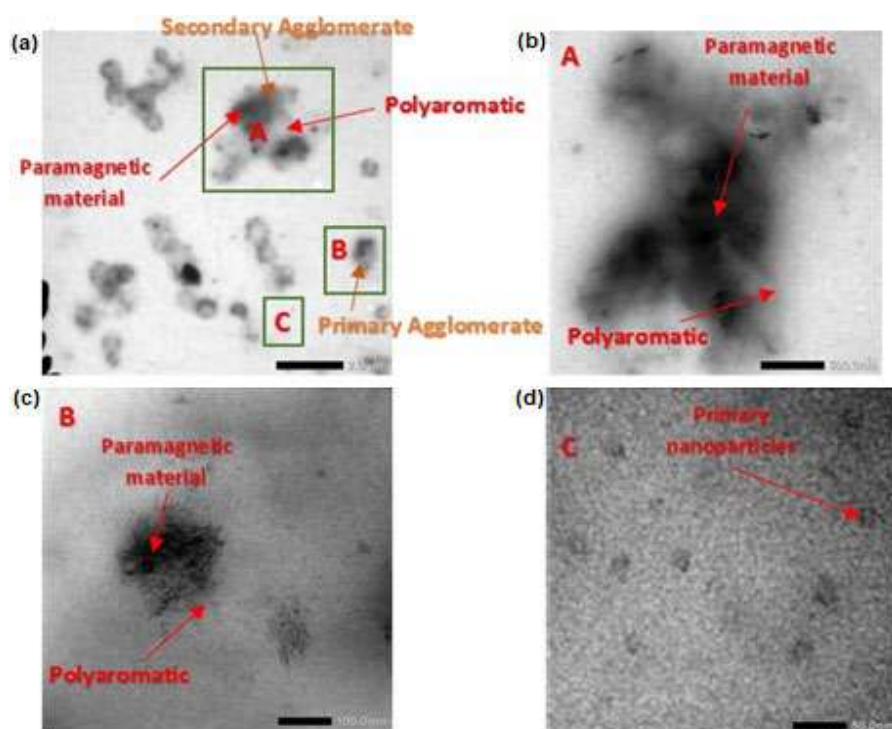


**Fig 3.** TEM images of solid organic fertilizer with a ratio of 3:1 showing (a) primary and secondary agglomerates, (b) primary agglomerate, (c) secondary agglomerate, and (d) primary nanoparticles

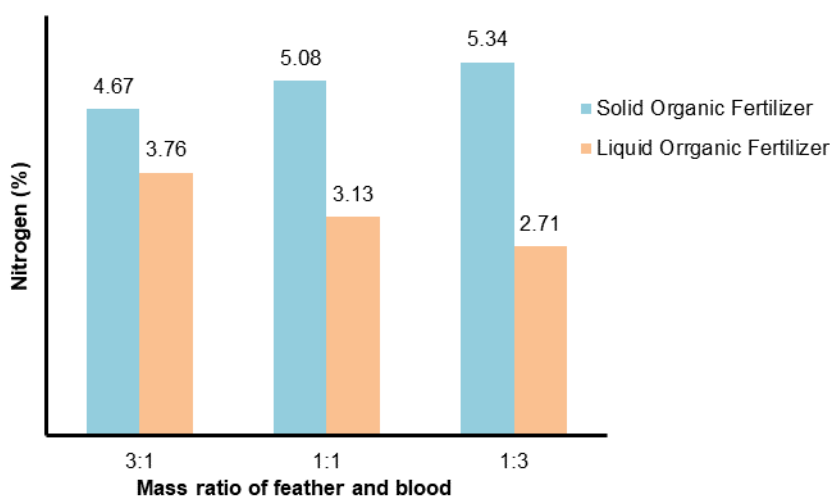


**Fig 4.** Nitrogen percentage of solid organic fertilizer and liquid organic fertilizer

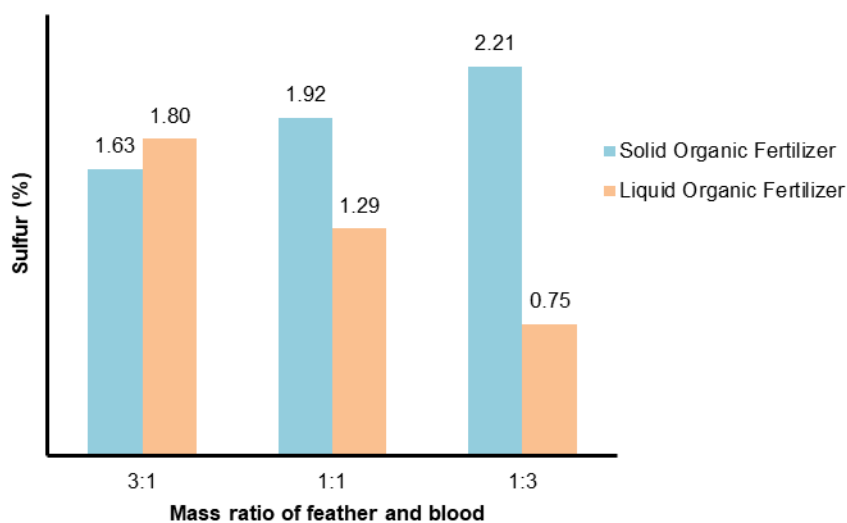


Fig 5. Sulfur percentage of solid organic fertilizer and liquid organic fertilizer

### Iron Analysis

The iron (Fe) contents of a solid organic fertilizer and liquid organic fertilizer are given in Table 1. The concentration of iron in the blood is much bigger than in feather, which is 1816.62 ppm [23] and 30 ppm [15] for blood and feather, respectively. It is in line with the AAS analysis of iron content where the ratio of 1:3 has the highest number of iron because it contained the highest amount of blood and a lower amount of feather. Otherwise, the 3:1 ratio has the lowest iron concentration because it contained the lowest amount of blood and a higher amount of feather.

The data was compared to the regulation of the Ministerial of Agriculture in Indonesia. According to the ministerial Regulation of Agriculture number 28 in 2009 on organic fertilizer, bio-fertilizers, and soil repair, which is now revised to Ministerial Regulation of Agriculture in 2011, to have a good quality of solid organic fertilizer, the iron contents should not exceed 9,000 ppm. This regulation necessitates that the formation of iron compounds in fertilizer should be below 9,000 ppm [20].

Based on the requirements above, the concentrations for every raw material and hydrolysate were below 9,000 ppm, which means the concentrations fit the standard regulation from the Ministerial of Agriculture in Indonesia. The solid organic fertilizer has an increment of iron concentration for every variation compared to raw material. Meanwhile, the liquid organic

fertilizer has a decrement of iron concentration for every variation compared to raw material. It means that the solid product probably chelated the iron more than the liquid product. The iron contents proved the paramagnetic character present in the solid aggregate of hydrolysate. In a solid organic fertilizer, the function of iron was to prevent the plant from chlorosis [21-22] and to control the electron transfer [21].

### Liquid Organic Fertilizer Characterization by HPLC

All ratios of liquid organic fertilizer were characterized by HPLC to determine the amounts and types of amino acids. Table 2 refers to the amounts and types of amino acids in the liquid organic fertilizer. Profile of amino acid content in the liquid phase indicated the potential as a liquid organic fertilizer. The potential of the liquid phase as a liquid organic fertilizer has been discussed in a previous study [16].

Results of nitrogen and sulfur analysis showed that

Table 1. The distribution of iron content in solid organic fertilizer and liquid organic fertilizer

Sample	Concentration (ppm)
Solid 1:1	6238.01
Solid 1:3	6393.86
Solid 3:1	3694.56
Liquid 1:1	307.15
Liquid 1:3	599.74
Liquid 3:1	221.56

**Table 2.** Amino acid profile of liquid hydrolysate

Amino acid	3:1	1:1	1:3
	Percentage (%)	Percentage (%)	Percentage (%)
Aspartic acid	3.44	7.74	4.08
Glutamic acid	17.70	16.30	17.15
Serine	1.54	2.55	2.69
Histidine	4.36	7.38	2.65
Glycine	9.66	7.32	6.89
Alanine	16.92	11.19	13.76
Tyrosine	1.99	4.72	2.40
Methionine	1.08	0.88	-
Valine	11.41	9.65	8.64
Phenylalanine	7.19	6.03	5.49
Isoleucine	6.52	5.52	0.71
Leucine	12.32	11.27	5.20
Lysine	5.88	9.45	30.33
Total amino acid	100.00	100.00	100.00

hydrolysate of 3:1 ratio undergoes maximum hydrolysis highest amino acid content for most detected amino acids, i.e., glutamic acid, glycine, alanine, methionine, valine, phenylalanine, isoleucine, and leucine, compared to other ratios. This result proved that the 3:1 ratio undergoes maximum hydrolysis.

## ■ CONCLUSION

The HTC process has an excellent effect on the degradation of keratin chicken feathers and high protein blood of chicken waste to produce solid organic fertilizer and liquid organic fertilizer. According to FTIR spectra of solid organic fertilizer, the functional groups that appeared were NH, OH, C=O, CH sp<sup>3</sup>, SH, Fe-O, CH aromatic, C=C aromatic, and C-O groups. TEM images showed the size of paramagnetic material coated by polyaromatic structure is less than 20 nm. A solid organic fertilizer started from a 1:1 ratio was optimally formed, indicated by a high degree of aromatization. Percentage of nitrogen and sulfur in solid organic fertilizer and liquid organic fertilizer were affected by ratios of feather and blood as precursors. HPLC analysis showed the potential of liquid organic fertilizer as a liquid protein source because of the high protein contents.

## ■ ACKNOWLEDGMENTS

This research was supported by the Ministry of Research and Technology and Higher Education of

Indonesia through the PPUPT project of UGM with Contract Number of 1929/UNI/DITLIT/DIT-LIT/PT2020.

## ■ REFERENCES

- [1] Tronina, P., and Bubel, F., 2008, Production of organic fertilizer from poultry wastes excluding the composting process, *Pol. J. Chem. Technol.*, 10 (2), 33–36.
- [2] Mazotto, A.M., Coelho, R.R.R., Cedrola, S.M.L., de Lima, M.F., Couri, S., de Souza, E.P., and Vermelho, A.B., 2011, Keratinase production by three *Bacillus* spp. using feather meal and whole feather as substrate in a submerged fermentation, *Enzyme Res.*, 2011, 523780.
- [3] Sams, A.R., 2000, *Poultry Meat Processing*, 1<sup>st</sup> Ed., Eds. Owens, C.M., Alvarado, C., and Sams, A.R., CRC Press, Boca Raton.
- [4] Sari, Ö.F., Özdemir, S., and Celebi, A., 2016, Utilization and management of poultry slaughterhouse wastes with new methods, *EurAsia Waste Management Symposium*, 2-4 May 2016, İstanbul, Türkiye.
- [5] Yaakob, M.A., Radin Mohamed, R.M.S., Al-Gheethi, A.A.S., and Mohd Kassim, A.H., 2018, Characteristics of chicken slaughterhouse wastewater, *Chem. Eng. Trans.*, 63, 637–642.
- [6] Wan, Y., Ghost, R., and Cui, Z., 2002, High resolution

- plasma protein fractionation using ultrafiltration, *Desalination*, 144 (1-3), 301–306.
- [7] Kuncaka, A., 2014, *Metode Memproduksi Pupuk Organik Paramagnetik Pelepasan Lambat*, IND. Patent No. P00201401530.
- [8] Hayes, M.H.B., Swift, R.S., Byrne, C.M., and Simpson, A.J., 2010, The isolation and characterization of humic substances and humin from Grey Brown Podzolic and Grey Grassland Soil, *19<sup>th</sup> World Congress of Soil Science, Soil Solution for Changing World*, 1-6 August 2010, Brisbane, Australia.
- [9] Adiati, U., Puastuti, W., and Mathius, I.W., 2004, Peluang pemanfaatan tepung bulu ayam sebagai bahan pakan ternak ruminansia, *Wartazoa*, 14, 39–44.
- [10] Widhyari, S.D., Esfandiari, A., and Herlina, 2011, Profil protein total, albumin dan globulin pada ayam broiler yang diberi kunyit, bawang putih dan Zinc (Zn), *JIPPI*, 16 (3), 179–184.
- [11] Putriani, S., Soma, I.G., and Ardana, I.B.K., 2012, Nilai hematokrit, kadar hemoglobin, dan total eritrosit ayam pedaging yang diinjeksi kombinasi tylosin dengan gentamicin, *Indones. Med. Veterinus*, 1 (4), 492–504.
- [12] Suwardi and Wijaya, H., 2013, Peningkatan produksi tanaman pangan dengan bahan aktif asam humat dengan zeolite sebagai pembawa, *JIPPI*, 18 (2), 79–84.
- [13] Gitosuwondo, S., 2010, Strategi efisiensi penggunaan bahan organik untuk kesuburan dan produktivitas tanah melalui pemberdayaan sumberdaya hayati tanah, *Jurnal Sumber Daya Lahan*, 4 (1), 13–25.
- [14] Las, I., and Setyorini, D., 2010, Kondisi lahan, teknologi, arah, dan pengembangan pupuk majemuk NPK dan pupuk organik, *Prosiding Semnas Peranan Pupuk NPK dan Organik dalam Meningkatkan Produksi dan Swasembada Beras Berkelanjutan*, Balai Besar Litbang Sumberdaya Lahan Pertanian, 24 February 2010, Bogor, Indonesia.
- [15] Sevilla, M., and Fuertes, A.B., 2009, The production of carbon materials by hydrothermal carbonization of cellulose, *Carbon*, 47 (9), 2281–2289.
- [16] Nurdiawati, A., Nakhshiniev, B., Zaini, I.N., Saidov, N., Takahashi, F., and Yoshikawa, K., 2017, Characterization of potential liquid fertilizers obtained by hydrothermal treatment of chicken feathers, *Environ. Prog. Sustainable Energy*, 37 (1), 375–382.
- [17] Gasco, G., Paz-Ferreiro, J., Álvarez, M.L., Saa, A., and Méndez, A., 2018, Biochars and hydrochars prepared by pyrolysis and hydrothermal carbonisation of pig manure, *Waste Manage.*, 79, 395–403.
- [18] Donar, Y.O., Çağlar, E., and Sinağ, A., 2016, Preparation and characterization of agricultural waste biomass based hydrochars, *Fuel*, 183, 366–372.
- [19] Namanga, J., Foba, J., Ndinteh, D.T., Yufanyi, D.M., and Krause, R.W.M., 2013, Synthesis and magnetic properties of a superparamagnetic nanocomposite "Pectin-magnetite nanocomposite", *J. Nanomater.*, 2013, 137275.
- [20] Cahyadi, Yuliani, N., and Srikandi, 2013, Penetapan ambang batas kadar Fe total dalam pupuk organik yang berpotensi menyebabkan keracunan Fe tanaman padi sawah, *Sains Natural*, 3 (2), 135–143.
- [21] Fattakhova, L.A., Shinkarev, A.A., Kosareva, L.R., Nurgaliev, D.K., Shinkarev Jr., A.A., and Bagautdinova, Y.S., 2016, Magnetic properties of different-aged chernozemic soil profiles, *ARPN J. Eng. Appl. Sci.*, 19 (11), 11383–11394.
- [22] Yunta, F., Di Foggia, M., Bellido-Díaz, V., Morales-Calderoñ, M., Tessarin, P., López-Rayó, S., Tinti, A., Kovács, K., Klencsár, Z., Fodor, F., and Rombola, A.D., 2013, Blood meal-based compound. Good choice as iron fertilizer for organic farming, *J. Agric. Food Chem.*, 61 (17), 3995–4003.
- [23] Kovács, K., Czech, V., Fodor, F., Solti, A., Lucena, J.J., Santos-Rosell, S., and Hernández-Apaolaza, L., 2013, Characterization of Fe-leonardite complexes as novel natural iron fertilizers, *J. Agric. Food Chem.*, 61 (50), 12200–12210.

## Synthesis, Characterization and Optimization of Oleyl Oleate Wax Ester Using Ionic Liquid Catalysts

Naowara Al-Arafi<sup>1</sup>, Nadia Salih<sup>2\*</sup>, and Jumat Salimon<sup>2</sup>

<sup>1</sup>Department of Chemistry, Faculty of Science, Benghazi University, P.O. Box 1308, Benghazi, Libya

<sup>2</sup>Department of Chemical Sciences, Faculty of Science and Technology, Universiti Kebangsaan Malaysia, 43600 Bangi, Selangor, Malaysia

\* **Corresponding author:**

email: [nadiaalnami@hotmail.com](mailto:nadiaalnami@hotmail.com)

Received: September 12, 2020

Accepted: November 11, 2020

DOI: 10.22146/ijc.59694

**Abstract:** In this work, the synthesis of oleyl oleate wax ester using Brønsted acidic ionic liquid catalysts was carried out. Confirmation of oleyl oleate molecular structure has been performed using FTIR, NMR, and ESI-MS spectroscopies. The ability of ionic liquid catalysts for catalyzing the esterification reaction of oleic acid and oleyl alcohol to produce oleyl oleate was optimized. The ionic liquid catalyst ([NMP][CH<sub>3</sub>SO<sub>3</sub>]) was found to be the best catalyst for the esterification reaction of oleic acid and oleyl alcohol compared with the other acidic ionic liquids studied. The optimal reaction conditions were determined at a reaction time of 8 h; oleic acid to oleyl alcohol mole ratio of 1:1; ([NMP][CH<sub>3</sub>SO<sub>3</sub>]) with 9.9 wt.%; and reaction temperature of 90 °C. Under these conditions, the percentage yield of oleyl oleate wax ester was 86%.

**Keywords:** wax ester; Brønsted acidic ionic liquid catalyst; esterification reaction; oleic acid; oleyl alcohol

### ■ INTRODUCTION

Esters have been used as biolubricants since the beginning of the nineteenth-century, in the form of natural esters in pig fat and whale oil. During World War II, a large number of synthetic fluids were developed, such as alcohol and long-chain acid esters that presented excellent low-temperature properties. The strongest effect of the ester group on the physical properties of lubricant is a decrease in its volatility and increase in its flashpoint. This is due to the strong dipole moment that keeps the ester molecules together. The ester group also affects other properties, such as thermal and hydrolytic stability, solvency, lubricity, and biodegradability [1]. The most important physical-chemistry properties of ester are viscosity, viscosity index (VI), pour point, lubricity, thermal, hydrolytic stabilities, and solvency. The main esters used as biolubricants are diesters, phthalates, trimethylates, C<sub>36</sub> dimerates, polyolesters, and wax ester. Wax esters, consisting of long-chain fatty acids esterified to long-chain fatty alcohols, have potential applications as lubricants, plasticizers, and cosmetics [2]. These kinds of

ester have excellent wetting properties at interfaces. Two good examples of naturally occurring wax esters are jojoba oil and sperm whale oil.

However, the supply of jojoba oil is inconsistent and sperm whale oil is diminishing, so a substitute for this wax ester is desired [3]. Esterification of carboxylic acids with alcohols using homogeneous and heterogeneous catalysts is well documented in the literature [4-6]. However, several limitations, such as an excess of the catalysts or amounts of reactants to achieve efficient conversion, removal of water during the reaction, long reaction times, and large amounts of effluent generation during work-up are associated with these processes [7]. The catalyst used in traditional esterification is mainly acidic homogeneous catalysts, such as sulphuric acid, as well as solid acid. Due to environmental concerns, the use of excess homogenous sulphuric acid can cause corrosion to the metallic equipment and this should be avoided. Solid acid catalysts have attracted considerable attention in recent years because of their significant advantages of eliminating corrosion, and environmental and toxicity

problems. Apart from recyclability and reusability, the disadvantages of solid acid catalysts are low activity, easy deactivation, and difficulty in product separation [8-9].

Ionic liquid, a kind of environmentally friendly solvent and catalyst, has gained the attention of scholars from various fields such as synthesis, catalysis, separation, and electrochemistry, due to its tunable physical and chemical properties [10]. Ionic liquids are salts with a melting point lower than 100 °C. Ionic liquids are usually composed of an organic cation, typically containing nitrogen or phosphorus, and a weakly coordinating anion. Some of the most common cations are imidazolium, phosphonium, pyridinium, and ammonium, while some common anions are  $\text{BF}_4$ ,  $\text{PF}_6$ ,  $\text{CF}_3\text{SO}_3$ , and  $\text{N}(\text{CF}_3\text{SO}_2)_2$ . Ionic liquids are non-flammable, thermally stable, exhibit negligible vapor pressure, and offer the potential for recyclability. For these reasons, the replacement of the current esterification protocols with a more environmentally benign process involving the use of ionic liquids was considered to be an area worthy of investigation. Deng et al. reported the esterification of carboxylic acids with alcohols in acidic chloroaluminate ionic liquid [11]. Some Brønsted acidic ionic liquids, including  $\text{SO}_3\text{H}$ -functionalized ionic liquid, ionic liquids with acidic counter anion, and protonated *N*-alkylimidazolium ionic liquids have also been used in esterification reactions [12-14]. Although elegant work has been done in this area; there still exist some drawbacks in the above-mentioned catalytic systems. Therefore, one of the driving forces for this research is the possibility of elucidating the merits of ionic liquids for esterification and preparing synthetic wax ester, which resembles naturally occurring waxes of commercial interest.

The objective of this work is to synthesis oleyl oleate wax ester by esterification reaction of oleic acid with oleyl alcohol using different Brønsted acidic ionic liquid catalysts MIM-PS,  $[\text{HSO}_3\text{-Pmim}][\text{CH}_3\text{SO}_3]$ ,  $[\text{NMP}][\text{CH}_3\text{SO}_3]$  and then optimizing the reaction with several variables that affect the yield, such as the molar ratio of oleic acid to oleyl alcohol, amount of catalyst, reaction time and reaction temperature.

## ■ EXPERIMENTAL SECTION

### Materials

Oleic acid (90%) and oleyl alcohol (85%) were purchased from Aldrich chemical company (Germany). Diethyl ether, 1,3-propane sulphone, toluene, and 1-methyl imidazole were purchased from System Chemical Company (Malaysia). Benzene and *N*-methyl-2-pyrrolidone were obtained from the ACE chemical company (Sydney). Methane sulphonic acid was purchased from J.T. Baker chemical company (USA). All other chemicals and reagents used in this study were analytical grade and used without further purification.

### Instrumentation

Fourier transforms infrared spectroscopy (FTIR) was carried out using a Perkin Elmer Spectrum GX spectrophotometer in the range of 400–4000  $\text{cm}^{-1}$ . Nuclear magnetic resonance spectroscopy (NMR) for  $^1\text{H}$  and  $^{13}\text{C}$  was carried with model Joel FCP 400 MHz with  $\text{CDCl}_3$  and  $\text{D}_2\text{O}$  solvent. The electrospray ionization mass spectra (ESI-MS) were recorded on a Bruker MicroTOF-Q (German) mass spectrometer equipped with a Kd Scientific Apparatus syringe pump (USA).

### Procedure

#### **Synthesis of 3-(1-methylimidazolium-3-yl) propane-1-sulphonate (MIM-PS)**

In an ice-bath, 1-3-propane sulphone was dissolved in toluene and an equal mole of 1-methyl imidazole was dropped slowly with vigorous stirring. After dropping, the mixture was slowly heated up to room temperature and was stirred for 2 h, and then the reaction mixture was filtered to obtain the white precipitate. The precipitate was washed three times with diethyl ether and was dried at 100 °C for 5 h to obtain MIM-PS as a white powder with 97% yield.

#### **Synthesis of 1-methyl-3-(3-sulphopropyl)-imidazolium methyl sulphate ( $[\text{HSO}_3\text{-Pmim}][\text{CH}_3\text{SO}_3]$ )**

First, MIM-PS was dissolved in water then an equal mole of methane sulphonic acid was dropped slowly at room temperature, after dropping, the reaction mixture was slowly heated up to 90 °C and was stirred for 2 h, and

then the water was removed under vacuum (5–10 mm Hg) at 90 °C, giving ([HSO<sub>3</sub>-Pmim][CH<sub>3</sub>SO<sub>3</sub>]) as a light yellow viscous liquid yield 98%.

### Synthesis of *N*-methyl-2-pyrrolidonium methyl sulfate ([NMP][CH<sub>3</sub>SO<sub>3</sub>])

Benzene 30 mL was mixed with *N*-methyl-2-pyrrolidone (0.1 mol, 9.9 g) in a 50 mL flask. Then, methane sulphonic acid (0.1 mol, 9.6 g) was dropped slowly into the flask within 30 min in an ice-bath. The reaction lasted for another 4 h at room temperature. Benzene was removed under reduced pressure and was further dried at 90 °C under 1–5 mm Hg for 1 h, giving ([NMP][CH<sub>3</sub>SO<sub>3</sub>]) as a dark yellow viscous liquid yield 96%.

### Synthesis of oleyl oleate wax ester

A weighted amount of oleic acid (1 mol), oleyl alcohol (1, 2, and 3 mol) and Brønsted acidic ionic liquid catalyst (4.2, 5.7, 8.5, 9.9, 11.3 and 15.6 wt.%) as a percentage of the weight of oleic acid were added to a flask reflux apparatus. The esterification reaction was typically carried out for (2, 4, 6, 8, 10, and 12 h) at a temperature of (30 °C, 50 °C, 70 °C, 90 °C, 100 °C, and 110 °C) with vigorous stirring. After the completion of the reaction, the reaction mixture was transferred into a separatory funnel and then 5 mL of methanol was added into the funnel, extraction was carried out. The aqueous layer was decanted and the product was dissolved with 20 mL of ethyl acetate, followed by 10 mL of water to remove the remaining methanol.

After the water layer was removed, the product was dried in a conical flask with a sufficient amount of Na<sub>2</sub>SO<sub>4</sub> anhydrous. The hydrated Na<sub>2</sub>SO<sub>4</sub> was filtered off, then, the product was rotary-evaporated to remove ethyl acetate at 77 °C, giving oleyl oleate as a viscous liquid.

## RESULTS AND DISCUSSION

### Characterization of Ionic Liquid Catalysts

The structure of MIM-PS was characterized by the presence of asymmetric and symmetric SO<sub>2</sub> stretching vibrations, which appeared as strong and weak bands at 1325 cm<sup>-1</sup> (asy SO<sub>2</sub>), 1194 cm<sup>-1</sup> (sy SO<sub>2</sub>), respectively, that were absent in 1-methyl imidazole. The S–O stretching vibration was also detected at 747 cm<sup>-1</sup>. These special FTIR peaks indicated that the sulphonic group was successfully introduced in 1-methyl imidazole molecule. Fig. 1 shows the FTIR spectrum of MIM-PS. Furthermore, the <sup>1</sup>H and <sup>13</sup>C-NMR spectra of MIM-PS are presented in Fig. 2 and 3, respectively. The most important peak in the <sup>1</sup>H-NMR spectrum of the compound MIM-PS is the triplet peak related to CH<sub>2</sub>-N, which was observed at 2.97 ppm. Besides, its <sup>13</sup>C-NMR spectrum confirmed the presence of 7 carbon atoms in the MIM-PS, which indicates that the compound MIM-PS was prepared successfully.

The structure of [HSO<sub>3</sub>-Pmim][CH<sub>3</sub>SO<sub>3</sub>] has been confirmed by the presence of the bands representing the S=O group (1336, 1196 cm<sup>-1</sup>), OH group (3443 cm<sup>-1</sup>),

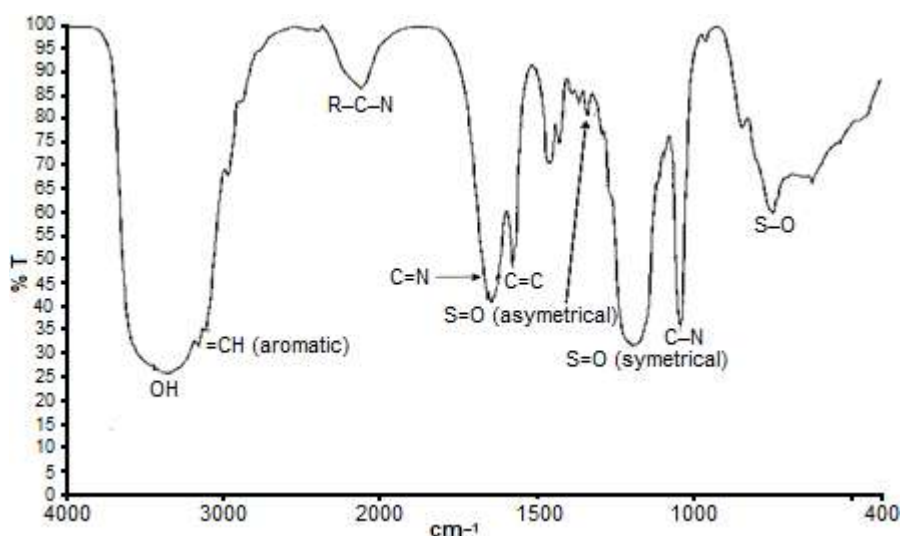


Fig 1. FTIR spectrum of MIM-PS

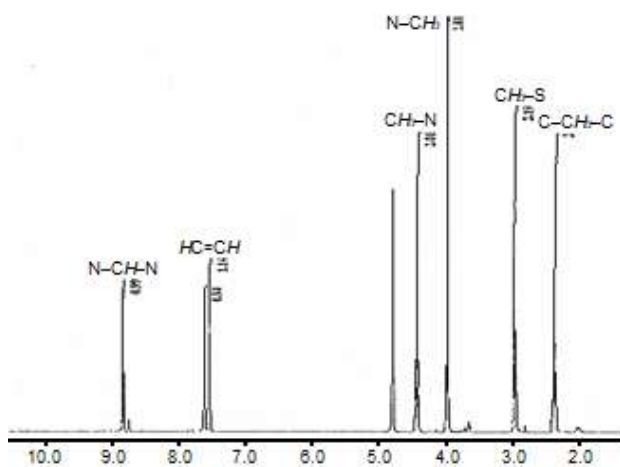


Fig 2.  $^1\text{H}$ -NMR spectrum of MIM-PS

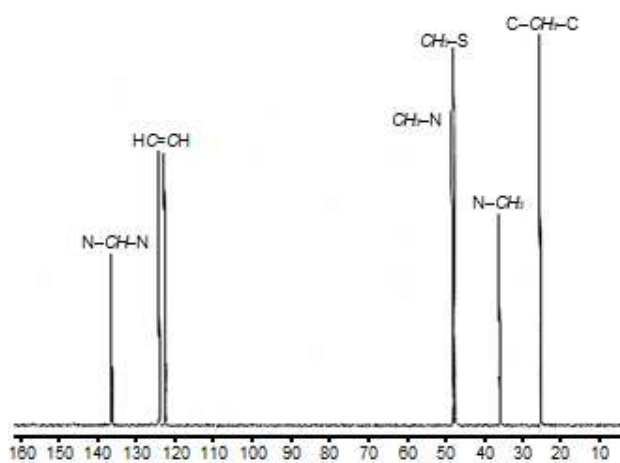


Fig 3.  $^{13}\text{C}$ -NMR spectrum of MIM-PS

S-O group ( $748\text{ cm}^{-1}$ ), C=N group ( $1644\text{ cm}^{-1}$ ), C-N group ( $1042\text{ cm}^{-1}$ ) and also =CH aromatic ( $3110, 3158\text{ cm}^{-1}$ ) as shown in Fig. 4. The  $^1\text{H}$  and  $^{13}\text{C}$ -NMR spectra of compound  $[\text{HSO}_3\text{-Pmim}][\text{CH}_3\text{SO}_3]$  were similar to  $^1\text{H}$  and  $^{13}\text{C}$ -NMR spectra of MIM-PS but with significant signals in  $^1\text{H}$  and  $^{13}\text{C}$ -NMR spectra of compound  $[\text{HSO}_3\text{-Pmim}][\text{CH}_3\text{SO}_3]$  at 2.18 ppm and 38.62 ppm, respectively. These peaks corresponded to methyl protons and carbon of methane sulphonic acid, which indicated that ionic liquid catalyst  $[\text{HSO}_3\text{-Pmim}][\text{CH}_3\text{SO}_3]$  was correctly synthesized. Furthermore, the signal due to the OH group (11–12 ppm) was not observed in the  $^1\text{H}$ -NMR spectrum of  $[\text{HSO}_3\text{-Pmim}][\text{CH}_3\text{SO}_3]$  due to the deuterium exchange where  $\text{D}_2\text{O}$  was used as the  $^1\text{H}$ -NMR solvent, as shown in Fig. 5 and 6.

Fig. 7 shows the representative FTIR spectrum of  $[\text{NMP}][\text{CH}_3\text{SO}_3]$ . The characteristic signals in the FTIR

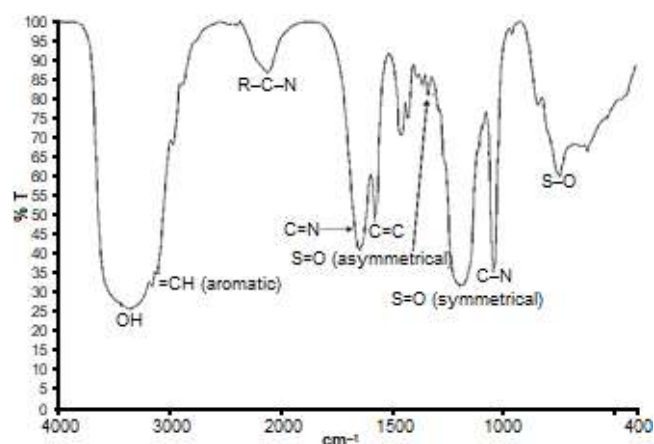


Fig 4. FTIR spectrum of  $[\text{HSO}_3\text{-Pmim}][\text{CH}_3\text{SO}_3]$

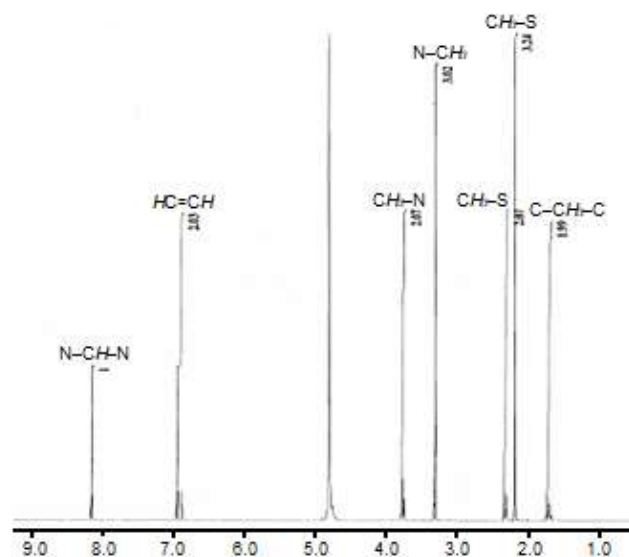


Fig 5.  $^1\text{H}$ -NMR spectrum of  $[\text{HSO}_3\text{-Pmim}][\text{CH}_3\text{SO}_3]$

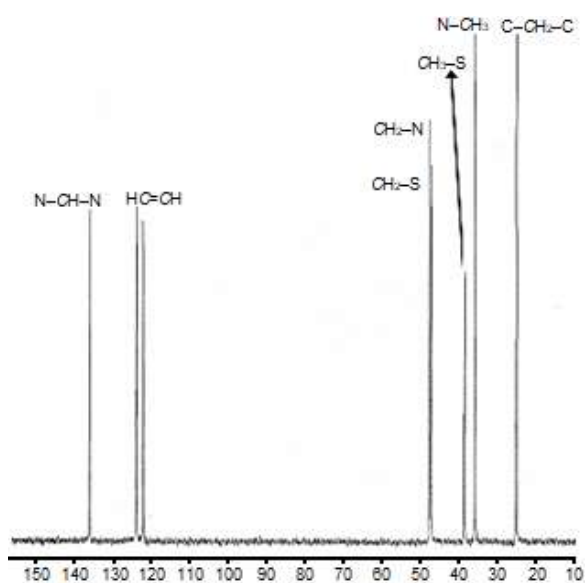


Fig 6.  $^{13}\text{C}$ -NMR spectrum of  $[\text{HSO}_3\text{-Pmim}][\text{CH}_3\text{SO}_3]$



spectrum of  $[\text{NMP}][\text{CH}_3\text{SO}_3]$  at 1200, 1307, and  $789\text{ cm}^{-1}$  corresponded to the  $\text{SO}_3$  and  $\text{S-O}$  groups, while the signal at  $1652\text{ cm}^{-1}$  showed the  $\text{C=O}$  group of *N*-methyl-2-pyrrolidone. This observation proved the success of the synthesis of the Brønsted acidic ionic liquid catalyst  $[\text{NMP}][\text{CH}_3\text{SO}_3]$ . The NMR spectra data gave additional support for the composition of the compound. The observed changes are evidence of the reaction that occurred because the chemical shift of a compound is deeply dependent on its electronic environment. Fig. 8 and 9 indicate the  $^1\text{H}$  and  $^{13}\text{C}$ -NMR spectra of  $[\text{NMP}][\text{CH}_3\text{SO}_3]$ , respectively. The result of the  $^1\text{H}$ -NMR spectrum of  $[\text{NMP}][\text{CH}_3\text{SO}_3]$  confirmed the appearance of the proton signals of  $\text{CH}_3\text{SO}_3\text{H}$  at about 2.56 ppm. Furthermore, at about  $\delta$  11.70 ppm, the proton signal of  $\text{N-H}$  as a broad signal appeared. Moreover, the  $\text{C=O}$  resonance group of the product appeared at about 174.60 ppm, while the  $\text{CH}_3$  group of compound  $\text{CH}_3\text{SO}_3\text{H}$  was detected at 39.90 ppm, which means that the reaction between *N*-methyl-2-pyrrolidone and methane sulphonic acid had taken place.

### Effect of Various Ionic Liquid Catalysts

Initially, the esterification reaction between oleic acid and oleyl alcohol at  $90\text{ }^\circ\text{C}$  under solvent-free conditions was tested. Three existing Brønsted acidic ionic liquids, including MIM-PS,  $[\text{HSO}_3\text{-Pmim}][\text{CH}_3\text{SO}_3]$ , and  $[\text{NMP}][\text{CH}_3\text{SO}_3]$  were used. Table 1 shows the yield percent of the experiments carried out under the same conditions.  $[\text{NMP}][\text{CH}_3\text{SO}_3]$  proved to be active, leading to a 45.41% yield of oleyl oleate within 2 h when 9.9 wt.% ionic liquid was used (percentage of the weight of oleic acid).  $[\text{HSO}_3\text{-Pmim}][\text{CH}_3\text{SO}_3]$  could also be used as a catalyst to promote the esterification reaction, but its activity seems to be slightly inferior compared with that of  $[\text{NMP}][\text{CH}_3\text{SO}_3]$ . However, repeating the reaction using MIM-PS only produced 32% of oleyl oleate at the same temperature and reaction time due to its hydrophobic nature which leads to catalyst deactivation. In general, the percentage yields of oleyl oleate produced from the esterification process catalyzed by ionic liquids is lower compared to homogeneous acidic catalysts such as sulfuric acid (94%), phosphoric acid (52.7%),

perchloric acid (54.9) and *p*-TSA (70%) for the same 2 h reaction time [15] and by using Lipozyme (75.66%) for 5 h reaction time [16]. However, because of the foregoing research,  $([\text{NMP}][\text{CH}_3\text{SO}_3])$  should be a suitable catalyst for the esterification reaction of oleic acid

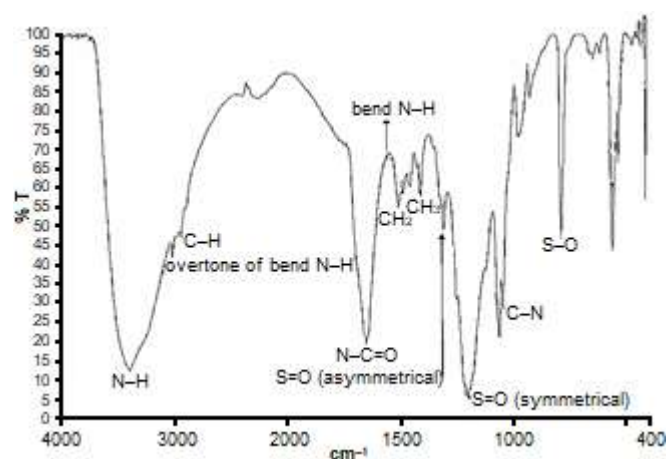


Fig 7. FTIR spectrum of  $[\text{NMP}][\text{CH}_3\text{SO}_3]$

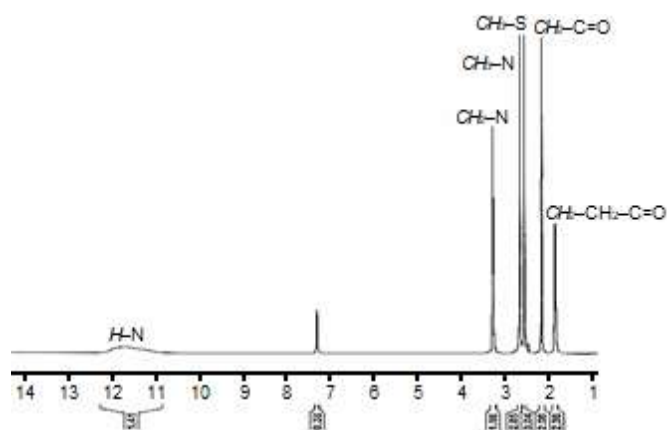


Fig 8.  $^1\text{H}$ -NMR spectrum of  $[\text{NMP}][\text{CH}_3\text{SO}_3]$

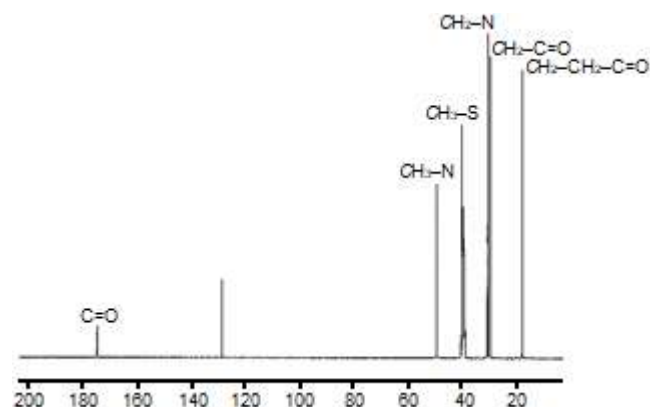


Fig 9. The  $^{13}\text{C}$  NMR spectrum of  $[\text{NMP}][\text{CH}_3\text{SO}_3]$

**Table 1.** The yields % of oleyl oleate wax ester based on the ionic liquid catalyst used

Duration	Ester yield (%)		
	MIM-PS	[(HSO <sub>3</sub> -Pmim)][CH <sub>3</sub> SO <sub>3</sub> ]	[(NMP)][CH <sub>3</sub> SO <sub>3</sub> ]
2 h	32.00 ± 3.1	35.00 ± 3.28	45.41 ± 2.15

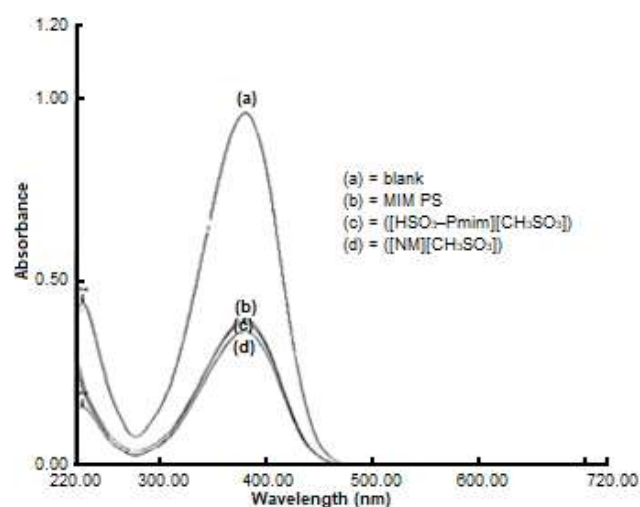
with oleyl alcohol to produce oleyl oleate. It offers significant improvements concerning the yield of products, simplicity in operation, and green aspects by avoiding toxic catalysts and solvents.

The esterification reaction proceeds through the addition of a proton and nucleophilic attack of the alcohol give a tetrahedral intermediate followed by dehydration. The three steps are all typical acid-catalyzed reactions. Therefore, the outcome of the esterification reaction depends very much on the acidity of the catalyst [17-18]. However, acidity determinations based on room temperature Brønsted acidic ionic liquids are a relatively new subject. The determination of the acidity of ionic liquid catalysts used in this research has not even been considered yet. A commonly used method to evaluate the acidity of acid in solution is the Hammett method [19], wherein a basic indicator has been used to trap the dissociative proton. The properties of the protons depend on both the nature of the solvent and the concentration of the chosen acid. The acidity was evaluated from the determination of the Hammett acidity functions, using UV-visible spectroscopy. In the present case, this method consists of evaluating the protonation extent of the uncharged indicator base (named I) in solution, in terms of the measurable ratio  $[I]/[IH^+]$ . In a given solvent (S), assumed as being dissociating, the Hammett function ( $H_0$ ) is defined as (Eq. (1)):

$$H_0 = pK(I)_{aq} + \log([I]_s/[IH^+]_s) \quad (1)$$

For comparison, the acidities of these three Brønsted acidic ionic liquid catalysts were examined using 4-

nitroaniline (Hammett constant is 0.99) as an indicator in distilled water; the results are shown in Table 2. The maximal absorbance of the unprotonated form of the indicator was observed at 380 nm in H<sub>2</sub>O. When an ionic liquid was added, the absorbance of the unprotonated form of indicator decreased. As shown in Fig. 10, the absorbance of the unprotonated form of the indicator on three ionic liquid catalysts decreased as follows: MIM-PS > [(HSO<sub>3</sub>-Pmim)][CH<sub>3</sub>SO<sub>3</sub>] > [(NMP)][CH<sub>3</sub>SO<sub>3</sub>]. By taking 4-nitroaniline as the initial reference (blank) the total unprotonated form of the indicator (when no acid is added to H<sub>2</sub>O solution, spectrum a), the ratio  $[I]/[IH^+]$  was determined from the measured absorbances after each ionic liquid (spectra b-d), and then the Hammett function ( $H_0$ ) was calculated.

**Fig 10.** Absorption spectra of 4-nitroaniline for Brønsted acidic ionic liquids in water**Table 2.**  $H_0$  values of various Brønsted acidic ionic liquid catalyst <sup>[a]</sup>

Ionic liquids	Absorbance [AU]	[I]%	[IH <sup>+</sup> ]%	$H_0$
4-nitroaniline	0.962	100	0	0
MIM-PS	0.39	41	59	0.8
[(HSO <sub>3</sub> -Pmim)][CH <sub>3</sub> SO <sub>3</sub> ]	0.388	40	59.7	0.82
[(NMP)][CH <sub>3</sub> SO <sub>3</sub> ]	0.36	37.4	62.6	0.76

<sup>[a]</sup>Concentration: 10 mmol/L

The smallest  $H_0$  was obtained in a 10 mmol/L  $H_2O$  solution of  $[(NMP)[CH_3SO_3]]$ , which indicated that Brønsted acidic ionic liquid  $[(NMP)[CH_3SO_3]]$  exhibits stronger acidity than the two other ionic liquid catalysts used in this work. The acidity of  $[HSO_3-Pmim][CH_3SO_3]$  is almost equal with MIM-PS, but slightly inferior compared with  $[(NMP)[CH_3SO_3]]$ . The result by using ionic liquid catalyst  $[(NMP)[CH_3SO_3]]$  shows the highest acidity, therefore a high % yield of oleyl oleate wax ester was obtained when the reaction was carried out using this catalyst.

### Effect of the Reaction Time

Fig. 11 shows the effect of the reaction time on the esterification reaction of oleic acid with oleyl alcohol.

The reactions were carried out within 2, 4, 6, 8, 10, 12 h. The other reaction conditions were as follows: substrates oleic acid and oleyl alcohol molar ratio of 1:1; amount catalyst of 9.9 wt.% as a percentage of the weight of the oleic acid; reaction temperature, 90 °C, and type of catalyst,  $[(NMP)[CH_3SO_3]]$ . The % yield of oleyl oleate wax ester increased with the increasing reaction time.  $[(NMP)[CH_3SO_3]]$  gave the highest percentage yield within a reaction period of 8 h (86%). Thereafter, the percentage yield of oleyl oleate decreased (47.37%) at 10 h. This behavior may be due to the production of water molecules, which increased the solvation process of the catalyst. According to Trubiano et al. [20], the presence of water only has an unfavorable effect on the equilibrium conversion. Since water is one of the products in the esterification reaction, it can promote the reverse hydrolysis reaction in the process. It is important to remove water during the reaction to achieve a high product yield. After 10 h the % yield of oleyl oleate was relatively reduced (41.95%). This may be due to the reaction having achieved the equilibrium state where the rate of the forward reaction is equal to the rate of backward reaction. Hence, the concentration of the product was unchanged.

### Effect of Molar Ratio of Substrates

To study the effect of the molar ratio in the esterification reaction of oleic acid with oleyl alcohol, the reaction was done using 1:1, 1:2, and 1:3 of oleic acid to

oleyl alcohol under the following conditions: reaction time of 8 h; the amount of catalyst, 9.9 wt.% as a percentage of the weight of the oleic acid; reaction temperature, 90 °C, and type of catalyst,  $[(NMP)[CH_3SO_3]]$ . The effect of the molar ratio of substrates on the esterification reaction is shown in Fig. 12. The optimal molar ratio of oleic acid to oleyl alcohol was 1:1, which gave 86% of oleyl oleate. Increasing the molar ratio of oleic acid to oleyl alcohol beyond this molar ratio 1:1 would decrease the esterification activity.

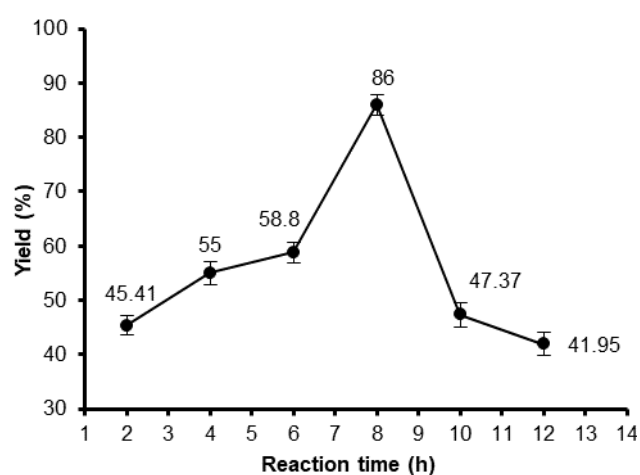


Fig 11. Effect of reaction time on the percentage yield of oleyl oleate wax ester. Values represent means  $\pm$  SD of three of triplicate determinations

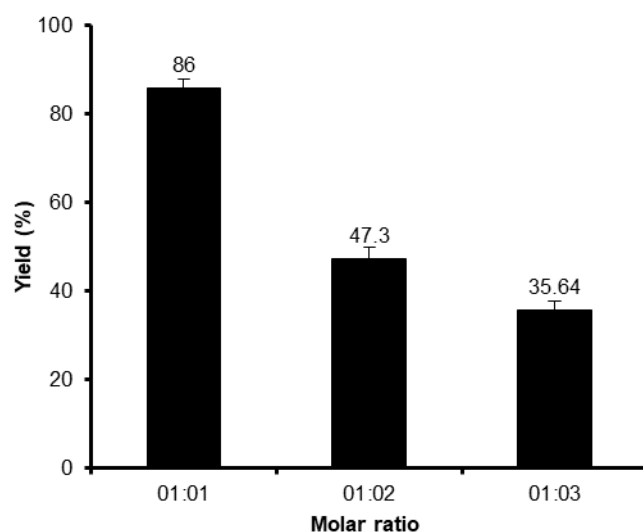


Fig 12. Effect of molar ratio of oleic acid and oleyl alcohol on the percentage yield of oleyl oleate wax ester. Values represent means  $\pm$  SD of three of triplicate determinations

This observation may reflect that an excess of oleyl alcohol would hinder the interaction frequency between the substrate and the catalyst [21-23]. Due to the high concentrations of oleyl alcohol, the viscosity of the reaction mixture surrounding the catalyst is increased, leading to ineffective mixing of substrates, thus decrease the rate of reaction.

### Effect of Amount of Catalyst

The influence of a varying amount of  $[(\text{NMP})[\text{CH}_3\text{SO}_3]]$  corresponding to 4.2, 5.7, 8.5, 9.9, 11.3, and 15.6 wt.% as a percentage of the weight of the oleic acid on the esterification reaction of oleyl alcohol and oleic acid at 90 °C, during 8 h using 1 mol of oleic acid: 1 mol oleyl alcohol is shown in Fig. 13. The % yield increased from 4.2% (28.4%) to 9.9% (86%) and decreased when the amount of catalyst increased to 11.3% (67.52). The amount of catalyst at 9.9% was sufficient to catalyze this esterification reaction. This result shows that an excess of catalyst amount did not contribute to the increase in the percentage yield, and, that, sometimes, it would decrease the yield of the product. This is due to the solvation of water from the Brønsted acidic ionic liquid catalyst becoming less, meaning that the water will excess on pre-condition and this will make the reversible reaction occur [24].

### Effect of Reaction Temperature

Changes in the reaction temperature can affect the activity and stability of the catalyst and thus the rate of reaction. Fig. 14 shows the influence of temperature on the esterification reaction within a temperature range of 30, 50, 70, 90, 100, and 110°. The other reaction conditions were as follows: reaction time, 8 h; the amount of catalyst, 9.9 wt.% as a percentage of the weight of the oleic acid; substrates molar ratio, 1:1 of oleic acid to oleyl alcohol and type of catalyst,  $[(\text{NMP})[\text{CH}_3\text{SO}_3]]$ . Initially, the % yield of oleyl oleate increased with the increasing temperature reaching the maximum at 90 °C (86%). This is because the energy received from the heat of higher temperature was used to increase the frequency of collision between the molecules thereby increasing the rate of reaction. However, the percentage yield started to decline to 56.39% at 100 °C and to 54.28% at 110 °C. Water

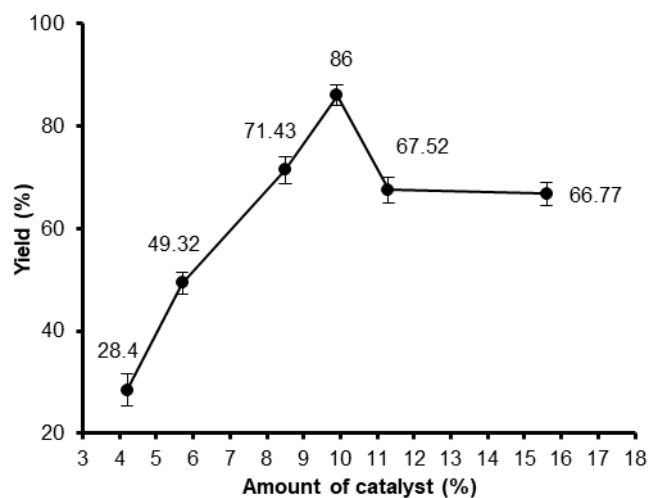


Fig 13. Effect of amount of catalyst on the percentage yield of oleyl oleate wax ester. Values represent means  $\pm$  SD of three of triplicate determinations

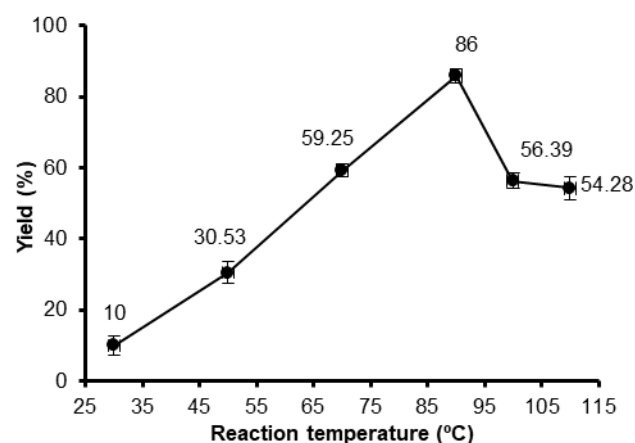


Fig 14. Effect of temperature on the percentage yield of oleyl oleate wax ester. Values represent means  $\pm$  SD of three of triplicate determinations

content simultaneously formed during the esterification reaction increased to higher temperatures, and better dissolved in the Brønsted acidic ionic liquid. This consequently, diluted the ionic liquid catalyst and greatly decreased the viscosity and acidity [25].

## CONCLUSION

The Brønsted acidic ionic liquid  $[(\text{NMP})[\text{CH}_3\text{SO}_3]]$  is non-flammable, easy to synthesize, thermally stable, and exhibits negligible vapor pressure. The  $[(\text{NMP})[\text{CH}_3\text{SO}_3]]$  as an esterification catalyst, has many advantages in which the Brønsted acidic ionic liquid

([NMP][CH<sub>3</sub>SO<sub>3</sub>]) exhibits good catalytic performance. The [NMP][CH<sub>3</sub>SO<sub>3</sub>] loads which are 9.9 wt.% (as a percentage of the weight of oleic acid) can be used to catalyze the esterification process to produce esters with high yield. Also, the procedure used for the preparation of [NMP][CH<sub>3</sub>SO<sub>3</sub>] is quite easy and inexpensive. The preliminary acidity determinations of three Brønsted acidic ionic liquids used in this research revealed that the acidities of the ionic liquids play a determining role in the rate acceleration of the esterification reaction. The esterification reaction could be done at moderate temperature; a high % yield of oleyl oleate wax ester was obtained. Therefore, using [NMP][CH<sub>3</sub>SO<sub>3</sub>] will decrease the cost of production. This methodology offers significant improvements concerning the yield of products, simplicity in operation, and green aspects by avoiding toxic catalysts and solvents.

#### ■ ACKNOWLEDGMENTS

The authors acknowledge the Universiti Kebangsaan Malaysia for funding (Code UKMGUP-NBT-08-27-113 and UKM-OUP-NBT-29-150/2011) and the direct contributions of the support staff from the Department of Chemical Sciences, the Faculty of Science and Technology, Universiti Kebangsaan Malaysia.

#### ■ REFERENCES

- [1] da Silva, J.A.C., 2011, "Biodegradable lubricants and their production via chemical catalysis" in *Tribology - Lubricants and Lubrication*, Eds. Kuo, C.H., IntechOpen, Rijeka, Croatia, 185–200.
- [2] Cheng, D., 2013, Wax ester biosynthetic pathway, *Dissertations*, Department of Biochemistry, Biophysics and Molecular Biology, Iowa State University, US.
- [3] Samidin, S., Salih, N., and Salimon, J., 2021, Synthesis and characterization of trimethylolpropane based esters as green biolubricant basestock, *Biointerface Res. Appl. Chem.*, 11 (5), 13638–13651.
- [4] Liu, T., Peng, X., Chen, Y., Zhang, J., Jiao, C., and Wang, H., 2020, Solid-phase esterification between poly(vinyl alcohol) and malonic acid and its function in toughening hydrogels, *Polym. Chem.*, 11 (29), 4787–4797.
- [5] Weng, S.S., Chen, F.K., and Ke, C.S., 2013, Direct esterification of carboxylic acids with alcohols catalyzed by iron(III) acetylacetonate complex, *Synth. Commun.*, 43 (19), 2615–2621.
- [6] Naik, S., Kavala, V., Gopinath, R., and Patel, B.K., 2006, Tetrabutylammonium tribromide mediated condensation of carboxylic acids with alcohols, *Arkivoc*, 2006 (1), 119–127.
- [7] Bartlewicz, O., Dąbek, I., Szymańska, A., and Maciejewski, H., 2020, Heterogeneous catalysis with the participation of ionic liquids, *Catalysts*, 10 (11), 1227.
- [8] Liang, S.T., Wang, H.Z., and Liu, J., 2018, Progress, Mechanism and application of liquid metal catalysis system: A review, *Chem. Eur. J.*, 24 (67), 17616–17626.
- [9] Gao, P., Zhang, L., Li, S., Zhou, Z., and Sun, Y., 2020, Novel heterogeneous catalysts for CO<sub>2</sub> hydrogenation to liquid fuels, *ACS Cent. Sci.*, 6 (10), 1657–1670.
- [10] Soleimani, O., 2020, Properties and applications of ionic liquids, *J. Chem. Rev.*, 2 (3), 169–181.
- [11] Deng, Y., Shi, F., Beng, J., and Qiao, K., 2001, Ionic liquid as a green catalytic reaction medium for esterification, *J. Mol. Catal. A: Chem.*, 165 (1-2), 33–36.
- [12] Vafaezadeh, M., and Alinezhad, H., 2016, Brønsted acidic ionic liquids: Green catalysts for essential organic reactions, *J. Mol. Liq.*, 218, 95–105.
- [13] Zhang, T., Li, X., Song, H., and Yao, S., 2019, Ionic liquid-assisted catalysis for glycosidation of two triterpenoid sapogenins, *New J. Chem.*, 43 (43), 16881–16888.
- [14] Al-Arafi, N., and Salimon, J., 2012, Production of oleic acid based wax ester using acidic homogeneous catalysts, *J. Chem.*, 9, 181249.
- [15] Sardar, S., Wilfred, C.D., and Leveque, J.M., 2017, One-pot Mannich base synthesis using task specific protic ionic liquids, *Malays. J. Anal. Sci.*, 21 (5), 1203–1209.

- [16] Salminen, E., Virtanen, P., and Mikkola, J.P., 2014, Alkaline ionic liquids applied in supported ionic liquid catalyst for selective hydrogenation of citral to citronellal, *Front. Chem.*, 2, 3.
- [17] Polesso, B.B., Bernard, F.L., Ferrari, H.Z., Duarte, E.A., Vecchia, F.D., and Einloft, S., 2019, Supported ionic liquids as highly efficient and low-cost material for CO<sub>2</sub>/CH<sub>4</sub> separation process, *Heliyon*, 5 (7), e02183.
- [18] Hu, Y.L., and Fang, D., 2016, Preparation of silica supported ionic liquids for highly selective hydroxylation of aromatics with hydrogen peroxide under solvent-free conditions, *J. Mex. Chem. Soc.*, 60 (4), 207–217.
- [19] Gu, Y., Zhang, J., Duan, Z., and Deng, Y., 2005, Pechmann reaction in non-chloroaluminate acidic ionic liquids under solvent-free conditions, *Adv. Synth. Catal.*, 347 (4), 512–516.
- [20] Trubiano, G., Borio, D., and Errazu, A., 2007, Influence of the operating conditions and the external mass transfer limitations on the synthesis of fatty acid esters using a *Candida antarctica* lipase, *Enzyme Microb. Technol.*, 40 (4), 716–722.
- [21] Ratti, R., 2014, Ionic Liquids: Synthesis and applications in catalysis, *Adv. Chem.*, 2014, 729842.
- [22] Salih, N., and Salimon, J., 2021, A Review on eco-friendly green biolubricants from renewable and sustainable plant oil sources, *Biointerface Res. Appl. Chem.*, 11 (5), 13303–13327.
- [23] Ishak, Z.I., Sairi, N.A., Alias, Y., Aroua, M.K.T., and Yusoff, R., 2017, A review of ionic liquids as catalysts for transesterification reactions of biodiesel and glycerol carbonate production, *Catal. Rev. Sci. Eng.*, 59 (1), 44–93.
- [24] Neto, B.A.D., and Spencer, J., 2012, The impressive chemistry, applications and features of ionic liquids: Properties, catalysis & catalysts and trends, *J. Braz. Chem. Soc.*, 23 (6), 987–1007.
- [25] Salimon, J., Salih, N., and Yousif, E., 2012, Industrial development and applications of plant oils and their biobased oleochemicals, *Arabian J. Chem.*, 5 (2), 135–145.

## Performance Improvements of Bixin and Metal-Bixin Complexes Sensitized Solar Cells by 1-Methyl-3-propylimidazolium Iodide in Electrolyte System

Winda Rahmalia<sup>1\*</sup>, Septiani<sup>1</sup>, Uray Amira Naselia<sup>1</sup>, Thamrin Usman<sup>1</sup>,  
Imelda Hotmarisi Silalahi<sup>1</sup>, and Zéphirin Mouloungui<sup>2,3</sup>

<sup>1</sup>Department of Chemistry, Faculty of Mathematics and Natural Sciences, Tanjungpura University,  
Jl. Ahmad Yani, Pontianak 78124, West Kalimantan, Indonesia

<sup>2</sup>Laboratoire de Chimie Agro-industrielle (LCA), Université de Toulouse, INP-ENSIACET,  
4 Allée Emile Monso, 31030 Toulouse, France

<sup>3</sup>INRA, UMR 1010 CAI, F-31030 Toulouse, France

### \* Corresponding author:

tel: +62-561-577963

email: [winda.rahmalia@chemistry.untan.ac.id](mailto:winda.rahmalia@chemistry.untan.ac.id)

Received: October 15, 2020

Accepted: December 13, 2020

DOI: 10.22146/ijc.60633

**Abstract:** Bixin is one of the potential natural sensitizers used in dye-sensitized solar cells (DSSCs). In this study, bixin was complexed with Cu(II) and Zn(II) to increase its stability. The formation of the complexes was indicated by shifting peaks absorption and the changes in the fine spectral structure observed from the UV-Vis absorption spectra. The metal-bixin complex occurs due to the interaction between the ester groups of bixin and the metal. Bixin, Cu-bixin, and Zn-bixin were used separately as sensitizers in DSSCs. The DSSCs performance was then improved by adding 1-methyl-3-propylimidazolium iodide (MPII) to the electrolyte system. The presence of MPII 0.4 M in KI-I<sub>2</sub> electrolyte produced a higher ionic conductivity value (20.44 mS cm<sup>-1</sup>) than that without MPII (11.14 mS cm<sup>-1</sup>). This electrolyte system significantly improved DSSCs performance. Under a light intensity of 300 W/m<sup>2</sup>, the maximum energy conversion efficiencies of DSSC with bixin, Cu-bixin, and Zn-bixin as sensitizers are 0.084, 0.081, and 0.005%, respectively. The Zn-bixin-based DSSC was stable under high light intensity. Under 700 W/m<sup>2</sup>, its maximum energy conversion efficiency reaches 0.125%. There was a synergistic work observed between the metal-bixin complex and the MPII based electrolyte. This result can open the way for constructing functional materials for solar cell applications.

**Keywords:** bixin; complex; dye-sensitized solar cells (DSSCs); 1-methyl-3-propylimidazolium iodide (MPII)

## ■ INTRODUCTION

Dye-sensitized solar cells (DSSCs) are a third generation of the photovoltaic cell. It is a low-cost solar cell belonging to thin-film solar cells due to inexpensive constituent materials and a simple fabrication process [1-2]. Dye sensitizer is one of the essential components of DSSCs [3]. Organic or natural dyes-based sensitizers offer a suitable alternative to high-cost inorganic dyes. Ruthenium and several materials used as inorganic dye sensitizers are also toxic and low natural abundance [4].

Among naturally occurring carotenoids, bixin (methyl hydrogen 9'-cis-6,6'-diapocarotene-6,6'-dioate, C<sub>25</sub>H<sub>30</sub>O<sub>4</sub>, CAS Number: 39937-79-5) is a potential dye that has been explored as a sensitizer in DSSCs because of its 9'-cis structure and two carboxylic groups, one of which is a methyl carboxy ester as shown in Fig. 1(a). The bixin's carboxylic group can react readily with the metal oxide's surface hydroxyl groups [5-7]. Bixin can absorb UV-A, UV-B, and UV-C with absorption coefficients in aprotic polar solvents of over 10<sup>4</sup> M<sup>-1</sup> cm<sup>-1</sup> [5,8], which is

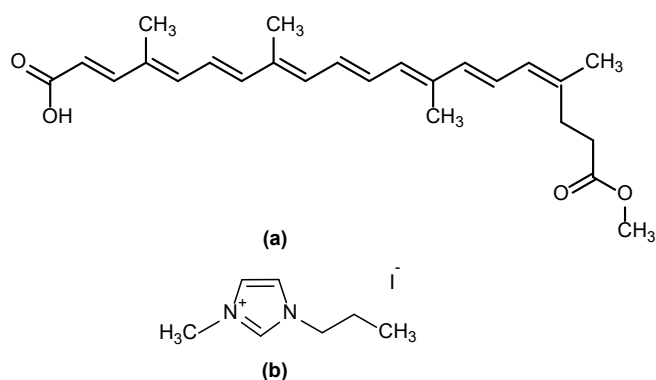


**Fig 1.** Structure of *cis*-bixin (a) and 1-methyl-3-propylimidazolium iodide (MPII) (b)

an advantage for dyes as sensitizers in DSSCs. However, due to their conjugated double bonds system, the stability of natural sensitizers like bixin in DSSCs is debated [9].

De Sousa Lobato et al. [10] have conducted research to increase bixin stability by using polymer encapsulation to produce bixin nanocapsules. This method was able to increase the stability of bixin up to  $100 \pm 0.02\%$ . However, encapsulation could inhibit the role of bixin as a sensitizer. Another way to increase the stability of the dye sensitizer is the complexation method. This method can prevent cloudiness or loss of color from the dye. Cortez et al. [11] reported that metal ions used in complex processes were shown to stabilize the dye extract color. Besides that, the oxidation state of metal ions plays a vital role in forming dye-metal complexes. Therefore, complexes of bixin with divalent transition metal ions ( $Zn^{2+}$  and  $Cu^{2+}$ ) were prepared. In a coordination complex, the transition group metals tend to act as a Lewis acid (an electron acceptor). They are bonded by ligands which act as Lewis bases (an electron donor) [12-13]. The different electronic properties of these two transition metals ( $Cu^{2+}$ ,  $Zn^{2+}$ ) are interesting to study because they will show different interactions with ligands in organometallic complexes [14-15].

In addition to the sensitizer stability, electrolyte stability also has an essential role in improving the DSSCs performance. The electrolyte is a charge transport medium produced by sensitizer and photoanode. The electrolyte system that has been widely used is the liquid electrolyte type of the redox  $I^-/I_3^-$  pair. Rahmalia [12] fabricated DSSC with a bixin-based sensitizer using liquid

electrolyte  $KI-I_2$ , showing a maximum performance of 0.08%. The low viscosity of liquid electrolytes makes it easy for the solvent to leak or evaporate, thereby drastically reducing performance.

Shi et al. [15] have reported that electrolyte stability can be improved by adding an additive ionic liquid such as imidazolium. This leads to an increase in the conductivity and energy conversion efficiency of the DSSC system. Ionic conductivity increases with increasing electrolyte density due to the increased concentration of free ions formed after adding imidazolium to the liquid electrolyte [16]. One of the imidazolium groups is 1-methyl-3-propylimidazolium iodides (MPII, Fig. 1(b)). The concentration of ionic liquid added to the electrolyte system affects the viscosity, conductivity, and mobility of electrons. Therefore, this study discusses the effect of MPII concentrations in the  $KI-I_2$  electrolyte system on the performance of bixin and bixin-metal complexes sensitized solar cells, focused on short circuit current ( $I_{sc}$ ), open-circuit voltage ( $V_{oc}$ ), and the maximum energy conversion efficiency.

## ■ EXPERIMENTAL SECTION

### Materials

Kesumba (*Bixa orellana* L.) seeds were obtained from West Kalimantan Indonesia,  $NH_4OH$ -activated metakaolinite prepared by Rahmalia et al. [17]. Acetone ( $CH_3COCH_3$ ,  $\geq 99.9\%$ ) was supplied by Mallinckrodt Chemicals, iodine ( $I_2$ ) by VWR Chemicals, plastisol by Solaronix, transparent conductive oxide (TCO) glass with fluorine-doped tin oxide (FTO) type thermal evaporation coating, 7–8 ohm/sq (TEC-7) conductive glass by SOLEM. Anatase nanopowder titanium dioxide ( $TiO_2 < 25$  nm particle size, 99.7% trace metals basis) and 1-methyl-3-propylimidazolium iodide (MPII) were supplied by Sigma Aldrich. Acetonitrile ( $C_2H_3N$ ,  $\geq 99.8\%$ ), ethyl acetate ( $C_4H_8O_2$ ,  $\geq 99.9\%$ ), potassium iodide (KI), copper sulfate ( $CuSO_4 \cdot xH_2O$ ), zinc sulfate ( $ZnSO_4 \cdot H_2O$ ), triton-x-100 ( $C_8H_{17}C_6H_4(OCH_2CH_2)_nOH$ ), acetylacetone ( $C_5H_8O_2$ ) absolute ethanol ( $C_2H_5OH$ ), and aluminium thin layer chromatography plate, silica gel coated with fluorescent indicator F254 (TLC F<sub>254</sub>) were supplied by Merck.



## Procedure

### Preparation of bixin and metal-bixin complexes

**Preparation of bixin.** Kesumba seeds (75 g) were immersed in 200 mL of ethyl acetate in an Erlenmeyer flask, stirred for 1 h, and filtered. The process was repeated until all the colors are extracted into the ethyl acetate solution, and it was then evaporated at 40 °C to give 6.9 g of crude residue (9.4%). The 2 g crude residue was chromatographed over silica gel 60 Å (70–230 mesh) using hexane, mixtures of hexane-ethyl acetate (9:1, 8:2, 7:3, 6:4, 1:1), acetone, a mixture of acetone-methanol (1:1), and methanol. The eluates were collected, monitored by thin-layer chromatography, and combined in major fractions. Bixin (0.13 g) was obtained from the last fractions.

**Preparation of complexes M-bixin (M = Zn(II) and Cu(II)).** ZnSO<sub>4</sub>·H<sub>2</sub>O and CuSO<sub>4</sub>·xH<sub>2</sub>O were separately heated at 100 °C for 24 h to remove hydrates. The complex of Zn-bixin was prepared as follows. An aqueous solution of Zn(II) (12.2 mg in 1 mL of distilled water) was added gradually into bixin solution (30.0 mg in 30 mL of acetone), then stirred until homogeneous. The mixture was refluxed for 1 h. It was evaporated on heating in an oven at 50 °C for 2 h to remove the solvent. The powder complex of Zn-bixin was obtained and stored in the dark at 4 °C until further treatment. The Cu-bixin complex was prepared by the same method by replacing Zn(II) with Cu(II) (12.3 mg in 1 mL of distilled water) and bixin solution (30.5 mg in 30 mL of acetone). The bixin (Bx), Zn-bixin (Zn-Bx), and Cu-bixin (Cu-Bx) complexes were analyzed by a double-beam Shimadzu UV-1800 UV-Vis and a Shimadzu FT-IR spectrophotometer.

### Fabrication of dye-sensitized solar cells (DSSCs)

**Preparation of transparent conductive oxide (TCO).** TEC7 FTO glasses measuring 2.5 × 2.0 cm<sup>2</sup> were washed using soap and water. The glasses were immersed in 70% ethanol using a bath sonicator for 30 min, then dried at a temperature of 100 °C for 1 h. The conductive side of the glasses was determined.

**Preparation of anode.** Photoanode was prepared by adopting the method of Rahmalia [12]. The mixture of anatase-TiO<sub>2</sub> (2.375 g) and a mixture of ammonia-activated metakaolinite (MKA, 0.126 g) were added with 15 mL of absolute ethanol, 16 drops of triton-x, and 12

drops of acetylacetone. The mixture was then stirred for 24 h to form a paste. The photoanode paste formed was sonicated for 3.0 h.

**Preparation of electrolytes.** The electrolyte used in this study is a redox pair (I<sup>-</sup>/I<sub>3</sub><sup>-</sup>), where KI (1.66 g) and I<sub>2</sub> (0.127 g, 0.05 M) were mixed in 20 mL acetonitrile and stirred until homogeneous. The electrolyte solution was stored in a dark and closed bottle. The electrolyte variation was carried out by adding MPEI ionic liquid with various concentrations of 0.3, 0.4, and 0.5 M. The electrolytes were determined their viscosity, density, pH, and ionic conductivity.

**Assembling of DSSCs.** DSSCs were prepared by doctor blading using TEC7 FTO-covered glass as follows. TiO<sub>2</sub>/MKA paste and plastisol paste were deposited on FTO glass with 1 cm<sup>2</sup> active side forming photoanode and cathode separately. The photoanode was heated in the furnace at 450 °C for 30 min, while the cathode was heated at 400 °C for 5 min. Photoanodes were immersed in sensitizer solution (Bx, Zn-Bx, and Cu-Bx) concentrated of 5 g/L (in acetone solvent) for 24 h. Furthermore, one drop of electrolyte was added to the photoanode, then covered with a cathode to form a layer like a sandwich. Each cell was tested for performance (I<sub>sc</sub> and V<sub>oc</sub>) using a scientific multimeter of 6.5 digits Agilent 34461A. The light source used in the test is a 500 W halogen lamp. The test conditions are carried out with variations in light intensity of 0–1000 W/m<sup>2</sup>.

## RESULTS AND DISCUSSION

### Characteristics of Bx, Zn-Bx, and Cu-Bx

The TLC analysis (as seen in Fig. 2) shows changes in R<sub>f</sub> after reacting bixin with metal precursors for 60 min. R<sub>f</sub> values' differences are due to the bonding of Zn<sup>2+</sup> and Cu<sup>2+</sup> to Bx molecules, which affects the resulting product polarity. The R<sub>f</sub> values of Bx, Zn-Bx, and Cu-Bx are 0.31, 0.73, and 0.26, respectively, indicating that the Zn-Bx and Cu-Bx had been formed with polarity properties Bx-Cu > Bx > Bx-Zn. This polarity can be influenced by the ion electronegativity of the Cu<sup>2+</sup> (1.90), which is greater than Zn<sup>2+</sup> (1.65).

The conjugated double bond system constitutes the light-absorbing chromophore of bixin, resulting in a

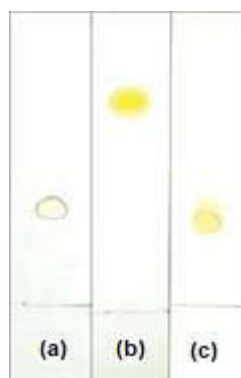


**Fig 2.** Thin layer chromatogram of Bx (a), Zn-Bx (b), and Cu-Bx (c)

strong absorption band above 400 nm, as seen in Fig. 3. Based on this figure, there are three characteristic peaks for Bx at 488, 459, and 430 nm. The nine conjugated double bonds influence the absorption spectra in the wavelength range above 400 nm on the Bx molecule. The peaks at the 488 and 459 nm wavelengths show an electron transition from  $\pi$  to  $\pi^*$ , which comes from the C=C conjugated double bond [8]. In contrast, the peak at 430 nm occurs due to the electron transition from  $n$  to  $\pi^*$ , originating from the carbonyl group (C=O) [8,17].

The UV-Vis absorption band of Zn-Bx coincides with the Bx, while the absorption band of Cu-Bx tends to shift towards a lower wavelength (hypsochromic) to 3 nm. The hydroxyl substitution of the carboxylate or ester group in Bx (as a ligand) interacting with the metal does not affect their chromophore group. Consequently, it will not affect the resulting absorption spectra [18]. The slightly blue shift occurs probably due to the transfer of electrons from the ligand ion to the metal [19]. The charge transfer in the Cu-Bx and Zn-Bx complexes is most likely derived from the transfer of charge from metal to ligand (Metal to Ligand Charge Transfer or MLCT). The interaction between Bx and  $Zn^{2+}$  or  $Cu^{2+}$  can also be identified by the change in the % III/II ratio (fine spectral structure) in the absorption spectrum, illustrated in Fig. 4 [17]. In this research, the ratios % III/II of Bx, Zn-Bx, and Cu-Bx are 51.89, 39.28, and 15.91%, respectively.

The FTIR spectrum of Bx (Fig. 5) shows the following bands: at  $3183\text{ cm}^{-1}$  for the -OH stretching vibration, at  $2937$ ,  $2924$ , and  $2852\text{ cm}^{-1}$  for the H-C-H bending vibration, at  $1716\text{ cm}^{-1}$  for the ester C=O group,

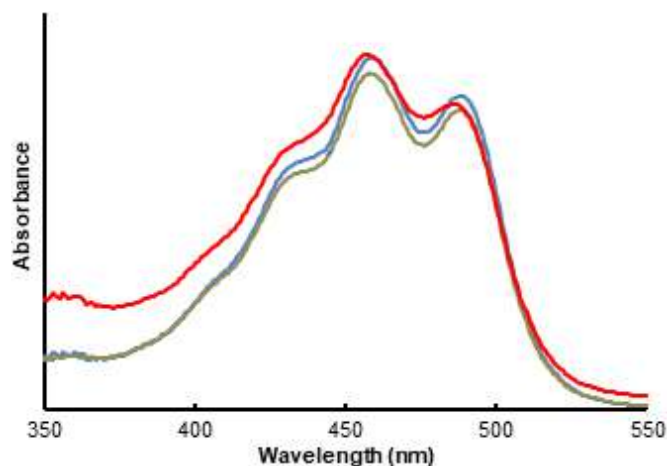


**Fig 3.** Normalized UV-Vis absorption spectra of Bx (blue), Cu-Bx (red), Zn-Bx (grey) in acetone

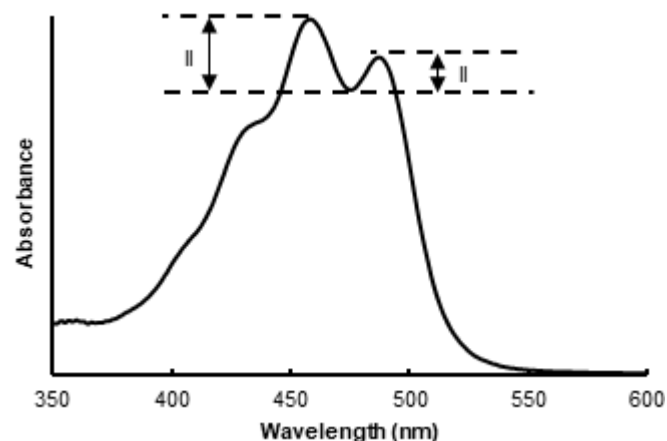


**Fig 4.** Calculation of %III/II for a carotenoid [17]

at  $1689\text{ cm}^{-1}$  for the carboxylic C=O group, at  $1608\text{ cm}^{-1}$  for the -OH bending vibration, at  $1563$  and  $1518\text{ cm}^{-1}$  for the alkene C=C stretching vibration, at  $1379\text{ cm}^{-1}$  for C-H bending vibration of the methyl groups, at  $1288$  and  $1255\text{ cm}^{-1}$  for the C=O stretching vibration of the ester functional group, at  $1160\text{ cm}^{-1}$  for the symmetric and asymmetric vibrations of the C-O-C ester group, at  $1011\text{ cm}^{-1}$  as the asymmetric C-H bending vibration, at  $728\text{ cm}^{-1}$  indicated methylene oscillating vibrations of *cis*-carotenoid. The FTIR analysis results in agreement with Rahmalia et al. [20] and Lóránd et al. [21] that presented FTIR analysis for *cis*-bixin compounds.

FTIR spectra of Zn-Bx and Cu-Bx do not show any significant differences compared to Bx. However, the -OH carboxylate group absorption band became wider, accompanied by a decrease in the absorption peak

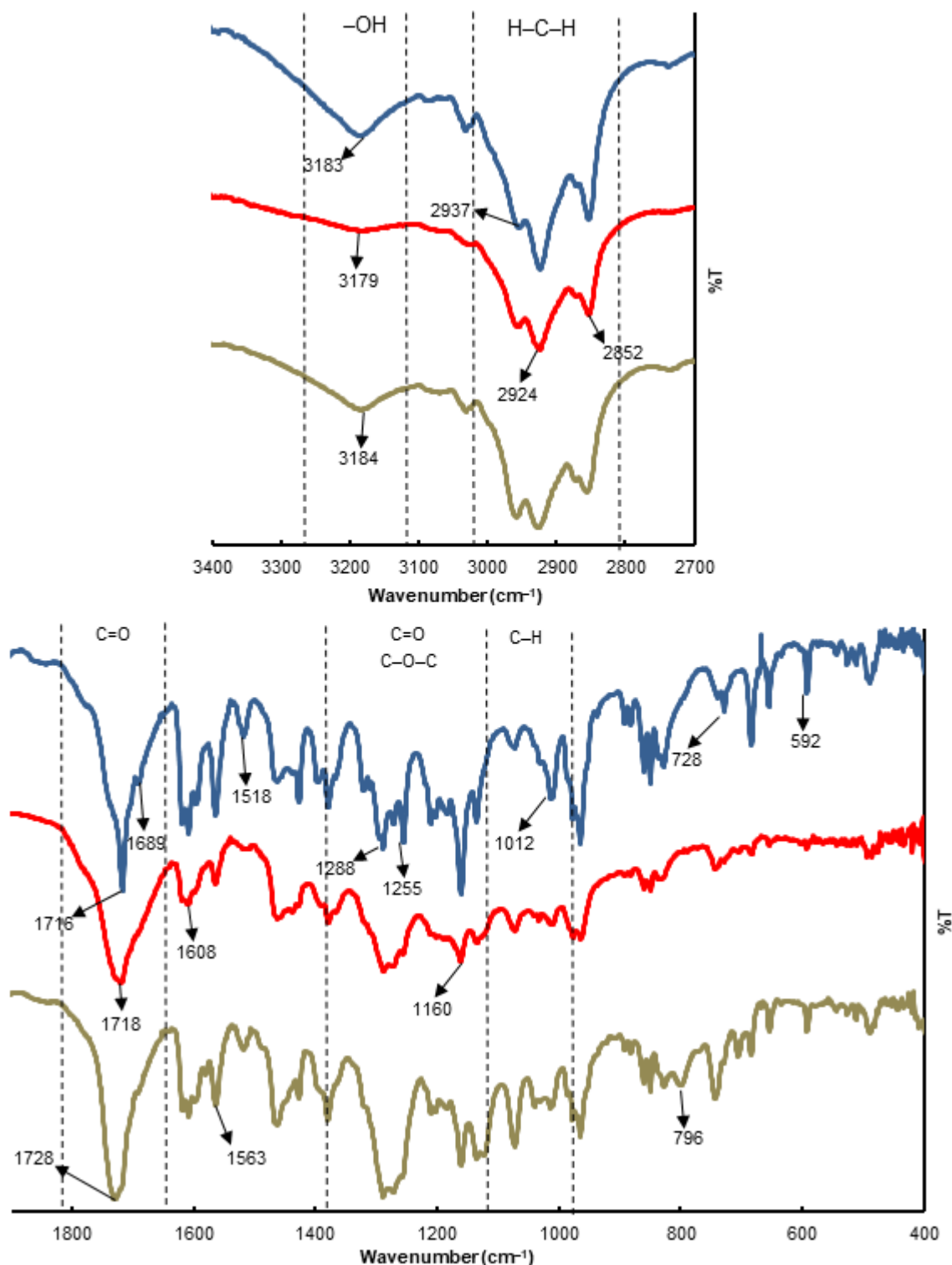


Fig 5. FTIR spectra of Bx (blue), Cu-Bx (red), and Zn-Bx (grey)

intensity. There is a shift to the lower wavenumber for the Cu-Bx complex (3179  $\text{cm}^{-1}$ ) and the longer wavenumber for the Zn-Bx complex at (3184  $\text{cm}^{-1}$ ) as compared to Bx

(3183  $\text{cm}^{-1}$ ). Tayyari et al. [22] postulated that a stronger hydrogen bond would show a wider absorption band accompanied by a decrease in absorption intensity. The

ester group's C=O absorption band undergoes a shift to a larger wavenumber, which for Bx-Cu and Bx-Zn show bands at 1718 and 1728  $\text{cm}^{-1}$ , respectively, as compared to Bx (1716  $\text{cm}^{-1}$ ). The absorption bands at 1288 and 1255  $\text{cm}^{-1}$  are observed to overlap into a wide peak. There were also decreases in the intensities of vibration peaks of the C–O–C ester group at 1160  $\text{cm}^{-1}$  and C–H bending vibration at 1011  $\text{cm}^{-1}$ . These phenomena indicated that the metal-bixin complex occurs due to the interaction between the ester groups of bixin and the metal [23-24]. According to FT-IR analysis data, the mechanism of complex formation is predicted as given in Fig. 6.

### Characteristics of the KI-I<sub>2</sub> Electrolyte with Various MPII Concentrations

Table 1 shows the characteristics of the KI-I<sub>2</sub> electrolyte with various concentrations of MPII. The greater the MPII concentration added leads to higher

density and viscosity values. This phenomenon is due to the increasing number of ion pairs formed by free ions moving randomly in the medium. MPII can form MPII<sup>+</sup> and I<sup>-</sup> ions. This is in good agreement with Chowdhury et al. [25], who investigated the effect of tetrabutylammonium iodide (TBAI) concentrations in the KI-I<sub>2</sub> electrolyte system in a polyacetonitrile (PAN) based gel electrolyte. They reported that the higher concentration of TBAI added caused the free ion density of TBA<sup>+</sup> and I<sup>-</sup> to increase.

The addition of MPII in the KI-I<sub>2</sub> electrolyte system increased the viscosity value almost two times. Although the increase in viscosity causes a decrease in fluid velocity and the rate of electrolyte diffusion, which can affect the transport of electrons in the electrolyte, it can decrease evaporation rate and prevent leakage electrolyte system from cells [26]. The addition of MPII

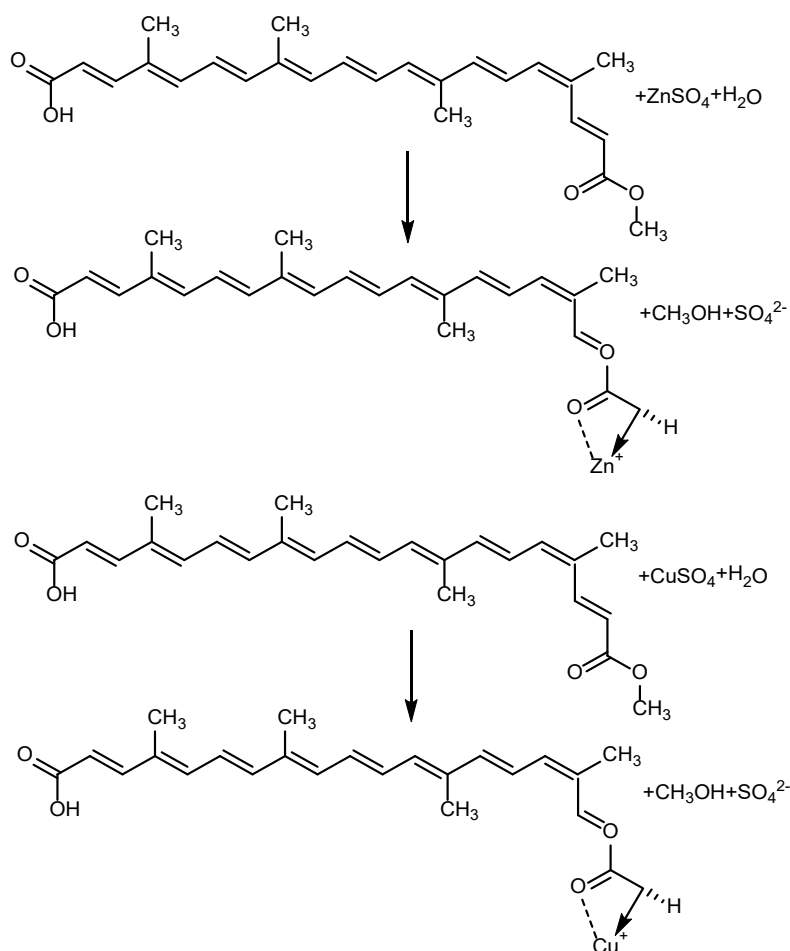


Fig 6. Prediction of the mechanism of complex formation

**Table 1.** The results of the electrolyte analysis

Electrolytes*	KI-I <sub>2</sub>	KI-I <sub>2</sub> /MPII 0.3 M	KI-I <sub>2</sub> /MPII 0.4 M	KI-I <sub>2</sub> /MPII 0.5 M
$\rho$ (g cm <sup>-3</sup> )	0.82	0.87	0.88	0.88
$\eta$ (mPa s)	0.27	0.46	0.48	0.49
pH	2.39	3.00	3.17	3.37
$\kappa$ (mS cm <sup>-1</sup> )	11.14	0.02	20.44	20.46

\*  $\rho$  = density (g cm<sup>-3</sup>),  $\eta$  = viscosity (mPa s),  $\kappa$  = ionic conductivity (mS cm<sup>-1</sup>)

did not have a significant effect on the pH of the electrolyte.

The ionic conductivity of the KI-I<sub>2</sub> electrolyte without MPII was 11.14 mS cm<sup>-1</sup>. The addition of 0.3 M MPII in the KI-I<sub>2</sub> electrolyte system significantly decreased the conductivity values. However, adding 0.4 and 0.5 M MPII significantly increased the viscosity values to 20.44 and 20.46 mS cm<sup>-1</sup>, respectively. MPII is an ionic liquid (IL) that increases the electron transport from electrolytes. These results are consistent with the research conducted by Shing et al. [27]. They reported that the addition of MPII in poly (ethylene oxide) polymer electrolyte (PEO) could increase the conductivity of electrons in the electrolyte. However, the excessive concentration MPII addition does not significantly affect the conductivity value and can even reduce the conductivity due to the ion aggregation process in the electrolyte. Therefore, based on the density, viscosity, and conductivity values, the optimum concentration of MPII added in the KI-I<sub>2</sub> electrolyte system in this study is 0.4 M.

### DSSC Performance

Fig. 7 shows the relationship between Voc, Isc, and the maximum energy conversion efficiency to the light intensity of the DSSCs using the KI-I<sub>2</sub> electrolyte without MPII. Voc is the maximum voltage available from a solar cell that occurs at zero current, while Isc is the current through the solar cell when the voltage across the solar cell is zero. They are the key parameters that govern the attainable power from a DSSC. The maximum energy conversion efficiency describes the performance of a DSSC, how much solar energy (photons) can be converted into electrical energy without considering the value of the fill factor. It is the ratio between power generated by DSSC and the power of the light sources.

As shown in Fig. 7, Voc and Isc increase logarithmically with light intensity. All DSSC have the

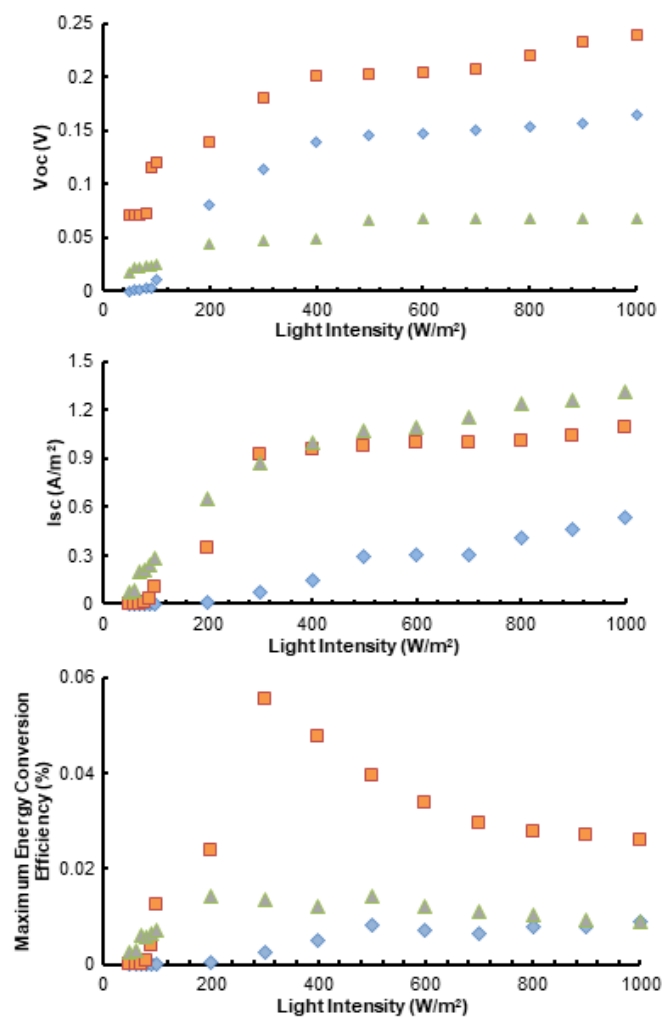


**Fig 7.** Performance parameter of DSSCs using Bx (◆), Bx-Zn (■), and Bx-Cu (▲) as sensitizer and KI-I<sub>2</sub> electrolyte system

same curve pattern. However, under various light intensities, Zn-Bx and Cu-Bx-based DSSCs showed higher Voc values than pure Bx-based DSSC. Voc is given by the difference of the electrons Fermi level in the TiO<sub>2</sub> and the electrolyte redox potential [28]. In this work, the presence of metal in the dye, which then covers

the semiconductor surface, may increase the semiconductor's electrons' Fermi level. Zn is a better redox catalyst than Cu, causing the highest Voc value under various light intensities. Zn-Bx and Cu-Bx-based DSSCs show higher Isc values than those based on pure Bx. This phenomenon indicated that  $Zn^{2+}$  and  $Cu^{2+}$  in the bixin molecule could increase the number of excited electrons from dye sensitizer and promote the rapid injection of these excited electrons into the semiconductor conduction band.

Based on Fig. 7, the maximum energy conversion efficiency of DSSCs using KI-I<sub>2</sub> electrolyte occurs under a light intensity of 300 W/m<sup>2</sup> with the values of 0.003, 0.055, and 0.013% for Bx, Zn-Bx, and Cu-Bx based DSSCs, respectively. The maximum energy conversion efficiency of DSSCs decreases under light intensity higher than 300 W/m<sup>2</sup>. This is due to increased cell temperature that may evaporate liquid electrolyte KI-I<sub>2</sub> and/or provoke charge recombination between dye sensitizer and semiconductor.

The effect of MPII 0.4 M addition in the KI-I<sub>2</sub> liquid electrolyte system on the performance of the DSSC based on Bx, Zn-Bx, and Cu-Bx has also been investigated. The relationship between Voc, Isc, and the maximum energy conversion efficiency to the light intensity with MPII 0.4 M addition can be seen in Fig. 8. The addition of MPII to the KI-I<sub>2</sub> electrolyte system significantly affects the Isc values. For all DSSC, Isc increases almost linearly with increasing light intensity, indicated that MPII plays a role in increasing the electrolyte stability. These results are in good agreement with Ramesh [29], who reported that MPII could increase Isc due to increased ionic conductivity of iodide ions or ion transfer in the MPII<sup>+</sup>I<sup>-</sup> electrolyte. The K<sup>+</sup> ions can intercalate into the semiconductor layer, causing a positive shift in the conduction band and increasing the charge injection rate. MPII is high ionic hopping, which can accelerate the dissociation initiation of KI.

The stability of the DSSCs performance under high light intensity is supported by the increase in the value of electrolyte viscosity due to MPII. Leakage and evaporation of liquid electrolytes were prevented. DSSC that used Zn-Bx as a sensitizer even shows good performance under

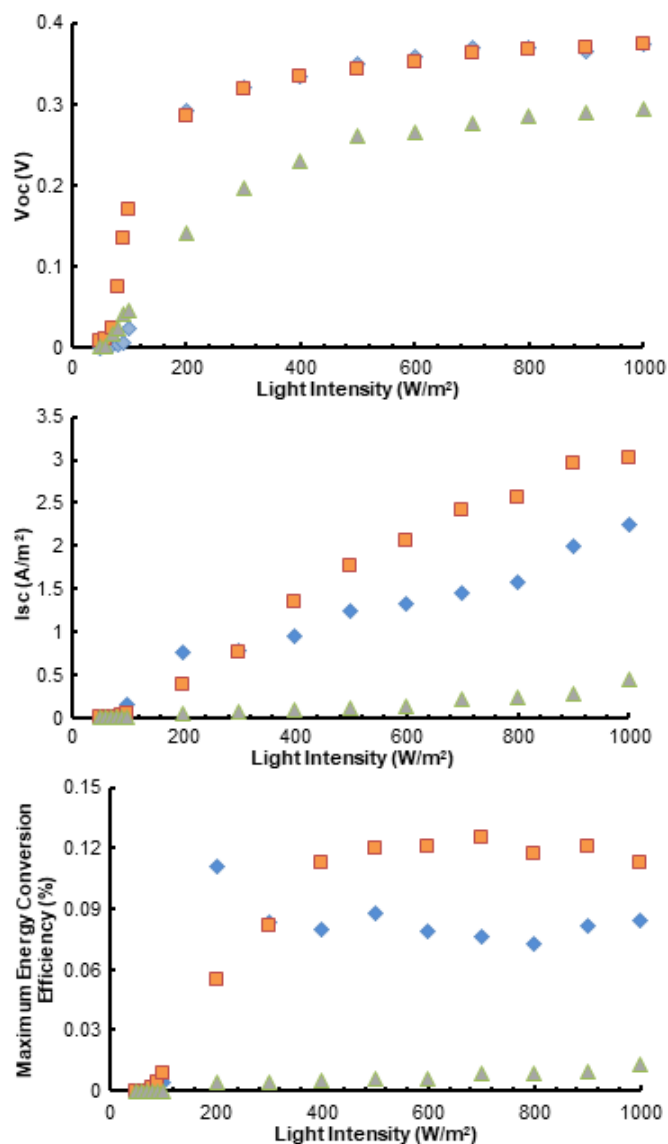


**Fig 8.** Performance parameters of DSSCs using Bx (◆), Bx-Zn (■), and Bx-Cu (▲) as sensitizer and KI-I<sub>2</sub> + MPII 0.4 M electrolyte system

700 W/m<sup>2</sup> of light intensity. Under this condition, the maximum energy conversion efficiency shows values of 0.076, 0.125, and 0.008% for Bx, Zn-Bx, and Cu-Bx-based DSSCs, respectively. This phenomenon proves that complexation bixin with  $Zn^{2+}$  can improve the stability and performance of bixin.  $Zn^{2+}$  is a metal ion that is not oxidized.

## CONCLUSION

The metal-bixin complexes were successfully synthesized due to the interaction between the ester

groups of bixin and the metal. Complexing bixin on metals has a positive impact on increasing bixin's stability and performance as a sensitizer. The presence of MPII in the KI-I<sub>2</sub> electrolyte system also produces several advantages, including an increase in the electrolyte's conductivity, density, and viscosity. A synergistic work was observed between the Zn-bixin complex and the KI-I<sub>2</sub>-MPII 0.4 M electrolyte system in the DSSC with a maximum energy conversion efficiency of 0.125 under 700 W/m<sup>2</sup> light intensity and no significant decrease when the light intensity increased. Although there are some problems with natural DSSCs, such as their stability and durability, this research's results can solve the disadvantages. Finally, with the advance of technology, their good application prospect will be apparent.

#### ■ ACKNOWLEDGMENTS

This study received financial support from the Ministry of Research Technology and the Higher Education Republic of Indonesia (KEMENRISTEK DIKTI) through the National Competitive Research (217/SP2H/LT/DRPM/2019).

#### ■ REFERENCES

- [1] Gong, J., Sumathy, K., Qiao, Q., and Zhou, Z., 2017, Review on dye-sensitized solar cells (DSSCs): Advanced techniques and research trends, *Renewable Sustainable Energy Rev.*, 68, 234–246.
- [2] Mariotti, N., Bonomo, M., Fagiolari, L., Barbero, N., Gerbaldi, C., Bella, F., and Barolo, C., 2020, Recent advances in eco-friendly and cost-effective materials towards sustainable dye-sensitized solar cells, *Green Chem.*, 22 (21), 7168–7218.
- [3] Prabavathy, N., Shalini, S., Balasundaraprabhu, R., Velauthapillai, D., Prasanna, S., and Muthukumarasamy, N., 2017, Enhancement in the photostability of natural dyes for dye-sensitized solar cell (DSSC) applications: A review, *Int. J. Energy Res.*, 41 (10), 1372–1396.
- [4] Semalti, P., and Sharma, S.N., 2020, Dye-sensitized solar cells (DSSCs) electrolytes and natural photosensitizers: A review, *J. Nanosci. Nanotechnol.*, 20 (6), 3647–3658.
- [5] Gómez-Ortíz, N.M., Vázquez-Maldonado, I.A., Pérez-Espadas, A.R., Mena-Rejón, G.J., Azamar-Barrios, J.A., and Oskam, G., 2010, Dye-sensitized solar cells with natural dyes from achiote seeds, *Sol. Energy Mater. Sol. Cells*, 94 (1), 40–44.
- [6] Hiendro, A., Hadary, F., Rahmalia, W., and Wahyuni, N., 2012, Enhanced performance of bixin-sensitized TiO<sub>2</sub> solar cells with activated kaolinite, *Int. J. Eng. Res. Innov.*, 4 (1), 40–44.
- [7] Hug, H., Bader, M., Mair, P., and Glatzel, T., 2013, Biophotovoltaics: Natural pigments in dye-sensitized solar cells, *Appl. Energy*, 115, 216–225.
- [8] Rahmalia, W., Fabre, J.F., Usman, T., and Mouloungui, Z., 2014, Aprotic solvents effect on the UV-visible absorption spectra of bixin, *Spectrochim. Acta, Part A*, 131, 455–460.
- [9] Kabir, F., Sakib, S.N., and Matin, N., 2019, Stability study of natural green dye based DSSC, *Optik*, 181, 458–464.
- [10] de Sousa Lobato, K.B., Paese, K., Forgearini, J.C., Guterres, S.S., Jablonski, A., and de Oliveira Rios, A., 2015, Evaluation of stability of bixin in nanocapsules in model systems of photosensitization and heating, *LWT Food Sci. Technol.*, 60 (1), 8–14.
- [11] Cortez, R., Luna-Vital, D.A., Margulis, D., and de Mejia, E.G., 2016, Natural pigments: Stabilization methods of anthocyanins for food applications, *Compr. Rev. Food Sci. Food Saf.*, 16 (1), 180–198.
- [12] Rahmalia, W., 2016, Paramètres de Performances de Photo-électrodes de TiO<sub>2</sub>/Kaolinite et d'Electrolyte à base de Carbonates Biosourcés dans la Cellule Solaire Sensibilisée par la Bixine, *Dissertation*, Institut National Polytechnique de Toulouse, France.
- [13] Soldatović, T., 2018, "Mechanism of interactions of zinc(II) and copper(II) complexes with small biomolecules" in *Basic Concepts Viewed from Frontier in Inorganic Coordination Chemistry*, IntechOpen, London, UK.
- [14] Lo, K.K.W., 2017, *Inorganic and Organometallic Transition Metal Complexes with Biological*

- Molecules and Living Cells*, 1<sup>st</sup> Ed., Academic Press, Cambridge, Massachusetts, USA.
- [15] Shi, L.Y., Chen, T.L., Chen, C.H., and Cho, K.C., 2013, Synthesis and characterization of a gel-type electrolyte with ionic liquid added for dye-sensitized solar cells, *Int. J. Photoenergy*, 2013, 834184.
- [16] Khanmirzaei, M.H., Ramesh, S., and Ramesh K., 2015, Hydroxypropyl cellulose-based non-volatile gel polymer electrolytes for dye-sensitized solar cell applications using 1-methyl-3-propylimidazolium iodide ionic liquid, *Sci. Rep.*, 5, 18056.
- [17] Britton, G., 1995, "UV/visible Spectroscopy" in *Carotenoids, Vol. 1B: Spectroscopy*, Eds., Britton, G, Liaaen-Jensen, S, and Pfander, H., Birkhäuser Verlag, Basel, Boston and Berlin.
- [18] Popova, A.V., 2017, Spectral characteristics and solubility of  $\beta$ -carotene and zeaxanthin in different solvents, *C. R. Acad. Bulg. Sci.*, 70 (1), 53–60.
- [19] Zebib, B., Mouloungui, Z., and Noirot, V., 2010, Stabilization of curcumin by complexation with divalent cations in glycerol/water system, *Bioinorg. Chem. Appl.*, 2010, 292760.
- [20] Rahmalia, W., Fabre, J.F., and Mouloungui, Z., 2015, Effects of cyclohexane/acetone ratio on bixin extraction yield by accelerated solvent extraction method, *Procedia Chem.*, 14, 455–464.
- [21] Lóránd, T., Molnar, P., Deli, J., and Tóth, G., 2002, FT-IR study of some seco- and apocarotenoids, *J. Biochem. Biophys. Methods*, 53 (1-3), 251–258.
- [22] Tayyari, S.F., Vakili, M., Nekoei, A.R., Rahemi, H., and Wang, Y.A., 2007, Vibrational assignment and structure of trifluorobenzoylacetone: A density functional theoretical study, *Spectrochim. Acta, Part A*, 66 (3), 626–636.
- [23] Rahmalia, W., Fabre, J.F., Usman, T., and Mouloungui, Z., 2020, Preparation of ammonia dealuminated metakaolinite and its adsorption against bixin, *Indones. J. Chem.*, 20 (4), 791–800.
- [24] Yang, C., and Wöll, C., 2017, IR spectroscopy applied to metal oxide surfaces: Adsorbate vibrations and beyond, *Adv. Phys.: X*, 2 (2), 373–408.
- [25] Chowdhury, F.I., Buraidah, M.H., Arof, A.K., Mellander, B.E., and Noor, I.M., 2020, Impact of tetrabutylammonium, iodide and triiodide ions conductivity in polyacrylonitrile based electrolyte on DSSC performance, *Sol. Energy*, 196, 379–388.
- [26] Gu, P., Yang, D., Zhu, X., Sun, H., Wangyang, P., Li, J., and Tian, H., 2017, Influence of electrolyte proportion on the performance of dye-sensitized solar cells, *AIP Adv.*, 7 (10), 105219.
- [27] Singh, P.K., Kim, K.W., and Rhee, H.W., 2009, Ionic liquid (1-methyl 3-propyl imidazolium iodide) with polymer electrolyte for DSSC application, *Polym. Eng. Sci.*, 49 (5), 862–865.
- [28] Raga, R., Barea, E.M., and Fabregat-Santiago, F., 2012, Analysis of the origin of open circuit voltage in dye solar cells, *J. Phys. Chem. Lett.*, 3 (12), 1629–1634.
- [29] Ng, H.M., Ramesh, S., and Ramesh, K., 2015, Efficiency improvement by incorporating 1-methyl-3-propylimidazolium iodide ionic liquid in gel polymer electrolytes for dye-sensitized solar cells, *Electrochim. Acta*, 175, 169–175.



## Surface Complexation of Chromium(VI) on Iron(III) Hydroxide: Mechanisms and Stability Constants of Surfaces Complexes

Mhamed Hmamou<sup>1\*</sup>, Fatima Ezzahra Maarouf<sup>1</sup>, Bouchaib Ammary<sup>1</sup>, and Abdelkebir Bellaouchou<sup>2</sup>

<sup>1</sup>Applied Chemistry Laboratory Materials, University Mohamed V, Faculty of Science, Ibn Batouta Avenue, Rabat, Morocco

<sup>2</sup>Nanotechnology Laboratory and Environment, University Mohamed V, Faculty of Science, Ibn Batouta Avenue, Rabat, Morocco

\* **Corresponding author:**

tel: +212-674908352

email: hmamou1965@gmail.com

Received: October 15, 2020

Accepted: November 20, 2020

DOI: 10.22146/ijc.60634

**Abstract:** The adsorption of chromate ions  $H_{2-y}A$  ( $y = 1, 2$ , and  $A = CrO_4^{2-}$ ) on iron(III) hydroxide was conducted as a function of adsorbent mass, solution pH, and hydration time. The surface complexation technique, based on the examination of the chromate distribution between the solid and liquid phases, was adopted to predict the adsorption mechanism. To specify stoichiometry of the chromate surface complexes, the proton ( $n > 0$ ) and hydroxyl ( $n < 0$ ) ion-exchange was evaluated at a pH range of 2–12. The obtained “n” values are ranging between -1 and 1. As a result, the sorption process involved specific chemical interaction with surface sites, resulting in  $1H^+$  and  $1OH^-$  the adsorbate molecule’s release. The surface species identified were  $\frac{>S(OH_2^+)(HA^-)}{>S(OH_2^+)(A^{2-})}$ ;  $\frac{>S(OH_2^+)(H_1A^{-1})}{>S(OH_2^+)(A^{2-})}$ ;  $\frac{>S(OH_1^0)(A^{2-})}{>(SOH_2^+) - (H_1A)H_{-1} - S^{(-2)}}$ ;  $\frac{>(SOH_2^+) - AH_{-1} - S^{(-1)}}{>S(OH)(A^{2-})}$  and  $\frac{>(SOH_2^+ - A - SOH)^{4-}}{>S(OH)(A^{2-})}$ . The logarithmic values of their complexing constants were:  $\log K_{00} = 1.81 \pm 0.04$ ;  $\log K_{11} = -3.53 \pm 0.07$ ;  $\log K_{21} = -1.03 \pm 0.23$ ,  $\log K_{1-1} = 7.15 \pm 0.14$  and  $\log K_{2-1} = 9.62 \pm 0.53$ . The results showed that the chromate adsorption on Fe(III) hydroxide was of electrostatic and chemical nature at pH lower than 5.5, and only of chemical nature at pH superior to 5.5. Therefore, Fe(III) hydroxide could be considered an excellent sorbent for removing Cr(VI) from wastewater solutions.

**Keywords:** chromium(VI); iron(III) hydroxide; adsorption; surface complexes; stability constants

### ■ INTRODUCTION

Chromium is widely used in many industrial fields such as tanning, painting, dyeing ceramics, wood treatment, and the paper industry. These Industrial activities generate substantial amounts of hazardous wastes containing high concentrations of chromium [1]. The hexavalent chromium has been considered one of the most toxic pollutants because of its mutagenic, carcinogenic, and teratogenic properties in humans [2-6]. This element’s discharge in the surface water is a severe threat to rivers, streams, and aquatic life. The presence of this metal is well controlled and the maximal concentration level of Cr(VI) allowed in drinking water, as determined by the US-Environmental Protection Agency (EPA), is 0.05 mg/L [7]. As a result, raising public concerns about environmental pollution requires

sustainable technologies for reducing the chromium ions in wastewater to an acceptable level. Wastewater discharge of the Cr(VI) industry is largely treated using different adsorbents to meet environmental regulation [8-13]. However, this process and subsequent treatments have high operating costs. Accordingly, wastewater is still a managing difficulty for Cr(VI).

For this purpose, methods have already been developed, such, ion exchange [14], solvent extraction [15], precipitation [16-17], and adsorption [18-21]. These techniques are usually performed using conventional or non-conventional adsorbents, especially, zeolites, and iron(III) hydroxide [22-25]. However, adsorption is a technique of choice for the removal of dissolved elements as Cr(VI) from aqueous solutions. One can note that this procedure is often

carried out using activated carbon [26-27], metal-organic frameworks [28-29], polymeric, and biomass materials [30-35]. A new study is recently conducted on hexavalent chromium adsorption and removal from the aqueous environment using chemically functionalized amorphous and mesoporous silica nanoparticles [36]. Nevertheless, iron oxyhydroxide or ferric oxyhydroxide ( $\text{FeO}(\text{OH})$ ), which has low solubility in water and often poorly crystalline, has a large surface area and more active sites for  $\text{Cr}(\text{VI})$  adsorption.

The relevant reported functional groups of  $\text{Fe}(\text{III})$  oxyhydroxide rich in defects are  $\text{Fe}-\text{O}$ ,  $\text{Fe}-\text{OH}$ , and  $\text{Fe}-\text{O}-\text{Fe}$  [37]. Thus,  $\text{FeO}(\text{OH})$  suspension develops surface charge ( $Q$ ) due to the exchange of  $\text{H}^+$  or  $\text{OH}^-$  ions resulting from the dissociation of hydration water molecules [38]. This exchange phenomenon's contribution to  $Q$  depends on the transfer of proton to hydroxo complex interface ( $>\text{SOH}$ ), which is a function of the medium suspension acidity [39]. As discussed previously, the proton transfer reaction can be treated as an acid-base equilibrium after protonation/deprotonation of  $>\text{SOH}$  [40].

This study's mean objective consists of surface complexation of hexavalent chromium ions on iron(III) hydroxide. For this purpose, the sorption of  $\text{Cr}(\text{VI})$  is examined through co-precipitation experiments from aqueous solution, as a function of contact time, the mass of adsorbent, and equilibrium pH of chromium solution  $10^{-5}$  M. The ion exchange method, which has already been successfully used in liquid-liquid extraction, is carried out, in order to examine the sorption and the complexation of ions chromates with the surface of amorphous  $\text{Fe}(\text{OH})_3 \cdot x\text{H}_2\text{O}$ .

## ■ EXPERIMENTAL SECTION

### Materials

Chemicals namely potassium dichromate ( $\text{K}_2\text{Cr}_2\text{O}_7$ , 99%), sodium hydroxide ( $\text{NaOH}$ , 99%), potassium permanganate ( $\text{KMnO}_4$ ), iron(III) chloride ( $\text{FeCl}_3$ , 99%), and nitric acid ( $\text{HNO}_3$ , 99%) were used and purchased from Sigma Aldrich. The reagents are of analytical grade and used without further purification [41]. High quality distilled water is used for all the experiments.

### Instrumentation

The equipment used in this research was a magnetic stirrer, laboratory balance ADB, KERN of precision  $10^{-4}$  g, and MIKRO 200 HETTICH benchtop centrifuge. The pH of sample solutions was measured using a METROHM pH-meter of precision  $10^{-3}$  pH unit, equipped with a previously calibrated double concentric electrode. Analysis of the dosage of chromium(VI) is carried out in the aqueous phases before and after adsorption by a GBC type 902 UV-Visible spectrophotometer.

### Procedure

The adsorption studies are carried out by co-precipitation of  $\text{Fe}(\text{OH})_3$ . The iron(III) masses used in this case are 60, 100, and 300 mg/L, while the contact time is varied in the range of 1–24 h. Co-precipitation experiments are examined using a  $10^{-5}$  M solution of potassium permanganate. The pH is adjusted by decimolar solutions of  $\text{NaOH}$  or  $\text{HNO}_3$ . Chromium co-precipitation is carried out with 100 ml of amorphous ferric oxyhydroxide solution at various pH and  $\text{Fe}^{3+}$  concentrations.

The co-precipitation efficiency is determined using the ratio of  $\text{Cr}(\text{VI})$  concentrations in solid and aqueous phases, which corresponds to the partition coefficient ( $D$ ). The concentration of hexavalent chromium is measured in the aqueous phase by using a UV-Visible spectrophotometry technique.

### Adsorption experiments

The dosage of chromium in the aqueous solution is carried out by UV-Visible spectrophotometry technique. For this purpose, 0.2 mL of the 1,5-diphenyl-carbazide complexing agent is acidified with 4 mL of 0.05 M sulfuric acid solution and completed to 5 mL with distilled water. The co-precipitation of chromium ions by the  $\text{Fe}(\text{OH})_3$  is examined according to the contact time, the pH of the suspension, and the mass of the iron hydroxide. The effect of pH on the partition of  $\text{Cr}(\text{VI})$  between the solution and the solid phase is examined for various contact times.

The effect of pH and mass of sorbent on  $\text{Cr}(\text{VI})$  sorption is described by Eq. (1).

$$\log D = \log K_{ap} + \log m + npH \quad (1)$$

$$D = \frac{[\text{Cr(VI)}]}{[\text{Cr(VI)}]} \quad (2)$$

$K_{ap}$  is adsorption constant, "m" is sorbent amount in g/L and the on lined species referrer to the solid phase. If "P" denotes the percentage of chromium fixation on iron(III) oxyhydroxide we obtain:

$$D = \frac{P}{1-P} \rightarrow P = \frac{D}{1+D} \quad (3)$$

## ■ RESULTS AND DISCUSSION

### Effect of pH

The experimental results of the adsorption of chromate ions on iron(III) hydroxide are given in Fig. 1, as a logarithmic variation of D with pH for iron contents equal to 60, 100, and 300 mg.L<sup>-1</sup> at contact times ( $t_{ct}$ ) of 0.5, 1, 2, 3, 4, and 26 h. One can note that these curves are to define the mechanisms of chromium adsorption involved in this case. Fig. 1 shows  $\log D = f(\text{pH})$  obtained

for various contact times and suspension amounts.

In acidic media,  $\log D = f(\text{pH})$  variations are linear until reaching a maximum ( $P \sim 90\%$ ) at  $\text{pH}_{\text{max}}$  ranging from 5 to 6, then decrease rapidly when the pH continues to rise. It must be noted that at given "m," the values of both  $\text{pH}_{\text{max}}$  and  $\delta \log D / \delta \text{pH}$  are dependent on the duration of adsorbent hydration. This indicates the absence of a predominant reaction and shows the absorption phenomenon's complexity, which seems to involve several reactions of fixation of Cr(VI) by iron hydroxide. According to the suspension medium's acidity, the variations in chromium(VI) retention with acidity are due to the protonation/deprotonation reaction of both chromic acid and sorbent surface groups ( $>\text{SOH}$ ). The first and second acidity constants of  $\text{H}_2\text{CrO}_4$  are respectively  $\text{p}K_{a1} = 0.75$  and  $\text{p}K_{a2} = 6.45$  [42]. At concentrations lower than 0.03 M, Cr(VI) exists mainly as hydrogen chromate  $\text{HCrO}_4^-$  at  $\text{pH} \leq 5.0$  ( $\geq 95\%$ ), chromate  $\text{CrO}_4^{2-}$  for  $\text{pH} \geq 7.6$  (95%), and as a

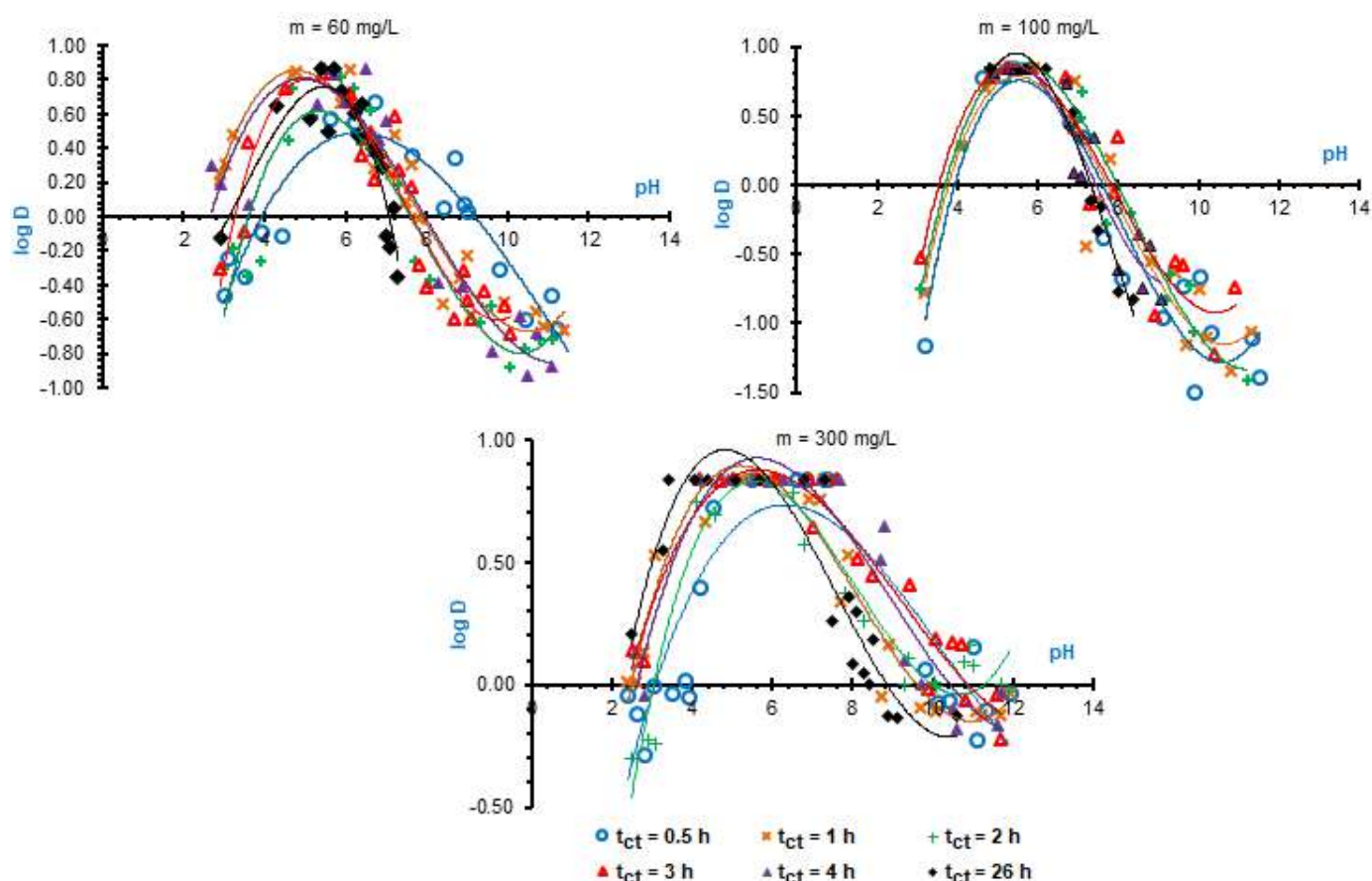


Fig 1. Log D versus pH for  $m = 60, 100,$  and  $300 \text{ mg/L}$  and contact times  $t_{ct} = 0.5, 1, 2, 3, 4,$  and  $26 \text{ h}$

mixture of these two species between pH 5.0 and 7.6. Moreover, the electrostatic and chemical sorption mechanisms are very rapid, that the kinetics cannot be used to differentiate between these two processes [43].

The maximum adsorption conditions are exhibited when the surface charge of the sorbent is opposite to that of the sorbate. Thus, the binding of weak acids is maximal at pH values close to the  $pK_a$  of these acids or to the PZC of the surface adsorbent materials [42-44]. Taking these considerations into account,  $H_2CrO_4$  can be considered a strong diprotic acid dissociated into  $HCrO_4^-$  and adsorbed electrostatically onto the positively charged hydroxide surface up to pH around PZC~7. It is shown from previous studies that the adsorption of Cr(VI) is, in general, optimal at pH values lower than 4 for various adsorbents such as some metal oxyhydroxides [45, 46], natural biosorbents such as larch bark [47], boiled tea leaves [48] and activated charcoal [49]. Also, optimum pH for adsorption of this metal ion is found to be ranging from 5 to 7 with various adsorbents such as clays [50], sands covered with oxides [50], zeolite and hydroxyapatite [51-52], aluminosilicate [50-53], apricot stone [54], bamboo waste [55] and seed-based biochar [56]. This acidity effect is considered to be due to the interaction of the surface sites ( $>SOH$ ) that is much greater with  $H^+$  ions than with sorbate anion. At pH greater than  $pH_{max}$ , Cr(VI) exhibits a typically anionic sorption behavior, and the adsorption decreases with increasing pH, as found in the retention of anions on iron oxides [57]. This behavior, usually observed at pH values higher than 6.0, is suggested to be due to the competition uptake of  $CrO_4^{2-}$  and  $OH^-$  anions by the surface of the adsorbent [58]. As a result, the obtained adsorption behavior involves the phenomena of protonation of the hydroxylated sites and the hydrolysis of chromium(VI). Thus, at pH higher than  $pH_{max}$ , the retention of Cr(VI) is due to the interaction of hydrogen chromate and/or chromate with  $>SOH$  surface groups rather than with  $>SOH_2^+$  groups that are predominating at pH below  $pH_{max}$  [59]. One can note that the non-integer values of  $\frac{\partial \log D}{\partial pH} = n$  is associated with two successive surface

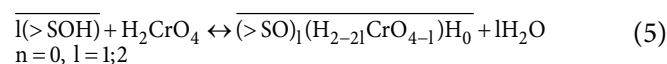
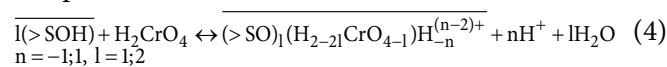
complexes [60].

### Variation of $\frac{\partial \log D}{\partial pH} = f(pH)$

As shown below in Eq. (15),  $\frac{\partial \log D}{\partial pH} = n$  corresponds to proton  $H^+$  ( $n > 0$ ) or hydroxyl  $OH^-$  ( $n < 0$ ), exchanged during the surface complexation reaction described by Eq. (9). Obtained results show that the mechanism of Cr(VI) adsorption with  $Fe(OH)_3$  sorbent occurs via electrostatic attraction or diffusion process ( $\frac{\delta \log D}{\delta pH} = 0$ ), proton ( $\frac{\delta \log D}{\delta pH} > 0$ ) and hydroxyl ( $\frac{\delta \log D}{\delta pH} < 0$ ) exchanges. In general, the adsorption phenomenon is a non-linear curve describing  $\log D = f(pH)$  variations. To determine the "n" value, equilibrium adsorption data are best fitted with cubic polynomial equation ( $R^2 > 0.99$ ), in various pH regions. Fig. 2 shows the variations  $n = f(pH)$  obtained for  $60 \text{ mg/L} \leq m \leq 300 \text{ mg/L}$ , at contact times varying between 0.5 and 26 h.

These results demonstrate that the pH of the sorbent system controls the ionic forms of the chromium solutions and the surface properties of the adsorbent. In all the cases, the variations  $n = f(pH)$  exhibits a similar behavior that is varying significantly with the contact time, in particular in acid conditions. The protonation/deprotonation of the sorbent is dependent on the surface coverage and varies between -1 and 1 for  $m = 60, 100, \text{ and } 300 \text{ mg/L}$ . The protonation phenomenon is prevailing at pH around 2, while coulombic/intra-particle diffusion adsorption is predominantly for pH ranging from 4.4 to 6.0. Furthermore, the deprotonation is prevailing at a pH of around 8 in all examined media.

Combining these mechanisms leads to the predominance of surface complexes ( $C_{in}$ ), whose nature depends on the acidity of the aqueous medium. These species are  $C_{00}$ ,  $C_{11}$ ,  $C_{21}$ ,  $C_{1-1}$ , and  $C_{2-1}$ . Taking these considerations into account, the predominant complexation reactions involved in this case are:



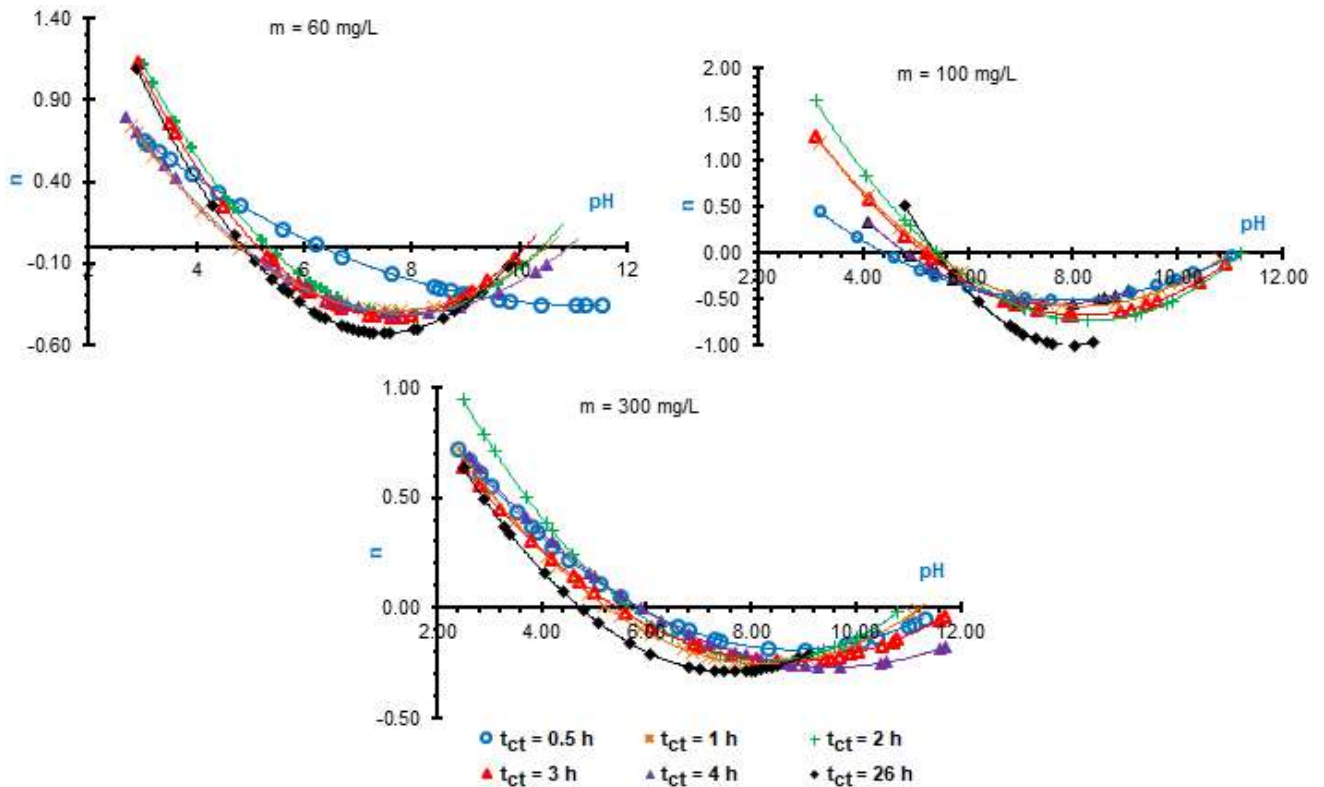
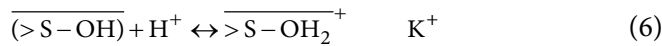


Fig 2. Variations of  $n = f(\text{pH})$  obtained for  $m = 60, 100, \text{ and } 300$  mg/L at contact times  $t_{ct} = 0.5, 1, 2, 3, 4, \text{ and } 26$  h

**Chromium(VI) Adsorption Mechanism and Stability Constants**

In general, the process of adsorption of ion metal with hydrated oxyhydroxides is described by the complexation reaction of a metal ion with active sites  $>S-OH$ . The acid-base properties of the surface of the adsorbents considered are attributed to the protonation/deprotonation reactions taking place on the surface of the sorbent and which can be expressed by:



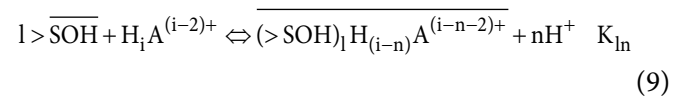
The highlighted species belong to the solid phase, so  $K^+$  and  $K^-$  refer to the stability constants for iron(III) hydroxide.

The symbols  $H_{-1}$  and  $H_1$  respectively denote the H atoms and the OH group. This leads therefore to:



The surface complexation of chromium ions,  $H_iCrO_4^{i-2}$ , by Iron hydroxide can be described by the Sillen notation,

generally adopted in complexing reactions in the aqueous phase.



with:  $i = 2; 1; 2, l = 1; 2, n = -1; 0; 1$ , and  $A = CrO_4^{2-}$   
Taking into account the expression of "D" given by:

$$D = \frac{|(>SOH)_l H_{i-n}A^{(i-n-2)+}|}{|H_iA^{(i-2)+}|} \quad (10)$$

The extraction constant is:

$$K_{ln} = \frac{|(>SOH)_l H_{i-n}A^{(i-n-2)+}| |H^+|^n}{|H_iA^{(i-2)+}| |>SOH|^l} \quad (11)$$

$$K_{ln} = \frac{|(>SOH)_l H_{i-n}A^{(i-n-2)+}| |H^+|^n}{|H_iA^{(i-2)+}| m^l} = \frac{D}{m^l} |H^+|^n \quad (12)$$

where  $|>SOH| = m$

$$\log K_{ln} = \log D - l \log m - npH \quad (13)$$

So that:

$$\log D = \log K_{ln} + l \log m + npH \quad (14)$$

According to these expressions, the study of the variation in the value of the distribution coefficient  $D$  as a function of  $pH$  makes it possible to verify the supposed binding mechanism and define the nature “ $n$ ” of the adsorbed species calculate the  $K_{ln}$  constants.

$$\frac{\partial \log D}{\partial pH} = n \quad (15)$$

$$\frac{\partial \log D}{\partial \log m} = l \quad (16)$$

### Study of Variations $A_{ln} = l \log m + \log K_{ln} = f(n)$

The surface complexation equilibrium constants are obtained from the line segments of the  $\log D = f(pH)$  curves. The slope of these segments leads to the value of “ $n$ ” while the y-intercept leads to  $A_{ln} = \log K_{ln} + l \log m$ . Fig. 3 illustrates the variations  $A_{ln} = f(n)$  for the successive contents of 60, 100, and 300 mg/L.

As shown, these variations are linear throughout the range of “ $n$ ” explored. They allow the calculation of  $A_{11}$ ;  $A_{10}$  and  $A_{1-1}$  relating to the various iron concentrations. So, the curve equation can be written in the form  $\log (A_{ln}) =$

$\log (A_{10}) + n \log (A_n - A_{10})$ . This equation can be obtained thermodynamically by considering that  $|n|$  also presents the fraction of the  $1 H^+$  or  $1 OH^-$  exchange reaction, contributing to the overall adsorption reaction.

### Study of the “ $l$ ” Order of Surface Complexes

The ordinate at the origin of the variations  $\log D = f(pH)$  is equal to  $A_{ln} = l \log m + \log K_{ln}$ . The exam of the variations  $A_{ln} = f(\log m)$  for  $n = 1; 0$  and  $-1$  (Fig. 4) make it possible to determine “ $l$ ” and  $\log K_{ln}$ .

Fig. 4 shows that the graphs  $A_{ln} = f(\log m)$  are linear whose slope values correspond to the “ $l$ ” parameter.

As a result, the adsorption process combines mononuclear and binuclear uptake mechanisms. Accordingly, the surface complexation constants are  $\log K_{1,1,1} = -3.28$ , and  $\log K_{1,3,-1} = 7.89$ . As shown,  $A_{10} = \log K_{10}$  are constants, indicating that the intrinsic reaction is no dependent on suspension amount. This means that this steeper Cr(VI) adsorption is, essentially, controlled by film diffusion. One can note that this external surface sorption is characterized by  $l = 0$ , in these conditions. The logarithmic variation of  $K_{ln}$  associated with different monodentate complexes resulting from surface

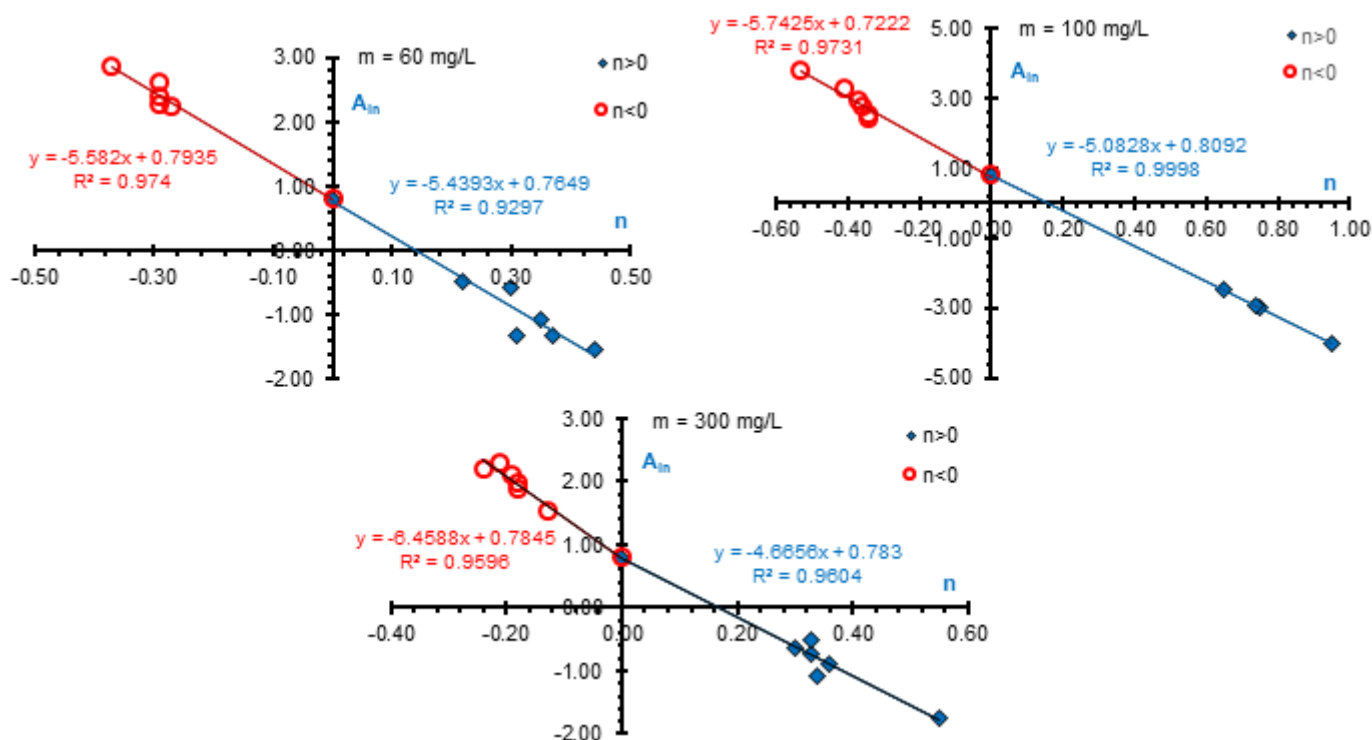


Fig 3. Variations of  $A_{ln} = f(n)$  obtained for  $m = 60, 100, \text{ and } 300 \text{ mg/L}$

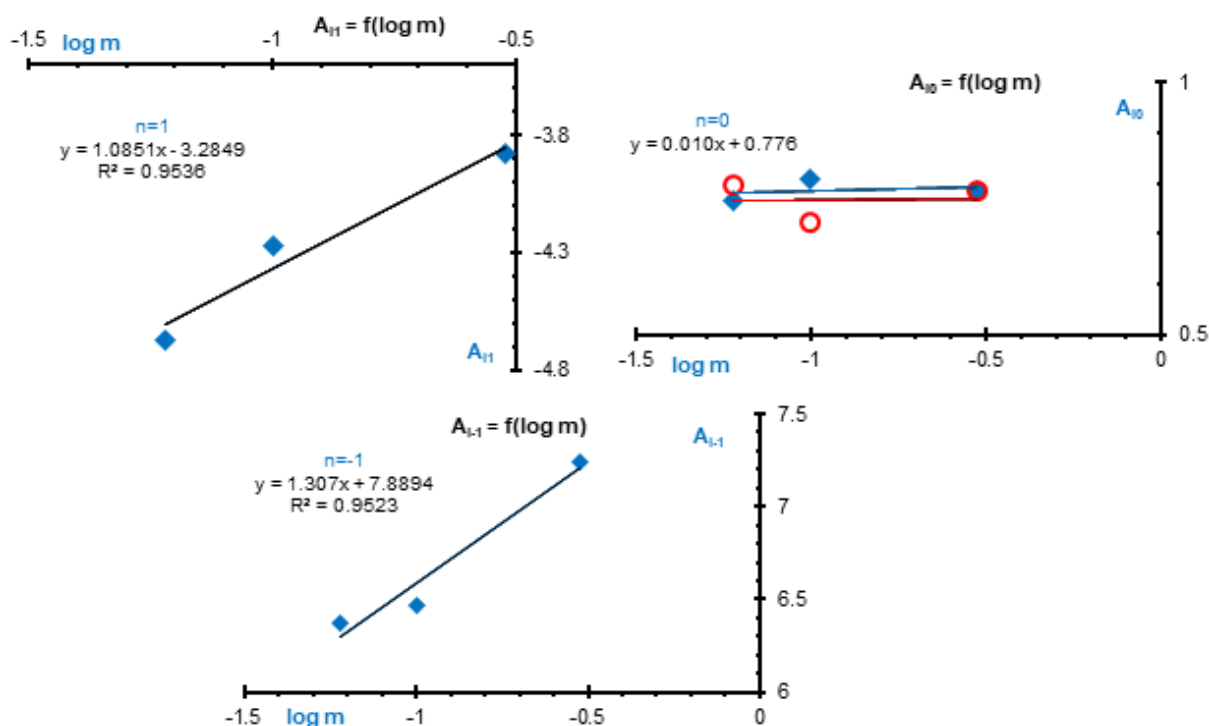


Fig 4. Variations of  $A_{ln} = f(\log m)$  obtained for  $n = -1; 0$  and  $1$  for different  $m$

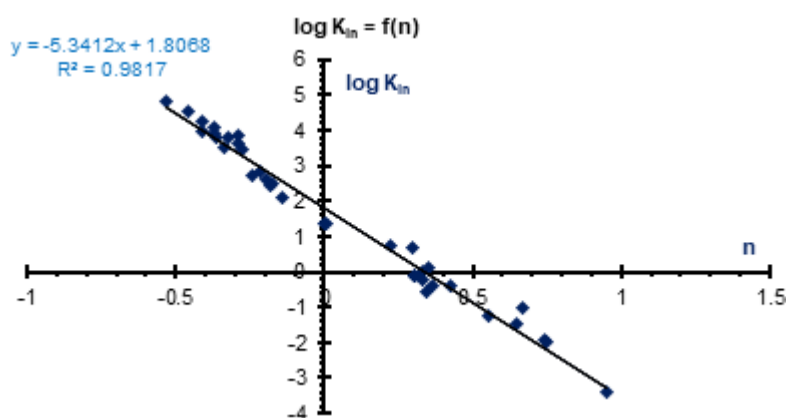


Fig 5. Variation  $\log K_{ln} = f(n)$  obtained from  $m = 60, 100$  and  $300$  mg/L

different surface protonation/deprotonation phenomena is shown in Fig. 5.

As found above, the straight line shows that the slope value equal to 'n', varies between -1 and 1. Therefore, the constants  $K_0$ ,  $K_{11}$  and  $K_{1-1}$  are the intersect and y-coordinates associated to (0,0); (1,1) and (1,-1) points of  $\log K_{ln} = f(n)$ , respectively. This information provides that the intrinsic constants  $K_{l0}$  or  $K_{00}$  (independent on  $l$ ), is such  $\log K_{00} = 1.81$ ,  $\log K_{11} = -3.53$ , and  $\log K_{1-1} = 7.15$ . The apparent constant value related to  $n = 0.35$  is such  $\log K_{10.35} = 0$ . Furthermore, the adsorption

reaction associated with apparent constant  $K_{l,z,1}$  is composed of mononuclear reaction ( $z\%$ ) and binuclear reaction ( $(1-z)\%$ ). This result can be used to calculate  $\log K_{2\pm 1}$  according to:

$$K_{1,1,1} = (K_{11})^{0.9}(K_{21})^{0.1}$$

$$K_{1,3,-1} = (K_{1-1})^{0.7}(K_{2-1})^{0.3}$$

This allows for obtaining  $\log K_{21} = -1.03$  and  $\log K_{2-1} = 9.62$ . Considering that adsorbed species are mono- and bidentate complexes, Table 1 summarizes the obtained results.

**Table 1.** Surface complexation and stability constants for Cr(VI) sorption onto Fe(III) hydroxide

(l,n)	Surface Complexation Reaction	log K <sub>ln</sub>	pH
(0,0)	$\overline{>SOH_2^+} + H_{2-y}A^{(y-2)} \Leftrightarrow \overline{(>SOH_2^+)(H_{2-y}A)^{-y}}$ y = 1; 2	1.81 ± 0.04	pH ≤ 5.5
(1,1)	$\overline{>SOH_2^+} + H_{2-y}A^{(y-2)} \Leftrightarrow \overline{>SOH_2^+ - (H_{2-y}A)H_{-1}^{(y-3)}} + H^+$ y = 1; 2	-3.53 ± 0.07	pH ≤ 5.5
(2,1)	$2\overline{>SOH_2^+} + H_{2-y}A^{(y-2)} \Leftrightarrow \overline{2(>SOH_2^+) - (H_{2-y}A)H_{-1} - S^{(y-3)}} + H_2O + H^+$ y=1; 2	-1.03±0.23	pH≤5.5
(1,-1)	$\overline{>SO^-} + A^{2-} + H_2O \Leftrightarrow \overline{>(SOH - A)^{2-}} + OH^-$	7.15 ± 0.14	pH ≥ 5.5
(2,-1)	$2\overline{>SO^-} + A^{2-} + H_2O \Leftrightarrow \overline{2(>(SOH - A - SO)^{4-})} + OH^-$	9.62 ± 0.53	pH ≥ 5.5

## ■ CONCLUSION

The adsorption of hexavalent chromium Cr(VI) on Fe(III) hydroxide was thoroughly investigated. For this purpose, a method was developed for studying the surface complexation of Fe(OH)<sub>3</sub> sorbent. The partition of Cr(VI) between the solid and liquid phases was examined as a sorbent mass function, contact time, and solution pH. The proton and hydroxyl ion exchange were evaluated to define the adsorption reaction and define surface complexes to achieve this purpose.

The study of log D = f(pH) experimental data (D = distribution coefficient = ratio of chromium in the solid and liquid phases), pointed out that the adsorption of Cr(VI) on Fe(III) hydroxide was greater than 90% in all cases, for pH values ranging between 4 and 6. Furthermore, the obtained results were used to specify the predominant chromium surface complexes. These results allowed the identification and formulation of these complexes according to the acidity of explored environments. These complexes concerned  $\overline{>S(OH_2^+)(HA^-)}$ ;  $\overline{>S(OH_2^+)(A^{2-})}$ ;  $\overline{>S(OH_2^+)(H_1A^{-1})}$ ;  $\overline{>S(OH_2^+)(A^{2-})}$ ;  $\overline{>S(OH_1^0)(A^{2-})}$ ;  $\overline{>(SOH_2^+) - (H_1A)H_{-1} - S^{(-2)}}$ ;  $\overline{>(SOH_2^+) - AH_{-1} - S^{(-1)}}$ ;  $\overline{>S(OH)(A^{2-})}$  and  $\overline{>(SOH_2^+ - A - SOH)^{4-}}$ . The complexing constants were calculated using the transformed curves of raw experimental data. The logarithmic values of these constants were: log K<sub>00</sub> = 1.81 ± 0.04, log K<sub>11</sub> = -3.53 ± 0.07, log K<sub>21</sub> = -1.03 ± 0.23, log K<sub>1,-1</sub> = 7.15 ± 0.14 and log K<sub>2,-1</sub> = 9.62 ± 0.53. Therefore, Fe(III) hydroxide exhibited high adsorption capacity for hexavalent chromium. Therefore,

this sorbent could be considered as excellent and reliable for the effective removal of Cr(VI) from wastewater solutions before dumping it into the environment.

## ■ ACKNOWLEDGMENTS

We are grateful for the facilities provided by the University Mohamed V, Rabat, to carry out this research work in the Applied Chemistry Laboratory Materials. It has provided us with all the necessary chemical products and measurement equipment. Also, we express our deepest gratitude and appreciation to Professor Bouhlassa S. and Sbihi K. (Ph.D. Student) for helping and making this research possible.

## ■ REFERENCES

- [1] Saha, R., Nandi, R., and Saha, B., 2011, Sources and toxicity of hexavalent chromium, *J. Coord. Chem.*, 64 (10), 1782–1806.
- [2] Praveen, P., and Loh, K.C., 2016, Thermodynamic analysis of Cr(VI) extraction using TOPO impregnated membranes, *J. Hazard. Mater.*, 314, 204–210.
- [3] Lim, S.F., and Lee, A.Y.W., 2015, Kinetic study on removal of heavy metal ions from aqueous solution by using soil, *Environ. Sci. Pollut. Res.*, 22 (13), 10144–10158.
- [4] Gorzin, F., and Abadi, M.M.B.R., 2017, Adsorption of Cr(VI) from aqueous solution by adsorbent prepared from paper mill sludge: Kinetic and thermodynamic studies, *Adsorpt. Sci. Technol.*, 36 (1-2), 149–169.
- [5] Nagajyoti, P.C., Lee, K.D., and Sreekanth, T.V.M., 2010, Heavy metals, occurrence and toxicity for



- plants: A review, *Environ. Chem. Lett.*, 8 (3), 199–216.
- [6] Singh, R., Gautam, N., Mishra, A., and Gupta, R., 2011, Heavy metals and living systems: An overview, *Indian J. Pharmacol.*, 43 (3), 246–253.
- [7] Zachara, J.M., Ainsworth, C.C., Brown, G.E., Catalano, J.G., McKinley, J.P., Qafoku, O., Smith, S.C., Szecsody, J.E., Traina, S.J., and Warner, J.A., 2004, Chromium speciation and mobility in a high level nuclear waste vadose zone plume, *Geochim. Cosmochim. Acta*, 68 (1), 13–30.
- [8] Duan, W., Chen, G., Chen, C., Sanghvi, R., Iddya, A., Walker, S., Liu, H., Ronen, A., and Jassby, D., 2017, Electrochemical removal of hexavalent chromium using electrically conducting carbon nanotube/polymer composite ultrafiltration membranes, *J. Membr. Sci.*, 531, 160–171.
- [9] Mayasari, H.E., and Sholeh, M., 2016, Kajian adsorpsi krom dalam limbah cair penyamakan kulit, *JKM*, 13 (2), 50–56.
- [10] Daraei, H., Mittal, A., Noorisepher, M., and Mittal, J., 2015, Separation of chromium from water samples using eggshell powder as a low-cost sorbent: Kinetic and thermodynamic studies, *Desalin. Water Treat.*, 53 (1), 214–220.
- [11] Athieh, M.A., 2011, Removal of chromium(VI) from polluted water using carbon nanotubes supported with activated carbon, *Procedia Environ. Sci.*, 4, 281–293.
- [12] Liu, H., Zhang, F., and Peng, Z., 2019, Adsorption mechanism of Cr(VI) onto GO/PAMAMS composites, *Sci. Rep.*, 9 (1), 3663.
- [13] Yussuff, A.S., 2019, Adsorption of hexavalent chromium from aqueous solution *Leucaena leucocephala* seed pod activated carbon: Equilibrium, kinetic and thermodynamic studies, *Arab J. Basic Appl. Sci.*, 26 (1), 89–102.
- [14] Li, I.L., Feng, X.Q., Han, R.P., Zang, S.Q., and Yang, G., 2017, Cr(VI) removal via anion exchange on a silver-triazolate MOF, *J. Hazard. Mater.*, 321, 622–628.
- [15] Pagilla, K.R., and Canter, L.W., 1999, Laboratory studies on remediation of chromium-contaminated soils, *J. Environ. Eng.*, 125 (3), 243–248.
- [16] Gheju, M., and Balcu, I., 2011, Removal of chromium from Cr(VI) polluted wastewaters by reduction with scrap iron and subsequent precipitation of resulted cations, *J. Hazard. Mater.*, 196, 131–138.
- [17] Golbaz, S., Jafari, A.J., Rafiee, M., and Kalantary, R.R., 2014, Separate and simultaneous removal of phenol, chromium, and cyanide from aqueous solution by coagulation/precipitation: Mechanisms and theory, *Chem. Eng. J.*, 253, 251–257.
- [18] Maximous, N.N., Nakhla, G.F., and Wan, W.K., 2010, removal of heavy metals from wastewater by adsorption and membrane processes: A comparative study, *World Acad. Sci. Eng. Technol.*, 40, 599–604.
- [19] Hu, J., Chen, G., and Lo, I.M.C., 2005, Removal and recovery of Cr(VI) from wastewater by maghemite nanoparticles, *Water Res.*, 39 (18), 4528–4536.
- [20] Yang, T., Han, C., Liu, H., Yang, L., Liu, D., Tang, J., and Luo, Y., 2019, Synthesis of Na-X zeolite from low aluminium coal fly: Characterization and high efficient As(V) removal, *Adv. Powder Technol.*, 30 (1), 199–206.
- [21] Nor, N.M., Kamil, N.H.N., Mansor, A.I., and Maarof, H.I., 2020, Adsorption analysis of fluoride removal using graphene oxide/eggshell adsorbent, *Indones. J. Chem.*, 20 (3), 579–586.
- [22] Razzouki, B., El Hajjaji, S., El Yahyaoui, A., Lamhamdi, A., Jaafar, A., Azzaoui, K., Bousaoud, A., and Zarouk, A., 2015, Kinetic investigation on arsenic(III) adsorption onto iron(III) hydroxide, *Pharm. Lett.*, 7 (9), 53–59.
- [23] Alvarez-Ayusco, E., Garcia Sanchez, A., and Querol, X., 2007, Adsorption of Cr(VI) from synthetic solutions and electroplating wastewaters on amorphous aluminium oxide, *J. Hazard. Mater.*, 142 (1-2), 191–198.
- [24] Hyder, A.H.M.G., Begum, S.A., and Egiebor, N.O., 2015, Adsorption isotherm and kinetic studies of hexavalent chromium removal from aqueous solution onto bone char, *J. Environ. Chem. Eng.*, 3 (2), 1329–1336.
- [25] Suryanti, V., Hastuti, S., Wahyuningsih, T.D., Mudasir, Kresnadipayana, D., and Wiratna, I., 2018, Heavy metal removal from aqueous solution using biosurfactants produced by *Pseudomonas*

- aeruginosa* with corn oil as substrate, *Indones. J. Chem.*, 18 (3), 472–478.
- [26] Selvi, K., Pattabhi, S., and Kadirvelu, K., 2001, Removal of Cr(VI) from aqueous solutions by adsorption onto activated carbon, *Bioresour. Technol.*, 80 (1), 87–89.
- [27] El Batouti, M., Ahmed, A.M.M., and Salam, S.M., 2016, Adsorption of toxic Ni(II) from aqueous solution by activated carbon, *Mor. J. Chem.*, 4 (4), 1130–1143.
- [28] Duranoğlu, D., Buyruklardan Kaya, İ.G., Beker, U., and Şenkal, B.F., 2012, Synthesis and adsorption properties of polymeric and polymer-based hybrid adsorbent for hexavalent chromium removal, *Chem. Eng. J.*, 181–182, 103–112.
- [29] Kobielska, P.A., Howarth, A.J., Farha, O.K., and Nayak, S., 2018, Metal-Organic frameworks for heavy metal removal from water, *Coord. Chem. Rev.*, 358, 92–107.
- [30] Yang, T., Han, C., and Luo, Y., 2019, Removal performance and mechanisms of Cr(VI) by an in-situ self-improvement of mesoporous biochar derived from chicken bone, *Environ. Sci. Pollut. Res.*, 27 (5), 5018–5029.
- [31] Kristianto, H., Daulay, N., and Arie, A.A., 2019, Adsorption of Ni(II) ion onto calcined eggshells: A study of equilibrium adsorption isotherm, *Indones. J. Chem.*, 19 (1), 143–150.
- [32] Taher, T., Irianty, Y., Mohadi, R., Said, M., Andreas, R., and Lesbani, A., 2019, Adsorption of cadmium(II) using Ca/Al layered double hydroxides intercalated with Keggin ion, *Indones. J. Chem.*, 19 (4), 873–881.
- [33] Mahatmanti, F.W., Nuryono, and Narsito, 2016, Adsorption of Ca(II), Mg(II), Zn(II), and Cd(II) on chitosan membrane blended with rice hull ash silica and polyethylene glycol, *Indones. J. Chem.*, 16 (1), 45–52.
- [34] Handayani, D.S., Jumina, Siswanta, D., Mustofa, Ohto, K., and Kawakita, H., 2011, Adsorption of Pb(II), Cd(II), and Cr(III) from aqueous solution by poly-5-allyl-calix[4]arene tetracarboxylic acid, *Indones. J. Chem.*, 11 (2), 191–195.
- [35] Abdul, A.S., Muhammad, A.S., Ibrahim, M.A., and Ibrahim, M.B., 2019, Thermodynamic study on the adsorptive removal of Cr(VI) and Ni(II) metal ions using Schiff base as adsorbent, *Mor. J. Chem.*, 7 (3), 506–515.
- [36] Jang, E.H., Pack, S.P., Kim, I., and Chung, S., 2020, A systematic study of hexavalent chromium adsorption and removal from aqueous environments using chemically functionalized amorphous and mesoporous silica nanoparticles, *Sci. Rep.*, 10, 5558.
- [37] Tang, B., and Hang, Z., 2014, Essence of disposing the excess sludge and optimizing the operation of wastewater treatment: Rheological behavior and microbial ecosystem, *Chemosphere*, 105, 1–13.
- [38] Jolivet, J.P., Henry, M., and Livage, J., 1994, *De la Solution à l'Oxyde. Condensation des cations en solution aqueuse, chimie de surface des oxydes*, CNRS Editions, Inter Editions, Paris.
- [39] Elyahyaoui, A., Ellouzi, K., Al Zabadi, H., Razzouki, B., Bouhlassa, S., Azzaoui, K., Mejdoubi, E., Hamed, O., Jodeh, S., and Lahmamdi, A., 2017, Adsorption of chromium(VI) on calcium phosphate: Mechanisms and stability constants of surface complexes, *Appl. Sci.*, 7 (3), 222.
- [40] Forsling, L., Wu, W., and Schindler, P.W., 1991, Surface complexation of calcium minerals in aqueous solution: 1. Surface protonation at fluorapatite-water interfaces, *J. Colloid Interface Sci.*, 147 (1), 178–185.
- [41] AFNOR-French Agency for Standardization, 1997, *Water Quality. Tome1: Terminology, Sampling and Assessment Methods*, 3<sup>rd</sup> Ed., AFNOR Publishing, Paris, France.
- [42] Samaké, D., 2008, *Traitement des eaux usées de tannerie à l'aide de matériaux à base d'argile, Dissertation*, Université Joseph Fourier-Grenoble et de Bamako, Mali.
- [43] Lorphensri, O., Intravijit, J., Sabatini, D.A., Kibbey, T.C.G., Osathaphan, K., and Saiwan, C., 2006, Sorption of acetaminophen, 17 $\alpha$ -ethynyl estradiol, nalidixic acid, and norfloxacin to silica, alumina and

- a hydrophobic medium, *Water Res.*, 40 (7), 1481–1491.
- [44] Harding, I.S., Rashid, N., and Hing, K.A., 2005, Surface charge and the effect of excess calcium ions on the hydroxyapatite surface, *Biomaterials*, 26 (34), 6818–6826.
- [45] Demetriou, A., and Pashalidis, I., 2012, Spectrophotometric studies on the competitive adsorption of boric acid (B(III)) and chromate (Cr(VI)) onto iron (oxy) hydroxide (Fe(O)OH), *Global NEST J.*, 14 (1), 32–39.
- [46] Chowdhury, S.R., and Yanful, E.K., 2010, Arsenic and chromium removal by mixed magnetite-maghemite nanoparticles and the effect of phosphate on removal, *J. Environ. Manage.*, 91 (11), 2238–2247.
- [47] Krishna, H.R., and Swamy, A.V.V.S., 2012, Investigation on the adsorption of hexavalent chromium from the aqueous solutions using powder of papaya seeds as a sorbent, *Int. J. Environ. Sci. Res.*, 2 (1), 119–125.
- [48] Talokar, A.Y., 2011, Studies on removal of chromium from waste water by adsorption using low cost agricultural biomass as adsorbents, *Int. J. Adv. Biotechnol. Res.*, 2 (4), 452–456.
- [49] Gholipour, M., Hashemipour, H., and Mollashahi, M., 2011, Hexavalent chromium removal from aqueous solution via adsorption on granular activated carbon: Adsorption, desorption, modeling and simulation studies, *ARPJ. Eng. Appl. Sci.*, 6 (9), 10–18.
- [50] Wu, X.W., Ma, H.W., and Zhang, Y.R., 2010, Adsorption of chromium(VI) from aqueous solution by a mesoporous aluminosilicate synthesized from microcline, *Appl. Clay Sci.*, 48, 538–541.
- [51] Pandey, P.K., Sharma, S.K., and Sambhi, S.S., 2010, Kinetics and equilibrium study of chromium adsorption on zeolite NaX, *Int. J. Environ. Sci. Technol.*, 7 (2), 395–404.
- [52] Soundarajan, M., Gomathi, T., and Sudha, P.N., 2013, Understanding the adsorption efficiency of chitosan coated carbon on heavy metal removal, *IJSRP*, 3 (1), 1–10.
- [53] Fellenz, N., Martin, P., Marchetti, S., and Bengoa, F., 2015, Aminopropyl-modified mesoporous silica nanospheres for the adsorption of Cr(VI) from water, *J. Porous Mater.*, 22 (3), 429–738.
- [54] Abbas, M., and Trari, M., 2015, Kinetic, equilibrium and thermodynamic study on the removal of Congo Red from aqueous solutions, *Process Saf. Environ. Prot.*, 98, 424–436.
- [55] Dula, T., Siraj, K., and Kitte, S.A., 2014, Adsorption of hexavalent chromium from aqueous solution using chemically activated carbon prepared from locally available waste of bamboo (*Oxytenanthera abyssinica*), *Int. Scholarly Res. Not.*, 2014, 438245.
- [56] Ghazi, M., Oladipo, A.A., and Azalok, K.A., 2018, High efficient and magnetically separable palm seed-based biochar for the removal of nickel, *Sep. Sci. Technol.*, 53 (7), 1124–1131.
- [57] Farley, K.J., Dzombak, D.A., and Morel, F.M.M., 1985, A surface precipitation model for the sorption of cations on metal oxides, *J. Colloid Interface Sci.*, 106 (1), 226–242.
- [58] Attia, A.A., Khedr, S.A., and Elkholy, S.A., 2010, Adsorption of chromium ion (VI) by acid activated carbon, *Braz. J. Chem. Eng.*, 27 (1), 183–193.
- [59] Correa, F.G., Gómez, J.S., and Martínez, J.B., 2010, “Síntesis y caracterización de materiales inorgánicos para ser empleados como adsorbentes de metales tóxicos y de interés nuclear” in *Contribuciones del Instituto Nacional de Investigaciones Nucleares al avance de la Ciencia y la Tecnología en México, Commemorative Edition 2010*, Instituto Nacional de Investigaciones Nucleares, Ocoyoacac, Mexico, 195–210.
- [60] Müller, A., and Sigg, L., 1992, Adsorption of lead(II) on the goethite surface: Voltammetric evaluation of surface complexation parameters, *J. Colloid Interface Sci.*, 148 (2), 517–532.

## Carotenoid Analysis from Commercial Banana Cultivars (*Musa spp.*) in Malang, East Java, Indonesia

Jodiawan<sup>1</sup>, Devi Natalia Chrisdiyanti<sup>1</sup>, Nur Vi'atin<sup>1</sup>, Monika Nur Utami Prihastyanti<sup>2</sup>, Rosita Dwi Chandra<sup>2</sup>, Heriyanto<sup>1,2,3</sup>, Chandra Ayu Siswanti<sup>2</sup>, Lia Hapsari<sup>4</sup>, and Tatas Hardo Panintingjati Brotosudarmo<sup>1,2\*</sup>

<sup>1</sup>Department of Chemistry, Faculty of Science and Technology, Universitas Ma Chung, Villa Puncak Tidar N-01, Malang 65151, East Java, Indonesia

<sup>2</sup>Ma Chung Research Center for Photosynthetic Pigments (MRCPP), Universitas Ma Chung, Villa Puncak Tidar N-01, Malang 65151, East Java, Indonesia

<sup>3</sup>Faculty of Biochemistry, Biophysics and Biotechnology, Jagiellonian University, Ul. Gronostajowa 7, 30-387 Krakow, Poland

<sup>4</sup>Purwodadi Botanic Garden, Research Center for Plant Conservation and Botanic Gardens, Indonesian Institute of Sciences (LIPI), Jl. Raya Surabaya – Malang KM. 65, Purwodadi, Pasuruan 67163, East Java, Indonesia

---

\* **Corresponding author:**

tel: +62-341-550171

email: tatas.brotosudarmo@machung.ac.id

Received: October 26, 2020

Accepted: January 8, 2021

DOI: 10.22146/ijc.60865

**Abstract:** Banana, as the world's most consumed fruit, is a good source of carbohydrate, potassium, fiber, and other essential nutrients such as pro-vitamin A carotenoids. The carotenoid contents and compositions in bananas commonly sold in fruit shops in Malang have become interesting studies. Five types of banana, i.e., Berlin, Mas, Cavendish, Candi, and Raja, were characterized using high-performance liquid chromatography and UV-Vis spectrophotometer. The carotenoid concentrations ranged between 347–3,660 µg/100 g dry weight (dw), with the level of vitamin A activity at the range between 6-139 µg RAE/100 g dw. The Mas banana had a higher carotenoid concentration compared to the Berlin, Candi, Raja, and Cavendish varieties.

**Keywords:** banana; carotenoid concentration; carotenoid identification; Malang; vitamin A activity

---

### ■ INTRODUCTION

Carotenoids have been proven as compounds that are able to support biological functions in the human cellular system, such as vitamin A activity, antioxidant functions, and immune system enhancers [1-3]. Nevertheless, several diseases in developing countries related to vitamin A deficiency, cancer, cardiovascular disease, cataracts, and age-related macular degeneration (AMD) are still becoming public attention issues [4]. Due to the inability of cells to biosynthesize carotenoids, humans need diet intake rich in carotenoids to reduce the risk of these chronic illnesses [5]. The main dietary carotenoids generally come from yellow-orange fruits or

vegetables, such as bananas which are food commodities that contain carotenoids [6-7].

Globally, people have labeled bananas as the world's fourth staple food after rice, wheat, and maize [8-9]. Interestingly, besides being rich in nutrients and energy, bananas also contain carotenoid pigments, which consist of three main carotenoids:  $\alpha$ -carotene,  $\beta$ -carotene, and lutein [10-11].  $\alpha$ -Carotene and  $\beta$ -carotene are pro-vitamin A carotenoids in which each compound can produce one and two retinal molecules in the body [5]. Lutein is a macular carotenoid that can protect the photoreceptor cell of the eye [12]. Consumption of banana flesh could provide supply of pro-vitamin A carotenoids to the human body [7].

As a tropical country, Indonesia has considerable potential for the diversity of bananas, which currently there were at least 1,000 cultivars distributed in 16 provinces of banana production centers in Indonesia [13]. Banana production in Indonesia has increased from 6.9 billion tons in 2014 to 7.3 billion tons in 2018, which means the production grew by 5.86% within 5 years. East Java produced 2.1 billion tons of banana in 2018, increasing 54.11% from 1.3 billion tons in 2014, leading to the largest banana production in Indonesia in the same year. Bananas are largely produced in certain regions in East Java, such as Malang, Jember, Lumajang, Bojonegoro, and Pasuruan. In Malang district itself, 32 banana varieties were cultivated by the local communities with a total production of approximately 9,728 tons in 2018, which was the largest production in East Java province [14-16].

The above-mentioned data suggest that an enormous number of bananas have been produced to fulfill consumers' need for a healthy diet. However, people's knowledge on bananas may be limited to Cavendish due to its considerable amount of trade. Food and Agriculture Organization (FAO) claimed that Cavendish dominated 45% of global production in which 50 billion tons of Cavendish have been globally produced annually. This considerable amount of Cavendish production may be due to its ability to generate high yields and its strength towards environmental issues, such as storms [17]. On the other hand, a lot of banana types have been cultivated in Indonesia other than Cavendish. In fact, 79 cultivars of bananas were found in East Java, moreover, 33 types among them have been cultivated in the Malang region [18]. Recent study on pro-vitamin A carotenoids in local banana cultivar widely grown in Lumajang, East Java, *i.e.* Agung Semeru banana (*Musa paradisiaca* L. AAB), revealed that vitamin A activity of it was at  $457.33 \pm 5.18$   $\mu\text{g}$  retinol activity equivalents (RAE)/100 g dry weight (dw) [19]. This fact indicates that local banana cultivars should be taken into consideration as they may have great potential to enhance people's diet of vitamin A.

This enormous amount of local banana cultivars production combined with the content of carotenoids

makes bananas as potential fruit source for daily nutrition intake. However, limited information on the total carotenoids of banana cultivars are reported, specifically, those cultivated and commercialized in the Malang region. Therefore, this study aimed to identify, quantify, and evaluate the carotenoid contents of selected bananas cultivated and commercialized in Malang, Indonesia. The selected banana cultivars to be observed were dessert bananas (Berlin, Cavendish, Mas), plantain bananas (Candi) and that which could be served as both (Raja). Identification and quantification of total carotenoids, major carotenoids, and vitamin A activity of five cultivars of banana were carried out by spectrophotometry and chromatographic methods. The information on carotenoid compositions and concentrations as well as vitamin A activity of these bananas obtained in this study may enrich people's knowledge on the function of carotenoid contents of these bananas, thus, leads to a comprehensive understanding on a healthy diet.

## ■ EXPERIMENTAL SECTION

### Materials

Five cultivars of banana were used in this study, *i.e.* Berlin (*Musa acuminata* AA), Mas (*M. acuminata* AA) and Cavendish (*M. acuminata* AAA), all of those were classified as dessert bananas, as well as Candi (*M. paradisiaca* AAB) which is classified as plantain, and Raja (*M. paradisiaca* AAB) which can play role both as dessert and plantain. The whole fruit and half-fruit longitudinal cross-section are depicted in Fig. 1. All the cultivars were purchased from several local markets in Malang, Indonesia. The selected bananas were the ones that had entered ripening stage 6 to 7, indicated by yellow skin color with several brown spots on the surface area, thus, were ready-to-eat [20]. For analytical purposes, the fresh flesh was taken, immediately sliced, ground using mortar, and stored in the sample tube. These following chemicals, *i.e.*, calcium carbonate ( $\text{CaCO}_3$ ), ethanol (EtOH), tetrahydrofuran (THF), *n*-hexane, acetone, methyl *tert*-butyl ether (MTBE), methanol (MeOH), water (Merck), and sodium-*L*-ascorbate (Chameleon), were used for extraction and

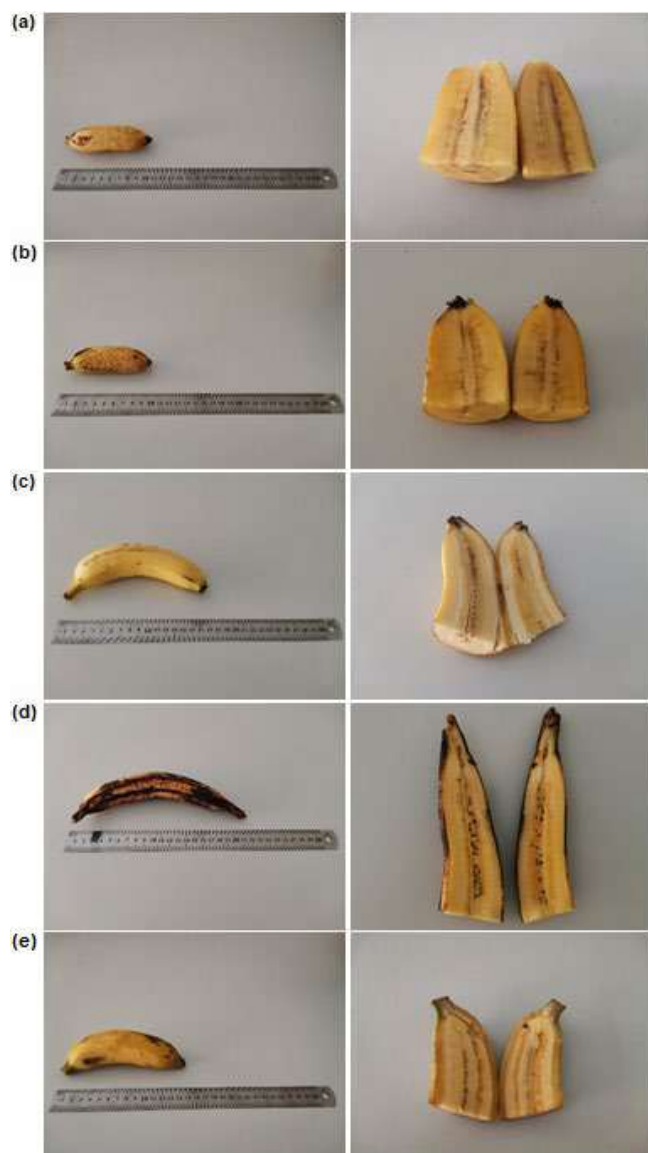


**Fig 1.** Whole fruit (left) and half-fruit longitudinal cross-section (right) of Berlin (a), Mas (b), Cavendish (c), Candi (d), and Raja (e) bananas

analytical purposes. Lutein,  $\alpha$ -carotene, and  $\beta$ -carotene standard pigments ( $\geq 95\%$  purity level) were obtained from NATChrom (Malang, Indonesia).

### Instrumentation

The absorption spectra of pigment extracts were recorded using a UV-Vis spectrophotometer (UV 1700 Shimadzu). It was also used for the total carotenoids determination of the bananas. High-performance liquid chromatography (HPLC) system (Shimadzu) equipped with a photodiode array detector (LC20A) and column

oven (CTO-20A) was used to determine the carotenoid compositions and concentrations of the banana cultivars.

### Procedure

#### Carotenoid extraction

Carotenoid extraction was performed based on a previously reported procedure with several modifications [10,19]. In a dark room, 3 g of flesh aliquot were mixed with trace amount of  $\text{CaCO}_3$  and sodium-*L*-ascorbate, then stirred for 10 min at 120 rpm in a 10 mL solvent extraction mixture containing EtOH and THF (4:3, v/v). The yellow filtrate containing carotenoids was collected, then the extraction process was repeated four times toward the residue until it became colorless. Furthermore, all carotenoid extracts were combined and transferred in a separatory funnel to be separated from any contaminants by the addition of water and *n*-hexane. The organic layer containing carotenoids was then collected, and the remaining solvent was removed using a rotary evaporator (Heidolph, Schwabach, Germany) at 35 °C. All extraction was performed in duplicate.

#### Total carotenoids analysis

The carotenoid extracts in acetone were subjected to UV-Vis spectroscopy measurement (UV-1700, Shimadzu) to record the absorption spectrum and then to determine the total carotenoids. Sample was diluted by 10 prior to the measurement. Total carotenoids (in  $\mu\text{g}$  carotenoid/100 g dw) were determined using formulation modified from Gross as follows [21]:

$$\text{Total Carotenoid} = \frac{A \times V \times 10^6}{A_{1\text{cm}}^{1\%} \times 100 \times G} \times \frac{100}{100 - \text{moisture content}(\%)} \quad (1)$$

where *A* represents absorbance at maximum absorption wavelength ( $\lambda_{\text{max}}$ ); *V* is volume of carotenoid extract (mL); *G* is weight of sample (g);  $A_{1\text{cm}}^{1\%}$  is specific absorbance extinction of carotenoid mixture in acetone, *i.e.* 2,500 (mL/(g × cm)). Moisture content was measured using a moisture analyser (MOC63u, Shimadzu).

#### Determination of carotenoid compositions and major carotenoid concentrations

The carotenoid compositions and major carotenoid concentrations were determined by means of

HPLC (Shimadzu, Kyoto, Japan), following the method suggested by Kurniawan et al. [22]. The dry carotenoid extract was re-dissolved in 1 mL of acetone and filtered using a PTFE membrane syringe (0.22  $\mu\text{m}$ , Shimadzu), then 20  $\mu\text{L}$  of the extract was injected into the reversed-phase (RP) HPLC. The separation of pigment was carried out by RP-HPLC using a YMC C30 column (150  $\times$  4.6 mm ID) (YMC, Wilmington, MA, USA), column oven (CTO-20A) at 30  $^{\circ}\text{C}$ , and photo-diode array detector (LC20A). The elution gradient program was regulated by a mixture of MeOH, MTBE, and H<sub>2</sub>O (81:15:4, v/v/v) at 0 min to (6:90:4, v/v/v) at 70 min at 30  $^{\circ}\text{C}$  with a flow rate of 1 mL/min.

Carotenoid identification was performed based on chromatography result of lutein,  $\alpha$ -carotene, and  $\beta$ -carotene standard pigments from a previously described report by Chandra et al. [19]. The lutein,  $\alpha$ -carotene, and  $\beta$ -carotene standard pigments in the chromatogram were eluted at 8.3 min, 23.5 min, and 26.4 min, respectively. The absorption spectrum properties of peaks (shape or pattern and  $\lambda_{\text{max}}$ ) from the banana samples obtained at the same retention time ( $t_{\text{R}}$ ) were compared with those of standard pigments to confirm pigments identification.

Peak area of major carotenoids at  $\lambda_{\text{max}}$  of each banana cultivars obtained from HPLC was used to calculate the concentration of lutein,  $\alpha$ -carotene, and  $\beta$ -carotene (in  $\mu\text{g}/100$  g dw) by using standard linear equations developed by Chandra et al. [19] and Kurniawan et al. [22], *i.e.*:

$$\text{Lutein : } y = 305.8x - 0.6335, R^2 = 0.9999 \quad (2)$$

$$\alpha\text{-carotene : } y = 232.04x - 47.906, R^2 = 0.9950 \quad (3)$$

$$\beta\text{-carotene : } y = 206.57x - 74.953, R^2 = 0.9982 \quad (4)$$

where  $y$  and  $x$  are peak area ( $\times 10^{-3}$ ) at  $\lambda_{\text{max}}$  and concentration of measured pigment ( $\mu\text{g}/\text{mL}$ ), respectively.

#### Vitamin A activity

Vitamin A activity was described based on concentrations of  $\alpha$ -carotene and  $\beta$ -carotene, both are known as pro-vitamin A carotenoids. The concentration of pro-vitamin A carotenoids was converted into retinol activity equivalent (RAE) using a conversion factor of 24:1 for  $\alpha$ -carotene and 12:1 for  $\beta$ -carotene.

#### Statistical analysis

All values were performed as means  $\pm$  standard deviation (SD) of two replicates. Statistical analysis of total carotenoids, lutein,  $\alpha$ -carotene, and  $\beta$ -carotene concentrations, and vitamin A activity was performed using one-way analysis of variance (ANOVA). When a significant difference was found, Tukey's Honest Significant Difference test was performed in Minitab software version 17 (Minitab, State College, PA, USA) with 95% confidence level ( $p < 0.05$ ).

## RESULTS AND DISCUSSION

The initial study of yellow pigment from five banana cultivars was carried out based on spectroscopic analysis by comparing the total carotenoids of each flesh crude extract. Fig. 2 shows the absorption spectra of crude carotenoid extracts from each sample in 1 g of dw basis, where the absorbance value at  $\lambda_{\text{max}}$  represents the total value of the carotenoid. Based on the absorbance height of each banana cultivar in Fig. 2, ones can observe that the banana cultivars showed a different concentration of carotenoid. For instance, having the highest absorbance

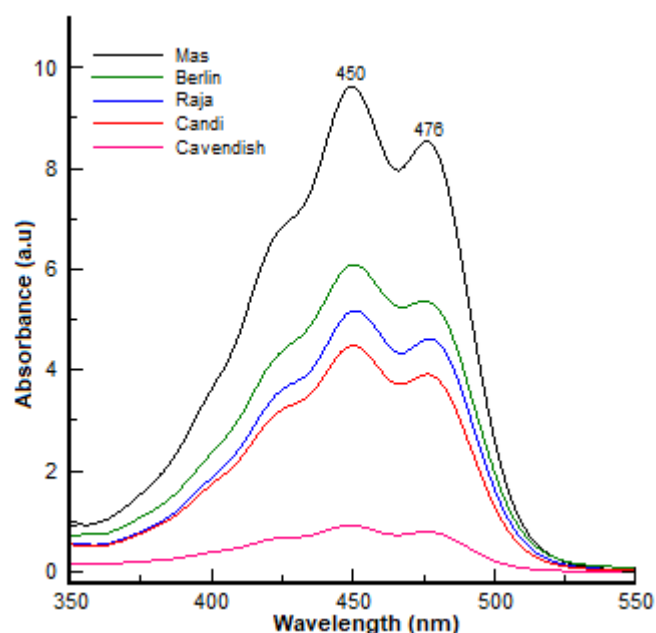


**Fig 2.** Absorption spectra of carotenoid crude extracts from Mas (black line), Berlin (green line), Raja (blue line), Candi (red line), and Cavendish (magenta line). All extracts were dissolved in 1 mL of acetone and calculated in 1 g dw basis

value, Mas banana would have the highest carotenoid concentration. On the other hand, Cavendish was most likely exhibiting the lowest carotenoid concentration based on its extremely low intensity. Moreover, all samples provided the same  $\lambda_{\max}$  and shoulder peak at 450 nm and 476 nm, respectively. This suggests that the major carotenoid compositions and concentrations will be further discussed.

The banana flesh color indicates the carotenoid contents as can be observed from Fig. 1. For instance, Mas banana exhibited the most intensive orange color among the five banana cultivars, whereas Cavendish showed the least intensive yellow. The difference in flesh color among the cultivars suggests that the carotenoid contents were also varied. One can roughly conclude that Mas banana would have the highest carotenoid content, while Cavendish showed the least. Table 1 shows the total carotenoids in the five banana cultivars which suggests that Mas bananas contained the highest total carotenoids compared to the other four cultivars with 3,660  $\mu\text{g}/100\text{ g dw}$ . On the contrary, Cavendish shows the least carotenoid among others with only 347  $\mu\text{g}/100\text{ g dw}$ . The value in Table 1 corresponds to the absorbance value of the bananas shown in Fig. 2. Higher absorbance value indicates higher concentration of carotenoid in the

bananas. The result of the ANOVA statistical test suggests significant differences among cultivars, with  $p$  values of 0.00 ( $p < 0.05$ ). Tukey's multiple comparisons confirmed that the total carotenoids in each sample were significantly different from one another, nevertheless, Raja was not significantly different from Berlin and Candi. According to the recommendation for the prevention of cancer and other chronic diseases from the National Academy of Sciences which recommends carotenoid consumption in the range of 9 to 18 mg/day [23], the human carotenoid requirement could be then fulfilled properly with consumption of 300 to 600 g of Mas banana.

Analysis of total carotenoids describes the total concentration of all carotenoid compounds contained in the bananas. Moreover, to understand the carotenoid compositions and contents, HPLC analysis was performed. HPLC chromatogram of pigment compositions is shown in Fig. 3 which reveals peaks of three major carotenoids possessed by the bananas, *i.e.* lutein,  $\alpha$ -carotene, and  $\beta$ -carotene. The identification of the major carotenoid compounds was based on the spectra shape,  $\lambda_{\max}$ , and retention time ( $t_R$ ) in the standard pigment chromatogram described in the previous study by Chandra et al. [19]. Peak #1 was identified as lutein,

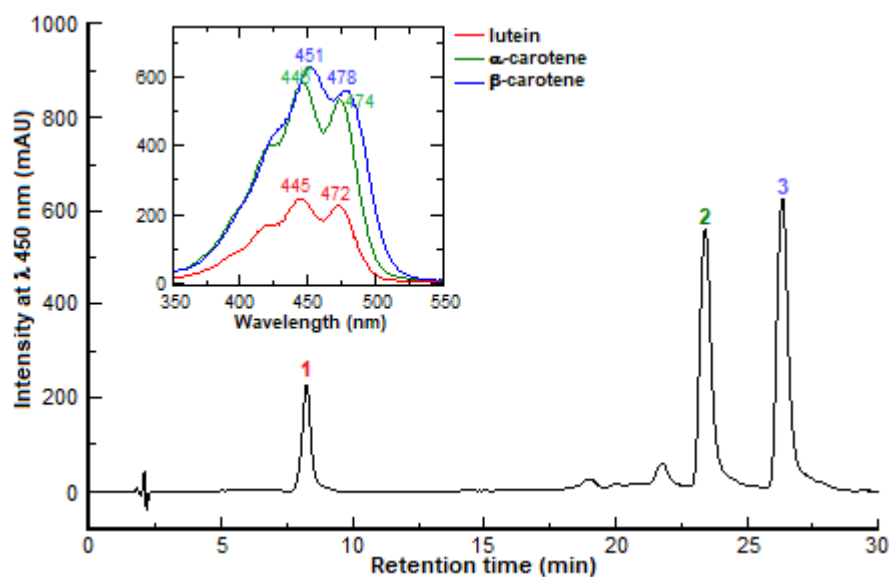


**Fig 3.** HPLC chromatogram detected at 450 nm of carotenoid crude extracts from Candi bananas. The intensity was calculated in 1 g dw basis. Inset: absorption spectra of lutein (red line, peak #1),  $\alpha$ -carotene (green line, peak #2), and  $\beta$ -carotene (blue line, peak #3) in HPLC eluent



with  $\lambda_{\text{max}}$  at 445 and 472 nm, and eluted at min 8.4. Peak #2 corresponds to  $\alpha$ -carotene due to its absorption at 446 and 474 nm and detected at min 23.4. Peak #3 was eluted at min 26.3 having  $\lambda_{\text{max}}$  at 451 and 478 nm, thus, identified as  $\beta$ -carotene. Previous studies also reported these compounds as major carotenoids in other banana cultivars in several regions in the world, such as in Australia, Africa, and Asia [10,24-27].

Table 1 and Fig. 4 show that each cultivar exhibited different trends in its carotenoid concentration. Raja contained  $\beta$ -carotene in a higher concentration than  $\alpha$ -carotene and lutein. Candi and Berlin seemed to follow the same pattern as Raja, however, only a slight difference was found in the concentration of  $\alpha$ -carotene and  $\beta$ -carotene between those two cultivars. On the other hand, Mas banana contained  $\alpha$ -carotene 1.7 and 6.0 times higher than  $\beta$ -carotene and lutein. Meanwhile, the amount of lutein in Mas, Berlin, Raja, and Candi was relatively low. Compared to  $\alpha$ -carotene and  $\beta$ -carotene, the amount of lutein in Mas bananas was 6.0 and 3.5 times

lower. In Raja, lutein was found 4.7 and 5.8 times lower than  $\alpha$ -carotene and  $\beta$ -carotene. Much lower concentration of lutein was also found in Candi, in which lutein was 10.6 and 10.9 times lower than  $\alpha$ -carotene and  $\beta$ -carotene, and in Berlin, where lutein was 12.8 and 13.0 times lower than  $\alpha$ -carotene and  $\beta$ -carotene. Interestingly, Cavendish bananas were known to produce lutein in a greater quantity than the other two compounds, covering approximately 50% of the whole major carotenoid.

Furthermore, the concentration of the major pigments varied among all cultivars. Mas bananas showed the highest content of lutein, *i.e.* 258.65  $\mu\text{g}/100$  g dw, followed by Raja, Cavendish, Berlin, and Candi bananas. Concentration of  $\alpha$ -carotene remains the highest in Mas bananas, followed by Berlin, Raja, Candi, and Cavendish bananas. On the other hand, Raja bananas showed a great amount of  $\beta$ -carotene among other cultivars, followed by Mas, Berlin, Candi, and Cavendish bananas. Table 1 shows that the concentration

**Table 1.** Concentration of total carotenoids and major carotenoids from five banana cultivars

Banana cultivars	Concentration ( $\mu\text{g}/100$ g dw $\pm$ SD)			
	Total carotenoids	Lutein	$\alpha$ -carotene	$\beta$ -carotene
Mas	3,669.59 $\pm$ 485.28 <sup>a</sup>	258.65 $\pm$ 35.80 <sup>a</sup>	1,556.22 $\pm$ 9.75 <sup>a</sup>	900.69 $\pm$ 73.57 <sup>ab</sup>
Berlin	2,554.14 $\pm$ 210.56 <sup>b</sup>	67.81 $\pm$ 4.94 <sup>c</sup>	870.89 $\pm$ 1.62 <sup>b</sup>	884.69 $\pm$ 54.70 <sup>ab</sup>
Raja	2,089.60 $\pm$ 206.29 <sup>bc</sup>	170.54 $\pm$ 34.05 <sup>ab</sup>	806.26 $\pm$ 5.03 <sup>c</sup>	983.85 $\pm$ 10.30 <sup>a</sup>
Candi	1,777.77 $\pm$ 278.80 <sup>c</sup>	64.38 $\pm$ 4.71 <sup>c</sup>	682.00 $\pm$ 14.93 <sup>d</sup>	699.44 $\pm$ 19.56 <sup>b</sup>
Cavendish	347.79 $\pm$ 23.45 <sup>d</sup>	97.43 $\pm$ 1.17 <sup>bc</sup>	59.43 $\pm$ 1.58 <sup>e</sup>	41.47 $\pm$ 2.24 <sup>c</sup>

\*values with different alphabet superscripts are significantly different at  $p < 0.05$

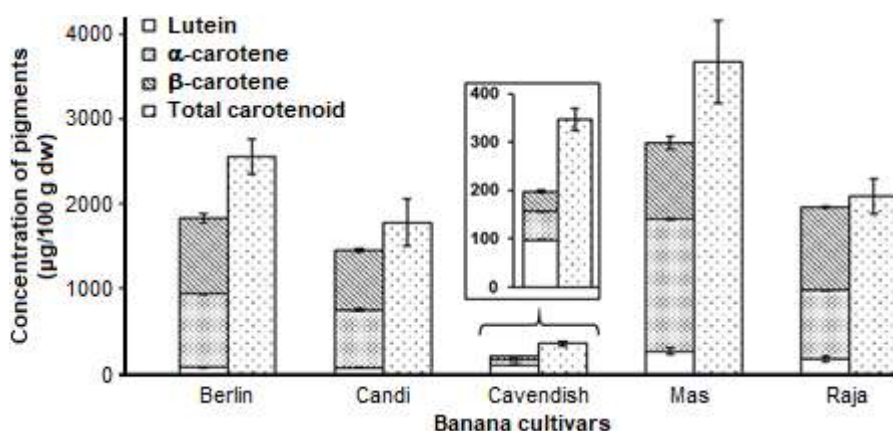


**Fig 4.** Comparison of major carotenoids (lutein,  $\alpha$ -carotene,  $\beta$ -carotene) and total carotenoids ( $\mu\text{g}/100$  g dw  $\pm$  SD) from five banana cultivars. Composition and concentration of major carotenoids were obtained from HPLC analysis, while total carotenoids were derived from spectrophotometry data

of  $\alpha$ -carotene in Mas bananas and  $\beta$ -carotene in Raja bananas were 1,556.22  $\mu\text{g}/100\text{ g dw}$  and 983.83  $\mu\text{g}/100\text{ g dw}$ , respectively. Being the most marketable banana cultivar, Cavendish shows a low amount of  $\beta$ -carotene which corresponds to previous reports suggesting that Cavendish contained 21 to 290  $\mu\text{g}/100\text{ g dw}$  of  $\beta$ -carotene [7,24,28].

Table 1 shows that  $\alpha$ -carotene concentrations were significantly different among the five banana cultivars, observed from the different letter as the result of statistical test calculation. In terms of  $\beta$ -carotene concentration, Raja, Candi, and Cavendish were distinguished over each other. Mas and Berlin showed no significant difference, however, they were significantly different from Cavendish. Moreover, lutein content among Berlin, Candi, and Cavendish could be considered not significantly different. Raja and Cavendish showed the same result as well as Mas and Raja. However, Mas showed a significant difference towards Berlin, Candi, and Cavendish.

In addition, a comparison between concentrations of three major pigments and total carotenoids is presented in Fig. 4, showing that the total carotenoids were greater than total concentrations of  $\alpha$ -carotene,  $\beta$ -carotene, and lutein. This result implies that more carotenoid compounds existed in the bananas, such as 5,8,5',6'-diepoxy- $\alpha$ -carotene or 5,6,5',8'-diepoxy- $\alpha$ -carotene, 13-*cis*- $\alpha$ -carotene, 15-*cis*- $\alpha$ -carotene, 5,8-epoxy- $\alpha$ -carotene, 13-*cis*- $\beta$ -carotene, 9-*cis*- $\alpha$ -carotene or 9'-*cis*- $\alpha$ -carotene and 9-*cis*- $\beta$ -carotene. Other carotenoid compounds that belong to the xanthophyll group also contribute to the total carotenoids. However, they could hardly be found in the HPLC chromatogram due to an extremely low amount [7,29-31].

The amount of vitamin A activity in the banana cultivars was calculated from the total of 1/24 of  $\alpha$ -carotene concentration and 1/12 of  $\beta$ -carotene concentration. Table 2 provides the result of vitamin A activity calculation from five samples in the range from between 5.92  $\pm$  0.12  $\mu\text{g RAE}/100\text{ g dw}$  and 139.90  $\pm$  6.54  $\mu\text{g RAE}/100\text{ g dw}$ . Through Table 2, it can be seen that there were significant differences between cultivars ( $p < 0.05$ ) and there were four groups regarding Tukey's multiple comparison. Berlin and Raja, however, show no

**Table 2.** Vitamin A activity from five banana cultivars

Banana cultivars	Vitamin A activity ( $\mu\text{g RAE}/100\text{ g dw} \pm \text{SD}$ )
Mas	139.90 $\pm$ 6.54 <sup>a</sup>
Berlin	113.63 $\pm$ 7.08 <sup>b</sup>
Raja	115.58 $\pm$ 1.07 <sup>b</sup>
Candi	84.23 $\pm$ 9.98 <sup>c</sup>
Cavendish	5.93 $\pm$ 0.12 <sup>d</sup>

\*values with different alphabet superscripts are significantly different at  $p < 0.05$

significant difference. The concentration of  $\alpha$ -carotene and  $\beta$ -carotene (Table 2) contribute to vitamin A activity. Therefore, Mas bananas contained the highest vitamin A activity among the other cultivars, while Cavendish became the lowest. Institute of Medicine (U.S) suggested the recommended dietary intake (RDI) values for vitamin A for females and males, 700  $\mu\text{g RAE}$  and 900  $\mu\text{g RAE}$ , respectively [32]. This means that to fulfill the dietary intake of vitamin A from these five banana cultivars, a considerable amount is needed. This number would be much greater for bananas with a very low amount of vitamin A, such as Cavendish.

## ■ CONCLUSION

Observational studies on the five banana cultivars in Malang were conducted to analyze the total carotenoids and to identify the dominant carotenoid pigments, *i.e.* lutein,  $\alpha$ -carotene, and  $\beta$ -carotene, as well as to determine their concentration. Each cultivar provided a different amount of major carotenoids. In addition, Mas bananas were found to contain the highest total carotenoids, *i.e.* 3,669  $\pm$  485.28  $\mu\text{g}/100\text{ g dw}$ . These bananas also presented the highest content of lutein and  $\alpha$ -carotene, while Raja bananas were known to have the highest  $\beta$ -carotene among other cultivars. On the other hand, Cavendish bananas, although they showed to provide the lowest amount of carotenoid, lutein was found in a higher amount than  $\alpha$ -carotene and  $\beta$ -carotene. Moreover, Mas banana exhibited the highest amount of vitamin A activity (139.90  $\pm$  6.54  $\mu\text{g RAE}/100\text{ g dw}$ ), suggesting a considerable amount of the bananas to fulfill the dietary intake of vitamin A.

## ■ ACKNOWLEDGMENTS

This study was supported by the Indonesian Ministry of Research, Technology, and Higher Education through the National Strategic Excellent Research (PUSNAS) Grant (No.: 120/SP2H/LT/DRPM/IV/2017) and Ministry of Research and Technology/National Agency for Research and Innovation and Indonesia Endowment Fund for Education through Covid-19 research and innovation funding program (No.: 8/FI/P-KCOVID-19.2B3/IX/2020).

## ■ AUTHOR CONTRIBUTIONS

J conducted the experiment, data analysis and wrote the manuscripts. DVC and NV conducted the experiment. MNUP conducted supervision, wrote and revise the manuscript. RDC performed supervision, data analysis, and revised the manuscript. CAS conducted experiment supervision. H performed supervision and revised the manuscript. LH provided literature review and consultation. THPB conducted supervision. All author agreed to the final version of this manuscript.

## ■ REFERENCES

- [1] Yadav, A., Kumari, R., Yadav, A., Mishra, J.P., Srivatva, S., and Prabha, S., 2016, Antioxidants and its function in human body – A review, *Res. Environ. Life Sci.*, 9 (11), 1328–1331.
- [2] Melendez-Martinez, A.J., 2019, An overview of carotenoids, apocarotenoids, and vitamin A in agro-food, nutrition, health, and disease, *Mol. Nutr. Food Res.*, 63 (15), 1801045.
- [3] Miller, A.P., Coronel, J., and Amengual, J., 2020, The role of  $\beta$ -carotene and vitamin A in atherogenesis: Evidences from preclinical and clinical studies, *Biochim. Biophys. Acta, Mol. Cell Biol. Lipids*, 1865 (11), 158635.
- [4] Sommer, A., and Vyas, K.S., 2012, A global clinical view on vitamin A carotenoids, *Am. J. Clin. Nutr.*, 96 (5), 1204S–1206S.
- [5] Lietz, G., Oxley, A., Boesch-Saadatmandi, C., and Kobayashi, D., 2012, Importance of  $\beta$ , $\beta$ -carotene 15,15'-monooxygenase 1 (BCMO1) and  $\beta$ , $\beta$ -carotene 9',10'-dioxygenase 2 (BCDO2) in nutrition and health, *Mol. Nutr. Food Res.*, 56 (2), 241–250.
- [6] Yuan, H., Zhang, J., Nageswaran, D., and Li, L., 2015, Carotenoid metabolism and regulation in horticultural crops, *Hortic. Res.*, 2, 15036.
- [7] Heng, Z., Sheng, O., Yan, S., Lu, H., Motorykin, I., Gao, H., Li, C., Yang, Q., Hu, C., Kuang, R., Bi, F., Dou, T., Xie, S., Deng, G., and Yi, G., 2017, Carotenoid profiling in the peel and pulp of 36 selected *Musa* varieties, *Food Sci. Technol. Res.*, 23 (4), 603–611.
- [8] Lokesh, V., Divya, P., Puthusseri, B., Manjunatha, G., and Neelwarne, B., 2014, Profiles of carotenoids during post-climacteric ripening of some important cultivars of banana and development of a dry product from a high carotenoid yielding variety, *LWT-Food Sci. Technol.*, 55 (1), 59–66.
- [9] Amah, D., van Biljon, A., Brown, A., Perkins-Veazie, P., Swennen, R., and Labuschagne, M., 2019, Recent advances in banana (*Musa* spp.) biofortification to alleviate vitamin A deficiency, *Crit. Rev. Food Sci. Nutr.*, 59 (21), 3498–3510.
- [10] Septiany, G.J., Putri, W.D.R., Panca, N.I., Heriyanto, and Limantara, L., 2019, Carotenoid analysis of ripe banana flesh and peel from three cultivars of banana, *Indones. J. Nat. Pigment.*, 1 (2), 60–64.
- [11] Aquino, C.F., Salomão, L.C.C., Pinheiro-Sant'ana, H.M., Ribeiro, S.M.R., De Siqueira, D.L., and Cecon, P.R., 2018, Carotenoids in the pulp and peel of bananas from 15 cultivars in two ripening stages, *Rev. Ceres*, 65 (3), 217–226.
- [12] Khoo, H.E., Ng, H.S., Yap, W.S., Goh, H.J.H., and Yim, H.S., 2019, Nutrients for prevention of macular degeneration and eye-related diseases, *Antioxidants*, 8 (4), 85.
- [13] Valmayor, R.V., Jamaluddin, S.H., Silayoi, B., Kusumo, S., Danh, L.D., Pascua, O.C., and Espino, R.R.C., 2000, *Banana cultivar names and synonyms in Southeast Asia*, INIBAP Regional Office for Asia and the Pacific, Laguna, Philippines.
- [14] Herlina, T., 2007, Peningkatan nilai tambah melalui pengembangan agroindustry pisang di kabupaten Lumajang, *Prosiding Seminar Nasional Agroindustri*, Bogor, 4 December 2007.

- [15] Hapsari, L., Wahyudi, D., Azrianingsih, R., and Arumingtyas, E.L., 2015, Genome identification of bananas (*Musa* L.) from East Java Indonesia assessed with PCR-RFLP of the internal transcribed spacers nuclear ribosomal DNA, *Int. J. Biosci.*, 7 (3), 42–52.
- [16] Badan Pusat Statistik, 2018, *Statistik Tanaman Buah-Buahan dan Sayuran Tahunan Indonesia 2018*, BPS, Jakarta.
- [17] Falcomer, A.L., Riquette, R.F.R., de Lima, B.R., Ginani, V.C., and Zandonadi, R.P., 2019, Health benefits of green banana consumption: A systematic review, *Nutrients*, 11 (6), 1222.
- [18] Hapsari, L., Kennedy, J., Lestari, D.A., Masrum, A., and Lestari, W., 2017, Ethnobotanical survey of bananas (*Musaceae*) in six districts of East Java, Indonesia, *Biodiversitas*, 18 (1), 160–174.
- [19] Chandra, R.D., Siswanti, C.A., Prihastyanti, M.N.U., Heriyanto, and Brotosudarmo, T.H.P., 2020, Evaluating pro-vitamin A carotenoids and polar metabolites composition during the ripening stages of Agung Semeru banana (*Musa paradisiaca* L. AAB), *Int. J. Food Sci.*, 2020, 8503923.
- [20] Stover, R.H., and Simmonds, N.W., 1987, *Bananas (Tropical Agriculture Series)*, 3<sup>rd</sup> Ed., Wiley, Hoboken, US.
- [21] Gross, J., 1991, *Pigments in Vegetables: Chlorophylls and Carotenoids*, Springer US.
- [22] Kurniawan, J.M., Yusuf, M.M., Azmi, S.S., Salim, K.P., Prihastyanti, M.N.U., Indrawati, R., Heriyanto, Shioi, Y., Limantara, L., and Brotosudarmo, T.H.P., 2019, Effect of drying treatments on the contents of lutein and zeaxanthin in orange- and yellow-cultivars of marigold flowers and its application for lutein ester encapsulation, *IOP Conf. Ser.: Mater. Sci. Eng.*, 509, 012060.
- [23] Institute of Medicine (US) Panel in Micronutrients, 2000, *Dietary Reference Intakes for Vitamin C, Vitamin E, Selenium, and Carotenoids*, National Academies Press, Washington DC.
- [24] Mbabazi, R., Harding, R., Khanna, H., Namanya, P., Arinaitwe, G., Tushemereirwe, W., Dale, J., and Paul, J.Y., 2019, Pro-vitamin A carotenoids in East African highland banana and other *Musa* cultivars grown in Uganda, *Food Sci. Nutr.*, 8 (1), 311–321.
- [25] Ekesa, B., Nabuuma, D., Blomme, G., and Van den Bergh, I., 2015, Provitamin A carotenoid content of unripe and ripe banana cultivars for potential adoption in eastern Africa, *J. Food Compos. Anal.*, 43, 1–6
- [26] Singh, B., Sing, J.P., Kaur, A., and Sing, N., 2016, Bioactive compounds in banana and their associated health benefits – A review, *Food Chem.*, 206, 1–11.
- [27] Ashokkumar, K., Elayabalan, S., Shobana, V.G., Sivakumar, P., and Pandiyan, M., 2018, Nutritional value of cultivars of banana (*Musa spp.*) and its future products, *J. Pharmacogn. Phytochem.*, 7 (3), 2972–2977.
- [28] Buah, S., Mlalazi, B., Khanna, H., Dale, J.L., and Mortimer, C.L., 2016, The quest for golden bananas: Investigating carotenoid regulation in a Fe'i group *Musa* cultivar, *J. Agric. Food Chem.*, 64 (16), 3176–3185.
- [29] Facundo, H.V.V., Gurak, P.D., Mercadente, A.Z., Lajolo, F.M., and Cordenunsi, B.R., 2015, Storage at low temperature differentially affects the colour and carotenoid composition of two cultivars of banana, *Food Chem.*, 170, 102–109.
- [30] Yan, L., Fernando, W.M.A.D.B., Brennan, M., Brennan, C.S., Jayasena, V., and Coorey, R., 2016, Effect of extraction method and ripening stage on banana peel pigments, *Int. J. Food Sci. Technol.*, 51 (6), 1449–1456.
- [31] Amah, D., Alamu, E., Adesokan, M., van Biljon, A., Maziya-dixon, B., Swennen, R., and Labuschagne, M., 2019, Variability of carotenoids in a *Musa* germplasm collection and implications for provitamin A biofortification, *Food Chem.: X*, 2, 100024.
- [32] Institute of Medicine (US) Panel in Micronutrients, 2001, *Dietary Reference Intakes for Vitamin A, Vitamin K, Arsenic, Boron, Chromium, Copper, Iodine, Iron, Manganese, Molybdenum, Nickel, Silicon, Vanadium, and Zinc*, National Academies Press, Washington DC.

## Anticancer Activities of Chemical Constituents from Leaves and Twigs of *Mitrephora winitii*

Sukee Sukdee<sup>1</sup>, Puttinan Meepowpan<sup>1\*</sup>, Narong Nantasaen<sup>2</sup>, Siriporn Jungsuttiwong<sup>3</sup>, Sarinya Hadsadee<sup>3</sup>, and Wilart Pompimon<sup>4</sup>

<sup>1</sup>Department of Chemistry, Center of Excellence for Innovation in Chemistry (PERCH-CIC), Faculty of Science, Graduate School, Chiang Mai University, 239 Huay Kaew Road, Chiang Mai 50200, Thailand

<sup>2</sup>The Forest Herbarium, Department of National Park, Wildlife and Plant Conservation, Ministry of Natural Resources and Environment, Bangkok, 10220, Thailand

<sup>3</sup>Center for Organic Electronic and Alternative Energy, Department of Chemistry and Center of Excellence for Innovation in Chemistry, Faculty of Science, Ubon Ratchathani University, Ubon Ratchathani, 34190, Thailand

<sup>4</sup>Laboratory of Natural Products, Faculty of Science and Center for Innovation in Chemistry, Lampang Rajabhat University, Lampang, 52100, Thailand

---

### \* Corresponding author:

tel: +668-69192120

email: pmeepowpan@hotmail.com

Received: November 4, 2020

Accepted: March 9, 2021

DOI: 10.22146/ijc.61085

**Abstract:** The genus *Mitrephora* has been investigated, and its anti-inflammatory, anti-bacterial, and anti-parasitical activities were examined along with its potential as an anti-cancer cell line and inhibitor for platelet aggregation. In this work, air-dried leaves and twigs of *M. winitii* were grounded and extracted with *n*-hexane, ethyl acetate, and methanol, respectively. Chromatographic separations of these extracts led to the isolation of three known compounds and one new compound (compound **2**). The chemical structures of these were identified using the spectroscopic investigation of 1D- and 2D-NMR, and the resulting data confirmed these as stigmaterol (**1**), (3,4-dimethoxyphenyl)(5-(3,4-dimethoxyphenyl)-4-(hydroxymethyl)tetrahydrofuran-3-yl)methanol (**2**), diayangambin (**3**), and methyl-L-inositol (**4**). The chemical constituents were reported the first time in *M. winitii*. Compound **2** showed anti-cancer cell lines with  $ED_{50}$  13.07  $\mu\text{g/mL}$  against KB cells and then was tested for cytotoxicity against MCF-7 cells with  $ED_{50}$  11.77  $\mu\text{g/mL}$ .

**Keywords:** *Mitrephora winitii*; anticancer; extraction; extract

---

## ■ INTRODUCTION

Within the pantropical family of shrubs, trees, and lianas, the *Annonaceae* family comprises an interesting group of medicinal plants. Consisting of roughly 130 genera and 2,500 species, the majority of these are found in Asia, Australia, and Pacific regions [1]. One of these is the genus *Mitrephora*, which is comprised of some 48 species found in Asia and Australia [2]. In Thailand, 12 species are found, and some plants in this genus have been used in the country for the production of folk medicine [3]. These genera have great potential for the treatment of cancers, bacterial infections, brain dysfunctions, and hypertension [1]. Phytochemical investigations have established that *Mitrephora* species contain diterpenoids,

polyacetylene carboxylic acids/esters, fatty acids, lignans, sesquiterpenes, alkaloids [4-9], the diterpenoids and alkaloids have shown significant anti-microbial, anti-malarial, anti-platelet aggregation, and cytotoxic potential [10-12]. Interestingly, the *M. winitii* was the new source and reported on the antitumor and potent cytotoxic activities of the genus showed high activity anticancer agents.

The *M. winitii* [13] extracts with solvents (*n*-hexane, ethyl acetate, and methanol) and isolated by column chromatography was found to contain four compounds. They were identified using IR, NMR, and ESI-MS spectrometry to yield stigmaterol (**1**), (3,4-dimethoxyphenyl)(5-(3,4-dimethoxyphenyl)-4-(hydroxy

methyl)tetrahydrofuran-3-yl)methanol (2), diyangambin (3), and methyl-L-inositol (4). In this paper, we investigated the cytotoxicity of the *n*-hexane extract of this plant tested against a panel of two mammalian cancer cell lines. We also report on the isolation and characterization of one new, and three known compounds were found in *M. winitii*.

## ■ EXPERIMENTAL SECTION

### Materials

*M. winitii* leaves and twigs were collected from Lampang Province in Thailand in January 2011. *M. winitii* was confirmed by the Forest Herbarium, Department of National Parks, Wildlife and Plant Conservation, Ministry of Natural Resources and Environment, Bangkok, Thailand, where a voucher specimen (BKF16447) has been deposited. Silica gel (Merck 7734, Mesh 70-230) and TLC 60 PF<sub>254</sub> sheets were purchased from Merck. All organic solvents used for extraction and chromatographic separation (CC) were distilled at their boiling point ranges of *n*-hexane, ethyl acetate, and methanol (laboratory grade), whereas AR grade solvents were used for crystallization were from Merck.

### Instrumentation

The melting points of the extracted compounds were measured on a digital electrothermal melting apparatus, and the uncorrected results were recorded in degrees Celsius (°C). IR spectra were recorded on KBr disks using a Shimadzu 8900 FTIR spectrophotometer, whereas major bands ( $\nu_{\max}$ ) were recorded at wavenumber ( $\text{cm}^{-1}$ ) unit, <sup>1</sup>H (400 MHz), and <sup>13</sup>C (100 MHz). NMR spectra were determined using either CDCl<sub>3</sub> or D<sub>2</sub>O solution. Chemical shifts were recorded in  $\delta$  values, which were referenced to TMS as the internal standard at  $\delta$  0.00 ppm. The signal of chloroform at  $\delta$  7.26 was used as a reference in the case of <sup>1</sup>H-NMR spectra and at  $\delta$  77.00 in the case of <sup>13</sup>C-NMR spectra. The instrument was achieved using a DPX on a Bruker AV 400 spectrometer for 1D and 2D determinations. Low resolution mass spectra were recorded on a Thermo Finnegan Polaris Q mass spectrometer at 70 eV (probe) for the EIMS. High-

resolution mass spectra (made using the electrospray ionization mode, ESI-MS) were measured on a micro massQ-TOF-2<sup>TM</sup> (Waters) spectrometer. Column chromatography was conducted on silica gel 60 (Merck 7734, 70–230 mesh). TLC was performed on aluminum backed pre-coated silica gel 60 PF<sub>254</sub> sheets, and detections were made using a UV detector at 254 and 365 nm.

### Procedure

#### Extraction and isolation

Dried and powdered leaves and twigs of *M. winitii* (2.0 kg) were treated at room temperature with *n*-hexane, ethyl acetate, and methanol successively. The *n*-hexane extract (25.0 g) was subjected to silica gel (Merck 7734, 70–230 mesh) column chromatography (CC) and eluted in a gradient system with an increasing concentration of *n*-hexane/ethyl acetate to yield fifteen fractions (A1-A15). Fraction A7 was found to contain a solid. This was recrystallized with a solution of ethyl acetate/ethanol (3:1) to afford stigmasterol (1). Fraction A10 was subjected to further CC on silica gel, eluted with a gradient of *n*-hexane/ethyl acetate to afford 150 mg of (3,4-dimethoxyphenyl)(5-(3,4-dimethoxyphenyl)-4-(hydroxymethyl)tetrahydrofuran-3-yl)methanol (2). The ethyl acetate extract (24.0 g) was subjected to silica gel (Merck 7734, 70–230 mesh) column chromatography (CC), eluted in a gradient system with an increasing concentration of *n*-hexane/ethyl acetate and ethyl acetate/methanol to give ten fractions (B1-B10). Fraction B8 was subjected to further CC on silica gel, eluted with a gradient of ethyl acetate/methanol to afford 200 mg of diyangambin (3). The methanol extract (72.0 g) was subjected to silica gel (Merck 7734, 70–230 mesh) column chromatography and eluted in a gradient system with an increasing concentration of ethyl acetate/methanol to give ten fractions (C1-C10). Fraction C4 was subjected to further CC on silica gel and eluted with a gradient of ethyl acetate/methanol to give 300 mg of methyl-L-inositol (4) (Fig. 1).

#### Evaluation of cytotoxic activity

The cytotoxic activities of the compounds extracted from *M. winitii* were tested using the *in-vitro* sulforhodamine B (SRB) method. Ellipticine was used as

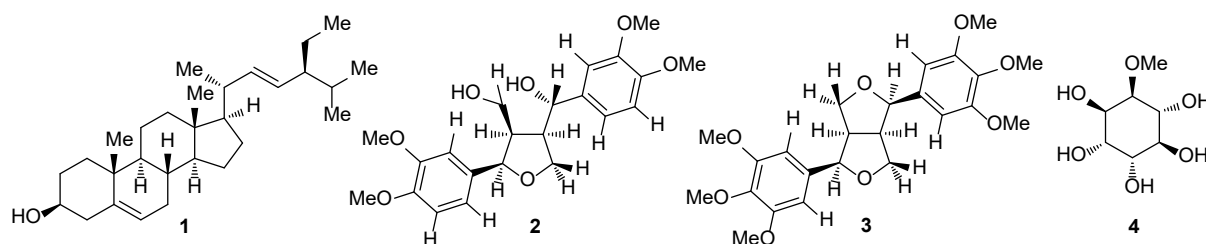


Fig 1. Structure of compounds from *M. winitii*

a positive control. Test samples were dissolved in dimethyl sulfoxide (DMSO) at a stock concentration of 3 mg/mL, and these were tested in triplicate with a final concentration of DMSO at 0.5%. The cancer cell lines were grown in a 96-well plate in the following media: P-388, in RPMI-1640 with 5% fetal bovine serum (FBS). The P-388, KB, HT29, MCF-7, A549, ASK, and HEK293 cell lines were cultured in MEM (minimum essential medium with Earle's salt and l-glutamine) with 10% FBS, while Lu-1 was grown in MEM with 5% FBS. After drug exposure was at 37 °C for 72 h (48h for P-388) with 5% CO<sub>2</sub> in air and 100% relative humidity, cells were then fixed with a final concentration of 10% trichloroacetic acid and stained with 0.4% SRB in 1% acetic acid. The bound and dried stain was solubilized with 10 mM Trizma base after removing the unbound dye by washing. Absorbance was read on a Fluostar optima BMG plate reader at a wavelength of 570 nm. The cytotoxic activity is expressed as a 50% effective dose (ED<sub>50</sub>) [14].

The ED<sub>50</sub> value was determined by:

$$\% \text{ Survival} = \frac{\text{OD (test sample)} - \text{OD (Day 0)}}{\text{OD (0.5\% DMSO control)} - \text{OD (Day 0)}}$$

Criteria of activity: Extracts having an ED<sub>50</sub> < 20 µg/mL and pure compounds having an ED<sub>50</sub> < 4 µg/mL = Active;  
No Response = ED<sub>50</sub> > 20 µg/mL

## RESULTS AND DISCUSSION

### Structure Elucidation

Compound **1** was obtained as a white powder; mp 163–164 °C. From the EIMS spectrum [M+H<sub>2</sub>O+H]<sup>+</sup> at *m/z* 395.37, this could be assigned the molecular formula C<sub>29</sub>H<sub>48</sub>O. The IR spectrum showed the broad absorption bands of a hydroxyl group at 3460 cm<sup>-1</sup>. Absorption bands appearing at 2955 and 2870 cm<sup>-1</sup> were due to C–H stretching. C–H bending showed weak absorption bands at

1465 cm<sup>-1</sup> and 1377 cm<sup>-1</sup>, and C=C stretching appeared as a weak absorption band at 1650 cm<sup>-1</sup>. The medium absorption band at 1050 cm<sup>-1</sup> was assigned to C–O stretching. The structure was further elucidated by examination with NMR techniques. The <sup>1</sup>H-NMR spectra of compound **1** showed the presence of six methyl signals, which appeared at δ 0.72 (3H, *s*, H-28), 0.81 (3H, *d*, *J*=5.0 Hz, H-27) 0.85 (3H, *d*, *J*=5.0 Hz, H-26), 0.87 (3H, *t*, *J*=5.0 Hz, H-24), 0.94 (3H, *d*, *J*=10.0 Hz, H-19), and 1.06 (3H, *s*, H-29). The spectra also showed protons at δ 5.03, 5.16, and 5.62 ppm, suggesting the presence of protons corresponding to a tri-substituted and a di-substituted olefinic bond. A comparison of the <sup>1</sup>H and <sup>13</sup>C-NMR spectral data to data in the literature, together with the melting point of the sample, points to the molecular structure of stigmasterol (**1**) [9,15].

Compound **2** was isolated as a colorless needle crystal; mp 126–127 °C. Its ESIMS gave a molecular ion peak [M+2H<sup>+</sup>] at *m/z* 406, consistent with the molecular formula C<sub>22</sub>H<sub>28</sub>O<sub>7</sub> (cal. for C<sub>22</sub>H<sub>28</sub>O<sub>7</sub>, 404). In addition, the mass spectrum of the compound found *m/z* 406 [M+2H<sup>+</sup>]. The key fragmentation ions in the mass spectrum were at 359, 324, 323, 249, and 151, which was useful in obtaining the structure of the compound (Fig. 2) [16]. The IR spectrum showed absorption bands attributable to hydroxyl at 3400 cm<sup>-1</sup> and aromatics at 1617, 1589, and 1519 cm<sup>-1</sup>. The absorption bands appearing at 2945 and 2850 cm<sup>-1</sup> were due to C–H stretching. The C–H bending appeared as weak absorption bands at 1464 and 1375 cm<sup>-1</sup>. In addition, the methoxy groups showed typical C–O stretching absorptions, which appeared at 1269 and in the range from 1234 to 1160 cm<sup>-1</sup>. The <sup>1</sup>H-NMR signals at δ 6.85–6.93 ppm (6H) represented a tri-substituted phenyl moiety. Two oxygen bearing methylene protons were

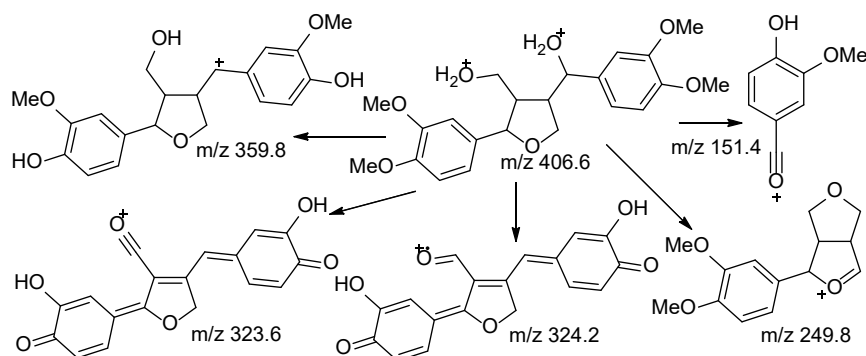


Fig 2. The mass spectral fragmentation of compound 2

suggested at  $\delta$  3.36 ppm (2H, *m*, H-3a) and two nonequivalent methylene protons at  $\delta$  3.85 (1H, *dd*,  $J=5.0$ , 10.0 Hz, H-5<sub>a</sub>) and 4.13 (1H, *d*,  $J=10.0$  Hz, H-5<sub>b</sub>) ppm. Four methine protons were indicated at  $\delta$  2.92 (1H, *dd*,  $J=5.0$ , 10.0 Hz, H-4), 3.32 (1H, *m*, H-3), 4.45 (1H, *d*,  $J=10.0$  Hz, H-4a), and 4.88 (1H, *d*,  $J=5.0$  Hz, H-2) ppm. Four methoxy groups were also indicated at  $\delta$  3.89, 3.87, 3.88, and 3.91 (each 3H, *s*) ppm in the <sup>1</sup>H-NMR spectrum. Further spectral evidence was required to confirm the structure of 2. The <sup>1</sup>H-<sup>1</sup>H COSY showed coupling correlations through the sequence of H-2 to H-3, H-3 to H-3a, H-4 to H-5, and H-4 to H-4a for the connectivity of the protons to the structure. The connectivity of the aromatic carbon skeleton (e.g., C-5', C-6', C-5'', and C-6'') was also confirmed by the COSY correlations (Fig. 3). The HMBC spectrum showed crossed peaks between the aromatic signals (H-2', H-5', and H-6') and C-1', C-2', C-3', and C-4' and between H-6', H-2' and C-2, which indicated the aromatic ring was connected to C-2. Further, the aromatic signals (H-2'', H-5'', and H-6'') and C-1'', C-2'', C-3'', and C-4'' and between H-6'', H-2'' and C-4a indicated the aromatic ring was connected to C-4a (Fig. 3). The <sup>1</sup>H-<sup>13</sup>C spectrum revealed signals from 22 atoms,

and DEPT experiments also showed 16 protonated carbon signals, thereby revealing the presence of six quaternary carbons in the molecule. The presence of a trisubstituted phenyl ring was evident from the signals at  $\delta$  109.11, 111.14, 117.76, 131.02, 148.09 and 148.92 (a ring connected C-2) and signals at  $\delta$  109.26, 111.14, 118.47, 133.75, 148.78 and 149.29 (a ring connected C-4a). Additionally, oxymethine carbon signals were found at  $\delta$  82.07, 87.63, and methoxy carbons at  $\delta$  55.93, 55.96, and 55.97. A literature search revealed that *cis*- and *trans*- orientation of substituents at C-2 and C-3 give a signal of H-2 at  $\delta$  4.76 and 4.91 ( $J=4$ , 4.8 Hz), respectively. The H-2 signal of compound 2 ( $\delta$  4.88 and  $J=5.0$  Hz) thus agreed well with the assignment of a *cis*-configuration. The relationship between the torsion angle and vicinal coupling constant <sup>3</sup>*J* is given theoretically by the Karplus equation:  ${}^3J(\text{HH}) = P_1 \cos^2\phi + P_2 \cos\phi + P_3 + \sum \Delta\chi_i \{P_4 + P_5 \cos^2(\xi_i\phi + P_6 |\Delta\chi_i|)\}$  [17]. So, the relative configuration at H-4 and H-4a could be determined by the <sup>3</sup>*J*<sub>4,4a</sub>, H-C-C-H (10 Hz) coupling constant, which would indicate that the two protons were located on opposite sides with a dihedral angle of 180°. Furthermore, the H-4a showed a signal at  $\delta$  4.45 ppm

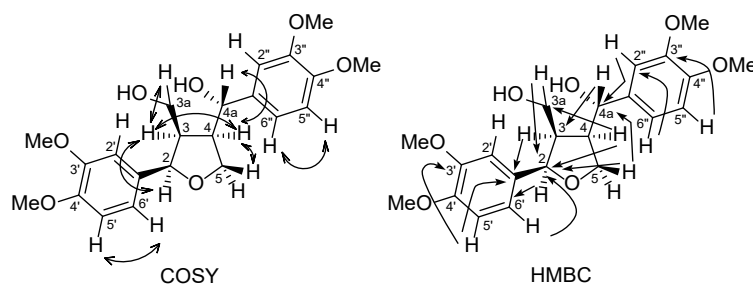


Fig 3. <sup>1</sup>H-<sup>1</sup>H COSY correlations and the selected HMBC correlations of compound 2



**Table 1.**  $^{13}\text{C}$  and  $^1\text{H}$ -NMR data of compound **2** and  $^1\text{H}$ - $^1\text{H}$ ,  $^1\text{H}$ - $^{13}\text{C}$  correlations exhibited in the 2D NMR spectra in  $\text{CDCl}_3$ 

Position	$\delta_{\text{C}}$ (ppm)	$\delta_{\text{H}}$ (ppm)	COSY	HMBC
1	"	"	"	"
2	82.07	4.88, <i>d</i> (5.0)	H-3	3, 3a, 1', 2', 6'
3	50.18	3.32, <i>m</i>	H-2, H-3a, H-4	2, 3a, 4, 4a
3a	69.73	3.36, <i>m</i>	H-3	2, 3, 4
4	54.50	2.92, <i>dd</i> (5.0,10.0)	H-3, H-4a, H-5	2, 4a, 1"
4a	87.63	4.45, <i>d</i> (10.0)	H-4	3, 4, 5, 1", 2", 6"
5	71.04	4.13, <i>d</i> (10.0) 3.85, <i>dd</i> (5.0,10.0)	H-4	2, 3, 4, 4a
1'	131.02			
2'	109.11	6.93, <i>s</i>		2, 1', 3', 4', 6'
3'	148.92			
4'	148.09			
5'	111.14	6.85, <i>m</i>	H-6'	2, 1', 2', 3', 4', 6'
6'	117.76	6.89, <i>m</i>	H-5'	2, 1', 2', 3', 4'
1"	133.75			
2"	109.26	6.92, <i>s</i>		4a, 1", 3", 4", 6"
3"	149.29			
4"	148.78			
5"	11.14	6.85, <i>m</i>	H-6"	1", 2", 3", 4", 6"
6"	118.47	6.90, <i>m</i>	H-5"	4a, 1", 2"
3'-OMe	55.96	3.89, <i>s</i>		3'
4'-OMe	55.93	3.87, <i>s</i>		4'
3"-OMe	55.97	3.88, <i>s</i>		3"
4"-OMe	55.96	3.91, <i>s</i>		4"

and  $J=10.0$  Hz, giving a spectra data assignment to the *trans*- configuration. On the basis of the above data [18-19], the structure of **2** was determined to be (3,4-dimethoxyphenyl)(5-(3,4-dimethoxyphenyl)-4-(hydroxyl methyl)tetrahydrofuran-3-yl)methanol, which has not been previously reported. The resonances for the protons of the tetrahydrofuran skeleton between two propanyl groups showed nonequivalent for H-3/H-4, H-2/H-4a, and H<sub>2</sub>-5/H<sub>2</sub>-3a; therefore, requiring an unsymmetrical substitution stereochemistry of the furan system; especially the chemical shifts of the benzylic oxymethine protons H-2 (4.88, 5.0 Hz, *d*) and H-4a (4.45, 10 Hz, *d*) confirmed that two the propanyl groups substituent are asymmetrical in compound **2** [18-19]. When compared, the protons for the furan system of compound **3** showed the equivalents of H-7/H-7' and H-8/H-8'; therefore, requiring a symmetrical substitution stereochemistry for

the aryl substituents and furan ring. Moreover, the few coupling constants and the chemical shifts of the benzylic oxymethine protons of H-7 and H-7', showed  $J=5.0$  Hz,  $\delta$  4.92, and for bridge carbons, C-8/C-8' (49.43/49.43) confirmed that two aryl substituents are symmetry in compound **3** [20]. Support the absolute configuration of compound **2** was studied by electronic circular dichroism (ECD) spectroscopy. The optimized structure of compound was performed by the density functional theory (DFT) calculation at the B3LYP/6-31G (d,p) level of theory (Fig. 4). ECD spectra were carried out by using TD-DFT method at the CAM-B3LYP/6-311G++(d,p) including PCM model (MeOH) (Fig. 5). The rotary strengths of 80 excited states were calculated. All calculations were performed using Gaussian09 program package. Gaussian bandshape with a bandwidth of 0.25 eV was used to simulate ECD spectra.

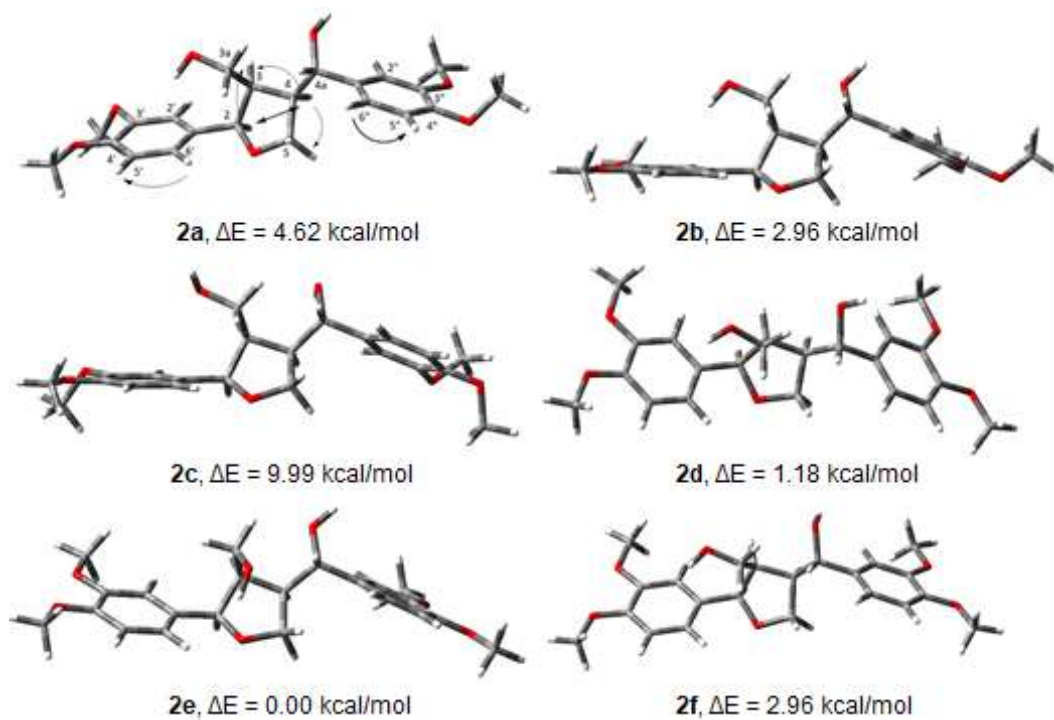


Fig 4. Optimized structures of compound 2 using B3LYP/6-31G(d,p)

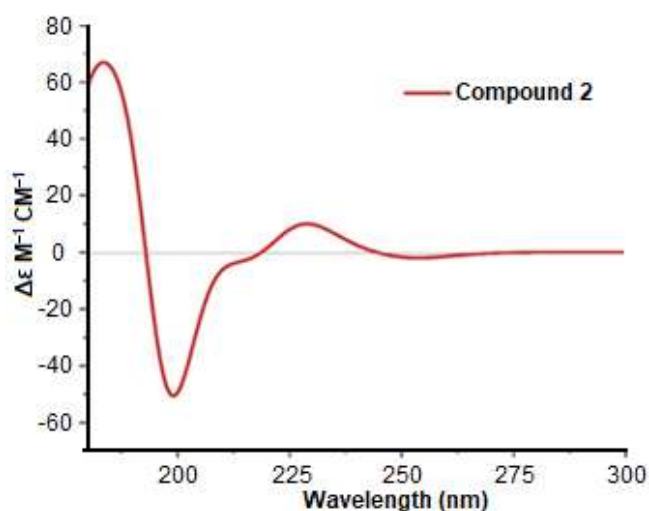


Fig 5. TDDFT calculated CD spectra of compound 2-2e at Cam-B3LYP/6 311++G)d,p

The ECD curve was generated by SpecDis 1.64 (University of Wurzburg, Wurzburg, Germany) softwares. The proposed biosynthesis pathway correctly showed to reasonably assure the specific structure for the unknown compound 2 (Fig. 6) [21].

Medicinal plants are important sources of bioactive compounds in cancer suppression and treatment [1]. Plants of the *Mitrephora* genera were used to treat sickness

in folk medicines [3]. The *in-vitro* sulforhodamine B (SRB) method assay to study the inhibition of cell viability on seven cancer cell lines P-388, KB, HT29, MCF-7, A549, ASK, and HEK293 by treatment of seven naturally occurring pure compounds, compared with an ellipticine drug. Compound 2 showed moderated anti-proliferative activity against KB and MCF-7 cell lines, with ED<sub>50</sub> values of 13.07, and 11.77 μg/mL, respectively, which is reported here for the first time.

Compound 3 was obtained as a white needle crystal; mp 144–145 °C. Its EIMS gave a molecular ion peak [M]<sup>+</sup> at *m/z* 445, which was consistent with the molecular formula C<sub>24</sub>H<sub>30</sub>O<sub>8</sub> (cal. for C<sub>24</sub>H<sub>30</sub>O<sub>8</sub><sup>+</sup>, 445). The mass showed the fragmentation characteristics described for liriosinol-*B* dimethyl ether. The EIMS spectrums showed fragmentation ions in the mass spectrum at *m/z* 249, 219, 195, 181, 177, and 165. The IR spectrum of the compound showed medium absorption bands at 1634, 1614, 1589, and 1509 cm<sup>-1</sup>, which were characterized as aromatic C=C stretching. The strong absorption bands at 2935 and 2840 cm<sup>-1</sup> were characterized as C-H stretching, while the corresponding bending vibrations appeared at 1422 and 1367 cm<sup>-1</sup>. The

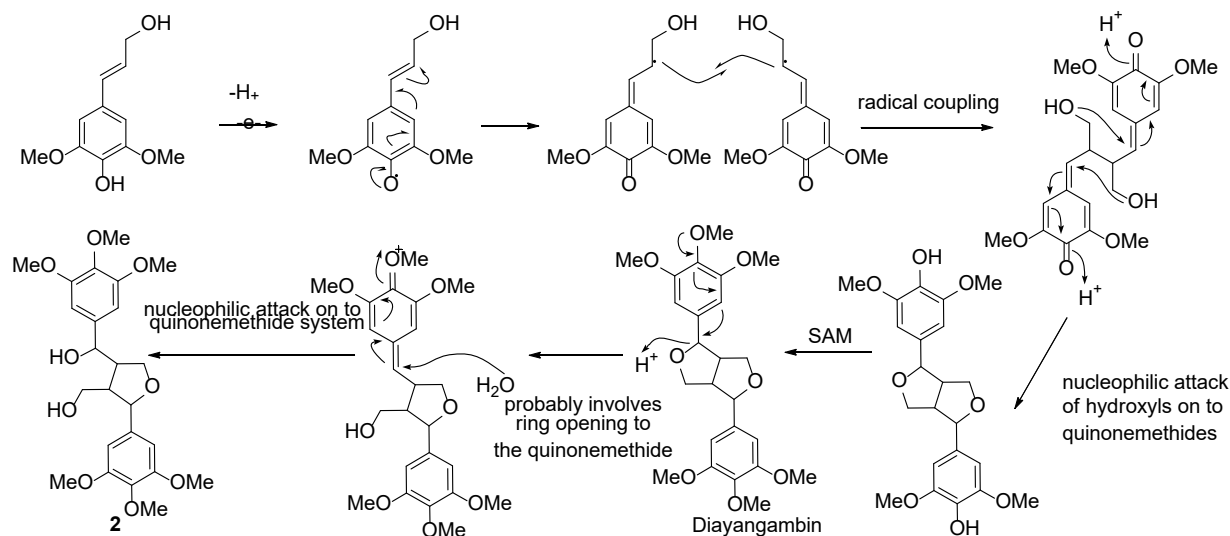


**Fig 6.** Proposed biosynthesis pathway of diayangambin and compound 2

C–O stretching showed medium absorption bands at 1129 and 1004  $\text{cm}^{-1}$ . The structure of compound 3 was further elucidated through 1D- and 2D-NMR experiments. The  $^1\text{H}$ -NMR spectrum showed the presence of tetra-substituted aromatic protons at  $\delta$  6.62 (4H, s, H-2,6,2',6') ppm. A doublet of methine proton H-7,7' was observed at  $\delta$  4.92 (2H, *d*,  $J=5.0$  Hz, H-7,7') ppm and the resonances at  $\delta$  3.90 (12H, s, 3,5,3',5'-OMe) and 3.87 (6H, s, 4,4'-OMe) ppm indicated a methoxy proton. A doublet of methylene protons ( $\text{H}_{\alpha,\beta}$ -9) on a tetrahydrofuran ring was observed at  $\delta$  3.74 (2H, *dd*,  $J_1=1.8$  Hz,  $J_2=9.6$  Hz,  $\text{H}_{\alpha}$ -9,9') and 3.58 (2H, *dd*,  $J_1=6.7$  Hz,  $J_2=9.6$  Hz,  $\text{H}_{\beta}$ -9,9') ppm. The  $^{13}\text{C}$ -NMR spectrum exhibited the resonances of a quaternary aromatic carbon at  $\delta$  153.22 (C-3,5,3',5'), 137.02 (C-1,1'), 134.58 (C-4,4'), and four aromatic methine carbons at  $\delta$  103.17 (C-2,6,2',6') ppm. Methine carbons were found at  $\delta$  84.08 (C-7,7') and 49.43 (C-8,8') ppm, and methylene carbons at  $\delta$  68.89 (C-9,9') ppm. Deshieldedoxymethyl carbons were indicated at  $\delta$  68.89 (C-9,9'), 60.89 (4,4'-OMe), and 56.10 (3,5,3',5'-OMe) ppm. The HMBC correlation of H-2 to C-4, C-6, and C-7, and H-7 to C-1, and C-9 confirmed an aromatic ring connecting to the tetrahydrofuran ring. These data were in accordance with those of diayangambin (3) [20,22].

Compound 4 was obtained as a white crystal; mp 190–192  $^{\circ}\text{C}$ . The IR spectrum showed the broad absorption band of a hydroxyl group at 3420  $\text{cm}^{-1}$ . The absorption bands at 2940 and 2840  $\text{cm}^{-1}$  were due to C–H

stretching. In addition, the hydroxyl and methoxy groups showed typical C–O stretching absorptions, which appeared at 1146  $\text{cm}^{-1}$  and in the range from 1119 to 1066  $\text{cm}^{-1}$ . The structure of the compound was further elucidated by 1D- and 2D-NMR experiments. The  $^1\text{H}$ -NMR displayed signals for protons of oxygenated carbons at  $\delta$  3.46 (1H, *m*, H-2), 3.48 (1H, *m*, H-3), 3.60 (1H, *m*, H-4), 3.92 (1H, *t*,  $J=5$  Hz, H-5), and 4.13 (1H, *t*,  $J=5$  Hz, H-6) ppm, while a methoxy group was indicated at  $\delta$  3.31 (3H, s, -OMe) ppm. One proton at  $\delta$  3.26 (1H, *m*, H-1) ppm was assigned to a methine proton adjacent to the oxygen of an ether group. The  $^{13}\text{C}$ -NMR spectrum showed a resonance signal at  $\delta$  80.06 ppm, which was assigned to a carbon of ether, while the methoxy carbon showed at  $\delta$  56.79 ppm. The signals at  $\delta$  72.74, 71.83, 70.27, 71.28, and 67.03 ppm also indicated oxymethine carbons. The COSY spectrum showed correlations between H-1 and H-2, H-2 and H-3, H-3 and H-4, H-4 and H-5, H-5 and H-6, H-6 and H-1. The HMBC spectrum demonstrated the correlation of H-OMe to C-1, indicating the methoxy was connected at C-1, and this confirmed the position of the methoxy group. These data were in accordance with those recorded for methyl-L-inositol (4) [23–25].

## CONCLUSION

The investigation focused on the phytochemical of medicinal plant together with biochemical evaluation.

The results presented four compounds derivative from *M. winitii* were carried out from crude extract of *M. winitii* found the compounds; stigmaterol (1), (3,4-dimethoxyphenyl)(5-(3,4-dimethoxyphenyl)-4-(hydroxymethyl)tetrahydrofuran-3-yl)methanol (2), diayangambin (3), and methyl-L-inositol (4). Chemical constituents were the first report isolated from *M. winitii*, in addition, compound 3,4-dimethoxyphenyl)(5-(3,4-dimethoxyphenyl)-4-(hydroxymethyl)tetrahydrofuran-3-yl)methanol (2) was new the structure. Other than the compound 2 can effectively inhibit the growth of the KB and MCF-7 cancer cell lines; when compared with an ellipticine as the positive control.

#### ■ ACKNOWLEDGMENTS

We would like to express our sincere thanks to the Department of Chemistry and Center for Innovation in Chemistry, Faculty of Science, Graduate School, Chiang Mai University, and Lampang Rajabhat University for financial support. We also would like to thank Mr. Daniel Rooney for editing this manuscript.

#### ■ REFERENCES

- [1] Florence, A.R., Joselin, J., Brintha, T.S.S., Sukumaran, S., and Jeeva, S., 2014, Preliminary phytochemical studies of select members of the family Annonaceae for bioactive constituents, *Biosci. Discovery*, 5 (1), 85–96.
- [2] Mols, J.B., and Kessler, P.J.A., 2003, The genus *Miliusa* (Annonaceae) in the Austro-Malesian area, *Blumea*, 48 (3), 421–462.
- [3] Rayanil, K., Limpanawisut, S., and Tuntiwachwuttikul, P., 2013, *Ent*-pimarane and *ent*-trachylobane diterpenoids from *Mitrephora alba* and their cytotoxicity against three human cancer cell lines, *Phytochemistry*, 89, 125–130.
- [4] Lee, N.H.S., Xu, Y.J., and Goh, S.H., 1999, 5-Oxonoraporphines from *Mitrephora* cf. *maingayi*, *J. Nat. Prod.*, 62 (8), 1158–1159.
- [5] Zgoda, J.R., Freyer, A.J., Killmer, L.B., and Porter, J.R., 2001, Polyacetylene carboxylic acids from *Mitrephora celebica*, *J. Nat. Prod.*, 64 (10), 1348–1349.
- [6] Li, C., Lee, D., Graf, T.N., Phifer, S.S., Nakanishi, Y., Burgess, J.P., Riswan, S., Setyowati, F.M., Saribi, A.M., Soejarto, D.D., Farnsworth, N.R., Falkinham, J.O., Kroll, D.J., Kinghorn, A.D., Wani, M.C., and Oberlies, N.H., 2005, A hexacyclicent-trachylobrane diterpenoid possessing an oxetane ring from *Mitrephora glabra*, *Org. Lett.*, 7 (25), 5709–5712.
- [7] Deepalard, K., Pengsuparp, T., Moriyasu, M., Kawanishi, K., and Suttisri, R., 2007, Chemical constituents of *Mitrephora maingayi*, *Biochem. Syst. Ecol.*, 35 (10), 696–699.
- [8] Li, C., Lee, D., Graf, T.N., Phifer, S.S., Nakanishi, Y., Riswan, S., Setyowati, F.M., Saribi, A.M., Soejarto, D.D., Farnsworth, N.R., Falkinham, J.O., Kroll, D.J., Kinghorn, A.D., Wani, M.C., and Oberlies, N.H., 2009, Bioactive constituents of the stem bark of *Mitrephora glabra*, *J. Nat. Prod.*, 72 (11), 1949–1953.
- [9] Husain, K., Jamal, J.A., and Jalil, J., 2012, Phytochemical study of *Cananga odorata* (Lam) Hook.F. & Thomson & Thoms (Annonaceae), *Int. J. Pharm. Pharm. Sci.*, 4 (4), 465–467.
- [10] Zgoda-Pols, J.R., Freyer, A.J., Killmer, L.B., and Porter, J.R., 2002, Antimicrobial diterpenes from the stem bark of *Mitrephora celebica*, *Fitoterapia*, 73 (5), 434–438.
- [11] Mueller, D., Davis, R.A., Duffy, S., Avery, V.M., Camp, D., and Quinn, R.J., 2009, Antimalarial activity of azafluorenone alkaloids from the Australian tree *Mitrephora diviversifolia*, *J. Nat. Prod.*, 72 (8), 1538–1540.
- [12] Moharam, B.A., Jantan, I., Jalil, J., and Shaari, K., 2010, Inhibitory effects of phylligenin and quebrachitol isolated from *Mitrephora vulpina* on platelet activating factor receptor binding and platelet aggregation, *Molecules*, 15 (11), 7840–7848.
- [13] Royal Botanic Gardens, 1922, “*Mitrephora winitii*” in *Bulletin of Miscellaneous Information*, Springer, Berlin/Heidelberg, 227–228.
- [14] Graidist, P., Martla, M., and Sukpondma, Y., 2015, Cytotoxic activity of *Piper cubeba* extract in breast cancer cell lines, *Nutrients*, 7 (4), 2707–2718.
- [15] Chaturvedula, V.S.P., and Prakash, I., 2012, Isolation

- of stigmasterol and  $\beta$ -sitosterol from the dichloromethane extract of *Rubus suavisissimus*, *Int. Curr. Pharm. J.*, 1 (9), 239–242.
- [16] Russell, G.B., and Fenemore, P.G., 1973, New lignans from leaves of *Macropiper excelsum*, *Phytochemistry*, 12 (7), 1799–1803.
- [17] Haasnoot, C.A.G., de Leeuw, F.A.A.M., de Leeuw, H.P.M., and Altona, C., 1981, The relationship between proton-proton NMR coupling constants and substituent electronegativities. II—Conformational analysis of the sugar ring in nucleosides and nucleotides in solution using a generalized Karplus equation, *Org. Magn. Reson.*, 15 (1), 43–52.
- [18] Jung, K.Y., Kim, D.S., Oh, S.R., Park, S.H., Lee, I.S., Lee, J.J., Shin, D.H., and Lee, H.K., 1998, Magnone A and B, Novel anti-PAF tetrahydrofuran lignans from the flower buds of *Magnolia fargesii*, *J. Nat. Prod.*, 61 (6), 808–811.
- [19] Tulake, A., Jiang, Y. and Tu, P.F., 2012, Nine lignans from *Atemisia absinthium* L., *J. Chin. Pharm. Sci.*, 21, 360–364.
- [20] Wang, T., Yuan, Y., Wang, J., Han, C., and Chen, G., 2012, Anticancer activities of constituents from the stem of *Polyalthia rumphii*, *Pak. J. Pharm. Sci.*, 25 (2), 353–356.
- [21] Dewick, P.M., 2002, “The shikimate pathway: Aromatic amino acids and phenylpropanoids” in *Medicinal Natural Products: A Biosynthetic Approach*, 2<sup>nd</sup> Ed., John Wiley & Sons, Ltd., UK, 121–166.
- [22] De León, E.J., Olmedo, D.A., Solis, P.N., Gupta, M.P., and Terencio, M.C., 2002, Diayagambin exerts immunosuppressive and anti-inflammatory effects *in vitro* and *in vivo*, *Planta Med.*, 68 (12), 1128–1131.
- [23] Júnior, H.V.N., Cunha, G.M.A., Moraes, M.O., Luciana, M.F.D., Oliveira, R.A., Maia, F.D., Nogueira, M.A.S., Lemos, T.L.G., and Rao, V.S., 2006, Quebrachitol (2-*O*-methyl-L-inositol) attenuates 6-hydroxydopamine-induced cytotoxicity in rat fetal mesencephalic cell cultures, *Food Chem. Toxicol.*, 44 (9), 1544–1551.
- [24] Sanseera, D., Niwatananun, W., Liawruangrath, B., Liawruangrath, S., Baramée, A., Trisuwan, K., and Pyne, S.G., 2012, Antioxidant and anticancer activities from aerial parts of *Acalypha indica* Linn, *Chiang Mai Univ. J. Nat. Sci.*, 11 (2), 157–168.
- [25] Abraham, R.J., Byrne, J.J., Griffiths, L., and Konioutou, R., 2005, <sup>1</sup>H chemical shifts in NMR: Part 22—Prediction of the <sup>1</sup>H chemical shifts of alcohols, diols and inositols in solution, a conformational and solvation investigation, *Magn. Reson. Chem.*, 43 (8), 611–624.

## Synthesis and DFT Study of the Complexation of Schiff Base Derived Curcumin and L-Tyrosine with Al(III), Ag(I), and Pb(II) Metal Ions

Ali Mahmood Ali<sup>1</sup>, Tagreed Hashim Al-Noor<sup>1</sup>, Eid Abdalrazaq<sup>2\*</sup>, and Abdel Aziz Qasem Jbarah<sup>2</sup>

<sup>1</sup>Department of Chemistry, Ibn Al-Haithem College of Education for Pure Science, Baghdad University, Baghdad, Iraq

<sup>2</sup>Department of Chemistry, College of Science, Al-Hussein Bin Talal University, Ma'an, Jordan

\* Corresponding author:

tel: +962-796862267

email: eidalzooby@yahoo.com

Received: December 13, 2020

Accepted: February 22, 2021

DOI: 10.22146/ijc.62188

**Abstract:** The multi-dentate Schiff base ligand ( $H_2L$ ), where  $H_2L=2,2'-(((1,3,5,6)-1-(3-((11-oxidaneryl)-15-methyl)-4-hydroxyphenyl)-7-(4-hydroxy-3-methoxyphenyl)hepta-1,6-diene-3,5-diylidene)bis(azanelylylidene))bis(3-(4-hydroxyphenyl)propanoic acid)$ , has been prepared from curcumin and L- Tyrosine amino acid. The synthesized Schiff base ligand ( $H_2L$ ) and the second ligand 1,10-phenanthroline (phen) are used to prepare the new complexes  $[Al(L)(phen)]Cl$ ,  $K[Ag(L)(phen)]$  and  $[Pb(L)(phen)]$ . The synthesized compounds are characterized by magnetic susceptibility measurements, micro elemental analysis (C.H.N), mass spectrometry, molar conductance, FT-infrared, UV-visible, atomic absorption (AA), <sup>13</sup>C-NMR, and <sup>1</sup>H-NMR spectral studies. The characterization of the synthesized complexes shows that the environment surrounding the central metal ion in the complexes adopted a distorted octahedral configuration. Moreover, the conductivity measurements show a non-electrolytic character for the  $[Pb(L)(phen)]$  complex and an electrolytic character for the  $[Al(L)(phen)]Cl$  and  $K[Ag(L)(phen)]$  complexes. The experimental infrared data are supported by density functional theory (DFT) calculations using the B3LYP level of theory and LANL2DZ basis set. The vibrational frequencies of the molecules are computed using the optimized geometry obtained from the DFT calculations. The calculated vibrational frequencies have been compared with obtained experimental values. <sup>1</sup>H and <sup>13</sup>C-NMR chemical shifts were computed for the  $H_2L$  ligand using the DFT/GIAO method. Additionally, the molecular electronic structures of the complexes have been investigated by DFT calculations.

**Keywords:** curcumin; L-tyrosine; silver; aluminium; lead; Schiff base

### ■ INTRODUCTION

Schiff base derived from curcumin has much attention due to its various medicinal properties against expanding and dangerous diseases, such as different types of cancer and diabetes. Curcumin has various biological activities includes antioxidant, anti-inflammatory, antiviral, antibacterial, and many more studies [1-2]. The curcumin Schiff base was coordinated to the metal ion due to their catalytic power and antioxidant activity of these complexes [3].

In drug design, targeting is an important phenomenon because toxicity is often encountered only if the drugs are not delivered to the specific tissues, cells, and receptors where they are required. If the active species of

drugs contain metal complexes, then the complexes can spontaneously undergo biological reactions such as ligand substitution and redox reactions. Thus, enumerating the mechanism of the active species on biological reactions is expected to yield valuable information about using the metal complexes as drugs [4].

During the last few decades, metal carboxylates have been the subject of extensive investigations because of their remarkable structural diversity and significant biological activity, for example, pesticidal, bactericidal, and antitumor agents [5]. The antimicrobial activities of lead compounds of Schiff base have been compared with the corresponding free Schiff bases and standard drugs

[6]. Silver-containing compounds are attractive because, in the range of the applicable concentrations, silver ions do not exhibit toxicity and carcinogenic activities. There is an increased interest in the potential use of silver (I) as a therapeutic agent for different antimicrobial applications [7].

Another attractive property of Schiff bases is their use as an effective corrosion inhibitor. They have been studied extensively as a class of ligands and are known to coordinate with metal ions through the azomethine nitrogen atom. The ligation nature of Schiff base shows a great potentiometric sensor as they have shown excellent selectivity, sensitivity, and stability for specific metal ions such as Ag(I), Al(III), Co(II), Cu(II), Gd(III), Hg(II), Ni(II), Pb(II), Y(III), and Zn(II), Fe(III), Cd(II). The bonding of Schiff base in their complexes is due to the donor nature of neutral N of azomethine linkage [8].

This research focused on the production and identification of Schiff bases derived from curcumin and L-Tyrosine amino acid and treatment with some metallic and non-metallic elements. Density functional theory (DFT) calculations, including geometry optimization, vibrational frequency analysis, and electronic structures, were reported for the synthesized molecules using the B3LYP level of theory and LANL2DZ basis set.

## ■ EXPERIMENTAL SECTION

### Materials

Aluminum chloride ( $\text{AlCl}_3$ , 99% Sigma-Aldrich, Germany), silver nitrate ( $\text{AgNO}_3$ ,  $\geq 99.0\%$ , Sigma-Aldrich, Germany), lead nitrate ( $\text{Pb}(\text{NO}_3)_2$ ,  $\geq 99.95\%$  Sigma-Aldrich, Germany), curcumin ( $\geq 98.0\%$  Sigma-Aldrich, Germany), L-Tyrosine ( $\geq 98\%$  Sigma-Aldrich, Germany), methanol ( $\geq 99.8\%$  Sigma-Aldrich, Germany) and dimethyl sulfoxide (DMSO,  $\geq 99.7\%$  Sigma-Aldrich, Germany) were used as supplied.

### Instrumentation

Melting points (M.P) were recorded by MPA160 – Digi Melt melting point apparatus. Elemental analyses (C, H, N) of ligand were performed by Eager300 for EA1112 Thermal Finnegan C.H.N.S 2400 elemental analyzer. The (AAS) analysis in complexes was recorded by using a fair

agreement method by used the device from type Shimadzu (A.A 620) atomic absorption spectrophotometer. The molar conductivity measurements of the complexes with  $10^{-3} \text{ mol L}^{-1}$  in dimethyl sulfoxide (DMSO) were performed by using a device digital conductivity series Ino.Lab.720. Magnetic measurements of the complexes were measured by using Balance Johnson Matthey. The mass spectrum of ligand was determined by using Ion source: Electron Impact (EI) 70eV mass spectra register on manufacturer company: Agilent Technology 1. MS Model: 5973 spectrometers. Ultraviolet-visible spectra were obtained by using DMSO as a solvent and a concentration of  $10^{-3} \text{ mol L}^{-1}$  for the ligand and complexes. Ultraviolet-visible spectra were carried by double-beam UV-visible spectrophotometry type U.V 160A (Shimadzu) at the range between 200 and 1100 nm with a 1 cm quartz cell. The Fourier-transform infrared spectra were recorded using KBr pellets on Shimadzu FT-IR 8400S spectrophotometry. The Fourier-transform infrared spectra were recorded at the range of 400 to  $4000 \text{ cm}^{-1}$ .  $^1\text{H}$  and  $^{13}\text{C}$ -NMR spectra were obtained from (DMSO- $d_6$  Solution using an Inova 500 MHz.

### Procedure

#### Preparation of the ligand

The ligand (Schiff base) was prepared by condensation of L-Tyrosine (0.362 g, 2 mmol) dissolved in 25 mL of hot water-ethanol mixture (1:1, ratio) solution and Curcumin (0.368 g, 1 mmol) dissolved in 25 mL of hot ethanol. The mixture was refluxed for about 10 h with the TLC technique observed until obtained a yellow-brown precipitate. It was filtered and purified by repeated washing with water-ethanol, as recrystallized from hot ethanol. The preparation of the Schiff base ligand  $\text{H}_2\text{L}$  is summarized in Scheme 1. The yield of the prepared Schiff base ligand,  $\text{H}_2\text{L}$ , was 81% (solid, Color: pale brown, m.p. 150–152 °C). FTIR (KBr,  $\text{cm}^{-1}$ ): 3508 ( $\nu(\text{O}-\text{H})$ ,  $-\text{COOH}$ ), 3400 ( $\nu(\text{O}-\text{H})$ , phenolic), 1629 ( $\nu(\text{C}=\text{N})$ ), 1595 ( $\nu_{\text{as}}(\text{COO})$ ,  $-\text{COOH}$ ), 1425 ( $\nu_{\text{s}}(\text{COO})$ ,  $-\text{COOH}$ ), 1244 ( $\nu(\text{C}-\text{O})$ , phenolic). UV-Vis spectroscopy ( $10^{-3} \text{ mol L}^{-1}$  concentration in DMSO,  $\lambda_{\text{max}}$  nm): 272, 433.  $^1\text{H}$ -NMR (500 MHz, DMSO-

d6):  $\delta$  9.66 (bs, 2H, OH), 7.54 (d, 4H, C<sub>6</sub>H<sub>4</sub>), 7.31 (d, 4H, C<sub>6</sub>H<sub>4</sub>), 7.15 (s, 2H, C=CH), 6.83–6.66 (m, 6H, C<sub>6</sub>H<sub>3</sub>), 6.06 (s, 2H, C=CH), 3.83 (s, 6H, OCH<sub>3</sub>), 3.74–3.36 (m, 8H, CH, CH<sub>2</sub>). <sup>13</sup>C-NMR (500 MHz, DMSO-d<sub>6</sub>):  $\delta$  183.2, 166.4, 149.4, 148.0, 147.0, 140.7, 140.4, 130.3, 126.3, 123.1, 121.1, 120.8, 119.6, 119.5, 115.9, 115.7, 111.3, 111.3, 100.8, 55.7. Anal. Calcd. for C<sub>39</sub>H<sub>38</sub>N<sub>2</sub>O<sub>10</sub> (694.25 g/mol): C, 67.43; H, 5.51; N, 4.03; O, 23.03%. Found: C, 66.41; H, 5.39; N, 4.09%.

### Preparation of the [Pb(L)(phen)] complex

1.0 mmol of lead(II) nitrate is dissolved in 10 mL of absolute ethanol to obtain metal ion (Pb<sup>2+</sup>) solution. A ligand solution is obtained by dissolving 1.0 mmol of Schiff base ligand, 2.0 mmol of potassium hydroxide, and 1.0 mmol of 1,10-phenanthroline in 15 mL of absolute ethanol. The ligand solution is gradually added to the metal ion (Pb<sup>2+</sup>) solution with constant stirring for 30 min to obtain the precipitate. The precipitate is filtrated and washed several times in a mixture of solvent (ethanol: distilled water, 50%). The precipitate is recrystallized from the hot ethanol. The preparation of the [Pb(L)(phen)] complex is summarized in Scheme 2. The yield of the [Pb(L)(phen)] complex, was 89% (solid, Color: brown, m.p. 156–158 °C). FTIR (KBr, cm<sup>-1</sup>): 3435 ( $\nu$ (O–H), phenolic), 1620 ( $\nu$ (C=N)), 1581 ( $\nu_{as}$ (COO), –COOH), 1384 ( $\nu_s$ (COO), –COOH), 1246 ( $\nu$ (C–O), phenolic), 576 ( $\nu$ (Pb–O)), 464 ( $\nu$ (Pb–N)). UV-Vis spectroscopy (10<sup>-3</sup> mol L<sup>-1</sup> concentration in DMSO,  $\lambda_{max}$  nm): 271, 435, 735. Metal percent in [Pb(L)(phen)] complex, calculated: 19.18%. Found: 18.01%. Molar conductivity (10<sup>-3</sup> mol L<sup>-1</sup> concentration in DMSO): 5.6  $\Omega^{-1}$  cm<sup>2</sup> mol<sup>-1</sup>.

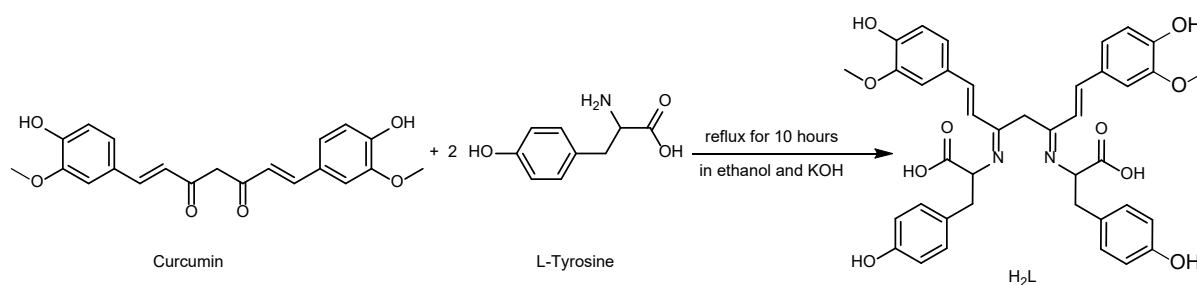
### Preparation of the [Al(L)(phen)]Cl complex

1.0 mmol aluminium(III) chloride is dissolved in 10 mL of absolute ethanol to obtain a homogeneous metal

ion (Al<sup>3+</sup>) solution. A ligand solution is obtained by dissolving 1.0 mmol of Schiff base ligand, 2.0 mmol of potassium hydroxide, and 1.0 mmol of 1,10-phenanthroline in 15 mL of absolute ethanol. The ligand solution is gradually added to the metal ion (Al<sup>3+</sup>) solution with constant stirring for 30 min to obtain the precipitate. The precipitate is filtrated and washed several times in a mixture of solvent (ethanol: distilled water, 50%). The precipitate is recrystallized from the hot ethanol. The preparation of the [Al(L)(phen)]Cl complex is summarized in Scheme 2. The yield of the [Al(L)(phen)]Cl complex, was 60% (solid, Color: pale yellow, m.p. 222–224 °C). FTIR (KBr, cm<sup>-1</sup>): 3398 ( $\nu$ (O–H), phenolic), 1612 ( $\nu$ (C=N)), 1589 ( $\nu_{as}$ (COO), –COOH), 1363 ( $\nu_s$ (COO), –COOH), 1244 ( $\nu$ (C–O), phenolic), 576 ( $\nu$ (Al–O)), 474 ( $\nu$ (Al–N)). UV-Vis spectroscopy (10<sup>-3</sup> mol L<sup>-1</sup> concentration in DMSO,  $\lambda_{max}$  nm): 279, 442, 802. Metal percent in [Al(L)(phen)]Cl complex, calculated: 2.88%. Found: 3.4%. Molar conductivity (10<sup>-3</sup> mol L<sup>-1</sup> concentration in DMSO): 42.5  $\Omega^{-1}$  cm<sup>2</sup> mol<sup>-1</sup>.

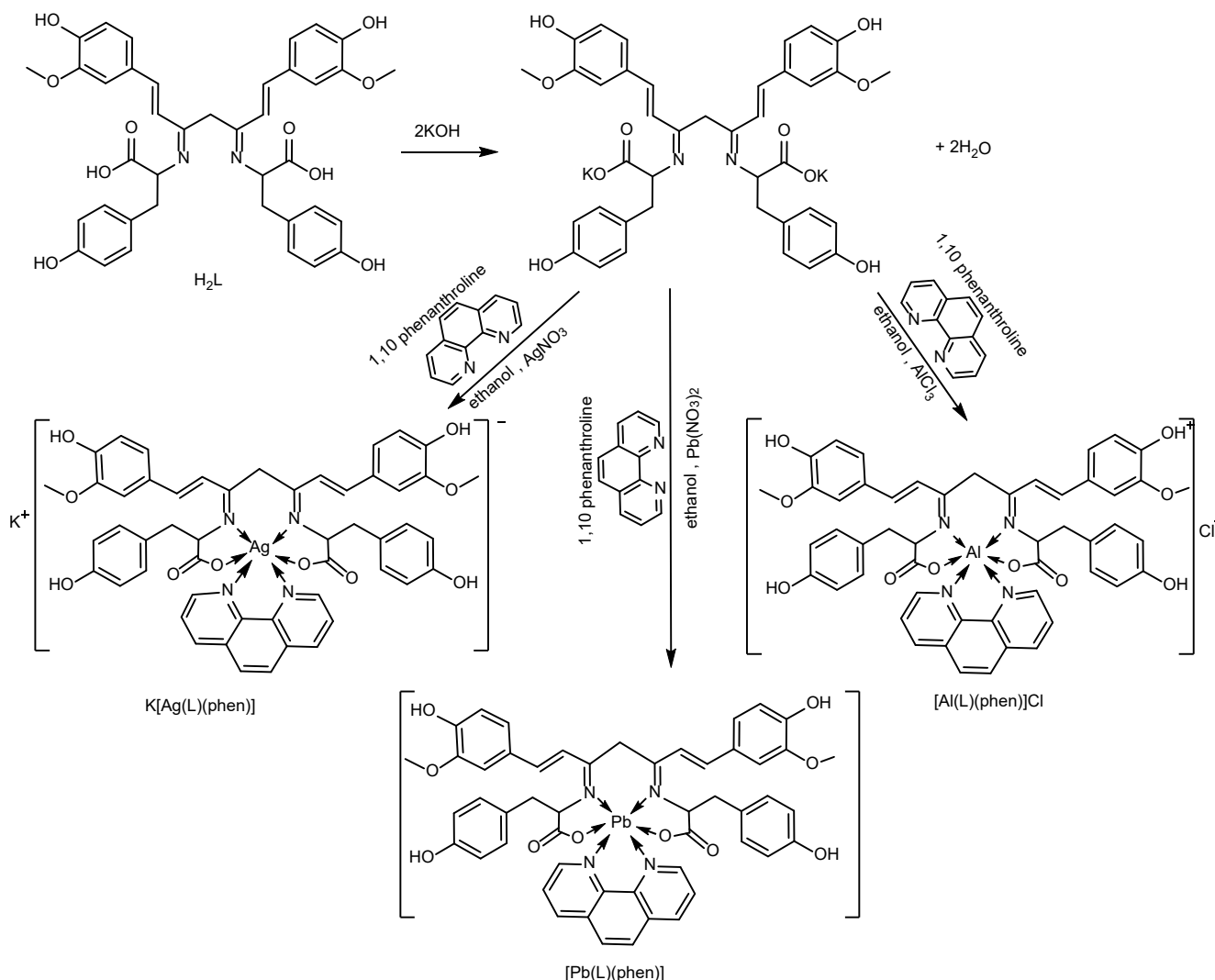
### Preparation of the K[Ag(L)(phen)] complex

1.0 mmol silver(I) nitrate is dissolved in 10 mL of absolute ethanol to obtain a homogeneous metal ion (Ag<sup>+</sup>) solution. A ligand solution is obtained by dissolving 1.0 mmol of Schiff base ligand, 2.0 mmol of potassium hydroxide, and 1.0 mmol of 1,10-phenanthroline in 15 mL of absolute ethanol. The ligand solution is gradually added to the metal ion (Ag<sup>+</sup>) solution with constant stirring for 30 min to obtain the precipitate. The precipitate is filtrated and washed several times in a mixture of solvent (ethanol: distilled water, 50%). The precipitate is recrystallized from the hot ethanol. The preparation of the K[Ag(L)(phen)] complex



Scheme 1. Preparation of the Schiff base ligand





**Scheme 2.** Preparation of the  $[\text{Pb}(\text{L})(\text{phen})]$ ,  $[\text{Al}(\text{L})(\text{phen})]\text{Cl}$  and  $\text{K}[\text{Ag}(\text{L})(\text{phen})]$  complexes

is summarized in Scheme 2. The yield of the  $\text{K}[\text{Ag}(\text{L})(\text{phen})]$  complex, was 79% (solid, Color: pale brown, m.p. 188–189 °C). FTIR (KBr,  $\text{cm}^{-1}$ ): 3396 ( $\nu(\text{O}-\text{H})$ , phenolic), 1620 ( $\nu(\text{C}=\text{N})$ ), 1583 ( $\nu_{\text{as}}(\text{COO})$ ,  $-\text{COOH}$ ), 1382 ( $\nu_{\text{s}}(\text{COO})$ ,  $-\text{COOH}$ ), 1244 ( $\nu(\text{C}-\text{O})$ , phenolic), 578 ( $\nu(\text{Ag}-\text{O})$ ), 474 ( $\nu(\text{Ag}-\text{N})$ ). UV-Vis spectroscopy ( $10^{-3}$  mol  $\text{L}^{-1}$  concentration in DMSO,  $\lambda_{\text{max}}$  nm): 286, 428, 707, 829. Metal percent in  $[\text{Al}(\text{L})(\text{phen})]\text{Cl}$  complex, calculated: 10.58%. Found: 7.92%. Molar conductivity ( $10^{-3}$  mol  $\text{L}^{-1}$  concentration in DMSO): 37.2  $\Omega^{-1} \text{cm}^2 \text{mol}^{-1}$ .

### Computational details

Gaussian 09 software [9] is used to perform the DFT calculations. All structures of the synthesized compounds were optimized at the B3LYP/LANL2DZ level of theory

[10]. Several researchers used the LANL2DZ as a basis set in DFT calculations of systems that included Ag and Pb atoms [11-12]. The GaussView 5.0, supported by Gaussian Inc. [9], was used to generate the input files that correspond to the DFT calculations. The GaussView 5.0 software is used to visualize and analyze the data obtained from Gaussian09 output results. A frequency calculation was performed to identify the most stable structures of the synthesized compounds. The absence of the imaginary frequencies in the calculated vibrational modes indicates that the corresponding optimized structure of the molecule is the most stable one. The obtained values of the vibrational modes from the DFT calculations were scaled by a factor of 0.966 [13]. The

DFT/GIAO (gauge-independent atomic orbital) method was used to calculate and assign the  $^1\text{H}$  and  $^{13}\text{C}$ -NMR chemical shifts for carbon and hydrogen atoms of the  $\text{H}_2\text{L}$  ligand. The isotropic atomic chemical shifts in ppm unit were calculated as differences between the atomic isotropic shielding of the  $\text{H}_2\text{L}$  ligand and the corresponding reference atoms in TMS (tetramethylsilane). The energies and electron densities of the frontiers' molecular orbitals were calculated using the B3LYP level of theory and the LANL2DZ as a basis set. The excited states were computed for all compounds at the same level of theory using the TD-DFT (Time-Dependent Density Functional Theory) method [14]. The TD-DFT calculations were performed in DMSO solvent using the CPCM solvation model (conductor-like polarizable continuum model) [15]. The Projected density of states (PDOS) has been obtained through the calculated orbital populations for all compounds at the same level of theory, using GAUSSSUM 3.0 program [16].

## ■ RESULTS AND DISCUSSION

Generally, this study included synthesis Schiff base ligand ( $\text{H}_2\text{L}$ ) multi-dentate ( $\text{N}_2\text{O}_2$ ) couple negative charge derived from (1 mmol) curcumin and (2 mmol) of L-Tyrosine amino acid. The synthesized Schiff base metal complexes and some physicochemical properties are listed in Table 1.  $\text{Cl}^-$  ions were not detected by the addition of  $\text{AgNO}_3$  solution to the solutions of the three complexes for  $\text{K}[\text{Ag}(\text{L})(\text{phen})]$  and  $[\text{Pb}(\text{L})(\text{phen})]$  but

detected for  $[\text{Al}(\text{L})(\text{phen})]\text{Cl}$  complex. The  $\text{K}[\text{Ag}(\text{L})(\text{phen})]$ ,  $[\text{Pb}(\text{L})(\text{phen})]$  and  $[\text{Al}(\text{L})(\text{phen})]\text{Cl}$  complexes are stable in the air environment and have higher melting points. The solubility test indicates that these complexes are soluble in DMF, DMSO, and concentrated HCl acid. They are insoluble in  $\text{H}_2\text{O}$  and partially soluble in ethanol, acetone methanol, and most organic solvents. The molar conductivity values for  $10^{-3}$  mol  $\text{L}^{-1}$  concentration of the  $\text{K}[\text{Ag}(\text{L})(\text{phen})]$ ,  $[\text{Pb}(\text{L})(\text{phen})]$  and  $[\text{Al}(\text{L})(\text{phen})]\text{Cl}$  complexes in DMSO solvent are listed in Table 1. For the  $\text{K}[\text{Ag}(\text{L})(\text{phen})]$  and  $[\text{Al}(\text{L})(\text{Phen})]\text{Cl}$  complexes the molar conductivity are 37.2 and  $42.5 \Omega^{-1} \text{ cm}^2 \text{ mol}^{-1}$ , respectively. These results suggest that these complexes are electrolytes. The molar conductivity of the  $[\text{Pb}(\text{L})(\text{phen})]$  complex is  $5.6 \Omega^{-1} \text{ cm}^2 \text{ mol}^{-1}$ , which is revealing a non-electrolyte nature of this complex.

### Mass Spectrum

The mass spectral fragmentation of the Schiff base ligand ( $\text{H}_2\text{L}$ ) is displayed in Fig. 1. In the spectrum (Fig. 1), the peak positions of the structure consist with the formulas  $[\text{C}_{39}\text{H}_{38}\text{N}_2\text{O}_{10}]$ ,  $[\text{C}_{39}\text{H}_{36}\text{N}_2\text{O}_{10}]$ ,  $[\text{C}_{39}\text{H}_{37}\text{N}_2\text{O}_9]$ ,  $[\text{C}_{39}\text{H}_{52}\text{N}_2\text{O}_7]$ ,  $[\text{C}_{37}\text{H}_{58}\text{N}_2\text{O}_3]$  and  $[\text{C}_{36}\text{H}_{68}\text{N}_2\text{O}_2]$  appears at  $m/z$  values of 694, 692, 676, 660, 579 and 555, respectively. These spectral fragmentations allowed us to determine the molecular weight of the  $\text{H}_2\text{L}$  ligand, which is consists of the chemical formula  $[\text{C}_{39}\text{H}_{38}\text{N}_2\text{O}_{10}]$ , and equal to  $694 \text{ g mol}^{-1}$ .

**Table 1.** Formula weight, melting point, color, metal percent, percentage yield and conductivity measurement of the  $\text{H}_2\text{L}$ , phen,  $\text{K}[\text{Ag}(\text{L})(\text{phen})]$ ,  $[\text{Pb}(\text{L})(\text{phen})]$  and  $[\text{Al}(\text{L})(\text{phen})]\text{Cl}$  compounds

Compound	Formula weight ( $\text{g mol}^{-1}$ )	Color	Melting point ( $^{\circ}\text{C}$ )	Metal %	$\Lambda_m$ ( $\Omega^{-1} \text{ cm}^2 \text{ mol}^{-1}$ )	% Yield
$\text{H}_2\text{L}$	694.25	Yellow brown	150–152	-	-	81
phen	180.21	-	-	-	-	-
$[\text{Al}(\text{L})(\text{phen})]\text{Cl}$	935.36	Pale yellow	222–224	2.88 <sup>a</sup> 3.4 <sup>b</sup>	37.2 <sup>c</sup>	60
$\text{K}[\text{Ag}(\text{L})(\text{phen})]$	1019.90	Pale brown	188–189	10.58 <sup>a</sup> 7.92 <sup>b</sup>	42.5 <sup>c</sup>	79
$[\text{Pb}(\text{L})(\text{phen})]$	1080.13	Brown	156–158	19.18 <sup>a</sup> 18.01 <sup>b</sup>	5.6 <sup>c</sup>	89

<sup>a</sup>: theoretical value calculated from the molecular formula of the complex, <sup>b</sup>: experimental value where determined according to the reported method in reference [17], <sup>c</sup>: measured in DMSO

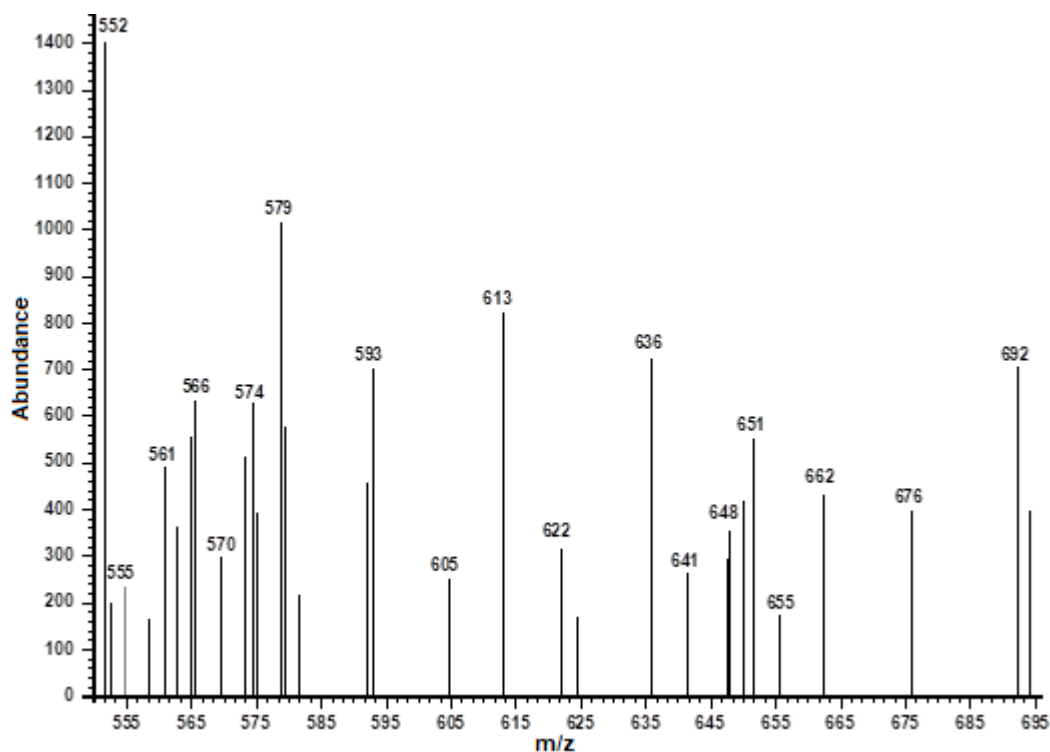


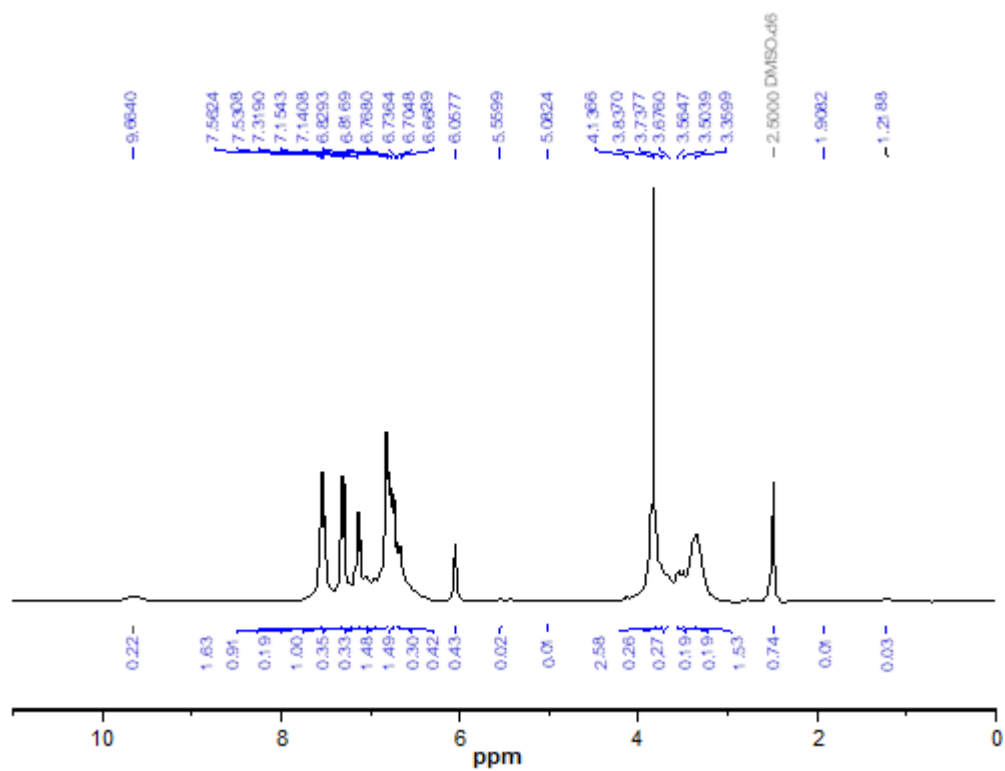
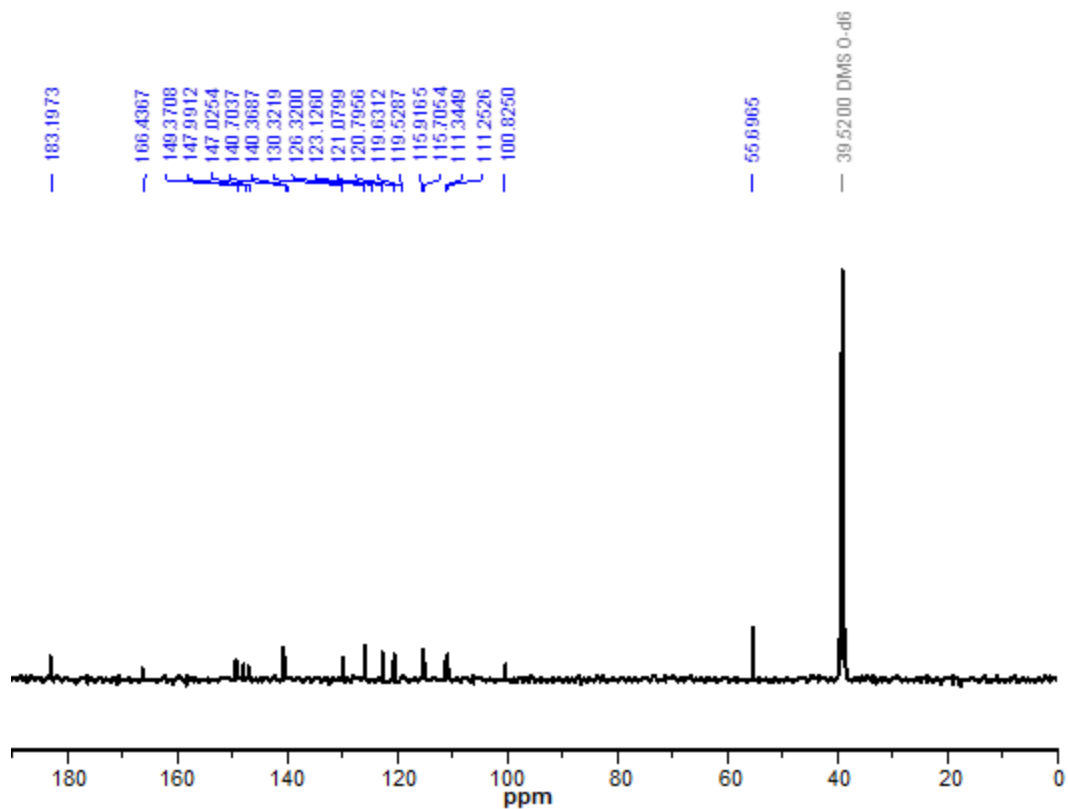
Fig 1. Fragmentation mass spectrum of Schiff base ( $H_2L$ )

### $^1H$ and $^{13}C$ -NMR Spectra of the Tetradentate Schiff Base Ligand ( $H_2L$ )

$^1H$ -NMR spectrum of the prepared Schiff base ligand,  $H_2L$ , in DMSO solvent is shown in Fig. 2. In Fig. 2, a signal appeared at 9.66 ppm which corresponds to the hydrogen atom of the phenolic hydroxyl group. According to the DFT/GIAO calculations, the theoretical chemical shift value of the proton of the phenolic hydroxyl group is obtained at 9.44 ppm. Multiples peaks appear in the range of 6.83–6.66 ppm and 7.56–7.32 ppm are corresponding to the benzene ring protons [18]. The calculated values for these peaks are in perfect agreement with those obtained experimentally, and they are observed in the range of 7.77–7.21 and 6.90–6.35 ppm. The peaks at 6.06 and 7.15 ppm are assigned to the protons of the  $C=CH$  group. The calculated chemical shift value of the  $C=CH$  group protons are at 5.74 and 7.10 ppm. The peak at 3.83 ppm is assigned to the protons of the  $OCH_3$  [19–20]. The calculated chemical shift value, obtained by the DFT/GIAO method, of the  $OCH_3$  protons, appeared at 3.80 ppm. The multiples peaks that appeared in the range 3.74–3.36 ppm correspond to the

CH and  $CH_2$  groups. The corresponding calculated chemical shift values of the proton of the CH and  $CH_2$  groups are in the range of 3.41–3.00 ppm. The missing of the carboxylic proton signal in the spectrum of Fig. 2 is due to hydrogen bonding in the ligand structure [21].

The  $^{13}C$ -NMR spectrum of tetradentate Schiff base ligand ( $H_2L$ ) is shown in Fig. 3. The spectrum of Fig. 3 shows a clear a strong peak at 183.2 ppm, which is an attribute to the carbonyl moiety of the carboxylic group [22]. The calculated chemical shift value of the carbon atom of the carboxylic group appears at 178.6 ppm. Also, peaks appeared at 149.4, 166.4, 148.0–147.0, 140.7–140.4, and 130.3 ppm are assigned to the carbons of the  $C-OH$  (carbon of benzene ring),  $C=N$  (azomethine),  $C-OCH_3$  (carbon of benzene ring),  $C=C$  (ethylene) and  $(HOOC-C-H-N)$  groups, respectively [23]. The calculated peaks corresponding to the chemical shift of the carbons of the  $C-OH$  (carbon of benzene ring),  $C=N$  (azomethine),  $C-OCH_3$  (carbon of benzene ring),  $C=C$  (ethylene), and  $(HOOC-C-H-N)$  groups are observed at 149.7, 163.8, 146.0–145.2, 143.7–143.0, and 136.4 ppm, respectively. In the recorded spectrum, the peaks correspond to the

Fig 2.  $^1\text{H}$ -NMR spectrum of tetradentate Schiff base ( $\text{H}_2\text{L}$ )Fig 3.  $^{13}\text{C}$ -NMR spectrum of tetradentate Schiff base ( $\text{H}_2\text{L}$ )

aromatic ring that appears in the range 111.3–126.3 ppm [24] and in the calculated one appears in the range 109.0–135.0 ppm. Additional signals appear at 55.7 ppm and are assigned to the methoxy carbons [25]. The calculated chemical shift value of the carbon atom of the methoxy carbon of the H<sub>2</sub>L is very close to each other and appears at 56.75 ppm and 56.59 ppm. The chemical shift value of the carbon of the methylene (CH<sub>2</sub>) group is observed at 100.8 ppm experimentally. The calculated chemical shift value of the carbon atom of the methylene group is 106.3 ppm.

### Vibrational Frequencies Results

Selected vibrational frequencies of infrared spectra of the [Al(L)(phen)]Cl, K[Ag(L)(phen)], and [Pb(L)(phen)] complexes and the H<sub>2</sub>L ligand are given in Table 2. The assignments for the observed infrared bands were based on the calculated vibrational modes and the literature data [26–30]. The spectrum of the H<sub>2</sub>L ligand shows a band at 3508, 3400, 1629, 1595, and 1425 cm<sup>-1</sup> which are attributed to  $\nu(\text{O-H})_{\text{carboxylic}}$ ,  $\nu(\text{O-H})_{\text{phenolic}}$ ,  $\nu(\text{C=N})_{\text{azomethine}}$ ,  $\nu_{\text{as}}(\text{COO})$  and  $\nu_{\text{s}}(\text{COO})$ , respectively. The  $\nu(\text{O-H})_{\text{carboxylic}}$  band disappeared in the infrared spectra of all complexes. This result confirms a complete replacement of the H<sup>+</sup> of the carboxylic group of the H<sub>2</sub>L ligand by K<sup>+</sup> during the synthesis steps of the complexes (Scheme 1). The  $\nu(\text{C=N})_{\text{azomethine}}$ ,  $\nu_{\text{as}}(\text{COO})$ , and  $\nu_{\text{s}}(\text{COO})$  bands appear at lower vibrational frequencies in the infrared spectra of all complexes as compared to those of the H<sub>2</sub>L ligand. The shifting to the lower frequencies of

these bands indicates coordination via the oxygen atom of the carboxylic group and nitrogen of the azomethine group of the H<sub>2</sub>L ligand with the metal ion. The phenolic  $\nu(\text{C-O})$  band appears in the infrared spectra of all complexes at wavenumbers very close to that of the H<sub>2</sub>L ligand (Table 2). This result indicates that the phenolic hydroxyl group of the H<sub>2</sub>L ligand did not participate in the coordination with the metal ions. In the infrared spectra of all complexes, new bands at 464–474 cm<sup>-1</sup> and 576–578 cm<sup>-1</sup> are observed and attributed to the  $\nu(\text{M-N})$  and  $\nu(\text{M-O})$ , respectively. The appearance of these bands supported the coordination of the H<sub>2</sub>L ligand with the metal ions via oxygen and nitrogen atoms.

### UV-Vis Spectra

The UV-vis spectra of the prepared ligand and its complex were recorded using 10<sup>-3</sup> M concentration of each compound in DMSO solvent. The results of the UV-visible measurements of these compounds are listed in Table 3. The UV-vis spectrum of the ligand L shows only two peaks. The first absorption peak appears at 272 nm (36765 cm<sup>-1</sup>) and is assigned to  $\pi \rightarrow \pi^*$ . This transition corresponds to the aromatic ring and double bonds fragments of the ligand L. The second absorption peak appears at 433 nm (23095 cm<sup>-1</sup>) and is assigned to  $n \rightarrow \pi^*$  transition. This transition corresponds to the azomethine (-C=NH), hydroxyl, amine, and methoxy groups of the ligand L. This conclusion is based on that these groups are possessing non-shared electronic pairs [31]. The UV-visible spectra of the K[Ag(L)(phen)],

**Table 2.** Infrared absorption (in cm<sup>-1</sup>) data as observed and calculated for the H<sub>2</sub>L, K[Ag(L)(phen)], [Pb(L)(phen)] and [Al(L)(phen)]Cl compounds

Compound	$\nu(\text{O-H})_{\text{carboxylic}}$	$\nu(\text{O-H})_{\text{phenolic}}$	$\nu(\text{C=N})$	$\nu_{\text{as}}(\text{COO})$	$\nu_{\text{s}}(\text{COO})$	$\nu(\text{C-O})_{\text{phenolic}}$	$\nu(\text{M-O})$	$\nu(\text{M-N})$
H <sub>2</sub> L	3508 (3579) <sup>a</sup>	3400 (3526) <sup>a</sup>	1629 (1622) <sup>a</sup>	1595 (1597) <sup>a</sup>	1425 (1445) <sup>a</sup>	1244 (1249) <sup>a</sup>	-	-
[Al(L)(phen)]Cl	-	3398 (3574) <sup>a</sup>	1612 (1601) <sup>a</sup>	1589 (1590) <sup>a</sup>	1363 (1366) <sup>a</sup>	1244 (1243) <sup>a</sup>	576 (583) <sup>a</sup>	474 (478) <sup>a</sup>
k[Ag(L)(phen)]	-	3396 (3527) <sup>a</sup>	1620 (1629) <sup>a</sup>	1583 (1580) <sup>a</sup>	1382 (1390) <sup>a</sup>	1244 (1242) <sup>a</sup>	578 (576) <sup>a</sup>	474 (480) <sup>a</sup>
[Pb(L)(phen)]	-	3435 (3592) <sup>a</sup>	1620 (1634) <sup>a</sup>	1581 (1582) <sup>a</sup>	1384 (1380) <sup>a</sup>	1246 (1244) <sup>a</sup>	576 (573) <sup>a</sup>	464 (456) <sup>a</sup>

<sup>a</sup>: Calculated value according to B3LYP/LANL2DZ level,  $\nu_{\text{s}}$ : symmetric stretching;  $\nu_{\text{as}}$ : asymmetric stretching;  $\nu$ : stretching; M: the corresponding metal

**Table 3.** Computed excitation energies, electronic transition configurations, and oscillator strengths ( $f$ ) for the optical transitions in the visible region of the L ligand and the complexes (transitions with  $f \geq 0.01$  are listed)

Compound	Experimental results		TD-DFT results	
	$\lambda_{\max}$ (nm)	$\lambda_{\max}$ (nm)	Oscillator strength ( $f$ )	Major contributions
$H_2L$	272	289	0.4171	$H_{-3} \rightarrow L, H_{-2} \rightarrow L, H_{-2} \rightarrow L_{+1}, H_{-1} \rightarrow L$
		282	0.1513	$H_{-3} \rightarrow L, H_{-2} \rightarrow L_{+1}, H_{-1} \rightarrow L_{+1}$
	433	427	0.4254	$H_{-1} \rightarrow L, H \rightarrow L_{+1}$
		425	0.2227	$H_{-3} \rightarrow L, H_{-1} \rightarrow L, H \rightarrow L_{+1}$
[Al(L)(phen)]Cl	279	290	0.0706	$H \rightarrow L_{+2}$
	442	427	0.2941	$H_{-2} \rightarrow L, H \rightarrow L$
		423	0.0624	$H_{-3} \rightarrow L_{+1}, H_{-3} \rightarrow L_{+2}, H_{-1} \rightarrow L$
K[Ag(L)(phen)]	802	795	0.0803	$H_{-2} \rightarrow L, H \rightarrow L$
	268	261	0.0444	$H_{-1} \rightarrow L_{+1}, H \rightarrow L_{+1}$
	428	411	0.0217	$H_{-1} \rightarrow L, H \rightarrow L$
	707	720	0.0251	$H_{-3} \rightarrow L, H_{-2} \rightarrow L, H \rightarrow L$
[Pb(L)(phen)]	829	335	0.0163	$H_{-3} \rightarrow L, H \rightarrow L, H \rightarrow L_{+1}, H \rightarrow L_{+2}$
	271	295	0.0144	$H_{-6} \rightarrow L, H \rightarrow L_{+2}$
	435	418	0.0122	$H_{-4} \rightarrow L, H_{-2} \rightarrow L, H \rightarrow L_{+1}$
	735	730	0.116	$H_{-3} \rightarrow L, H_{-1} \rightarrow L$
728		0.0137	$H \rightarrow L$	

H: HOMO, L: LUMO

[Al(L)(phen)] Cl, and [Pb(L)(phen)] complexes show appearing of peaks at different frequency values from that of the ligand  $H_2L$ . Also, the UV-visible spectra of the complexes show the appearance of new frequencies that corresponds to charge transfer. These results support the coordination of the ligand L with metal ions.

In the UV-visible spectrum of [Al(L)(phen)]Cl complex three peaks appeared. The first peak appeared at 279 nm ( $358842 \text{ cm}^{-1}$ ) with high intensity and corresponded to intra ligand transition. The second peak is due to the charge transfer and appears at 442 nm ( $22624 \text{ cm}^{-1}$ ). The third peak appears at 802 nm ( $12469 \text{ cm}^{-1}$ ). This peak is attributed to metal (Al)  $\rightarrow$  ligand (L) transition. The Al $\rightarrow$ L transition was detected by monitoring  $4s \rightarrow 3p$  emission from Al(4s) atoms produced by pre disengagement of the excited complex [32].

The UV-visible spectrum of K[Ag(L)(phen)] complex shows the appearance of four peaks at 268 nm ( $37313 \text{ cm}^{-1}$ ), 428 nm ( $23364 \text{ cm}^{-1}$ ), 707 nm ( $14144 \text{ cm}^{-1}$ ) and 829 nm ( $12063 \text{ cm}^{-1}$ ). The peaks at 268 nm ( $37313 \text{ cm}^{-1}$ ) and 428 nm ( $23364 \text{ cm}^{-1}$ ) correspond to  $\pi \rightarrow \pi^*$  and  $n \rightarrow \pi^*$  transitions, respectively. The other two peaks are assigned to ligand-metal charge transfer transitions [23].

The UV-visible spectrum of [Pb(L)(phen)] complex shows a three peaks at 271 nm ( $36900 \text{ cm}^{-1}$ ), 435 nm ( $22989 \text{ cm}^{-1}$ ) and 735 nm ( $13605 \text{ cm}^{-1}$ ). The transitions at 271 nm ( $36900 \text{ cm}^{-1}$ ) and 435 nm ( $22988 \text{ cm}^{-1}$ ) correspond to conjugated  $\pi$  system and they are due to  $\pi \rightarrow \pi^*$  and to  $n \rightarrow \pi^*$  transitions, respectively. The third peak appeared at the visible area and corresponds to L-M charge transfer (C.T) transitions from COO $^-$  groups [32-33]. The three complexes are also diamagnetic as expected from their electron configuration [18]. The electronic spectral studies confirm the octahedral geometry of these complexes [33]. Furthermore, the complexes K[Ag(L)(phen)], [Al(L)(phen)]Cl and [Pb(L)(phen)] are diamagnetic as indicated from its magnetic moment measurements. These results support the conclusion drawn from the electronic spectral data of these complexes. The experimental data, which are obtained from the electronic spectra and the magnetic measurements values of the complexes, are in good agreement with the calculated optimized structure of these.

#### DFT Calculations and Electronic Structures

The optimized structures of the K[Ag(L)(phen)],

[Al(L)(phen)]Cl, and [Pb(L)(phen)] complexes according to the B3LYP/LANL2DZ level of theory are displayed in Fig. 4. Selected bond distances and bond angles of the optimized structures of these complexes are listed in Table 4. The observations from the calculated geometries that displayed in Fig. 4 show that the environment surrounding the central metal ion in [Al(L)(phen)]Cl, K[(Ag(L)(phen))] and [Pb(L)(phen)] complexes adopted distorted octahedral configuration. The distorted octahedral of the environment surrounding the central metal atom of these complexes is due to the tension that comes from the formation of three rings around the central metal upon complexation.

The calculated bond length of Ag(1)-N(45), Ag(1)-N(46), Ag(1)-N(2) and Ag(1)-N(3) of the K[Ag(L)(phen)] complex (Table 4) are 2.534, 2.663, 2.590 and 2.383 Å, respectively. The typical Ag-N bond lengths are reported within the range 2.1–2.7 Å [34–37]. Moreover, the calculated Ag-N bond lengths of the

K[Ag(L)(phen)] complex is shorter than the sum of the van der Waals radii of N and Ag atoms (1.55 and 1.72 Å, respectively) [38]. The calculated bond length of Ag(1)-O(5) and Ag(1)-O(4) of the K[Ag(L)(phen)] complex (Table 4) are 2.685 and 2.291 Å, respectively. These values are within the reported Ag-O bond lengths range (2.032–2.754 Å) [35,39–40]. It should be noted that the calculated Ag-O bond lengths are not larger than the sum of the van der Waals radii of O and Ag atoms, which are 1.52 and 1.72 Å, respectively [38].

The optimized geometry of the [Al(L)(phen)]K complex (Fig. 4, Table 4), shows that the bond length of Al(86)-N(45), Al(86)-N(44), Al(86)-N(2), Al(86)-N(1), Al(86)-O(4) and Al(86)-O(3) are 2.173, 2.104, 2.035, 2.072, 1.852 and 1.862 Å, respectively. Previous studies concerning the complexation of Al<sup>3+</sup> with Schiff base reported that the bond lengths of Al-N and Al-O are within the range of 1.988–2.013 Å and 1.809–1.881 Å, respectively [41–42]. The values of Al-N and Al-O bond

**Table 4.** Selected bond lengths (Å) and bond angles (°) of the computed structures of the [Al(L)(phen)]Cl, K[(Ag(L)(phen))] and [Pb(L)(phen)] according to B3LYP/LANL2DZ level of theory

Bond Lengths (Å) of [Al(L)(phen)]Cl		Bond Lengths (Å) of K[(Ag(L)(phen))]		Bond Lengths (Å) of [Pb(L)(phen)]	
N(45)-Al(86)	2.173	Ag(1)-N(45)	2.534	N(45)-Pb(86)	2.839
N(44)-Al(86)	2.104	Ag(1)-N(46)	2.663	N(44)-Pb(86)	2.834
O(4)-Al(86)	1.852	Ag(1)-O(5)	2.685	O(4)-Pb(86)	2.212
O(3)-Al(86)	1.869	Ag(1)-O(4)	2.291	O(3)-Pb(86)	2.198
N(2)-Al(86)	2.035	Ag(1)-N(2)	2.590	N(2)-Pb(86)	2.805
N(1)-Al(86)	2.072	Ag(1)-N(3)	2.383	N(1)-Pb(86)	2.876
Angles (°) of [Al(L)(phen)]Cl		Angles (°) of K[(Ag(L)(phen))]		Angles (°) of [Pb(L)(phen)]	
N(45)-Al(86)-N(44)	76.971	N(45)-Ag(1)-N(46)	64.660	N(45)-Pb(86)-N(44)	58.427
N(45)-Al(86)-O(4)	87.035	N(45)-Ag(1)-O(5)	125.009	N(45)-Pb(86)-O(4)	72.281
N(45)-Al(86)-O(3)	162.718	N(45)-Ag(1)-O(4)	77.569	N(45)-Pb(86)-O(3)	120.065
N(45)-Al(86)-N(2)	91.706	N(45)-Ag(1)-N(2)	104.920	N(45)-Pb(86)-N(2)	119.812
N(45)-Al(86)-N(1)	96.998	N(45)-Ag(1)-N(3)	140.505	N(45)-Pb(86)-N(1)	170.595
N(44)-Al(86)-O(4)	93.885	N(46)-Ag(1)-O(5)	71.337	N(44)-Pb(86)-O(4)	113.284
N(44)-Al(86)-O(3)	86.462	N(46)-Ag(1)-O(4)	140.734	N(44)-Pb(86)-O(3)	74.989
N(44)-Al(86)-N(2)	168.384	N(46)-Ag(1)-N(2)	134.896	N(44)-Pb(86)-N(2)	178.054
N(44)-Al(86)-N(1)	97.718	N(46)-Ag(1)-N(3)	93.132	N(44)-Pb(86)-N(1)	117.487
O(4)-Al(86)-O(3)	99.112	O(5)-Ag(1)-O(4)	128.663	O(4)-Pb(86)-O(3)	97.193
O(4)-Al(86)-N(2)	82.802	O(5)-Ag(1)-N(2)	129.654	O(4)-Pb(86)-N(2)	64.938
O(4)-Al(86)-N(1)	168.303	O(5)-Ag(1)-N(3)	70.209	O(4)-Pb(86)-N(1)	116.531
O(3)-Al(86)-N(2)	105.033	O(4)-Ag(1)-N(2)	63.609	O(3)-Pb(86)-N(2)	105.833
O(3)-Al(86)-N(1)	80.200	O(4)-Ag(1)-N(3)	124.233	O(3)-Pb(86)-N(1)	63.777
N(2)-Al(86)-N(1)	86.098	N(2)-Ag(1)-N(3)	66.915	N(2)-Pb(86)-N(1)	64.387

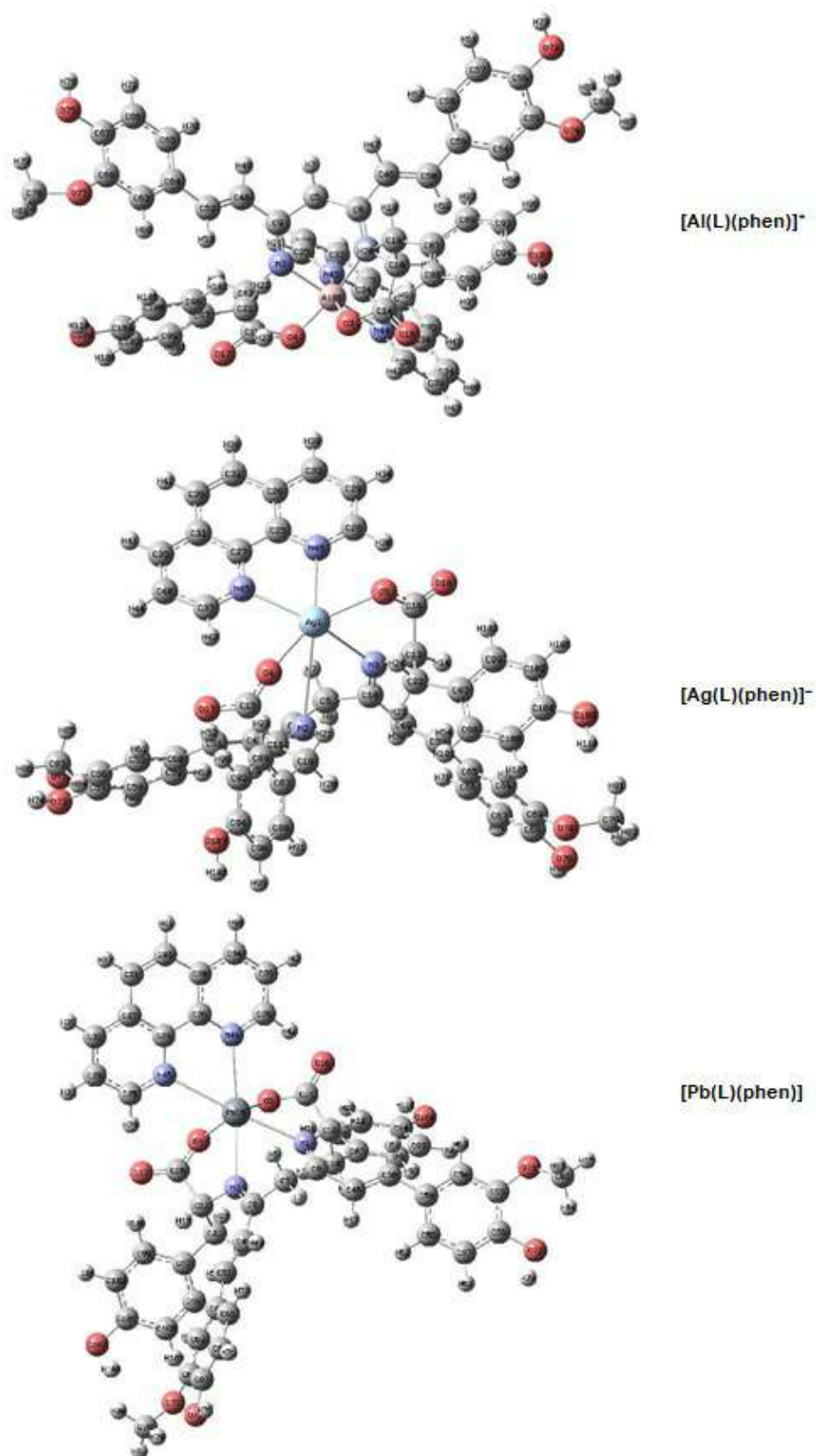


**Fig 4.** Optimized structures of [Al(L)(phen)]<sup>+</sup>, [Ag(L)(phen)]<sup>-</sup> and [Pb(L)(phen)] complexes according to B3LYP/LANL2DZ level of theory



lengths reported in these studies are very close to those obtained in our study.

The bond lengths of Pb(86)–N(45), Pb(86)–N(44), Pb(86)–N(2), Pb(86)–N(1), Pb(86)–O(4) and Pb(86)–O(3) that presented by the optimized structure of the [Pb(L)(phen)] complex (Fig. 4, Table 4) are 2.839, 2.834, 2.805, 2.876, 2.212 and 2.198 Å, respectively. These bond lengths are in the range of the Pb–N and Pb–O bond lengths reported in the literature [43-45].

The UV-Vis measurements of the synthesized H<sub>2</sub>L ligand and complexes were performed in DMSO solvent. All these compounds show several absorption bands in the UV-Vis region (Table 3). TD-DFT (Time-Dependent Density Functional Theory) calculations were performed on the optimized geometries of the synthesized complexes and H<sub>2</sub>L ligand to assign these bands. The calculated absorption spectra of the compounds, which are obtained from the output of the TD-DFT computations, were simulated using the GaussSum software. The simulated and experimental UV-Vis spectra of the synthesized H<sub>2</sub>L ligand and complexes are in good agreement (Table 3). To demonstrate the electronic properties of the synthesized

complexes, investigations were performed on the calculated energies and electron densities of the frontiers molecular orbitals. Fig. 5 summarizes the energy profile of the highest occupied molecular orbitals (HOMO's) and lowest unoccupied molecular orbital (LUMO's), and HOMO-LUMO gaps for [Ag(L)(phen)]<sup>-</sup>, [Al(L)(phen)]<sup>+</sup> and [Pb(L)(phen)] complexes, which are calculated at the B3LYP/LANL2DZ level of theory. The higher HOMO-LUMO energy gap is associated with the [Pb(L)(phen)] complex. The orbital energies and percent composition of selected frontier occupied and virtual molecular orbitals of complexes, expressed in terms of composing fragments, calculated at the B3LYP/LANL2DZ level are listed in Table 5. As shown in Table 5, the metal of the [Al(L)(phen)]<sup>+</sup> complex is contributing only 1% to the LUMO, and LUMO<sub>+1</sub> orbitals. The presented frontier occupied orbitals of the [Al(L)(phen)]<sup>+</sup> complex in Table 5 are completely localized on the L ligand, while the virtual orbitals are mostly localized on the phen ligand. The HOMO and LUMO contour plots of [Al(L)(phen)]<sup>+</sup> complex are shown in Fig. 6.

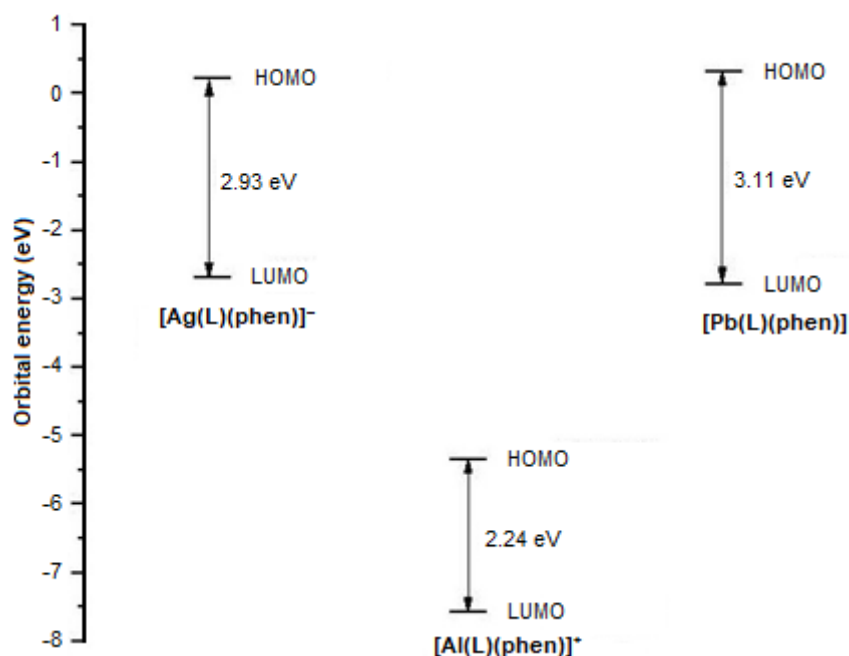


**Fig 5.** Energy profile of the highest occupied molecular orbitals (HOMO's) and lowest unoccupied molecular orbital (LUMO's), and HOMO-LUMO gaps for [Ag(L)(phen)]<sup>-</sup>, [Al(L)(phen)]<sup>+</sup> and [Pb(L)(phen)] complexes, calculated at the B3LYP/ LANL2DZ level of theory

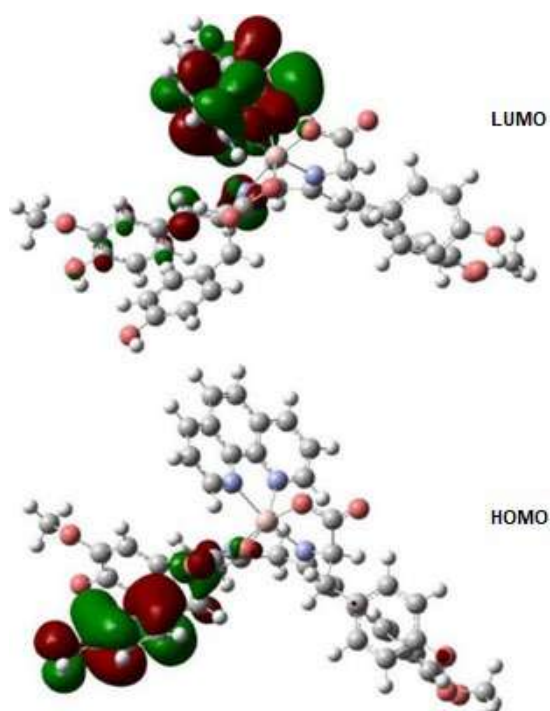


**Fig 6.** The frontier orbitals HOMO and LUMO of  $[\text{Al}(\text{L})(\text{phen})]^+$  calculated at the B3LYP/LANL2DZ level of theory, with the surface isovalue is 0.02

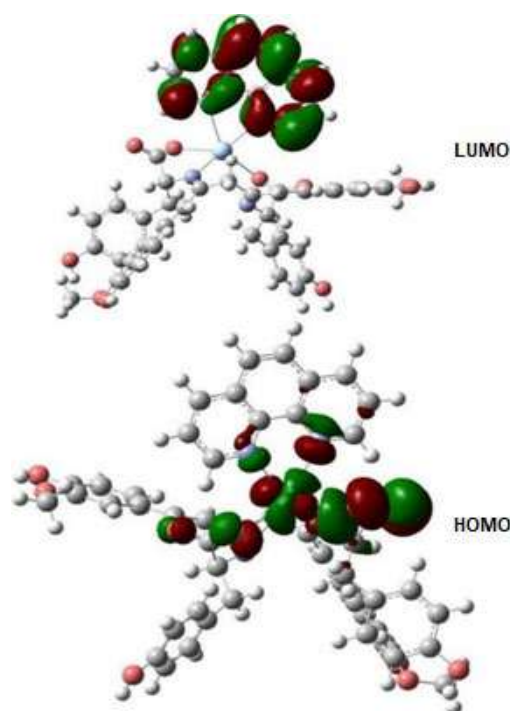


**Fig 7.** The frontier orbitals HOMO and LUMO of  $[\text{Ag}(\text{L})(\text{phen})]^-$  calculated at the B3LYP/LANL2DZ level of theory, with the surface isovalue is 0.02

The percent composition of the frontier molecular orbitals of  $[\text{Ag}(\text{L})(\text{phen})]^-$  complex are different from that of  $[\text{Al}(\text{L})(\text{phen})]^+$  as shown in Table 5. The metal of the  $[\text{Ag}(\text{L})(\text{phen})]^-$  complex is a notable contribution to the HOMO, HOMO<sub>-1</sub>, and HOMO<sub>-2</sub> orbitals with the percentage of 25, 18, and 18%, respectively. The presented frontier occupied orbitals of the  $[\text{Ag}(\text{L})(\text{phen})]^-$  complex is mostly localized on the L ligand. Concerning the virtual orbitals, LUMO and LUMO<sub>+2</sub>, are localized with the percentage of 100 and 99%, respectively on the phen ligand. The virtual orbital, LUMO<sub>+1</sub>, is localized with a percentage of 99% on the L ligand. The HOMO and LUMO contour plots of  $[\text{Ag}(\text{L})(\text{phen})]^-$  complex is shown in Fig. 7.

The presented frontier orbitals, LUMO<sub>+1</sub>, LUMO, HOMO, HOMO<sub>-1</sub>, HOMO<sub>-2</sub>, HOMO<sub>-3</sub>, HOMO<sub>-4</sub>, HOMO<sub>-5</sub>, and HOMO<sub>-6</sub> of the  $[\text{Pb}(\text{L})(\text{phen})]$  complex are localized on the L ligand with the percentage of 100, 99, 94, 90, 98, 84, 85, 93 and 98%, respectively. The LUMO<sub>+2</sub> orbital is completely localized on phen ligand. The metal of the  $[\text{Pb}(\text{L})(\text{phen})]$  complex is contributed only to the HOMO<sub>-1</sub>, HOMO<sub>-2</sub>, HOMO<sub>-3</sub>, HOMO<sub>-4</sub>, HOMO<sub>-5</sub>, and

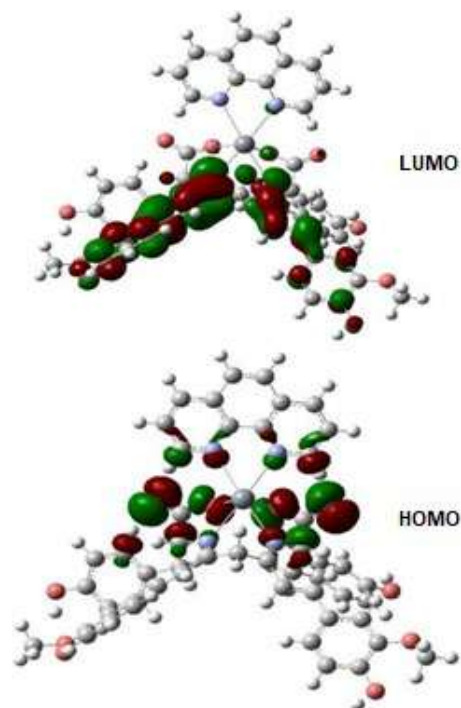


**Fig 8.** The frontier orbitals HOMO and LUMO of  $[\text{Pb}(\text{L})(\text{phen})]$  calculated at the B3LYP/LANL2DZ level of theory, with the surface isovalue is 0.02

**Table 5.** Percent composition in terms of composing fragments of selected frontier molecular orbitals (MO's) and molecular orbitals energies of the complexes calculated at the B3LYP/LANL2DZ level

Complexes	MO	MO energy (eV)	Fragment		
			Metal	phen ligand	L ligand
[Al(L)(phen)]Cl	L <sub>+2</sub>	-5.00	0	82	17
	L <sub>+1</sub>	-5.23	1	26	73
	L	-5.34	1	89	10
	H	-7.58	0	0	100
	H <sub>-1</sub>	-7.65	0	0	100
	H <sub>-2</sub>	-8.16	0	0	100
	H <sub>-3</sub>	-8.30	0	0	100
K[Ag(L)(phen)]	L <sub>+2</sub>	0.31	1	99	0
	L <sub>+1</sub>	0.28	0	1	99
	L	0.23	0	100	0
	H	-2.70	25	6	69
	H <sub>-1</sub>	-2.79	18	5	77
	H <sub>-2</sub>	-3.01	18	2	80
	H <sub>-3</sub>	-3.19	5	3	92
[Pb(L)(phen)]	L <sub>+2</sub>	0.76	0	100	0
	L <sub>+1</sub>	0.53	0	0	100
	L	0.32	0	1	99
	H	-2.79	0	6	94
	H <sub>-1</sub>	-2.92	5	5	90
	H <sub>-2</sub>	-3.04	1	1	98
	H <sub>-3</sub>	-3.14	13	3	84
	H <sub>-4</sub>	-3.38	5	10	85
H <sub>-5</sub>	-3.43	2	4	93	
H <sub>-6</sub>	-3.51	1	1	98	

H: HOMO, L: LUMO

HOMO<sub>-6</sub> orbitals. The HOMO and LUMO contour plots of [Pb(L)(phen)] complex are shown in Fig. 8.

## ■ CONCLUSION

The Schiff base ligand (H<sub>2</sub>L) has been prepared from curcumin and L- Tyrosine amino acid. The synthesized Schiff base ligand (H<sub>2</sub>L) and the second ligand 1,10-phenanthroline (phen) are used to prepare the new mixed ligand complexes [Al(L)(phen)]Cl, K[Ag(L)(phen)] and [Pb(L)(phen)]. The results obtained from the UV-visible spectra and the magnetic moments values of the complexes are in good agreement with the optimized structures of these compounds, which are calculated according to B3LYP/LANL2DZ level of the theory. The optimized structures of [Al(L)(phen)]Cl, K[Ag(L)(phen)]

and [Pb(L)(phen)] that calculated according to B3LYP/LANL2DZ level of the theory show that the environment surrounding the central metal ion in these complexes adopted distorted octahedral configuration. The computed energies and electron densities of the frontiers molecular orbitals were reported. All these results indicate that experimental and theoretical calculations were consistent.

## ■ AUTHOR CONTRIBUTIONS

The authors Ali Mahmood Ali and Tagreed Hashim Al-Noor conducted the synthesise and measurement experiments, and the authors Eid Abdalrazaq, and Abdel Aziz Qasem Jbarah conducted the DFT calculations, wrote and revised the manuscript. All authors agreed to

the final version of this manuscript.

## ■ REFERENCES

- [1] Omidi, S., and Kakanejadifard, A., 2020, A review on biological activities of Schiff base, hydrazone, and oxime derivatives of curcumin, *RSC Adv.*, 10 (50), 30186–30202.
- [2] Mahal, A., Wu, P., Jiang, Z.H., and Wei, X., 2019, Schiff bases of tetrahydrocurcumin as potential anticancer agents, *ChemistrySelect*, 4 (1), 2019, 366–369.
- [3] Kareem, A., Khan, M.S., Nami, S.A.A., Bhat, S.A., Mirza, A.U., and Nishat, N., 2018, Curcumin derived Schiff base ligand and their transition metal complexes: Synthesis, spectral characterization, catalytic potential and biological activity, *J. Mol. Struct.*, 1167, 261–273.
- [4] Priyadharshini, N., Iyyam, P.S., Subramanian, S., and Venkatesh, P., 2015, Synthesis, spectroscopic characterization and DNA interaction of Schiff base curcumin Cu(II), Ni(II) and Zn(II) complexes, *Der Pharma Chem.*, 7 (10), 186–201.
- [5] Ferenc, W., Osypiuk, D., Sarzyński, J., and Gluchowska, H., 2020, Complexes of Mn(II), Co(II), Ni(II), Cu(II) and Zn(II) with ligand formed by condensation reaction of isatin with glutamic acid, *Eclética Quím. J.*, 45, 12–27.
- [6] Bhanuka, S., and Singh, H.L., 2016, Synthesis, spectroscopic and molecular studies of lead(II) complexes of Schiff bases derived from 4-methoxybenzaldehyde and amino acids, *Rasāyan J. Chem.*, 9 (4), 614–626.
- [7] Shukla, S., and Mishra, A.P., 2013, Synthesis, structure, and anticancerous properties of silver complexes, *J. Chem.*, 2013, 527123.
- [8] Pradhan, A., and Kumar, A., 2015, A review: An overview on synthesis of some Schiff bases and their metal complexes with antimicrobial activity, *Chem. Process Eng. Res.*, 35, 84–86.
- [9] Frisch, M.J., Trucks, G.W., Schlegel, H.B., Scuseria, G.E., Robb, M.A., Cheeseman, J.R., Scalmani, G., Barone, V., Mennucci, B., Petersson, G.A., Nakatsuji, H., Caricato, M., Li, X., Hratchian, H.P., Izmaylov, A.F., Bloino, J., Zheng, G., Sonnenberg, J.L., Hada, M., Ehara, M., Toyota, K., Fukuda, R., Hasegawa, J., Ishida, M., Nakajima, T., Honda, Y., Kitao, O., Nakai, H., Vreven, T., Montgomery Jr., J.A., Peralta, J.E., Ogliaro, F., Bearpark, M., Heyd, J.J., Brothers, E., Kudin, K.N., Staroverov, V.N., Keith, T., Kobayashi, R., Normand, J., Raghavachari, K., Rendell, A., Burant, J.C., Iyengar, S.S., Tomasi, J., Cossi, M., Rega, N., Millam, J.M., Klene, M., Knox, J.E., Cross, J.B., Bakken, V., Adamo, C., Jaramillo, J., Gomperts, R., Stratmann, R.E., Yazyev, O., Austin, A.J., Cammi, R., Pomelli, C., Ochterski, J.W., Martin, R.L., Morokuma, K., Zakrzewski, V.G., Voth, G.A., Salvador, M.P., Dannenberg, J.J., Dapprich, S., Daniels, A.D., Farkas, O., Foresman, J.B., Ortiz, J.V., Cioslowski, J., and Fox, D.J., 2009, *Gaussian 09, Revision D.01*, Gaussian, Inc., Wallingford CT.
- [10] Al-Razaq, E.A., Buttrus, N., Al-Kattan, W., Jbarah, A.A., and Almatarneh, M., 2011, Reactions of Pd<sup>2+</sup> and Pt<sup>2+</sup> with pyrrolidinedithio carbamate and cystine ligands: Synthesis and DFT calculations, *J. Sulfur Chem.*, 32 (2), 159–169.
- [11] Thanakit, P., Suramitr, S., and Phromyothin, D., 2017, The study of metal binding properties and electronic transitions of dithienopyrrole derivatives, *Mater. Today: Proc.*, 4 (5), 6585–6591.
- [12] Chen, X., Hu, Y., Gao, J., Zhang, Y., and Li, S., 2013, Interaction of melamine molecules with silver nanoparticles explored by surface-enhanced Raman scattering and density functional theory calculations, *Appl. Spectrosc.*, 67 (5), 491–497.
- [13] Assefa, M.K., Devera, J.L., Brathwaite, A.D., Mosley, J.D., and Duncan M.A., 2015, Vibrational scaling factors for transition metal carbonyls, *Chem. Phys. Lett.*, 640, 175–179.
- [14] Cossi, M., and Barone, V., 2001, Time-dependent density functional theory for molecules in liquid solutions, *J. Chem. Phys.*, 115 (10), 4708–4717.
- [15] Cossi, M., Rega, N., Scalmani, G., and Barone V., 2003, Energies, structures, and electronic properties of molecules in solution with the C-PCM solvation model, *J. Comput. Chem.*, 24 (6), 669–681.

- [16] O'Boyle, N.M., Tenderholt, A.L., and Langner, K.M., 2008, cclib: A library for package-independent computational chemistry algorithms, *J. Comput. Chem.*, 29 (5), 839–845.
- [17] Ali, H.R.H., Saleh, G.A., Hussein, S.A., and Hassan, A.I., 2013, Preparation, characterization and atomic absorption spectroscopic determination of some metal complexes of glipizide, *Der Pharma Chem.*, 5 (6), 156–163.
- [18] Shahraki, S., and Delarami, H.S., 2018, Magnetic chitosan-(D-glucosimine methyl)benzaldehyde Schiff base for Pb<sup>+2</sup> ion removal. Experimental and theoretical methods, *Carbohydr. Polym.*, 200, 211–220.
- [19] Shah, A.D., Raval, D.J., Jatakiya, V.P., Sen, D.J., and Badmanaban, R., 2012, Comparison study of antimicrobial activity with effect of DPPH for antioxidant study of synthesized Schiff bases of Mannich bases of resacetophenone having variable electronegative atoms, *Int. J. Drug Dev. Res.*, 4 (2), 205–215.
- [20] Yousif, E., Majeed, A., Al-Sammarrae, K., Salih, N., Salimon, J., and Abdullah, B., 2017, Metal complexes of Schiff base: Preparation, characterization and antibacterial activity, *Arabian J. Chem.*, 10 (Suppl. 2), S1639–S1644.
- [21] Dehkhodaei, M., Khorshidifard, M., Rudbari, H.A., Sahihi, M., Azimi, G., Habibi, N., Taheri, S., Bruno, G., and Azadbakht, R., 2017, Synthesis, characterization, crystal structure and DNA, HSA-binding studies of four Schiff base complexes derived from salicylaldehyde and isopropylamine, *Inorg. Chim. Acta*, 466, 48–60.
- [22] Gandhi, S.R., Kumar, D.S., Tajudeen, S.S., and Sheriff, A.K.I., 2017, Studies on synthetic, structural characterization, thermal, DNA cleavage, antimicrobial and catalytic activity of tetradentate (N<sub>4</sub>) Schiff base and its transition metal complexes, *Asian J. Chem.*, 29, 1076–1084.
- [23] Singh, H.L., and Singh, J.B., 2012, Synthesis and characterization of new lead(II) and organotin(IV) complexes of Schiff bases derived from histidine and methionine, *Int. J. Inorg. Chem.*, 2012, 568797.
- [24] Balić, T., Marković, B., and Medvidović-Kosanović, M., 2015, Electrochemical and structural analysis of a novel symmetrical bis-Schiff base with herringbone packing motif, *J. Mol. Struct.*, 1084, 82–88.
- [25] de Lima, D.P., Giannesi, G.C., dos Santos, E.A., Freitas, T.S.E., Lopes, R.S., Lopo, M.N., Beatriz, A., Marques, M.R., and Marchetti, C.R., 2017, N-acetylation of aromatic amines by the soil fungus *Aspergillus japonicus* (UFMS 48.136), *Lett. Org. Chem.*, 14 (4), 227–230.
- [26] Abdel-Rahman, L.H., Ismail, N.M., Ismael, M., Abu-Dief, A.M., and Ahmed, E.A.H., 2017, Synthesis, characterization, DFT calculations and biological studies of Mn(II), Fe(II), Co(II) and Cd(II) complexes based on a tetradentate ONNO donor Schiff base ligand, *J. Mol. Struct.*, 1134, 851–862.
- [27] Keypour, H., Aidi, M., Mahmoudabadi, M., Karamian, R., Asadbegy, M., and Gable, R.W., 2019, Synthesis, X-ray crystal structural, antioxidant and antibacterial studies of new Cu(II) macrocyclic Schiff base complex with a ligand containing homopiperazine moiety, *J. Mol. Struct.*, 1198, 126666.
- [28] Singh, H.L., and Singh, J., 2014, Synthesis, spectroscopic, molecular structure, and antibacterial studies of dibutyltin(IV) Schiff base complexes derived from phenylalanine, isoleucine, and glycine, *Bioinorg. Chem. Appl.*, 2014, 716578.
- [29] Hemalatha, S., Dharmaraja, J., Shobana, S., Subbaraj, P., Esakkidurai, T., and Raman, N., 2020, Chemical and pharmacological aspects of novel hetero MLB complexes derived from NO<sub>2</sub> type Schiff base and N<sub>2</sub> type 1,10-phenanthroline ligands, *J. Saudi Chem. Soc.*, 24 (1), 61–80.
- [30] Nakamoto, K., 2006, "Infrared and Raman spectra of inorganic and coordination compounds" in *Handbook of Vibrational Spectroscopy*, Eds. Chalmers, J.M., and Griffiths, P.R., John Wiley & Sons, Inc., Hoboken, New Jersey, US.
- [31] Savithri, K., Kumar, B.C.V., Vivek, H.K., and Revanasiddappa, H.D., 2018, Synthesis and characterization of cobalt(III) and copper(II)

- complexes of 2-((E)-(6-fluorobenzo[d]thiazol-2-ylimino)methyl)-4-chlorophenol: DNA binding and nuclease studies—SOD and antimicrobial activities, *Int. J. Spectrosc.*, 2018, 8759372.
- [32] Cotton, F.A., Wilkinson, G., Murillo, C.A., and Bochmann, M., 1999, *Advanced Inorganic Chemistry*, 6<sup>th</sup> Ed., John Wiley & Sons, Ltd., Chichester, UK.
- [33] Lever, A.B.P., 1984, *Inorganic Electronic Spectroscopy*, Series: Studies in Physical and Theoretical Chemistry, Vol. 33, Elsevier, Amsterdam.
- [34] Gulbransen, J.L., and Fitchett, C.M., 2012, Anion directed control of supramolecular structure in silver complexes through weak interactions, *CrystEngComm*, 14 (7), 5394–5397.
- [35] Pettinari, C., Marchetti, F., Orbisaglia, S., Pettinari, R., Ngoune, J., Gómez, M., Santos, C., and Álvarez, E., 2013, Group 11 complexes with the bidentate di(1*H*-indazol-1-yl)methane and di(2*H*-indazol-2-yl)methane ligands, *CrystEngComm*, 15 (19), 3892–3907.
- [36] Nunes, J.H.B., de Paiva, R.E.F., Cuin, A., Lustrì, W.R., and Corbi, P.P., 2015, Silver complexes with sulfathiazole and sulfamethoxazole: Synthesis, spectroscopic characterization, crystal structure and antibacterial assays, *Polyhedron*, 85, 437–444.
- [37] Kim, Y., and Kang, S.K., 2015, Crystal structure of bis-[2-(1*H*-benzimidazol-2-yl)aniline]silver(I) nitrate, *Acta Crystallogr., Sect. E: Crystallogr. Commun.*, 71 (Pt 9), 1058–1060.
- [38] Bondi A., 1964, van der Waals volumes and radii, *J. Phys. Chem.*, 68 (3), 441–451.
- [39] Soliman, S.M., Mabkhot, Y.N., Barakat, A., and Ghabbour, H.A., 2017, A highly distorted hexacoordinated silver(I) complex: synthesis, crystal structure, and DFT studies, *J. Coord. Chem.*, 70 (8), 1339–1356.
- [40] Bergamini, F.R.G., Ferreira, M.A., de Paiva, R.E.F., Gomes, A.F., Gozzo, F.C., Formiga, A.L.B., Corbi, F.C.A., Mazali, I.O., Alves, D.A., Lancellotti, M., and Corbi, P.P., 2012, A binuclear silver complex with L-buthionine sulfoximine: Synthesis, spectroscopic characterization, DFT studies and antibacterial assays, *RSC Adv.*, 2 (27), 10372–10379.
- [41] Asadi, Z., Asadi, M., and Shorkaei, M.R., 2016, Synthesis, characterization and DFT study of new water-soluble aluminum(III), gallium(III) and indium(III) Schiff base complexes: Effect of metal on the binding propensity with bovine serum albumin in water, *J. Iran. Chem. Soc.*, 13 (3), 429–442.
- [42] Truscott, J.C., Conradie, J., Swart, H.C., Duvenhage, M.M., and Visser, H.G., 2019, Synthesis, crystal structures, photoluminescence, electrochemistry and DFT study of aluminium(III) and gallium(III) complexes containing a novel tetra-dentate Schiff base ligand, *Acta Crystallogr., Sect. C: Cryst. Struct. Commun.*, 75 (8), 1045–1052.
- [43] Ghanbari, B., and Zarepour-Jevinani, M., 2016, Synthesis and characterization of M(II) (M = Cd, Hg and Pb) complexes with naphthodiaza-crown macrocyclic ligand and study of metal ion recognition by fluorescence, <sup>1</sup>H NMR spectroscopy, and DFT calculation, *J. Coord. Chem.*, 69 (18), 2793–2803.
- [44] Platas-Iglesias, C., Esteban-Gómez, D., Enríquez-Pérez, T., Avecilla, F., de Blas, A., and Rodríguez-Blas, T., 2005, Lead(II) thiocyanate complexes with bibracchial lariat ethers: An X-ray and DFT study, *Inorg. Chem.*, 44 (7), 2224–2233.
- [45] Mahmoudi, G., Seth, S.K., Riera, A.B., Zubkov, F.I., and Frontera, A., 2020, Novel Pb(II) complexes: X-ray structures, Hirshfeld surface analysis and DFT calculations, *Crystals*, 10 (7), 568.

## A Theoretical Study on Vibrational Energies of Molecular Hydrogen and Its Isotopes Using a Semi-classical Approximation

Redi Kristian Pingak<sup>1\*</sup>, Albert Zicko Johannes<sup>1</sup>, Fidelis Nitti<sup>2,3</sup>, and Meksianis Zadrak Ndii<sup>4</sup>

<sup>1</sup>Department of Physics, Universitas Nusa Cendana, Jl. Adisucipto Penfui, Kupang 85001, Nusa Tenggara Timur, Indonesia

<sup>2</sup>Department of Chemistry, Universitas Nusa Cendana, Jl. Adisucipto Penfui, Kupang 85001, Nusa Tenggara Timur, Indonesia

<sup>3</sup>School of Chemistry, University of Melbourne, Masson Road, Parkville, Victoria 3052, Australia

<sup>4</sup>Department of Mathematics, Universitas Nusa Cendana, Jl. Adisucipto Penfui, Kupang 85001, Nusa Tenggara Timur, Indonesia

\* **Corresponding author:**

tel: +62-82147618836

email: rpingak@staf.undana.ac.id

Received: January 18, 2021

Accepted: March 2, 2021

DOI: 10.22146/ijc.63294

**Abstract:** This study aims to apply a semi-classical approach using some analytically solvable potential functions to accurately compute the first ten pure vibrational energies of molecular hydrogen ( $H_2$ ) and its isotopes in their ground electronic states. This study also aims at comparing the accuracy of the potential functions within the framework of the semi-classical approximation. The performance of the approximation was investigated as a function of the molecular mass. In this approximation, the nuclei were assumed to move in a classical potential. The Bohr-Sommerfeld quantization rule was then applied to calculate the vibrational energies of the molecules numerically. The results indicated that the first vibrational transition frequencies ( $\nu_{1 \leftarrow 0}$ ) of all hydrogen isotopes were consistent with the experimental ones, with a minimum percentage error of 0.02% for ditritium ( $T_2$ ) molecule using the Modified-Rosen-Morse potential. It was also demonstrated that, in general, the Rosen-Morse and the Modified-Rosen-Morse potential functions were better in terms of calculating the vibrational energies of the molecules than Morse potential. Interestingly, the Morse potential was found to be better than the Manning-Rosen potential. Finally, the semi-classical approximation was found to perform better for heavier isotopes for all potentials applied in this study.

**Keywords:** semi-classical approximation; classical potential functions; hydrogen isotopes; Bohr-Sommerfeld quantization

### ■ INTRODUCTION

The molecular hydrogen ( $H_2$ ) and its isotopes are of great importance in molecular quantum chemistry. The fact that the experimental energies of the systems are consistent with their corresponding theoretical values has long been considered an initial platform for testing and developing the practical techniques and theoretical models [1-2].

Exact experimental vibrational levels for  $H_2$  and deuterium-bearing hydrogen molecules, i.e., hydrogen deuteride (HD) and dideuterium ( $D_2$ ) have been widely reported in the literature [3-5]. On the other hand, physical properties of the tritium-bearing hydrogen molecules, i.e., tritiated hydrogen (HT), deuterium-

tritium (DT), and ditritium ( $T_2$ ), have been less frequently measured. The reason was due to the stringent safety requirements to hold the radioactive species, which results in limited access and handling difficulty in the experimental study of these systems [6]. Some of the empirical studies on the first vibrational frequencies for these systems were reported for  $T_2$  molecule [7], DT molecule [8], and the most recent one for HT, DT, and  $T_2$  molecules [6]. With these recent experimental reports, theoretical models to study the systems, especially for the fundamental tone, can be tested for all molecular hydrogen isotopes.

From the theoretical point of view, highly accurate energy calculations of isotopes of molecular hydrogen

have also been thoroughly performed. Various types of theoretical calculations have been developed, including the moment constant summability method [9], free-complement variational theory [10-11] and matrix Numerov method [12] for the H<sub>2</sub> molecule. The non-relativistic calculations were also reported on energy levels of D<sub>2</sub> molecule [13] and of HD molecule [14]. Similarly, a theoretical study on vibrational energy levels of the hydrogen molecule and its isotopes was presented [15]. Besides, highly accurate ab-initio calculations have also been extended to investigate the effects of vibrations on the chemical and physical properties of other quantum systems. These studies include the use of the first-principle DFT calculation to investigate vibrational effects on vacancies in silicon [16], nitrogen-doped diamond [17], germanene [18], monolayer hexagonal boron nitride [19]. DFT also was used to investigate the potential of halogen-substituted N-methyl-4-piperidones curcumin analog compounds as candidates for optoelectronic materials [20]. First-principle vibrational free energy calculations have also been conducted to study defects in silicon [21-22].

Moreover, DFT was used along with ab-initio correlated wavefunction theory (WFT) methods to obtain highly accurate potential energy curves (PECs) of fluorine adsorption on coronene [23], setting up a high-level benchmark for theoretical studies on graphene functionalization. The results generated from the above-mentioned first-principle calculations are in excellent agreement with their corresponding experimental values and other ab-initio products. These findings indicate that DFT and correlated WFT are among the most accurate theoretical methods. Therefore, they are recommended for performing precise high calculations on rovibrational, electronic, structural, optical, and other properties of materials for investigating their potential use in devices.

Recently, the semi-classical method has been applied to study the vibrational states of molecules [24-25]. One approach in this method is to use the Bohr-Sommerfeld quantization rule. One can apply the potential analytical surfaces such as the Morse potential rather than applying a more complex ab-initio potential. Despite being simple, the Morse potential has been proven accurate in studying the diatomic molecules [26-

27]. In our previous study [28], we have successfully applied a semi-classical approach using the Morse potential [29] to calculate the vibrational energies of the molecular H<sub>2</sub>. In this study, we observed that 10 out of 15 vibrational levels of H<sub>2</sub> could be generated with reasonable accuracy. In addition to the Morse potential, there have also been other analytically solvable potentials, including the Rosen-Morse [30], Manning-Rosen [31], and the Modified-Rosen-Morse potential [32]. These potentials have been extensively applied to study the interactions in molecules. However, they have not been explored to calculate the vibrational energies of molecular hydrogen isotopes within the framework of the semi-classical approximation.

Since their introduction, most of the potential functions have been widely explored and compared for their performance in describing the molecular interaction of diatomic molecules. Consequently, a variety of claims have been drawn by different researchers that a particular potential is better than the others or vice versa. For instance, Deng and Fan [33] claimed that the Deng-Fan potential was better than Morse potential in describing the interactions of diatomic molecules. Moreover, Liu et al. [34] reported that vibrational levels predicted by Manning-Rosen potential model were better than those predicted by the Morse potential model for a  $^3\Sigma_u^+$  of the Li<sub>2</sub> molecule. Wang et al. [35] made a contradictory claim that the Morse potential was better than Deng-Fan, Manning-Rosen, and the Schiöberg potential in describing the interaction of diatomic molecules. Therefore, more comprehensive theoretical studies on different chemical-physical properties of various diatomic molecules using these potentials are crucial in testing the accuracy of the potentials.

This present paper aims to apply the semi-classical method using the Morse, Manning-Rosen, Rosen-Morse, and the modified Rosen-Morse potential to calculate the first 10 vibrational energies of molecular H<sub>2</sub> and its isotopes (HD, HT, D<sub>2</sub>, DT, and T<sub>2</sub>) in their ground electronic state  $X\Sigma_g^+$ . Also, the accuracy of the calculation in the framework of the semi-classical approximation was examined. Finally, the performance



of the approximation was evaluated as a function of the molecular mass.

## ■ COMPUTATIONAL METHODS

### The Semi-Classical Approximation Using Analytically Solvable Potentials

The semi-classical method used in this article was applied within the framework of the Born-Oppenheimer approximation. In this approximation, the nuclei and electrons were assumed to move independently. The further assumption would be that the vibrational and the rotational motion were separated. Therefore the vibrational bound states of the molecular hydrogen isotopes can be obtained by solving the time-independent Schrödinger equation for the nuclei shown in Eq. (1):

$$(\hat{T} + \hat{V})|\Psi\rangle = E_n|\Psi\rangle \quad (1)$$

In the semi-classical approximation, one does not need to solve Eq. (1) directly for  $E_n$  but needs to assume that the nuclei move in a classical potential  $V(r)$  and then apply the Bohr-Sommerfeld quantization rule to approximate vibrational energy eigenvalues  $E_n$ . Hence, using the quantization rule led to dimensionless action  $S$  at a particular energy  $E_n$  [36]:

$$S(E_n) = \left(\frac{2\mu}{\hbar^2}\right)^{1/2} \int_{r_{in}}^{r_{out}} (E_n - V(r))^{1/2} dr - \left(n + \frac{1}{2}\right)\pi \quad (2)$$

Despite  $S(E_n)$  is dimensionless, all other quantities contained in  $S(E_n)$  still have their standard units. All physical quantities were defined in a way that they are dimensionless. Therefore, Eq. (2) can be written as:

$$s(\varepsilon_n) = \gamma \int_{x_{in}}^{x_{out}} (\varepsilon_n - v(x))^{1/2} dx - \left(n + \frac{1}{2}\right)\pi \quad (3)$$

where  $s(\varepsilon_n)$  is the new dimensionless action. All other unknown dimensionless quantities defined to arrive at Eq. (3) are described as follows. Firstly, dimensionless position  $x$  was defined as  $x \equiv r/\delta$ . Here,  $\delta$  is a parameter with the dimension of length introduced to make position  $x$  dimensionless. This  $\delta$  parameter also appeared in the potential functions as shown in Eq. (8) to Eq. (11). This parameter has a physical meaning of controlling the width of the potential functions. Hence, it has to be fitted to experimental values for given energy using a particular potential function. Similarly,  $\gamma$  is a dimensionless quantity

introduced to make the constants just before the integral in Eq. (2) dimensionless and to account for  $\delta$  and equilibrium potential  $D_e$  in the calculation. This  $\gamma$  value, shown in Eq. (4), represents the quantum nature of the problem where more significant matters of  $\gamma$  correspond to systems with a more negligible quantum effect. In other words, the systems behave more classically for larger  $\gamma$  and vice versa.

$$\gamma = \left(\frac{2\mu D_e \delta^2}{\hbar^2}\right)^{1/2} \quad (4)$$

Here,  $D_e$  is the potential at the equilibrium position  $r_e$ , and  $\mu$  is the reduced mass of the nuclei. Secondly,  $x_{in}$  and  $x_{out}$  in Eq. (3) are the scaled classical turning points obtained by first solving  $r_{in}$  and  $r_{out}$  using:

$$V(r_{in}) = V(r_{out}) = E_n \quad (5)$$

Next,  $\varepsilon_n$  in Eq. (3) is the scaled vibrational energy for a particular vibrational quantum state  $n$ , defined as

$$\varepsilon_n \equiv \frac{E_n}{D_e} \quad (6)$$

Finally,  $v(x)$  in Eq. (3) is the scaled classical potential governing the motion of the nuclei. This  $v(x)$  function can be determined from  $v(r)$ , which was defined as

$$v(r) \equiv \frac{V(r)}{D_e} \quad (7)$$

In this article, the potential functions used were the Morse potential  $V_M(r)$  [29] shown in Eq. (8). The Manning-Rosen potential  $V_{MR}(r)$  in the form presented in [35] as shown in Eq. (9). The Rosen-Morse potential  $V_{RM}(r)$  in the form presented in [37] as shown in Eq. (10), and the modified Rosen-Morse potential  $V_{MRM}(r)$  [32] demonstrated in Eq. (11). It was important to note that there was a slight change in each equation where  $-D_e$  was added, which only yielded  $-D_e$  at the potential minimum but did not affect the physical properties of the potentials at all. It is also important to note that the bond length  $r_e$  used in this article was taken as a pre-computed parameter.

$$V_M(r) = D_e \left( \left( 1 - e^{-(r-r_e)/\delta} \right)^2 - 1 \right) \quad (8)$$

$$V_{MR}(r) = D_e \left( \left( \frac{1 - e^{r_e/\delta}}{e^{r/\delta} - 1} \right)^2 - 1 \right) \quad (9)$$

$$V_{RM}(r) = D_e \left( \left( 1 - \frac{e^{2r_e/\delta} + 1}{e^{2r/\delta} + 1} \right)^2 - 1 \right) \quad (10)$$

$$V_{MRM}(r) = D_e \left( \left( 1 - \frac{e^{2(r_e - r_{ij})/\delta} + 1}{e^{2(r - r_{ij})/\delta} + 1} \right)^2 - 1 \right) \quad (11)$$

### Computational Details

Overall, the computational details used in this research followed the same procedures described in [28]. Calculation of the vibrational energies of the molecular hydrogen isotopes was done by solving Eq. (3) numerically. The numerical methods used in calculating the vibrational energies in Eq. (3) were numerical integration using the Simpson's rule and root finding using the false position method, with 1024 divisions and a tolerance of  $10^{-7}$ . The steps involved are as follows. First, the dimensionless quantity  $\gamma$  was determined using Eq. (4). Second, the classical turning points were determined for all potentials using Eq. (5). After that,  $\gamma$  values, classical turning points, and the potential functions were substituted into Eq. (3). Finally, Eq. (3) was solved numerically to obtain the pure vibrational energies of the molecules. In this final step, the value of  $\delta$  was varied to get the first vibrational energy which can match its experimental value. This  $\delta$  value was then used to solve the higher vibrational energy levels of the molecules.

## RESULTS AND DISCUSSION

### Physical Constants Used in the Calculation

Reduced mass  $\mu$  of nuclei of the molecules were 0.50391261 a.m.u., 0.67171137 a.m.u., 0.75540394 a.m.u., 1.00705111 a.m.u., 1.20764393 a.m.u., and 1.50802486 a.m.u., for H<sub>2</sub>, HD, HT, D<sub>2</sub>, DT and T<sub>2</sub> respectively [38]. The bond length value used in the calculation for all molecules in this study was 0.74142 Å [38]. Using an experimental value for  $D_e = 38287 \text{ cm}^{-1}$  and the reduced mass of the molecules, the values of the dimensionless quantity  $\gamma$  of the molecules were calculated using Eq. (4), and they were found to be 33.830 $\delta$ , 39.059 $\delta$ , 41.421 $\delta$ , 47.825 $\delta$ , 52.372 $\delta$ , and 58.524 $\delta$  respectively, where  $\delta$  in Å.

### Classical Turning Points

The classical turning points for the Morse potential

(M) had been presented before in [28], from which the classical turning points were

$$r_{in(M)} = r_e - \delta \ln(1 + \sqrt{\epsilon_n + 1}) \quad (12a)$$

$$r_{out(M)} = r_e - \delta \ln(1 - \sqrt{\epsilon_n + 1}) \quad (12b)$$

Using similar procedures, i.e., by applying Eq. (5) to Eq. (9), (10), and (11), the classical turning points for the Manning-Rosen (MR), Rosen-Morse (RM), and the Modified-Rosen-Morse (MRM) potentials were derived and respectively shown in Eq. (13), (14) and (15).

$$r_{in(MR)} = \delta \ln \left( 1 + \frac{e^{r_e/\delta} - 1}{1 + \sqrt{\epsilon_n + 1}} \right) \quad (13a)$$

$$r_{out(MR)} = \delta \ln \left( 1 + \frac{e^{r_e/\delta} - 1}{1 - \sqrt{\epsilon_n + 1}} \right) \quad (13b)$$

$$r_{in(RM)} = \frac{\delta}{2} \ln \left( \frac{e^{2r_e/\delta} + 1}{1 + \sqrt{\epsilon_n + 1}} - 1 \right) \quad (14a)$$

$$r_{out(RM)} = \frac{\delta}{2} \ln \left( \frac{e^{2r_e/\delta} + 1}{1 - \sqrt{\epsilon_n + 1}} - 1 \right) \quad (14b)$$

$$r_{in(MRM)} = r_{ij} + \frac{\delta}{2} \ln \left( \frac{e^{2(r_e - r_{ij})/\delta} + 1}{1 + \sqrt{\epsilon_n + 1}} - 1 \right) \quad (15a)$$

$$r_{out(MRM)} = r_{ij} + \frac{\delta}{2} \ln \left( \frac{e^{2(r_e - r_{ij})/\delta} + 1}{1 - \sqrt{\epsilon_n + 1}} - 1 \right) \quad (15b)$$

For the Modified-Rosen-Morse potential,  $r_{ij}$  values were calculated using Eq. (16) [32].

$$r_{ij} = r_e - \sqrt{\frac{KD_e}{k_e}} \quad (16)$$

where K is a dimensionless constant given by

$$K = \frac{d^2 v(r)}{dr^2} \Big|_{r'=1; r'} = \frac{r - r_{ij}}{r_e - r_{ij}} \quad (17)$$

### Vibrational Energy Levels of H<sub>2</sub>, HD, HT, D<sub>2</sub>, DT, and T<sub>2</sub> Molecules

The calculated first ten vibrational energies for the molecular hydrogen and its isotopes in their ground electronic state  $X\Sigma_g^+$  are presented in this section. Eq. (3) was numerically evaluated using values given in the previous section. The equation had already been solved for the H<sub>2</sub> molecule using the Morse potential in our earlier study [28], but it was recalculated in this research using the most recent experimental values to obtain the

results comparable to that of the hydrogen isotopes calculated in this study. The most recent experimental values used here were  $36118.06962\text{ cm}^{-1}$  [39],  $36405.78366\text{ cm}^{-1}$  [40], and  $36748.36286\text{ cm}^{-1}$  [3] for the first vibrational energy levels of  $\text{H}_2$ , HD, and  $\text{D}_2$ , respectively. Meanwhile, the most recent theoretical values for the first vibrational energy levels for HT, DT, and  $\text{T}_2$  were  $36512.19957\text{ cm}^{-1}$ ,  $36881.2812\text{ cm}^{-1}$ , and  $37028.49625\text{ cm}^{-1}$  [41], respectively. Values of  $\delta$  matching the corresponding experimental first vibrational levels for  $\text{H}_2$ , HD, HT,  $\text{D}_2$ , DT, and  $\text{T}_2$  are shown in Table 1. These  $\delta$  values were then used to calculate the first ten vibrational energy levels for all molecules. For the Modified-Rosen-Morse potential, the  $r_{ij}$  values used are also presented in Table 1, calculated using Eq. (16) and (17) based on diatomic constants adapted from [38]. Calculated results of the first ten vibrational energies of the molecules are presented in Table 2.

It is evident from Table 2 that our calculated energies using Rosen-Morse and Modified Rosen Morse potential functions were consistent with the corresponding energies reported in [42], with errors below 1% for all molecules. Similarly, the results for the first 5 vibrational energy levels for all molecules were also in good agreement when using the Morse potential (error below 1%). Still, for sizeable vibrational quantum numbers, it was clear that the difference between the calculation and the experimental data became significant. On the other hand, only the first three vibrational levels with errors of less than 1% could be generated using the Manning-Rosen potential. For  $\text{H}_2$  molecule with  $n = 9$ , the use of Manning-Rosen potential resulted in a much

higher percentage of error compared to that of the Morse, Rosen-Morse, and Modified Rosen Morse potential, with up to 54.81% of error compared to 12.83%, 0.47% and 0.17% for the respective potential functions. The accuracy of these potential functions within the framework of the semi-classical approximation is discussed further in the following section.

It is also clear from Table 2 that for any vibrational level calculated using any potential function, isotopic shifts in vibrational energies occurred when other isotopes substituted one atom or both atoms. The reason was due to the difference in the reduced mass of the molecules containing different isotopes, which leads to the increase or decrease in the corresponding calculated energy. The substitution of an atom or both atoms with heavier isotopes led to the lower vibrational energies and hence results in more chemically stabilized vibrational states. This stabilization, in addition to some other factors explained in the next section, led to more accurate vibrational levels for heavier molecules.

Regarding the dissociation energy, it is clear that any change to the molecule with heavier isotopes led to a higher bond dissociation energy of the molecule. Therefore, the chemical bond of such molecules became more muscular, which eventually affects the molecules' behavior in any chemical reaction, which involves bond cleavage. The stronger the chemical bond between isotopes, the higher the energy required to break the chemical bond within the molecule from its first vibrational state into its unexcited constituent atoms/isotopes. As chemical reactions between two atoms

**Table 1.** Values of  $\delta$  and  $r_{ij}$  used in the calculation

Molecule	$\delta_M$ (Å)	$\delta_{MR}$ (Å)	$\delta_{RM}$ (Å)	$\delta_{MRM}$ (Å)	$r_{ij}$ (Å)
$\text{H}_2$	0.71715238100	0.97932457700	0.92625240460	0.92405655150	0.01480561
HD	0.71734847950	0.98070005400	0.92634829660	0.92411931120	0.01500609
HT	0.71743336176	0.98123423230	0.92639796470	0.92412744480	0.01527452
$\text{D}_2$	0.71765735300	0.98249317680	0.92654899188	0.92426980660	0.01531373
DT	0.71780750840	0.98325158400	0.92666155500	0.92436195030	0.01543833
$\text{T}_2$	0.71800402150	0.98415409740	0.92682071850	0.92451846200	0.01544307

**Table 2.** Calculated energies with % errors<sup>†</sup> for first 10 vibrational energies of the molecules using the Morse (M), Manning-Rosen (MR), Rosen-Morse (RM), and Modified-Rosen-Morse (MRM) potentials. Calculated energies from ab-initio methods in [42]<sup>†</sup> are also presented

Molecule	n	$E_{n(M)}/\text{cm}^{-1}$ (% error)	$E_{n(MR)}/\text{cm}^{-1}$ (% error)	$E_{n(RM)}/\text{cm}^{-1}$ (% error)	$E_{n(MRM)}/\text{cm}^{-1}$ (% error)	$E_n^\dagger/\text{cm}^{-1}$
H <sub>2</sub>	0	-36118.070 (0.00)	-36118.070 (0.00)	-36118.070 (0.00)	-36118.070 (0.00)	-36118.074
	1	-31969.921 (0.04)	-32085.512 (0.40)	-31941.486 (0.05)	-31940.867 (0.05)	-31956.927
	2	-28074.723 (0.16)	-28427.373 (1.41)	-27984.898 (0.16)	-27982.911 (0.17)	-28031.088
	3	-24432.479 (0.40)	-25108.677 (3.18)	-24254.567 (0.33)	-24250.572 (0.35)	-24335.689
	4	-21043.186 (0.84)	-22098.637 (5.90)	-20757.141 (0.53)	-20750.621 (0.56)	-20867.698
	5	-17906.847 (1.59)	-19370.069 (9.89)	-17499.678 (0.72)	-17490.265 (0.77)	-17626.119
	6	-15023.460 (2.81)	-16898.893 (15.65)	-14489.684 (0.84)	-14477.179 (0.92)	-14612.257
	7	-12393.027 (4.76)	-14663.724 (23.95)	-11735.138 (0.80)	-11719.538 (0.93)	-11830.105
	8	-10015.546 (7.85)	-12645.513 (36.17)	-9244.540 (0.46)	-9226.068 (0.66)	-9286.901
	9	-7891.020 (12.83)	-10827.248 (54.81)	-7026.942 (0.47)	-7006.079 (0.17)	-6993.907
HD	0	-36405.784 (0.00)	-36405.784 (0.00)	-36405.784 (0.00)	-36405.784 (0.00)	-36405.778
	1	-32785.512 (0.04)	-32873.724 (0.31)	-32763.984 (0.03)	-32763.511 (0.03)	-32773.635
	2	-29354.790 (0.12)	-29627.277 (1.05)	-29286.222 (0.11)	-29284.694 (0.12)	-29318.920
	3	-26113.619 (0.29)	-26643.017 (2.32)	-25976.499 (0.24)	-25973.402 (0.25)	-26038.161
	4	-23061.999 (0.58)	-23899.984 (4.24)	-22839.027 (0.39)	-22833.925 (0.41)	-22928.893
	5	-20199.930 (1.05)	-21379.384 (6.95)	-19878.246 (0.56)	-19870.791 (0.60)	-19989.738
	6	-17527.412 (1.78)	-19064.321 (10.71)	-17098.829 (0.71)	-17088.776 (0.77)	-17220.515
	7	-15044.445 (2.89)	-16939.573 (15.85)	-14505.710 (0.80)	-14492.927 (0.89)	-14622.386
	8	-12751.029 (4.53)	-14991.400 (22.90)	-12104.090 (0.77)	-12088.577 (0.90)	-12198.059
	9	-10647.165 (6.98)	-13207.369 (32.71)	-9899.461 (0.53)	-9881.364 (0.71)	-9952.060
HT	0	-36512.200 (0.00)	-36512.200 (0.00)	-36512.200 (0.00)	-36512.200 (0.00)	-36512.166

**Table 2.** Calculated energies with % errors<sup>†</sup> for first 10 vibrational energies of the molecules using the Morse (M), Manning-Rosen (MR), Rosen-Morse (RM), and Modified-Rosen-Morse (MRM) potentials. Calculated energies from ab-initio methods in [42]<sup>†</sup> are also presented (*Continued*)

Molecule	n	$E_{n(M)}/\text{cm}^{-1}$ (% error)	$E_{n(MR)}/\text{cm}^{-1}$ (% error)	$E_{n(RM)}/\text{cm}^{-1}$ (% error)	$E_{n(MRM)}/\text{cm}^{-1}$ (% error)	$E_n^\dagger/\text{cm}^{-1}$
	1	-33088.949 (0.04)	-33167.879 (0.27)	-33069.743 (0.02)	-33069.314 (0.02)	-33077.320
	2	-29834.167 (0.11)	-30079.091 (0.93)	-29772.814 (0.09)	-29771.425 (0.10)	-29800.557
	3	-26747.854 (0.26)	-27225.971 (2.05)	-26624.747 (0.20)	-26621.924 (0.21)	-26678.870
	4	-23830.010 (0.51)	-24590.639 (3.71)	-23629.042 (0.34)	-23624.377 (0.36)	-23710.043
	5	-21080.637 (0.90)	-22156.968 (6.05)	-20789.374 (0.49)	-20782.532 (0.53)	-20892.705
	6	-18499.733 (1.50)	-19910.379 (9.24)	-18109.606 (0.64)	-18100.334 (0.69)	-18226.406
	7	-16087.298 (2.39)	-17837.669 (13.53)	-15593.795 (0.75)	-15581.935 (0.83)	-15711.716
	8	-13843.334 (3.69)	-15926.855 (19.30)	-13246.209 (0.78)	-13231.709 (0.89)	-13350.363
	9	-11767.839 (5.58)	-14167.046 (27.11)	-11071.339 (0.66)	-11054.266 (0.82)	-11145.411
D <sub>2</sub>	0	-36748.363 (0.00)	-36748.363 (0.00)	-36748.363 (0.00)	-36748.363 (0.00)	-36748.349
	1	-33765.748 (0.03)	-33825.769 (0.21)	-33751.239 (0.01)	-33750.915 (0.01)	-33754.742
	2	-30909.347 (0.09)	-31097.461 (0.70)	-30862.703 (0.06)	-30861.650 (0.06)	-30880.242
	3	-28179.160 (0.20)	-28550.209 (1.52)	-28084.890 (0.13)	-28082.738 (0.14)	-28122.759
	4	-25575.189 (0.37)	-26171.943 (2.71)	-25420.029 (0.24)	-25416.448 (0.25)	-25480.643
	5	-23097.432 (0.63)	-23951.635 (4.35)	-22870.443 (0.36)	-22865.149 (0.38)	-22952.701
	6	-20745.889 (1.01)	-21879.188 (6.53)	-20438.557 (0.49)	-20431.313 (0.52)	-20538.231
	7	-18520.562 (1.55)	-19945.349 (9.37)	-18126.900 (0.60)	-18117.528 (0.66)	-18237.066
	8	-16421.450 (2.32)	-18141.622 (13.03)	-15938.116 (0.69)	-15926.497 (0.77)	-16049.615
DT	0	-36881.281 (0.00)	-36881.281 (0.00)	-36881.281 (0.00)	-36881.281 (0.00)	-36881.271
	1	-34148.713 (0.03)	-34199.145 (0.18)	-34136.568 (0.00)	-34136.296 (0.00)	-34137.946

**Table 2.** Calculated energies with % errors<sup>†</sup> for first 10 vibrational energies of the molecules using the Morse (M), Manning-Rosen (MR), Rosen-Morse (RM), and Modified-Rosen-Morse (MRM) potentials. Calculated energies from ab-initio methods in [42]<sup>†</sup> are also presented (*Continued*)

Molecule	n	$E_{n(M)}/\text{cm}^{-1}$ (% error)	$E_{n(MR)}/\text{cm}^{-1}$ (% error)	$E_{n(RM)}/\text{cm}^{-1}$ (% error)	$E_{n(MRM)}/\text{cm}^{-1}$ (% error)	$E_n^{\ddagger}/\text{cm}^{-1}$
T <sub>2</sub>	2	-31521.306 (0.09)	-31680.242 (0.59)	-31482.126 (0.04)	-31481.236 (0.04)	-31494.199
	3	-28999.061 (0.18)	-29314.359 (1.26)	-28919.567 (0.10)	-28917.744 (0.11)	-28948.381
	4	-26581.978 (0.31)	-27092.105 (2.24)	-26450.569 (0.18)	-26447.526 (0.19)	-26499.146
	5	-24270.057 (0.52)	-25004.835 (3.56)	-24076.875 (0.28)	-24072.356 (0.30)	-24145.463
	6	-22063.298 (0.81)	-23044.578 (5.29)	-21800.294 (0.39)	-21794.084 (0.42)	-21886.630
	7	-19961.700 (1.21)	-21203.979 (7.51)	-19622.710 (0.50)	-19614.630 (0.55)	-19722.304
	8	-17965.265 (1.77)	-19476.236 (10.33)	-17546.081 (0.60)	-17535.999 (0.66)	-17652.523
	9	-16073.991 (2.53)	-17855.059 (13.89)	-15572.444 (0.67)	-15560.275 (0.75)	-15677.744
	0	-37028.496 (0.00)	-37028.496 (0.00)	-37028.496 (0.00)	-37028.496 (0.00)	-37028.481
	1	-34574.579 (0.03)	-34615.299 (0.15)	-34564.814 (0.00)	-34564.595 (0.00)	-34563.983
2	-32204.784 (0.08)	-32333.895 (0.48)	-32173.161 (0.02)	-32172.445 (0.02)	-32179.461	
3	-29919.112 (0.15)	-30176.855 (1.01)	-29854.684 (0.06)	-29853.213 (0.07)	-29873.687	
4	-27717.562 (0.26)	-28137.285 (1.78)	-27610.570 (0.13)	-27608.104 (0.14)	-27645.628	
5	-25600.134 (0.41)	-26208.789 (2.80)	-25442.044 (0.21)	-25438.369 (0.22)	-25494.449	
6	-23566.830 (0.63)	-24385.422 (4.12)	-23350.378 (0.30)	-23345.302 (0.32)	-23419.519	
7	-21617.648 (0.92)	-22661.653 (5.79)	-21336.886 (0.39)	-21330.245 (0.42)	-21420.429	
8	-19752.589 (1.31)	-21032.333 (7.87)	-19402.931 (0.48)	-19394.591 (0.53)	-19497.002	
9	-17971.653 (1.83)	-19492.660 (10.44)	-17549.922 (0.56)	-17539.781 (0.62)	-17649.309	

<sup>†</sup>Percentage errors in our results were calculated based on ab initio results in [42]

occur when the chemical bond is cleaved, molecules with heavier isotopes would undergo slower chemical reactions. The reason is that the amount of energy required to cleave the chemical bond in the molecules

with heavier isotopes is more significant than those of the lighter isotopes. It can also be inferred from Table 2 that molecules with heavier isotopes tend to have more dense vibrational states, which can be seen from the

smaller spacing between their adjacent states compared to the lighter ones. These findings indicate that the energy required to excite a molecule with heavier isotopes from a particular state into its next vibrational level is lower than that of the molecule with lighter isotopes. This argument has long been used in spectroscopic studies to infer the previously unknown heavy isotopes in a mix of diatomic molecules with different isotopes.

Fig. 1 illustrates the comparison of the first ten energy levels between our results using the Morse and Modified Rosen Morse potentials and those obtained from the ab-initio calculations [42] for the  $H_2$  molecule. The forms of the potential functions were also plotted in the exact figure. It is evident from Fig. 1(a) that the difference between our results and ab-initio results [42] became more apparent for higher vibrational states using the Morse potential. The large discrepancy at higher vibrational states was significantly reduced by using the modified Rosen-Morse potential function, as shown in Fig. 1(b). This finding is a clear indication that the modified Rosen-Morse potential was a better potential function than the Morse potential.

### Accuracy of the Semi-classical Approximation

#### Comparison with experimental values and literature

In most of the reported literature, the experimental data are not fully available for all vibrational energies of the molecules. The only complete data available for the

molecules are the first vibrational transition frequencies ( $\nu_1 \leftarrow 0$ ). Therefore, the accuracy of our calculations was assessed using these experimental values as shown in Table 3. As can be seen from Table 3, for the first transition frequencies, our analyses are in good agreement with the most accurate and recent corresponding experimental values. The most accurate results from our calculations came from the use of Rosen-Morse and the Modified-Rosen-Morse potential.

Based on Table 3, the errors resulted from the calculation of vibrational frequencies of molecular hydrogen isotopes using the Morse potential were significantly lower than those from the Manning-Rosen potential, indicating that the Morse potential was much better than the Manning-Rosen potential. This result also implied that the Morse potential was also better than the Deng-Fan potential and Schiöberg potential in describing some diatomic molecular interactions as it had been previously proven in [35] that despite being different in their initial forms, Manning-Rosen, Deng-Fan, and the Schiöberg potentials were empirically the same. Our finding agrees with the study by Wang et al. [35] where the calculations of anharmonicity  $\omega_e \chi_e$  and vibrational rotational coupling parameter  $\alpha_e$  for 16 diatomic molecules were conducted, and the results were compared to the experimental values. The authors indicated that the classic Morse potential was better than the Deng-Fan, Manning-Rosen, and the Schiöberg potential. This finding

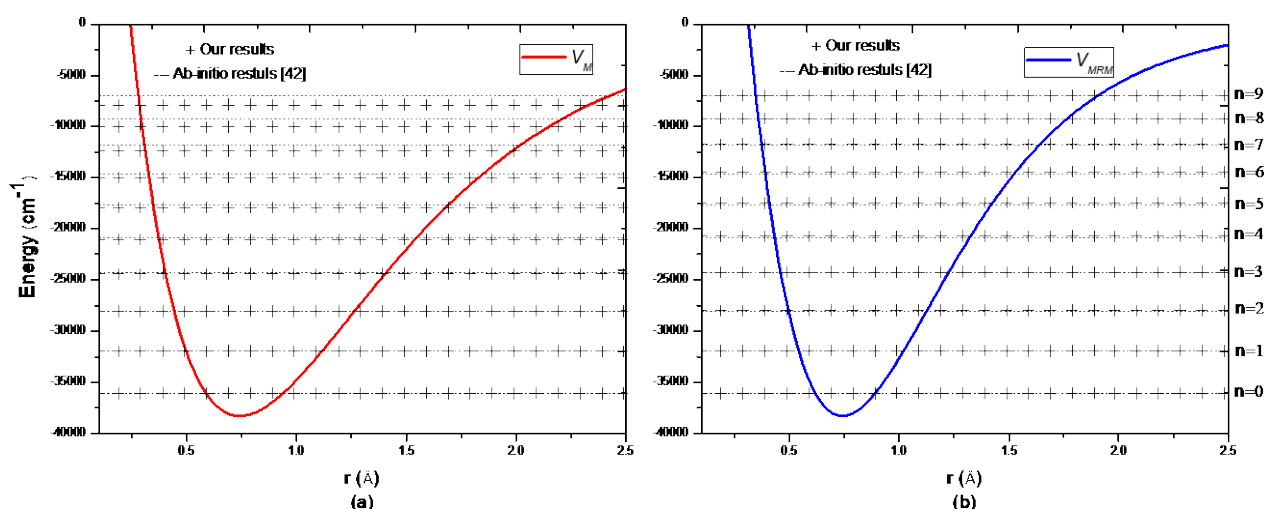


**Fig 1.** (a) First 10 vibrational energies of  $H_2$  molecule using the Morse potential  $V_M$  and (b) Modified Rosen-Morse potential  $V_{MRM}$ . Energies from ab-initio results [42] are also shown

**Table 3.** First vibrational frequencies  $\nu_{1 \leftarrow 0}$  ( $\Delta J=0$ ) with % errors<sup>1</sup> using the Morse (M), Manning-Rosen (MR), Rosen-Morse (RM), and Modified-Rosen-Morse (MRM) potentials. Exact and accurate corresponding values from the most recent experiments are also presented

Molecule	$\nu_{1 \leftarrow 0(M)}$ in $\text{cm}^{-1}$ (% error)	$\nu_{1 \leftarrow 0(MR)}$ in $\text{cm}^{-1}$ (% error)	$\nu_{1 \leftarrow 0(RM)}$ in $\text{cm}^{-1}$ (% error)	$\nu_{1 \leftarrow 0(MRM)}$ in $\text{cm}^{-1}$ (% error)	$\nu_{1 \leftarrow 0}$ in $\text{cm}^{-1}$ (exp.)
H <sub>2</sub>	4148.149 (0.31)	4032.557 (3.09)	4176.583 (0.37)	4177.203 (0.39)	4161.166 <sup>a</sup>
HD	3620.272 (0.33)	3532.060 (2.76)	3641.799 (0.27)	3642.273 (0.28)	3632.161 <sup>a</sup>
HT	3423.251 (0.34)	3344.321 (2.63)	3442.456 (0.22)	3442.885 (0.24)	3434.812 <sup>b</sup>
D <sub>2</sub>	2982.615 (0.37)	2922.593 (2.37)	2997.124 (0.12)	2997.448 (0.13)	2993.617 <sup>a</sup>
DT	2732.568 (0.39)	2682.136 (2.23)	2744.713 (0.05)	2744.986 (0.06)	2743.342 <sup>b</sup>
T <sub>2</sub>	2453.917 (0.43)	2413.197 (2.08)	2463.682 (0.03)	2463.901 (0.02)	2464.504 <sup>b</sup>

<sup>1</sup>Percentage errors in our results were calculated based on the corresponding experimental data shown in column 6

<sup>a,b</sup>Experimental data were obtained from [4]<sup>a</sup> and [6]<sup>b</sup>

was also supported by the study of Royappa et al. [43], who compared 21 potential empirical functions, including the Morse, Deng-Fan. The Rosen-Morse potential functions in fitting experimental data for some first- and second-row diatomic molecules and suggested that the Morse potential was significantly better than Deng-Fan potential in describing diatomic molecular interaction. Their results also powerfully revealed that the Rosen-Morse potential was considerably better than the Morse potential, consistent with our results as shown in Table 3, particularly for HD, D<sub>2</sub>, HT, and T<sub>2</sub> molecules. Our results are in agreement with the study of Wang et al. [35], and Royappa et al. [43] strongly suggested that the Morse potential was better than Manning-Rosen (and therefore Deng-Fan and Schiöberg potential) in describing the interaction of some diatomic molecules. This finding was in contrast to the claim that Deng-Fan potential was better than the Morse potential made by Deng and Fan [33]. The Morse potential was better than the Manning-Rosen potential in predicting vibrational levels of electronic ground states of molecular hydrogen isotopes obtained here was interesting since it was in contrast to results obtained by [34] for the Li<sub>2</sub> molecule. Thus, it suggests that a further investigation on the vibrational energies of these two kinds of molecules for different electronic states is of interest.

The results presented in Table 3 showed that the Modified Rosen Morse potential function was also more accurate in obtaining the first vibrational frequency of the HD, D<sub>2</sub>, HT, and T<sub>2</sub> molecules. This finding suggested

that the modified Rosen Morse potential was more potent than the Morse potential in describing the interaction of diatomics. This conclusion was supported by the study of Tang et al. [44], who solved the Schrödinger equation of some diatomics with some potential functions and found that the Modified Rosen Morse potential was better in fitting with experimental data. It is interesting to note that for the H<sub>2</sub> molecule (the lightest molecule considered here), the Morse potential was somehow better than both Rosen Morse and the Modified Rosen Morse potential, with errors about 0.31%, 0.37%, and 0.39%, respectively. These errors were related to the accuracy of the semi-classical approximation used in this article which was less accurate for lighter molecules.

To further evaluate our results, the first vibrational frequencies for the molecules generated from our calculations were compared with the most accurate ab-initio estimates adapted from [7,13-14,45-46]. The comparison, shown in Table 4, clearly indicates that our calculations, although having slightly higher % error, are reasonably comparable to the results generated from the ab-initio calculations. The fact that the ab-initio calculations resulted in better accuracy since the ab-initio analysis involved the Born-Oppenheimer, adiabatic, non-adiabatic, relativistic, and quantum electrodynamics effects, which are more comprehensive in comparison to our calculation that only affects the Born-Oppenheimer term applied in a semi-classical approach. As can be seen from Table 4, ab-initio calculations in [45] generated the



**Table 4.** First vibrational frequencies  $\nu_{1\leftarrow 0}$  ( $\Delta J=0$ ) with % errors<sup>†</sup> using the most accurate potential in this study: Rosen-Morse (RM) and Modified-Rosen-Morse (MRM) potential functions are compared with most accurate corresponding values from ab-initio calculations

Molecule	$\nu_{1\leftarrow 0(\text{RM})}$ in $\text{cm}^{-1}$ (% error)	$\nu_{1\leftarrow 0(\text{MRM})}$ in $\text{cm}^{-1}$ (% error)	$\nu_{1\leftarrow 0(\text{ab-initio})}$ in $\text{cm}^{-1}$ (% error)	$\nu_{1\leftarrow 0}$ in $\text{cm}^{-1}$ (exp.)
H <sub>2</sub>	4176.583 (0.37)	4177.203 (0.39)	4161.166 (0) [45] 4161.185(0.0005) [46]	4161.166 <sup>a</sup>
HD	3641.799 (0.27)	3642.273 (0.28)	3632.160 (0.00003) [45] 3632.179 (0.0005) [46] 3632.158 (0.00008) [14]	3632.161 <sup>a</sup>
HT	3442.456 (0.22)	3442.885 (0.24)	-	3434.812 <sup>b</sup>
D <sub>2</sub>	2997.124 (0.12)	2997.448 (0.13)	2993.617 (0) [45] 2993.636 (0.0006) [46] 2993.615 (0.00007) [13]	2993.617 <sup>a</sup>
DT	2744.713 (0.05)	2744.986 (0.06)	-	2743.342 <sup>b</sup>
T <sub>2</sub>	2463.682 (0.03)	2463.901 (0.02)	2464.502 (0.00008) [7]	2464.504 <sup>b</sup>

<sup>†</sup>Percentage errors were calculated based on the corresponding experimental data in column 5

<sup>a</sup>bExperimental data were obtained from [4]<sup>a</sup> and [6]<sup>b</sup>

exact experimental values for the first vibrational frequency of H<sub>2</sub> and D<sub>2</sub>. They were in excellent agreement with experimental ones for HD (with % error of order 10<sup>-5</sup>).

Similarly, the first vibrational frequencies reported in [7,13-14,46] were very accurate with % errors in the order of 10<sup>-5</sup>-10<sup>-4</sup> compared to ours with % errors in 10<sup>-2</sup>-10<sup>-1</sup>. However, it can be inferred that the Born-Oppenheimer term made the most significant contribution to the vibrational energies of the molecules. The contribution of the Born-Oppenheimer term can reach about 99.9% from the most accurate ab-initio results for the first vibrational frequency  $\nu_{1\leftarrow 0}$  of the molecules [45]. Therefore, despite involving only Born-Oppenheimer approximation in a semi-classical approximation, our products can generate reasonably accurate results with an error below 0.4% for the first vibrational frequencies of the molecules.

#### **Accuracy as a function of the vibrational quantum number and molecular mass**

To further clarify the accuracy of the potentials used, the percentage errors provided in Table 2 are plotted against the vibrational levels. The plot for the Morse potential is shown in Fig. 2(a). The pattern for other potentials is similar and hence is not shown.

The results obtained in Fig. 2(a) indicated that at higher vibrational levels, the accuracy of our calculations decreased, as indicated by the increase in the percentage of errors for higher vibrational energies for all molecules considered. This trend was also observed for other isotopes used in this study, as can be seen from Table 2. This finding was interesting since semi-classical approximation should work better for higher energies as for much higher energies, wave functions of the systems should approach the classical free particle wave functions. The more significant errors observed for higher vibrational states in this research were because the values of  $\delta$  used for a particular molecule using a particular potential were fitted only once for the ground vibrational state energy and used to calculate other higher vibrational energies of the molecules.

Additionally, the use of the Rosen-Morse and the Modified-Rosen-Morse potentials have significantly reduced the errors obtained using the Morse potential, especially for higher vibrational states of the H<sub>2</sub> molecule. This finding can be seen in Fig. 2(b) and Table 2, where the % errors resulted from the use of Rosen-Morse and the Modified-Rosen-Morse potentials were below 1%. These percentage errors were significantly lower than those calculated using the Morse potential,

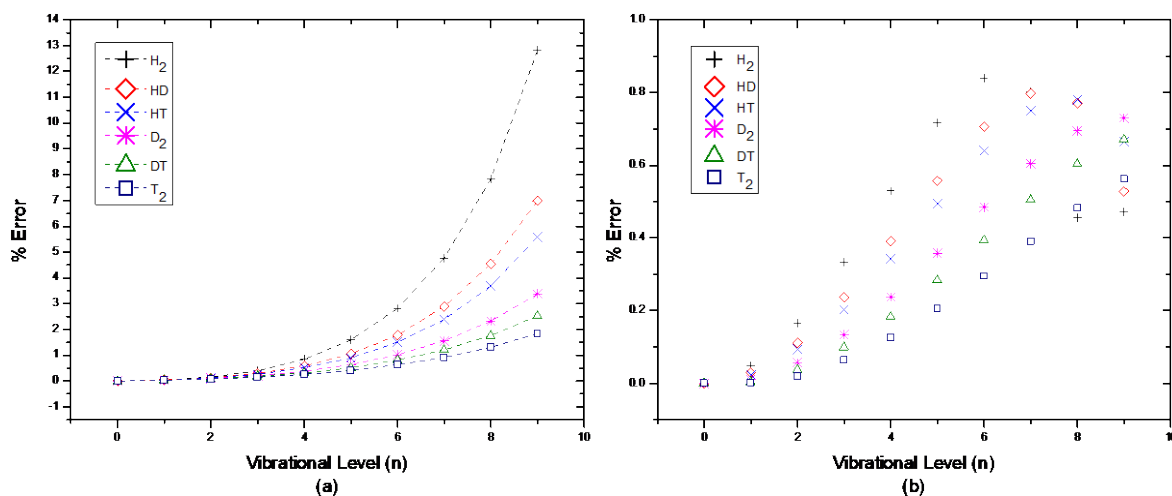


**Fig 2.** (a) % Errors in our vibrational energies are plotted against the vibrational energy levels for all molecules using the Morse potential and (b) Rosen-Morse potential

with the highest % errors of 12.83%. It was also important to note from Fig. 2(a) that better accuracy was obtained for heavier isotopes. This result was indicated by the more minor errors for heavier isotopes. The argument can explain that the heavier the molecules, the more “classical” they become (the larger  $\gamma$  values they have). This discrepancy was mainly due to the semi-classical approximation is based on the assumption that the nuclei move in classical potential wells. Therefore they have continuous energy like any classical object before their subsequent quantization using the Bohr-Sommerfeld quantization rule.

Consequently, less accurate results generated from this approximation in comparison to the ab-initio calculations would be anticipated. However, better accuracy using this approximation was expected following the substitution of the lighter isotopes with their heavier counterparts within the molecules. As previously described, this change was due to the more classical dynamics of the molecules as the mass of the isotopes increases. This was described as the  $\gamma$  value in Eq. (4). Larger  $\gamma$  values correspond to more ‘classical’ molecules and more accurate results for the semi-classical approximation. Chemically, this can be attributed to the fact that heavier isotopes have more stable vibrational states than lighter ones, as previously described.

With these two essential observations, investigations of the accuracy of this method on the

calculation of vibrational energies of more ‘classical’ diatomic molecules are therefore attractive. A more comprehensive study on this topic is the subject of our following paper which is in preparation.

### Improved Vibrational Energies from the (Modified) Rosen Morse Potential

In our previous study [28], the semi-classical method using the Morse potential has been successfully applied to calculate low-lying vibrational energies of the molecular hydrogen H<sub>2</sub>. However, as can be seen from Fig. 2(a), a declining trend in the accuracy was observed for higher vibrational states. This decreasing trend, particularly for higher vibrational states and lighter molecules, was fixed by Rosen-Morse and the Modified-Rosen-Morse potential. This can be seen in Fig. 2(b).

Fig. 2(b) demonstrates that the increase in the errors when using the Morse potential for higher vibrational states of the molecules could be fixed by using the Rosen-Morse potential function. This result was shown by a significant decreasing trend of the % errors for the H<sub>2</sub> molecule, particularly from  $n = 7$  onwards. A similar pattern can also be seen for the HD molecule starting at  $n = 8$ . For heavier molecules: HT, D<sub>2</sub>, DT, and T<sub>2</sub>, the practice is not seen, but a decrease of errors for higher vibrational states ( $n > 9$ ) is highly expected from the pattern shown in Fig. 2(b). This finding implies that the use of the Rosen-Morse and the

Modified-Rosen-Morse potential function within the framework of the semi-classical approximation has significantly improved the accuracy of the calculation of vibrational energies from the Morse potential, especially for higher vibrational states. This finding was also reported by Tang et al. [44]. They fitted the potentials to the well-known Rydberg-Klein-Rees (RKR) data points of the  $\text{Li}_2$  molecule. They found that the modified Rosen Morse potential showed a much better fit with the experimental data than Morse potential, especially for high vibrational states. Zhang et al. [32] also reported the same finding when examining some other diatomic molecules in their study, including  $\text{ICl}$ ,  $\text{I}_2$ ,  $\text{Cs}_2$ ,  $\text{MgH}$ , and  $\text{Li}_2$  molecules. This argument was also valid for other diatomic molecules, including  $\text{SiC}$ ,  $\text{SCL}$ ,  $\text{Cs}_2$ , and  $\text{Na}_2$  molecules, as reported in [47-49]. These observations strongly indicated that the Rosen Morse and the modified Rosen Morse potential were better than the Morse potential (and therefore the Manning-Rosen, Deng-Fan, and the Schiöberg potential) in describing the interaction of some diatomic molecules. More comprehensive studies on other physical and chemical properties of other diatomic molecules in different electronic, vibrational, and rotational states are therefore essential to further evaluate and compare the accuracy of the potential functions in describing the interaction of the molecules.

## ■ CONCLUSION

The semi-classical method has been successfully applied to obtain the first ten vibrational energies of all isotopes of the molecular hydrogen in their ground electronic state  $X\Sigma_g^+$ . The results showed that the Rosen-Morse and the Modified Rosen Morse potential were the most accurate potentials used in this study, with errors below 1%. It was also found that the Morse potential was better than the Manning-Rosen potential function in calculating vibrational energy levels of all isotopes of the diatomic hydrogen, using the semi-classical approximation. Finally, the accuracy of the approximation becomes better for heavier isotopes. The semi-classical approximation could be applied to study vibrational energies of diatomic molecules, especially

those with larger reduced mass using various classical potential functions.

## ■ ACKNOWLEDGMENTS

The authors thank Prof. Pekik Nurwantoro from the Department of Physics CoECS FMIPA Universitas Gadjah Mada for beneficial discussions and valuable comments on our manuscript.

## ■ REFERENCES

- [1] Puchalski, M., Komasa, J., and Pachucki, K., 2017, Relativistic corrections for the ground electronic state of molecular hydrogen, *Phys. Rev. A*, 95 (5), 052506.
- [2] Korobov, V.I., Hilico, L., and Karr, J.P., 2017, Fundamental transitions and ionization energies of the hydrogen molecular ions with few ppt uncertainty, *Phys. Rev. Lett.*, 118 (23), 233001.
- [3] Liu, J., Sprecher, D., Jungen, C., Ubachs, W., and Merkt, F., 2010, Determination of the ionization and dissociation energies of the deuterium molecule ( $\text{D}_2$ ), *J. Chem. Phys.*, 132 (15), 154301.
- [4] Dickenson, G.D., Niu, M.L., Salumbides, E.J., Komasa, J., Eikema, K.S.E., Pachucki, K., and Ubachs, W., 2013, Fundamental vibration of molecular hydrogen, *Phys. Rev. Lett.*, 110 (19), 193601.
- [5] Wójtewicz, S., Gotti, R., Gatti, D., Lamperti, M., Laporta, P., Jóźwiak, H., Thibault, F., Wcisło, P., and Marangoni, M., 2020, Accurate deuterium spectroscopy and comparison with ab initio calculations, *Phys. Rev. A*, 101 (5), 052504.
- [6] Lai, K.F., Hermann, V., Trivikram, T.M., Diouf, M., Schlösser, M., Ubachs, W., and Salumbides, E.J., 2020, Precision measurement of the fundamental vibrational frequencies of tritium-bearing hydrogen molecules:  $\text{T}_2$ ,  $\text{DT}$ ,  $\text{HT}$ , *Phys. Chem. Chem. Phys.*, 22 (16), 8973–8987.
- [7] Trivikram, T.M., Schlösser, M., Ubachs, W., and Salumbides, E.J., 2018, Relativistic and QED effects in the fundamental vibration of  $\text{T}_2$ , *Phys. Rev. Lett.*, 120 (16), 163002.
- [8] Lai, K.F., Czachorowski, P., Schlösser, M., Puchalski, M., Komasa, J., Pachucki, K., Ubachs, W., and Salumbides, E.J., 2019, Precision tests of non-

- adiabatic perturbation theory with measurements on the DT molecule, *Phys. Rev. Res.*, 1 (3), 033124.
- [9] Kalinin, K.V., 2011, Calculation of hydrogen molecule energy levels using the moment constant summability method with specialized weight, *Atmos. Oceanic Opt.*, 24 (1), 17–21.
- [10] Kurokawa, Y.I., Nakashima, H., and Nakatsuji, H., 2019, Solving the Schrödinger equation of hydrogen molecules with the free-complement variational theory: Essentially exact potential curves and vibrational levels of the ground and excited states of the  $\Sigma$  symmetry, *Phys. Chem. Chem. Phys.*, 21 (12), 6327–6340.
- [11] Kurokawa, Y.I., Nakashima, H., and Nakatsuji, H., 2020, Solving the Schrödinger equation of hydrogen molecules with the free-complement variational theory: Essentially exact potential curves and vibrational levels of the ground and excited states of the  $\Pi$  symmetry, *Phys. Chem. Chem. Phys.*, 22 (24), 13489–13497.
- [12] Desai, A.M., Mesquita, N., and Fernandes, V., 2020, A new modified Morse potential energy function for diatomic molecules, *Phys. Scr.*, 95 (8), 085401.
- [13] Pachucki, K., and Komasa, J., 2019, Non-relativistic energy levels of  $D_2$ , *Phys. Chem. Chem. Phys.*, 21 (20), 10272–10276.
- [14] Pachucki, K., and Komasa, J., 2018, Non-relativistic energy levels of HD, *Phys. Chem. Chem. Phys.*, 20 (41), 26297–26302.
- [15] Komasa, J., Puchalski, M., Czachorowski, P., Łach, G., and Pachucki, K., 2019, Rovibrational energy levels of the hydrogen molecule through non-adiabatic perturbation theory, *Phys. Rev. A*, 100 (3), 032519.
- [16] Sholihun, S., Saito, M., Ohno, T., and Yamasaki, T., 2015, Density-functional-theory-based calculations of formation energy and concentration of the silicon monovacancy, *Jpn. J. Appl. Phys.*, 54 (4), 041301.
- [17] Sholihun, S., Kadarisman, H.P., and Nurwantoro, P., 2018, Density-functional-theory calculations of formation energy of the nitrogen-doped diamond, *Indones. J. Chem.*, 18 (4), 749–754.
- [18] Hastuti, D.P., Nurwantoro, P., and Sholihun, S., 2019, Stability study of germanene vacancies: The first-principles calculations, *Mater. Today Commun.*, 19, 459–463.
- [19] Amalia, W., Nurwantoro, P., and Sholihun, S., 2018, Density-functional-theory calculations of structural and electronic properties of vacancies in monolayer hexagonal boron nitride (h-BN), *Comput. Condens. Matter*, 18, e00354.
- [20] Hutama, A.S., Huang, H., and Kurniawan, Y.S., 2019, Investigation of the chemical and optical properties of halogen-substituted *N*-methyl-4-piperidone curcumin analogs by density functional theory calculations, *Spectrochim. Acta, Part A*, 221, 117152.
- [21] Al-Mushadani, O.K., and Needs, R.J., 2003, Free-energy calculations of intrinsic point defects in silicon, *Phys. Rev. B*, 68 (23), 235205.
- [22] Sanati, M., and Estreicher, S.K., 2003, Defects in silicon: The role of vibrational entropy, *Solid State Commun.*, 128 (5), 181–185.
- [23] Hutama, A.S., Hijikata, Y., and Irle, S., 2017, Coupled cluster and density functional studies of atomic fluorine chemisorption on coronene as model systems for graphene fluorination, *J. Phys. Chem. C*, 121 (27), 14888–14898.
- [24] Ceotto, M., Valleau, S., Tantardini, G.F., and Aspuru-Guzik, A., 2011, First principles semi-classical calculations of vibrational eigenfunctions, *J. Chem. Phys.*, 134 (23), 234103.
- [25] Vázquez, F.X., Talapatra, S., and Geva, E., 2011, Vibrational energy relaxation in liquid HCl and DCl via the linearized semi-classical method: Electrostriction versus quantum delocalization, *J. Phys. Chem. A*, 115 (35), 9775–9781.
- [26] Walton, J.R., Rivera-Rivera, L.A., Lucchese, R.R., and Bevan, J.W., 2016, Morse, Lennard-Jones, and Kratzer potentials: A canonical perspective with applications, *J. Phys. Chem. A*, 120 (42), 8347–8359.
- [27] Roy, A.K., 2013, Accurate ro-vibrational spectroscopy of diatomic molecules in a Morse oscillator potential, *Results Phys.*, 3, 103–108.
- [28] Pingak, R.K., and Johannes, A.Z., 2020, Penentuan tingkat-tingkat energi vibrasi molekul hidrogen pada keadaan elektronik dasar menggunakan potensial Morse, *Wahana Fisika*, 5 (1), 1–9.

- [29] Morse, P.M., 1929, Diatomic molecules according to the wave mechanics II: Vibrational levels, *Phys. Rev.*, 34 (1), 57–64.
- [30] Rosen, N., and Morse, P.M., 1932, On the vibrations of polyatomic molecules, *Phys. Rev.*, 42 (2), 210–217.
- [31] Manning, M.F., and Rosen, N., 1933, A potential function for the vibrations of the diatomic molecules, *Phys. Rev.*, 44, 953.
- [32] Zhang, G.D., Liu, J.Y., Zhang, L.H., Zhou, W., and Jia, C.S., 2012, Modified Rosen-Morse potential-energy model for diatomic molecules, *Phys. Rev. A*, 86 (6), 062510.
- [33] Deng, Z.H., and Fan, Y.P., 1957, A potential function of diatomic molecules, *J. Shandong Univ.*, 1, 162–166.
- [34] Liu, J.Y., Zhang, G.D., and Jia, C.S., 2013, Calculation of the interaction potential energy curve and vibrational levels of the  $a^3\Sigma_u^+$  state of  $^7\text{Li}_2$  molecule, *Phys. Lett. A*, 377 (21-22), 1444–1447.
- [35] Wang, P.Q., Zhang, L.H., Jia, C.S., and Liu, J.Y., 2012, Equivalence of the three empirical potential energy models for diatomic molecules, *J. Mol. Spectrosc.*, 274, 5–8.
- [36] Koonin, S.E., and Meredith, D.C., 1998, *Computational Physics: Fortran Version*, 1<sup>st</sup> Ed., CRC Press, Boca Raton, Florida, US.
- [37] Jia, C.S., Diao, Y.F., Liu, X.J., Wang, P.Q., Liu, J.Y., and Zhang, G.D., 2012, Equivalence of the Wei potential model and Tietz potential model for diatomic molecules, *J. Chem. Phys.*, 137 (1), 014101.
- [38] Huber, K.P., and Herzberg, G., 1979, *Molecular Spectra and Molecular Structure. IV. Constants of Diatomic Molecules*, 1<sup>st</sup> Ed., Springer, US.
- [39] Sprecher, D., Jungen, C., Ubachs, W., and Merkt, F., 2011, Towards measuring ionisation and dissociation energies of molecular hydrogen with sub-MHz accuracy, *Faraday Discuss.*, 150, 51–70.
- [40] Sprecher, D., Liu, J., Jungen, C., Ubachs, W., and Merkt, F., 2010, Communication: The ionization and dissociation energies of HD, *J. Chem. Phys.*, 133 (11), 111102.
- [41] Puchalski, M., Komasa, J., Spyszkiwicz, A., and Pachucki, K., 2019, Dissociation energy of molecular hydrogen isotopologues, *Phys. Rev. A*, 100 (2), 020503.
- [42] Schwartz, C., and Le Roy, R.J., 1987, Non-adiabatic eigenvalues and adiabatic matrix elements for all isotopes of diatomic hydrogen, *J. Mol. Spectrosc.*, 121 (2), 420–439.
- [43] Royappa, A.T., Suri, V., and McDonough, J.R., 2006, Comparison of empirical closed-form functions for fitting diatomic interaction potentials of ground state first- and second-row diatomics, *J. Mol. Struct.*, 787 (1-3), 209–215.
- [44] Tang, H.M., Liang, G.C., Zhang, L.H., Zhao, F., and Jia, C.S., 2014, Diatomic molecule energies of the modified Rosen-Morse potential energy model, *Can. J. Chem.*, 92 (4), 341–345.
- [45] Niu, M.L., Salumbides, E.J., Dickenson, G.D., Eikema, K.S.E., and Ubachs, W., 2014, Precision spectroscopy of the  $X^1\Sigma_g^+$ ,  $v=0 \rightarrow 1$  ( $J=0''-''2$ ) rovibrational splittings in  $\text{H}_2$ , HD and  $\text{D}_2$ , *J. Mol. Spectrosc.*, 300, 44–54.
- [46] Wolniewicz, L., 1983, The  $X^1\Sigma_g^+$  state vibration-rotation energies of the  $\text{H}_2$ , HD, and  $\text{D}_2$  molecules, *J. Chem. Phys.*, 78 (10), 6173–6181.
- [47] Yanar, H., Aydoğdu, O., and Salti, M., 2016, Modelling of diatomic molecules, *Mol. Phys.*, 114 (21), 3134–3142.
- [48] Liu, J.Y., Hu, X.T., and Jia, C.S., 2014, Molecular energies of the improved Rosen-Morse potential energy model, *Can. J. Chem.*, 92 (1), 40–44.
- [49] Tan, M.S., He, S., and Jia, C.S., 2014, Molecular spinless energies of the improved Rosen-Morse potential energy model in D dimension, *Eur. Phys. J. Plus*, 129 (12), 264.

## A Green Method for Synthesis of Silver-Nanoparticles-Diatomite (AgNPs-D) Composite from Pineapple (*Ananas comosus*) Leaf Extract

Sapriani Hamdiani<sup>1,2</sup> and Yeng-Fong Shih<sup>1\*</sup>

<sup>1</sup>Department of Applied Chemistry, Chaoyang University of Technology, No. 168, Jifeng E. Rd., Wufeng District, Taichung 41349, Taiwan

<sup>2</sup>Department of Chemistry, Faculty of Mathematics and Natural Sciences, University of Mataram, Jl. Majapahit No.62, NTB 83115, Indonesia

\* **Corresponding author:**

tel: +04-23323000 ex 4308, 7272  
email: syf@cyut.edu.tw

Received: January 25, 2021  
Accepted: March 15, 2021

DOI: 10.22146/ijc.63573

**Abstract:** This study aims to develop a green method to load silver nanoparticles (AgNPs) into the diatomite (D) pores to produce AgNPs-D composite material. The AgNPs were synthesized by pineapple leaf extract at the temperature of 70 °C for 30 min. The composite formation was characterized by UV-Vis, FTIR, TGA, particle sizes analysis, gravimetric, and color observation. The appearance of surface plasmon bands in 440–460 nm confirms the AgNPs formation. The percentage of the AgNO<sub>3</sub> which converted to AgNPs was 99.8%. The smallest particle size of AgNPs was 30 nm, obtained in an AgNO<sub>3</sub> concentration of 1 mM with a stirring time of 24 h at 70 °C. The colloidal AgNPs were stable for up to 7 days. The adsorption process of AgNPs was marked by the appearance of –C=O and –C–O– groups peak at 1740 and 1366 cm<sup>-1</sup> on the FTIR spectrum. By adsorption and gravimetric technique, as much as 1 wt.% of AgNPs were loaded into D pores. The color of diatomite material changes from white to reddish-brown. The TGA analysis showed that the remaining D and AgNPs-D at 580 °C are 98.22% and 95.74%, respectively. The AgNPs loading through the green technology technique was expected to increase diatomite application in the biomedical field.

**Keywords:** pineapple leaf extract; diatomite; silver nanoparticles; green method

### ■ INTRODUCTION

Diatomite is an inorganic material naturally formed from fossilized single-celled aquatic algae called diatomite [1]. The main diatomite composition is SiO<sub>2</sub>; other components include Al<sub>2</sub>O<sub>3</sub>, Fe<sub>2</sub>O<sub>3</sub>, CaO, MgO, and other organics [2]. The material's physical properties are lightweight, low density, thermal conductivity, high porosity, and surface area, inertness, and high absorption capacity [3-4]. The composition and excellent physical properties make diatomite potential for application as a filler of composite material in industrial and biomedical applications [5].

In the industrial field, diatomite is applied as a filler in many applications such as for the adsorption of dye materials [6], separation of oil from crude oil [7], sensors [8], catalyst support, thermal storage [9], and pollution prevention of heavy metals in drinking water [10]. In the

biomedical field, diatomite is applied as a drug delivery material [11], biosensing [12], a filler for making scaffold and bone tissue regeneration [13]. As a filler for scaffold and bone tissue regeneration, diatomite is used for reinforced porous polyurethane foam (PUF) [14] and chitosan composite membrane [15]. The addition of diatomite increases the mechanical strength and water uptake capacity of the polymer. Another biomedical application for diatomite is a precursor for leusite synthesis. Leusite is an essential material in Porcelain-Fused-to-Metal (PFM) and all-ceramic restoration systems. This material produces transparency, depth of color, and texture of natural teeth [16]. However, the use of diatomite in the biomedical field is limited because it does not contain antibacterial properties. The large porosity of diatomite makes antibacterial substrate easy to load into the diatomite pores. Diatomite, as matrix

minerals for antibacterial carrier agents, is a promising economic material.

One of the elements that possessed excellent antibacterial properties is silver nanoparticles (AgNPs). The substances are not toxic to humans but have high toxicity to microorganisms such as bacteria, viruses, and fungi [17-19]. The resulting silver nanoparticles (AgNPs) will be loaded into the diatomite (D) pores to obtain silver-nanoparticle diatomite (AgNPs-D) composite material. Several methods were used to load silver nanoparticles into the diatomite pores. Chen et al. (2020) have used the  $\text{Ag}^+$  adsorption method from an electrolytic cell and calcination in high temperatures of 500 and 800 °C [20]. Qi et al. (2020) fabricated silver-diatomite nanocomposite ceramic with silver nitrate adsorption by diatomite. The composite was then added with a carboxymethyl cellulose solution followed by calcination at 400 °C [21]. Besides, the researchers used chemicals such as sodium borohydride solution [22], hydrogen peroxide [23], and Tollens' reagent [24-25] to produce AgNPs. However, some of these methods are not environmentally friendly and expensive because they use high calcination temperatures and toxic reducing agents.

The environmentally friendly, non-toxic, safe, and low-cost method to produce AgNPs-D composites is necessary to develop. The method used is synthesized silver nanoparticles using the leaf extract from agricultural waste [26-27]. One of the ample abundances of agricultural waste in Taiwan is pineapple (*Ananas comosus* L) leaf. Every year, more than 5 million tons of pineapple leaf trash are produced [28]. The phytochemical content in the leaf extract acts both as a reducing and capping agent for the formation of AgNPs [29-30]. The phytochemical compound in the pineapple leaf extract includes terpenoids, flavonoids, cardiac glycosides, phytosterols, alkaloids, and saponins [31], causing the reduction process of  $\text{Ag}^+$  to  $\text{Ag}^0$ . The reduction process is then followed by stabilization to form stable oligomeric clusters of silver nanoparticles. The AgNPs are loaded into the diatomite pores by the adsorption process. Adsorption is an effective and efficient method for loading metal nanoparticles into the pores of porous materials [32]. The resulting silver

nanoparticle-diatomite (AgNPs-D) composite will potentially be applied as a filler in the biomedical field.

## ■ EXPERIMENTAL SECTION

### Materials

Pineapple leaf was collected from the pineapple plantation area in Wufeng District, Taiwan,  $\text{AgNO}_3$  (Sigma-Aldrich chemicals), and diatomite (Cellite® 577; density = 0.47 g/cm<sup>3</sup>, content: 80~90%  $\text{SiO}_2$ , 2~4%  $\text{Al}_2\text{O}_3$ , and 0.5~2%  $\text{Fe}_2\text{O}_3$ ) was supplied by Imerys Filtration Minerals Inc.

### Instrumentation

FTIR (Perkin Elmer Two Spectrum, USA), UV-Visible Spectrophotometer (Perkin Elmer PDA UV-Vis, Lambda 265, USA), Laser particle sizer (Fritsch Analysette 22), and TA Instruments TGA Q50 thermogravimetric analyzer.

### Procedure

#### **Preparation of leaf extract**

Fresh pineapple leaf was washed and chopped. The leaf was then dried at room temperature and extracted with distilled water. Next, 10 g of the dried leaf was added with 200 mL of distilled water and boiled at 60 °C for 1 h. The mixture was then filtered with no.1 Whatman filter paper. The filtrate was collected and kept at 4 °C and was further used to synthesize the silver nanoparticles.

#### **Synthesis of silver nanoparticles using the pineapple leaf extract**

The filtrate (5 mL) of pineapple leaf extract was added to 50 mL of 1 mM, 2 mM, and 3 mM aqueous solution of  $\text{AgNO}_3$ . The solution was heated at 70 °C for 30 min, and the color change was observed. Afterward, the solution was stirred for 4, 8, 24, 28, and 30 h, respectively, at a speed of 800 rpm to complete the nanoparticle formation. The sample was taken for UV-Visible and particle size analysis.

#### **Stability of particle size distribution in silver nanoparticles (AgNPs) solution**

Stability of Particle Size Distribution in Silver Nanoparticles (AgNPs) solution: The 1 mM solution of

synthesized AgNPs was stored at the period of 3, 7, 9, 14, 21, and 30 days. At the range of the periods, the distribution of particle size was measured by particle size analysis equipment.

#### **Preparation of AgNPs-D (diatomite, which loaded by AgNPs)**

Diatomite was processed to enhance the surface area and total pore volume by the calcination process at 400 °C for 2 h. The diatomite was added to the silver nanoparticles solution at room temperature. It stirred continuously for 8 h to complete the adsorption of AgNPs into the diatomite pores. The mixture was heated at 60 °C for 24 h to remove the solvents, and AgNPs-D powder was obtained.

## ■ RESULTS AND DISCUSSION

### **The Phytochemical Compound in Pineapple Leaf Extracts for AgNPs Formation**

Collecting the phytochemical compound, such as secondary metabolite in pineapple leaf extract, is carried out by the extraction process in distilled water. Before processing, the pineapple leaves were dried at room temperature. The drying process aims to reduce the presence of water. The reduced water content will create more space for the solvent to penetrate the cells and increase the secondary metabolites extracted from the leaves [33]. Pineapple leaf extract contains secondary metabolites include 13 types of phenolic constituents. There are five major phenolic compounds: caffeic acid, *p*-coumaric acid, 1-O-caffeoylglycerol, 1-O-coumaroylglycerol, and 1,3-O-dicaffeoylglycerol (ananasate) [34-36]. The secondary metabolites of leaf extract play an essential role in reducing and capping silver nanoparticle formation. Carbonyl and hydroxyl functional groups found in the pineapple leaf extract forces the reduction process. The groups as a reduction agent and stabilize the nanoparticles by preventing aggregation [37]. The reduction and stabilization process occurs in one single step:

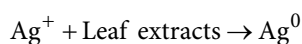
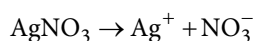


Illustration of reduction and stabilization of silver

nanoparticles by the phytochemical compound in pineapple leaf extract shown in Fig. 1. The nanoparticle formation occurred in 3 steps. The steps are reduction, nucleation, and crystal growth. Reduction occurs because the carbonyl and hydroxyl groups have a higher redox potential than other groups and become the electron source that transfers to metal [38]. The reduction process causes the beginning of crystal nanoparticle formation (nucleation). During the process of crystal formation completed, the carbonyl and hydroxyl will stabilize the nanoparticle crystals formed.

### **UV-Visible Spectroscopy**

The formation of silver nanoparticles was detected by UV-Visible Spectroscopy analysis shown in Fig. 2. The characteristic plasmon band for silver nanoparticle formation was ranging between 440–460 nm (a). The peak appears due to the reduction of  $\text{Ag}^+$  to  $\text{Ag}^0$ , the nucleation process, and the complete crystal growth process. Completing the crystal growth process is characterized by a change in the  $\text{AgNO}_3$  solution color of the reddish-brown [39]. The color change is caused by the excitation process and changes in electronic energy on the surface plasmon band vibrations due to silver nanoparticle formation. In general, free electrons in metals vibrate after being exposed to UV light. Electron vibrations resonate with light waves, resulting in the highest absorption characteristic at the peak of 425 nm.

### **Particle Size Analysis**

In this study, the synthesis of AgNPs involves the heating process at a temperature of 70 °C for 30 min. The heat treatment affects the formation and average diameter of AgNPs. According to research conducted by Hongyu Liu et al. (2020), the particle size of AgNPs is smaller at the temperature of 70 °C than between 75–90 °C [40]. A static laser light scattering technique conducted distribution and particle size measurement. The method can cover a particle measuring range from approximately ten nanometers up to a few millimeters. The particle size distribution of the AgNPs in the variation of concentration and stirring time is shown in Table 1.



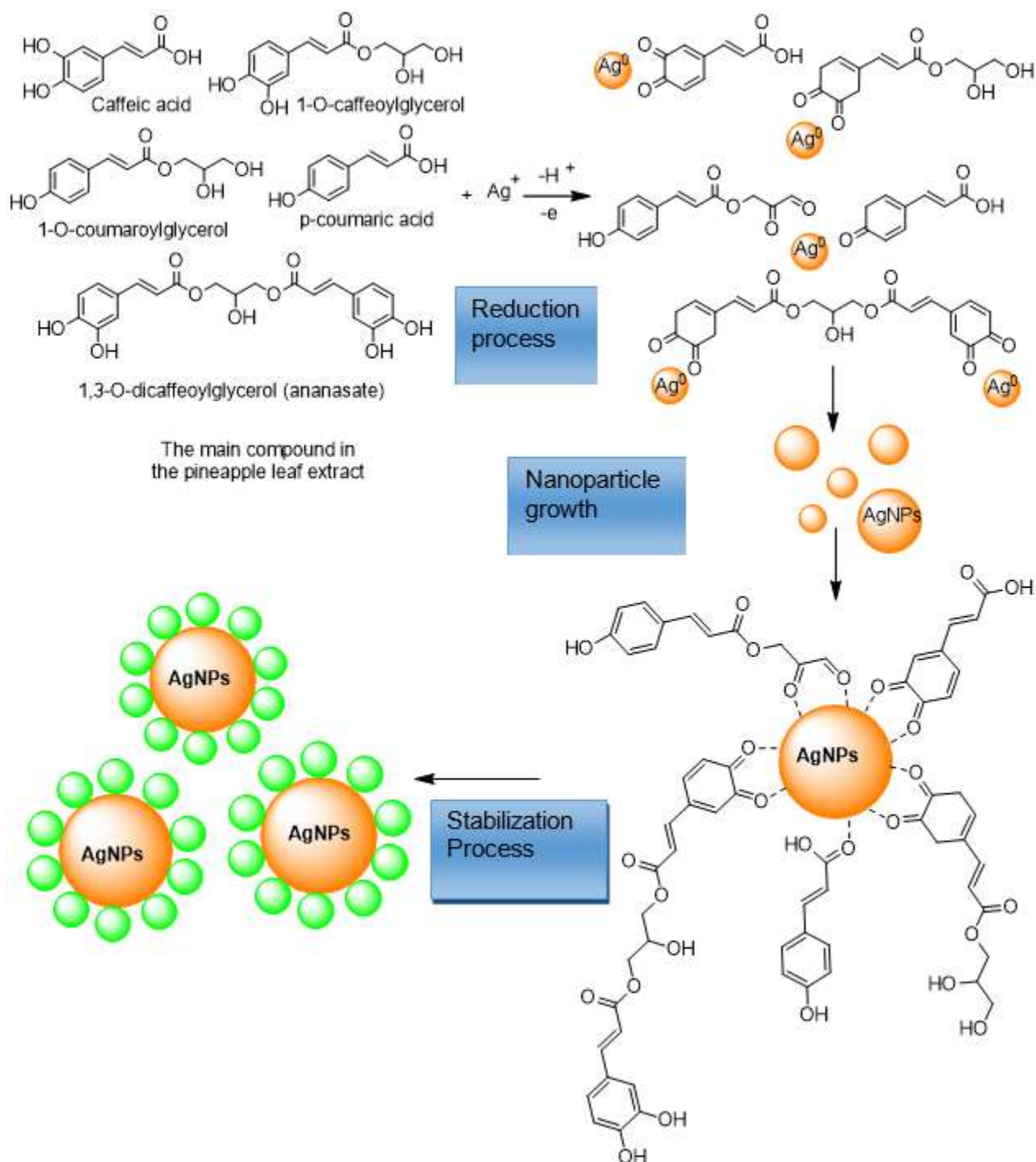


**Fig 1.** Illustration of silver nanoparticle formation and stabilization by the phytochemical compounds in the pineapple leaf extract

Table 1 shown that heat treatment and stirring time also affect the particle size and distribution of nanoparticles [41]. For AgNPs 1 mM, the variation of stirring time of 4, 8, 16, and 24 h affected the percentage,

mean, and median values of AgNPs. At 16 and 24 h, the nanoparticle formation percentages were 99.5% and 99.8%. The smallest mean and median values were obtained during the stirring process for 24 h. At the

higher AgNPs concentrations (2 and 3 mM), the longer stirring times of 28 and 30 h were required for AgNPs formation. The histogram of the particle size distribution is shown in Fig. 3.

### Stability of Particle Size Distribution of AgNPs Solution

The stability of AgNPs in the solution was determined by measuring changes in particle size with different storage times. The stabilities of the AgNPs in the leaf extract lasted in 7 days. At the storage time of 9, 14, 21, and 30 days, the particle sizes of AgNPs became more than 100 nm. The increase of nanoparticle sizes in solution, influenced by pH, ionic strength, the formation of Ag<sub>2</sub>O, and electrolyte type [42]. In the synthesis of nanoparticles using leaf extracts, a longer storage time will increase the amount of Ag<sup>+</sup> species. The Ag<sup>+</sup> ion released then forms a black precipitate which is most likely Ag<sub>2</sub>O.

This can be seen from the darker color of the solution and the formation of black deposits in the AgNPs solution

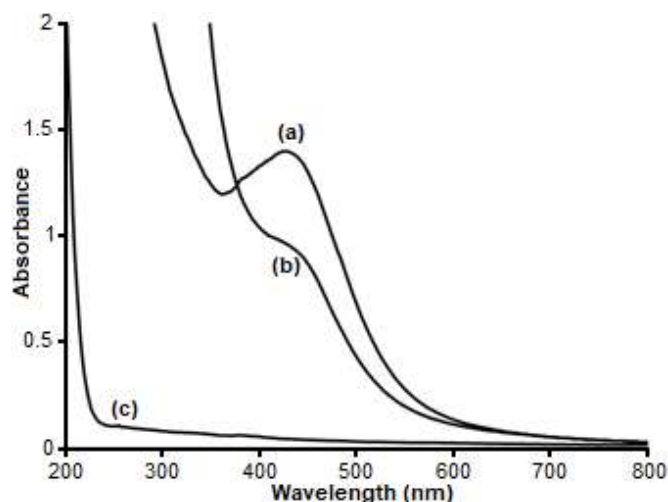


**Fig 2.** UV-Visible spectra of: (a) AgNPs, (b) Pineapple leaf extract, (c) AgNO<sub>3</sub> solution

**Table 1.** The particle size distribution of silver nanoparticle in variation AgNO<sub>3</sub> concentration and stirring time

[AgNO <sub>3</sub> ] (mM)	T (°C)	Total stirring time (h)	Particle size (nm)	%	Mean (nm)	Median (nm)
1	70	4	< 100	89.1	350	50
			101–200	7.2		
			> 300	3.7		
1	70	8	< 100	93.4	300	30
			101–200	4.3		
			> 300	2.3		
1	70	16	< 100	99.5	100	20
			101–200	0.2		
			> 300	0.3		
1	70	24	< 100	99.8	30	20
			101–200	0.2		
			300	0		
2	70	4	< 100	83.6	92	50
			101–200	9.0		
			>300	7.4		
2	70	28	< 100	98.3	70	30
			101–200	1.1		
			> 300	0.6		
3	70	4	< 100	0.3	11730	641
			101–200	17.8		
			> 300	81.9		
3	70	30	< 100	99.4	50	20
			101–200	0.4		
			> 300	0.2		

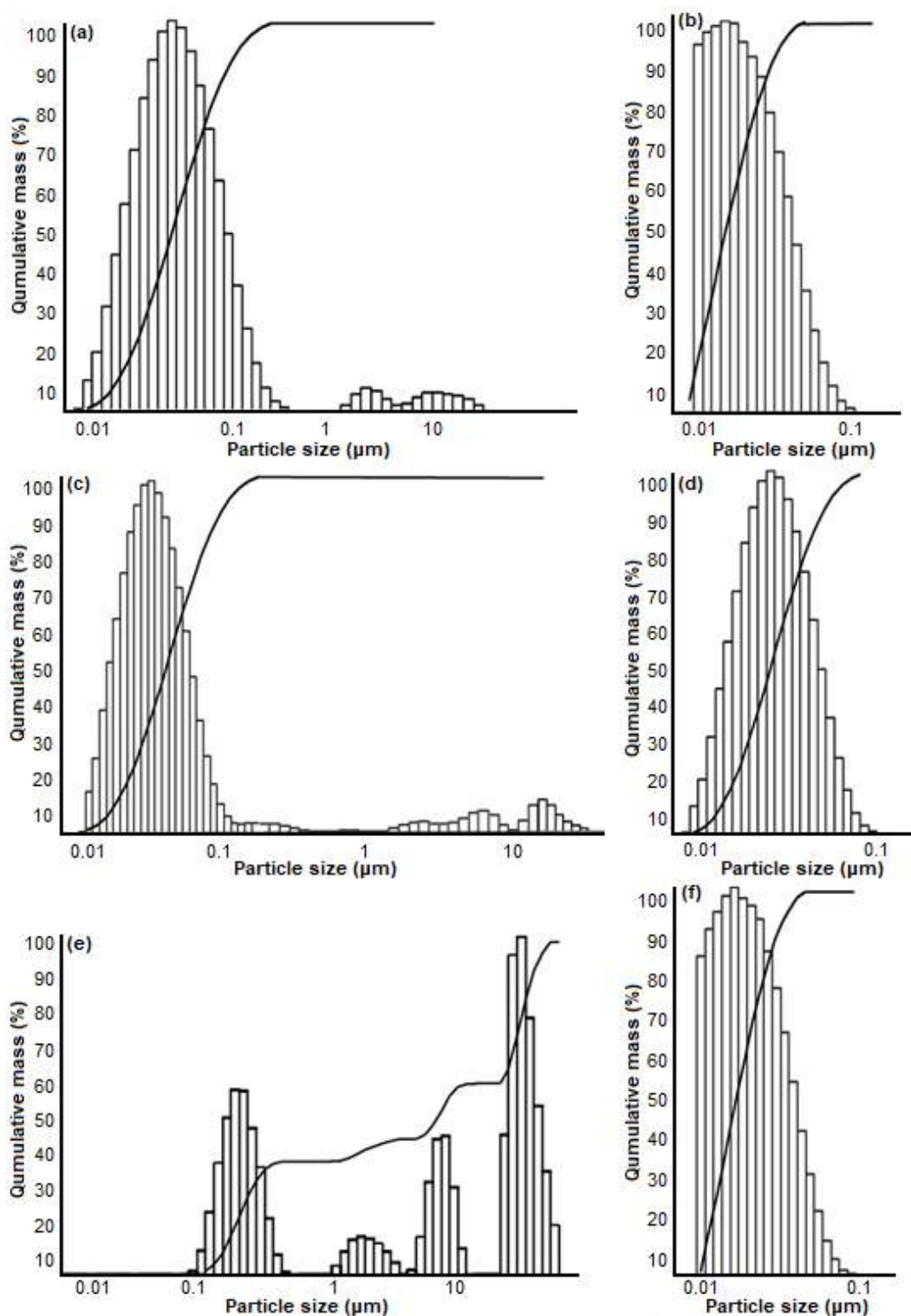


**Fig 3.** Histogram of the particle size distribution in (a) 1 mM AgNPs, stirred for 4 h and (b) 24 h, (c) 2 mM AgNPs, stirred for 4 h and (d) 28 h, (e) 3 mM AgNPs, stirred for 4 h and (f) 30 h

stored for more than 7 days. The formation of  $\text{Ag}_2\text{O}$  increases the particle sizes of nanoparticles [43]. The

formation of the darker color of the solution is shown in Fig. 4. The particle size distribution of the AgNPs 1 mM

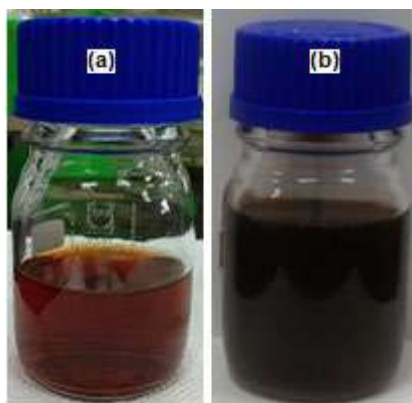


Fig 4. AgNPs solution after (a) 24 h and (b) 30 days

with variations in storage time is shown in Table 2 and Fig. 5.

#### FTIR Spectroscopy for AgNPs

Fig. 6. exhibits FTIR spectra of pineapple leaf extract (a) shows the broad peak at  $3369\text{ cm}^{-1}$  could be assigned to O–H stretch, while the peaks at  $2972$ ,  $1375$ , and  $1218\text{ cm}^{-1}$  could be attributed to C–H stretching vibration. The peak at  $1375$  and  $1218\text{ cm}^{-1}$  could be identified as –C–O single bond absorption. The adsorption band at  $1722$  and  $1641\text{ cm}^{-1}$  could be identified as –C=O carbonyl and –C=C stretching of the cyclic aromatic ring. These peaks

correspond to the functional groups of five major compounds found in the pineapple leaf extract. Fig. 6(b) showed the spectra of the AgNPs. The shift in wavenumbers for the functional groups –OH, –C=O and the increase in the –C–O groups transmittance because these functional groups affect the reduction and stabilization processes in forming AgNPs. The presence of the AgNPs influenced the additional peaks at  $1596$ ,  $1039$ , and  $770\text{ cm}^{-1}$  [44-46]. A few characteristic peaks of pineapple leaf extract were exhibited in AgNPs. The work observed that AgNPs still contain organic material from pineapple leaf extract.

#### Silver Nanoparticles Loaded on Diatomite (AgNPs-D)

An adsorption process carried out the loaded process of AgNPs into the diatomite pore. Diatomite was heated at  $400\text{ }^{\circ}\text{C}$  for 2 h to maximize the adsorption of AgNPs. According to research by Shih et al. (2020), the heating process to diatomite waste at  $400\text{ }^{\circ}\text{C}$  increases the surface area and pore volume [47]. The percentage of AgNPs loaded into the diatomite pore was measured using a gravimetric technique. The technique is based on the weighing process before and after adsorption to determine

Table 2. The particle size of 1 mM of AgNPs in the storage time variation

No.	Storage time (day)	Particle size (nm)	%	Mean	Median
1	3	< 100	99.8	30.0 nm	20.0 nm
		101–200	0.2		
		> 100	-		
2	7	< 100	99.8	30.0 nm	20.0 nm
		101–200	0.2		
		> 100	-		
3	9	< 100	-	5.36 $\mu\text{m}$	5.34 $\mu\text{m}$
		101–200	-		
		> 100	100		
4	14	< 100	-	377.4 $\mu\text{m}$	373.4 $\mu\text{m}$
		101–200	-		
		> 100	100		
5	21	< 100	-	534.3 $\mu\text{m}$	532.5 $\mu\text{m}$
		101–200	-		
		> 100	100		
6	30	< 100	-	754.8 $\mu\text{m}$	746.69 $\mu\text{m}$
		101–200	-		
		> 100	100		

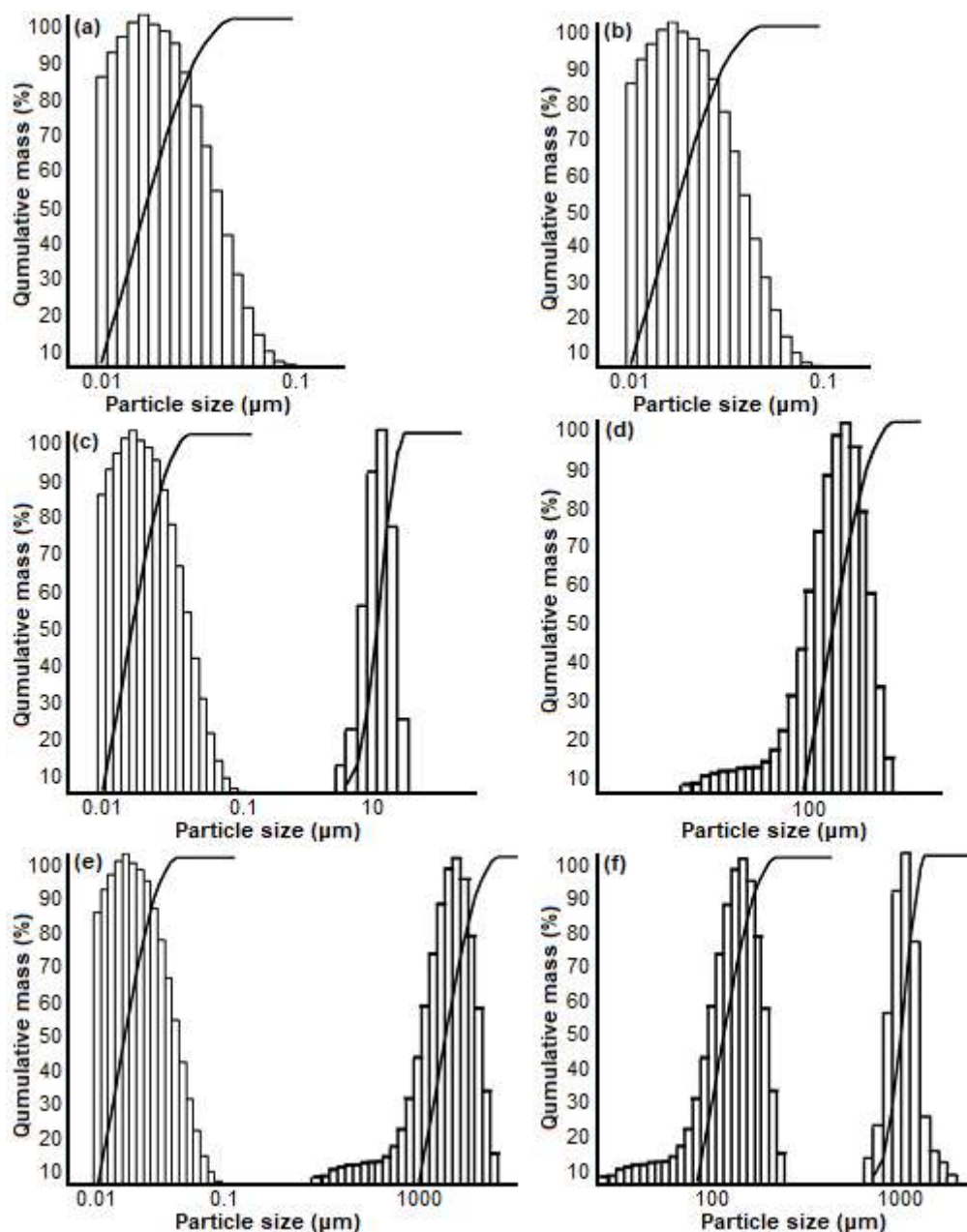


**Fig 5.** Histogram of the particle size distribution of 1 mM AgNPs stored for (a) 3, (b) 7, (c) 9, (d) 14, (e) 21, and (f) 30 days

the amount of AgNPs loaded into the diatomite pores.

In this study, as much as 1 wt.% of silver nanoparticles were loaded into the diatomite pores. Based on the gravimetric analysis, the initial weight of diatomite ( $w_0$ ) was 0.8692 g. The adsorption of AgNPs into diatomite pores produces AgNPs-D. The AgNPs-D composite was then dried and heated at 200 °C. The drying and heating process of AgNPs-D composites

resulted in the final weight ( $w_f$ ) = 0.8792 g. The weight increased of AgNPs-D was 1 wt.%, indicating that 1% of AgNPs was successfully loaded in the diatomite pores. The loading of AgNPs into the diatomite pores was also evidenced by the change in the diatomite color from white to reddish-brown (the characteristic color of AgNPs), as shown in Fig. 7. FTIR spectra of diatomite and AgNPs-D are demonstrated in Fig.8.

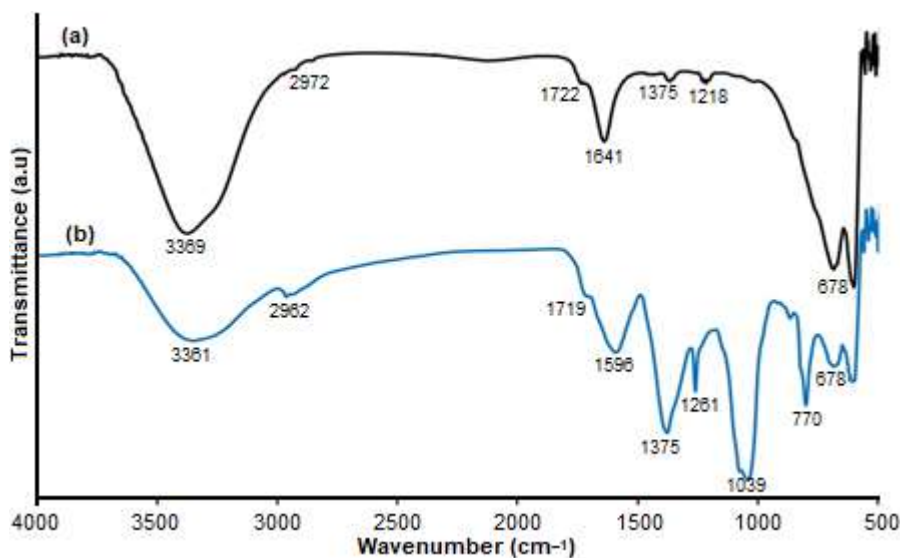


Fig 6. FTIR spectra of (a) pineapple leaf extract and (b) AgNPs

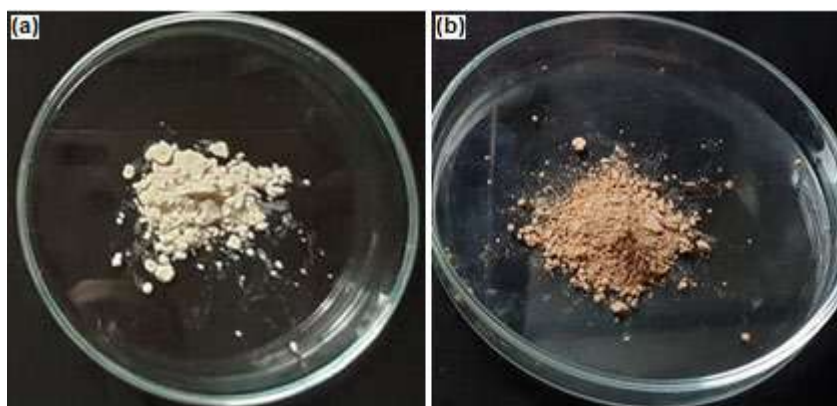


Fig 7. (a) Diatomite, (b) AgNPs-D composite

Fig. 8(b) shows the FTIR spectra for AgNPs-D. The characteristic peaks indicated the loaded AgNPs into the diatomite pores are observed at 1740 and 1366  $\text{cm}^{-1}$ , attributable to the  $\text{-C=O}$  groups and  $\text{C-H}$  stretching vibration. This absorption indicates that the AgNPs loaded into the diatomite pores still contain organic compounds from pineapple leaf extract. The wavenumber shifts for the  $\text{Si-O-Si}$  and  $\text{Si-O}$  groups from 1088 to 1090  $\text{cm}^{-1}$  and 803 to 799  $\text{cm}^{-1}$  caused by the entry of AgNPs into the diatomite pores.

#### Thermal Analysis of Diatomite and AgNPs-D

Diatomite is a potential filler to enhance the thermal properties of the composite material. Thermal analysis (TGA) was performed to determine the effect of AgNPs

on the thermal resistance of AgNPs-D. TGA thermogram of D and AgNPs-D are shown in Fig. 9. The remaining material measured by thermal analysis for D and AgNPs-D were 98.22 and 95.74%, respectively. The organic compounds in AgNPs cause the remaining material to be reduced compared to D. The insertion of AgNPs to D was successfully proved by the organic compound found in AgNPs-D. In D and AgNPs-D material, weight loss occurs in the range of 100–580  $^{\circ}\text{C}$ . At a temperature of 100–200  $^{\circ}\text{C}$ , the decrease in weight due to the loss of water molecules. In the next phase, the reduction in the weight percentage of D and AgNPs-D occurred at temperatures of 141–430  $^{\circ}\text{C}$  and 142–450  $^{\circ}\text{C}$ . The decrease was caused by the decomposition of organic matter. Based on Kristl (2015), organic matter

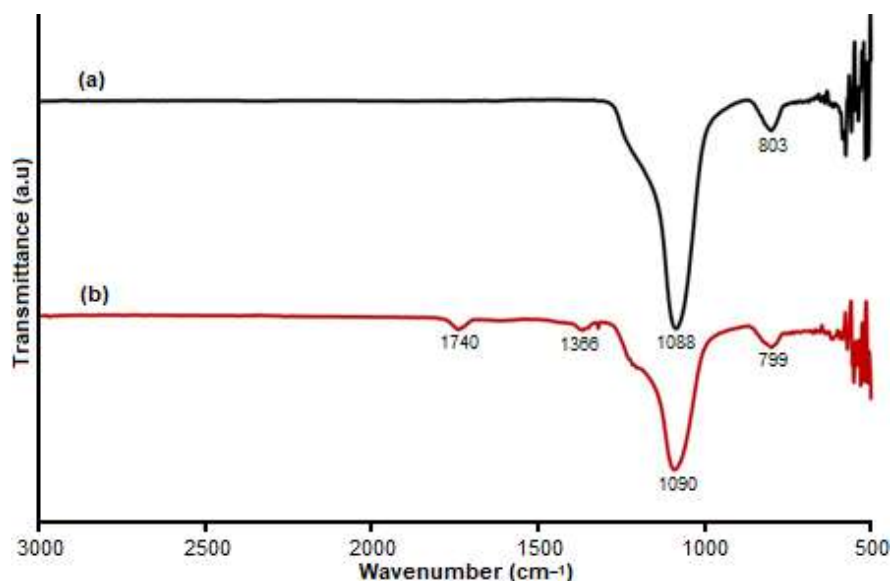


Fig 8. FTIR spectra of (a) Diatomite and (b) AgNPs-D

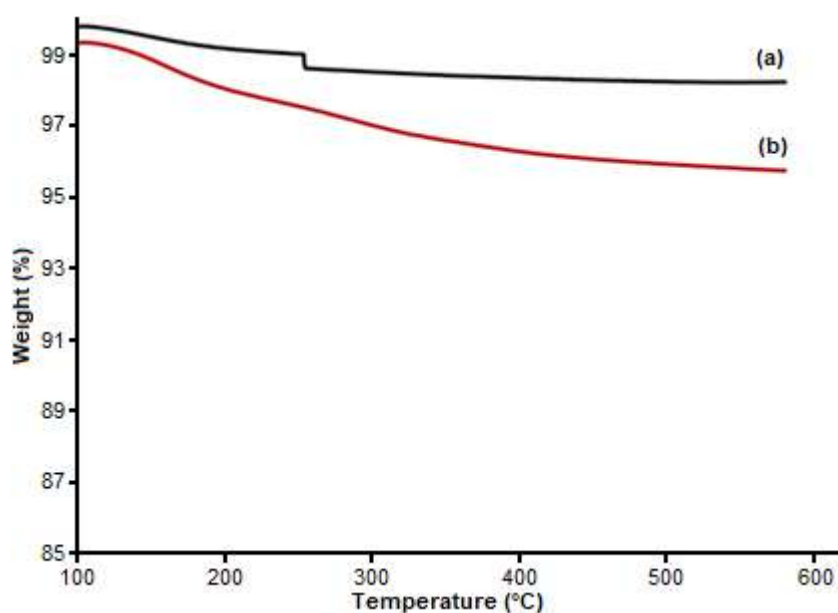


Fig 9. TGA Thermogram of (a) D, (b) AgNPs-D

decomposition will begin at a temperature of 180–450 °C [48]. Besides, the weight loss percentage is not caused by the breakdown of diatomites minerals because the process takes place at temperatures above 650 °C [49].

## ■ CONCLUSION

Research has been conducted on developing a green method to prepare AgNPs from pineapple leaf extract loaded on diatomite pores. The results showed that the pineapple leaf extract plays an essential role in converting

the 99.8% AgNO<sub>3</sub> solution into AgNPs. The size distribution of the AgNPs was affected by the temperature and the total stirring time. The smallest mean and median values for AgNPs 1 mM were 30 and 20 nm, obtained after the stirring time for 24 h. The stability of the AgNPs solution lasts for seven days. The particle size was more than 100 nm after seven days of storage. After one month of storage, the particle size was recorded as 754.8 μm (mean) and 746.69 μm (median). The successful loading of AgNPs into D exhibited by

gravimetric techniques, as much as 1 wt.% of AgNPs, was loaded into diatomite pores. The diatomite changes color to reddish-brown. The appearance of the peak for  $\text{-C=O}$  and  $\text{-C-O-}$  groups at 1719 and  $1375\text{ cm}^{-1}$  indicates that AgNPs still contain organic compounds from pineapple leaf extract. The TGA analysis showed that the residual material D and AgNPs-D were 98.22% and 95.74% at  $580\text{ }^\circ\text{C}$ . The AgNPs loaded to diatomite pores will improve the performance of the material as an antibacterial agent. The properties will expand the applications of AgNPs-D composites in the biomedical and industrial fields.

### ■ AUTHOR CONTRIBUTIONS

Conceptualization of the presented idea, S. Hamdiani (Sapri Hamdiani) and Y.F. Shih (Yeng-Fong Shih); methodology, S. Hamdiani, and Y.F. Shih; fabricated the sample and data curation, S. Hamdiani; writing—original draft preparation, S. Hamdiani, and Y.F. Shih; writing—review and editing, S. Hamdiani and Y.F. Shih. All authors have read and agreed to the published version of the manuscript.

### ■ REFERENCES

- [1] Lutyński, M., Sakiewicz, P., and Lutyńska, S., 2019, Characterization of diatomaceous earth and halloysite resources of Poland, *Minerals*, 9 (11), 670.
- [2] Pookmanee, P., Wannawek, A., Satienperakul, S., Putharod, R., Laorodphan, N., Sangsrichan, S., and Phanichphant, S., 2016, Characterization of diatomite, leonardite and pumice, *Mater. Sci. Forum*, 872, 211–215.
- [3] Galán-Arboledas, R.J., Cotes-Palomino, M.T., Bueno, S., and Martínez-García, C., 2017, Evaluation of spent diatomite incorporation in clay based materials for lightweight bricks processing, *Constr. Build. Mater.*, 144, 327–337.
- [4] Yu, H., Li, C., Zhang, K., Tang, Y., Song, Y., and Wang, M., 2020, Preparation and thermophysical performance of diatomite-based composite PCM wallboard for thermal energy storage in buildings, *J. Build. Eng.*, 32, 101753.
- [5] Tramontano, C., Chianese, G., Terracciano, M., de Stefano, L., and Rea, I., 2020, Nanostructured biosilica of diatoms: From water world to biomedical applications, *Appl. Sci.*, 10 (19), 6811.
- [6] Xia, K., Liu, X., Chen, Z., Fang, L., Du, H., and Zhang, X., 2020, Efficient and sustainable treatment of anionic dye wastewaters using porous cationic diatomite, *J. Taiwan Inst. Chem. Eng.*, 113, 8–15.
- [7] Xu, H., Wang, J., and Ren, S., 2019, Removal of oil from a crude oil-in-water emulsion by a magnetically recyclable diatomite demulsifier, *Energy Fuels*, 33 (11), 11574–11583.
- [8] Kong, X., Yu, Q., Li, E., Wang, R., Liu, Q., and Wang, A.X., 2018, Diatomite photonic crystals for facile on-chip chromatography and sensing of harmful ingredients from food, *Materials*, 11 (4), 539.
- [9] Li, C., Wang, M., Xie, B., Ma, H., and Chen, J., 2020, Enhanced properties of diatomite-based composite phase change materials for thermal energy storage, *Renewable Energy*, 147, 265–274.
- [10] Zhao, Y., Tian, G., Duan, X., Liang, X., Meng, J., and Liang, J., 2019, Environmental applications of diatomite minerals in removing heavy metals from water, *Ind. Eng. Chem. Res.*, 58 (27), 11638–11652.
- [11] Janićijević, J., Krajišnik, D., Čalića, B., Vasiljević, B.N., Dobričić, V., Daković, A., Antonijević, M.D., and Milić, J., 2015, Modified local diatomite as potential functional drug carrier—A model study for diclofenac sodium, *Int. J. Pharm.*, 496 (2), 466–474.
- [12] Shen, Z., Fan, Q., Yu, Q., Wang, R., Wang, H., and Kong, X., 2021, Facile detection of carbendazim in food using TLC-SERS on diatomite thin layer chromatography, *Spectrochim. Acta, Part A*, 247, 119037.
- [13] Tamburaci, S., Kimna, C., and Tihminlioglu, F., 2019, Bioactive diatomite and POSS silica cage reinforced chitosan/Na-carboxymethyl cellulose polyelectrolyte scaffolds for hard tissue regeneration, *Mater. Sci. Eng., C*, 100, 196–208.
- [14] Mustafiov, S.D., Sen, F., and Seydibeyoglu, M.O., 2020, Preparation and characterization of diatomite and hydroxyapatite reinforced porous polyurethane foam biocomposites, *Sci. Rep.*, 10 (1), 13308.
- [15] Tamburaci, S., and Tihminlioglu, F., 2017, Diatomite reinforced chitosan composite



- membrane as potential scaffold for guided bone regeneration, *Mater. Sci. Eng., C*, 80, 222–231.
- [16] Novembre, D., Gimeno, D., and Poe, B., 2019, Synthesis and characterization of leucite using a diatomite precursor, *Sci. Rep.*, 9 (1), 10051.
- [17] Susanthi, D., Santosa, S.J., and Kunarti, E.S., 2020, Antibacterial activity of silver nanoparticles capped by *p*-aminobenzoic acid on *Escherichia coli* and *Staphylococcus aureus*, *Indones. J. Chem.*, 20 (1), 182–189.
- [18] Akinsiku, A.A., Adekoya, J.A., and Dare, E.O., 2021, *Nicotiana tabacum* mediated green synthesis of silver nanoparticles and Ag-Ni nanohybrid: Optical and antimicrobial efficiency, *Indones. J. Chem.*, 21 (1), 179–191.
- [19] Uddin, A.K.M.R., Siddique, M.A.B., Rahman, F., Ullah, A.K.M.A., and Khan, R., 2020, *Cocos nucifera* leaf extract mediated green synthesis of silver nanoparticles for enhanced antibacterial activity, *J. Inorg. Organomet. Polym Mater.*, 30 (9), 3305–3316.
- [20] Chen, J.X., Zhu, J.Q., Luo, S.Y., and Zhong, X.Y., 2020, A green method to the preparation of the silver-loaded diatomite with enhanced antibacterial properties, *Chem. Pap.*, 74 (3), 859–866.
- [21] Qi, X., Chen, J., Li, Q., Yang, H., Jiang, H., Deng, Y., Song, Q., and Liang, T., 2020, Antibacterial silver-diatomite nanocomposite ceramic with low silver release, *Water Supply*, 20 (2), 633–643.
- [22] Gao, L., Wang, L., Yang, L., Zhao, Y., Shi, N., An, C., Sun, Y., Xie, J., Wang, H., Song, Y., and Ren, Y., 2019, Preparation, characterization and antibacterial activity of silver nanoparticle/graphene oxide/diatomite composite, *Appl. Surf. Sci.*, 484, 628–636.
- [23] Kubasheva, Z., Sprynskyy, M., Railean-Plugaru, V., Pomastowski, P., Ospanova, A., and Buszewski, B., 2020, Synthesis and antibacterial activity of (AgCl, Ag)NPs/diatomite hybrid composite, *Materials*, 13 (15), 3409.
- [24] Sherief, M.A., El-Bassyouni, G.T., Gamal, A.A., and Esawy, M.A., 2021, Modification of diatom using silver nanoparticle to improve antimicrobial activity, *Mater. Today: Proc.*, 43, 3369–3374.
- [25] Sun, H., Wen, X., Zhang, X., Wei, D., Yang, H., Li, C., and Yang, L., 2018, Biocompatible silver nanoparticle-modified natural diatomite with anti-infective property, *J. Nanomater.*, 2018, 7815810.
- [26] Nilavukkarasi, M., Vijayakumar, S., and Kumar, S.P., 2020, Biological synthesis and characterization of silver nanoparticles with *Capparis zeylanica* L. leaf extract for potent antimicrobial and anti proliferation efficiency, *Mater. Sci. Energy Technol.*, 3, 371–376.
- [27] Thirumagal, N., and Jeyakumari, A.P., 2020, Structural, optical and antibacterial properties of green synthesized silver nanoparticles (AgNPs) using *Justicia adhatoda* L. leaf extract, *J. Cluster Sci.*, 31 (2), 487–497.
- [28] Shih, Y.F., Chou, M.Y., Chang, W.C., Lian, H.Y., and Chen, C.M., 2017, Completely biodegradable composites reinforced by the cellulose nanofibers of pineapple leaves modified by eco-friendly methods, *J. Polym. Res.*, 24 (11), 209.
- [29] Alsultani, A.M., 2017, *Conocarpus erectus* leaf extract for green synthesis of silver nanoparticles, *Indones. J. Chem.*, 17 (3), 407–414.
- [30] Emeka, E.E., Ojiefoh, O.C., Aleruchi, C., Hassan, L.A., Christiana, O.M., Rebecca, M., Dare, E.O., and Temitope, A.E., 2014, Evaluation of antibacterial activities of silver nanoparticles green-synthesized using pineapple leaf (*Ananas comosus*), *Micron*, 57, 1–5.
- [31] Hartati, R., Suarantika, F., and Fidrianny, I., 2020, Overview of phytochemical compounds and pharmacological activities of *Ananas Comosus* L., *Merr., Int. J. Res. Pharm. Sci.*, 11 (3), 4760–4766.
- [32] Miftiyati, S.D., Hamdiani, S., and Darmayanti, M.G., 2018, Synthesis of paramagnetic merkpto silica hybrid from rice husk ash for Ag(I) adsorbent, *Acta Chim. Asiana*, 1 (2), 30–36.
- [33] Justine, V.T., Mustafa, M., Kankara, S.S., and Go, R., 2019, Effect of drying methods and extraction solvents on phenolic antioxidants and antioxidant activity of *Scurrula ferruginea* (Jack) Danser (Loranthaceae) leaf extracts, *Sains Malays.*, 48 (7), 1383–1393.

- [34] Ma, C., Xiao, S., Li, Z., Wang, W., and Du, L., 2007, Characterization of active phenolic components in the ethanolic extract of *Ananas comosus* L. leaves using high-performance liquid chromatography with diode array detection and tandem mass spectrometry, *J. Chromatogr. A*, 1165 (1-2), 39–44.
- [35] Xie, W., Wang, W., Su, H., Xing, D., Cai, G., and Du, L., 2007, Hypolipidemic mechanisms of *Ananas comosus* L. leaves in mice: Different from fibrates but similar to statins, *J. Pharmacol. Sci.*, 103 (3), 267–274.
- [36] Wang, W., Ding, Y., Xing, D.M., Wang, J.P., and Du, L.J., 2006, Studies on phenolic constituents from leaves of pineapple (*Ananas comosus*), *China J. Chin. Mater. Med.*, 31 (15), 1242–1244.
- [37] Aritonang, H.F., Koleangan, H., and Wuntu, A.D., 2019, Synthesis of silver nanoparticles using aqueous extract of medicinal plants' (*Impatiens balsamina* and *Lantana camara*) fresh leaves and analysis of antimicrobial activity, *Int. J. Microbiol.*, 2019, 8642303.
- [38] Gomes, J.F., Garcia, A.C., Ferreira, E.B., Pires, C., Oliveira, V.L., Tremiliosi-Filho, G., and Gasparotto, L.H.S., 2015, New insights into the formation mechanism of Ag, Au, and AgAu nanoparticles in aqueous alkaline media: Alkoxides from alcohols, aldehydes, and ketones as universal reducing agents, *Phys. Chem. Chem. Phys.*, 17 (33), 21683–21693.
- [39] Nayak, D., Ashe, S., Rauta, P.R., Kumari, M., and Nayak, B., 2016, Bark extract mediated green synthesis of silver nanoparticles: Evaluation of antimicrobial activity and antiproliferative response against osteosarcoma, *Mater. Sci. Eng., C*, 58, 44–52.
- [40] Balavandy, S.K., Shameli, K., Biak, D.R.A., and Abidin, Z.Z., 2014, Stirring time effect of silver nanoparticles prepared in glutathione mediated by green method, *Chem. Cent. J.*, 8 (1), 11.
- [41] Liu, H., Zhang, H., Wang, J., and Wei, J., 2020, Effect of temperature on the size of biosynthesized silver nanoparticle: Deep insight into microscopic kinetics analysis, *Arabian J. Chem.*, 13 (1), 1011–1019.
- [42] Bélteky, P., Rónavári, A., Igaz, N., Szerencsés, B., Tóth, I.Y., Pfeiffer, I., Kiricsi, M., and Kónya, Z., 2019, Silver nanoparticles: Aggregation behavior in biorelevant conditions and its impact on biological activity, *Int. J. Nanomed.*, 14, 667–687.
- [43] Izak-Nau, E., Huk, A., Reidy, B., Uggerud, H., Vadset, M., Eiden, S., Voetz, M., Himly, M., Duschl, A., Dusinska, M., and Lynch, I., 2015, Impact of storage conditions and storage time on silver nanoparticles' physicochemical properties and implications for their biological effects, *RSC Adv.*, 5 (102), 84172–84185.
- [44] Halawani, E.M., 2017, Rapid biosynthesis method and characterization of silver nanoparticles using *Zizyphus spina christi* leaf extract and their antibacterial efficacy in therapeutic application, *J. Biomater. Nanobiotechnol.*, 08, 22–35.
- [45] Das, G., Patra, J.K., Debnath, T., Ansari, A., and Shin, H.S., 2019, Investigation of antioxidant, antibacterial, antidiabetic, and cytotoxicity potential of silver nanoparticles synthesized using the outer peel extract of *Ananas comosus* (L.), *PLoS One*, 14 (8), e0220950.
- [46] Poadang, S., Yongvanich, N., and Phongtongpasuk, S., 2017, Synthesis, characterization, and antibacterial properties of silver nanoparticles prepared from aqueous peel extract of pineapple, *Ananas comosus*, *Chiang Mai Univ. J. Nat. Sci.*, 16 (2), 123–133.
- [47] Shih, Y.F., Wang, C.H., Tsai, M.L., and Jehng, J.M., 2020, Shape-stabilized phase change material/nylon composite based on recycled diatomite, *Mater. Chem. Phys.*, 242, 122498.
- [48] Kristl, M., Muršec, M., Šuštar, V., and Kristl, J., 2016, Application of thermogravimetric analysis for the evaluation of organic and inorganic carbon contents in agricultural soils, *J. Therm. Anal. Calorim.*, 123 (3), 2139–2147.
- [49] Ibrahim, S.S., and Selim, A.Q., 2012, Heat treatment of natural diatomite, *Physicochem. Probl. Miner. Process.*, 48 (2), 413–424.

**Short Communication:****Data Fusion of UV-Vis and FTIR Spectra Combined with Principal Component Analysis for Distinguishing of *Andrographis paniculata* Extracts Based on Cultivation Ages and Solvent Extraction**

Antonio Kautsar<sup>1,2</sup>, Wulan Tri Wahyuni<sup>1,2</sup>, Utami Dyah Syafitri<sup>3</sup>, Syifa Muflihah<sup>1</sup>, Nursifa Mawadah<sup>1</sup>, Eti Rohaeti<sup>1</sup>, Zulhan Arif<sup>1</sup>, Bambang Prajogo<sup>4</sup>, Muhammad Bachri Amran<sup>5</sup>, Abdul Rohman<sup>6</sup>, and Mohamad Rafi<sup>1,2\*</sup>

<sup>1</sup>Department of Chemistry, Faculty of Mathematics and Natural Sciences, IPB University, Jl. Tanjung Kampus IPB Dramaga, Bogor 16680, Indonesia

<sup>2</sup>Tropical Biopharmaca Research Center- Institute of Research and Community Services, IPB University, Jl. Taman Kencana No. 3 Kampus IPB Taman Kencana, Bogor 16128, Indonesia

<sup>3</sup>Department of Statistics, Faculty of Mathematics and Natural Sciences, IPB University, Jl. Meranti Kampus IPB Dramaga, Bogor 16680, Indonesia

<sup>4</sup>Department of Pharmacognosy and Phytochemistry, Faculty of Pharmacy, Universitas Airlangga, Jl. Mulyorejo Kampus C Unair, Surabaya 60286, Indonesia

<sup>5</sup>Analytical Chemistry Research Group, Institut Teknologi Bandung, Jl. Ganesha No. 10, Bandung 40132, Indonesia

<sup>6</sup>Department of Pharmaceutical Chemistry Faculty of Pharmacy, Universitas Gadjah Mada, Sekip Utara, Yogyakarta 55281, Indonesia

**\* Corresponding author:**

email: mra@apps.ipb.ac.id

Received: October 3, 2020

Accepted: March 15, 2021

DOI: 10.22146/ijc.60321

**Abstract:** *Andrographis paniculata* is one of the medicinal plants used for the treatment of antidiabetic. Cultivation ages and solvent extraction affected metabolites' composition and concentration that directly cause the plant's efficacies. This research aimed to distinguish *A. paniculata* based on cultivation ages and solvent extraction using data fusion of UV-Vis and FTIR spectra combined with principal component analysis (PCA). *A. paniculata* with 2, 3, and 4 months post-planting were extracted by water, 50% ethanol, 70% ethanol, and ethanol. In each extract, we measured UV-Vis and FTIR spectra. Then, we used the data fusion from both spectra. We used UV-Vis and FTIR absorbance from 200–400 nm and 1800–400 cm<sup>-1</sup>, respectively. Each extract gives a similar pattern of UV-Vis and FTIR spectra, only differ in their intensities. PCA score plot in two and three-dimensional showed *A. paniculata* extracts could be distinguished based on cultivation ages and solvent extraction with a total variance of 86 and 92%, respectively. Furthermore, this study confirms the data fusion of UV-Vis and FTIR spectra could distinguished *A. paniculata* extracts combined with chemometrics based on cultivation ages and solvent extraction.

**Keywords:** *A. paniculata*; data fusion; FTIR; UV-Vis; PCA

**■ INTRODUCTION**

*Andrographis paniculata* is a medicinal plant commonly found in South and Southeast Asian countries such as Indonesia, India, Malaysia, Pakistan, and Sri

Lanka [1]. In Indonesia, it is known as *sambiloto*. *A. paniculata* is mostly used as a traditional medicine in some countries. It has several biological activities, such as antibacterial, antimalarial, antipyretic, anti-

inflammatory, and antidiabetic [2-4]. It is well known that bioactive compounds from medicinal plants are responsible for their biological activity. The main compounds in *A. paniculata* are included in the diterpene lactone class, such as andrographolide, neoandrographolide, and 14-deoxyandrographolide [5]. Yusuf et al. [6] reported that *A. paniculata* has a different accumulation of active components in the early generative stages. The highest andrographolide content is in the leaves, while the smallest content is in the seeds. Biological activities in plants are influenced by several factors, such as growing conditions, cultivation ages, and post-harvest processes [7]. Furthermore, the type and concentration of extracting solvents can affect the extracted metabolite's composition and concentration [8].

Data fusion is a new branch in chemometrics analysis. It has been widely used in recent years because it can combine several different analytical techniques to improve the quality and quantity of information obtained [9]. The resulting data has a large dimension and matrix of several instruments used, so it requires a combination of multivariate analysis in understanding the data as a whole. In general, data fusion is divided into three levels: low, medium, and high. Low-level data fusion consists of a series of simple data with different origins, while medium-level data fusion is a combination of data extracted from original data with data reduction. High-level data fusion is built from several data fusion models separately in each data, and then the model produces a final fusion of the data. Data fusion has been widely used in food analysis, bioinformatics, soil mapping, business, herbal medicine, etc. [10].

FTIR and UV-Vis spectroscopies have been widely used for quality control in food and herbal medicinal products because of their advantages, such as fast, cheap, and easy. FTIR provides spectrum information of functional groups with different and complex fingerprint patterns. UV-Vis produces a spectrum with visual parameters from the variation of UV-Vis light absorption in the sample but has limitations for characterization and authentication [11]. The combination of FTIR and UV-Vis can produce information that is more accurate and

useful in interpreting data than it is used separately in multivariate analysis.

Application of data fusion has been extensively used in improving the quality of herbal medicines with a lot of data fusion research that leads to the discrimination of origin and types of medicinal plants. There are several papers that have reported using data fusion of UV-Vis and FTIR spectra, such as discrimination of porcini mushrooms [12], traceability of Boletaceae mushrooms [13], differentiation and comparison of *Wolfiporia cocos* raw materials [14], discrimination of wild *Paris Polyphylla* Smith var. *yunnanensis* [15], discrimination of species in Ganodermataceae mushrooms [16], and geographical traceability of *Eucommia ulmoides* leaves [17]. However, improving herbal medicines' quality at the specific age of harvest and solvent extraction for *A. paniculata* is still limited. This study aims to distinguish *A. paniculata* with differences in harvest age and solvent extraction using UV-Vis and FTIR spectra fusion data combined with multivariate analysis, such as principal component analysis.

## ■ EXPERIMENTAL SECTION

### Materials

*A. paniculata* was collected as 2, 3, 4-month post-planting (MPP) from *Pusat Studi Biofarmaka Tropika* medicinal plant garden (IPB University, Bogor, Indonesia) in 2019. Ethanol p.a. (Merck, Darmstadt Germany), potassium bromide spectroscopy grade (Sigma Aldrich, Missouri, USA), Whatman filter paper No.40 (Merck, Darmstadt, Germany) and distilled water (Hydro, Jakarta, Indonesia) was used in this work.

### Instrumentation

Rotary evaporator-114 (Buchi, Flawil, Switzerland) was used for the evaporation of solvent extraction, and freeze-dryer ALPHA 1-2 LDPlus (Christ, Osterodeam Harz, Germany) was used for drying the extract. UV-Vis spectra were performed in UV-Vis spectrophotometer U-2000 (Hitachi, Tokyo, Japan). FTIR spectra were measured in Bruker Tensor 37 FTIR spectrophotometer (Bruker Optik GmbH, Karlsruhe, Germany).

## Procedure

### Sample preparation and extraction

Samples were sorted then cleaned by washing with water. Afterward, samples were dried and pulverized into a powder. About 2.5 g of powder was added to 25 mL of extraction solvent then sonicated for 30 min at room temperature. The solvents used for extraction were water, and 50% ethanol, 70% ethanol, and ethanol p.a. with four replication. The filtrate was collected, then concentrated by rotary evaporator R-100 (Buchi, Flawil, Switzerland), then dried using a freeze-dryer ALPHA 1-2 LDPlus (Christ, Osterodeam Harz, Germany).

### UV-Vis spectra measurement

About 7.5 mg of extract was added into 100 mL of each solvent that was used for extraction. Each solution was analyzed by a UV-Vis spectrophotometer U-2000 (Hitachi, Tokyo, Japan) in a range of 200–800 nm with an interval of 0.5 nm. Afterward, all of the spectra were recorded and converted in MS. Excel.

### FTIR spectra measurement

About 2.0 mg of extract was mixed with potassium bromide into a pellet. Furthermore, the pellet was analyzed by FTIR spectrophotometer Tensor 37 (Bruker, Ettlingen, Germany) with deuterated triglycine sulfate (DTGS) detector. FTIR spectra were recorded in the region of 4000–400  $\text{cm}^{-1}$  with a resolution of 4  $\text{cm}^{-1}$  and 32 scans/min controlled by OPUS 4.2 software (Bruker, Ettlingen, Germany). All of the spectra were collected and converted into MS. Excel.

### Chemometrics analysis

Significant differences in the extraction yield results were determined using analysis of variance (ANOVA) followed by the Duncan test. PCA was used to

discriminate *A. paniculata* extracts based on cultivation ages and solvents extraction. UV-Vis and FTIR spectra data (absorbance) were used as variables for data fusion. PCA was performed with the Unscrambler X version 10.4 (CAMO, Oslo, Norwegia).

## RESULTS AND DISCUSSION

### Extraction Yield of *A. paniculata*

*A. paniculata* metabolites were extracted using sonication at room temperature with different solvent extraction. We found that the percentage yield of extraction using various solvents and cultivation ages have slight differences (Table 1). According to Cui et al. [18], the composition and concentration of chemicals present in the plant are affected by solvent extraction used and cultivation ages. In this study, we got that cultivation ages and solvent extraction give a different level of metabolites extracted in *A. paniculata*.

The highest percentage of yield was obtained using 70% ethanol extract from 4 MPP, and the lowest is water extract from 2 MPP of *A. paniculata*. The trend in the percentage of yield showed that the pattern was increased except on 50% ethanol and ethanol. When extracted using different solvent extraction, *A. paniculata* from different cultivation ages showed that 50% ethanol extract has the highest yield in 2 and 3 MPP of *A. paniculata*. Whereas for the 4 MPP of *A. paniculata*, 70% ethanol extract gave the highest yield value. From the results obtained, at the age of 4 MPP, the more polar metabolites are extracted more in *A. paniculata*.

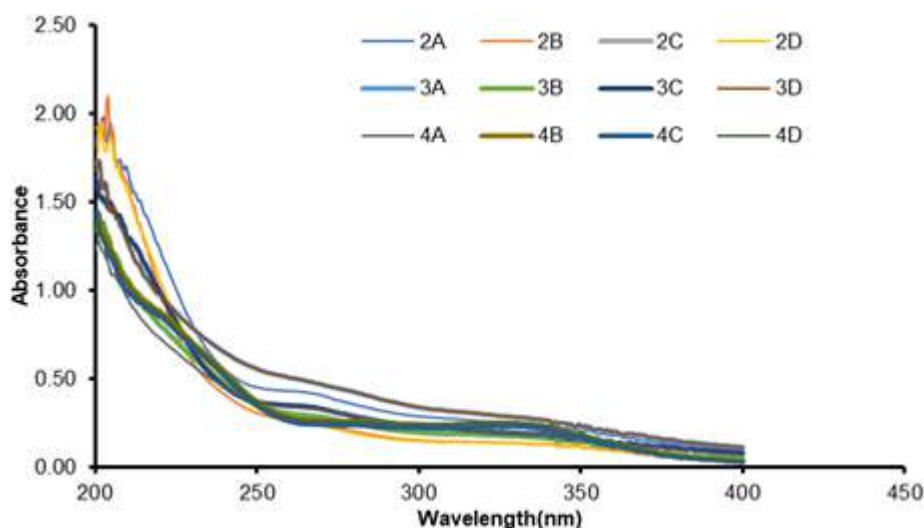
### UV-Vis Spectra of *A. paniculata*

Fig. 1 shows the UV-Vis spectra of all sample extract solutions. As shown in Fig. 1, a similar pattern was

**Table 1.** Yield of *A. paniculata* extracts

Extraction solvents	Yield (%)		
	2 MPP	3 MPP	4 MPP
Water	16.24 ± 1.83 <sup>a</sup>	16.99 ± 0.96 <sup>a</sup>	21.90 ± 0.83 <sup>b</sup>
50 % ethanol	22.97 ± 2.35 <sup>b</sup>	23.80 ± 1.57 <sup>b</sup>	18.76 ± 1.16 <sup>a</sup>
70 % ethanol	22.06 ± 0.41 <sup>b</sup>	22.24 ± 1.58 <sup>b</sup>	23.37 ± 2.80 <sup>b</sup>
Ethanol	18.58 ± 2.90 <sup>a</sup>	18.31 ± 0.49 <sup>a</sup>	16.62 ± 1.46 <sup>a</sup>

The reported values are mean ± SD of the quadruplicate for each sample. The mean ± SD within each extract in the same column followed with different superscript letters represent significant differences at  $p < 0.05$



**Fig 1.** UV-Vis spectra of *A. paniculata* extracts: 2 MPP: water (2A), 50% ethanol (2B), 70% ethanol (2C), ethanol (2D); 3 MPP: water (3A), 50% ethanol (3B), 70% ethanol (3C), ethanol (3D); 4 MPP: water (4A), 50% ethanol (4B), 70% ethanol (4C), ethanol (4D)

obtained from all UV-Vis spectra of the samples. Differences were only found for their intensity. It means no differences in the composition of metabolites extracted only differ for their level of concentration. About two regions with a maximum absorption appeared in the range of 270–290 nm and 310–330 nm. Both of the peaks resulted from the absorption of carbonyl chromophore with an electron transition from  $n \rightarrow \pi^*$ .

#### FTIR Spectra of *A. paniculata*

FTIR spectra of *A. paniculata* extracts (Fig. 2) also showed a similar pattern and differences only in each peak's absorbance intensities. This confirms the UV-Vis spectra measurement results, which also produce the same thing, which is different for the extracted metabolites' concentration level. The difference can be seen on the peak at wavenumber 3400, 2930, 2852, 1728, 1620, 1386, and 1076  $\text{cm}^{-1}$ . Each peak is representing a functional group from metabolites present in the *A. paniculata*. The peak at 3400  $\text{cm}^{-1}$  is from the stretching vibration of hydroxyl (-OH). Meanwhile, peaks at 2930, 2852, and 1386  $\text{cm}^{-1}$  are from the stretching vibration of methyl (C-H). Other peaks on 1728 and 1620 correspond to the stretching vibration of the carbonyl (C=O) functional group, and the peak at 1076  $\text{cm}^{-1}$  is from the stretching vibration of aliphatic amine (C-N).

Absorbance intensity showed a variation value on each sample. A peak at 1728  $\text{cm}^{-1}$  in water extract has low intensity than other extracts used in this study. However, a peak at 1620  $\text{cm}^{-1}$  showed that the absorbance intensity is higher than the other extracts. Pandey and Mandal [19] reported that the type of solvents could affect the distribution and concentration of composition extracted, while part of the plants can also impact the extraction.

#### Discrimination of *A. paniculata* Extracts

We used a combination of data fusion from absorbance data of UV-Vis and FTIR spectra in the range of 200–400 nm and 1800–400  $\text{cm}^{-1}$ , respectively. Preprocessing of spectra was performed before we used it for the PCA. Preprocessing aims to enhance the quality of data, for example, reducing noise to give better result output of the grouping sample [20]. We used multiple preprocessing for UV-Vis, such as baseline, normalize, and smoothing, while for FTIR spectra, we used baseline, standard normal variate, and smoothing.

PCA works by simplifying variables by reducing their dimension into principal components. Two and three-dimensional (2D and 3D) PCA score plots of *A. paniculata* (Fig. 3) showed that all extracts were grouped according to the cultivation ages and solvent extraction

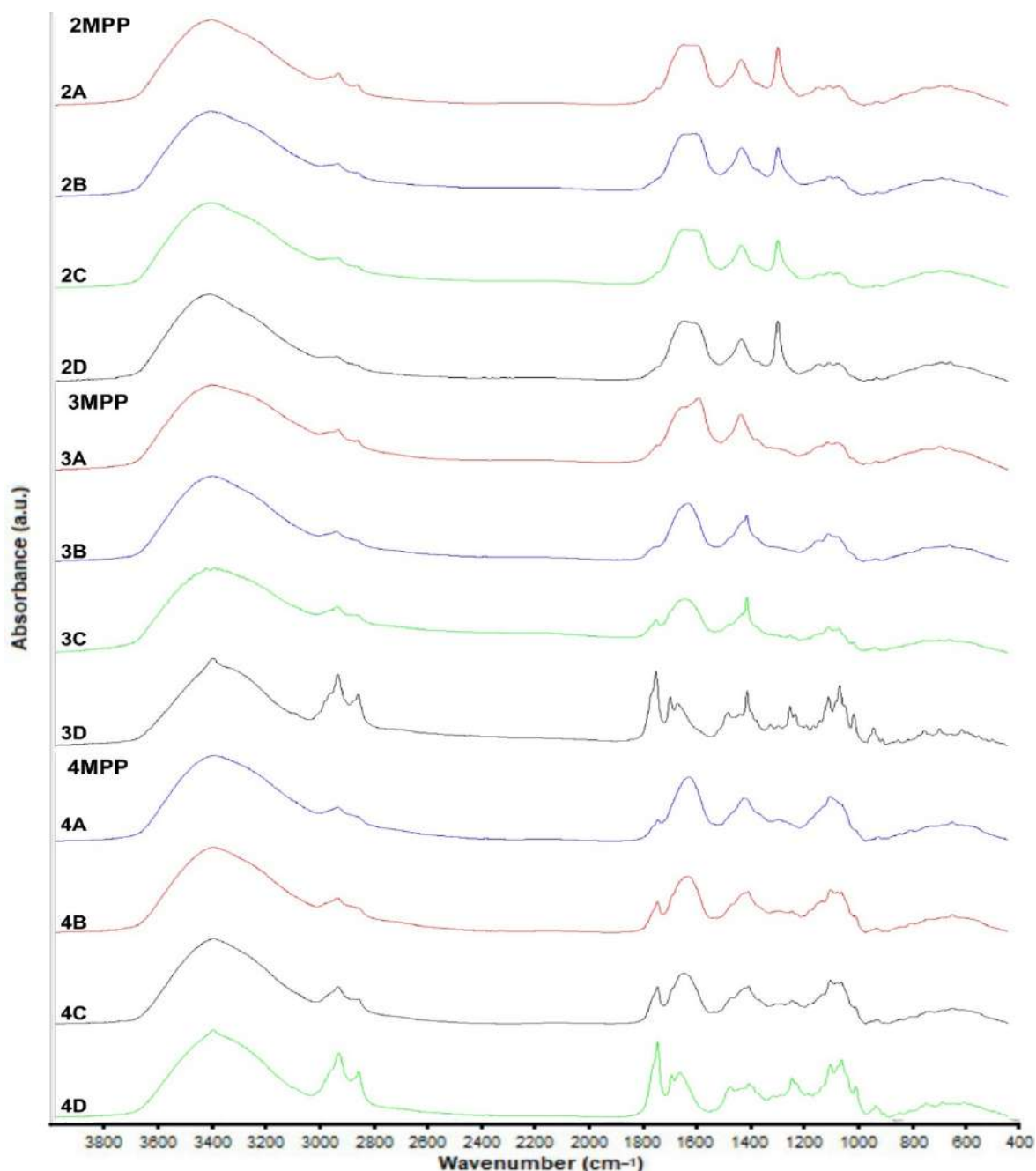


**Fig 2.** FTIR spectra *A. paniculata* extracts: 2 MPP: water (2A), 50% ethanol (2B), 70% ethanol (2C), ethanol (2D); 3 MPP: water (3A), 50% ethanol (3B), 70% ethanol (3C), ethanol (3D); 4 MPP: water (4A), 50% ethanol (4B), 70% ethanol (4C), ethanol (4D)

with a good separation of group. Only water extract of 2 MPP and 3 MPP is very close to each other in the two PCA score plots because the level concentration of extracted metabolites is not different in the two samples. According to Table 1, it can be seen that water extract of 2 MPP and 3 MPP are not significantly different from the Duncan

test. The cumulative percentage of principal components is 86% and 92% using 2D and 3D PCA score plots, respectively. The cumulative percentage of all PC used in the 2D and 3D score plot is higher than 70%, giving good 2D and 3D visualization.

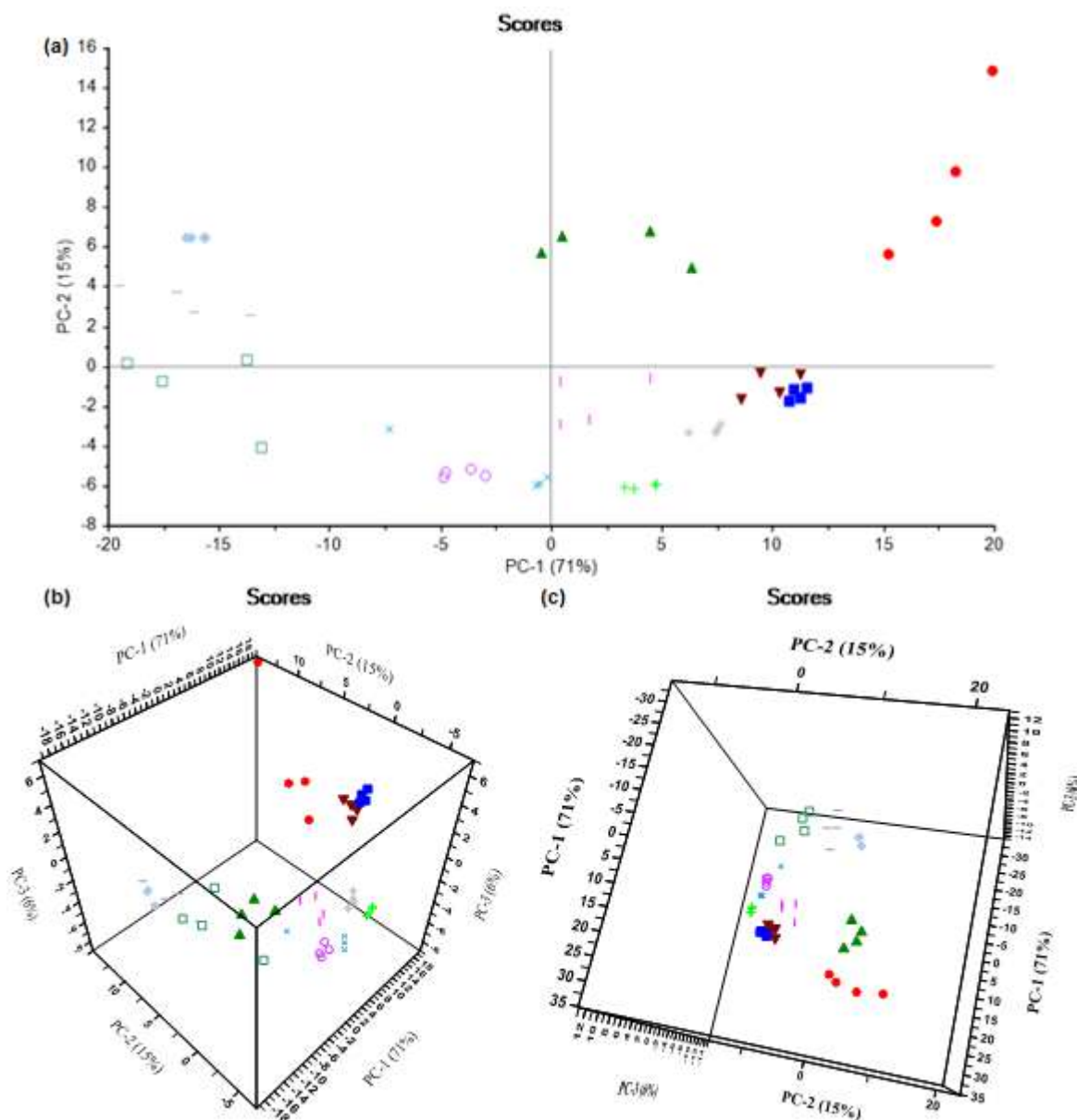


**Fig 3.** (a) 2 dimension PCA score plot, (b) 3 dimension PCA score plot, and (c) 3 dimension PCA score plot rotated 270 degrees to Z axis. 2 MPP: water (■), 50% ethanol (●), 70% ethanol (▲), and pure ethanol (◆); 3 MPP: water (▼), 50% ethanol (\*), 70% ethanol (◻), and pure ethanol (—); 4 MPP: water (+), 50% ethanol (×), 70% ethanol (○), and pure ethanol (◻)

## ■ CONCLUSION

UV-Vis and FTIR spectra of *A. paniculata* extracts with different cultivation ages and solvent extraction have similar profiles. The differences only in their absorbance intensity. The four months post-planting of *A. paniculata* extracted with 70% ethanol provide a higher yield percentage than other extracts. A combination of UV-Vis

and FTIR data with PCA enabled clustering *A. paniculata* extracts according to their cultivation ages and extraction solvents.

## ■ ACKNOWLEDGMENTS

The authors gratefully acknowledged the Ministry of Research, Technology, and Higher Education of the Republic of Indonesia through the World Class



University Program of IPB University to support this research by *Riset Kolaborasi Indonesia* Grant 2019 (No: 0847/IT3.L1/PN/2019).

## ■ REFERENCES

- [1] Valdiani, A., Kadir, M.A., Tan, S.G., Talei, D., Abdullah, M.P., and Nikzad S., 2012, Nain-e Havandi *Andrographis paniculata* present yesterday, absent today: A plenary review on underutilized herb of Iran pharmaceutical plants, *Mol. Biol. Rep.*, 39 (5), 5409–5424.
- [2] Tandon, C., Mathur, P., and Sen, M., 2015, *Andrographis paniculata* Nees (Kalmegh): A review on its antibacterial activities and phytochemicals, *Eur. J. Med. Plants*, 8 (1), 1–10.
- [3] Elumalai, S., Banupriya, R., Sangeetha, T., and Madhumathi, S., 2016, Review on phytopharmacological activities of *Andrographis paniculata* (Burm. f.) Nees, *Int. J. Pharm. Bio Sci.*, 7 (4), 183–200.
- [4] Aneesh, A., George, A.J., Kariyil, B.J., Khrisna, D., and Sajitha, I.S., 2018, Phytochemical evaluation of *Andrographis paniculata* (L.), *J. Pharmacogn. Phytochem.*, 7 (4), 1949–1953.
- [5] Sajeeb, B.K., Kumar, U., Halder, S., and Bachar, S.C., 2015, Identification and quantification of andrographolide from *Andrographis paniculata* (Burm. f.) Wall. ex Nees by RP-HPLC method and standardization of its market preparations, *Dhaka Univ. J. Pharm. Sci.*, 14 (1), 71–78.
- [6] Yusof, N.A., Isha, A., Ismail, I.S., Khatib, A., Shaari, K., Abas, F., and Rukayadi, Y., 2015, Infrared-metabolomics approach in detecting changes in *Andrographis paniculata* metabolites due to different harvesting ages and times, *J. Sci. Food Agric.*, 95 (12), 2533–2543.
- [7] Brinckman J.A., 2013, Emerging importance of geographical indications and designations of origin - authenticating geo-authentic botanicals and implications for phytotherapy, *Phytother. Res.*, 27 (11), 1581–1587.
- [8] Kunle, O.F., Egharevba, H.O., and Ahmadu, P.O., 2012, Standardization of herbal medicines - A review, *Int. J. Biodivers. Conserv.*, 4 (3), 101–112.
- [9] Silvestri, M., Bertacchini, L., Durante, C., Marchetti, A., Salvatore, E., and Cocchi, M., 2013, Application of data fusion techniques to direct geographical traceability indicators, *Anal. Chim. Acta*, 769, 1–9.
- [10] Lahat, D., Adali, T., and Jutten, C., 2015, Multimodal data fusion: An overview of methods, challenges, and prospects, *Proc. IEEE*, 103 (9), 1449–1477.
- [11] Borràs, E., Ferré, J., Boqué, R., Mestres, M., Aceña, L., and Busto, O., 2015, Data fusion methodologies for food and beverage authentication and quality assessment - A review, *Anal. Chim. Acta*, 891, 1–14.
- [12] Qi, L.M., Li, J.Q., Liu, H.G., Li, T., and Wang, Y.Z., 2018, An additional data fusion strategy for the discrimination of porcini mushrooms from different species and origins in combination with four mathematical algorithms, *Food Funct.*, 9 (11), 5903–5911.
- [13] Yao, S., Li, T., Liu, H., Li, J., and Wang, Y., 2017, Traceability of Boletaceae mushrooms using data fusion of UV-Vis and FTIR combined with chemometrics methods, *J. Sci. Food Agric.*, 98 (6), 2215–2222.
- [14] Li, Y., and Wang Y., 2018, Differentiation and comparison of *Wolfiporia cocos* raw materials based on multi-spectral information fusion and chemometric methods, *Sci. Rep.*, 8 (1), 13043.
- [15] Wu, X.M., Zuo, Z.T., Zhang, Q.Z., and Wang, Y.Z., 2018, FT-MIR and UV-vis data fusion strategy for origins discrimination of wild *Paris Polyphylla* Smith var. *yunnanensis*, *Vib. Spectrosc.*, 96, 125–136.
- [16] Li, X.P., Li, J., Liu, H., and Wang, Y.Z., 2020, A new analytical method for discrimination of species in Ganodermataceae mushrooms, *Int. J. Food Prop.*, 23 (1), 227–240.
- [17] Wang, C.Y., Tang, L., Jiang, T., Zhou, Q., Li, J., Wang, Y.Z., and Kong, C.H., 2021, Geographical traceability of *Eucommia ulmoides* leaves using attenuated total reflection Fourier transform infrared and ultraviolet-visible spectroscopy combined with chemometrics and data fusion, *Ind. Crops Prod.*, 160, 113090.

- [18] Cui, Y., Wang, Y., Ouyang, X., Han, Y., Zhu, H., and Chen, Q., 2009, Fingerprint profile of active component for *Andrographis paniculata* Nees by HPLC-DAD, *Sens. Instrum. Food Qual. Saf.*, 3 (3), 165–179.
- [19] Pandey, A.K., and Mandal, A.K., 2010, Variation in morphological characteristics and andrographolide content in *Andrographis paniculata* (Burm. f) Nees of Central India, *Iran. J. Energy Environ.*, 1 (2), 165–169.
- [20] Purwakusumah, E.D., Rafi, M., Safitri, U.D., Nurcholis, W., and Adzkiya, M.A.Z., 2014, Identifikasi dan autentikasi jahe merah menggunakan kombinasi spektroskopi FTIR dan kemometrik, *Agritech*, 34 (1), 82–87.

**Short Communication:****Synthesis of Colloidal Silver Nanoparticles in Various Liquid Media Using Pulse Laser Ablation Method and Its Antibacterial Properties**

Syifa Avicenna, Iis Nurhasanah, and Ali Khumaeni\*

Department of Physics, Faculty of Science and Mathematics, Diponegoro University,  
Jl. Prof. Soedarto SH, Tembalang, Semarang 50275, Indonesia

**\* Corresponding author:**

email: khumaeni@fisika.fsm.undip.ac.id

Received: October 4, 2020

Accepted: January 1, 2021

DOI: 10.22146/ijc.60344

**Abstract:** The silver nanoparticles (AgNPs) have been applied as an antibacterial agent in consumer products, cosmetics, and food industries. In this present work, AgNPs were synthesized in various mediums of polyvinylpyrrolidone (PVP), polyethylene glycol (PEG), and chitosan using the pulse laser ablation synthesis method. Experimentally, a pulse Nd:YAG laser beam (1064 nm, 7 ns, 30 mJ) was directed using a silver mirror and focused using a quartz lens with a focal length of 30 mm on a silver metal plate placed in a petri dish containing liquid mediums for 120 min to produce colloidal silver nanoparticles. The results certified that All AgNPs have a spherical shape with polydisperse size in all media, including PVP, PEG, and chitosan. The smallest AgNPs have been produced in PVP medium with an averaged smallest size of 11.62 nm. Based on this result, PVP is the preferred medium to produce AgNPs with the smallest size and good stability. The produced silver nanoparticles have been successfully employed as an antibacterial agent, which is experimentally demonstrated by using *Escherichia coli* and *Staphylococcus aureus*. The result certified that the produced silver nanoparticles could effectively kill the bacteria with a killing percentage of 99.6 to 100%.

**Keywords:** silver nanoparticles; pulse laser ablation technique; Nd:YAG laser; liquid media of PVP; PEG; chitosan

**■ INTRODUCTION**

Silver nanoparticles (AgNPs) have been well known as commercialized nano-material, having many beneficial applications. Due to their unique chemical and physical characteristics, including electrical, optical, thermal properties, the AgNPs have been employed in broad subjects including health care, medical, and industrial fields [1-3]. The AgNPs have been applied as an antibacterial agent in consumer products, cosmetics, medical tool coatings, and food industries [4-6]. In medical applications, the AgNPs have been used as anticancer agents in medical therapy, contrast agents in diagnostics, drug delivery, and agent of anticancer drugs. Thus, the synthesis of AgNPs has recently become an interesting subject.

Various techniques are suggested for the synthesis of AgNPs, such as sol-gel, precipitation, chemical

reduction, ion sputtering techniques [7-8]. The techniques can successfully produce silver nanoparticles with quite good stability. However, the techniques involve high energy requirements and hazardous chemicals, which need further purification and are complicated in the synthesis process due to the fact the chemical contamination. Hence, the AgNPs cannot be employed readily for medical purposes or human-related products. Therefore, alternative techniques to produce high-purity AgNPs with good stability without involving dangerous chemical agents are necessary for specific applications in medical purposes and human-related products.

The other technique for the synthesis of AgNPs is the pulse laser ablation (PLA) technique [9]. In this technique, a pulse laser is used to ablate the metal material samples from their surface to induce a

luminous plume. The plume then expands with time to disperse in a medium environment around the sample. When the medium is liquid, the ablated material disperses in the liquid medium, and finally, new material in the form of nanoparticles is produced. Compared to other chemical techniques, pulse laser ablation has several strong points. Namely, the produced nanoparticles have high purity because it does not involve chemical agents during the synthesis process and only needs pure metal and liquid medium such as deionized water. Furthermore, the pulse laser ablation technique has a much simple experimental setup than the case chemical technique. Many reports have been published on the synthesis of AgNPs using the PLA technique [10-15]. Tsuji et al. used the pulsed laser ablation technique to produce AgNPs in a water medium under the various wavelength of pulse laser, including 1064 nm, 532 nm, and 355 nm [15]. However, AgNPs cannot disperse well and is not quite stable because the particles will agglomerate and precipitate. To solve the problem, Bae et al. synthesized AgNPs by the laser pulse ablation method in NaCl solution, which resulted in an average nanoparticle size of 26.4 nm and very low stability compared to distilled water [10]. Then, in a dilute solution of sodium dodecyl sulfate (SDS) using the same method, the size of the AgNPs produced an average of 14 nm [13].

Valverde-Alva et al. used an ethanol medium to avoid agglomeration and precipitation [9]. Darroudi et al. employed gelatin solution to produce AgNPs having an average diameter ranging from 9 nm to 15 nm [12]. Al-Azawi et al. studied the effect of various liquid mediums, including deionized water, ethanol, and polyvinylpyrrolidone (PVP), on the particle size, resulting in the finer particle size for PVP liquid medium compared to the case of deionized water and ethanol [16]. It should be mentioned that the above reports are mainly used high-energy pulse laser, namely more than 50 mJ. Furthermore, they only studied the synthesis of silver nanoparticles and their characterization, including pulse laser energy dependence and liquid medium dependence. They did not report simultaneously the application of the produced silver nanoparticles for an antibacterial agent.

In this present work, we conducted a study on the

synthesis of AgNPs in various mediums of polyvinylpyrrolidone (PVP), polyethylene glycol (PEG), and chitosan using the pulse laser ablation synthesis method. The laser energy used was only 30 mJ. As mentioned above, the use of the pulsed laser ablation technique for the preparation of AgNPs in this study is because this technique can produce high-purity nanoparticles without additional hazardous chemical agents for medical applications and human-related products. The liquid medium has a role in regulating the size of a nanoparticle, where the addition of a polymer medium can produce a smaller and more uniform nanoparticle size. The effect of the liquid medium on the averaged sizes of produced AgNPs was studied. Characterization of AgNPs was carried out using the Ultraviolet-Visible Spectroscopy (UV-Vis) method, Particle Size Analyzer (PSA), Transmission Electron Microscope (TEM), and Fourier Transform Infrared spectroscopy (FTIR). Furthermore, produced silver nanoparticles are then applied as antibacterial agents, which are experimentally demonstrated by using *Escherichia coli* and *Staphylococcus aureus*. The result certified that the produced silver nanoparticles could effectively kill the bacteria with a killing percentage of 99.6 to 100%.

## ■ EXPERIMENTAL SECTION

### Materials

A silver metal plate with a purity of 99.9% and a dimension of  $5 \times 10 \times 20 \text{ mm}^3$  was used as a material target to produce AgNPs. The liquid medium for making colloidal AgNPs used were PVP, PEG, and Chitosan.

### Instrumentation

The experimental setup used in this work is shown in Fig. 1. The radiation source used was Nd:YAG laser (New Wave Research, Polaris II, 20 Hz) with a wavelength of 1064 nm and pulse width of 7 ns. Laser Exec II software was used to set laser parameters (energy, repetition rate). The laser energy was set at 30 mJ with a repetition rate of 10 Hz. The other instruments used in this work include a transmission electron microscope

(TEM, JEOL) equipped with an energy dispersive X-ray spectrometer (EDX) and ultraviolet-visible (UV-Vis) absorption spectrometer (Shimadzu 1240 SA).

## Procedure

### Synthesis of silver nanoparticles

Experimentally, a pulse laser beam was directed using a silver mirror and focused using a quartz lens with a focal length of 30 mm on a silver metal plate placed in a petri dish containing liquid mediums for 11 h. With increasing the number of laser bombardment, the color of the liquid medium changes from transparent to light yellow and finally become brownies yellow. The experimental setup used in this work is shown in Fig. 1.

### Characterization of silver nanoparticles

The produced colloidal AgNPs were characterized using various techniques, including transmission electron microscope (TEM), particle size analyzer (PSA), ultraviolet-visible (UV-Vis) spectroscopy, and Fourier Transform Infra-red (FTIR) spectroscopy to obtain a morphological view, average size, optical plasmon resonance, and molecular ingredient of colloidal AgNPs, respectively. The morphology of the nanoparticles produced was analyzed using a transmission electron microscope (TEM, JEOL) equipped with an energy dispersive X-ray spectrometer (EDX). The optical properties and surface plasma resonance of the product were characterized by an ultraviolet-visible (UV-Vis) absorption spectrometer (Shimadzu 1240 SA).

### Antibacterial testing

The antibacterial test was made using AOAC 960.09 the year 2013 with slight modification [17]. The bacteria used were *Escherichia coli* (ATCC 8739) and *Staphylococcus*

*aureus* (ATCC 6538). The temperature of incubation was 35 °C, and the temperature of the examination was 24 °C. A sample of 10 ppm AgNPs was inoculated with microorganisms tests including *E. coli* and *S. aureus* with a concentration of  $1.3 \times 10^6$  CFU/mL and  $1.1 \times 10^6$  CFU/mL, respectively, at a contact time of 10 min. One mL of AgNPs was poured with 1 mL of test suspension. This mixture was then striated in the solid medium of TSA in four quadrants with 4 striae each on the surface of the agar. Each quadrant was incubated for 48 h at 35 °C. After incubation, the growth of the inoculated microorganism in each quadrant was counted.

## RESULTS AND DISCUSSION

### Effect of Liquid Medium on Silver Nanoparticles (AgNPs)

First, we examined the physical characteristics of colloidal silver nanoparticles produced in various liquid media. Fig. 2 shows photographs of colloidal AgNPs produced in (a) PEG, (b) PVP, and (c) chitosan using the pulse laser ablation method. For producing these colloidal AgNPs, the Nd:YAG laser beam with a pulse repetition rate of 10 Hz was bombarded and focused on a high-purity Ag metal plate for 11 h. It can be seen in the figure that the formation of colloidal AgNPs in the three liquid mediums is identified by the color changing of the liquid medium that was previously colorless or clear to golden yellow. The golden yellow color of colloidal silver nanoparticles indicates the formation of silver nanoparticles as reported elsewhere [18].

The darker color of the colloid indicates a higher concentration of AgNPs [19]. The distinctive color of AgNPs is the result of the localized surface plasmon

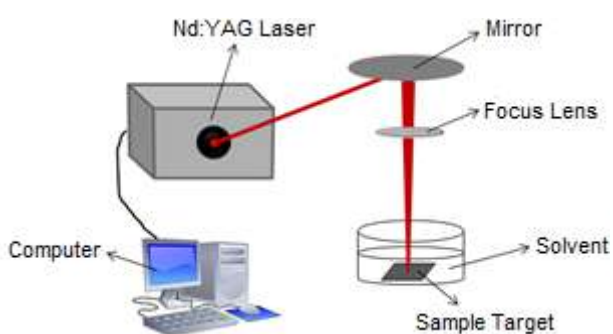


Fig 1. Experimental setup

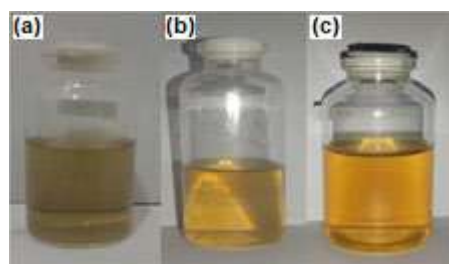


Fig 2. Colloidal AgNPs synthesized by pulsed laser ablation technique in liquid medium (a) PEG, (b) PVP, and (c) Chitosan

resonance (LSPR) phenomenon where silver material absorbs. The LSPR of AgNPs ranges from 380 to 425 nm, which means that they absorb blue or red light, so it will reflect the yellow color [18,20-22]. For further information, it will be discussed in the characterization section.

The colloidal AgNPs were subsequently stored in transparent bottles at room temperature for several weeks. The results showed that AgNPs were the most stable in the chitosan medium because they managed to survive without precipitation for 6 weeks, whereas in the PEG medium, nanoparticles were stable for 5 weeks. Also, in the PVP medium, the nanoparticles lasted for 4 weeks until black sedimentation appeared at the bottom of the bottle.

### Analysis of Morphology and Size of Silver Nanoparticles

To determine the morphology and size of the nanoparticles, measurements were made using a transmission electron microscope (TEM) and a particle size analyzer (PSA), respectively. The PSA uses a dynamic light scattering (DLS) principle that takes advantage of the properties of particles, which experience Brownian motion. Brownian motion of the liquid particles collides with each other so that when a laser beam is fired, it will cause scattering of light with various frequencies. This frequency will later be converted into a light signal form, which is then converted again into a digital signal, which is then processed into a counting series [23]. Fig. 3 shows the histogram of the size distribution and morphology of AgNPs in liquid media of PVP, PEG, and chitosan. Fig. 3(a) shows the size distribution of AgNPs in PVP, which consists of two peaks. For the large group average size, which is above 100 nm, it has an average particle size of  $275.80 \pm 38.96$  nm, then for the small size group, it is  $11.62 \pm 5.03$  nm. Fig. 3(b) shows a histogram of the size distribution of AgNPs in PEG, which also consists of two peaks. Namely, the peaks of the large particle groups had an average particle size of  $146.60 \pm 28.02$  nm and the peaks of the small particle groups had an average particle size of  $21.02 \pm 3.38$  nm. Then, Fig. 3(c) shows the average histogram size distribution of AgNPs in chitosan liquid medium, which is also divided into two peaks, that is a large particle group with an average particle size of  $480.60$

$\pm 163.40$  nm and a small particle group with an average particle size of  $71.60 \pm 19.43$  nm.

From the size distribution data above, it is known that the colloidal AgNPs formed to have two nanoparticle size distributions. This certified that the AgNPs colloids consist of polydisperse colloids composed of more than one peak or have different sizes that are quite far apart from each other [24]. The non-uniform size of the nanoparticles produced in each sample is due to the Brownian motion that occurs due to the pulse laser ablation method, as also reported in a paper here [25]. In addition, the type of colloid medium affects the uniformity of the size of the produced AgNPs. PVP polymers have a smaller aggregate ability than others, resulting in more small particle sizes. If the particles are agglomerated, they will produce large size nanoparticles [26], such as in PEG and chitosan, which have a size larger than PVP. The results of the size distribution of the

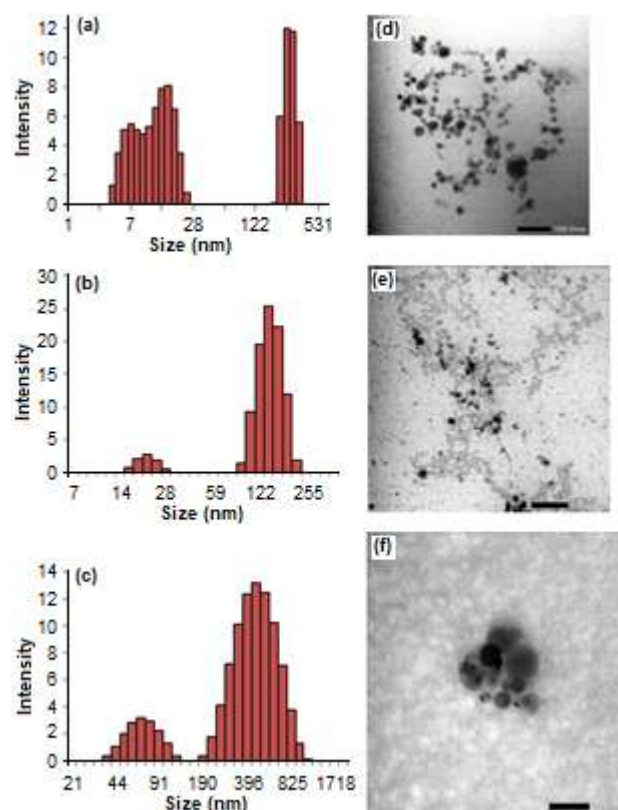


**Fig 3.** Histograms of the size distribution of AgNPs in (a) PVP, (b) PEG, (c) chitosan, and AgNPs morphology in (d) PVP, (e) PEG, and (f) chitosan using PSA and TEM

three colloids indicate that AgNPs have been successfully synthesized according to the literature, which is between 1–1000 nm in size [26-27].

### Optical Properties of AgNPs Using UV-Vis Spectrometer

To study the optical characteristics of produced AgNPs, the UV-Vis spectrometer was used. Based on the image shown in Fig. 4, all three graphs have absorbance peaks around the 400 nm wavelength. This peak is defined as the peak of localized surface plasmon resonance. Light single Plasmon resonance (LSPR) is an important parameter to identify the type of particles contained in a solution. LSPR is a resonance phenomenon between light waves and electrons on the metal surface, which oscillate with each other. LSPR occurs when the frequency of the photons matches the collective oscillations of the metal nanoparticles. The frequency and intensity of LSPR absorption depend on the type of material (metal), size, shape of the nanostructures, and the environment [28].

LSPR occurs when the frequency of the photons matches the collective oscillations of the metal nanoparticles. The frequency and intensity of LSPR absorption depend on the type of material (metal), size, shape of the nanostructures, and the environment [21]. The LSPR peak of silver nanoparticles in the PVP medium is at a wavelength of 408 nm with an absorbance of 1.118. Then, in the PEG medium, the peak is at a wavelength of 422 nm with an absorbance of 0.648. Whereas, in the chitosan medium, the SPR was at a wavelength of 408 nm with an absorbance of 1.012. According to literature, silver has an LSPR peak of around 380–425 nm [21-22]. The peak shift of 14 nm, as shown in the PEG graph, shows a larger size of the nanoparticles. Also, the absorbance amount can also indicate the size because the larger the nanoparticle size also provides a high absorbance. This is because the higher the absorbance usually indicates a higher concentration. High concentrations tend to give larger nanoparticles size [29].

### Compound Composition of AgNPs Colloidal

Fourier transform infrared (FTIR) was used to determine the compounds contained in colloids. The colloidal infrared transmittance spectrum of AgNPs can

be seen in Fig. 5. It shows a graph of the wavenumber ( $\text{cm}^{-1}$ ) against the percent transmittance passing through the material (% T). The absorption band of AgNPs at a wavenumber of  $3359 \text{ cm}^{-1}$  showed a vibration of O–H stretching with a transmittance of 86%.

Then, the wavenumber  $1739 \text{ cm}^{-1}$  indicates the presence of a carbonyl group C=O with a transmittance of 92%. The absorption bands at wavenumbers  $3359 \text{ cm}^{-1}$  and  $1739 \text{ cm}^{-1}$  indicate the presence of other molecules absorbed from the chitosan medium associated with AgNPs. The wavenumber of  $528 \text{ cm}^{-1}$  shows a stretching vibration of the Ag–O bond with a transmittance of 80%. This is evidence of the existence of AgO and  $\text{Ag}_2\text{O}$  [30].

### Application of AgNPs as an Antibacterial Agent

Finally, the application of AgNPs was demonstrated as an antibacterial agent. To this end, colloidal AgNPs produced in PVP medium with a concentration of 10 mg/kg AgNPs were examined as an

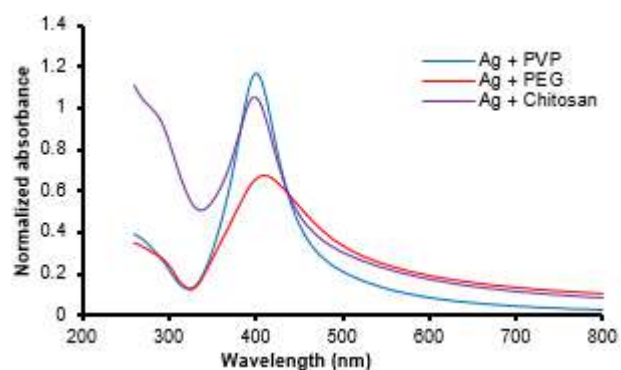


Fig 4. UV-Vis spectrum of AgNPs colloid in PVP, PEG, and Chitosan liquid medium

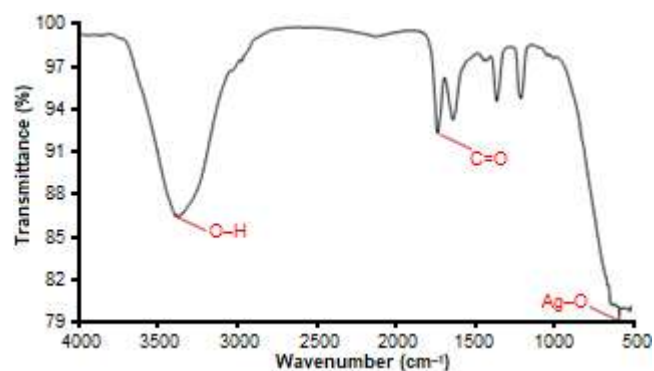


Fig 5. IR transmittance spectrum of colloidal AgNPs on chitosan medium

**Table 1.** AgNPs as an antibacterial agent in gram-negative *Escherichia coli* and gram-positive *Staphylococcus aureus*

Contamination time (sec)	Number of initial bacteria (CFU/mL)	Number of remaining bacteria (CFU/mL)	Number of dead bacteria (%)
<i>Escherichia coli</i>			
30	$1.3 \times 10^6$	0	100
60	$1.3 \times 10^6$	0	100
<i>Staphylococcus aureus</i>			
30	$1.1 \times 10^6$	$3.9 \times 10^3$	99.64
60	$1.1 \times 10^6$	$1.1 \times 10^2$	99.99

antibacterial agent. The produced AgNPs used in this antibacterial agent has a spherical shape with an average small diameter of 11.62 nm.

Table 1 shows the examination results of AgNPs as an antibacterial agent in gram-negative *Escherichia coli* and gram-positive *Staphylococcus aureus*. For this experiment, the number of initial bacteria is  $1.3 \times 10^6$  CFU/mL and  $1.1 \times 10^6$  CFU/mL, respectively. It can be seen that after 30 sec of AgNPs treatment to *E. coli* bacteria, 100% of bacteria are dead, and completely no bacteria remain. For *S. aureus*, 99.64% of *S. aureus* bacteria are dead. The dead bacteria increased up to 99.99% when the interaction time of bacteria with AgNPs was much longer, up to 60 sec. This result certified that the produced colloidal AgNPs in PVP medium with a concentration of 10 mg/kg could effectively be used as an antibacterial agent. As reported here [31], the interaction mechanism between AgNPs and bacteria is as follows: the AgNPs attach to the surface of the cell wall and membrane. After that, the AgNPs penetrates inside the cell and inducing cellular toxicity and oxidative stress by generating reactive oxygen species and free radicals, damaging intracellular structures, and biomolecules.

## ■ CONCLUSION

We demonstrated in this work that colloidal nanosilver particles have been successfully produced by using the pulse laser ablation method in various liquid media, including PVP, PEG, and chitosan. In this work, a pulse Nd:YAG laser with a laser wavelength of 1064 nm, laser energy of 30 mJ, and a pulse repetition rate of 10 Hz was employed as an energy source. The results certified that All AgNPs have a spherical shape with polydisperse size in all media, including PVP, PEG, and chitosan. The

smallest AgNPs have been produced in PVP medium with an average smallest size of 11.62 nm. Furthermore, AgO compounds were also produced during the synthesis process. Based on this result, PVP is the preferred medium to produce AgNPs with the smallest size and good stability. In this present work, AgNPs have been successfully applied as antibacterial agents in *Escherichia coli* and *Staphylococcus aureus* bacteria.

## ■ ACKNOWLEDGMENTS

This work has been financially supported by Research Grant from the Ministry of Education and Culture, Indonesia, under the research contract of PTUPT with a contract No. 225-135/UN7.6.1/PP/2020.

## ■ REFERENCES

- [1] Kruszewski, M., Brzoska, K., Brunborg, G., Asare, N., Dobrzyńska, M., Dušinská, M., Fjellsbø, L.M., Georgantzopoulou, A., Gromadzka-Ostrowska, J., Gutleb, A.C., Lankoff, A., Magdolenová, Z., Pran, E.R., Rinna, A., Instanes, C.J., Sandberg, W., Schwarze, P., Stępkowski, T., Wojewódzka, M., and Refsnes, M., 2011, Toxicity of silver nanomaterials in higher eukaryotes, *Adv. Mol. Toxicol.*, 5, 179–218.
- [2] Marassi, V., Di Cristo, L., Smith, S.G.J., Ortelli, S., Blosi, M., Costa, A.L., Reschiglian, P., Volkov, Y., and Prina-Mello, A., 2018, Silver nanoparticles as a medical device in healthcare settings: A five-step approach for candidate screening of coating agents, *R. Soc. Open Sci.*, 5 (1), 171113.
- [3] Jing, X., and Guo, Z., 2019, Multifunctional WS<sub>2</sub>&M-AgNPs superhydrophobic conductive sponges for application in various sensors, *New J. Chem.*, 43 (4), 5287–5296.



- [4] Natsuki, J., Natsuki, T., and Hashimoto, Y., 2015, A review of silver nanoparticles: Synthesis methods, properties and applications, *Int. J. Mater. Sci. Appl.*, 4 (5), 325–332.
- [5] Carbone, M., Donia, D.T., Sabbatella, G., and Antiochia, R., 2016, Silver nanoparticles in polymeric matrices for fresh food packaging, *J. King Saud Univ. Sci.*, 28 (4), 273–279.
- [6] Divya, M., Kiran, G.S., Hassan, S., and Selvin, J., 2019, Biogenic synthesis and effect of silver nanoparticles (AgNPs) to combat catheter-related urinary tract infections, *Biocatal. Agric. Biotechnol.*, 18, 101037.
- [7] Lkhagvajav, N., Yaşa, I., Çelik, E., Koizhaiganova, M., and Sari, Ö., 2011, Antimicrobial activity of colloidal silver nanoparticles prepared by sol-gel method, *Dig. J. Nanomater. Biostruct.*, 6 (1), 149–154.
- [8] Mishra, Y.K., Mohapatra, S., Kabiraj, D., Mohanta, B., Lalla, N.P., Pivin, J.C., and Avasthi, D.K., 2007, Synthesis and characterization of Ag nanoparticles in silica matrix by atom beam sputtering, *Scr. Mater.*, 56 (7), 629–632.
- [9] Valverde-Alva, M.A., García-Fernández, T., Villagrán-Muniz, M., Sánchez-Aké, C., Castañeda-Guzmán, R., Esparza-Alegria, E., Sánchez-Valdés, C.F., Sánchez Llamazares, J.L., and Herrera, C.E.M., 2015, Synthesis of silver nanoparticles by laser ablation in ethanol: A pulsed photoacoustic study, *Appl. Surf. Sci.*, 355, 341–349.
- [10] Bae, C.H., Nam, S.H., and Park, S.M., 2002, Formation of silver nanoparticles by laser ablation of a silver target in NaCl solution, *Appl. Surf. Sci.*, 197–198, 628–634.
- [11] Boutinguiza, M., Comesaña, R., Lusquiños, F., Riveiro, A., del Val, J., and Pou, J., 2015, Production of silver nanoparticles by laser ablation in open air, *Appl. Surf. Sci.*, 336, 108–111.
- [12] Darroudi, M., Ahmad, M.B., Zamiri, R., Abdullah, A.H., Ibrahim, N.A., Shameli, K., and Shahril Husin, M., 2011, Preparation and characterization of gelatin mediated silver nanoparticles by laser ablation, *J. Alloys Compd.*, 509 (4), 1301–1304.
- [13] Mafune, F., Kohno, J., Takeda, Y., and Kondow, T., 2000, Formation and size control of silver nanoparticles by laser ablation in aqueous solution, *J. Phys. Chem. B*, 104 (39), 9111–9117.
- [14] Rhim, J.W., Wang, L.F., Lee, Y., and Hong, S.I., 2014, Preparation and characterization of bionanocomposite films of agar and silver nanoparticles: Laser ablation method, *Carbohydr. Polym.*, 103, 456–465.
- [15] Al-Azawi, M.A., Bidin, N., Bououdina, M., Abbas, K.N., Al-Asedy, H.J., Ahmed, O.H., and Thahe, A.A., 2016, The effects of the ambient liquid medium on the ablation efficiency, size and stability of silver nanoparticles prepared by pulse laser ablation in liquid technique, *J. Teknol.*, 78 (3), 7–11.
- [16] Song, X., Vossebein, L., and Zille, A., 2019, Efficacy of disinfectant-impregnated wipes used for surface disinfection in hospitals: A review, *Antimicrob. Resist. Infect. Control*, 8 (1), 139.
- [17] Mulfinger, L., Solomon, S.D., Bahadory, M., Jeyarajasingam, A.V., Rutkowsky, S.A., and Boritz, C., 2007, Synthesis and study of silver nanoparticles, *J. Chem. Educ.*, 84 (2), 322–325.
- [18] Ahmed, B.S., Rao, A.G., Sankarshan, B.M., Vicas, C.S., Namratha, K., Umesh, T.K., Somashekar, R., and Byrappa, K., 2016, Evaluation of gold, silver, and silver-gold (bimetallic) nanoparticles as radiosensitizers for radiation therapy in cancer treatment, *Cancer Oncol. Res.*, 4 (3), 42–51.
- [19] Abadeer, N.S., and Murphy, C.J., 2016, Recent progress in cancer thermal therapy using gold nanoparticles, *J. Phys. Chem. C*, 120 (9), 4691–4716.
- [20] Evanoff, D.D., and Chumanov, G., 2005, Synthesis and optical properties of silver nanoparticles and arrays, *ChemPhysChem*, 6 (7), 1221–1231.
- [21] Rodríguez-León, E., Iñiguez-Palomares, R., Navarro, R.E., Herrera-Urbina, R., Tánori, J., Iñiguez-Palomares, C., and Maldonado, A., 2013, Synthesis of silver nanoparticles using reducing agents obtained from natural sources (*Rumex hymenosepalus* extracts), *Nanoscale Res. Lett.*, 8 (1), 318.
- [22] Nuraeni, W., Daruwati, I., Widyasari, E.M., and Sriyani, M.E., 2013, Verifikasi kinerja alat particle size analyzer (PSA) HORIBA LB-550 untuk

- penentuan distribusi ukuran nanopartikel, *Prosiding Seminar Nasional Sains dan Teknologi Nuklir*, PTNBR-BATAN, Bandung, 4 July 2013, 266–271.
- [23] Lichtenegger, T., and Pirker, S., 2018, CFD-DEM modeling of strongly polydisperse particulate systems, *Powder Technol.*, 325, 698–711.
- [24] Kim, M., Osone, S., Kim, T., Higashi, H., and Seto, T., 2017, Synthesis of nanoparticles by laser ablation: A review, *KONA Powder Part. J.*, 34, 80–90.
- [25] Tejamaya, M., Merrifield, R.C., and Lead, J.R., 2012, Stability of citrate, PVP, and PEG coated silver nanoparticles in ecotoxicology media, *Environ. Sci. Technol.*, 46 (13), 7011–7017.
- [26] Tiyaboonchai, W., 2003, Chitosan nanoparticles: A promising system for drug delivery, *Naresuan Univ. J.*, 11 (3), 51–66.
- [27] Beyene, H.D., Werkneh, A.A., Bezabh, H.K., and Ambaye, T.G., 2017, Synthesis paradigm and applications of silver nanoparticles (AgNPs), a review, *Sustainable Mater. Technol.*, 13, 18–23.
- [28] Chhatre, A., Solasa, P., Sakle, S., Thaokar, R., and Mehra, A., 2012, Color and surface plasmon effects in nanoparticle systems: Case of silver nanoparticles prepared by microemulsion route, *Colloids Surf., A*, 404, 83–92.
- [29] Hosseinpour-Mashkani, S.M., and Ramezani, M., 2014, Silver and silver oxide nanoparticles: Synthesis and characterization by thermal decomposition, *Mater. Lett.*, 130, 259–262.
- [30] Dakal, T.C., Kumar, A., Majumdar, R.S., and Yadav, V., 2016, Mechanistic basis of antimicrobial actions of silver nanoparticles, *Front. Microbiol.*, 7, 1831.

### Supplementary Data

This supplementary data is a part of paper entitled "Solvatochromism and Theoretical Studies of Dicyanobis(phenylpyridine)iridium(III) Complex Using Density Functional Theory".

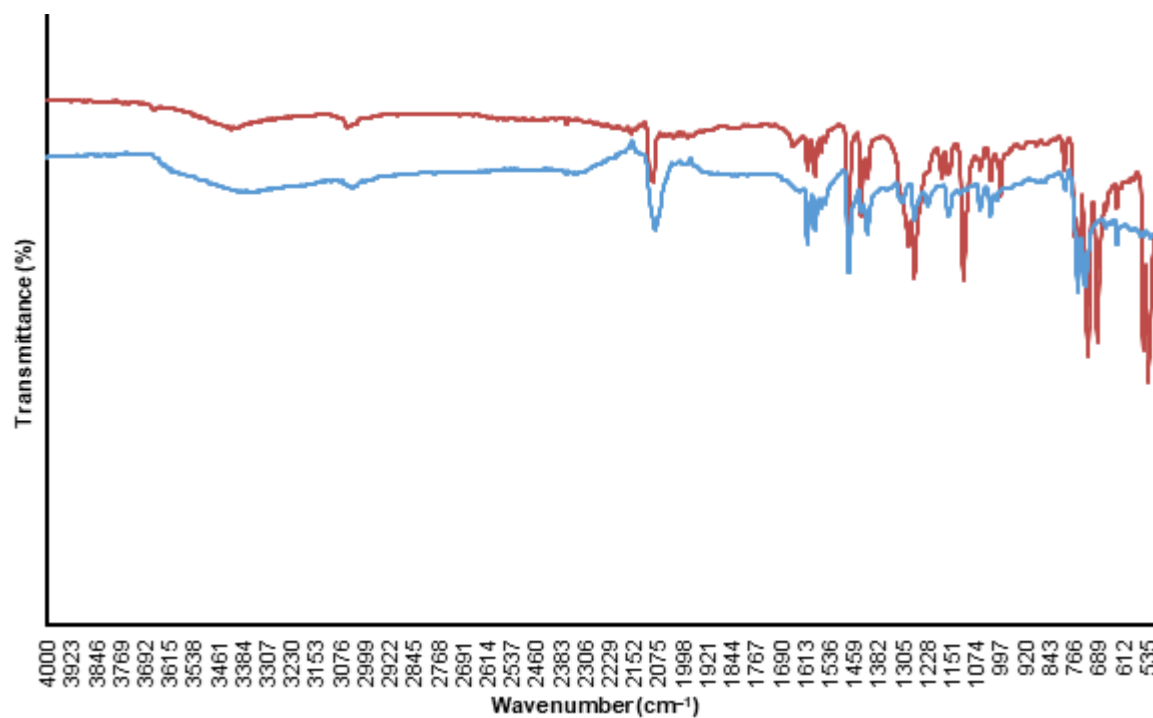


**Fig S1.** IR spectra of PPN[ $\text{Ir}(\text{ppy})_2(\text{CN})_2$ ] (red line) and  $\text{K}[\text{Ir}(\text{ppy})_2(\text{CN})_2]$  (blue line)

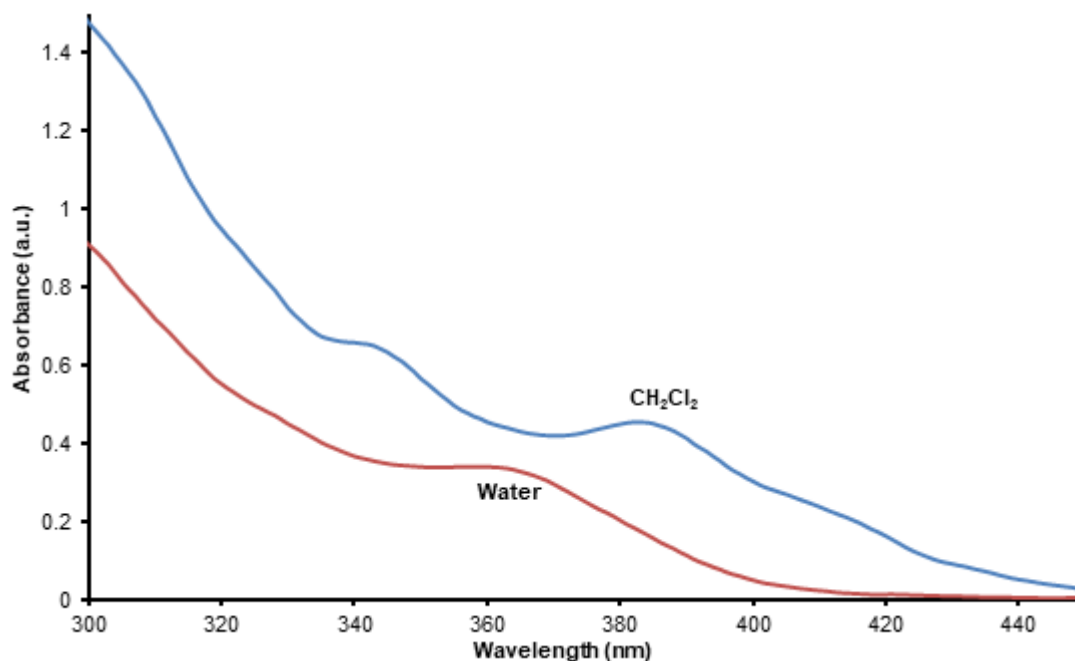


**Fig S2.** UV-Vis absorption spectra of  $[\text{Ir}(\text{ppy})_2(\text{CN})_2]^-$ , as its  $\text{PPN}^+$  salt (in  $\text{CH}_2\text{Cl}_2$ ) and as its  $\text{K}^+$  salt (in water)